University of ROMA TRE

PhD in Physics

Class XXXIII

Frascati National Laboratories (LNF-INFN)

Test of the Standard Model in the $H \rightarrow ZZ^* \rightarrow 4l$ decay channel with the Effective Lagrangian framework and construction and performance of the Micromegas chambers for the ATLAS New Small Wheel upgrade

Student

Chiara Arcangeletti

Supervisors

Dott. Mario Antonelli

Dott.ssa Giada Mancini

Contents

Introduction

The Higgs boson is the keystone particle of the Standard Model (SM) and its existence explains the massive nature of matter.

The Large Hadron Collider, located at CERN laboratory in Geneva, is the largest particle accelerator in the world and it is designed to allow the search for new processes at the TeV scale. At the LHC, the Higgs boson can be produced via different processes. The gluon fusion (ggF) process represents the main production mode, followed by the vector-boson fusion production (VBF), vector-boson associated production (VH) and the associated production with a top quark pairs ($t\bar{t}H$). The Higgs boson decays into pairs of fermions or bosons, and it can be detected through the different final states in several decay channels. The most sensitive decay channels at LHC are: $H \to W^+W^-$, $H \to \gamma\gamma$ and $H \to ZZ^* \to 4l$.

The first measurements performed during the Run1 at the Large Hadron Collider (LHC) allowed for the discovery of the Higgs boson [1] [2], announced by the ATLAS [3] and CMS [4] collaborations in July 2012. Since that moment, one of the main goal of the ATLAS experiment has been to study the Higgs boson properties.

An ambitious upgrade programme of the LHC is planned, which will take place in two phases (Phase I [5] and Phase II [6]), aimed to reach peak luminosity of 5 - 7 times the initial design values and a final integrated luminosity of about 3000 fb^{-1}. The expected increase in particle rate will be unsustainable for many of the current detectors. Therefore the ATLAS experiment has planned several upgrades to stay operative. One of the most important Phase I upgrade project is the New Small Wheel project [7], consisting of the replacement of the innermost muon station in the endcaps with a completely new detectors technology: the Micromegas (MM) [8] [9] and sTGC [10] [11].

The first part of this thesis describes the Micromegas chambers construction and testing of the SM1 module type, in which INFN is deeply involved since the first large prototype [12]. At LNF an assembly procedure of the chambers to guarantee the alignment of the readout strips has been developed, together with a validation procedure to test the functioning of the detectors, in which I personally worked during these PhD years, especially on the high voltage stability test. The high voltage stability has been a critical point of the Micromegas detector commissioning for the ATLAS upgrade. A limited R&D program has been restarted addressing the main issues, which has been overcame implementing additional steps in the assembly and validation procedure to optimise the detector performances.

The integration of the modules in the New Small Wheel is also presented in this thesis work. I took part in the integration activity at CERN of the Micromegas detector. It consists in several test activities of the modules: gas tightness and high voltage test performed once the modules arrive at CERN, irradiation tests at the Gamma Ray Irradiation Facility (GIF++) and the integration of the modules in the sector of the New Small Wheel, called *Double-Wedge* (DW). I worked on the high voltage validation of all the DWs of the small sectors that will be part of the New Small Wheel A, working on the HV powering scheme aimed to group HV sections with same behaviour together to achieve the optimal voltage conditions for the full chamber. The final validation of the DW is done performing cosmic test to estimate the efficiency and then its performance once it will be in ATLAS.

The second part of this thesis is focused on the analysis work performed on the $H \to ZZ^* \to 4l$ Higgs boson decay channel. This channel is one of the best channel to study the Higgs boson properties, due to the high signal-background ratio (~ 2) and to the clear signature, despite the low Branching Ratio ($(1.25 \pm 0.03) \times 10^{-4}$ [13]). In the Run 2 the improvements implemented in the analysis of this channel together with the enhancement of the statistics up to 139 fb^{-1} have allowed more precise measurements of the Higgs boson cross section in the different production modes, increasing the information also in the differential cross section measurements for observables sensitive to possible Beyond Standard Model (BSM) effects.

This thesis describes the Higgs boson fiducial cross section measurements, both inclusively and differentially, performed with full Run 2 dataset and published in [14], together with their interpretation, in which I have directly worked on. The *fiducial* attribute means that we are going to perform a measurement less model dependent as possible, given that it is done in the fiducial volume of the detector, factorising out the model-dependency related to the detector model itself. This kind of measurements are very important to test the predicted properties of the Higgs boson in the Standard Model framework, as well as to discover possible new physics effects measuring deviations from those predictions. The presence of anomalies in the Higgs boson interaction with the Standard Model particles due to a new massive undetected particle or to a modification of the couplings strength with respect to the Standard Model expectation, can be detected from Higgs cross section measurements.

In this thesis work the couplings of the Higgs boson with bosons and fermions have been tested, putting constraints on anomalous Higgs boson interactions with them. The limits on Higgs boson effective couplings have been derived in different theoretical framework and based on observables sensitive to different Higgs boson properties. The amplitude decay of an on-shell Higgs boson has been interpreted using the Pseudo-Observable framework [15], which feature the Higgs boson decay properties in an extension of the Standard Model. The Higgs boson Yukawa coupling with the charm quark instead has been probed by measurements of transverse momentum distributions in Higgs production [16].

The spin-parity of Standard Model Higgs boson is expected to be a 0^+. In this thesis also the CP properties have been tested, looking for possible CP-violation effects in the Higgs sector. This search has been performed looking to the impact of a possible BSM CP-odd coupling both on the rates, with fiducial cross section measurement, and on the shape of observables sensitive to anomalous CP contributions, with a shape-based analysis. In this context an Effective Field Theory (EFT) approach has been used [17], studying the operators which describe the BSM CP-odd interactions between the Higgs and the other SM particles in the production mechanisms as well as in the HZZ decay to test the interaction with Z boson. In this analysis I have directly worked on the unfolding studies of several CP-odd sensitive observables to provide preliminary fiducial differential cross section measurements for those and the relative EFT interpretation, and on the background estimations on both cross section and shape-based analysis. This study is focused to look for CP-odd contributions in the VBF production, then also the possibility to have a fiducial VBF cross section measurement has been investigated.

This thesis is organised as follow. In Chapter 1 the Higgs boson mechanism is described from the theoretical point of view in the Electroweak theory framework, as well as different Beyond Standard Model frameworks used in the $H \to ZZ^* \to 4l$ analysis. The production modes and the decay channels most relevant at LHC are described and an overview of the more recent results with the full Run 2 dataset is presented to give a picture of state of the art on the Higgs boson study. Chapter 2 concerns the ATLAS experiment at LHC. Its structure, composed by an Inner Detector, Calorimeters, Muon Spectrometers and Trigger, and related sub-detectors are described in detail, with an overview of the future upgrades. A second part of this chapter is dedicated to the description of the identification and reconstruction performances for muons, electrons and jets, important elements of the analysis performed.

Starting from the work done on the Micromegas detectors for the ATLAS upgrade, Chapter 3 introduce the New Small Wheel project, highlighting the limitation of the detectors currently installed and the improvements on the performances that will get from the use of the new detectors. A description of the sTGC and MM detectors is also presented. In Chapter 4 the construction of the SM1 modules is described together with the extensive work done to improve the high voltage performances of the chambers. In the first part the assembly and validation procedure developed at LNF is presented. The second part is focused on the HV stability issues and to the relative solutions found to overcome them.

Moving to the $H \to ZZ^* \to 4l$ analysis part, chapter 5 introduces the general $H \to ZZ^* \to 4l$ analysis within the ATLAS experiment. The event selection of this process is described, together with the background estimation. In Chapter 6 the fiducial inclusive and differential cross section measurements are shown. The observables on which the measurements has been performed are described, together with the fiducial selection and the unfolding procedure used to extract the cross section measurements. The observed results on the variables published in [14] are presented compared with SM expectations and on the CP-odd sensitive observables will be reported the preliminary expected results. In the last section of the chapter the prospect of a fiducial VBF measurement in the $H \to ZZ^* \to 4l$ decay channel is described. In Chapter 7 the interpretations of the results described in the previous chapter to constrain possible BSM contact interactions in the Pseudo-Observable framework, or non-SM values of the b- and c-quark Yukawa couplings are presented. In this section also an EFT interpretation of the preliminary results on CP-sensitive observable is described, constraining the anomalous Higgs boson couplings which can be probed in the HVV vertex. This results is compared with a shape-based analysis, described at the end of this chapter, which not take into account of possible BSM effects on the rate but only on the shape of the observables.

Chapter 1

The Standard Model and the Higgs boson

Contents

1.1 The Standard Model

The Standard Model describes three out of the four fundamental interactions of elementary particles in the framework of Quantum Field Theory: the electromagnetic interaction, responsible for the interaction between charged particles; the weak interaction, responsible for the existence of radioactive decays; and the strong interaction, responsible for the formation of proton and neutron and consequently nuclei. The gravitational interaction is too weak at the particle physics energy scales, and is not incorporated in the Standard Model (SM).

The elementary particles are divided into two groups:

- **Fermions**, have half-integer spin and are the constituents of matter. They are divided into *leptons* and *quarks*; the latter are involved in the strong interactions. They are grouped in three generations, each composed of two quarks and two leptons.

- **Bosons**, have integer spin. The gauge bosons have spin 1 and mediate the fundamental interactions: the *photon* is the massless mediator of electromagnetic interaction, the W^+, W^- and Z^0 are the massive mediator of weak interaction and the eight massless *gluons* mediate the strong interaction. The Higgs boson is a scalar boson which explains the massive nature of the particles within the SM.

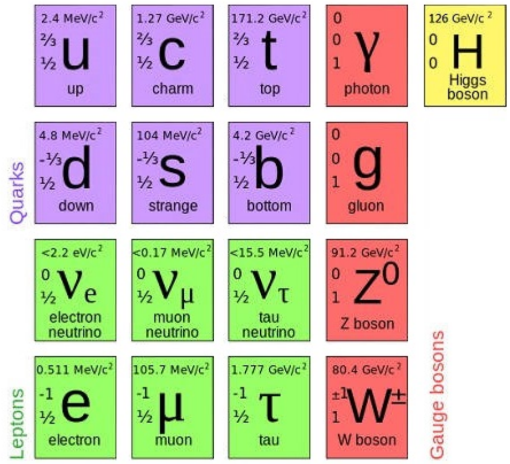

Figure 1.1: The elementary particles of the Standard Model.

The Standard Model is a gauge theory based on the local symmetry group $SU(3)_C \times SU(2)_L \times U(1)_Y$, where the subscripts C, L, and Y denote colour, left-handed chirality and weak hypercharge, respectively.

The $SU(3)_C$ group describes the colour symmetry of the strong interaction. The theory of the strong interactions between quarks and gluons is called Quantum Chromodinamycs (QCD), and the charge in QCD is referred to as colour charge and it could be of three types: red, green and blue. Only quarks and gluons are colour-charged particles and they cannot be isolated and exist only within colour neutral hadrons or high-temperature plasmas (*colour confinement*). The $SU(2)_L$ and the $U(1)_Y$ groups will be described in the next section.

The gauge group uniquely determines the interactions and the number of vector gauge bosons that correspond to the generators of the group. The electroweak interactions, based on the symmetry group $SU(2)_L \times U(1)_Y$, can be studied separately from strong interactions, because the symmetry under the colour group $SU(3)_C$ is unbroken and there is no mixing between $SU(3)_C$ and $SU(2)_L \times U(1)_Y$ sectors; on the other hand, as we will see, electromagnetic and weak interactions must be treated together because there is a mixing between the neutral gauge bosons of $SU(2)_L$ and $U(1)_Y$.

Electroweak Theory

The electroweak unification was first formalized in 1960 by Glashow [18] and then refined in 1967 by Weinberg and Salam [19] [20]. They discovered a way to combine the electromagnetic and weak interactions. To discuss about the electroweak part of the SM Lagrangian is sufficient to consider only the $SU(2)_L \times U(1)_Y$ symmetry group.

The symmetry group $SU(2)_L$ is called *weak isospin*. The elements of the group act only on the left-handed chiral components of the fermion fields (the right-handed chiral components are singlets under weak isospin transformations). This group has three generators, for which we use the notation T_i (i = 1, 2, 3) and they satisfy the commutation relations:

$$[T_i, T_j] = i\epsilon_{ijk}T_k \ , \tag{1.1.1}$$

where ϵ_{ijk} is the totally antisymmetric tensor. The weak isospin group is a non-abelian group and the generators are $T_i = \tau_i/2$, where τ_1, τ_2 and τ_3 are the three Pauli matrices:

$$\tau_1 = \begin{pmatrix} 0 & 1 \\ 1 & 0 \end{pmatrix} \qquad \tau_2 = \begin{pmatrix} 0 & -i \\ i & 0 \end{pmatrix} \qquad \tau_3 = \begin{pmatrix} 1 & 0 \\ 0 & -1 \end{pmatrix} \ . \tag{1.1.2}$$

The symmetry group $U(1)_Y$ is called *hypercharge*, and it is an abelian group. It is generated by the hypercharge operator Y, which is connected to T_3 and the charge operator Q by the *Gell-Mann–Nishijima relation*:

$$Q = T_3 + \frac{Y}{2} \ . \tag{1.1.3}$$

This relation is necessary in order to fix the action of the hypercharge operator Y on the fermion fields and implies the unification of weak and electromagnetic interactions.

In order to have local gauge invariance, one must introduce three vector gauge boson fields W_i^μ (i = 1, 2, 3) associated with the three generators T_i (i = 1, 2, 3) of the group $SU(2)_L$, and one vector gauge boson field B_μ associated with the generator Y of the group $U(1)_Y$. The covariant derivative D_μ, which in gauge theories replaces the normal derivative ∂_μ in the Lagrangian, is:

$$D_\mu = \partial_\mu + igW^i_\mu T_i + ig' B_\mu \frac{Y}{2} \ . \tag{1.1.4}$$

The two independent coupling constants g and g' are associated with the $SU(2)_L$ and $U(1)_Y$ groups respectively.

The choice of the representations for the fermion fields has been guided by the previous theory for the weak interaction, namely the $V - A$ theory, and the two-component theory of the neutrino. Thus, the fermions are divided into *left-handed* and *right-handed* components. Since the W bosons couple only to the left-handed particles, while the Z boson and the photon couple to both left-handed and right-handed particles, the left-handed chiral components of the fermion fields are grouped into *weak isospin doublets*, while the right-handed components are assumed to be singlets under the weak isospin group of transformations:

$$\begin{pmatrix} u \\ d \end{pmatrix}_L , \begin{pmatrix} \nu_e \\ e \end{pmatrix}_L \qquad \begin{pmatrix} c \\ s \end{pmatrix}_L , \begin{pmatrix} \nu_\mu \\ \mu \end{pmatrix}_L \qquad \begin{pmatrix} t \\ b \end{pmatrix}_L , \begin{pmatrix} \nu_\tau \\ \tau \end{pmatrix}_L \tag{1.1.5}$$

$$u_R,\ d_R,\ e_R \qquad c_R, s_R,\ \mu_R \qquad t_R,\ b_R,\ \tau_R\ . \tag{1.1.6}$$

The left-handed and right-handed components of the fermion fields transform differently under rotations of $SU(2)_L \times U(1)_Y$. The unitarity transformation is defined as:

$$U(\alpha(x), \overline{\beta}(x)) = e^{i\alpha(x)\frac{Y}{2} + i\overline{\beta}(x)\cdot\frac{\overline{\tau}}{2}}\ , \tag{1.1.7}$$

where $(\alpha(x), \overline{\beta}(x))$ is a set of 1+3 parameters, with $\overline{\beta}(x) = (\beta_1(x), \beta_2(x), \beta_3(x))$. The transformation of the left-handed doublets and of right-handed singlets are given by:

$$\psi_L \longrightarrow \psi'_L = e^{i\alpha(x)\frac{Y}{2} + i\overline{\beta}(x)\cdot\frac{\overline{\tau}}{2}}\psi_L\ , \qquad \psi_R \longrightarrow \psi'_R = e^{i\alpha(x)\frac{Y}{2}}\psi_R\ . \tag{1.1.8}$$

The resulting electroweak Lagrangian is:

$$\begin{aligned}\mathcal{L} =& -\frac{1}{4}W^i_{\mu\nu}W_i^{\mu\nu} - \frac{1}{4}B_{\mu\nu}B^{\mu\nu} + i\overline{\psi}\gamma^\mu D_\mu\psi = \\ =& -\frac{1}{4}W^i_{\mu\nu}W_i^{\mu\nu} - \frac{1}{4}B_{\mu\nu}B^{\mu\nu} + i\overline{\psi_L}\gamma^\mu\partial_\mu\psi_L + i\overline{\psi_R}\gamma^\mu\partial_\mu\psi_R + \\ & - \overline{\psi_L}\gamma^\mu\left(g\frac{\tau_i}{2}W^i_\mu + g'\frac{Y}{2}B_\mu\right)\psi_L - \overline{\psi_R}\gamma^\mu\left(g'\frac{Y}{2}B_\mu\right)\psi_R\ ,\end{aligned} \tag{1.1.9}$$

where $W^i_{\mu\nu}$ and $B_{\mu\nu}$ are the field tensors:

$$W^i_{\mu\nu} = \partial_\mu W^i_\nu + \partial_\nu W^i_\mu - g\epsilon_{ijk}W^j_\mu W^k_\nu\ , \tag{1.1.10}$$

$$B_{\mu\nu} = \partial_\mu B_\nu + \partial_\nu B_\mu\ . \tag{1.1.11}$$

Then to satisfy gauge invariance, the covariant derivative must transform as:

$$D_\mu \longrightarrow D'_\mu = U(\alpha(x), \overline{\beta}(x))D_\mu U^{-1}(\alpha(x), \overline{\beta}(x)) \tag{1.1.12}$$

This means that the gauge boson fields transform as:

$$W^i_\mu\tau^i \longrightarrow W^{i\prime}_\mu\tau^i = U(\alpha(x), \overline{\beta}(x))\left[W^i_\mu\tau^i - \frac{i}{g}\partial_\mu\right]U^{-1}(\alpha(x), \overline{\beta}(x)) \tag{1.1.13}$$

$$B_\mu\frac{Y}{2} \longrightarrow B'_\mu\frac{Y}{2} = U(\alpha(x), \overline{\beta}(x))\left[B_\mu\frac{Y}{2} - \frac{i}{g'}\partial_\mu\right]U^{-1}(\alpha(x), \overline{\beta}(x)) \tag{1.1.14}$$

A mass term for a fermion in the Lagrangian would be of the form: $-m\overline{\psi}\psi$, but such terms are not allowed as they are not gauge invariant, since

$$-m\overline{\psi}\psi = -m[\overline{\psi_R}\psi_L + \overline{\psi_L}\psi_R]\ , \tag{1.1.15}$$

but the left-handed and right-handed components transform in a different way under the transformations of the gauge group as seen before. In the same way, the invariance of the Lagrangian is achieved by replacing the partial derivative by a covariant derivative and introducing a new vector field with specific transformation properties (see 1.1.13 and 1.1.14). Under these symmetry requirements it is not possible for a gauge boson to acquire mass, e.g. in QED:

$$\frac{1}{2}m_\gamma^2 A_\mu A^\mu \to \frac{1}{2}m_\gamma^2 \left(A_\mu - \frac{i}{e}\partial_\mu\right)\left(A^\mu - \frac{i}{e}\partial^\mu\right) \neq \frac{1}{2}m_\gamma^2 A_\mu A^\mu \ . \tag{1.1.16}$$

The interaction Lagrangian that describes the coupling of the fermions with the gauge bosons is the last line of the equation 1.1.9 and in order to derive the explicit interaction term for the fermions, the definitions of Pauli matrices are used and ψ_u and ψ_d as the *up* component and *down* component of fermion fields are defined:

$$\mathcal{L}_I = -\frac{1}{2}(\overline{\psi}_{uL}\ \overline{\psi}_{dL}) \begin{pmatrix} g\not{W}_3 - g'\not{B} & g(\not{W}_1 - i\not{W}_2) \\ g(\not{W}_1 + i\not{W}_2) & -g\not{W}_3 - g'\not{B} \end{pmatrix} \begin{pmatrix} \psi_{uL} \\ \psi_{dL} \end{pmatrix} + g'\frac{Y}{2}\overline{\psi}_{uR}\not{B}\psi_{uR} + g'\frac{Y}{2}\overline{\psi}_{dR}\not{B}\psi_{dR} \ . \tag{1.1.17}$$

A field W^μ that annihilates W^+ bosons and creates W^- bosons can be defined, and its hermitian conjugate $W^{\mu\dagger}$, as a linear combination of W_1^μ and W_2^μ:

$$W^\mu = \frac{W_1^\mu - iW_2^\mu}{\sqrt{2}} \quad \Longrightarrow \quad W^{\mu\dagger} = \frac{W_1^\mu + iW_2^\mu}{\sqrt{2}} \ . \tag{1.1.18}$$

The theory must include the electromagnetic interactions described by the quantum electrodynamic (QED) Lagrangian. As such, the electromagnetic field A^μ can be expressed as an appropriate linear combination of B^μ and W_3^μ and write the orthogonal combination, which defines the vector boson field Z^μ. This performs a rotation in the plane of the B^μ, W_3^μ fields through an angle θ_W:

$$\begin{pmatrix} A^\mu \\ Z^\mu \end{pmatrix} = \begin{pmatrix} \cos\theta_W & \sin\theta_W \\ -\sin\theta_W & \cos\theta_W \end{pmatrix} \begin{pmatrix} B^\mu \\ W_3^\mu \end{pmatrix} \qquad \text{with } \tan\theta_W = \frac{g'}{g} \ . \tag{1.1.19}$$

The angle θ_W is called the *Weinberg angle*. The weak mixing angle is chosen in order to obtain the QED Lagrangian for the coupling between the electromagnetic field and the fermion fields.

Separate the interaction Lagrangian into a *charged-current* (CC) and *neutral-current* (NC):

$$\mathcal{L}_I^{(CC)} = -\frac{g}{\sqrt{2}}\left\{\overline{\psi}_{uL}\not{W}\psi_{dL} + \overline{\psi}_{dL}\not{W}^\dagger\psi_{uL}\right\} \ , \tag{1.1.20}$$

$$\begin{aligned} \mathcal{L}_I^{(NC)} = -\frac{g}{2\cos\theta_W}&\left\{2g_L^U\overline{\psi}_{uL}\not{Z}\psi_{uL} + 2g_L^D\overline{\psi}_{dL}\not{Z}\psi_{dL} + 2g_R^U\overline{\psi}_{uR}\not{Z}\psi_{uR} + 2g_R^D\overline{\psi}_{dR}\not{Z}\psi_{dR}\right\} + \\ &- g\sin\theta_W\frac{Y}{2}\overline{\psi}\not{A}\psi \ , \end{aligned} \tag{1.1.21}$$

Then,

$$\mathcal{L}_I^{(NC)} = -\frac{g}{2\cos\theta_W}\left\{\overline{\psi}_u \not{Z}(g_V^U - g_A^U\gamma^5)\psi_u + \overline{\psi}_d \not{Z}(g_V^D - g_A^D\gamma^5)\psi_d\right\} - g\sin\theta_W \frac{Y}{2}\overline{\psi}\not{A}\psi \ , \tag{1.1.22}$$

where the coefficients $g_{L,R}^{U,D}$, $g_V^{U,D}$ and $g_A^{U,D}$ have been introduced. In general, the values of the coefficients g_L^f and g_R^f for fermion field f are given by:

$$g_L^f = T_3^f - q_f \sin^2\theta_W \ , \qquad g_R^f = -q_f \sin^2\theta_W \ , \tag{1.1.23}$$

where the T_3^f is the value of the third component of the weak isospin and q_f is the electric charge of the fermion in units of the elementary electric charge e.

The $V - A$ structure of the weak interaction is shown by the fact that in 1.1.20 the coupling of W bosons is only with left-handed fermions $(1-\gamma^5)$, and in 1.1.22 the Z boson has a vector and an axial coupling with fermion fields, expressed by $(g_V - g_A\gamma^5)$.

1.1.1 The Higgs mechanism

In the previous section, a gauge-invariant and renormalisable unified theory of weak and electromagnetic interactions has been obtained. However, all fermions and gauge bosons need to have zero mass, since it has been shown that the *ad hoc* addition of mass terms to the Lagrangian density spoils the gauge invariance and the renormalisability of the theory. In order to obtain a renormalisable theory, it is essential to introduce the masses by a mechanism which retains the gauge invariance of the Lagrangian density: the *spontaneous symmetry breaking*.

In the Standard Model, the masses are generated through a spontaneous symmetry breaking of a local gauge theory, known as the *Higgs mechanism* [21] [22]. This is implemented by an additional $SU(2)_L$ isospin doublet of complex scalar fields with hypercharge $Y = 1$:

$$\Phi(x) = \begin{pmatrix} \phi^+(x) \\ \phi^0(x) \end{pmatrix} \ , \tag{1.1.24}$$

where $\phi^+(x)$ is a charged field and $\phi^0(x)$ is a neutral field. The Higgs doublet transforms under $SU(2)_L \times U(1)_Y$ transformation as follows:

$$\Phi \longrightarrow \Phi' = e^{i\alpha(x)\frac{Y}{2} + i\overline{\beta}(x)\cdot\frac{\overline{\tau}}{2}}\Phi \ . \tag{1.1.25}$$

The Higgs part of the SM Lagrangian is composed by a kinetic term, with the covariant derivative, and a potential term, that it could be thought as an expansion in powers of $\Phi(x)$ and $\Phi(x)^\dagger$ about the stable equilibrium configuration $\Phi(x) = 0$:

$$\mathcal{L}_{Higgs} = (D_\mu\Phi)^\dagger(D^\mu\Phi) - \mu^2\Phi^\dagger\Phi - \lambda(\Phi^\dagger\Phi)^2 \ . \tag{1.1.26}$$

The Higgs potential is:

$$V(\Phi) = -\mu^2\Phi^\dagger\Phi - \lambda(\Phi^\dagger\Phi)^2 \;, \tag{1.1.27}$$

and the $\lambda(\Phi^\dagger\Phi)^2$ term can be treat by perturbation theory.

The coefficient λ of the quadratic self-couplings of the Higgs fields must be positive in order to have a potential which is bounded from below. On the other hand, the squared mass-like coefficient μ^2 must be negative in order to realise the spontaneous breaking of the symmetry

$$SU(2)_L \times U(1)_Y \rightarrow U(1)_Q \;, \tag{1.1.28}$$

where $U(1)_Q$ is the gauge symmetry group of electromagnetic interactions, associated with the conservation of the electric charge. This invariance guarantees the existence of a massless gauge boson associated with the symmetry group $U(1)_Q$, which is the photon.

In the case of $\mu^2 > 0$, the potential has a unique minimum at $\Phi = 0$, which in quantum field theory corresponds to the vacuum and has the lowest energy state (ground state). This means that the field Φ has zero *vacuum expectation value* (VEV), defined as $\langle 0|\Phi|0\rangle$, and the vacuum is thus invariant under $SU(2)_L \times U(1)_Y$ and gauge bosons have to be massless in order to respect this symmetry. In the case of $\mu^2 < 0$, a non vanishing vacuum expectation value for Φ in the physical vacuum state is obtained. The potential assumes a shape known as the *"Mexican hat"* (Figures 1.2 and 1.3), with a local maximum at $\Phi = 0$. Defining:

$$v \equiv \sqrt{-\frac{\mu^2}{\lambda}} \;, \tag{1.1.29}$$

the Higgs potential can be written (neglecting constant term $v^4/4$) as:

$$V(\Phi) = \lambda\left(\Phi^\dagger\Phi - \frac{v^2}{2}\right)^2 \;. \tag{1.1.30}$$

Then the potential is minimum at:

$$\Phi^\dagger\Phi = \frac{v^2}{2} \;. \tag{1.1.31}$$

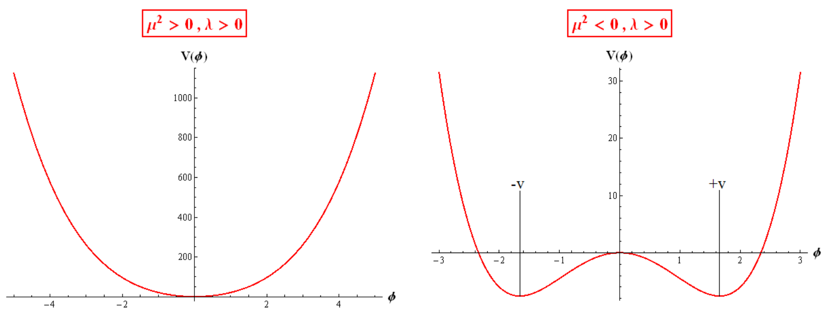

Figure 1.2: The Higgs potential $V(\Phi)$ as a function of the complex scalar field Φ for $\mu^2 > 0$ (*on the left*) and $\mu^2 < 0$ (*on the right*).

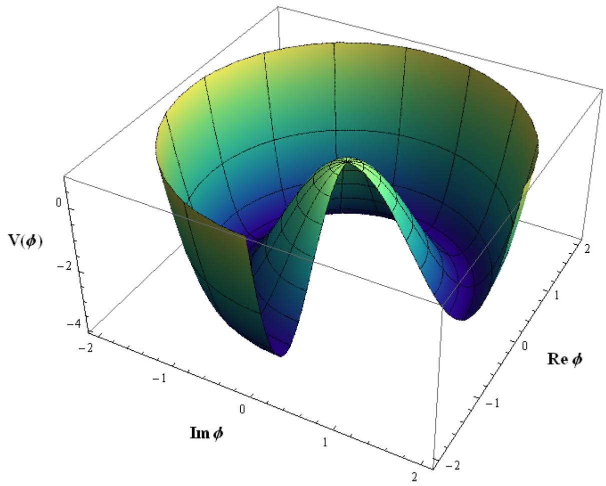

Figure 1.3: The Higgs potential shape known as the "mexican hat".

The minimum of the potential corresponds to the ground state and the quantised excitations of each field above the vacuum correspond to the particle states. Fermion and vector boson fields carry a non-zero spin, then they must have a zero vacuum expectation value, in order to preserve the invariance under spatial rotation; also charged scalar fields must have zero value in the vacuum because it is electrically neutral. On the other hand, neutral scalar fields (no charge and no spin) can have a non-zero vacuum expectation value. Then to have an electrically neutral vacuum, the VEV of the Higgs fields must be due to ϕ^0:

$$\langle\Phi\rangle = \frac{1}{\sqrt{2}}\begin{pmatrix}0\\ v\end{pmatrix} \ . \tag{1.1.32}$$

The minimum of the potential is no longer a unique value of Φ, but there are an infinite number of states. The fields are expressed with quantum fluctuations about this minimum and the scalar doublet Φ can be written as:

$$\Phi(x) = e^{\frac{i\vec{\xi}(x)\cdot\vec{\tau}}{2v}}\begin{pmatrix}0\\ \frac{v+H(x)}{\sqrt{2}}\end{pmatrix} \ , \tag{1.1.33}$$

where $\xi_i(x)$ $(i = 1, 2, 3)$ are the massless real fields (Goldstone bosons) and $H(x)$ is the real scalar Higgs field, the massive Higgs field. The Goldstone bosons correspond to angular excitations from the ground state, that leave the potential energy unchanged, while the the scalar Higgs field describes radial excitations, changing the potential energy. Since the Lagrangian in locally $SU(2)_L$ invariant, the three massless scalar bosons $\xi_i(x)$ could correspond to the phases parameter $\beta_i(x)$ in $SU(2)_L$ transformations and disappear from the Lagrangian. Then Φ can be replaced by:

$$\Phi(x) = \begin{pmatrix}0\\ \frac{v+H(x)}{\sqrt{2}}\end{pmatrix} \ . \tag{1.1.34}$$

This transformation defines the so-called *unitary gauge*. In this gauge, the Higgs Lagrangian becomes:

$$\begin{aligned}\mathcal{L}_{Higgs} =& \frac{1}{2}(\partial H)^2 - \lambda v^2 H^2 - \lambda v H^3 - \frac{\lambda}{4}H^4 + \frac{g^2 v^2}{4} W^\dagger_\mu W^\mu + \frac{g^2 v^2}{8\cos^2\theta_W} Z_\mu Z^\mu + \\ & \frac{g^2 v}{2} W^\dagger_\mu W^\mu H + \frac{g^2 v}{4\cos^2\theta_W} Z_\mu Z^\mu H + \\ & \frac{g^2}{2} W^\dagger_\mu W^\mu H^2 + \frac{g^2}{8\cos^2\theta_W} Z_\mu Z^\mu H^2 \ .\end{aligned} \tag{1.1.35}$$

The first term is the kinetic term for the Higgs boson. The second term is the mass term for the Higgs boson, from which the mass of the Higgs boson is given by:

$$m_H = \sqrt{2\lambda v^2} \ . \tag{1.1.36}$$

The fifth and the sixth terms are mass terms for the W and Z gauge bosons. The other terms are the trilinear and quadrilinear self-couplings of the Higgs field and the couplings of the Higgs field with the gauge bosons.

The mass of the $W^\pm$ and the Z bosons are related to each other through the following relation:

$$M_Z \cos\theta_W = M_W = \frac{1}{2} v g \quad \Longrightarrow \quad M_W = \frac{vg}{2} \ , \quad M_Z = \frac{v}{2}\sqrt{g^2 + g'^2} \ . \tag{1.1.37}$$

The fermions masses, like bosons, are generated by coupling between the Higgs doublet and the fermions. There are Yukawa coupling terms in the SM Lagrangian with this form:

$$\mathcal{L}_Y = -g^f_y \ \overline{\psi_L} \Phi \psi_R + h.c. \ , \tag{1.1.38}$$

where the g_y is the Yukawa coupling constant of the fermions with the Higgs boson. In the unitary gauge, the Higgs doublet has the expression given by the equation 1.1.34, and the Higgs-lepton Yukawa Lagrangian becomes:

$$\mathcal{L}_Y = -g^f_y \left(\frac{v + H(x)}{\sqrt{2}} \right) \overline{\psi_L} \psi_R + h.c. \ . \tag{1.1.39}$$

The term proportional to the VEV (v) of the Higgs doublet is the mass term for the charged fermion, whereas the term proportional the Higgs boson field $H(x)$ gives the trilinear couplings between the fermions and the Higgs boson. Then, the mass of the fermions is given by:

$$m_f = \frac{g^f_y v}{\sqrt{2}} \ . \tag{1.1.40}$$

1.1.1.1 The Higgs boson discovery

The announcement of the Higgs boson has been done on July 4^{th} 2012 by the ATLAS [1] and CMS collaborations [2]. The ATLAS experiment used a dataset corresponding to integrated luminosities of approximately 4.8 fb^{-1} collected at $\sqrt{s}$=7 TeV during 2011 and 5.8 fb^{-1} at $\sqrt{s}$=8 TeV during 2012. The CMS experiment used a data samples corresponding to integrated luminosities of approximately 5.1 fb^{-1} at $\sqrt{s}$=7 TeV and 5.3 fb^{-1} at $\sqrt{s}$=8 TeV.

Figure 1.4 shows the distribution of the four-lepton invariant mass m_{4l} from the $H \to ZZ^* \to 4l$ decay channel analysis, compared to the background expectation, for the combination of the 7 TeV and 8 TeV data. The distribution shows a clear signature of a new particle production, in good agreement with the signal expectation for a SM Higgs with m_H=125 GeV.

Figure 1.5 shows the diphoton invariant mass distribution from the $H \to \gamma\gamma$ decay channel analysis, with a clear peak over the continuum background distribution, consistent with the SM Higgs boson expectations.

The current estimation of the Higgs boson mass from the latest results obtained by combining the most sensitive channels from the ATLAS and CMS experiments is [23]:

$$m_H = (125.09 \pm 0.21(stat.) \pm 0.11(syst.))\ \mathrm{GeV} \tag{1.1.41}$$

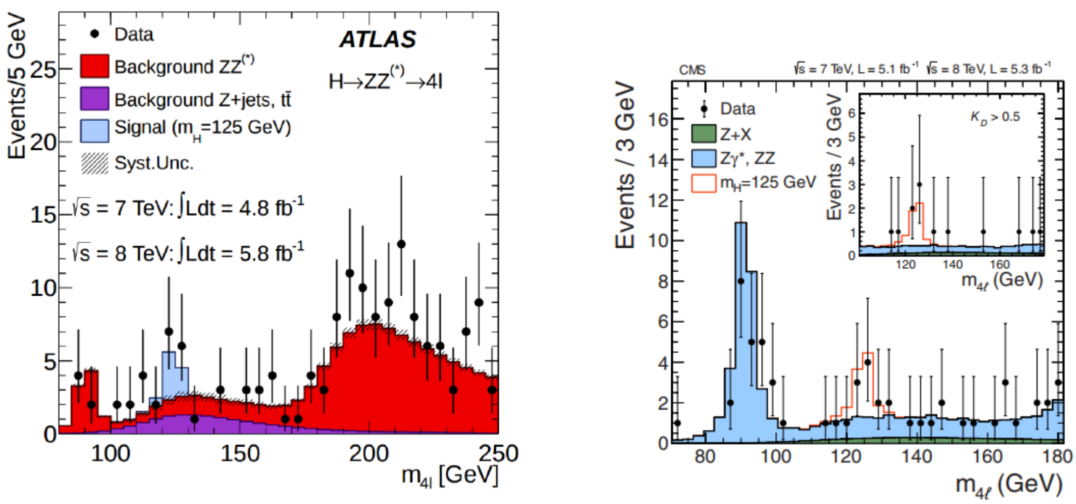

Figure 1.4: The distribution of the four-lepton invariant mass m_{4l}. The signal and the background expectation are shown and compared with the combination of the 7 TeV and 8 TeV data . *On the left*: ATLAS Collaboration [1]. *On the right*: CMS Collaboration [2].

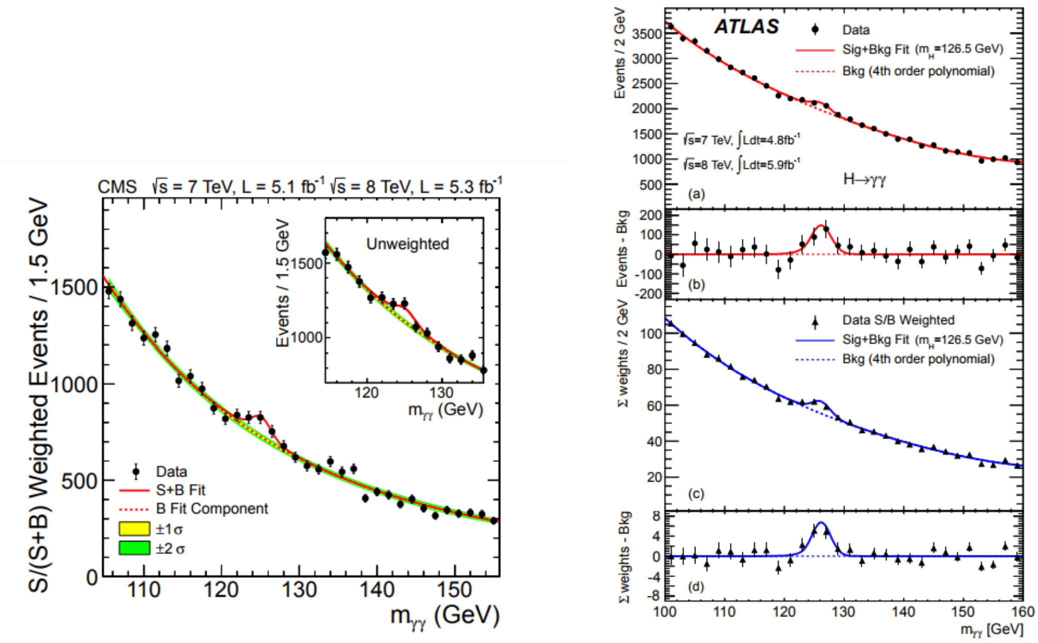

Figure 1.5: The diphoton invariant mass distribution. The result of a fit to the combined 7 TeV and 8 TeV data of the sum of a signal and a background component is superimposed. *On the left*: CMS Collaboration [2]. *On the right*: ATLAS Collaboration (the inclusive sample (a,b) and a weighted version (c,d) are shown) [1].

1.1.2 Beyond the Standard Model Higgs boson frameworks

The Standard Model is expected not to be the ultimate theory of particle physics, given that many fundamental questions are still not solved soon as the presence of the dark matter or the matter-antimatter asymmetry. For this reason, the investigation of the Higgs boson properties is crucial to search signs of possible New Physics effects in the Higgs sector, beyond the Standard Model (BSM).

It is reasonable to assume that new BSM particles are much heavier than the Standard Model particles, otherwise they would have already been detected by LHC experiments. In this case, the SM can represent only a simplification of a more complex underlying theoretical framework. To deal with this assumptions, the Beyond Standard Model physics in the electroweak sector can be described by an *Effective Field Theory* (EFT). In this framework, possible new heavy physical states can be expressed as an expansion in operator dimensions of an Effective Lagrangian. The EFT approach provides a useful tool to bring the SM and different BSM models closer. This is due to is "dual" nature: *top-down* and *bottom-up* approaches.

The top-down approach starts from a well known and defined High Energy (HE) theory to obtain a Low Energy (LE) theory to describe the low energy physics which the experiments are sensitive to. This is done by "integrate out" (removing) the heavier particles from the HE theory and "matching" onto a LE theory at a given scale Λ. It can be schematically represented as:

$$\mathcal{L}_{\mathrm{HE}} \quad \to \quad \sum_n \mathcal{L}_{\mathrm{LE}}^{(n)} \,, \tag{1.1.42}$$

where the sum in n is an expansion in decreasing relevance. $\mathcal{L}_{\mathrm{HE}}$ and $\mathcal{L}_{\mathrm{LE}}$ need to agree in the infrared (IR) but differs in the ultraviolet (UV). This approach indeed is strongly dependent on the model implemented in the HE theory.

In the bottom-up approach the underlying theory is unknown, or at least partially known, such as if it is Lorentz invariant, a gauge theory, etc. Then it is built writing down the most general possible operators in which the SM Lagrangian is the leading order term and the effects of new physics are encoded in higher-dimensional operators constructed out of the SM fields at higher energy scales $\Lambda^2 \gg m^2$:

$$\sum_n \mathcal{L}_{\mathrm{LE}}^{(n)} \quad \to \quad \mathcal{L}_{\mathrm{EFT}} = \mathcal{L}_{\mathrm{SM}} + \frac{c^{(5)}}{\Lambda}\mathcal{O}^{(5)} + \sum_i \frac{c^{(6)}}{\Lambda^2}\mathcal{O}^{(6)} + \ldots \tag{1.1.43}$$

where $\mathcal{O}^{(d)}$ are the operators of dimension-d and $c^{(d)}$ are the corresponding dimensionless coupling constant, called *Wilson coefficients*. These couplings are unknown, but they can be constrained from the experimental measurements. This approach is more model-independent with respect to the top-down one.

Several theoretical frameworks have been developed to probe anomalous Higgs boson couplings. The simplest interpretation was developed during Run 1 looking for deviations from the SM expectation by defining coupling modifiers in the so-called κ-framework [26]. This approach is an intuitive language but the formulation is limited to leading order effects on the Higgs boson couplings. During Run 2, with the statistics enhancement, the precision of the measurements improves by a sizeable factor, which allows more complete frameworks to be used for the interpretation of the results as the Standard Model Effective Field Theory (SMEFT) [17] and the Pseudo-Observable (PO) [15] framework. This last approach represents a generalisation of the κ-framework for higher precision studies of the on-shell Higgs decays, given that the Higgs PO are defined from a general decomposition of on-shell amplitudes involving the Higgs boson and a momentum expansion assuming no new particles below the Higgs mass. The Higgs PO can be then match a wider class of New Physics model than the coupling modifiers, including the determination of the Wilson coefficients in the EFT context [25].

1.1.2.1 Coupling modifier: κ-framework

The first interpretation framework put in place during Run 1 was the so-called κ-framework [26]. In this framework, multiplicative coupling modifiers κ are introduced to parametrise deviations of the Higgs boson couplings from the SM predictions under the assumption of a single CP-even Higgs boson state and of the SM tensor coupling structure. Only the coupling strength are allowed to be modified by BSM physics. The measured Higgs boson cross sections can then be interpreted in this framework. Assuming the narrow-width approximation, the production and the decay can be factorised such that:

$$\sigma \cdot \mathcal{B}(i \to H \to f) = \sigma_i(\kappa) \cdot \frac{\Gamma_f(\kappa)}{\Gamma_H} \ , \tag{1.1.44}$$

where σ_i is the production cross section from the initial state i and $\mathcal{B}$ and Γ_f are the branching ratio and partial decay width for the decay into the final state f, and Γ_H is the total width of the Higgs boson. The coupling modifiers for the Higgs production and decay process are defined as:

$$\kappa_i^2 = \frac{\sigma_i}{\sigma_i^{\mathrm{SM}}} \qquad \text{and} \qquad \kappa_f^2 = \frac{\Gamma_f}{\Gamma_f^{\mathrm{SM}}} \ . \tag{1.1.45}$$

1.1.2.2 Standard Model Effective Field Theory

As mentioned before, an Effective Field Theory approach can be used to parametrise new physics at an energy scale Λ higher than the electroweak scale. This framework defines new operators consisting of SM fields with dimensions larger than the SM Lagrangian operators.

In the Standard Model Effective Field Theory (SMEFT), a complete set of dimension-six operators invariant under the SM gauge group $SU(3)_C \times SU(2)_L \times U(1)_Y$ is built from the SM fields [17] . The general effective Lagrangian is the one described by the Equation 1.1.43.

Dimension-five operators violates lepton number (L conservation), while dimension-seven violate the observed $B - L$ symmetry (B is the baryon number). Both these effects in previous experiments have been shown to be suppressed. Therefore, the leading contributions to physical observables are expected from dimension-six operators and the SMEFT Lagrangian becomes:

$$\mathcal{L}_{\mathrm{SMEFT}} = \mathcal{L}_{\mathrm{SM}} + \sum_i \frac{c_i}{\Lambda^2} O_i^{(6)} \ . \tag{1.1.46}$$

There are several complete sets of these dimension-six operators. The historical one is the so-called *Warsaw basis*, which contains 59 independent operators assuming lepton and baryon number conservation. These operators are divided into eight classes according to the field content and the number of covariant derivatives, class 1: X^3, class 2: Φ^6, class 3: $\Phi^4 D^2$, class 4: $X^2\Phi^2$, class 5: $\psi^2\Phi^3$, class 6: $\psi^2 X\Phi$, class 7: $\psi^2\Phi^2 D$ and class 8: ψ^4, where $X = G^A_{\mu\nu}, W^I_{\mu\nu}, B_{\mu\nu}$ are the gauge field strength tensors, Φ the scalar doublet Higgs field, ψ the fermion spinor of $SU(2)_L$ eigenstates and D_μ the covariant derivative.

Considering three independent flavours, the 59 operators lead to 2499 independent real parameters. These can be reduced if we impose some assumptions, like flavour symmetry. This assumption lead to a reduced number of parameters, in particular to 52 CP-even and 17 CP-odd ones. Focusing on the operators which can affect the $H \to ZZ^*$ measurement, the remaining couplings are the top Yukawa coupling, which can be probed by the $t\bar{t}H$ production, the gluon coupling probed in the ggF production and the couplings to the weak gauge bosons, which can be measured in the VBF and VH, as well as in the decay vertex HZZ. The 5 CP-even and 5 CP-odd coupling remain are listed in Table 1.1.

CP-even			CP-odd			Impact on	
Operator	Structure	Coupling	Operator	Structure	Coupling	Production	Decay
$O_{\Phi G}$	$\Phi^\dagger \Phi G^A_{\mu\nu} G^{\mu\nu A}$	c_{HG}	$O_{\Phi\tilde{G}}$	$\Phi^\dagger \Phi \tilde{G}^A_{\mu\nu} G^{\mu\nu A}$	$c_{H\tilde{G}}$	ggF	-
$O_{u\Phi}$	$(\Phi^\dagger\Phi)(\tilde{Q}_p u_r \tilde{\Phi})$	c_{uH}	$O_{\tilde{u}\Phi}$	$(\Phi^\dagger\Phi)(\tilde{Q}_p u_r \tilde{\Phi})$	$c_{\tilde{u}H}$	ttH	-
$O_{\Phi W}$	$\Phi^\dagger \Phi W^I_{\mu\nu} W^{\mu\nu I}$	c_{HW}	$O_{\Phi\tilde{W}}$	$\Phi^\dagger \Phi \tilde{W}^I_{\mu\nu} W^{\mu\nu I}$	$c_{H\tilde{W}}$	VBF,VH	Yes
$O_{\Phi B}$	$\Phi^\dagger \Phi B_{\mu\nu} B^{\mu\nu}$	c_{HB}	$O_{\Phi\tilde{B}}$	$\Phi^\dagger \Phi \tilde{B}_{\mu\nu} B^{\mu\nu}$	$c_{H\tilde{B}}$	VBF,VH	Yes
$O_{\Phi WB}$	$\Phi^\dagger \tau^I \Phi W^I_{\mu\nu} B^{\mu\nu}$	c_{HWB}	$O_{\Phi\tilde{W}B}$	$\Phi^\dagger \tau^I \Phi \tilde{W}^I_{\mu\nu} B^{\mu\nu}$	$c_{H\tilde{W}B}$	VBF,VH	Yes

Table 1.1: SMEFT CP-even and CP-odd dimension-six operators in the Warsaw basis relevant for the measurement in the $H \to ZZ^* \to 4\ell$ decay channel

An alternative complete set of operators can be defined, based on the mass eigenstates instead of the fields (then after the spontaneous symmetry breaking explained in Section 1.1.1). This formulation is expressed in terms of the physical states W^+, W^-, Z and γ. The effective Lagrangian in terms of these alternative couplings, focused on the HVV couplings, is:

$$\begin{aligned}
\mathcal{L}^{\text{SM+d=6}}_{\text{HVV}} =& \frac{h}{c}\Bigg[(1+\delta c_w)\frac{g^2 v^2}{2} W^+_\mu W^{\mu-} + (1+\delta c_z)\frac{(g^2+g'^2)v^2}{4} Z_\mu Z^\mu + \\
& c_{ww}\frac{g^2}{2} W^+_{\mu\nu} W^{\mu\nu-} + \tilde{c}_{ww}\frac{g^2}{2} W^+_{\mu\nu}\tilde{W}^{\mu\nu-} + c_{w\Box} g^2 (W^-_\mu \partial_\nu W^{\mu\nu+} + \text{h.c}) + \\
& c_{gg}\frac{g_s^2}{4} G^a_{\mu\nu} G^{\mu\nu a} + c_{\gamma\gamma}\frac{e^2}{4} A_{\mu\nu} A^{\mu\nu} c_{z\gamma}\frac{e\sqrt{g^2+g'^2}}{4} Z_{\mu\nu} A^{\mu\nu} + c_{zz}\frac{g^2+g'^2}{4} Z_{\mu\nu} Z^{\mu\nu} + \\
& c_{z\Box} g^2 Z_\mu \partial_\nu Z^{\mu\nu} + c_{\gamma\Box} g g' Z_\mu \partial_\nu A^{\mu\nu} \\
& \tilde{c}_{gg}\frac{g_s^2}{4} G^a_{\mu\nu}\tilde{G}^{\mu\nu a} + \tilde{c}_{\gamma\gamma}\frac{e^2}{4} A_{\mu\nu}\tilde{A}^{\mu\nu}\tilde{c}_{z\gamma}\frac{e\sqrt{g^2+g'^2}}{4} Z_{\mu\nu}\tilde{A}^{\mu\nu} + \tilde{c}_{zz}\frac{g^2+g'^2}{4} Z_{\mu\nu}\tilde{Z}_{\mu\nu}\Bigg]
\end{aligned} \tag{1.1.47}$$

From this Lagrangian it is possible to build another basis which can probe the effects of the Higgs boson couplings with the other particles, parametrising them with only one coefficients instead of a linear combination of other coefficients. This is called *Higgs basis*, and the recommended choice for the independent couplings is the following:

$$\delta c_z, c_{gg}, c_{\gamma\gamma}, c_{z\gamma}, c_{zz}, c_{z\Box}, \tilde{c}_{gg}, \tilde{c}_{\gamma\gamma}, \tilde{c}_{z\gamma}, \tilde{c}_{zz}\ , \tag{1.1.48}$$

where $\tilde{c}$ denote coefficients of the CP-violating operators, while the other are the CP-conserving ones.

The $H \to ZZ^* \to 4\ell$ analysis performed in this thesis, especially in the CP-violation search, is focused on the study of the couplings in the HVV vertex, which can be probed mainly in the decay and in the VBF and VH production. In the end only three operators are needed:

- Warsaw basis: $c_{H\widetilde{W}}$, $c_{H\widetilde{B}}$, $c_{H\widetilde{W}B}$
- Higgs basis: $\tilde{c}_{zz}$, $\tilde{c}_{za}$, $\tilde{c}_{aa}$

The Warsaw basis is implemented in the SMEFTsim package [27] which interfaced with various Monte Carlo generators. To simulate samples in the Higgs basis, the couplings of the two bases need to be translated. The relations between them are listed below:

$$\tilde{c}_{zz} = 4\left(\frac{g^2 c_{H\tilde{W}} + g'^2 c_{H\tilde{B}} + gg' c_{H\tilde{W}B}}{(g^2+g'^2)^2}\right)\frac{v^2}{\Lambda^2}\ , \tag{1.1.49}$$

$$\tilde{c}_{z\gamma} = 4\left(\frac{c_{H\tilde{W}} - c_{H\tilde{B}} - \frac{g^2-g'^2}{2gg'} c_{H\tilde{W}B}}{g^2+g'^2}\right)\frac{v^2}{\Lambda^2}\ , \tag{1.1.50}$$

$$\tilde{c}_{\gamma\gamma} = 4\left(\frac{1}{g^2} c_{H\tilde{W}} + \frac{1}{g'^2} c_{H\tilde{B}} - \frac{1}{gg'} c_{H\tilde{W}B}\right)\frac{v^2}{\Lambda^2}\ , \tag{1.1.51}$$

and these translation formula are implemented in the ROSETTA framework [28].

1.1.2.3 Pseudo-Observable

Several phenomenological analyses about the effective couplings of the Higgs boson to SM fields have appeared after its discovery in 2012, mainly based on the κ-framework or signal-strength results reported by ATLAS and CMS.

The purpose of the work presented in Ref. [15] is to provide a generalisation of the "κ-framework" suitable for high-precision studies of on-shell Higgs decays. It relies on the hypothesis the Higgs boson (denoted as h(125)) is a spin zero particle and that there is no new particle with mass below (or around) m_H ∼125 GeV. In this regime the Effective Field Theory (EFT) approach is applicable, and no further assumption have been done in order to specify if the h(125) state is part of $SU(2)_L$ doublet, and global symmetry hypothesis (lepton-universality, CP invariance) are not imposed and can be tested from data. The only key assumption is to neglect terms in the decay amplitudes with a non-vanishing tree-level contribution from local operators with D>6.

The old κ-framework cannot describe modifications of the Higgs-cross sections that cannot be reabsorbed into a simple overall re-scaling with respect to the SM. A set of *effective-couplings* Pseudo-Observable (PO) can be defined to parametrise the on-shell production and decay amplitudes. These can be extracted from the measurements performed in the LHC Higgs analysis.

The $h \to 4f$ amplitudes are particularly interesting since they allow to investigate the effective hW^+W^- and hZZ interaction terms. The purpose of this approach is to probe this interactions in model-independent way taking into account all possible additional contribution to $h \to 4f$ from contact terms and effective Higgs couplings. It is needed to characterise the three point function of the Higgs boson and two fermion currents:

$$\langle 0|\mathcal{T}\{J_f^\mu(x), J_f^\nu(x), h(0)\}|0\rangle \ , \tag{1.1.52}$$

which can be probed by the experiments in $h \to 4f$ decays. Extracting a kinematical structure of the decay from data, it will allow to determine the effective coupling of the h to all the SM gauge bosons, and also to investigate possible couplings to new massive state (New Physics).

It is possible to define a limited set of POs from the momentum expansion of the on-shell electroweak Higgs decay amplitudes around the physical poles due to exchange of SM electroweak gauge bosons. The effective coupling PO that appear in these channels consist of four sets:

- 3 flavour-universal charged-current PO: $\{\kappa_{WW}, \epsilon_{WW}, \epsilon_{WW}^{CP}\}$
- 7 flavour-universal neutral-current PO: $\{\kappa_{ZZ}, \epsilon_{ZZ}, \epsilon_{ZZ}^{CP}\}$ and $\{\kappa_{\gamma\gamma}, \delta_{\gamma\gamma}^{CP}, \kappa_{Z\gamma}, \delta_{Z\gamma}^{CP}\}$
- set of flavour non-universal charged-current PO: $\{\epsilon_{Wf}\}$
- set of flavour non-universal neutral-current PO: $\{\epsilon_{Zf}\}$

in which the number of flavour non-universal PO depends on the fermion species.

Focusing on the $h \to 4f$ neutral currents, it is possible to write a most generic expression of the decay amplitude of an on-shell Higgs boson to $h \to f\bar{f} + f'\bar{f}'$ final state as function of the POs:

$$A = i\frac{2m_Z^2}{v_F}\sum_{f=f_L,f_R}\sum_{f'=f'_L,f'_R}(\bar{f}\gamma_\mu f)(\bar{f}'\gamma_\nu f')T^{\mu\nu}(q_1,q_2) \ , \tag{1.1.53}$$

$$T^{\mu\nu}(q_1,q_2) = \left[F_L^{ff'}(q_1^2,q_2^2)g^{\mu\nu} + F_T^{ff'}(q_1^2,q_2^2)\frac{q_1\cdot q_2 g^{\mu\nu} - q_2^\mu q_1^\nu}{m_Z^2} + F_{CP}^{ff'}(q_1^2,q_2^2)\frac{\epsilon^{\mu\nu\rho\sigma}q_{2\rho}q_{1\sigma}}{m_Z^2}\right] \ , \tag{1.1.54}$$

where $F_L^{ff'}(q_1^2,q_2^2)$, $F_T^{ff'}(q_1^2,q_2^2)$ and $F_{CP}^{ff'}(q_1^2,q_2^2)$ are the form factors which describe the longitudinal and transverse part of the current, as in the SM, and the CP-violating part of the interaction:

$$F_L^{ff'}(q_1^2,q_2^2) = k_{ZZ}\frac{g_Z^f g_Z^{f'}}{P_Z(q_1^2)P_Z(q_2^2)} + \frac{\epsilon_{Zf}}{m_Z^2}\frac{g_Z^{f'}}{P_Z(q_2^2)} + \frac{\epsilon_{Zf'}}{m_Z^2}\frac{g_Z^f}{P_Z(q_1^2)} \ , \tag{1.1.55}$$

$$F_T^{ff'}(q_1^2,q_2^2) = \epsilon_{ZZ}\frac{g_Z^f g_Z^{f'}}{P_Z(q_1^2)P_Z(q_2^2)} + \epsilon_{Z\gamma}\left(\frac{eQ_{f'}g_Z^f}{q_2^2 P_Z(q_1^2)} + \frac{eQ_f g_Z^{f'}}{q_1^2 P_Z(q_2^2)}\right) + \epsilon_{\gamma\gamma}\frac{eQ_f Q_{f'}}{q_1^2 q_2^2} \ , \tag{1.1.56}$$

$$F_{CP}^{ff'}(q_1^2,q_2^2) = \epsilon_{ZZ}^{CP}\frac{g_Z^f g_Z^{f'}}{P_Z(q_1^2)P_Z(q_2^2)} + \epsilon_{Z\gamma}^{CP}\left(\frac{eQ_{f'}g_Z^f}{q_2^2 P_Z(q_1^2)} + \frac{eQ_f g_Z^{f'}}{q_1^2 P_Z(q_2^2)}\right) + \epsilon_{\gamma\gamma}^{CP}\frac{eQ_f Q_{f'}}{q_1^2 q_2^2} \ , \tag{1.1.57}$$

where g_Z^f are the Z-pole PO.

Choosing as example decay channel $h \to 2e2\mu$, the independent contributions of the three form factors to the decay rate are:

$$\frac{d\Gamma^{LL}}{dm_1 dm_2} \propto f_L(m_1, m_2) \sum_{f,f'} |F_L^{ff'}|^2 \ , \qquad \frac{d\Gamma^{TT}}{dm_1 dm_2} \propto f_T(m_1, m_2) \sum_{f,f'} |F_T^{ff'}|^2 \ ,$$
$$\frac{d\Gamma^{CP}}{dm_1 dm_2} \propto f_{CP}(m_1, m_2) \sum_{f,f'} |F_{CP}^{ff'}|^2 \ , \tag{1.1.58}$$

where $m_{1(2)} = \sqrt{q^2_{1(2)}}$ and $f_{L,T,CP}(m_1, m_2)$ are factors function of $q^2_{1(2)}$. By integrating over m_1 and m_2, we can obtain the partial decay rate as:

$$\Gamma(h \to 2e2\mu) = \Gamma(h \to 2e2\mu)^{SM} \times \sum_{j \geq i} X_{ij}^{2e2\mu} \kappa_i \kappa_j \ , \tag{1.1.59}$$

where $X_{ij}^{2e2\mu}$ are numerical coefficients and κ_i are the effective-coupling PO.

Imposing the CP invariance of the Higgs boson, the term $F_{CP}^{ff'}(q_1^2, q_2^2)$ cancels out and the most interesting effects which can be probed by the $H \to ZZ^* \to 4\ell$ analysis are in the $F_L^{ff'}$ term. Then at the end we have 5 POs: k_{ZZ}, ϵ_{ZeL}, $\epsilon_{Z\mu L}$, ϵ_{ZeR}, $\epsilon_{Z\mu R}$ which represent the coupling to the hZZ vertex and the contact terms of the Z boson with leptons respectively.

1.2 The Higgs boson at LHC

The Large Hadron Collider provides $p-p$ collisions at very high energies. It is crucial to know the production modes and the decay channels to search for the Higgs boson.

1.2.1 Production modes

The main Higgs production mechanism at the LHC is the gluon-gluon fusion (ggF) then, ordered by importance, the vector-boson fusion (VBF), the associated production with a gauge boson (VH), the associated production with a pair of top quarks ($t\bar{t}H$), then with a pair of bottom quarks and the production in association with a single top quark (tH). Figure 1.6 shows the Feynman diagrams for different production modes and Figure 1.7 shows the Higgs boson production cross sections in $p-p$ collisions at $\sqrt{s} = 13$ TeV as a function of the Higgs boson mass. Table 1.2 shows the Higgs boson production cross sections for $m_H = 125$ GeV in p-p collisions at $\sqrt{s} = 13$ TeV with their overall uncertainties. The theoretical uncertainties are those associated with limitations of perturbative calculations of the partonic cross sections, which are estimated by varying factorisation and renormalisation QCD scales and, hence, they are frequently referred to as "QCD scale uncertainties". The PDF uncertainties also contribute directly to the overall uncertainties, because different collaborations making PDF fits provide their best-fit parameters with uncertainties, but they do not necessarily lead to the exact same cross sections. For this reason the overall uncertainties cross sections are estimated taking an envelope of all results from different PDF-fitting collaboration. In the end, also the uncertainties on fundamental input parameters, such as α_S, affects the overall uncertainties. The four main production modes are described below.

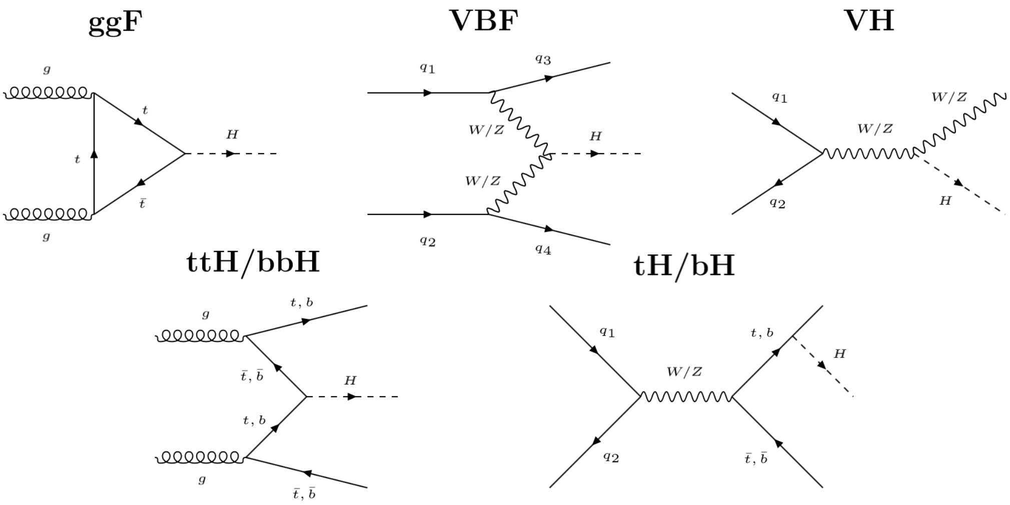

Figure 1.6: Examples of leading-order Feynman diagram for Higgs boson production via ggF, VBF, VH, ttH/bbH and tH/bH production processes.

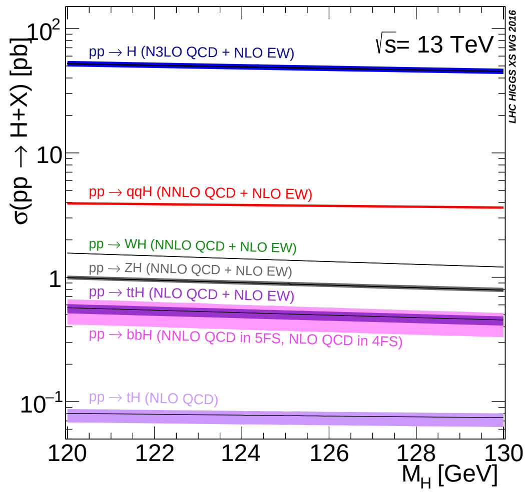

Figure 1.7: Standard Model Higgs boson production cross sections at $\sqrt{s} = 13$ TeV as a function of the Higgs boson mass [25].

Cross section (in pb) $^{+}_{-}$ QCD scale % $\pm$ (PDF + α_s) %							
ggF	**VBF**	**VH**		**ttH+tH**		**bbH**
$48.58^{+4.6\%}_{-6.7\%} \pm 3.2\%$	$3.78^{+0.4\%}_{-0.3\%} \pm 2.1\%$	**WH**	$1.37^{+0.5\%}_{-0.7\%} \pm 1.9\%$	**ttH**	$0.51^{+5.8\%}_{-9.2\%} \pm 3.6\%$	$0.49^{+20.2\%}_{-23.9\%}$
		ZH	$0.88^{+3.8\%}_{-3.1\%} \pm 1.6\%$	**tH**	$0.074^{+6.5\%}_{-14.9\%} \pm 3.7\%$	

Table 1.2: Standard Model Higgs boson production cross section for $m_H = 125$ GeV in p-p collisions at $\sqrt{s} = 13$ TeV with their theoretical uncertainties [25]. The theoretical uncertainty reported for the $b\bar{b}H$ production is the total $^{+}_{-}$ (QCD scale + PDF + α_s) %.

Gluon-gluon Fusion. At high-energy hadron colliders, the Higgs boson production mechanism with the largest cross section is the gluon-fusion process, $gg \to H + X$, mediated by a quark loop in which the heavy top quark gives the main contribution.

Vector-Boson-Fusion. The SM Higgs production mode with the second-largest cross section at the LHC is vector boson fusion. The $qq \to qqH$ process via VBF proceeds by the scattering of two (anti-)quarks, mediated by $t-$ or $u-$channel exchange of a W or Z boson, with the Higgs boson radiated off the weak-boson propagator. The scattered quarks give rise to two jets with high transverse momentum p_T in the forward and backward regions of the detector, respectively.

Associated production with a vector boson. It is also called *Higgsstrahlung* because the Higgs boson is produced in association with W and Z gauge bosons.

Associated production with a pair of top quarks. The Higgs radiation of top quarks, $pp \to t\bar{t}H$, can provide important information on the top-Higgs Yukawa coupling.

1.2.2 Decay channels

According to the Standard Model, the Higgs boson can decay into pairs of fermions or bosons.

The Higgs couplings to the particles are proportional to the particle masses. The heavier is the particle, the stronger the coupling with the Higgs boson is and thus the higher the branching ratio of the Higgs in this channel.

The sensitivity of a search channel for Higgs boson, for a given mass, depends on its production cross section, its decay branching ratio, the reconstructed mass resolution, the selection efficiency and the level of background in the final state. For the Higgs boson with mass $m_H = 125$ GeV, there are five decay channels that play the major role at the LHC. The $H \to \gamma\gamma$ and the $H \to ZZ^* \to 4l$ channels played a key role in the Higgs boson discovery. In fact, in these decay channels, all final state particles can be very precisely measured and therefore they present the best m_H resolution because the $H \to \gamma\gamma$ channel is characterised by a narrow resonant peak above the continuum background and the $H \to ZZ^* \to 4l$

channel has a good signal over background ratio, despite the low branching ratio. The $H \to WW^* \to l\nu l\nu$ decay channel has relatively large branching ratio but the presence of neutrinos affects the m_H resolution. Finally the $H \to b\bar{b}$ and the $H \to \tau^+\tau^-$ channels suffer from large backgrounds and poor mass resolution. Figure 1.8 shows the Higgs boson decay branching ratios as a function of the Higgs boson mass.

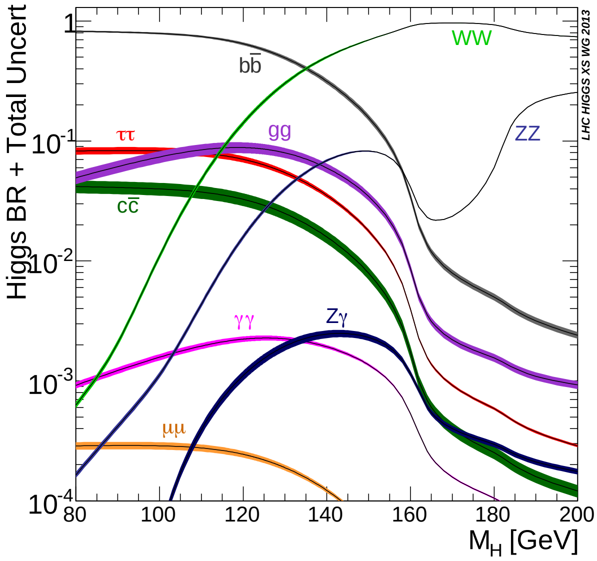

Figure 1.8: Standard Model Higgs boson decay branching ratios as a function of the Higgs boson mass [26].

1.2.3 Status of the Higgs boson measurement at the LHC

With the increasing statistics of the Run 2, large improvements on the precision of the property measurements have been achieved. The results also have been interpreted via theoretical frameworks on top of the κ-framework to put constraints on anomalous couplings of the Higgs boson with the other SM particles and to probe New Physics phenomena.

1.2.3.1 First observations with Run 2

$H \to \tau^+\tau^-$ decay channel

During the early Run 2, the $H \to \tau^+\tau^-$ signal has been observed for the first time by the ATLAS (36.1 fb^{-1}) [31] and CMS experiments (35.9 fb^{-1}) [32]. The analyses have been performed in different event categories designed to target Higgs boson signal from ggF and VBF production, categorising the events on the basis of the number of jets and the Higgs boson transverse momentum.

Combining these results with the Higgs boson decays to τ lepton pairs measurements performed during Run 1 at energies of 7 and 8 TeV, the observed significance amounts to 6.4 σ with ATLAS and to 5.9 σ with CMS experiment. Figures 1.9a and 1.9b show the distribution of the invariant mass of the τ lepton pair $m_{\tau\tau}$.

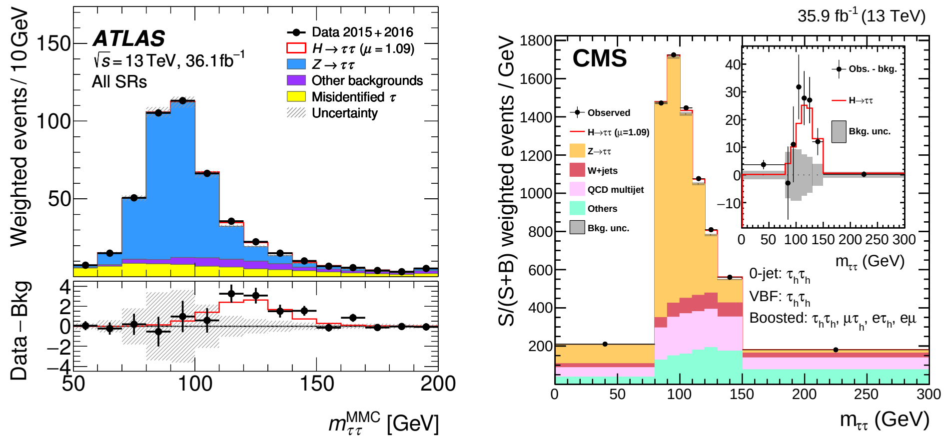

(a) (b)

Figure 1.9: Distribution of the reconstructed di-τ invariant mass $m_{\tau\tau}$ from (a) ATLAS [31] and (b) CMS experiments [32].

ttH production

The detection of the $t\bar{t}H$ production is a direct probe of the Higgs Yukawa coupling to the top quark. During Run 2 both ATLAS and CMS experiments have observed this process for the first time.

ATLAS experiment has combined the $t\bar{t}H$ measurement at 13 TeV performed in $H \to ZZ^* \to 4\ell$ and $H \to \gamma\gamma$ with data collected at 79.8 fb^{-1}with the measurements performed in $H \to b\bar{b}$ and multi-lepton decay channels at 36.1 fb^{-1} [33]. A combined fit using also the results from Run 1 gives an observed (expected) significance of 6.3 (5.1) σ. Figure 1.10a shows the combined $t\bar{t}H$ production cross section, as well as cross sections measured in the individual analyses.

CMS experiment has combined the $t\bar{t}H$ measurements with the 13 TeV data collected at 35.9 fb^{-1}in $H \to ZZ^*, WW^*, \gamma\gamma, \tau^+\tau^-$ and $b\bar{b}$ decay channels to extract the signal strength [34]. Combining the results from Run 1 analyses an observed significance of 5.2 σ has been obtained. Figure 1.10b show the best fit value of the $t\bar{t}H$ signal strength modifier for each decay channel and the combined results.

The overall results for the two experiment are:

$$(\sigma_{\mathrm{ttH}}/\sigma_{\mathrm{ttH}}^{SM})^{\mathrm{ATLAS}} = 1.32^{+0.28}_{-0.26} \qquad \mu_{\mathrm{ttH}}^{\mathrm{CMS}} = 1.26^{+0.31}_{-0.26} \tag{1.2.1}$$

$H \to b\bar{b}$ decays in the VH production

This channel is the one with the highest Branching Ratio ($\sim$ 58%), but it is affected by large backgrounds from multi-jet production, which make the search in the dominant ggF production very challenging. The most sensitive production mode for the decay channel detection is the associated production with a vector boson which decays leptonically. The

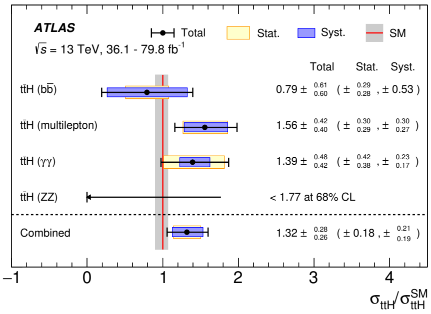

(a)

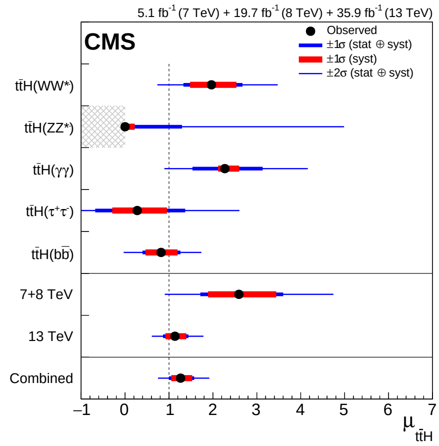

(b)

Figure 1.10: (a) combined $t\bar{t}H$ production cross section, as well as cross sections measured in the individual analyses performed by ATLAS experiment [33]. (b) the best fit value of the $t\bar{t}H$ signal strength modifier for each decay channel and the combined results performed by CMS experiment [34].

first observation of the decay of the Standard Model Higgs boson into a $b\bar{b}$ pair produced in association with a W or Z boson has been done by ATLAS and CMS detectors.

The measurement performed by the ATLAS detector is based on the data corresponding to an integrated luminosity of 79.8 fb^{-1} [35]. The search is performed in final states including 0,1 or 2 charged leptons (depending on the W or Z boson decay) and two identified bottom quark jets. The signal extraction method is performed using multivariate discriminants as fit observable and cross-checked with the dijet-mass analysis, in which the signal is extracted by fitting m_{bb} (Figure 1.11a). The result of the multivariate analysis has been combined with the previous measurements performed during Run 1, with other searches for $b\bar{b}$ decays of the Higgs boson and with other searches in the VH production. The combined results from other searches in Run 1 and in Run 2 for the Higgs boson in the $b\bar{b}$ decay mode show an excess over the expected SM background with an observed (expected) significance of 5.4 (5.5) σ, providing a direct observation of the Higgs boson decay into b-quarks. The measured signal strength relative to the SM expectation is:

$$\mu^{\text{ATLAS}}_{H\to b\bar{b}} = 1.01 \pm 0.12(\text{stat.})^{+0.17}_{-0.15}(\text{syst.}) \tag{1.2.2}$$

Additionally, a combination of Run 2 results searching for the Higgs boson produced in association with a vector boson yields an observed (expected) significance of 5.3 (4.8) standard deviations. Figures 1.12a and 1.12c show the signal strength $\mu_{H\to b\bar{b}}$ and μ_{VH} for individual search channels and their combination.

Similar analysis strategy has been followed also by the CMS experiment in VH, $H \to b\bar{b}$ process, using data collected up to 77.2 fb^{-1}at 13 TeV [36]. A combination of all CMS measurements of the $H \to b\bar{b}$ decay in all the other production modes (Figure 1.12b), yields an observed (expected) significance of 5.6 (5.5) σ and the signal strength is:

$$\mu^{\mathrm{CMS}}_{H\to b\bar{b}} = 1.04 \pm 0.20. \tag{1.2.3}$$

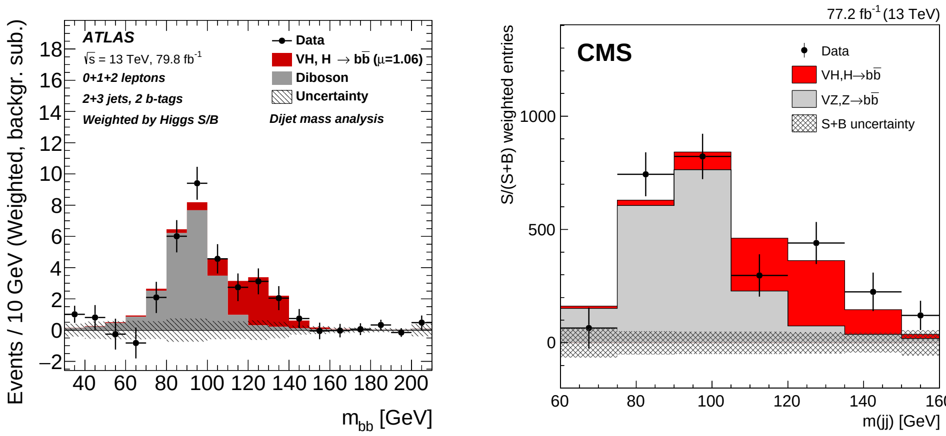

(a) (b)

Figure 1.11: Distribution of the reconstructed di-jet invariant mass m_{bb} from (a) ATLAS [35] and (b) CMS experiment [36].

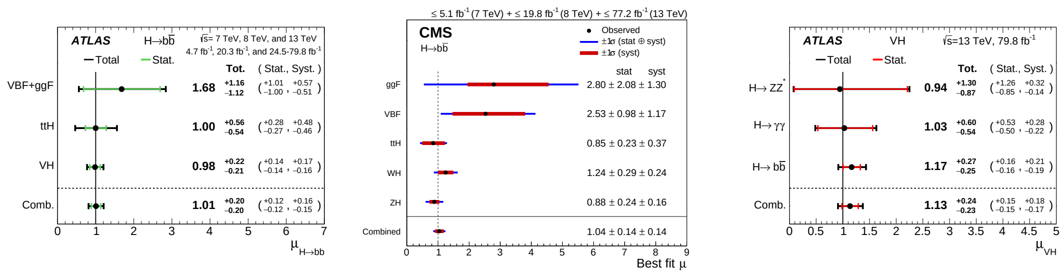

(a) (b) (c)

Figure 1.12: Signal strength $\mu_{H\to b\bar{b}}$ for individual search channels and their combination for the (a) ATLAS [35] and (b) CMS experiment [36]. (c) Signal strength μ_{VH} (b) for each decay channel search and the combined result for the ATLAS experiment [35].

Evidence for rare $H \to \mu\mu$ Higgs boson decay

ATLAS and CMS experiments announced new results which show the first indication of the Higgs boson decay into two muons. This is one of the most rare decay process of the Higgs boson with a branching ratio of 0.23%. These results are crucial because they indicate for the first time that the Higgs boson interacts with second-generation elementary particles.

ATLAS experiment performed the search for $H \to \mu\mu$ decay channel [37] with the full Run 2 statistics. The analysis selects event with two opposite-charge muons and classifies them into mutually exclusive categories based on the event topology (related to the production mode) and multivariate discriminants to increase the signal sensitivity. The signal yield is then extracted from a fit on the dimuon mass $m_{\mu\mu}$. Observed (expected) significance have been found of 2 (1.7) σ with a best-fit value of the signal strength parameter of:

$$\mu^{\text{ATLAS}}_{H\to\mu\mu} = 1.2 \pm 0.6 \tag{1.2.4}$$

The observed upper limit on the cross section times branching ratio for $pp \to H \to \mu\mu$ is 2.2 times the SM prediction at 95% CL, while the expected assuming absence (presence) of a SM signal is 1.1 (2.0).

CMS experiment performed the same search using the full Run 2 statistics of 137 fb^{-1} [38], observing an excess of events in data with a significance of 3.0 σ, where the SM expectation is 2.5. The measured signal strength is:

$$\mu^{\text{CMS}}_{H\to\mu\mu} = 1.19^{+0.41}_{-0.39}(\text{stat})^{+0.17}_{-0.16}(\text{sys}) \tag{1.2.5}$$

Figure 1.13 show the dimuon invariant mass distribution for ATLAS and CMS experiments.

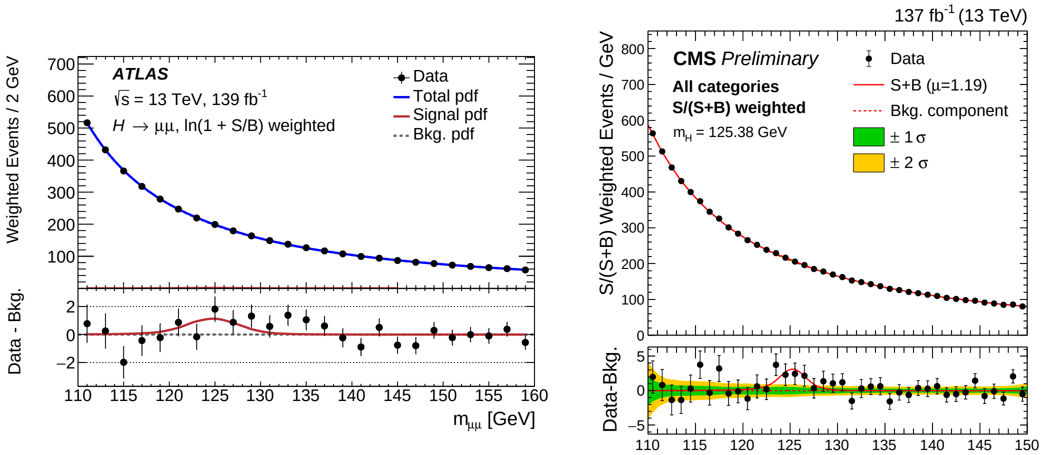

(a) (b)

Figure 1.13: Dimuon invariant mass spectra from (a) ATLAS [37] and (b) CMS experiment [38].

1.2.3.2 Higgs boson mass measurements

The ATLAS and CMS Collaborations have independently measured the Higgs boson mass during Run 1. The Higgs boson mass measurement has been performed in two of the most sensitive decay channels $H \to ZZ^* \to 4l$ and $H \to \gamma\gamma$, because they offer the best mass resolution. Due to their low BR, the total uncertainties on the mass measurement are dominated by the statistical term, and the systematic ones by the experimental effects related to the muon momentum and photon energy scales.

The results in the two channels with the partial Run 2 statistics of 36 fb^{-1} collected by the ATLAS experiment has been combined with the Run 1 results and they are shown in

Figure 1.14a [39]. The combined measurement of the Higgs boson mass is:

$$m_{\rm H}^{\rm ATLAS} = 124.97 \pm 0.24\ (\pm 0.16)\ {\rm GeV} \tag{1.2.6}$$

Same combination has been performed by CMS experiment in these decay channels with the data collected up ti 35.9 fb^{-1}during Run 2 together with the Run 1 results (Figure 1.14b) [41]. The combined measurement is:

$$m_{\rm H}^{\rm CMS} = 125.38 \pm 0.14\ (\pm 0.11)\ {\rm GeV} \tag{1.2.7}$$

Preliminary mass measurement in $H \to ZZ^* \to 4l$ channel with the full Run 2 statistics has been published [40] by ATLAS experiment:

$$m_{\rm H}^{\text{ATLAS-FullRun2}} = 124.92^{+0.21}_{-0.20}\ {\rm GeV} \tag{1.2.8}$$

showing an improvement of about 40% with respect to the previous analysis in this channel.

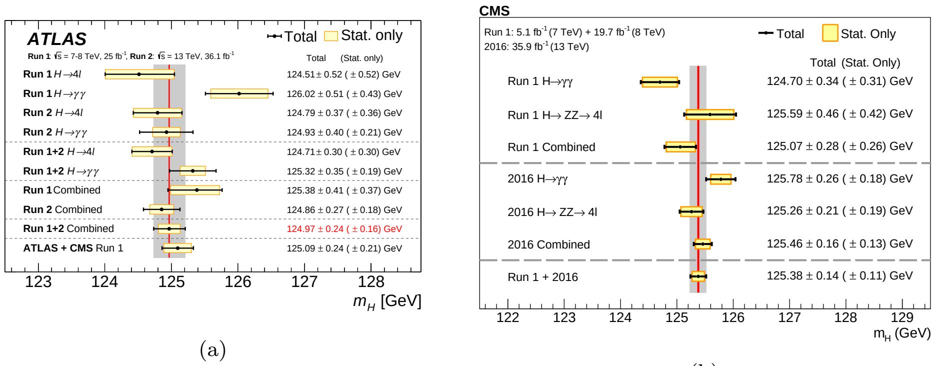

(a)

(b)

Figure 1.14: Summary of Higgs boson mass measurements from the individual analyses of (a) ATLAS and (b) CMS.

1.2.3.3 Spin-CP measurements

The spin-CP of the Higgs boson in the Standard Model is predicted to be $J^{CP} = 0^{++}$, but Beyond Standard Model theories predict the boson with other states of spin or CP, or even a mixture of CP-even and CP-odd states. Measurements of the Higgs spin-parity and tensor structure are based on angular analysis of decays to vector boson pairs. The presence of anomalous non-scalar components would indicate a mixed state and new physics.

Run 1 ATLAS and CMS results During Run 1 several alternatives hypothesis of spin-parity have been tested to assert the Higgs boson as a CP-even scalar particle. In the ATLAS experiment, the hypothesis are based on the Effective Field Theory approach, which assumes a general effective Lagrangian compatible with Lorentz invariance [42]. In contrast, in the

CMS experiment, the spin-CP models are based on an anomalous coupling approach, which assumed the general amplitude compatible with the Lorentz and gauge invariance [43].

The SM hypothesis $J^P = 0^+$ has been compared to alternative spin– models: a pseudo-scalar boson $J^P = 0^-$ and a BSM scalar boson $J^P = 0^+_h$, which describe the interaction of the Higgs boson with the SM vector bosons with an effective couplings. Also graviton-like tensor models with $J^P = 2^+$ have been investigated. The analysis rely on observables chosen to be sensitive to the spin and parity signal in the most sensitive decay channels: $H \to \gamma\gamma$, $H \to ZZ^* \to 4\ell$ and $H \to WW^* \to e\nu\mu\nu$. In these tests of fixed spin and parity hypothesis, it is assumed that the resonance decay involves only one CP eigenstate. Figure 1.15 show the expected and observed distributions of the test statistics of the SM hypothesis against all alternative spin-parity hypotheses for ATLAS and CMS experiments. In all the cases the quantum number predicted by the SM $J^P = 0^+$ are favoured by the data.

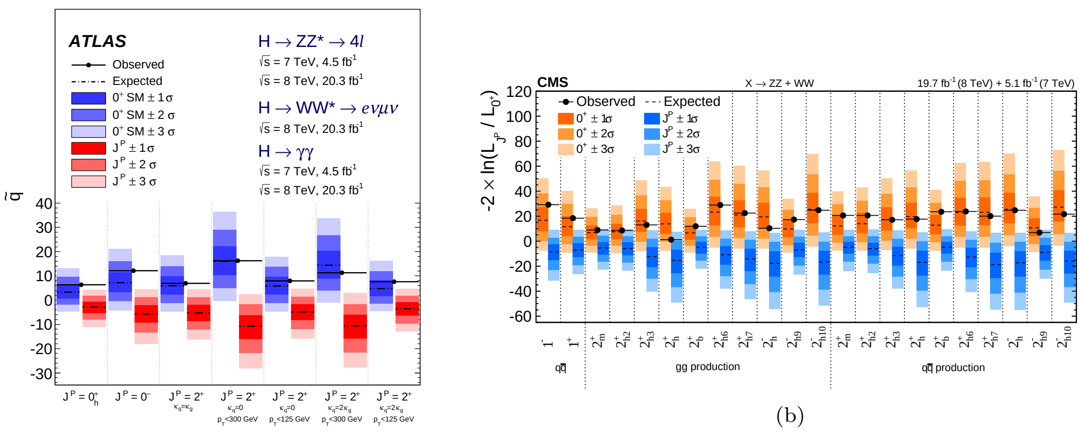

(a)

(b)

Figure 1.15: Distribution of the test statistics of the SM hypothesis $J^P = 0^+$ against the alternative spin-parity hypothesis $J^P = 0^-, 1^+, 1^-, 2^+$ for (a) ATLAS [42] and (b) CMS [43]. The spin-1 hypothesis in in principle excluded due to the observation of the $H \to \gamma\gamma$ decays and the Landau-Yang theorem, which forbids the decay of a spin-1 particle into two massless vector bosons. Then this hypothesis is not shown in the ATLAS results which includes also the $H \to \gamma\gamma$ channel in the combination.

In addition to the fixed hypothesis test, also the possible presence of BSM terms in the Lagrangian describing the HVV vertex of the spin-0 resonance has been investigated, and the relative fractions of the CP-odd and CP-even BSM contributions to the observed Higgs boson decays are constrained.

ATLAS experiment has set limits on the corresponding BSM tensor couplings expressed as the ratio couplings $\tilde{\kappa}_{HVV}/\kappa_{SM}$ and $\tilde{\kappa}_{AVV}/\kappa_{SM} \cdot \tan\alpha$ which are related to the coupling constant corresponding to the interaction of the SM (κ_{SM}), BSM CP-even ($\tilde{\kappa}_{HVV}$) and BSM CP-odd ($\tilde{\kappa}_{AVV}$) spin-0 particle, and α represents the CP-mixing angle. Table 1.3 shows the expected and observed best-fit values of $\tilde{\kappa}_{HVV}/\kappa_{SM}$ and $\tilde{\kappa}_{AVV}/\kappa_{SM} \cdot \tan\alpha$ and 95% CL excluded regions obtained in the combination of $H \to ZZ^* \to 4\ell$ and $H \to WW^* \to e\nu\mu\nu$

analyses.

Coupling ratio combined	Best fit value observed	95% CL Exclusion regions	
		Expected	Observed
$\tilde{\kappa}_{AVV}/\kappa_{SM} \cdot \tan\alpha$	-0.68	$(-\infty, -2.33] \cup [2.30, \infty)$	$(-\infty, -2.18] \cup [0.83, \infty)$
$\tilde{\kappa}_{HVV}/\kappa_{SM}$	-0.48	$(-\infty, -0.55] \cup [4.80, \infty)$	$(-\infty, -0.73] \cup [0.63, \infty)$

Table 1.3: Expected and observed best-fit values of $\tilde{\kappa}_{HVV}/\kappa_{SM}$ and $\tilde{\kappa}_{AVV}/\kappa_{SM} \cdot \tan\alpha$ and 95% CL excluded regions obtained in the combination of $H \to ZZ^* \to 4\ell$ and $H \to WW^* \to e\nu\mu\nu$ analyses from ATLAS experiment [42].

CMS experiment has put limits on the couplings a_i (i=1,2,3) present in the general scattering amplitude which describes interactions of a spin-zero boson with the gauge bosons. In particular a_1 represent the parity-conserving interaction of a scalar Higgs to VV bosons at tree-level, which is related to the Λ_1 BSM physics scale at which a possible new particles can contribute to the HVV vertex; while a_2 is generated through radiative corrections. Finally a_3 represent the parity-conserving interaction of a pseudo-scalar Higgs. Table 1.4 show a summary of the allowed 95% CL intervals on the anomalous couplings in HVV interactions in combination of $H \to ZZ^*$ and $H \to WW^*$ measurements.

Parameter	Observed	Expected
$(\Lambda_1\sqrt{\lvert a_1\rvert})\cos(\phi_{\Lambda_1})$	$(-\infty, -100\text{GeV}] \cup [-103\text{GeV}, \infty)$	$(-\infty, -43\text{GeV}] \cup [-116\text{GeV}, \infty)$
a_2/a_1	$[-0.58, 0.76]$	$[-0.45, 1.67]$
a_3/a_1	$[-1.54, 1.57]$	$[-2.65, 2.65]$

Table 1.4: Summary of the allowed 95% CL intervals on the anomalous couplings in HVV interactions in combination of $H \to ZZ^*$ and $H \to WW^*$ measurements [43].

CP structure of the Higgs boson Yukawa coupling with top quark

In the $H \to \gamma\gamma$ decay, the $t\bar{t}H$ production vertex has been studied to put strong constraint on possibile CP-odd couplings between the Higgs boson and the top quark. The ATLAS experiment has excluded a pure CP-odd coupling (mixing angle $\alpha = 90(180)°$) at 3.9 σ [44]. A comparable study from the CMS experiment excluded $\alpha = 90°$ at 3.2 σ [45]. A possible mixture of CP-even and CP-odd has been investigated. ATLAS has put directly a limit on the mixing angle $|\alpha| < 43°$ at 95% CL. Instead CMS experiment performed the measurement of the quantity:

$$f_{\text{CP}}^{\text{ttH}} = \frac{|\tilde{\kappa}_t|^2}{|\tilde{\kappa}_t|^2 + |\tilde{\kappa}_t|^2}\text{sign}(\tilde{\kappa}_t/\kappa_t) \tag{1.2.9}$$

where κ_t and $\tilde{\kappa}_t$ are the CP-even and CP-odd Yukawa couplings. It is constrained to be $f_{\text{CP}}^{\text{ttH}} = 0.00 \pm 0.33$ at 68% CL.

Test of CP invariance in VBF production

In the $H \to \tau\tau$ decay, the coupling between the Higgs boson and the vector boson has been investigated by ATLAS experiment in the VBF production vertex and described in an Effective Field Theory framework [46]. The parameter $\tilde{d}$ represents the strength of CP violation and it has been constrained to the interval [-0.090,0.035] at the 68% CL, based on the fit of Optimal Observable distribution (Figure 1.16a), a matrix element based variable able to discriminate CP-odd contribution.

CP structure of the Higgs boson Yukawa coupling with τ lepton

CMS experiment has performed the first measurement of the effective mixing angle $\phi_{\tau\tau}$ between a scalar and pseudo-scalar $H\tau\tau$ coupling using the full Run 2 statistics of 137 fb^{-1} [47]. The hypothesis for a pure CP-odd pseudo-scalar boson is rejected at 3.2 (2.3) observed (expected) standard deviations and the observed mixing angle is found to be $4 \pm 17°$, which is compatible with the expected value of $0 \pm 23°$. Figure 1.16b shows a 2-dimensional scan of CP-even κ_τ and CP-odd $\tilde{\kappa}_\tau$ Yukawa coupling.

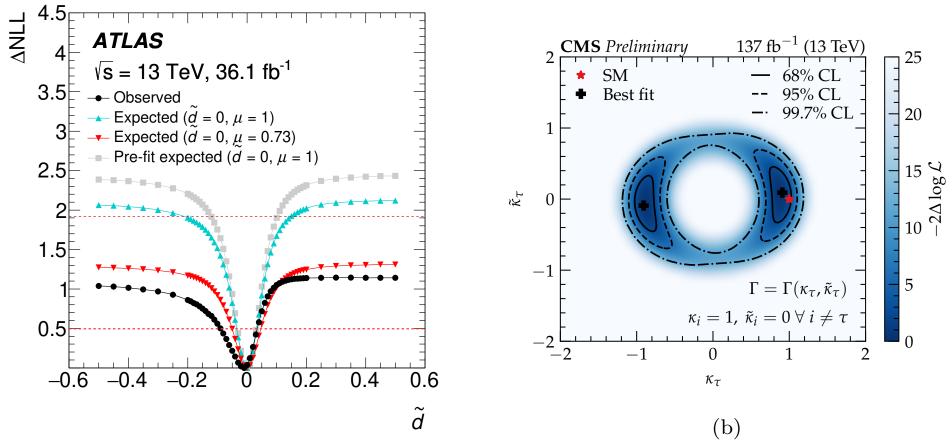

Figure 1.16: (a) The observed and expected negative log-likelihood (NLL) scan curve as a function of $\tilde{d}$ values [46]. (b) Two-dimensional scan of CP-even κ_τ and CP-odd $\tilde{\kappa}_\tau$ Yukawa coupling between Higgs boson and τ lepton [47].

1.2.3.4 Constraints on the Higgs boson width

A direct measurement of Higgs width is limited by the experimental resolution which is orders of magnitude greater than the one needed for the measurement. The $H \to ZZ^*$ decay channel can set a constraint on the Higgs boson width, obtained by measuring the off-shell Higgs boson production event yields normalised to the on-shell $\mu_{\text{off-shell}}/\mu_{\text{on-shell}}$, assuming identical coupling modifiers for on-shell and off-shell Higgs boson.

The combined results in the $ZZ^* \to 4l$ and $ZZ^* \to 2l2\nu$ decay channels using data collected by ATLAS experiment at 36.1 fb^{-1}, set an observed (expected) upper limit on the off-shell signal strength and on the Higgs width:

$$\mu^{\text{ATLAS}}_{\text{off-shell}} < 3.8\ (3.4) \text{ at } 95\%\ CL \qquad (\Gamma_{\text{H}}/\Gamma^{\text{SM}}_{\text{H}})^{\text{ATLAS}} < 3.5\ (3.7) \text{ at } 95\%\ CL. \tag{1.2.10}$$

CMS experiment performed the same measurement using data collected up to 80.2 fb^{-1}and combined the results with those obtained during Run 1. The Higgs boson width is constrained to be:

$$\Gamma_{\mathrm{H}}^{\mathrm{CMS}} = 3.2^{+2.8}_{-2.2} \ , \ [0.08, 9.16] \text{ at } 95\% \ CL. \tag{1.2.11}$$

1.2.3.5 Fiducial inclusive and differential cross section measurements

Fiducial cross sections are measured to minimise the model dependency of the extrapolation to phase-space regions not covered by the detector acceptance and are corrected for detector effects to be directly compared to theoretical calculation.

ATLAS experiment has published new measurement with the full Run 2 statistics in the $H \to \gamma\gamma$ [50] and $H \to ZZ^* \to 4l$ [14] decay channels. This thesis work has contributed to the second analysis. The current measurement of the inclusive fiducial cross section in the $H \to \gamma\gamma$ and $H \to ZZ^* \to 4l$ decay channels are:

$$\sigma^{\mathrm{ATLAS}}_{fid,\gamma\gamma} = 65.2 \pm 7.1 \text{ fb} \ , \tag{1.2.12}$$

$$\sigma^{\mathrm{ATLAS}}_{fid,ZZ\to 4l} = 3.28 \pm 0.32 \text{ fb} \ , \tag{1.2.13}$$

in agreement with the Standard model predictions of 63.6 ± 3.3 fb and 3.41 ± 0.18 fb respectively. A combined measurement in this two channels has been performed [51] and the total Higgs boson production cross section has been measured:

$$\sigma^{\mathrm{ATLAS}}_{tot} = 55.4^{+4.3}_{-4.2} \text{ pb} \ , \tag{1.2.14}$$

in agreement with the Standard model prediction 55.6 ± 2.5 pb.

CMS experiment has performed a combined measurement in the $H \to \gamma\gamma$, $H \to ZZ^* \to 4l$ and $H \to b\bar{b}$ with data collected up to 35.9 fb^{-1} [53]. The measured total cross section is:

$$\sigma^{\mathrm{CMS}}_{tot} = 61.1 \pm 6.0(\text{stat}) \pm 3.7(\text{syst}) \text{ pb} \ . \tag{1.2.15}$$

The more recent results with the full Run 2 statistics in the $H \to ZZ^* \to 4l$ [54] measured a fiducial cross section of:

$$\sigma^{\mathrm{CMS}}_{fid,ZZ\to 4l} = 2.73^{+0.23}_{-0.22}(\text{stat})^{+0.24}_{-0.19}(\text{syst}) \ . \text{ fb} \tag{1.2.16}$$

Differential cross sections measurements have been also performed with observables sensitive to the Higgs-boson production and decay modes. Figure 1.17 shows the differential fiducial cross sections as a function of $p_{T,H}$ and N_{jets} in the $H \to ZZ^* \to 4l$ decay channel measured by ATLAS and CMS. These results have been used to test the couplings of the Higgs boson with Standard Model particles and also to put constraints on anomalous Higgs-boson interactions with them in different theoretical framework. In Chapter 6, the analysis performed in the $H \to ZZ^* \to 4l$ decay channel with the ATLAS detector is described and in Chapter 7 the interpretations of the results are presented.

Figure 1.18 show the combined differential cross section as function of $p_{T,H}$ for the ATLAS experiment using data up to 139 fb^{-1}($H \to \gamma\gamma$ and $H \to ZZ^* \to 4l$) and for the CMS experiment using data up to 35.9 fb^{-1}.

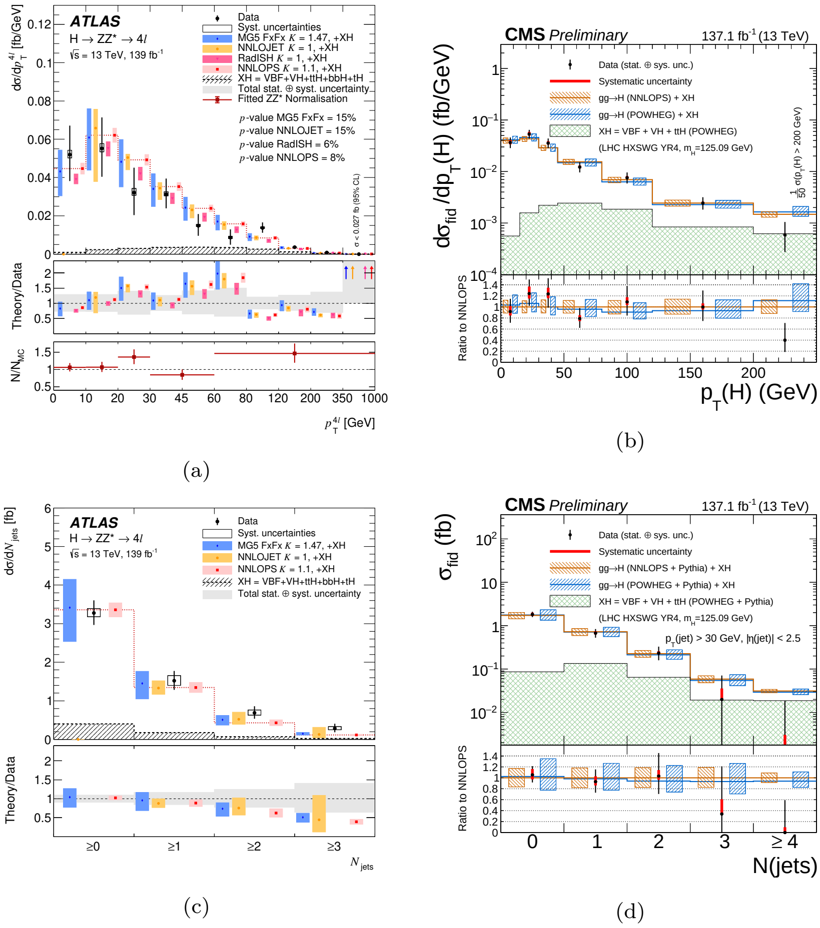

Figure 1.17: (a) - (d) Differential cross sections as function of $p_{T,H}$ and N_{jets} in the $H \to ZZ^* \to 4l$ decay channel measured by ATLAS [14] and CMS [54].

1.2.3.6 Higgs boson production cross section and couplings

The production cross section measurements represent an additional way to probe the strength of the Higgs boson coupling with the other Standard Model particles and test possible beyond SM effects. A way to perform this measurement is in the *Simplified Template Cross Section* framework (STXS) [55], defining exclusive regions of the Higgs phase space (called STXS bins) based on its kinematics and of the particle and jets produced in association to identify the different production modes: the transverse momentum of the Higgs boson p_T^H, the number of jets N_{jets}, the invariant mass of the di-jet system m_{jj} and the transverse momentum of the vector boson p_T^V produced in association with the Higgs. The definitions of the STXS bins are motivated by maximising the experimental sensitivity

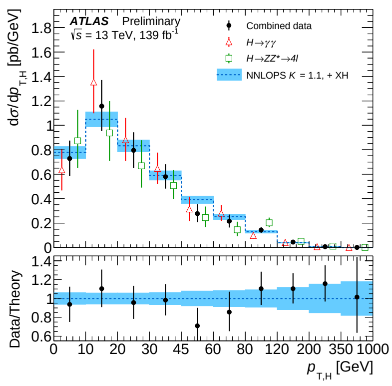

(a)

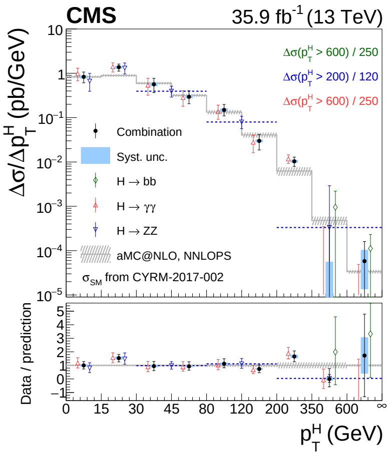

(b)

Figure 1.18: Combined differential cross section as function of $p_{T,H}$ from measurement performed in $H \to \gamma\gamma$ and $H \to ZZ^* \to 4l$ by (a) ATLAS [51] and (b) CMS [53].

and minimising the dependency on theoretical uncertainties. Different STXS stages can be defined, corresponding to increasingly fine granularity, but not all the analyses are sensitive to all the STXS bins. The STXS measurement is performed defining a reco-level categorisation, which is chosen as close as possible to the STXS one to minimise the extrapolation dependency.

The combination of the production cross section measurements in the main processes ggF, VBF, WH, ZH and $ttH + tH$ has been performed by ATLAS experiment (as shown in Figure 1.19a) [56]. The observed significance in each production mode is larger than 5 σ. Also the STXS (Stage 1.2) measurements have been combined and the results show a compatibility with the SM expectation of 95%. On the tH STXS measurement, an upper limit $< 8.4 \times \sigma_{\mathrm{tH}}^{\mathrm{exp}}$ has been set. These results have been interpreted in the well-known κ-framework. An interpretation assuming a universal coupling of vector bosons and fermions κ_V and κ_F has been performed, and also considering the coupling strength to W, Z, t, b,τ and μ independently. To probe BSM effect in the loop, the modified couplings with gluons κ_g and photons κ_γ have been studied. They may contribute to the total Higgs width, which is sensitive to possible invisible decay (B_i) and undetected decay (B_u). The different constraints are put on the couplings based on the different assumptions that have been made. The best-fit values of the Higgs boson coupling modifiers including effective photon and gluon couplings with and without BSM contributions to the total width are shown in Figure 1.19b.

The CMS experiment have combined the production and decay rates of the Higgs boson measurements, providing the results in terms of signal strength, coupling modifiers and also an interpretation in effective field theory, parametrising deviations in the cross section in terms of Wilson coefficients c_i (Figure 1.19c). All the results are found compatible with the SM expectation.

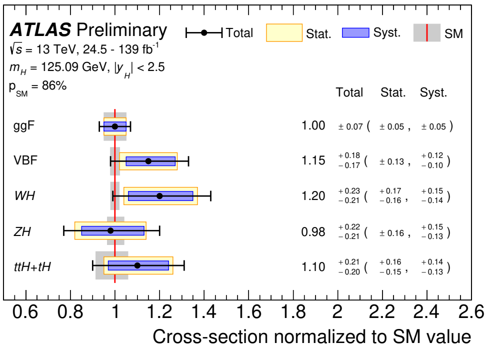

(a)

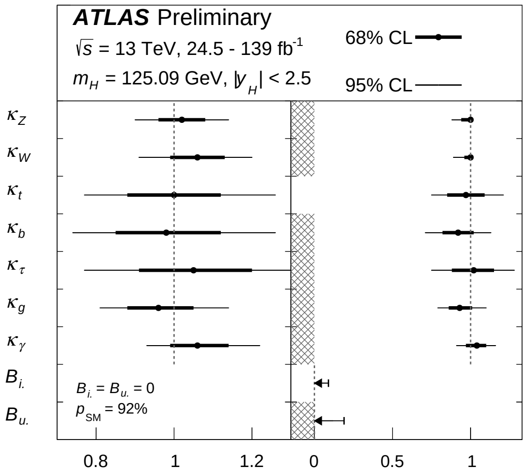

(b)

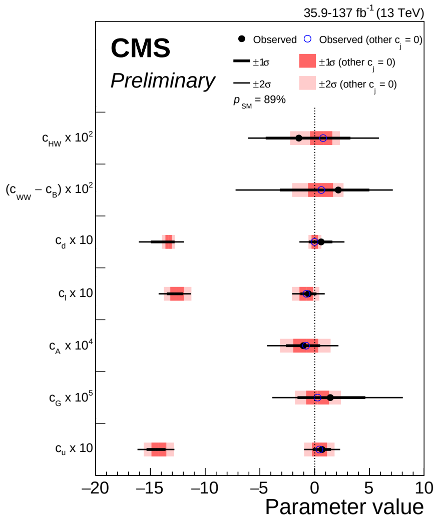

(c)

Figure 1.19: (a) Measured cross sections for ggF, VBF, WH, ZH and $ttH + tH$ normalised to their SM predictions, measured assuming SM values for the decay branching fractions [56]. (b) Best-fit values and uncertainties for Higgs boson coupling modifiers per particle type with effective photon and gluon couplings and either $B_i = B_u = 0$ (left), or include them as free parameters (right) [56]. (c) Summary plot for the effective couplings scans. The best fit values when profiling (fixing) the other parameters are shown by the solid black (hollow blue) points. The $\pm 1\sigma$ and $\pm 2\sigma$ confidence intervals are represented by the thick and thin black lines respectively for the profiled scenario, and the green and yellow bands respectively for the fixed scenario [57].

Chapter 2

The ATLAS Experiment at the LHC

Contents

2.1 The Large Hadron Collider

The Large Hadron Collider (LHC) [58] [59] at CERN is the highest energy collider ever built, dedicated to accelerating and colliding protons. It was designed to provide proton-proton (*pp*) collisions with a centre-of-mass energy of 14 TeV and an instantaneous luminosity of 10^{34} cm^{-2} s^{-1} and also lead-ion collisions at a centre-of-mass energy of 2.76 TeV per nucleon and an instantaneous luminosity of 10^{27} cm^{-2} s^{-1}.

Housed in the tunnel built between 1984 and 1989 for LEP (Large Electron-Positron Collider), the LHC is a 27 km long superconducting hadron collider. The tunnel is located between 45 m and 170 m below the ground surface. LHC magnets are made of niobium-titanium (NbTi) cables and are cooled to less than 2 K with superfluid helium, in order to reach the superconductivity state.

Beams are injected into the LHC in a series of bunches of 1.15×10^{11} protons and every beam is designed to have 2808 circulating proton bunches, arranged in "trains" of 72 bunches with 25 ns spacing within the trains, and 12 empty bunches between two trains. A schematic view of the LHC and the accelerator chain in shown in Figure 2.1.

ATLAS [3], CMS [4], ALICE [60] and LHCb [61] are the four main experiments, located at the interaction regions where the beams cross and are brought to collision. The first two experiments, ATLAS and CMS, are multipurpose, high luminosity detectors and have been designed for the Higgs boson search and new physics searches. ALICE is optimised to study heavy ion collisions, in order to understand quark-gluon plasma; and LHCb is a specialised B-physics experiment and searches for new physics beyond the SM.

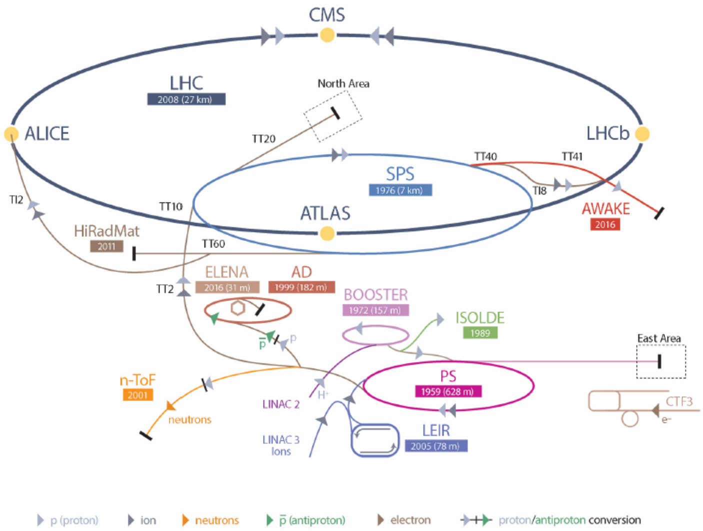

Figure 2.1: The layout of the Large Hadron Collider and the CERN accelerator complex.

Luminosity

The number of events N of a particular process per second generated in LHC collisions depend on the cross section $\sigma(\sqrt{s})$ of the process and the instantaneous luminosity, L, of the accelerator and is given by

$$N = L \cdot \sigma(\sqrt{s}) \ . \tag{2.1.1}$$

The cross section depends on the $\sqrt{s}$ which corresponds to the available energy in the centre of mass frame.

The machine luminosity depends on the beam parameters such as the number of particles per bunch N_b, the number of the bunches n_b, the relativistic gamma factor γ_r, the circulating frequency f_{rev}, the geometric luminosity reduction factor F which is due to the crossing angle at the interaction point, the normalised transverse beam emittance ϵ_n and the transverse beam amplitude β^* at the interaction point according to the relation

$$L = \frac{N_b^2 n_b \gamma_r f_{rev} F}{4\pi \epsilon_n \beta^*} \ . \tag{2.1.2}$$

The integral of the instantaneous luminosity over time, the integrated luminosity:

$$\mathcal{L}_{\text{int}} = \int L dt \ , \tag{2.1.3}$$

gives the amount of recorded events per unit cross section in the time interval. Figure 2.2 shows delivered luminosities as function of time for the 2011-2018 period.

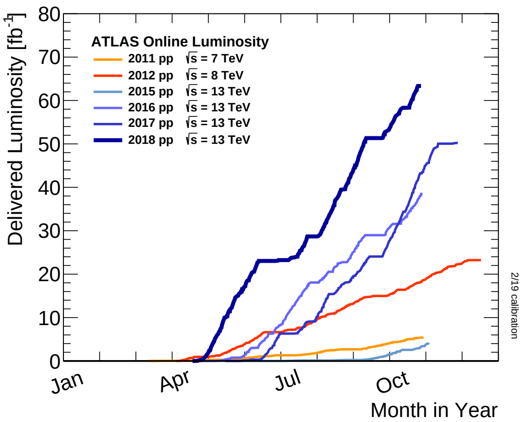

Figure 2.2: Cumulative luminosity versus day delivered to ATLAS during stable beams and for high energy p-p collisions [62].

LHC delivered proton-proton collisions at 7 TeV centre of mass energy in 2011. During this period ATLAS collected an integrated luminosity of about 5 fb^{-1}. Then, the energy was increased up to 8 TeV, allowing ATLAS to collect 20 fb^{-1} during 2012. This data-taking period is called *Run-1*. The ATLAS *Run-2* started in 2015 when LHC delivered proton-proton collisions at 13 TeV. During the 2015 data-taking, ATLAS collected an integrated luminosity of 3.9 fb^{-1}. In 2016 the instantaneous luminosity grow-up, reaching in the 2016 summer the nominal value of 10^{34} cm^{-2} s^{-1} and ATLAS collected an integrated luminosity of 38 fb^{-1}. During 2017 and 2018 ATLAS collected further 49 fb^{-1} and 62 fb^{-1} respectively of integrated luminosity.

Each ATLAS run is divided in several *luminosity blocks*, called simply lumi-blocks, defined as the period of time O($\sim$ 1 min), during which the data-taking is considered “good”. The list of lumi-blocks used the analysis is called *Good Run List* (GRL).

2.2 The ATLAS Detector

The ATLAS (**A** **T**oroidal **L**HC **A**pparatu**S**) detector [3] is a multi-purpose detector designed to exploit a wide range of physics topics at the LHC.

The physics program of the ATLAS experiment covers precision measurements of SM processes at the highest energies; measurement of the properties of the Higgs boson and the search for new physics phenomena beyond the SM, which comprises Supersymmetry searches, high precision tests of QCD, flavour physics and electroweak interactions; measurements of the properties of the top quark and searches for new vector bosons and for extra-dimensions.

The difficulty given by the nature of proton-proton collisions is the QCD jet production cross-sections, which dominate over the rare processes. The identification of such final states for these processes therefore imposes some requirements for the detector:

- Fast, radiation-hard electronics and sensor elements.
- High detector granularity to handle the particle fluxes and to reduce the influence of overlapping events.
- Large acceptance in pseudorapidity with almost full azimuthal angle coverage.
- Good charged-particle momentum resolution and reconstruction efficiency in the inner tracker.
- Very good electromagnetic calorimetry for electron and photon identification and measurements, complemented by full-coverage hadronic calorimetry for accurate jet and missing transverse energy measurements.
- Good muon identification and momentum resolution over a wide range of momenta and the ability to determine unambiguously the charge of muons with high transverse momentum.
- Highly efficient triggering on low transverse-momentum objects with sufficient background rejection.

The ATLAS detector has the typical layout of a collider experiment with a forward-backward symmetry with respect to the collision point with cylindrical *barrel* layers of detectors around the beam pipe and disk-shaped *endcaps* to have the range of coverage of the solid angle as large as possible. A schematic overview of the ATLAS detector is shown in Figure 2.3.

ATLAS is composed of an inner tracking system, calorimeters, and a muon spectrometer. The inner detector provides track, charge and the momentum measurement of charged particles in a solenoidal magnetic field of a cylindrical superconducting coil. The calorimeter system surrounds the inner detector and allows for identification of photons, electrons and hadrons combined with the measurement of their energies. It also measures the missing transverse energy from transverse momentum imbalance due to neutrinos. The outermost sub-system is the muon spectrometer which operates in a toroidal magnetic field of eight superconducting coils in the barrel and the endcaps and provides tracking, identification and momentum measurement of muons, as they are the only charged particles penetrating the whole ATLAS detector.

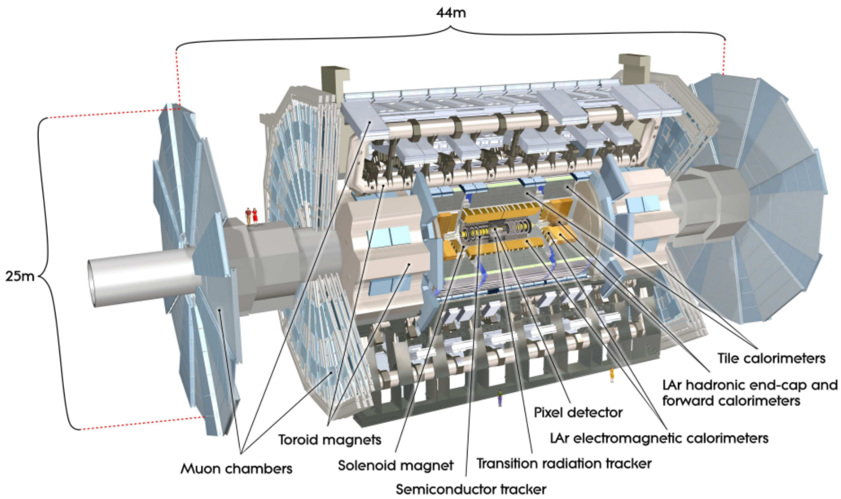

Figure 2.3: The cut-away view of the ATLAS detector. The various detector sub-systems are labelled. The dimensions of the detector are 25 m in height and 44 m in length. The overall weight of the detector is approximately 7000 tonnes [3] .

2.2.1 The Coordinate System

The ATLAS detector uses a right-handed coordinate system with its origin at the interaction point in the center of the detector. The z-axis points along the beam pipe, the x-axis points from the interaction point to the center of the LHC ring and the y-axis points upwards. In the plane transverse to the beam cylindrical coordinates (r, θ, ϕ) are used, where θ is the polar angle measured from the positive z-axis and $r = \sqrt{x^2 + y^2}$ is the radial distance from the interaction point, ϕ is the azimuthal angle around the beam pipe. The pseudorapidity η is defined in terms of the polar angle θ as

$$\eta = -\ln\left(\tan\frac{\theta}{2}\right) \ , \tag{2.2.1}$$

which approaches the rapidity in the limit where $E \gg m$

$$y = \frac{1}{2}\ln\left(\frac{E + p_z}{E - p_z}\right) \ , \tag{2.2.2}$$

where p_z is the longitudinal projection of the particle momentum and E is the particle energy. The pseudorapidity, according to this definition, is zero in the transverse plane and infinity along the z-axis, with $\eta = 1$ at 45° from the axis. The distance between two particles or tracks, in the $\eta - \phi$ plane, is measured by the distance parameter

$$\Delta R = \sqrt{\Delta\eta^2 + \Delta\phi^2}\ . \tag{2.2.3}$$

The energy and momentum of outgoing particles, E and p, are often projected onto the transverse plane: the transverse momentum conservation can be required, since the initial component is known to be zero, whereas the initial component along the z-axis is not known. The transverse momentum and the transverse energy are then

$$p_T = \sqrt{p_x^2 + p_y^2} = p \cdot \sin\theta\ , \qquad E_T = E \cdot \sin\theta\ . \tag{2.2.4}$$

The transverse impact parameter, d_0, is the distance of closest approach of a track to the reconstructed primary interaction vertex in the $r - \phi$ projection. The longitudinal impact parameter, z_0, is the distance of closest approach to the interaction point in the longitudinal z-direction.

2.2.2 The Magnetic Field

ATLAS uses four superconducting magnets to provide the magnetic field for bending charged tracks [63]. This magnetic system is 22 m in diameter and 26 m in length, and it consists of a central solenoid, a barrel toroid and two endcap toroids (Figure 2.4).

Central Solenoid. The central solenoid is aligned on the beam axis and provide a 2 T axial magnetic field for the inner detector. In this way, the field bends tracks in the ϕ direction in the inner detector .

To reduce the material thickness and the resulting energy loss of tracks, the solenoid has a thickness of ∼0.66 radiation lengths (X_0). This required that the solenoid windings and the electromagnetic calorimeter to share a common vacuum vessel.

The single-layer coil is wound with a high-strength conductor consisting of Niobium-Titanium Rutherford cables embedded in a high purity Aluminum stabiliser (Al-stabilised NbTi), cooled to 4.5 K. The flux is returned by the steel of the hadronic calorimeter and its girder structure.

Barrel and endcap Toroids. The barrel toroid and two endcap toroids produce a toroidal magnetic field of 0.5 T and 1 T for the muon detectors in the central and end-cap regions respectively, bending tracks in the η direction in the muon spectrometer.

The cylindrical volume surrounding the calorimeters and both endcap toroids are filled by the magnetic field of the barrel toroid, which consists of eight coils encased in individual racetrack-shaped, stainless-steel vacuum vessels.

Each endcap toroid consists of a single cold mass built up from eight flat, square coil units and eight keystone wedges, bolted and glued together into a rigid structure.

The conductor and coil-winding technology is the same in the barrel and endcap toroids and it is based on winding a pure Al-stabilised Nb/Ti/Cu conductor into pancake-shaped coils, cooled to 4.6 K.

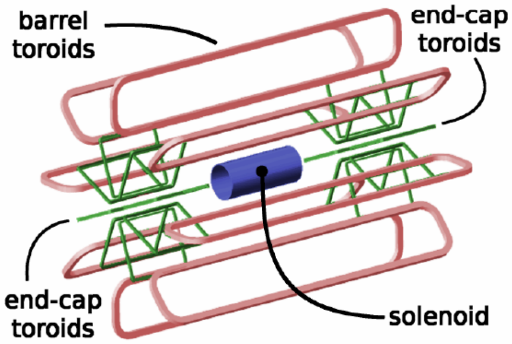

Figure 2.4: The ATLAS magnetic system.

2.2.3 The Inner Detector

The ATLAS Inner Detector (ID) [64] [65] is designed to provide pattern recognition, excellent momentum resolution and both primary and secondary vertex measurements for charged tracks above a given p_T threshold (nominally 0.5 GeV) and within the pseudorapidity range $|\eta|<2.5$. It also provides electron identification for $|\eta|<2.0$ over a wide range of energies (between 0.5 GeV and 150 GeV).

The ID consists of three independent but complementary sub-detectors, as shown in Figure 2.5. At inner radii, high-resolution pattern recognition capabilities are available using discrete space-points from silicon pixel layers and stereo pairs of silicon microstrip (SCT) layers. At larger radii, the transition radiation tracker (TRT) comprises many layers of gaseous straw tube elements interleaved with transition radiation material. With an average of 36 hits per track, it provides continuous tracking to enhance the pattern recognition, improves the momentum resolution over $|\eta|<2.0$ and provides electron identification complementary to that of the calorimeter over a wide range of energies.

Silicon Pixel Tracker. The pixel detector is the closest component to the beam. Formed of layers of silicon pixels, it is designed to have a very high granularity for resolving primary and secondary interaction vertices.

It is composed by three cylindrical layers in the barrel region, closed by an endcap consisting of three disks at each end. The B-layer, the closest layer to the beam pipe, positioned at a radius of 50.5 mm, plays an important role in detecting secondary vertices for the identification of b-jets.

During the first long shutdown, fourth pixel layer inside the existing detector, the Insertable B-Layer (IBL) [66], has been inserted at a radius of 33 mm from the beam axis.

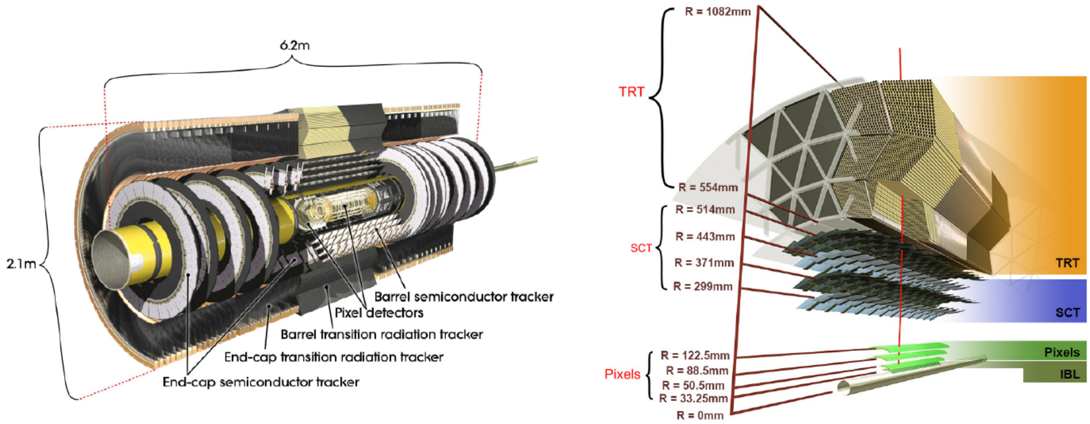

Figure 2.5: The ATLAS Inner Detector (ID) scheme [3] . On the right is shown a detailed layout of th ID including the new Insertable B-Layer (IBL).

The new pixel layer provides an additional space point very close to the interaction point, which keeps the performance of the tracking while the older B-layer continues to degrade, due to the high radiation dose.

The pixel detector allows for a resolution of σ_ϕ=10 µm in the bending direction ($r - \phi$ plane), and σ_z = 115 µm in the z direction. This detector provides uniform coverage in ϕ and up to $|\eta|$<2.5.

Semiconductor Tracker (SCT). The SCT is a silicon strip detector, composed of four barrel layers and two endcaps consisting of nine disks each. The barrel layers consist of 2112 separate modules; each endcap consists of 988 modules, arranged in such a way that a particle will pass through four layers of the detector.

The SCT are based on reverse-biased semiconductor technology. Charged particles passing through the depletion layer of the module junction produce electron-hole pairs, which are swept apart by the bias voltage. The electrons are collected on the top of the chip, producing a signal which can be read out. The spatial resolution of the detector is σ_ϕ=17 µm in the bending direction ($r - \phi$ plane), and σ_z = 580 µm in the z direction.

Transition Radiation Tracker (TRT). The Transition Radiation Tracker is a straw drift tube tracker, with additional particle identification capabilities from transition radiation. It is composed of modules formed from bundles of 4 mm diameter straws, filled with a gas mixture consisting of 70% Xe, 27% CO_2 and 3% O_2. The charge is collected through a tungsten wire that runs down the centre of the tube. Some modifications to the TRT have been made for Run 2, as well as the gas system, that has been modified to use a Ar-based gas mixture.

Charged particles with p_T>0.5 GeV and $|\eta|$<2.0 traverse at least 36 straws, except in the barrel to endcap transition region (0.8<$|\eta|$<1.0) where only 22 straws are traversed. In the bending direction ($r - \phi$ plane in the barrel and $z - \phi$ plane in the endcap) the spatial resolution is σ_ϕ=130 µm. Despite the low resolution compared to the silicon trackers, the TRT contributes significantly to the pattern recognition and momentum resolution due to the large number of measurements and longer measured track length.

2.2.4 The Calorimeters

The ATLAS calorimeter system [67] sit outside the inner detector and its magnetic field. Its purpose is to measure the energy and position of particles. In fact a particle entering the calorimeter produces a shower of secondary particle and the energy of this shower, proportional to the particle one, is then measured.

ATLAS uses sampling calorimeters: different materials are sandwiched together in layers. The absorber layer is used to initiate the shower development, and the active layer to measure the energy of its constituents. This allows for a more compact design and, hence, better shower containment.

The position measurement is obtained by segmenting the calorimeter in the z and ϕ directions. Different absorbers are required depending on whether the particle interacts via the electromagnetic or the strong force, because the nature of the interaction and the shower development is different.

ATLAS calorimeter system is divided into two distinct subsystems: the *electromagnetic calorimeter* and the *hadronic calorimeter*. An electromagnetic shower consists of electrons, positrons and photons, and is normally fully contained in the calorimeter and can be fully detected. Hadronic showers involve many more particle types, including the undetectable ones like neutrons, muons and neutrinos, and tend to be longer and wider. For this reason, the hadronic shower is often not fully contained, the energy is not fully detected and a calibration of the energy response is needed. It is important for the calorimeter to provide good containment of electromagnetic and hadronic showers to allow a good missing transverse energy measurement, and to avoid that the electromagnetic particles and the hadrons reach the muon system.

A cutaway view showing the location of the various calorimeter elements is shown in Figure 2.6. The calorimeters cover the range $|\eta|$<4.9.

Electromagnetic Calorimeter. The electromagnetic (EM) calorimeter (referred to as LAr) uses liquid argon as the active detector material, and lead as an absorber. Charged particles in the shower ionize the liquid argon and the ionising electrons drift to copper electrodes in the presence of an electric field. The LAr consists of two half barrels (referred to as EMB), extending to $|\eta|$<1.475 (with a 4 mm gap at z = 0), and two coaxial wheels on each side (referred to as EMEC), the first covering 1.375<$|\eta|$<2.5 and the second covering 2.5<$|\eta|$<3.2. Both in the barrel and in the endcap region, the calorimeter has an *accordion* structure (Figure 2.7) in order to avoid azimuthal cracks and to provide full ϕ symmetry.

The thickness of the lead layers change as a function of η from 1.5 mm for $|\eta|$<0.8 up to 2.2 mm for 0.8< $|\eta|$<3.2; the radial thickness of the liquid argon volumes is 2.1 mm in the barrel and goes from 0.9 mm up to 3.1 mm in the endcaps. The total active thickness of a

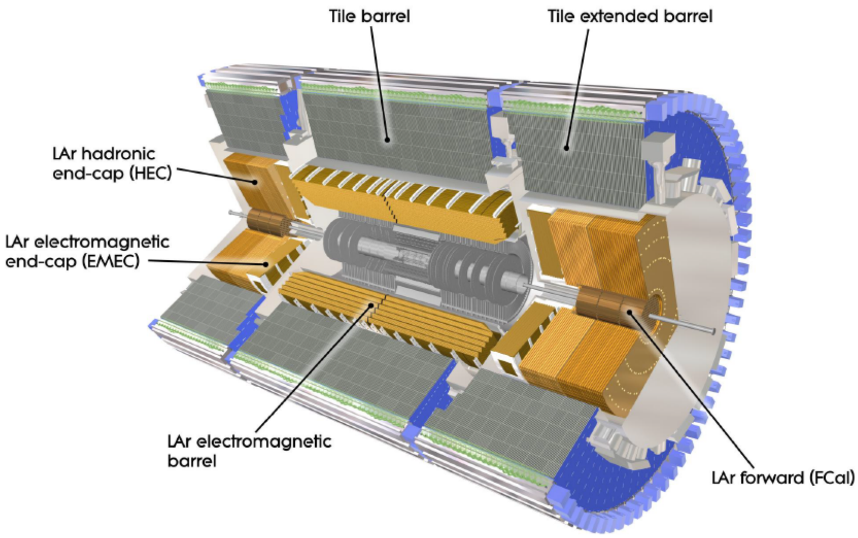

Figure 2.6: The ATLAS Calorimeter System [3] .

barrel module increases as a function of the radiation lengths (X_0), from 22 X_0 to 30 X_0 for $0 \leq |\eta| \leq 0.8$ and goes from 24 X_0 to 33 X_0 between $0.8 \leq |\eta| \leq 1.3$; while, in the endcap, goes from 24 to 38 X_0.

The energy resolution of an electromagnetic calorimeter is given by the relation:

$$\frac{\sigma(E)}{E} = \frac{a}{\sqrt{E}} \oplus \frac{b}{E} \oplus c \; , \tag{2.2.5}$$

where a is the stochastic term, b takes into account the electronic noise, and c is the constant term that reflects local non-uniformities in the response of the calorimeter. For the ATLAS electromagnetic calorimeter, $a = 10\%$, $b = 0.5\%$ and $c = 0.7\%$. In the energy range 15-180 GeV, the reconstructed energy response is linear within $\pm 0.1\%$.

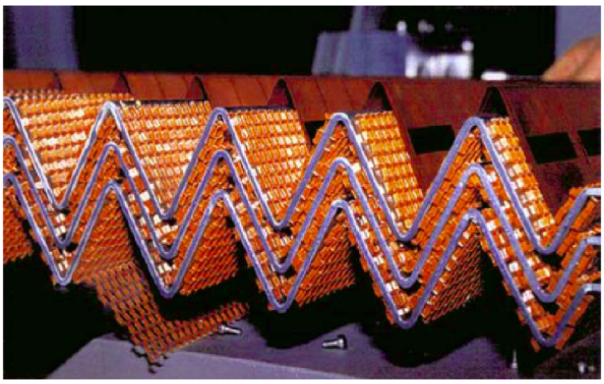

Figure 2.7: The accordion structure of Electromagnetic Barrel Calorimeter. Honeycomb spacers position the electrodes between the lead absorber plates.

Hadronic Calorimeter. The hadronic calorimeter consists of a plastic scintillator tile calorimeter (referred to as TileCal) covering $|\eta|<1.7$ and a liquid argon endcap calorimeter (referred to as HEC), covering $1.5<|\eta|<3.2$.

The TileCal consists of a barrel covering $|\eta|<0.8$ and two extended barrels covering $0.8<|\eta|<1.7$, and is located immediately behind the EM calorimeter. The active material consists of 3 mm thick layers of the plastic scintillator placed perpendicular to the beam direction, sandwiched between steel absorbers. The scintillators are connected at each end to readout photomultiplier tubes by wavelength-shifting fibres.

The HEC consists of two wheels per endcap located directly behind the EMEC and sharing the same cryostat. Each wheel has two layers of cells. The HEC covers $1.5<|\eta|<3.2$ and so overlaps with the Tile calorimeter on one side and the Forward Calorimeter (FCAL) on the other, thus avoiding cracks in the transition regions.

The ATLAS hadronic calorimeter is characterised by two different energy resolution depending on the η region:

$$\frac{\sigma(E)}{E} = \frac{50\%}{\sqrt{E[\text{GeV}]}} \oplus 3\% \qquad |\eta| \leq 3 \ , \tag{2.2.6}$$

$$\frac{\sigma(E)}{E} = \frac{100\%}{\sqrt{E[\text{GeV}]}} \oplus 10\% \qquad 3 \leq |\eta| \leq 5 \ . \tag{2.2.7}$$

The number of the interaction length in the TileCal is about 9 λ, in the endcap regions (including the EMEC) is 12 λ.

The response of the hadronic calorimeter to the non-electromagnetic components of the hadronic shower is different with respect to the electromagnetic components, due to the invisible energy coming from undetectable signals, like neutrinos. The consequence are non-linear response and the degradation of the energy resolution. A hadronic calorimeter needs to compensate for this invisible energy. The compensation has to be made when the fraction of the electromagnetic particles detected by the calorimeter over the hadronic ones e/h is $\neq$1. In the TileCal $e/h \sim 1.4$, then it is an under-compensating calorimeter.

Forward Calorimeter. The forward calorimeter (FCAL) covers the region $3.1<|\eta|<4.9$. To reduce the neutron flux, the FCAL begins 1.2 m away from the EM calorimeter front face. Due to the high particle fluxes and energies in the forward region, the calorimeter must contain relatively long showers in the small volume allowed by design constraints, and thus must be very dense.

The FCAL is divided into three sections. The first is designed for electromagnetic measurements, and uses copper as a passive material with liquid argon as active material. The other two compartments are designed for hadronic measurements, and use tungsten as a passive material, chosen for its high density to provide containment and minimise the lateral spread of hadronic showers.

The number of the interaction lengths in the FCAL is about 10 λ.

2.2.5 The Muon Spectrometer

The ATLAS Muon Spectrometer (MS) [68], shown in Figure 2.8, is the outermost component of the ATLAS detector. It is designed to reconstruct the muon trajectories, measuring the muon momentum independently from the ID, and to provide muon trigger signals. Muons are the only charged particles able to escape from the calorimeter system. The MS is instrumented with precision tracking and trigger detectors.

The MS measures the muon momentum in a pseudorapidity range $|\eta|<2.7$. Within the range $|\eta|<1.4$, the magnetic bending is provided by the large air core toroid. In the range $1.6<|\eta|<2.7$, muon tracks are bent by two smaller air core toroid endcap magnets inserted into the extremities of the barrel toroid. In the region $1.4<|\eta|<1.6$, the magnetic deflection is provided by a combination of barrel and endcap fields.

The MS consists of four different technologies, two connected mainly to the trigger and two mainly connected to the precise tracking. The precision tracking consists of the Monitored Drift Tubes (MDT) and the Cathode Strip Chambers (CSC), while for the trigger measurement, the Resistive Plate Chambers (RPC) and the Thin Gap Chambers (TGC) are used.

The most important parameters that have been optimised in the design phase of this sub-detectors are the resolution in p_T for a good reconstruction of final state decays in two or four muons and the second coordinate measurement with a resolution better than 1 cm in order to obtain a better track reconstruction.

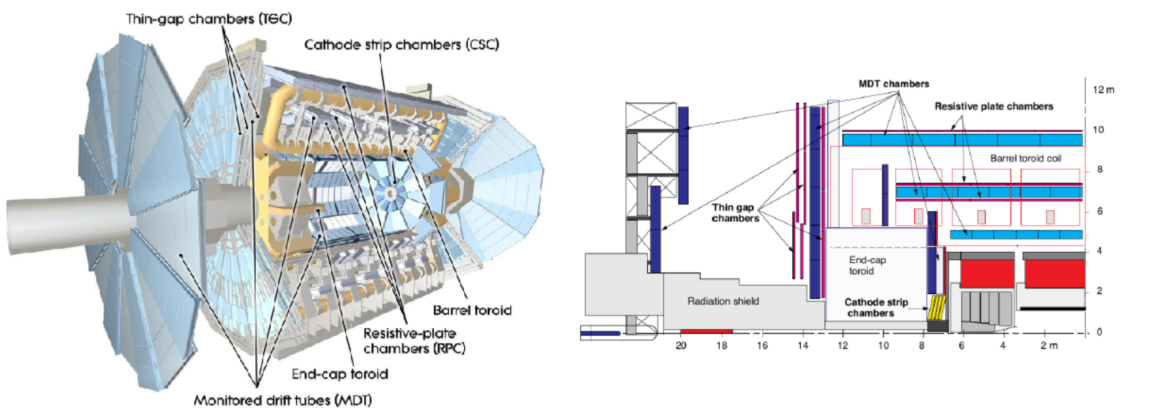

Figure 2.8: The ATLAS Muon Spectrometer [3]. On the right is shown the layout of the muon spectrometer in a quarter of the $y-z$ plane, with the interaction point located in the lower right corner.

Muon Drift Chamber (MDT). The MDT system is composed by 1088 chambers: each chamber is made of two multi-layers of three or four layers of tubes of 29.97 mm diameter and 400 µm thick aluminum walls. When a muon crosses the tube, the gas ionises and the ionising electrons are collected at the central tungsten-rhenium wire (50 µm diameter).

The gas mixture is 93% Ar + 7% CO_2 + 10^3ppm H_2O operating at 3 bar pressure and at 3080 V in order to work in the avalanche regime.

The MDT are located in both the barrel and endcap regions. In the barrel region, $|\eta|<1.3$, the chambers are divided in 16 sectors along ϕ. In each sector, there are large and small chambers. This allows a full coverage and an overlap between chambers that ensure a robust muon momentum measurement. In the endcap, the MDTs cover the region $1.3<|\eta|<2.4$.

Cathode Strip Chamber (CSC). The Cathode Strip Chambers (CSCs) are multi-wire proportional chambers, with the wires oriented in the radial direction and located between $2.0<|\eta|<2.7$. They are designed to provide high precision tracking in the detector region near to the beam pipe.

The CSCs are divided in 16 sectors for each of the two wheels, 8 small and 8 large. The chambers, composed of four layers, overlap to ensure no loss of coverage. The chambers are mounted in the $r-\phi$ plane such that the muon track position will be measured by the interpolation of the induced charges in different strips of the layers.

The gas mixture is Ar+CO_2 and the typical spatial resolution is 40 µm in the magnet field direction and 5 mm in the azimuthal direction. The time resolution is about 7 ns.

Resistive Plate Chamber (RPC). The Resistive Plate Chambers (RPCs) are gaseous detectors used in the barrel in the range $|\eta|<1.05$, to produce the muon trigger signal and to measure the second coordinate in the non bending direction. They are complementary to the MDTs.

The RPC system consists of 544 chambers, located in three concentric layers connected to the MDT. Each chamber has 2 layers of gas gap, filled with a gas mixture of 94.74% $C_2H_2F_4$ (Thetrafluoroethane) + 5% isoC_4H_{10} (isobutane) + 0.3% SF_6 (Sulfur Hexafluoride), where the last one is added to limit the charge avalanches in the chamber. The RPC chambers are made with bakelite plates of 2 mm and readout strips with pitches of about 3 cm. The inner distance between the middle and the outer layers permits the trigger to select tracks with 9 GeV$<p_T<$35 GeV while the two middle chambers provide the low-p_T trigger (6 GeV$<p_T<$9 GeV).

The RPC works at 4.9 kV/mm in order to have a formation of the avalanche along the ionizing track, and provide a time resolution of $\sim$1 ns.

Thin Gap Chamber (TGC). The Thin Gap Chambers (TGCs) are multi-wire proportional chambers dedicated to the trigger system on the endcap part of the ATLAS detector. They cover the forward region in the pseudorapidity range $1.05<|\eta|<2.7$.

The TGCs, like the RPCs, provide also a measurement of the muon track coordinate orthogonal to the one provided by the precision tracking chambers. The nominal spatial resolution for the TGCs is 3.7 mm in the $r-\phi$ plane.

The TGC system is divided in 4 layers, one innermost (TGI) and three in the endcap (TGC1, TGC2 and TGC3). The TGC1 covers $1.05<|\eta|<1.92$, while the others TGC layers cover up to $|\eta|$=2.7. TGC1 is composed of three chambers while TGC2 and TGC3 are composed of two chambers. The gas mixture used for these chambers is 55 %CO_2 and 45% C_5H_{12}. TGC chambers work at 2.9 kV and their time resolution is about 4 ns.

2.2.6 The Trigger System

The trigger system is one of the fundamental component for high-luminosity experiments. The ATLAS Trigger system filters out events, produced by proton-proton collisions in LHC, without physics interest, lowering the average output rate (about 40 MHz) to a level of few hundreds Hz. It is organised in three level: each trigger level refines the decision made by the previous level and it is based on fast and crude reconstruction of physics object like muons, electrons, photons and jets.

The Level-1 Trigger (LVL1)

The Level-1 trigger is the first level of the ATLAS trigger chain [69]. It is a hardware-based trigger and makes a first selection using the RPC and TGC chambers to identify muons with high transverse momenta and the calorimeters for high E_T photons and electrons, jets, τ decaying into hadrons.

Cuts on the energy and p_T are applied and events passing the LVL1 trigger selection are transferred to the next trigger level. The output rate of the LVL1 trigger is lowered from 40 MHz up to ∼100 kHz, with a maximum latency of 2.5 µs required to make the final decision.

In each event, the L1 trigger also defines one or more *Regions-of-Interest* (RoIs), that are the geographical coordinates in η and ϕ of regions within the detector, where its selection process has identified interesting features. The RoI data include the information on the type of identified feature and the passed criteria (e.g. a threshold). This information are subsequently used by the High Level Trigger (HLT).

For the ATLAS Run-II, a new approach for the trigger has also been used. It consists of L1 topological triggers which allows the combination of L1 objects from the Calorimeter and Muon systems to reconstruct interesting kinematic signatures. This is achieved by using FPGAs, which return topological decisions in nearly real time, exploiting particular criteria to accept or reject events, such as isolation requirements, overlap removals, angular relations, invariant mass and global quantities such as the missing transverse momentum.

The High-Level Trigger (HLT)

The final stage of the event selection is carried out by the High Level Trigger [70]. Its selections are implemented using off-line analysis procedures, within an average event processing time of 0.2 s. This stage reduces the event rate from 100 kHz at L1 to an average of about 200 Hz. The HLT is divided in two sub-levels: second-level trigger (LVL2) and the event filter level (EF).

The Level-2 Trigger (LVL2). This level is a software-based trigger that is seeded by the RoI information provided by the LVL1 trigger. The information with full granularity and precision is used to reconstruct within a RoI only the events that satisfy a certain set of selection on the measured quantities of physics object pass this trigger level. The trigger rate is reduced to approximately 2-3 kHz, with an event processing time of about 40 ms.

The Event Filter (EF). This is the final stage of the entire trigger selection and it reduces the event rate to ∼200 Hz. Here only events that pass at least one of the LVL2 trigger algorithm are processed. This level have access to the whole event, using the full granularity and all the ATLAS detector information. The EF use the off-line analysis procedure, such as detailed reconstruction algorithms and the mean processing time for one event at the event filter is ∼4 seconds.

The fully triggered events, also known as *Raw Data*, are stored on tape drives that can be accessed to produce *Event Data Summary* (EDS) files and *Analysis Object Data* (AOD) files which are then used for analysis.

2.2.7 ATLAS Upgrade

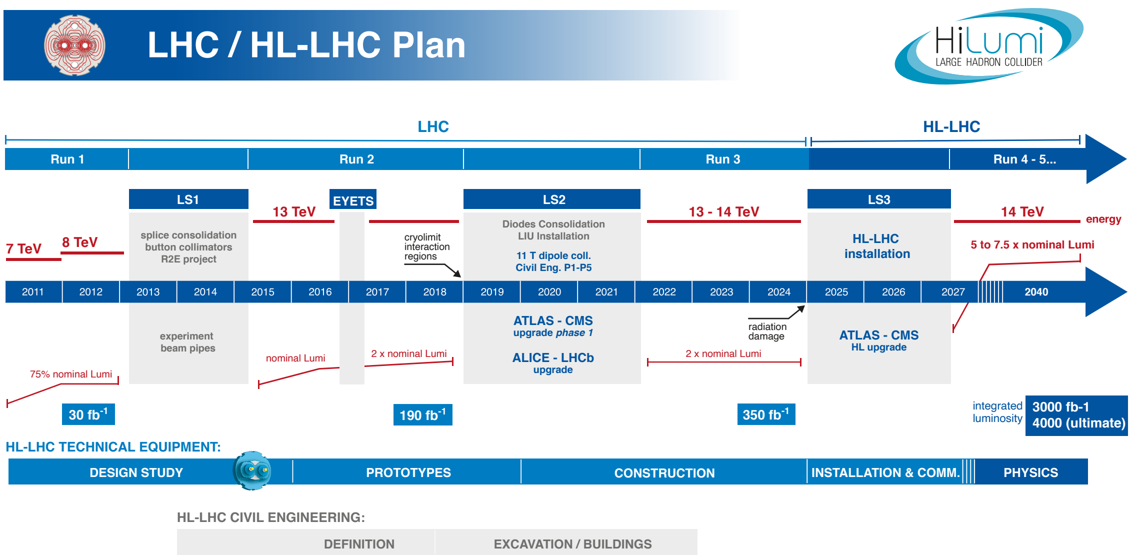

Figure 2.9: LHC plan for High Luminosity.

An upgrade programme is planned for LHC to reach a peak luminosity of 5-7 times the initial design values, and an integrated luminosity of about 3000 fb^{-1}. Upgrades will involve the machine elements, as the triplet magnets, cryogenics, collimators and two new shorter dipoles which produce a stronger magnet fields; as well as the detectors. The luminosity increasing will imply an higher number of interactions per beam crossing, which is called *pile-up*. The expected value at High-Luminosity LHC (HL-LHC) [71] is of about 140 interactions per beam crossing compared to the 30/40 that we have today. This will imply that the detectors will not be able to deal with an increasing of the particle rate.

During the two long shutdown periods (LS2 and LS3), ATLAS will undergo two major upgrade steps called Phase I [5] and Phase II [6] respectively. One of the most important Phase I upgrade is the New Small Wheel project [7], which will be described in Chapter 3 and involves the Muon Spectrometer. Furthermore new trigger readout boards will be implemented in the electromagnetic and forward calorimeters to exploit the longitudinal sampling of the calorimeter as well as including a higher trigger granularity comparable to that presently available in the full calorimeter readout.

During the Phase II the biggest upgrade consists in the replacement of all the Inner Detector with a silicon brand new one, called Inner Tracker (ITk) [72]. It will have a large impact on the physics performance, extending the coverage of the current inner detector, reducing the forward jets pile-up and improving the vertexing capabilities. The very high luminosities also present significant challenges to the performance of the other detector system. Then a new trigger architecture will be implemented exploiting the upgrades of the detector readout systems that will maintain and improve the event selection. Finally also the hadronic endcap calorimeter readout electronics and the forward calorimeter detector design will be upgraded, as well as the MDT/RPC electronics.

2.3 Physics objects definition and reconstruction

In proton-proton collisions, a large variety of processes that involve different particles like leptons, photons and jets are produced. For this reason, it is very important to have an excellent object reconstruction and identification in a wide range of the energy spectrum.

A particle passing through the detector can be identified by combining all the information coming from the tracking devices, the calorimeters, and by detecting radiation emitted by charged particles.

2.3.1 Track and vertex reconstruction

Charged particles that travel the inner detector, have an approximately helical path, due to the homogeneous magnetic field and leave hits in the detector due to the interaction with its various components that they traverse (Pixel, SCT and TRT).

The particle tracks are then reconstructed from these hits in order to identify and measure particles, in a procedure known as tracking. The tracks are used to reconstruct vertices and identify the primary vertex (PV). The PV is defined as the vertex with the largest $\sum_i^N (p_T^i)^2$, where N is the number of tracks associated to each vertex and p_T^i is the transverse momentum of the i-th track. The Figure 2.10 shows the picture of two different events recorded by ATLAS: a proton-proton collision event at 8 TeV with 25 reconstructed primary vertices, in which a $Z \to \mu\mu$ event could be reconstructed, and a proton-proton collision event at 13 TeV with 8 primary vertices.

In the ATLAS ID, the track reconstruction is split into several steps [73]. In the first step, seed tracks are reconstructed using the Pixel and, partially, the SCT information. These tracks are then extended through all the SCT to collect additional hits. As next step, ambiguity needs to be resolved, as several tracks candidates can share the same hits. The track is refitted with a more precise χ^2 fit and a score is assigned to each track. The ambiguities are solved by choosing the track with the largest score. The tracks with limited hits and not passing the quality criteria are rejected. The remaining tracks are extended to the TRT to collect new hits and refit with the full information from all the ID detectors.

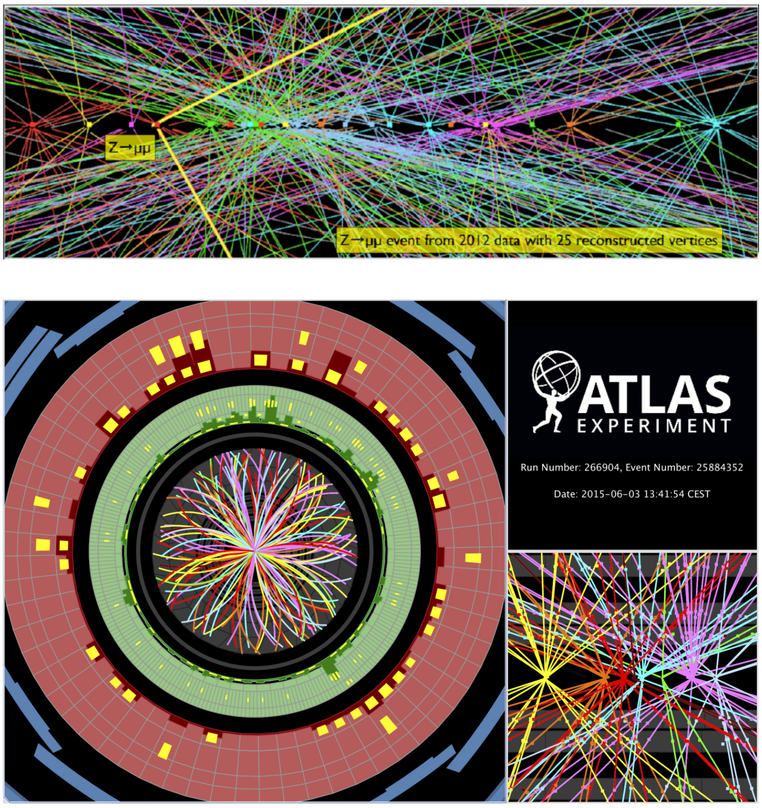

Figure 2.10: *On the top*: Picture of a $Z \to \mu\mu$ event recorded by ATLAS with 25 reconstructed primary vertices in 8 TeV collision. *On the bottom*: Display of a proton-proton collision event recorded by ATLAS on 3 June 2015, with the first LHC stable beams at a collision energy of 13 TeV. Tracks originate from 8 primary vertices recorded in one event.

Particle trajectories in a solenoidal magnetic field can be parametrised with a five parameter vector:

$$\tau = \tau(d_0, z_0, \phi, \theta, q/p) \tag{2.3.1}$$

where d_0 and z_0 are the transverse and the longitudinal impact parameter, which represent the distance between the track and the primary vertex, ϕ and θ are the azimuthal and the polar angles respectively, and q/p is the ratio between the particle charge and its momentum.

Once the tracks are reconstructed using all the ID information, they can be used for vertex reconstruction [74], which is performed by associating the tracks to a particular vertex candidate and performing a fit to determine the exact position. The procedure consist of selecting the tracks in the interaction region and creating a single seed vertex. An iterative fit between the vertex and the tracks is carried out, and tracks are assigned a weight depending on their consistency with the vertex: the process stops when the fit converges. The excluded tracks are used to build a second vertex seed. A fit is performed using the two vertices, and again the remaining tracks are used to fit a new vertex. The procedure stops when none of the remaining tracks fits with any vertex give a χ^2 probability of more than 1%.

2.3.2 Electron reconstruction and identification

Electrons are charged particles that leave tracks in the ID. The electron energy is measured in the ECAL. The identification and reconstruction of electrons in ATLAS is challenging because a good separation from hadronic jets and non-prompt electrons, originating from photon conversions and heavy flavour hadron decays, is needed. Electron candidates are reconstructed from energy clusters in the ECAL which are matched to ID tracks in the region of $|\eta|<2.47$ [75].

The reconstruction proceeds in several steps:

- *Topo-cluster reconstruction.* Clusters of cells are built from the deposit in both ECal and HCal calorimeter [76]. Proto-clusters are selected from cells which have energy significance $E_{cell}/\sigma_{cell}^{noise} > 4$, where E_{cell} is the energy of a single cell and σ_{cell}^{noise} is the expected noise. Neighbouring cells are then added iteratively, lowering the significance threshold to two and then to zero. A proto-cluster is split if it contains two or more cells with E_{cell} >500 MeV and at least four neighbours with lower signal.

- *Track reconstruction.* It consists in two steps. In the pattern recognition step, a track seed (three hits in the ID) with a p_T> 1 GeV, is extended to a full track of at least seven hits using first the pion hypothesis for energy loss and, if it fails, using an electron hypothesis for larger energy losses. Tracks that have significant number of precision hits ($\geq$4) and are loosely associated to electron clusters are refit using an optimised *Gaussian Sum Filter* (GSF), which takes into account the non-linear bremsstrahlung effects.

- *Cluster-track matching.* Tracks are considered matched if $|\eta_{track} - \eta_{clus}| < 0.05$ and $-0.10 < q \cdot (\phi_{track} - \phi_{clus}) < 0.05$, where q is the charge associated to the track and the cluster coordinate are taken as the second layer cell barycentre. In case of several matched track, the one with the best ΔR is kept.

- *Super-cluster reconstruction.* The track-matched topo-cluster are used to build a *supercluster*. This method consists of including additional *satellite* clusters to the cluster selected as the *seed* cluster (Figure 2.11). In this way clusters coming from bremsstrahlung radiation are taken into account. The seed topo-cluster is required to have energy greater than 1 GeV and with an associated track with at least four silicon hits. A cluster is considered satellite for an electron if it falls within a window of $\Delta\eta \times \Delta\phi = 0.075 \times 0.125$ around the seed cluster barycentre and also if it is in a window of $\Delta\eta \times \Delta\phi = 0.125 \times 0.300$ and share the same track as of the seed cluster. Finally an ambiguity resolution algorithm is applied on the superclusters to determine if it belongs to an electron or to a photon.

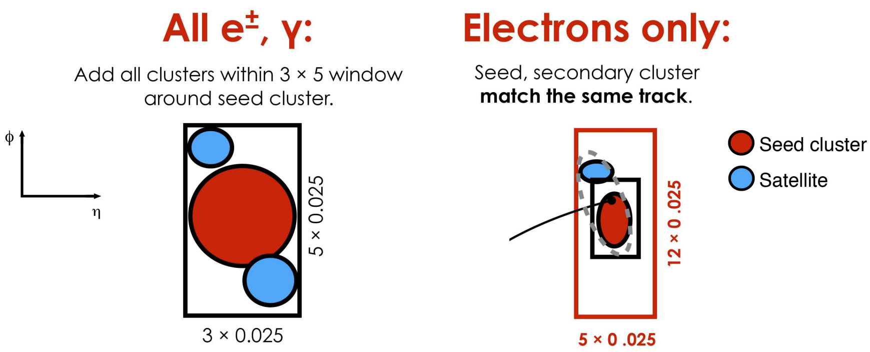

Figure 2.11: Diagram of superclustering algorithm for electrons. Seed clusters are shown in red, satellite clusters in blue.

To determine whether the reconstructed electron candidates are signal-like objects or background-like objects such as hadronic jets or converted photons, algorithms for electron identification (ID) are applied. The ID algorithms use quantities related to the electron cluster and track measurements including calorimeter shower shapes, information from the transition radiation tracker, track-cluster matching related quantities, track properties, and variables measuring bremsstrahlung effects to distinguishing signal from background.

For Run 2, the number of hits in the IBL pixel layer is also used for discriminating between electrons and converted photons because it provides measurement of space point very close to the primary vertex. Furthermore, a likelihood method based on the TRT high-threshold hits is introduced to compensate for the lower transition radiation absorption probability of the argon.

The re-optimization of the ID algorithms for Run-2 is based on MC simulation samples. Electron candidates from MC simulations of $Z \to ee$ and dijet events are used, in addition to $J/\phi \to ee$ and minimum bias events at low E_T. The baseline ID algorithm used for Run-2 data analyses is the likelihood-based (LH) method. It is a multivariate analysis (MVA) technique that simultaneously evaluates several properties of the electron candidates when making a selection decision. The LH method uses the signal and background probability density functions (PDFs) of the discriminating variables and an overall probability is calculated for the object to be signal or background.

Three levels of identification operating points are typically provided for electron ID: *Loose*, *Medium* and *Tight*, in order of increasing background rejection. The distributions of electron shower shapes depend on the amount of material the electrons pass through, and therefore vary with the $|\eta|$ and the E_T of the electron candidates. The performance of the

LH identification algorithm is illustrated in Figure 2.12. Depending on the operating point the identification efficiency varies with increasing E_T: for Loose (Tight) operating point it varies from 86% (58%) at $E_T = 4.5$ GeV to 95% (88%) at $E_T = 100$ GeV.

The $H \to ZZ^{(*)} \to 4\ell$ analysis uses the Loose operating point, providing the highest identification efficiency, but also the lowest background rejection.

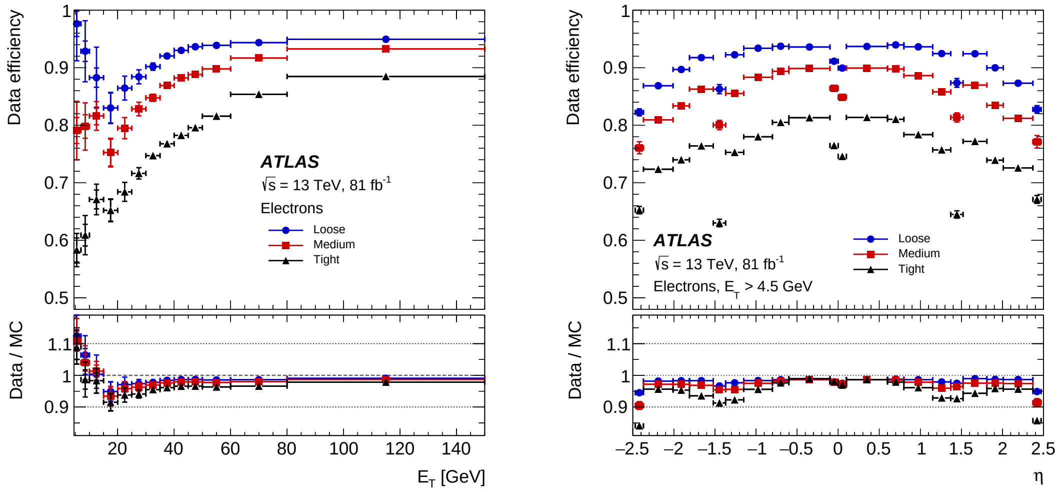

(a)

(b)

Figure 2.12: The efficiency to identify electrons from $Z \to ee$ decays as function of (a) E_T and as function of (b) η for Loose, Medium and Tight operating point [75].

In addition to the identification criteria described above, most analyses require electrons to fulfill isolation requirements, to further discriminate between signal and background. The isolation variables quantify the energy of the particles produced around the electron candidate and allow to disentangle prompt electrons (from heavy resonance decays, such as $W \to e\nu$, $Z \to ee$) from other, non-isolated electron candidates. Two discriminating variables have been designed for that purpose:

- a *calorimetric* isolation energy, E_T^{cone20}, defined as the sum of transverse energies of topological clusters within a cone of $\Delta R = 0.2$ around the candidate electron cluster.
- a *track* isolation, $p_T^{varcone20(30)}$, defined as the sum of transverse momenta of all tracks within a cone of $\Delta R = min(0.2(0.3), 10\ GeV/E_T)$ around the candidate electron track and originating from the reconstructed primary vertex of the hard collision.

The implementation of isolation criteria is specific to the physics analysis needs, as it results a compromise between a highly-efficient identification of prompt electrons, isolated or produced in a busy environment, and a good rejection of electrons from heavy-flavour decays or light hadrons misidentified as electrons. The details on the isolation working point used in the $H \to ZZ^{(*)} \to 4\ell$ analysis are described in Section 5.2.

2.3.3 Muon reconstruction and identification

Muon reconstruction is firstly performed independently in the ID and MS [77]. The information from individual sub-detectors is then combined to form the muon tracks that are used in physics analyses. In the ID, muons are reconstructed like any other charged particles as described in the Section 2.3.1.

Muon reconstruction in the MS starts with a search for hit patterns inside each muon chamber. In the selected areas, close hits in the same chamber are fitted in a straight line to produce *segments*. In each MDT chamber and nearby trigger chamber, the hits aligned on a trajectory in the bending plane of the detector are searched. The RPC or TGC hits measure the coordinate orthogonal to the bending plane. Segments in the CSC detectors are built using a separate combinatorial search in the η and ϕ detector planes.

Muon track candidates are then built by fitting together hits from segments in different layers. The algorithm used for this task performs a segment-seeded combinatorial search that starts by using the segments generated in the middle layers of the detector where more trigger hits are available as seeds. The search is then extended to use the segments from the outer and inner layers. The segments are selected using criteria based on hit multiplicity and fit quality and are matched using their relative positions and angles.

At least two matching segments are required to build a track, except in the barrel–endcap transition region. The same segment can initially be used to build several track candidates, but later, an overlap removal algorithm selects the best assignment to a single track, or allows for the segment to be shared between two tracks. The hits associated with each track candidate are fitted using a global χ^2 fit. A track candidate is accepted if the χ^2 of the fit satisfies the selection criteria.

Four different types of muons are defined in ATLAS, depending on which sub-detectors are used in reconstruction. They are listed below:

- *Combined (CB) muons*: track reconstruction is performed independently in the ID and MS, and a combined track is formed with a global fit that uses the hits from both the ID and MS sub-detectors. Muons are firstly reconstructed in the MS and then extrapolated inward and matched to an ID track. They are the most commonly used muons in physics analyses since they have the highest purity and the best resolution. An alternative algorithm is used to built what are called *Inside-out (IO) combined muons*. It requires an ID reconstructed track and hits in the MS (without requiring a MS reconstructed track). In this case, the trajectory is reconstructed by extrapolating the ID tracks to the MS in order to search for MS hits to be used in a combined fit track. The combined muons are defined only in the region $|\eta| < 2.5$.

- *Segment-tagged (ST) muons*: a track in the ID is classified as a muon if, once extrapolated to the MS, it is associated with at least one local track segment in the MDT or CSC chambers. ST muons are used when muons cross only one layer of MS chambers, either because of their low p_T or because they pass through regions with reduced MS acceptance.

- *Calorimeter-tagged (CT) muons*: a track in the ID is identified as a muon if it can be matched to an energy deposit in the calorimeter compatible with a minimum-ionising particle (MIP). This kind of muon has the lowest purity with respect to all the other muon types but they allow to recover the acceptance in regions where the MS is partially instrumented. The identification criteria for CT muons are optimised for that region ($|\eta|$<0.1) and a momentum range of 15 < p_T<100 GeV.

- *Stand-Alone (SA) muons* or *Extrapolated (ME) muons*: the muon trajectory is reconstructed based only on the MS track and a loose requirement on compatibility with originating from the interaction point. The muon is required to traverse at least two layers of MS chambers to provide a track measurement. SA muons are mainly used to extend the acceptance for muon reconstruction into the region 2.5<$|\eta|$<2.7, which is not covered by the ID.

Muon identification is performed by applying quality requirements that suppress background, mainly from pion and kaon decays, while selecting prompt muons with high efficiency and/or guaranteeing a robust momentum measurement. The identification algorithm uses the following variables for CB tracks:

- *q/p significance*, the absolute value of the difference between ratio of the charge and momentum of the muons measured in the ID and MS divided by the quadrature sum of the corresponding uncertainties.

- ρ', the absolute value of the difference between the p_T measurements in the ID and MS divided by the p_T of the combined track.

- normalised χ^2 of the combined track fit.

Five muon identification selections (*Loose, Medium, Tight*, *High-*p_T and *Low-*p_T) are provided to address the specific needs of different physics analyses. In the *Loose, Medium*, and *Tight* categories, such as in the electron case, the selected muons that pass tighter requirements are also included in the looser categories.

- *Loose muons*: the *Loose* identification criteria are designed to maximise the reconstruction efficiency while providing good-quality muon tracks and it is optimised for the Higgs searches. All muon types are used. It accepts CB and SA muons requiring to have at least two precision stations except in the region $|\eta| < 0.1$, where muons are included but can have at most one muon precision station. The q/p significance must be less than 7 to ensure a loose compatibility between the ID and MS measurements. The acceptance is extended outside the ID coverage by including SA muons with at least three precision stations in the range $2.5 < |\eta| < 2.7$. CT and ST muons are restricted to the $|\eta|$<0.1 region. In the region $|\eta|$<2.5, about 97% of the *Loose* muons are CB or IO.

- *Medium muons*: the *Medium* identification criteria provide the default selection for muons in ATLAS. This selection minimises the systematic uncertainties associated with muon reconstruction and calibration. Only CB (including IO) tracks within the ID acceptance $|\eta|<2.5$ and SA tracks within $2.5 < |\eta| < 2.7$ are used. They have the same requirements of the *Loose* working point. In the region $|\eta| < 2.5$, more than 98% of the muons are CB muons.

- *Tight muons*: the *Tight* selection maximises the purity of muons at the expense of an higher inefficiency. Only CB (including IO) muons with hits in at least two stations of the MS and satisfying the *Medium* selection criteria are considered. Requirements are placed on the normalised χ^2 of the combined track fit, on the q/p significance and on ρ' depending on the p_T and $|\eta|$ of the muon.

- *High-p_T muons*: the *High-p_T* selection aims to maximise the momentum resolution for tracks with transverse momentum above 100 GeV. The selection is optimised for searches for high-mass Z' and W' resonances. CB muons passing the *Medium* selection and having at least three hits in three MS stations are selected.

- *Low-p_T muons*: the *Low-p_T* selection targets the lowest-p_T muons which are less likely to be independently reconstructed as full tracks in the MS, so that the identification based on MS segments is necessary. Two versions of the Low-p_T WP have been developed: a cut-based selection, which reduces the kinematic dependencies of the background efficiencies, and a multivariate WP which maximises the overall performance.

Muon reconstruction efficiency as a function of $|\eta|$ is shown in Figure 2.13 for *Loose*, *Medium* and *Tight* muons.

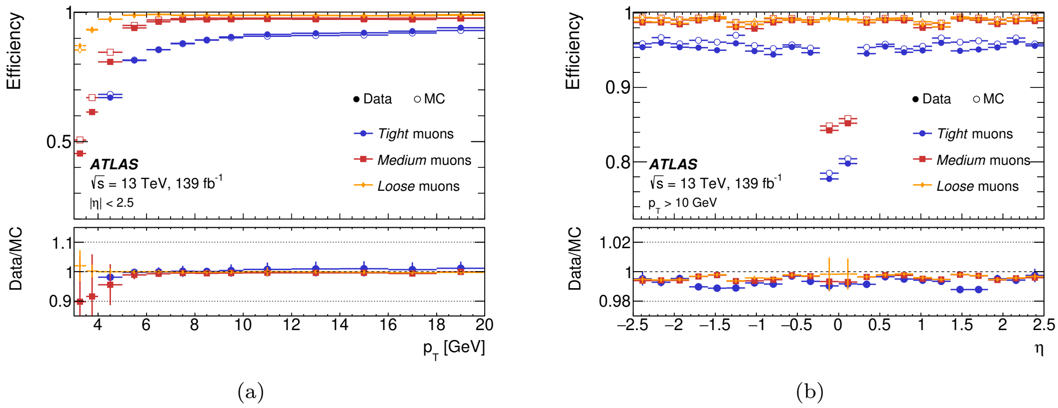

Figure 2.13: Muon reconstruction and identification efficiency for *Loose, Medium* and *Tight* criteria (a) from $J\psi \to \mu\mu$ events as function of p_T and (b) from $Z \to \mu\mu$ events as function of η for muons with $p_T > 10$ GeV(*on the right*) [77].

As done for the electrons, an isolation requirement on the muons is applied to improve the separation from fake muons. Based on the same variables defined in the previous section, several working points have been defined by ATLAS. The details on the isolation working point used in the $H \to ZZ^{(*)} \to 4\ell$ analysis are described in Section 5.2.

2.3.4 Jet reconstruction and identification

Quarks and gluons produced in particle interactions hadronise and produce collimated *jets* of particles. The goal of jet reconstruction is to combine those particles in order to obtain a physics object describing the characteristics of the initial parton.

For the jet reconstruction, an algorithm which combines tracking information and energy deposits in the calorimeters is used and it is called *particle flow* [78]. It does a cell-based energy subtraction to remove the overlap between them. Each track is matched to a single topo-cluster by a reduced error-corrected angular separation and its energy-momentum compatibility. The expected energy deposit in the cluster is then calculated based on cluster position and track momentum. The expected energy is then subtracted cell by cell from the set of matched clusters. Finally, if the energy in the system is consistent with the expected shower fluctuations of a single particle's signal, the topo-cluster remnants are removed. If the remnant energy is above the threshold, the clusters are kept and treated as additional particles. This procedure is applied to tracks sorted in descending p_T-order, firstly to the cases where only a single topo-cluster is matched to the track, and then to the other selected tracks.

Particle flow jets are reconstructed using $anti - k_t$ algorithm [79]. It is a clustering algorithm that builds jets with an iterative procedure. The main input object of the $anti-k_t$ algorithm are the topological clusters surviving the energy subtraction step and the selected tracks that are matched to the hard-scatter primary vertex.

This algorithm combines objects according to the distance parameters

$$d_{i,j} = \min\left(p_{T,i}^{-2}, p_{T,j}^{-2}\right) \cdot \frac{\Delta R}{R} \qquad \text{and} \qquad d_{i,beam} = p_{T,i}^{-2} \tag{2.3.2}$$

where $p_{T,i}$ is the transverse momentum of object i and ΔR is the distance between the topological clusters i and j. The parameter R controls the size of the jet and for the particle flow jets R is equal to 0.4. The four-momentum of the jet is simply the four-momenta sum of the constituent objects.

The energy of the jets reconstructed in ATLAS needs to be calibrated to the true energy of the corresponding jet of stable hadronic particles. The calibration takes into account several effects, such as the non-compensation of the hadronic calorimeters, the leakage effects when the showers reaching the outer edge of the calorimeters, the pile-up, the energy deposits below noise threshold and the energy lost in inactive areas of the detector [78].

b-tagging.

The identification of jets coming from b-quarks fragmentation (*b-tagging*), is crucial for analyses looking for one or more b-quarks in the final state. For example, the ttH production mode, which contains two top quarks that decay exclusively into bottom quarks ($t \to Wb$) [80].

Three different b-tagging algorithm are used in ATLAS. A log-likelihood-ratio-based algorithm, $IP3D$, takes track impact parameters as input to assign a weight to all the tracks which are then combined as the score of the jet. The $SV1$ algorithm instead attempts to reconstruct the secondary vertex fitting the track associated with the jet. Finally the $JetFitter$ algorithm reconstruct the decay chains from the interaction point through the $b-$ and $c-$ hadrons inside the jets using Kamal filters.

The final algorithm is a based on Multi-Variate Analysis (MVA) techniques, $MV2c10$, which combines the output of the three algorithms into a Boosted Decision Tree (BDT). The working point are defined by making cut on BDT score to achieve b-jets efficiencies of 85%, 77%, 70% and 60%. The distribution of the output discriminant of the algorithm for b-jets, c-jets and *light*-jets is shown in Figure 2.14.

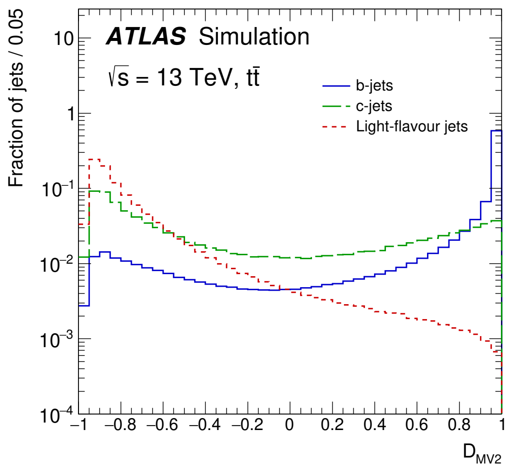

Figure 2.14: The b-tagging discriminant used to distinguish b-jets from jets containing charm and other light flavours. [80].

Chapter 3

The New Small Wheel Project and the Micromegas detector

Contents

The New Small Wheel (NSW) upgrade [7] of the ATLAS experiment consists of replacing all the detectors currently installed in the innermost muon station in the forward region, the so-called *Small Wheel* (SW).

3.1 New Small Wheel Requirements

LHC will reach a luminosity peak of $2-3\times10^{34}$ cm^{-2}s^{-1} during the Run III (with Phase-I upgrade), which corresponds to 55-80 mean interactions per bunch crossing, and up to $5-7\times10^{34}$ cm^{-2}s^{-1} during HL-LHC runs (with the Phase-II upgrade), corresponding to 140 pileup events. The New Small Wheel has been designed to operate efficiently for all the future LHC runs at higher particle flux.

3.1.1 Limitations of the Small Wheel in view of Run 3

The current Small Wheel consists of two detector technologies: CSC and MDT. With the LHC luminosity increase, a degradation of the performance of the MDT detectors is

Figure 3.1: ATLAS New Small Wheels.

expected, with an efficiency of about 80% at rate of 15 kHz/cm^2. Also the Level 1 trigger needs to be improved in order to discard the fake muon triggers produced by particles not coming from the interaction point. These are referred to as "cavern background".

Precision Tracking performance

During the next LHC phases the luminosity will reach a peak of $5 - 7 \times 10^{34}$ cm^{-2}s^{-1}, with an expected particle rate up to 15 kHz/cm^2. This maximum hit rate can be extracted from Figure 3.2. It shows the observed hit rates as function of the radial distance from the beam line in the MDT (r>210 cm) and CSC (r<200 cm) scaled to the value corresponding to the nominal Run III luminosity. The yellow band indicates the area corresponding to a hit rate of 200-300 kHz per tube of MDT.

Figure 3.3 shows the MDT tube efficiency as a function of the hit rate. In the plot, the track segments efficiency is reported, which are built using the hits in a given station of the detector. The other curve represents the efficiency at chamber level, which shows higher values than the tube level one, because only a subset of all available hits is required. This curve decreases rapidly with the enhancement of the flux, reaching efficiency levels of 70% for the expected hit rate of 300 kHz/Tube and results in a degradation of the spectrometer performance.

Trigger selection

In the endcap region, the rate of fake triggers is high due to the background, as shown in Figure 3.4. It shows the η distribution of candidates selected by the ATLAS Level-1 trigger as muons with a transverse momentum greater than 10 GeV. More than 80% of the

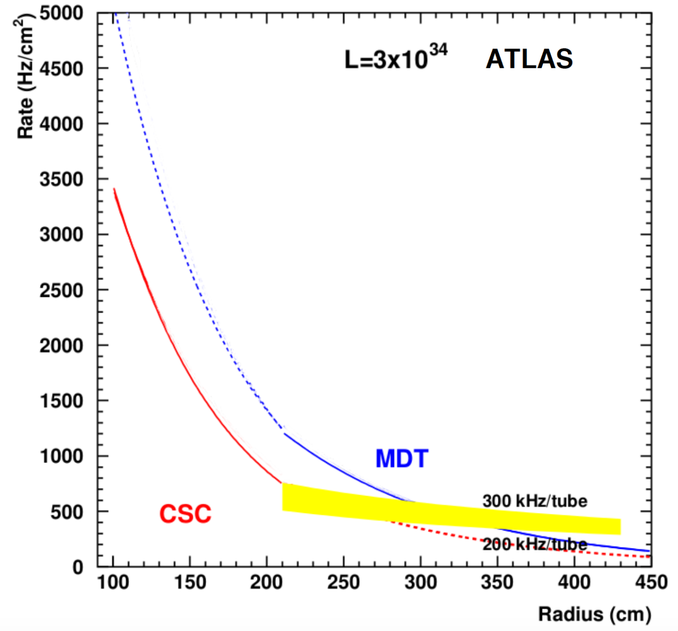

Figure 3.2: Extrapolated hit rate in the CSC and MDT regions for a luminosity of 3×10^{34} cm^{-2}s^{-1} at $\sqrt{s}$=7 TeV as a function of the radial distance from the beam line. The yellow band is the range of tube rates of 200-300 kHz [7].

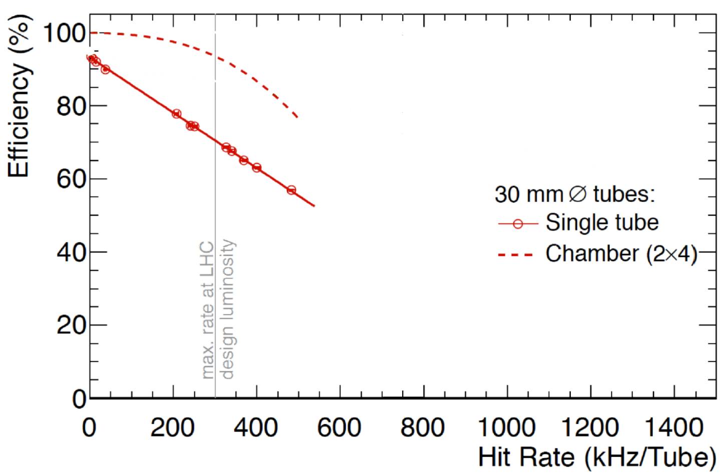

Figure 3.3: MDT tube hit (solid line) and track segment efficiency (dashed line, referring to a MDT chamber with 2x4 tube layers) as a function of tube rate estimated with test-beam data. Instantaneous luminosity of 1×10^{34} cm^{-2}s^{-1} is referred in this plot as 'design luminosity'. Points on the plots are result of test beam measurements [7].

muon trigger rate is from the endcaps ($|\eta|$>1.0) and most of the triggered objects are not reconstructed offline.

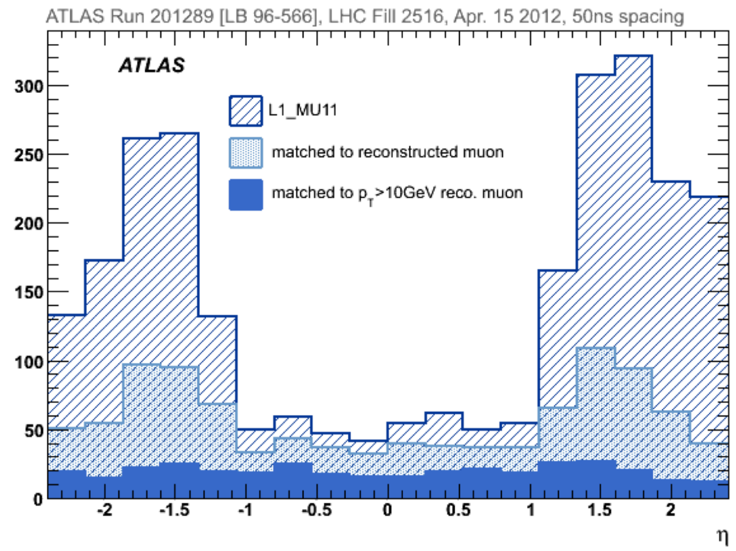

Figure 3.4: η distribution of Level-1 muon signal (p_T>10 GeV) (L1_MU11) with the distribution of the subset with matched muon candidate (within ΔR<0.2) to an offline well reconstructed muon (combined inner detector and muon spectrometer track with p_T>3 GeV), and offline reconstructed muons with p_T>10 GeV [7].

At higher luminosity, the fake trigger signals will increase and saturate the full bandwidth of 100 kHz available for the Level 1 trigger. Trigger simulations have been performed to see the improvements that can be reached by the New Small Wheel by applying offline cuts:

1. the presence of track segments in the Small Wheel: $SW\ segment > 0$
2. the segment points the IP in θ: $d\theta\ cut$
3. the segment matches in (η-ϕ) to the triggering segment in the Big Wheel: $dL\ cut$

Figure 3.5 shows how those cuts simulate where the NSW can aid the Big Wheel in reject fake triggers. It can be seen that among the three possible cases which produce a hit in the Big Wheel, only the case "A" is a real track, and it will be confirmed as such by the NSW. Instead the case "B" will be rejected because the NSW does not find a track coming from the IP that matches the Big Wheel candidate (simulated by $dL\ cut$), and the case "C" will be rejected because the NSW does not point to the interaction point (simulated by $d\theta\ cut$). Then the upcoming New Small Wheel are expected to maintain a Level 1 trigger rate around 20 kHz at a luminosity of 3×10^{34} cm^{-2}s^{-1}.

3.1.2 Upgrade requirements

The New Small Wheel detectors are designed to be able to work efficiently in high luminosity environment. These detectors have the following requirements:

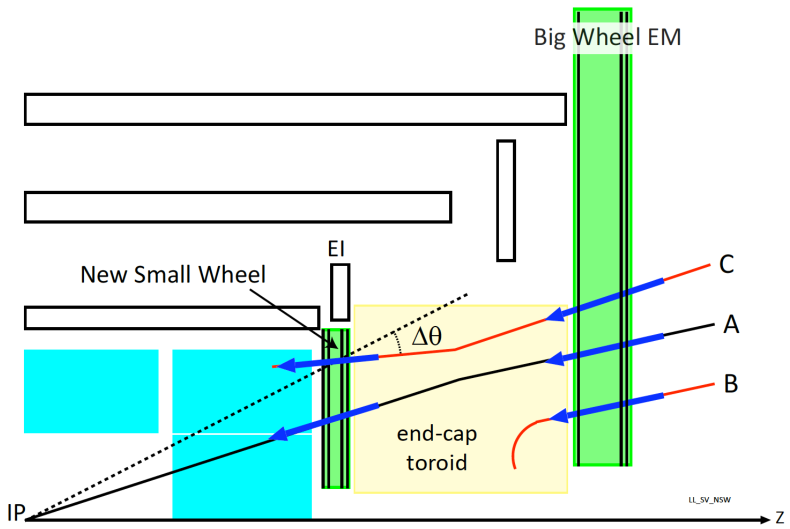

Figure 3.5: Schematic of the Muon endcap trigger. The existing Big Wheel trigger accepts all three tracks shown. With the NSW enhancement of the Muon endcap trigger only track 'A', the desired track, which is confirmed by both the Big Wheel and the New Small Wheel, will be accepted. Track 'B' will be rejected because the NSW does not find a track coming from the interaction that matches the Big Wheel candidate. 'C' will be rejected because the NSW track does not point to the interaction point. The NSW logic requires that $\Delta\theta < \pm$ 7 mrad

- Measure the transverse momentum (p_T) of passing muons with a precision of 10% for 1 TeV muons in the full rapidity coverage of the Small Wheel (up to $|\eta|$=2.7). It will be able to reconstruct track segments with a position resolution better than 100 µm per plane
- Segment finding efficiency better than 97% for muons with p_T>10 GeV
- Efficiencies and resolutions do not degrade at very high momenta
- Measure the second coordinate with a resolution of 1-2 mm to facilitate good matching between MS and ID tracks for the combined muon reconstruction
- Track segment information arrives at the Sector Logic[1] not later than 1.088 µs after a collision. This is the current delay of the Big Wheel TGC
- Track segment reconstruction for triggering with an angular resolution of 1 mrad or better
- Track segments with a granularity better than 0.04 × 0.04 in the η-ϕ plane will match to one of the current muon trigger system.

[1]The muon trigger electronics that combine information from the various detectors to provide one or more Regions of Interest per bunch crossing.

- Track segments reconstructed online with high efficiency in the full η coverage of the detector (1.3 $<|\eta|$ 2.5).
- Online track segment reconstruction efficiency greater than 95%.

Furthermore, the detectors will be able to operate in high background environment and reject spurious hits caused by δ-rays, neutron or other background particles.

3.2 NSW Design

To fulfil the requirements explained before, two detector technologies have been chosen for the New Small Wheel: the Micro Mesh Gaseous Chambers (Micromegas, MM) and the Small Thin Gap Chambers (sTGCs). This choice lead to a robust and redundant tracking system, given that both detectors can operate as tracking and trigger detector. Nevertheless, the Micromegas detectors are mostly devoted as tracker for their exceptional precision tracking capability, while the sTGCs mainly contribute to provide trigger signal given their single bunch crossing identification capability.

The NSW consists of 16 detector planes in two multilayers. Each multilayer comprises four sTGC and four MM detector planes.

The choice of eight plane per detector has been dictated by the need to provide a robust and fully functional detector system over its whole lifetime. Given that the NSW will work in a high background environment, it could lead to a detector deterioration, which will compromise the track segment reconstruction efficiency and resolution. The redundancy will ensure an appropriate detector performance even if some planes fail to work, or have to work with a lower high voltage settings. Furthermore, the layout of the NSW is defined to have a trigger acceptance of $1.3<|\eta|<2.5$ and a precision tracking acceptance of $1.3<|\eta|<2.7$.

3.2.1 Layout of the NSW

In the NSW, the detectors are arranged to maximise the distance between the sTGCs of the two multilayers, optimising the online track resolution: sTGC - MM - MM - sTGC (Figure 3.6) in z direction.

To ensure compatibility with the existing tracking detectors and the endcap alignment system, the 16 sectors of precision chambers are grouped in 8 small sectors and 8 large sectors, with a small of overlap between them.

The barrel toroid magnet structure imposes a division into 16 sectors for the muon instrumentation in the barrel region. The sectors in the barrel are numbered consecutively starting with sector 1 which contains the positive x-axis ($\phi = 0$), and increase with increasing ϕ, as shown in Figure 3.7. The endcap detector have to follow the same convention as consequence. This numbering scheme implies that the large sectors are labelled with odd numbers, and the small sectors with even numbers.

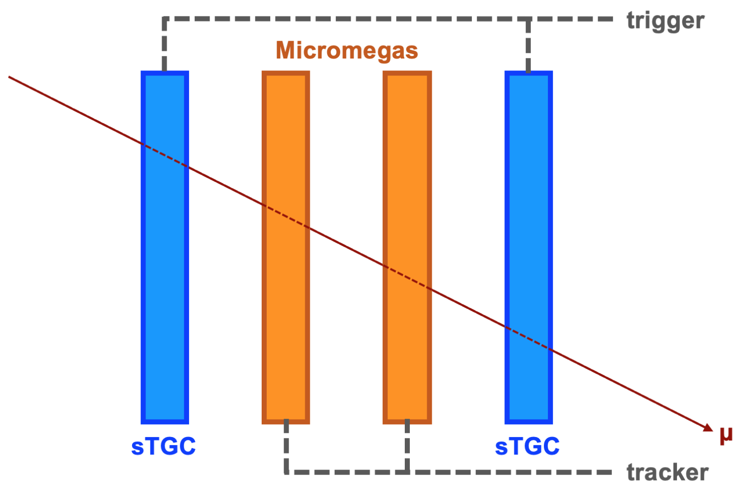

Figure 3.6: Detector order in z direction in the NSW: sTGC - MM - MM - sTGC.

There is also a nomenclature convection for each component of the New Small Wheel, starting from the basic detector element of a specific technology up to the final sector of the wheel, and it will be used in this thesis.

- **Plane or Layer:** a single detector gas gap with the readout structures.
- **Multiplet or Quadruplet or Module:** assembly of n planes of a single technology (sTGC or MM) in z-direction (n=1 to 4).
- **Wedge:** assembly of modules of a single technology type (sTGC or MM) in z direction, covering a full sector in $r - \phi$ plane.
- **Double-Wedge:** assembly of two modules of a single technology (sTGC or MM) in the z direction and one or more modules in the r direction which constitute a single independent object. It might include an internal or external spacer frame between the modules in the z direction. The two wedges in the z direction are called *IP side* or *HO side*, based on where they are facing: the interaction point (IP) or the external side of ATLAS (HO).
- **Sector:** $1/16^{\text{th}}$ of the NSW on side A or C [2] (corresponding to a large or small geometric sector), comprised of two sTGCs wedges and two MM wedges (corresponding to one MM double-wedge) placed as in Figure 3.6.

Each NSW wedge has a radial segmentation in modules of different sizes and shape. In particular, each MM wedge consists of two types of MM quadruplets distributed along r and in small/large sectors, while each sTGC wedge is composed of three different quadruplet types. They are labelled (counting from the smaller radius sectors up to bigger radius ones) as follow:

[2]The detector part in the positive z direction is called side A, the part in the negative z direction side C

- **Micromegas.** Small Modules: ***SM1***, ***SM2***; Large Module: ***LM1***, ***LM2***.
- **sTGC.** Quadruplets Small: ***QS1***, ***QS2***, ***QS3***; Quadruplets Large: ***QL1***, ***QL2***, ***QL3***.

The right picture in Figure 3.7 shows the scheme of the four different Micromegas modules (two large and two small) in the NSW. A wedge is the part of the wheel sector made by a Module of type 1 and a Module of type 2 for the MM and also type 3 for the sTGC, to have 4 layers of a single technology covering the full $|\eta|$ range.

The production is distributed over different institutes and industries. For the Micromegas, the production sites are: Italy (SM1), Germany (SM2), France (LM1) and Russia-Greece-CERN (LM2). For the sTGC, the production sites are: Canada (QS3, QL2), Chile (QS1), China (QS2) and Israel (QL1, QL3).

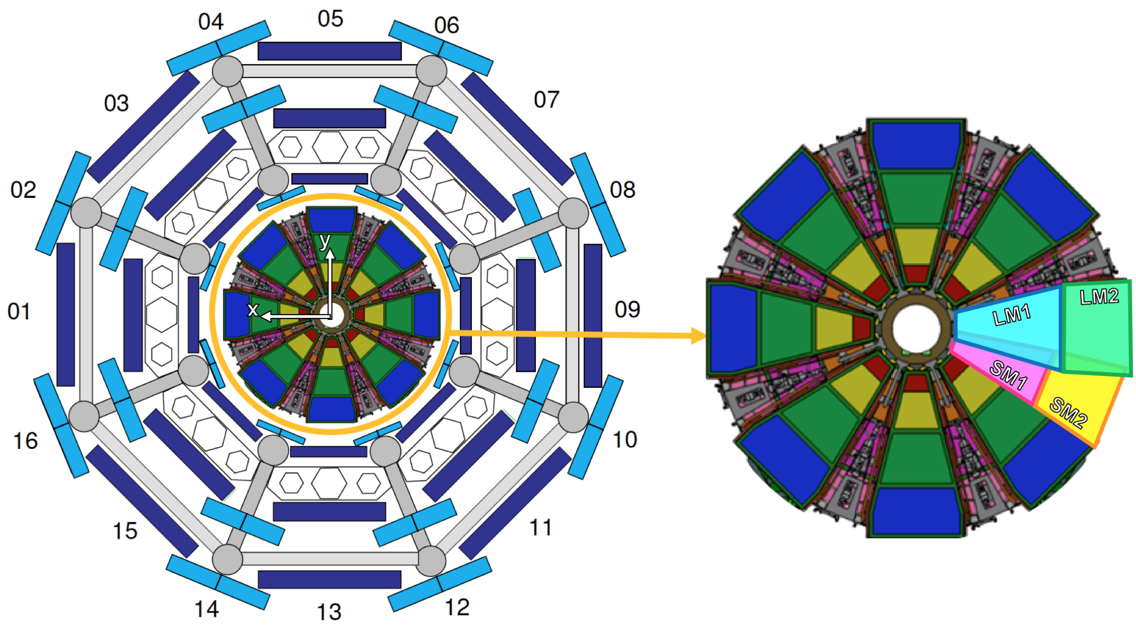

Figure 3.7: The left picture show the barrel scheme with the definition of the 16 sectors of the ATLAS muon spectrometer (dark blue sectors represent the *large* sectors, the light blue represent the *small* ones. Inside of the barrel scheme a sketch of the NSW is represented and the detailed view is shown in the right picture. This shows the 8 large sectors in which only the sTGC wedge are visible. The large and small MM sectors with the corresponding LM1, LM2, SM1 and SM2 modules segmentation are also represented.

3.3 NSW detectors: sTGC and MM

3.3.1 small-strip Thin Gap Chambers (sTGC)

The sTGC detectors have been chosen to be the main triggering detector in the NSW, featuring bunch crossing identification, and good time and angular resolution for online reconstructed segments.

The basic small-strip Thin Gap Chamber structure is shown in Figure 3.8a. It consists of an array of 50 µm diameter gold plated tungsten wires held at a potential of 2.85 kV, with a 1.8 mm pitch, sandwiched between two cathode planes located at a distance of 1.4 mm from the wire plane [81]. The cathode planes are made of graphite-epoxy mixture with a typical surface resistivity of 100 or 200 kΩ/□ sprayed on a 100 or 200 µm thick G10 plane for the inner and outer chambers, respectively. Behind the cathode planes, on one side of the anode plane, there are copper strips for precise coordinate reconstruction that run perpendicular to the wires. On the other side of the anode plane, there are copper pad which is used for fast trigger purposes. Both strips and pads act as readout electrodes. The pads cover large rectangular surfaces on a 1.5 mm thick PCB with the shielding ground on the opposite side. The strips have a 3.2 mm pitch, which is much smaller than the pitch of the current ATLAS TGC of 150-490 mm. This is why they are called "small-strip" TGC.

The sTGC quadruplet consists of four pad-wire-strip planes shown in Figure 3.8b. The pads are used for a 3-out-4 coincidence to identify the muon tracks pointing back to the interaction point and to define a Region Of Interest to determine the strips that should be read out to obtain the precise position measurement η. The azimuthal coordinate is obtained from the wires readout. The operational gas mixture is 55:45 $CO_2 : n - petane$.

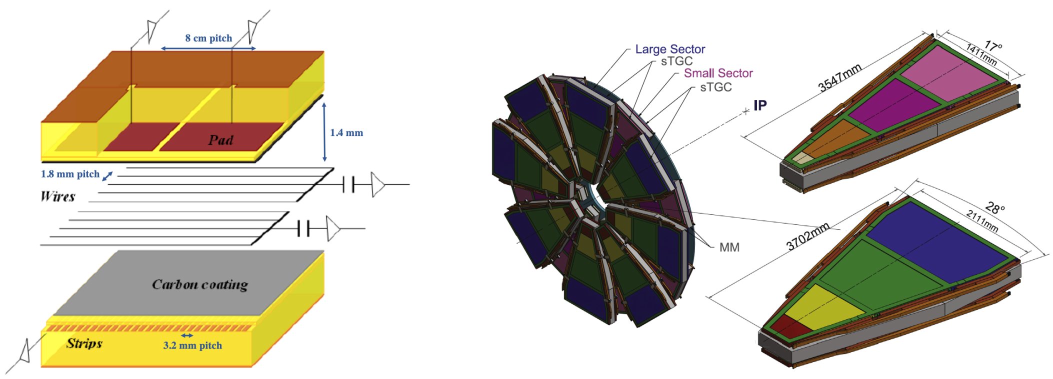

(a) (b)

Figure 3.8: Schematic diagram of the basic sTGC structure (a) and the scheme of the small and large sectors that make up the New Small Wheel (b). Each sector consists of two quadruplets of sTGC with eight Micromegas(MM) detector plane in between [81].

The timing performance of the sTGC is the crucial point for trigger performance. The features of the sTGC, ensure good time properties, since the total drift time for most electrons is shorter than 25 ns, and the high amplification ensures high efficiency. The time spectrum for normally incident muons on an sTGC operated at 2.85 kV has been studied comparing simulation and measurements. The experimental and simulated data agree well and demonstrate that 95% of the total events are contained within a 25 ns time window, as shown in Figure 3.9a [7]. A test beam has been also performed at Fermilab on the first full-size sTGC prototype detector to determine the position resolution. It has been estimated based on adjacent sTGC strip-layer position residual distributions. A representative result of about 41 μm for a sTGC standalone data taking run is shown in Figure 3.9b [81].

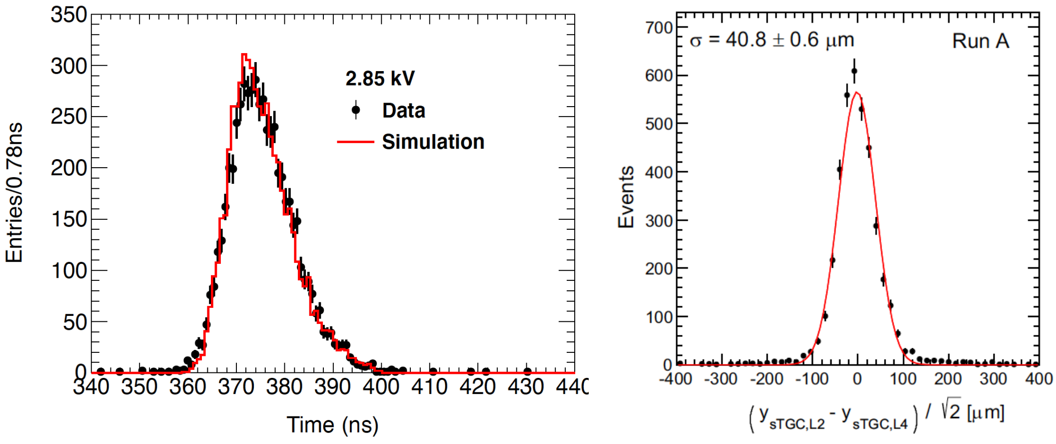

(a) (b)

Figure 3.9: Comparison of a simulated time spectrum with experimental data taken using wire voltage of 2.85 kV (a). The horizontal axis has an arbitrary offset [7]. In (b) the resolution estimate based on adjacent sTGC strip-layer position residual distributions for a representative sTGC standalone data taking run is reported [81].

3.3.2 Micromegas detector

Micromegas (MM) chambers is an abbreviation for MICRO MEsh GASeous Structure and it is an innovative design concept for Micro-Pattern Gaseous Detectors first introduced by Charpak and Giomataris during the 1990s. These chambers have been chosen as new precision tracking detectors for the upgrade of the forward muon spectrometer of the ATLAS experiment [9].

Micromegas are gas detectors in which a 5 mm gap between two parallel electrodes is filled with a typical 93 : 7 Ar : CO_2 gas mixture and a thin metallic micromesh is placed between the two electrodes, held by isolating *pillars* with a pitch of few millimetres and a height of about 128 μm (Figure 3.10). The drift electrode, with a -300 V voltage applied, and the mesh, which is grounded, define the drift region, where the ionisation takes place and the low electric field (∼600 V/cm) guides the produced electrons towards the mesh. Following the field lines the electrons enter the very thin amplification region between the mesh and the readout electrode, which is segmented into strips with a pitch of about 400 μm, where 570 V voltage is applied. Due to the very high electric field (40 - 50 kV/cm), the electrons produce avalanches with a gain of the order of 10^4. The thin amplification gap allows a fast ions evacuation, which occurs in about 100 ns, and allows MM to operate in highly radiated environments. The produced signal is then read by the readout strips capacitively coupled to the resistive ones in order to reduce the performance degradation due to discharges in the detector.

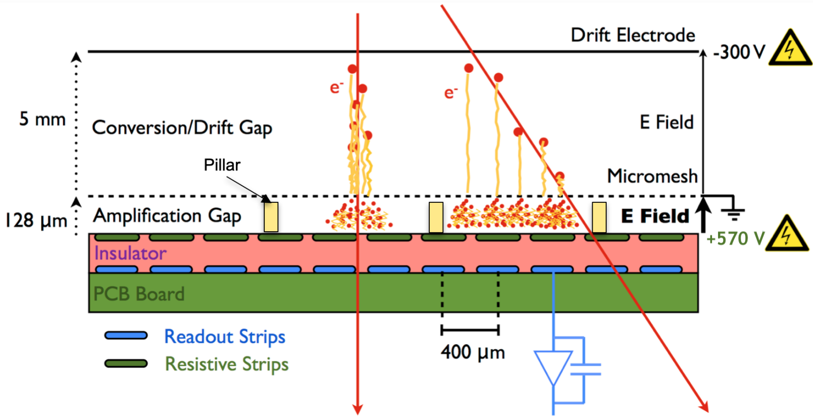

Figure 3.10: Schematic view of the Micromegas detector and the principles of operation.

3.3.2.1 Development of Micromegas detectors for ATLAS

In the NSW upgrade, large area Micromegas chambers will be used for the first time in high-energy physics. This application turned out to be a real challenge, leading to years of research and development on the Micro Pattern Gas detectors, to improve their performance. The operational principle described in the previous section is the result of the R&D activity which started in 2008 with the Muon ATLAS MicroMegas Activity (MAMMA) [11].

Spark protection The weak point of the Micromegas original design was their vulnerability to sparking. The readout plane was designed as a copper readout strips layer. Sparks occur when the total number of electrons in the avalanche reaches $\sim 10^7$ (Raether limit [85]). Given that the amplification factor for a MIP is of the order of 10^4, this limit can be reached with a ionisation process produces more than 1000 electrons, such as low-energy alpha-particles. These sparks may damage the detector and the readout electronics, leading to large dead times as a result of HV breakdown. To solve this problem, a spark protection system has been developed, adding a layer of resistive strips on top of a thin insulator directly above the readout electrode. In this way, the readout electrode is no longer directly exposed to the charge and the signals are capacitively coupled to it. The strips resistivity should be the order of ~ 10 MΩ/cm. The principle of the resistive spark protection is schematically shown in Figure 3.11.

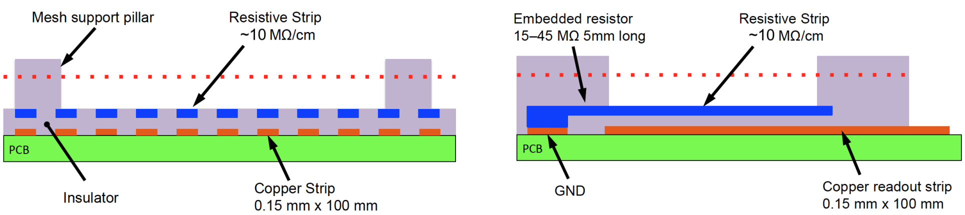

Figure 3.11: Spark protection principle.

Floating mesh The amplification gap of Micromegas is obtained by suspending a mesh over the anode strips. The precise gap is obtained by using insulating spacers, called *pillars*, etched on top of the anode plane by conventional lithography of a photoresistive film. The mesh is stretched and glued on a frame and then rested on top of the pillars. The positioning of the mesh in order to obtain a good flatness and parallelism between the anode and cathode represents a challenge in the construction, especially for large area chambers.

The first Micromegas prototypes was built with the so-called "bulk" design [86]. The entire sensitive detector is produced in a single process based on the PCB (Printed Circuit Board), in which the mesh is embedded into the readout PCB structure itself. This method lower the production cost, but it is limited by the industrial manufacturing of the PCB boards to a medium-sized area detectors.

The need for very large area detectors forced ATLAS to develop a new technique: the so-called "*floating mesh*". It consists of the integration of the mesh in the panel containing the cathode plane instead of the readout PCB plane. In this way, the drift gap is formed separately from the readout PCB, removing the dimension limitations. The floating mesh scheme is shown in Figure 3.12: the mesh is integrated in the so-called *drift panel* (the cathode plane) and the *readout panel* (the anode plane) is separate (on the *left*) and then coupled together (on the *right*) .

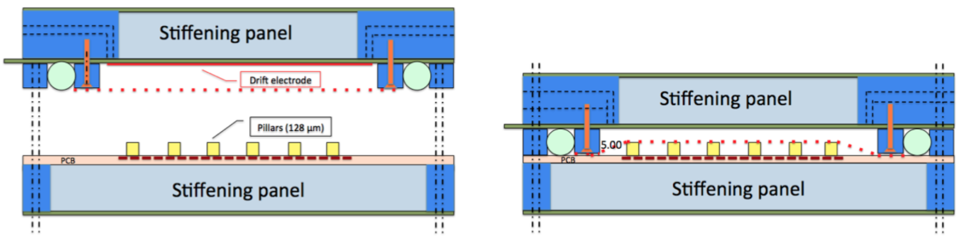

Figure 3.12: Schematic of a single MM plane assembly. *On the left*: the drift panel (top) and the readout panel (bottom) are shown in open position. The mesh is an element integrated in the drift panel, glued on an aluminum frame (the mesh frame). *On the right*: the drift panel is coupled up to the readout panel.

Inverted HV scheme The MM usually adopts a HV scheme applying negative HV on the mesh and keeping the resistive strips at ground. A new scheme has been developed in which the mesh has been grounded and positive HV is applied on the resistive strips. It brings several improvements. The absence of HV on the mesh simplifies the chamber construction, especially with the floating mesh scheme, and it reduces the risk of HV leaks. This scheme also allows for an easier implementation of segmenting the HV on the readout boards. It was observed from the tests that this provides a more stable detector performance allowing for operation of the detectors at higher gas gains [11].

3.3.2.2 Micromegas in the New Small Wheel

The NSW structure consist of 8 large sectors and 8 small sectors, with 4 Micromegas modules per sectors. Micromegas chambers are produced in 4 different shapes: LM1, LM2, SM1 and SM2, in order to cover different $|\eta|$ regions of the wheel. In Figure 3.13, the four different shapes are shown with the corresponding dimensions in millimeters. The chamber size is ~2 m^2 for small modules (SM1 and SM2) and ~3 m^2 for large modules (LM1 and LM2), and the volumes are ~40 L for SM1, ~42 L for SM2, ~60 L for LM1 and ~61 L for LM2. Each Micromegas chamber consists of five (type 1) or three (type 2) printed circuit boards (PCB) per layer, numbered respectively from 1 to 5 (type 1) and 6 to 8 (type 2), as they are assembled in sequence in a wedge.

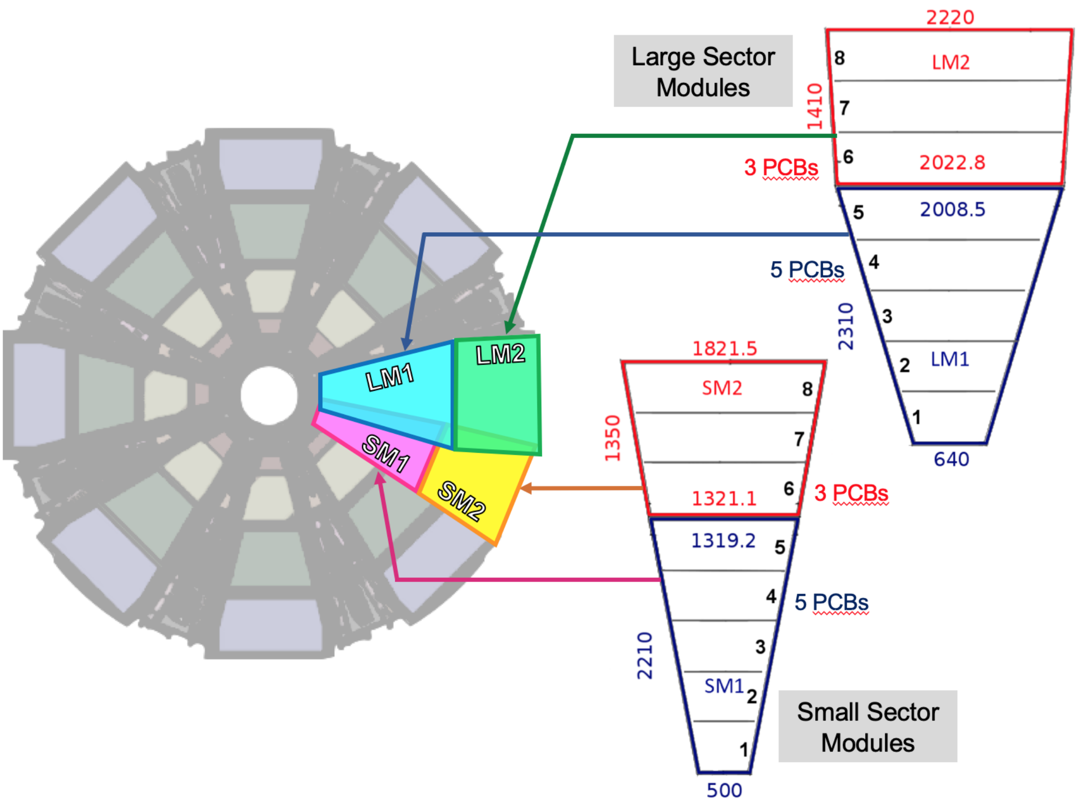

Figure 3.13: The New Small Wheel subdivision in small (S) and large (L) sectors and the division of the sectors' readout planes into 8 anode PCBs grouped in two modules (5 PCBs + 3 PCBs)

The INFN has committed to build all the 32 quadruplets of type SM1, under the responsibility of the INFN groups of Cosenza, Frascati, Lecce, Napoli, Pavia, Roma Tre and Roma Sapienza.

Figure 3.14 shows a schematic view of a quadruplet. Each quadruplet is composed of five panels, to have four active gaps. Three out of the five panels (panels 1, 3 and 5 in the figure) are called *Drift panels*, and are made of the drift PCB cathode and meshes. The panels 1 and 5 are the *external* drift panels (or *outer*) while the panel 3 is the *central* one. The cathode layers consist of PCBs with copper layers and they are placed, as for the meshes, on the inner face of the external panels and on both sides of the central. The panels 2 and 4 are called *Readout panels* and the active area is composed by the anode readout PCBs.

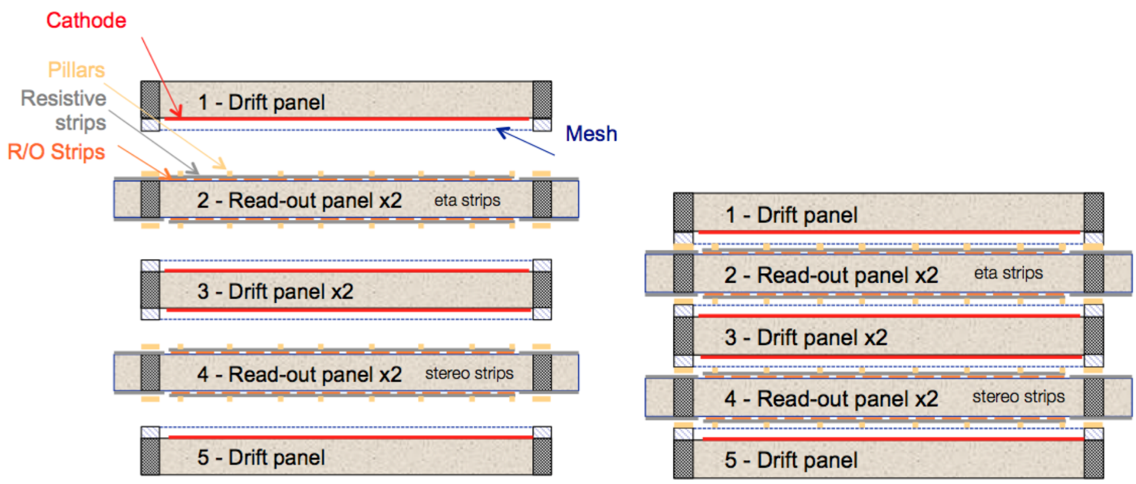

Figure 3.14: A schematic view of the five panels of a MM quadruplet.

The readout PCB consists of a 500 µm thick FR4 layer on top of which copper strips of 17 µm height are printed via photolitography. The strips are 300 µm wide for all the modules with a pitch of 425 - 450 ± 20 µm for small and large modules respectively. The shape of the resistive strip foils is almost identical as the readout PCBs. They are composed of a 50 µm thick Kapton® substrate glued on the readout strips, with screen-printed resistive strips, 8-10 µm thick. The resistive strips are split in two in the middle so that each side of the PCB has a separate high voltage supply line. Consequently, the MM module of type 1 has 10 HV sections in each layer (40 HV sections in total) and the MM module of type 2 has 6 HV sections in each layer (24 HV sections in total).

In the quadruplet layout, the strips of the first two layers are parallel to the chamber bases, and almost orthogonal to the bending plane of the tracks in the ATLAS experiment. The panel that forms these two layers is called *Eta panel*. In the case of the third and fourth layer, formed by the *Stereo panel*, the strips are inclined by ± 1.5° with respect to the strips of the *Eta panel*. This configuration, schematically shown in Figure 3.15a, allows not only a precise determination of the X coordinate, orthogonal to the strips and necessary for the momentum measurement, but also a determination of the second Y coordinate, although with less precision.

Figure 3.15b shows the layout of one PCB readout board for each type (*Eta* and *Stereo*). Each PCB readout board consists of 512 readout strips, half of them routed to the upper right corner to be readout while the other half, to the bottom left. This scheme balances the load for electronic boards on each side of the detector. The figure shows also an extra space for the electronics and the services on the PCB side.

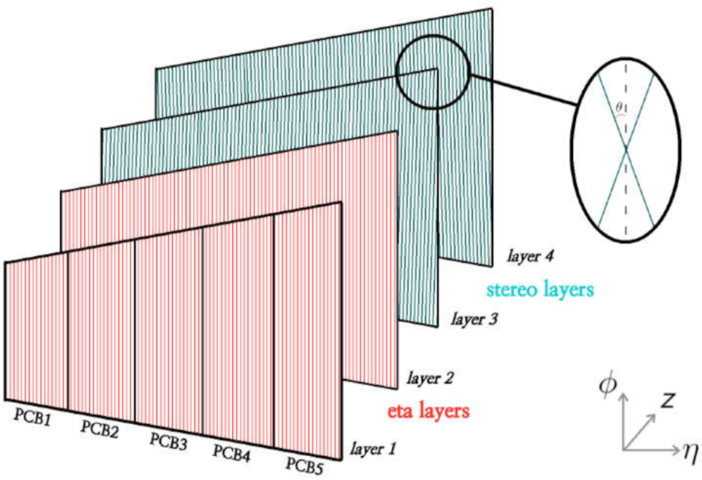

(a) Eta and Stereo readout panel layout.

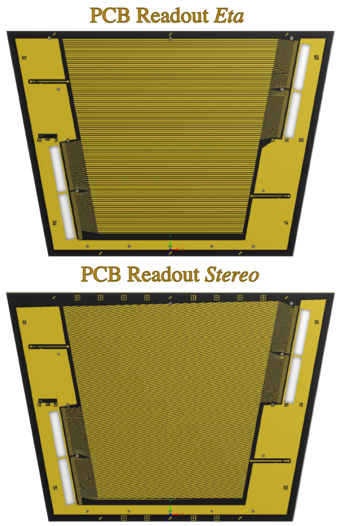

(b) Eta and Stereo readout PCB layout.

Figure 3.15: Layout of the Eta and Stereo readout (a) panel and (b) PCB.

Chapter 4

SM1 Micromegas production and High Voltage stability studies

Contents

4.1 Assembly and Validation of SM1 modules

A MicroMegas module for the NSW is made of four gas gap (*Quadruplet*) and it consists of 5 panels: two external Drift panels, one central Drift Panel and two Readout panels, the *Eta* (with vertical strip to measure the η coordinate) and the *Stereo* (with strip tilted at $\pm 1.5°$ to allow also the measurement of the second ϕ coordinate).

The INFN Italian production for the SM1 chambers is summarised as shown in Figure 4.1.

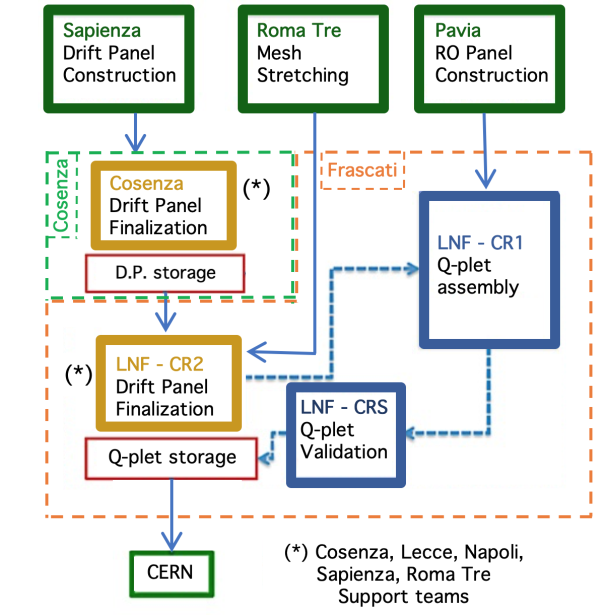

Figure 4.1: INFN production scheme of SM1.

In this section, an overview of the panels construction and a detailed description of the assembly of a full SM1 quadruplet are presented, together with the quality control performed at LNF to validate the modules performance with respect to the ATLAS requirements.

4.1.1 Panel construction

4.1.1.1 Drift Panel

The *bare* drift panels (without the mesh) is prepared at Roma-1 in the clean room using the so called *vacuum bag technique* [82] . The PCBs are placed with the copper face down on the granite table and the lateral frames, the inner bars and the honeycomb are glued on the PCB layer. Then a second set of PCBs is positioned on the already assembled components and finally the glue is fixed with a vacuum bag, that produces an underpressure of 100-150 mbar, using an aluminum mask to guarantee a uniform pressure. In this way a good planarity level can be achieved for the drift panel, below the 37 µm required. This measurement, together with the panel thickness, is made with a specific tool called *limbo*, which consists of a bar instrumented with 10 height gauges.

The meshes are prepared in parallel at Roma-3. The mesh lays on the stretching table and it is held with 28 clamps that are gradually moved until a tension of ~ 9 N/m is reached. Then a map of the mesh tension is performed using a tensiometer for textile fabric. The drift panel is finalised in Cosenza and then at LNF, where a frame 5 mm thick is fixed on the bare drift panel to build the ionisation gap and the stretched mesh is glued over this frame. The mesh tension is checked during this steps, and finally the High Voltage and the gas tightness tests are performed to ensure the operation of the drift panel. Some pictures of the drift panels construction phases are shown in Figure 4.2. Figure 4.3 shows an example of the planarity measurements of the drift panel and the mesh tension map.

(a)

(b)

Figure 4.2: Drift panel construction steps: (a) the vacuum bag technique (*on the top*), the mesh on the stretching table (*on the bottom*) and (b) the drift panel finalised.

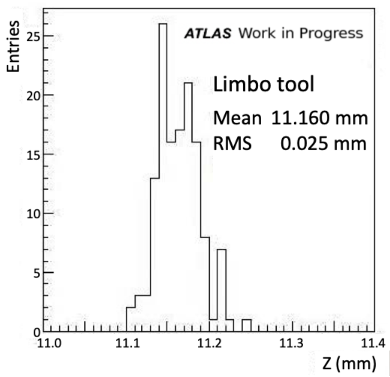

(a)

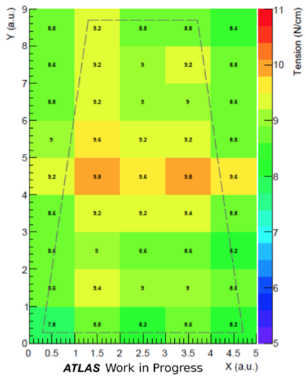

(b)

Figure 4.3: (a) Measurement of the thickness and planarity for a drift panel and (b) the mesh tension map.

4.1.1.2 Readout Panel

The two readout panels of the SM1 modules are prepared in Pavia in the clean room using the *stiff-back technique* [83] (Figure 4.4a). A readout panel has 5 PCBs for each side, and these PCBs are made of a layer of copper strips, the insulator layer and the layer of resistive strips. The assembly starts by placing the first PCB skin on the granite table, precisely positioned using reference pins, and sucked on this with a vacuum pump, and the second skin is placed on the stiff-back. Then the frames and the honeycomb are glued over the first PCB skin. The stiff-back is rotated upside-down and moved over the table to put the second skin on top of the assembled panel. The finalised panel is shown in Figure 4.4b.

As for the drift panels, the planarity of the readout panels is refined to be lower than 37 µm. The planarity measurement of the panel is performed with the CMM (*Coordinate Measuring System*) machine, a device for dimensional measurements mounted on a bridge over the granite table. An example of the planarity measurement is shown in Figure 4.5a.

An important step of the readout panel construction is the test of the readout strip alignment. This measurement is performed with a custom-made optical tool called Rasfork (based on the *Rasnik* system [84]). It is able to read the coded masks placed on the PCB external side through contact-CCDs. These tools perform measurements both of the mis-alignments and rotations of the strips PCB-to-PCB and of the strip alignment Layer-to-Layer. The tolerance for the absolute alignment is $|\Delta\eta| < 40$ µm, while for the relative alignment between the two side of the panel it is $|\Delta\eta| < 60$ µm. A partial statistics of the readout SM1 panel measurements is shown in Figure 4.5b.

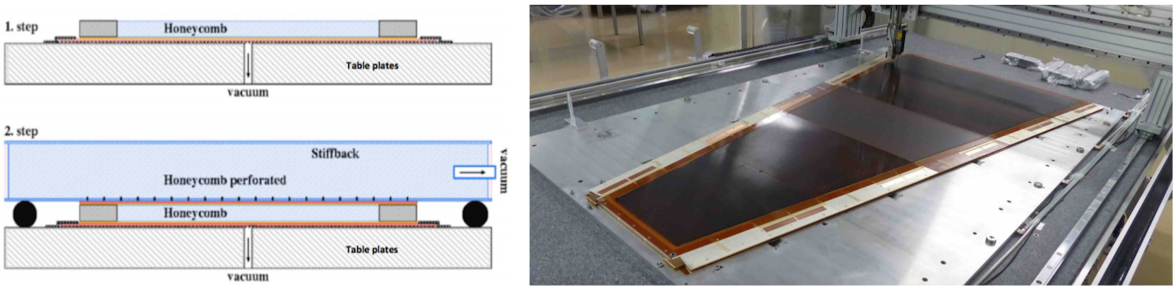

(a) (b)

Figure 4.4: (a) The stiff-back technique scheme and (b) the final readout panel.

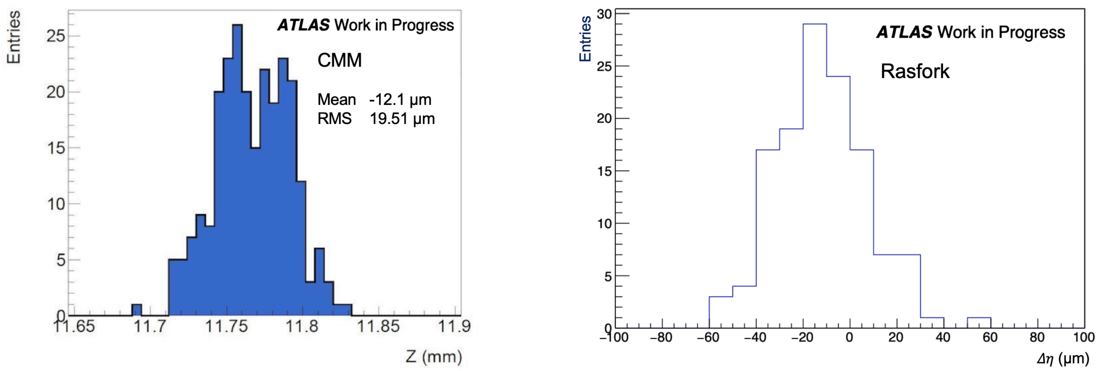

(a) (b)

Figure 4.5: (a) Mean and RMS value of a stereo panel planarity measurements and (b) mis-alignment of the readout strips along the precise coordinate measured with the *Rasfork*.

4.1.2 Assembly procedure

The assembly of a full MM quadruplet takes about one week. It includes the assembly steps itself, but also the intermediate HV tests performed at each gap closure. A gap is built when the active areas of a Drift panel and of a Readout one are placed face-to-face to each other.

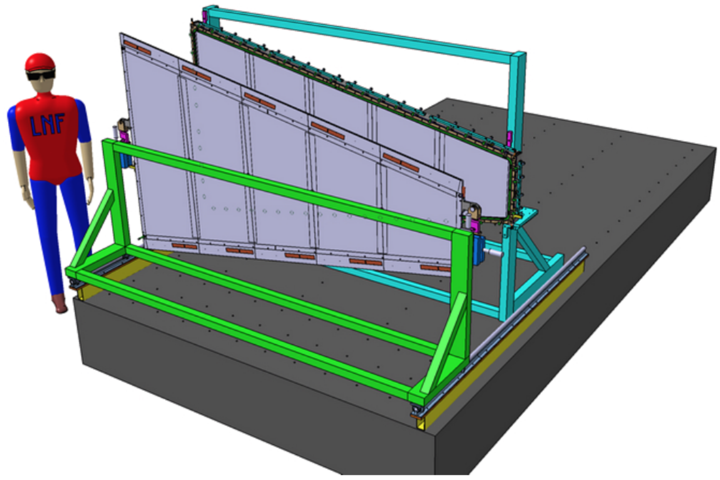

Figure 4.6: Picture of the assembly tool installed in the Clean Room at LNF.

4.1.2.1 Layer 4 - External Drift Panel

The assembly starts from the gap which represents the *Layer 4* in the SM1 nomenclature, i.e. the last gap of the detector. The External Drift panel is positioned on the *stiff-frame*, placed on the granite table. The stiff-frame is a mechanical structure used to guarantee the panel planarity during the assembly procedure. It is made with Al profile glued with Al brackets with mechanical tolerances of $\sim$ 100 µm. The panel is aligned to the stiff-frame border within 3 mm using adjustment screws. The stiff-frame with the panel is then moved on the assembly tool, mounted on the granite table. It is fixed on that tool using two clamps on the top and with two support brackets with slot on the bottom. The External Drift is then put in vertical position on the granite table as shown in Figure 4.7. Other two support brackets with inserted screws are mounted on both panel sides, and the screws are tuned in such a way that the weight of the panel and the stiff frame is loaded on the iron platforms on the tool side, instead of on the whole assembly structure. The o-ring is inserted in the frame slot along the perimeter of the Drift panel, to guarantee the gas tightness of the gap.

4.1.2.2 Layer 4 and 3 - Readout Stereo Panel

The Layer 4 is a Stereo layer (as also the Layer 3). To close the first gap, the Stereo Readout panel is put in vertical position on the *assembly cart*. This is a movable assembly

Figure 4.7: First External Drift in vertical position on the assembly tool.

tool mounted on a trolley. The panel is held on that cart by two brackets equipped with spherical joints on both sides, as shown in Figure 4.8. The height of the trolley is fixed such that it is aligned with the tracks on the granite table in which the cart have to slide. The cart has two degree of freedom, one along the central axis and one along the bases of the panel, to align the holes for the assembly screws on all panels.

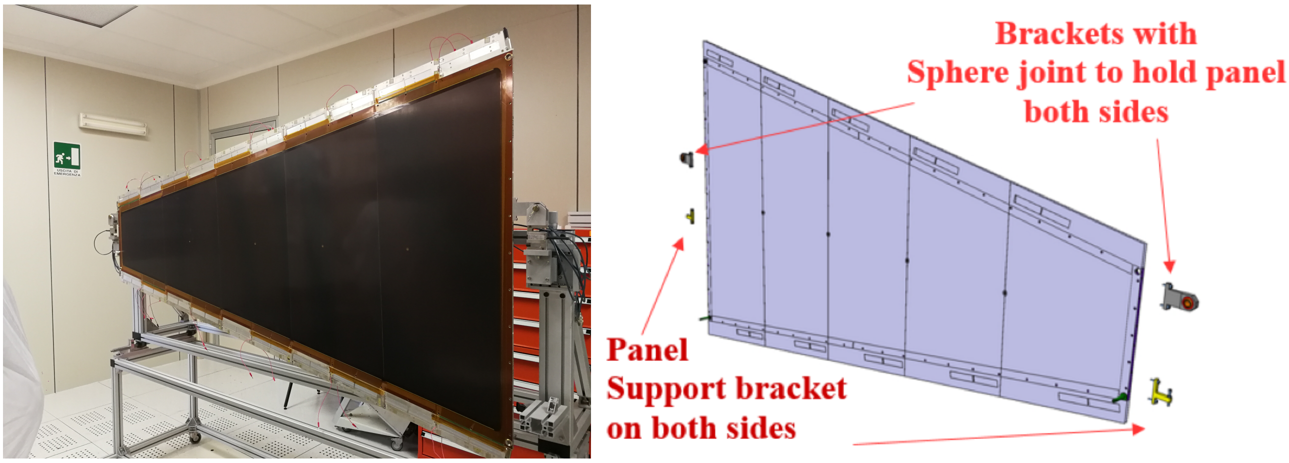

(a) (b)

Figure 4.8: (a) Stereo Readout panel on the movable assembly tool. (b) Support bracket to hold the panel on the tool.

When both the panels are in vertical position, a *dry cleaning* procedure is performed on the panel surfaces, removing the dust with a vacuum cleaner and then with an electrostatic roller, as shown in Figure 4.9.

The assembly trolley is brought closer to the granite table and fixed to the tracks. In this way, the cart with the Readout panel can slide along the tracks to approach it to the Drift panel (Figure 4.10a). To align the Readout and the Drift panels, two *Delrin*® pins

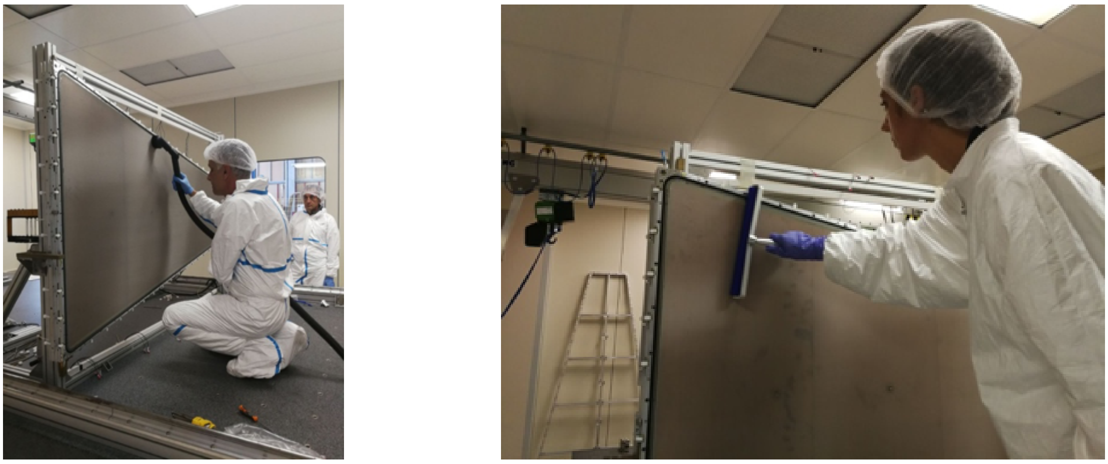

(a) (b)

Figure 4.9: Dry cleaning procedure performed on the panel surfaces (a) with vacuum cleaner and (b) with electrostatic roller.

of 6 mm diameter are inserted in the holes for the closure of the gap. As for the Drift panel, and for both sides of the Readout panel, two support brackets with inserted screws are installed for not-loading the panel weight on the assembly structure. In this case, the screw is a micrometrical screw, which allows for a finer alignment of the panel.

The capacitors of the HV filters installed on the Readout panel are tested by connecting the HV of each section of the layer (10 sections for the SM1 modules). The two panels are then connected using *expansion rods*, as shown in Figure 4.10b, on half of the screw holes. The expansion rods are designed to be fixed by turning the screw on one side and locking them with a wheel on the other side. In this way the panels are fixed and the o-ring compression is ensured without leaving metallic dust inside the gap.

When the first gap is closed, the HV test in air is performed by applying 750 V and requiring current values smaller than $\sim$ 10-20 nA. If some sections show instabilities, or do not work properly, the gap is re-opened, checked for defects on the panels and cleaned again.

4.1.2.3 Layer 3 and 2 - Central Drift Panel

To close the second gap (*Layer 3*), the Central Drift panel is added at this stage. It is a double-faced panel, then it builds the Layer 3 gap as well as the Layer 2 gap. As for the Stereo Readout, the Drift panel is put on the assembly trolley facing the Layer 3 - side of the Stereo panel. The dry cleaning is performed, the panel is aligned with respect to the Readout panel screw holes using Delrin® pins and the capacitors are tested. Then the gap is closed, assembling the new Drift panel and the Stereo one using the expansion rods on the second half screw holes. The support brackets are mounted on the sides of the panel. Finally the HV test in air is performed as for the previous gap.

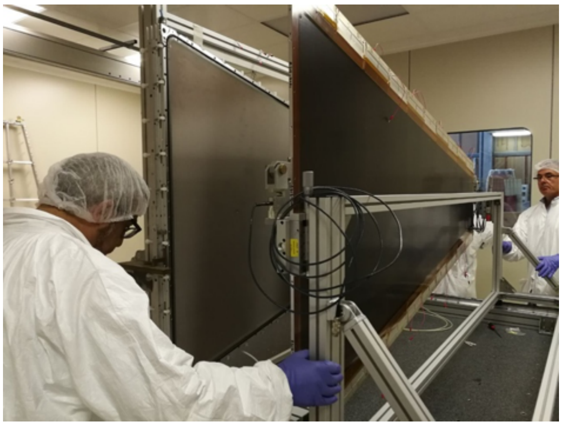

(a) Closure of the first gap.

(b) Expansion Rods

Figure 4.10: (a) Closure of the first gap approaching the Stereo readout to the drift panel installed on the assembly tool.(b) The Expansion rods used to fix the two panels during the assembly procedure, compressing the o-ring.

4.1.2.4 Layer 2 and 1 - Readout Eta Panel

The assembly of the Eta panel closes the third gap (*Layer 2*). As before, the panel is put on the assembly cart and subject to the described cleaning procedure and capacitor test.

In this case the alignment procedure is finer, as at this stage the alignment of the readout strips between the Stereo panel and the Eta one is performed. The Eta panel needs to be aligned with respect to the two *Alignment Pins* (Figure 4.11) installed at two angles of the Stereo panel, which are put on the bottom side during the assembly of the Stereo panel. The alignment is performed using load cells installed on the assembly cart, which measure the weight of the Eta panel loaded on the two alignment pins. The micrometrical screws on the cart, which tune the vertical position of the panel, are turned slowly to reduce the weight loaded on the pins as much as possible, with a tolerance of 200-300 grams.

Once an acceptable value is achieved on both sides of the panel, the Eta Readout is closed to the Central Drift panel by applying clamps on both tracks to fix the position of the sliding tool. Then the capacitors are tested and the gap is closed with the expansion rods used to fix the Stereo Readout panel. During this step, it is important that the values of the weight loaded on the pins do not change.

4.1.2.5 Layer 1 - External Drift Panel

Finally, the last External Drift panel is assembled to close the fourth gap (*Layer 1*). Following the same procedure explained before for the assembly of the Central Drift panel, the panel is put on the cart, cleaned, and closed to the Eta Readout panel, performing the alignment with the Delrin® pin.

Before the module completion and the closure with the final screws, the gap is again closed with the expansion rods used to close the Central Drift panel. Interconnection plugs with o-rings on both side of the module are inserted to minimise the gas leakage. Then

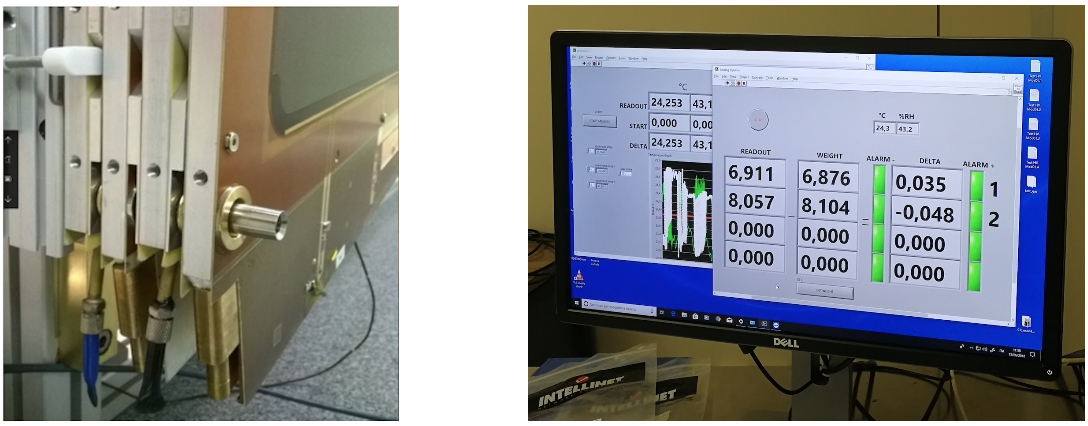

(a) Alignment Pin (installed on the Stereo panel) inserted in the pin slot (installed on the Eta panel).

(b) Monitoring of the weight loaded on the two pins using load cells.

Figure 4.11: The Eta panel need to be aligned to the Stereo one during the assembly. Load cells are used to measured the weight loaded on the alignment pins, with a tolerance of 200-300 grams.

a preliminary HV test in Ar:CO_2 is performed, ramping up the HV value up to 550 V. The test is not performed up to the operational HV value of 570 V given that the Relative Humidity (RH) value in the Clean Room is usually quite high ($\sim 40\%$) and the gas tightness of the module is not the optimal one.

If the module passes this preliminary HV test, the expansion rods are substituted with the final screws, closing the gaps with a dynamometric key. The module is then taken out from the assembly tool and put in horizontal position on the granite table to start the QA/QC tests (Figure 4.12).

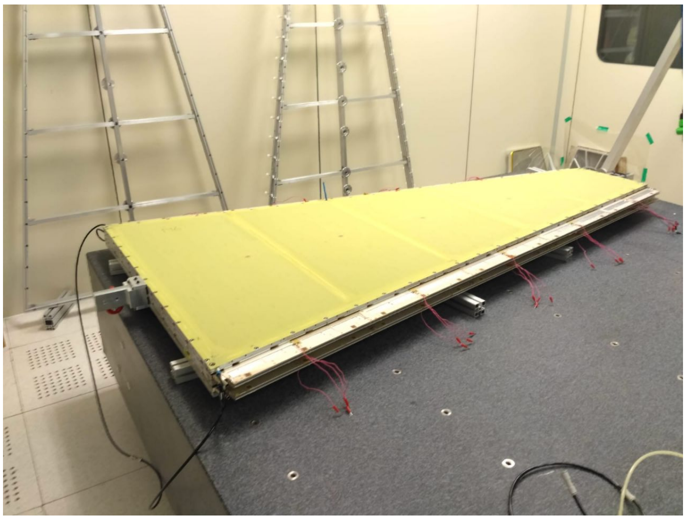

Figure 4.12: Assembled module on the granite table, ready to start the QA/QC tests.

4.1.3 Validation of SM1 Module at LNF

Several quality tests are performed on the Micromegas modules to ensure their correct functioning and the adherence to the construction requirements.

- *Planarity* of the module, required to be < 80 µm but values up to 200 µm are tolerated, and *thickness* is required to be consistent between the modules.
- *Gas tightness.* It is an important requirement, given that a gas leak in the module can lead to a contamination of the gas mixture with air and water, based on the humidity level. This effect would compromise the performance of the chambers. The ATLAS requirement is that the relative variation of the gas volume inside the chamber in time to be $< 10^{-5}$ Vol/min.
- *Strip alignment* measurement to have be performed to map the mis-alignments or rotations of the readout strips. This is to correct the track reconstruction taking into account of these effects. Mis-alignments < 60 µm are required, and tolerated up to 100 µm.
- *High Voltage stability.* Fundamental test to guarantee the functioning of the chamber at the nominal voltage without discharges. The nominal HV working point is 570 V in Ar:CO_2 93:7 gas mixture.
- *Cosmic Ray test* to estimate the efficiency of the chamber and its performance. At least 85% of the chamber must have an efficiency > 90%.

4.1.3.1 Planarity and Thickness

This test is performed in the clean room, positioning the quadruplet on several supports on the granite table, as shown in the scheme of Figure 4.13a. The support plane represents the reference plane (z=0) for planarity and thickness measurements.

The measurement is made with a Laser Tracker [87]. This tool is based on the laser interferometer to measure relative distance. It works on the principle of light interference in which one beam is used as a reference while the other beam is reflected back from a mirror or retro-reflector at some distance, producing interference. The distance can be calculated from the number of interference fringes, given that the wavelength of the laser is well known.

The laser tracker is first calibrated by taking the supports as the reference plane for the measurement. The module is then positioned on them to start the measurement. Figure 4.13b shows the laser tracker during the data taking of one module. The laser points to the retro-reflective target, the tool is then moved on the module surface and the height map of more than ∼3000 points is built for each side of the module.

A planar fit is performed on the cloud points. Figure 4.14 shows the measured points and interpolated surface for both side of one module. The thickness of the module is then extracted from the mean value of all the measurements and the planarity from the RMS.

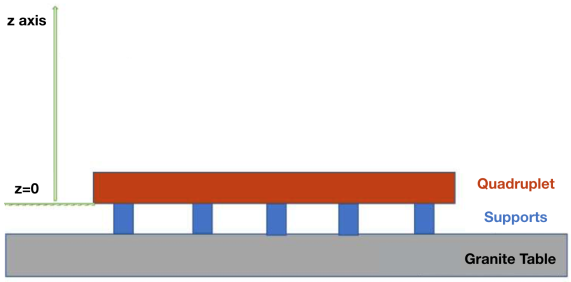

(a) Setup for planarity measurement

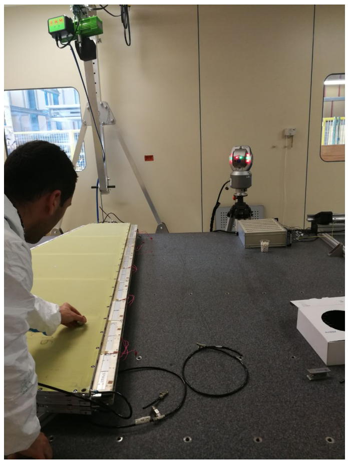

(b) Data acquisition with Laser Tracker

Figure 4.13: Setup during the planarity measurement. The Module is positioned on several aluminium supports which represents the reference plane z=0 for the measurement performed with the laser tracker.

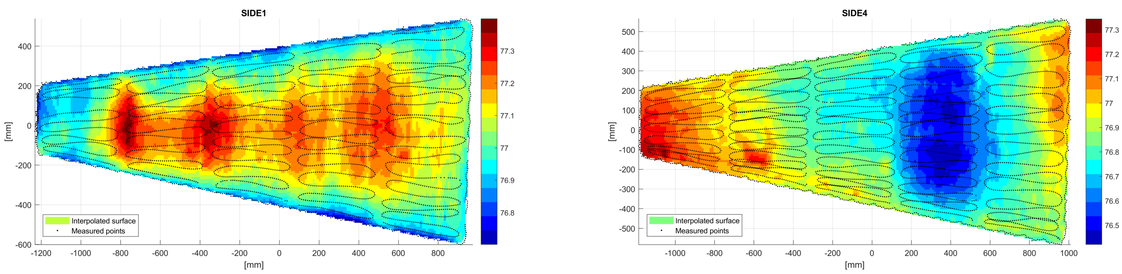

Figure 4.14: Point clouds obtained with the Laser Tracker and the interpolated surfaces of the two sides of the module for the planarity and thickness measurements.

A study has been done to estimate the deformation of the modules due to the gas pressure. This test has been performed on one prototype of the final Micromegas SM1 module, called *Doublet* as it was built with just two gas gaps (i.e. with only one readout and two external panels). Two sets of measurement have been collected, one without pressure and the other with an overpressure of ∼3 mbar.

The results are summarised in Table 4.1, which show the difference of the mean thickness $\Delta <z>$ of the panel with and without pressure is about 100 μm. Given that the deformation is due to the external panels, that deformation will be almost the same for the Quadruplet. As the SM1 modules have a volume of 40 L and a surface area of 2 m^2, a thickness variation of 100 μm can be translated in a volume variation of 0.2 L. The relative volume variation due to the deformation of the chamber in an overpressure regime is about 0.5 %.

Side 1		**Side 2**	
Δz (mm)	RMS (mm)	Δz (mm)	RMS (mm)
0.097	0.055	0.107	0.056

Table 4.1: Results from laser tracker measurements of the Doublet thickness difference with and without pressure.

4.1.3.2 Gas Leak Test

The tightness of the module is an important parameter to guarantee the performance of the chamber. This test is performed with the module in horizontal position on the granite table in Clean Room. The gas leak is measured with the *Pressure Drop* technique. The module is over-pressured in a static way (no continuous gas flushing) and then the variation of the pressure in time is measured.

Given the ideal gas law:

$$PV = nRT \ , \tag{4.1.1}$$

the gas leak in a given volume V, pressure P and temperature T is due to a variation of the gas mass, related to Δn. Then assuming a constant pressure in the chamber during the gas flushing, usually evaluated in terms of L/hour, this mass variation can be expressed as a gas volume variation ΔV.

The ATLAS requirement for the gas leak is expressed in terms of relative variation of the gas volume inside the chamber in time:

$$\frac{\Delta V}{V}\frac{1}{\Delta t} < 10^{-5}\mathrm{min}^{-1} \ . \tag{4.1.2}$$

This formula can be translated to relative variation of the pressure inside the chamber with respect to the atmosphere pressure outside the chamber during a pressure drop measurement. In this case, there is no constant gas flushing in the chamber and the pressure variation in the chamber is just due to a possible leak:

$$\frac{\Delta P}{P} = \frac{\Delta V}{V} \implies \text{ATLAS Limit: } \frac{\Delta P}{\Delta t} = 0.64 \text{ mbar} \cdot \text{hour}^{-1} \ , \tag{4.1.3}$$

assuming an external pressure P = 1 atm and a constant volume V= 40 L for the SM1 modules. This relation is based on the assumption that the volume of the chamber does not change with the gas flushing. As shown in the previous section, the volume deformation in overpressure condition is about 0.5% of the volume. As such, the effect on the relative variation $\Delta V/V$ is negligible.

The measurement is performed connecting the gas input line of the module to a pump of 200 mL capacity and the gas output to a sensor to measure the pressure inside the chamber (Figure 4.15). The value of the initial pressure inside the chamber is taken as reference and then air is injected with the pump in the chamber until an over-pressure of $\sim$3 mbar is reached. The pressure variation is then monitored together with the temperature.

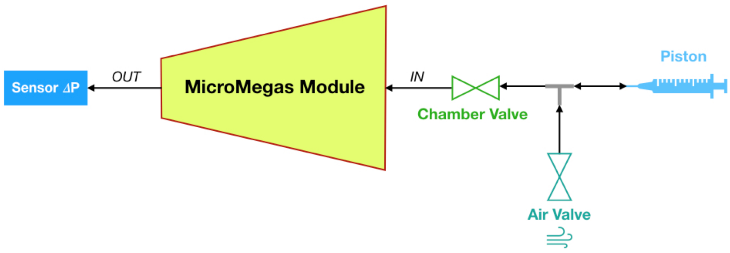

Figure 4.15: Setup scheme used at LNF to perform the pressure drop measurement.

Figure 4.16 shows the pressure drop due to the chamber leakage. A linear fit is then performed to extract a measurement of the leakage expressed in terms of mbar/hour. The duration of the measurement is about 15-20 minutes. In this short time range, the temperature variation ΔT is negligible as shown on the bottom panel of the plot in Figure 4.16, and also its effect on the pressure variation.

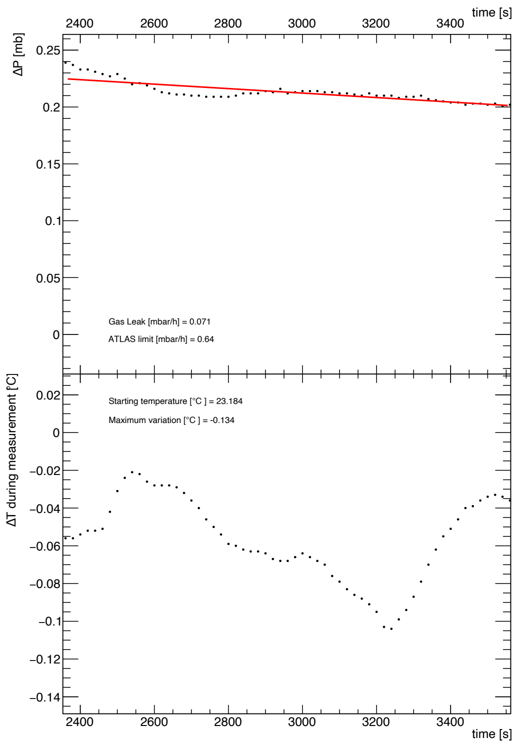

Figure 4.16: Pressure drop plot to measure the gas tightness of the chamber. The red line represent the linear fit to extrapolate the gas leak measurement. The bottom panel shows the Clean Room temperature variation during the measurement.

4.1.3.3 Strip and Panel Alignment

It is very important to ensure that there are no displacements or rotations between one PCB and another to achieve a high spatial resolution. For this purpose, many alignment measurements are performed during the construction of MM modules to measure all the possible parameters which can affect the track reconstruction. The as-built parameters to be determined with the alignment measurements are:

- PCB shape parameters: Strip sagitta and elogantions
- PCB alignment in-Layer: PCB translation and rotation and the in-Layer coordinate system
- Layer alignment in-Panel: Layer translation and rotation and the in-Panel coordinate system
- Panel alignment in-Module: Panel translation and rotation and the in-Module coordinate system

From a complete map of any displacements and rotations between the PCB, it is possible to perform a combined fit of all available measurements to reconstruct the full module metrology, which can be used at the muon reconstruction level. These parameters are measured several times with different tools, given that the individual measurement set does not cover the full module metrology.

At LNF, the panel-to-panel alignment is measured after the module assembly. The measurement is performed using a custom-made tool called *4 - Rasfork*, based on the *Rasnik* system [84] and developed in Saclay, that is able to measure the misalignment of corresponding PCB on the two panels. The ATLAS requirement on the Panel-to-Panel mis-alignment along the precision coordinate is $\Delta\eta < 60$ µm.

The Micromegas PCBs have three coded masks etched on the copper layer along each PCB side. These masks can be analysed by *Rasnik* system, using a contact CCD (cCCD) coupled with a LEDs. This projects the PCBs coded masks onto the cCCD camera. The *Rasnik Mask* (Rasmask) is a chessboard, as shown in Figure 4.17 with some squares switched from black to white, and other switched from white to black in way to indicate to a camera which part of the mask it is looking at, despite only seeing a small portion of the mask. The images of the masks are analysed by a dedicated LWDAQ software developed by Brandeis University [88]. The software performs the analysis of the rasmask pattern and determines the center of the mask with respect to the cCCD center (image sensor), defining the *rasnik position*. Then the final Rasnik measurement consists of the x and y coordinates of a point in the mask, the magnification of the mask image and the rotation of the mask with respect to the image sensor.

The 4-Rasfork instrument has the same working principle of the 2-Rasfork used for the layer-to-layer (within the same readout panel) alignment measurement performed in Pavia but it consists of four channels instead of two to be able to measure both the layer-to-layer and panel-to-panel alignment.

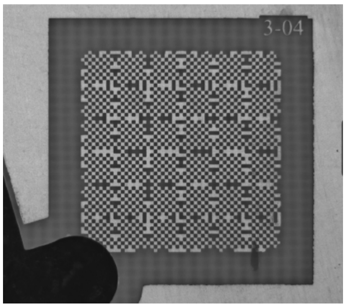

Figure 4.17: Rasmask installed on the PCBs.

It is made of four Rasfork tubes and a circuit of 4 cCCDs and a support block. A Rasfork tube consists of a prism holder, equipped with a prism and a LED circuit, and a tube consisting of 2 half tubes, a lens and a diaphragm at their junction. Due to the LED circuit, the light reflected by the rasmasks is guided by the prism, that works in total internal reflection, in the tubes and reaches the cCCD (one for each tube). The measurement setup is shown in Figure 4.18a. The module is placed on precise shims (the same used for the planarity measurement), so that the Rasfork can be inserted correctly.

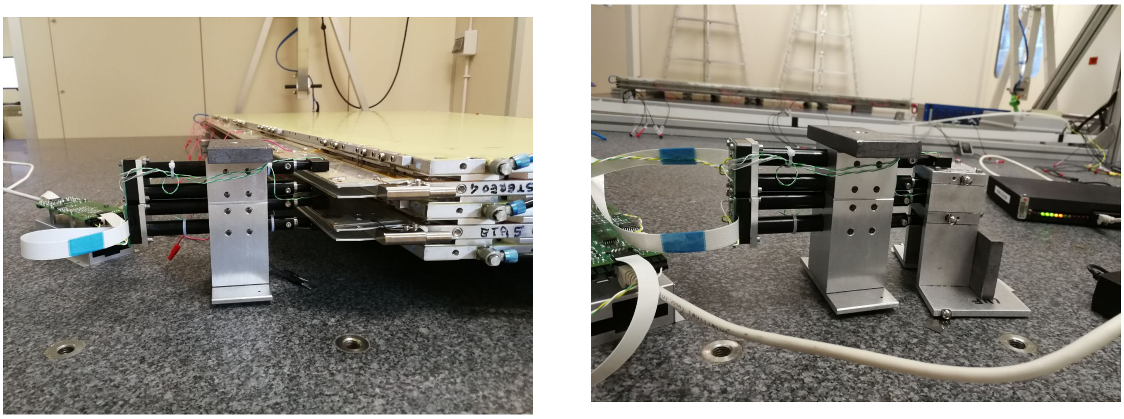

(a) 4-Rasfork setup during a measurement.

(b) 4-Rasfork during the calibration step at LNF using the Calirasfork.

Figure 4.18: 4-Rasfork measurement of the panel-to-panel alignment.

4-Rasfork Calibration The Rasfork tool needs to be calibrated, and for this another instrument called *Calirasfork* is used. The Calirasfork is made of a support sitting on 3 balls, holding four glass rasmasks, placed as the masks on the two panel sides. The position and the orientations of the *calimasks* are determined with an accuracy < 3 µm with an optical CMM in Saclay. This calibration is made only once.

At LNF the first time that the Rasfork is used, or if it is damaged or lacks precision, the Rasfork is calibrated placing the Calirasfork in the Rasfork (Figure 4.18b). The Rasfork acquires the images at different translation in x, y and different heights (placing shims of 1, 2 and 3 µm below the Calirasfork) and different angular orientation. Then a fit of the positions is made to validate the Rasfork calibration. Each time that a new alignment measurement is performed on a new Module, the calibration have to be checked.

4-Rasfork Measurement The Rasfork measurement on the module is performed on all the 30 rasmasks (3 masks each PCB side). The most relevant measurements are the ones performed on the PCB central masks, which give the real magnitude of the mis-alignment between the panels, instead the others are sensitive also to possible PCB shape deformations.

An example of map of the mis-alignment $(\Delta x, \Delta y)$ measurements is shown in Figure 4.19. The y coordinate represents the precision coordinate η in the ATLAS coordinate system.

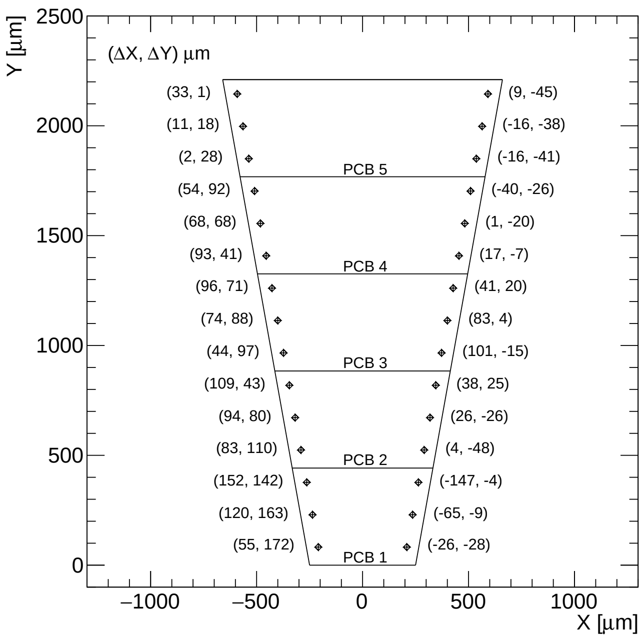

Figure 4.19: Scheme of the ΔX and ΔY displacement of the readout strips between the Eta and the Stereo readout panel.

4.1.3.4 High Voltage Stability Test

The High Voltage stability has been a crucial point of the MM performance during the commissioning phase. In Section 4.2, the different issues met during the production of the MM detectors will be described in detail together with the corresponding solutions. They include several additional steps, as the cleaning procedure and the readout panel passivation, to the MM module construction.

A further step to improve the HV performance of the chambers is the so-called *conditioning* procedure in High Voltage. This procedure consists in a slow ramp up of the HV voltage applying an initial voltage of 400 V in the amplification region. It is slowly increased until it reaches the nominal working point of 570 V. Once the nominal HV is reached, a long term stability test is performed and the behaviour of the chamber is monitored for several days (also weeks).

HV setup and acquisition The final HV test is performed at Cosmic Ray Stand. All the HV sections are connected to the CAEN power supply (PS) SY4527 through the 48 independent HV channels board A7038AP, a Common Floating Return board which allows on-detector grounding, reducing the noise level. In this setup it is possible to power all the 40 HV sections of the module independently, to have a *full-granularity* configuration.

The setting and monitoring of the main HV parameters is performed using the CAEN interface GECO2020. It is the GEneral COntrol Software developed by CAEN for High Voltage boards and systems, which brings the HV control and management via external Host PC using a simple GUI.

The more interesting HV parameters are *VMon* (monitored HV) and *IMon* (monitored current). These values are constantly recorded by a DCS code developed at LNF. The code interfaces with the PS recording data each second using the CAEN HV Wrapper Library functions. Grafana dashboards [1] is used to monitor the trend of the current for each HV section. Figure 4.20 shows an example of the current monitoring in real-time.

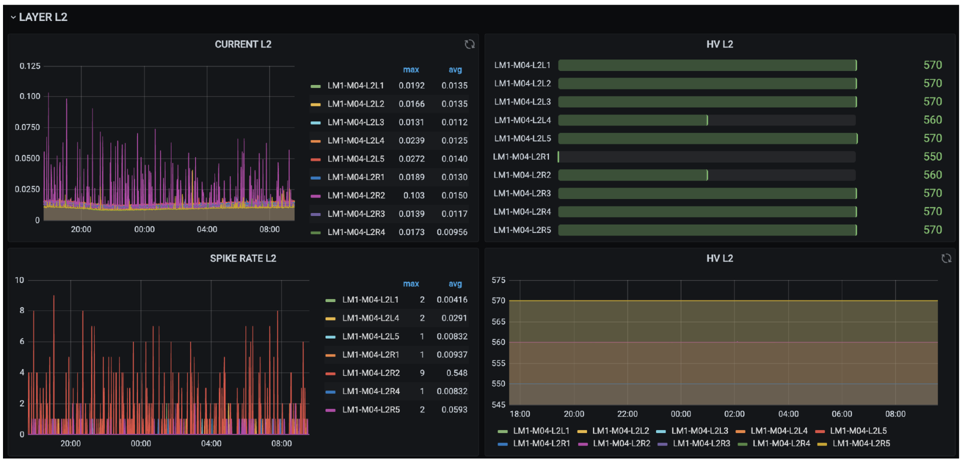

Figure 4.20: HV monitoring system used at LNF to perform the HV test uses Grafana dashboard to monitor the currents of different HV sections.

Procedure and Criteria The HV test is performed while flushing the chamber with Ar:CO_2 with a gas flux of ∼20 L/h. The HV ramp up starts when the gas RH reaches a value $< 10\%$. First of all the HV sections are switched on at 100 V to check there are no shorts. Therefore each section is ramped up at 400 V, and then at steps defined by the

[1]open source analytical and visualisation tool

following chain:

$$400V \rightarrow 450V \rightarrow 500V \rightarrow 510V \rightarrow 520V \rightarrow 530V \rightarrow 540V \rightarrow 550V \rightarrow 560V \rightarrow 570V \tag{4.1.4}$$

For the first modules, in which low resistivity issue was present (then cured through the passivation technique described in Section 4.2.4.3), the ramp up phase was very slow, taking 1-2 hours between one step and another. In the last modules, with higher strip resistivity, this step became much faster (5-10 minutes each step).

This test is important also to evaluate which is the maximum HV value that a section can reach, which can be lower than the nominal: 570 V. To identify the maximum HV value for which a section is stable, some acceptance criteria have been defined. These are based on the current drawn by the section and on the *spark rate*. The *spark rate* is the frequency in which the HV section current goes above a defined current *threshold*. It is computed defining a *spark* as an IMon value > 100 nA in a second. Then if a section draws a current >100 nA for 6 seconds, it is counted as 6 sparks. The spark rate is defined as the number of sparks per minute.

The HV sections can be flagged as GOOD, CONDITIONING or BAD sections based on the following criteria:

- **GOOD**: if the section IMon value is < 10 nA and stable (spark rate ~ 0) $\rightarrow$ The HV value can be ramped up to the next step
- **CONDITIONING**: if the section IMon value shows *rare instabilities* ($0 <$ spark/min < 6) or few sparks order of hundreds nA $\rightarrow$ The section is left to condition at the corresponding HV value
- **BAD**: if the section IMon value shows continuous instabilities (spark/min > 6) $\rightarrow$ The HV is lowered until the IMon value became stable again. The HV could be lowered by 5 V but also by 50 V if needed. The section is left at this HV value for several hours and if it becomes stable, it can be ramped up again following the described procedure.

Figure 4.21 shows the three different behaviour described above. These criteria are needed also to evaluate if a module has passed the requirements or not.

The ATLAS HV acceptance requirement for a MM module is that the 85% of the sections have to pass the following criteria:

- Nominal HV of 570 V
- Spark Rate < 6/min

If a section fails even one of the requirements, it is not considered as accepted. For the SM1, a module is accepted if at least 34/40 HV sections pass the requirements.

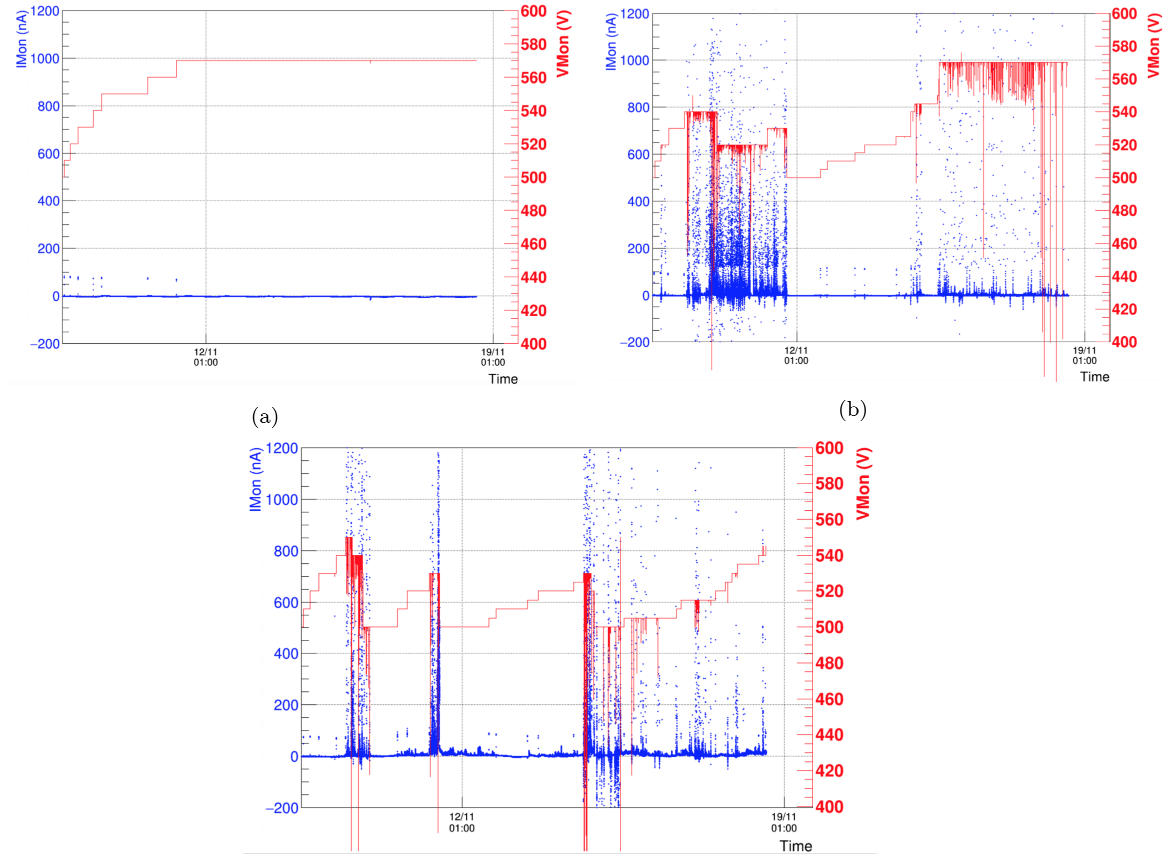

(a)

(b)

(c)

Figure 4.21: Different HV behaviour. Each plot show in red the monitored HV (VMon) and in blue the monitored current (IMon). In (a) it is shown an example of a good sector. In particular in this plot it can be seen also the ramp-up step at the beginning of the plot. In (b) it is shown an example of a sector which shows a bad HV behaviour at the beginning. For this reason the HV has been lowered up to 500 V, when it became again stable. Then the ramp up procedure has been performed again and the sector reached 570 V showing a number of spark $< 6/\text{min}$, and it has been left at this HV value to condition. In (c) it is shown an example of a bad behaving section. This plot shows the continuous HV drops due to the sparks which can be recovered just lowering the HV up to 500 V, and finally show a spiky behaviour even at this HV value.

4.1.3.5 Cosmic Ray Stand Test

The modules are then validated at the LNF Cosmic Ray Stand to estimate their performances, in terms of efficiency of each layer. The experimental setup (Figure 4.22) consists of:

- two array of plastic scintillators for the trigger coincidence, achieving a trigger rate of 50 Hz. The trigger logic is the OR between the scintillators on the same plane and the AND between the two plane.
- 35 cm of iron absorber to cut muons <0.6 GeV
- MM Module

The module is equipped with 40 APV25 front-end electronic boards. The APV25 boards have a signal sampling time of 25 ns, sent to the Scalable Readout System (SRS) to be read.

Figure 4.22: Experimental setup at the ATLAS LNF Cosmic Ray Stand.

The software efficiency is computed with a *self-tracking* algorithm. This method is able to estimate the efficiency on the layer i by reconstructing the track on the other $N-1$ layer (Figure 4.23). At LNF, for the SM1 modules, the events selected to reconstruct a track on the i-layer requires 1 cluster on the other 3 layers. The efficiencies on the Eta and Stereo layers are then estimated with the 3 over 4 method.

Efficiency on Eta Layer The track is reconstructed by using the cluster on the other Eta layer and building a *super-point* (SP) from the Stereo layers, both for the precision coordinate η and the second coordinate ϕ. The super-point coordinates are defined:

$$\begin{cases} \eta_{sp} = \dfrac{\ell_3 + \ell_4}{2\cos\theta} \\ \phi_{sp} = \dfrac{\ell_3 - \ell_4}{2\sin\theta} \end{cases} \tag{4.1.5}$$

where ℓ_3 and ℓ_4 are the local coordinates in the Stereo layers 3 and 4 respectively. The tracks are selected with angles within $\pm$ 0.5 rad (geometrical acceptance) and the extrapolation of the expected position on the Eta layer to be measured is done by looking for a cluster on that layer within $\pm$ 10 mm from the expected position.

Efficiency on Stereo Layer The track is reconstructed using the clusters on the two Eta layers, used to determine the precision coordinate η. The second coordinate ϕ is defined building a *super-point* from the other Stereo layer and one of the Eta layer. The super-point coordinates are:

$$\begin{cases} \eta_{sp} = \ell_2 \\ \phi_{sp} = \dfrac{\ell_2\cos\theta - \ell_4}{\sin\theta} \end{cases} \tag{4.1.6}$$

where ℓ_2 and ℓ_4 are the local coordinates in one of the Eta layers (layer 2 for example) and in the other Stereo layer (layer 4 for example) respectively. Also in this case, the tracks are selected with angles within $\pm$ 0.5 rad and the extrapolation of the expected position on the Stereo layer to be measured is done by looking for a cluster on that layer in a window of $\pm$ 25 mm.

Figure 4.24 shows an example of 1D efficiency plot along the precision coordinate (X corresponds to η) and the 2D efficiency map for Layer 1 and Layer 3 of one module.

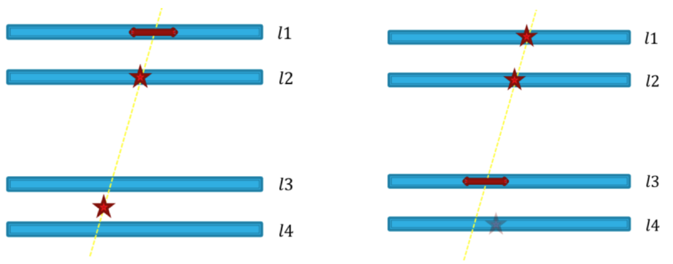

Figure 4.23: The *self-tracking* algorithm is used to estimate the efficiency on the layer i reconstructing the track on the other $N-1$ layer. The method to estimate the efficiency on the Eta layer is shown on the left, in which a super-point from the Stereo layer is used, instead on the right is shown the method used for the Stereo layer (super-point from the other Stereo layer and one of the Eta layer).

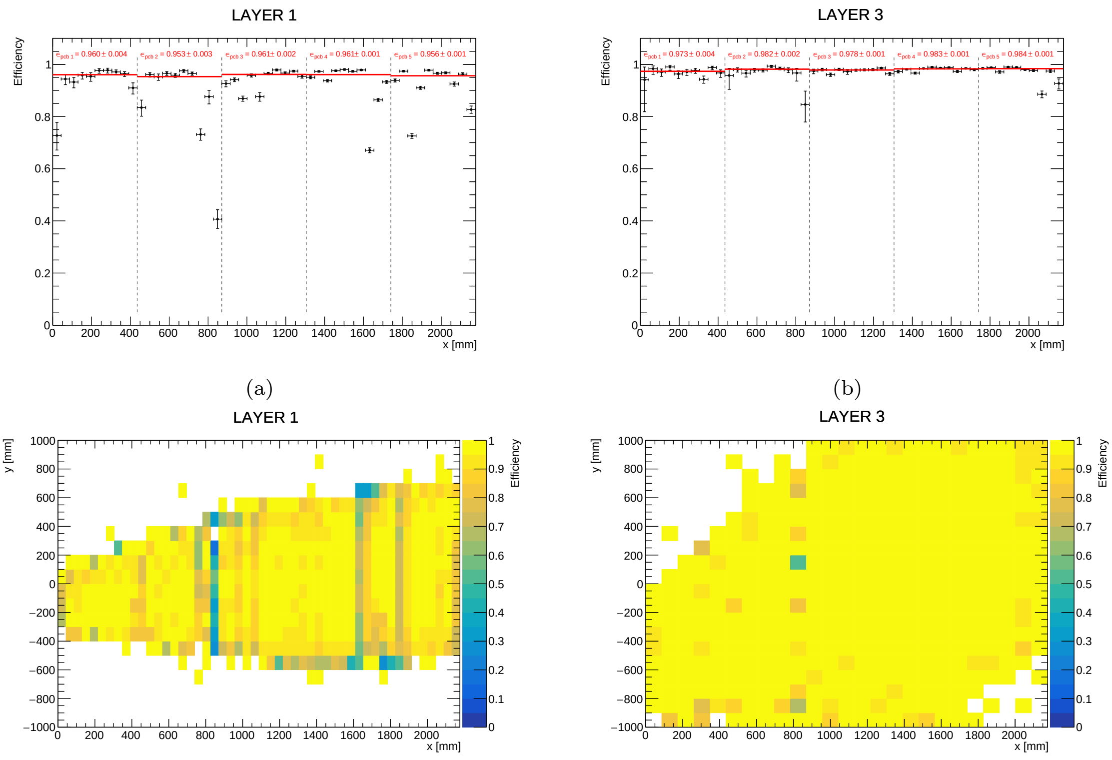

(a) (b) (c) (d)

Figure 4.24: 1D e 2D efficiency plot per Layer 1 and Layer 3.

4.1.3.6 Results of SM1 modules produced by INFN

In this section, a summary of the QA/QC tests results on SM1 modules performed at LNF is presented. In Figures 4.25-4.30, the summary of the QA/QC measurements on the SM1 modules produced are reported.

The planarity measurements results are within the tolerance value of 200 µm for almost all the module. In Figure 4.25b it is clear that the measurements on the two sides sometimes are quite different. This can be explained by possible defects on the external drift panels, which impact on the measurement on one side, but not on the other. The planarity measurements are indeed sensitive to possible defects on the external drifts and also on the supports used for the measurement. For this reason, also modules that show values far from the tolerance have been accepted.

The gas leak results also are in the tolerance, except for a couple of modules. Cosmic rays tests showed good performances also for these chambers, then they can be accepted.

The Δy (then $\Delta\eta$ in ATLAS coordinate) alignment results shows a couple of module out of the tolerance. In this case, as explained in Section 4.1.3.3, it is possible to fully reconstruct the geometry of the strips using also the other measurements performed on the single panels and PCBs. Then also modules with alignments a bit outside the tolerance can be accepted.

The most important requirement on the HV: at least 85% of the HV sections at 570 V, is respected by all the modules.

In Table 4.2, the status of all the SM1 modules is summarised. It shows the percentage of the detector area which is set at nominal voltage of 570 V and the corresponding mean efficiency of the module. The last column shows if the module has been disassembled because it does not pass some validation criteria, or at LNF or at CERN, or if it has been integrated on a Double-Wedge (defined in Section 3.2.1), which is labelled as A# or C#, if it belongs to the NSW-A or NSW-C.

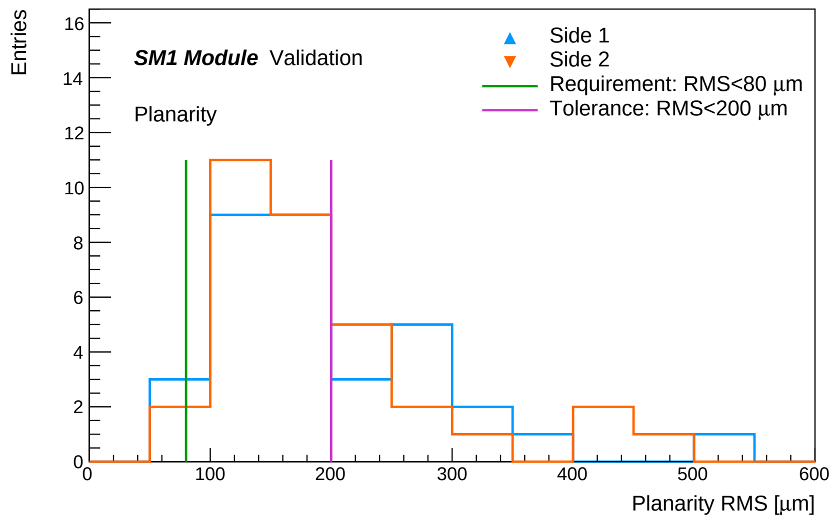

(a)

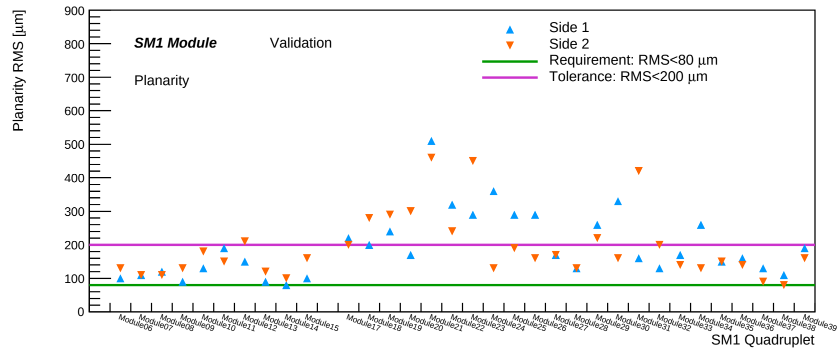

(b)

Figure 4.25: Summary planarity measurements.

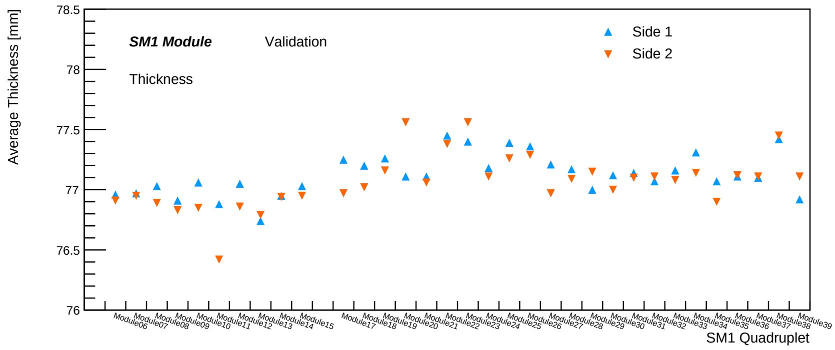

Figure 4.26: Summary thickness measurements.

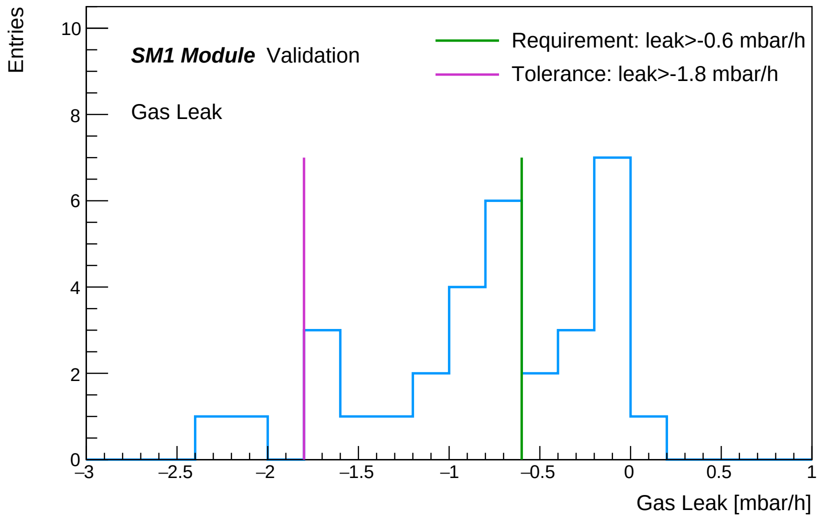

(a)

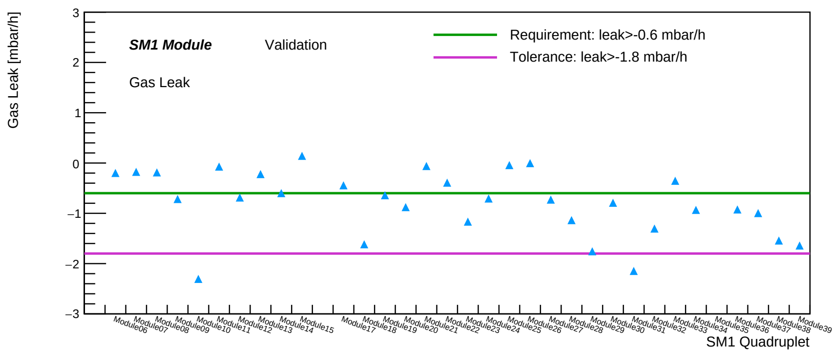

(b)

Figure 4.27: Summary gas leak measurements.

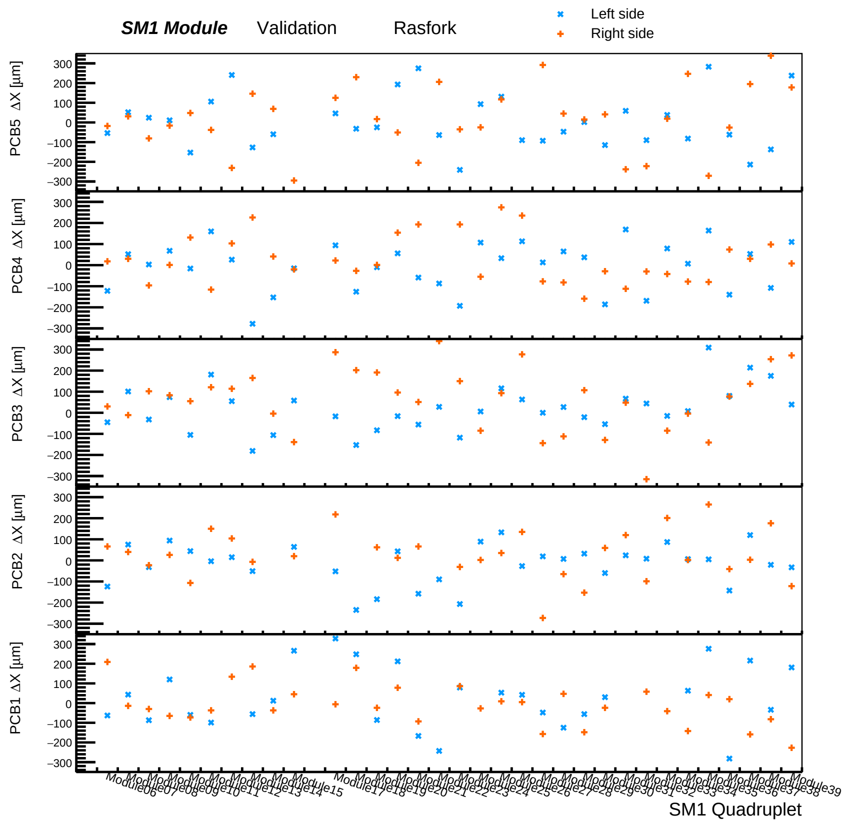

(a)

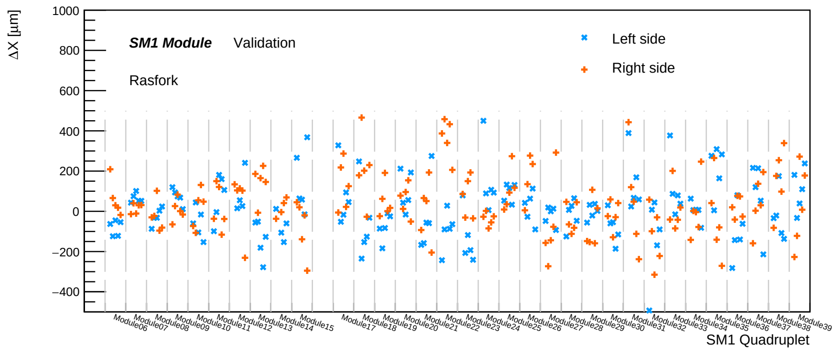

(b)

Figure 4.28: Summary ΔX measurements from rasfork.

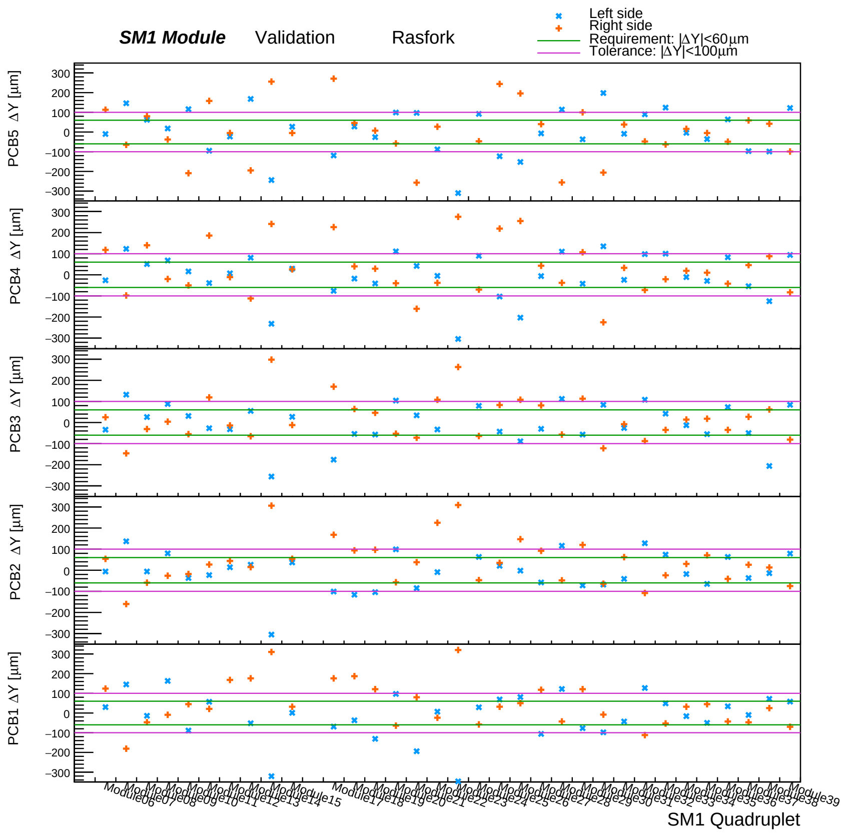

(a)

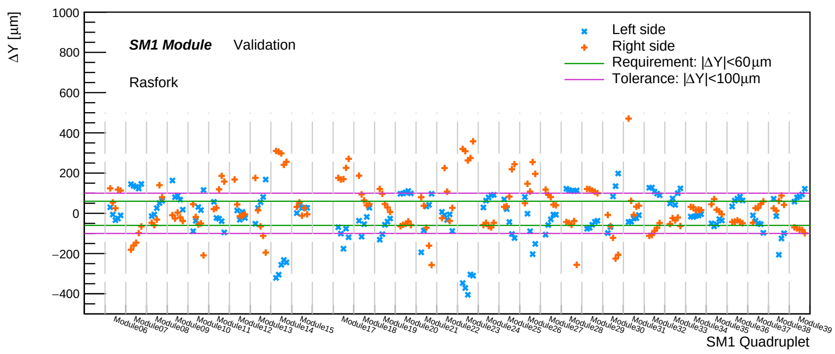

(b)

Figure 4.29: Summary ΔY measurements from rasfork.

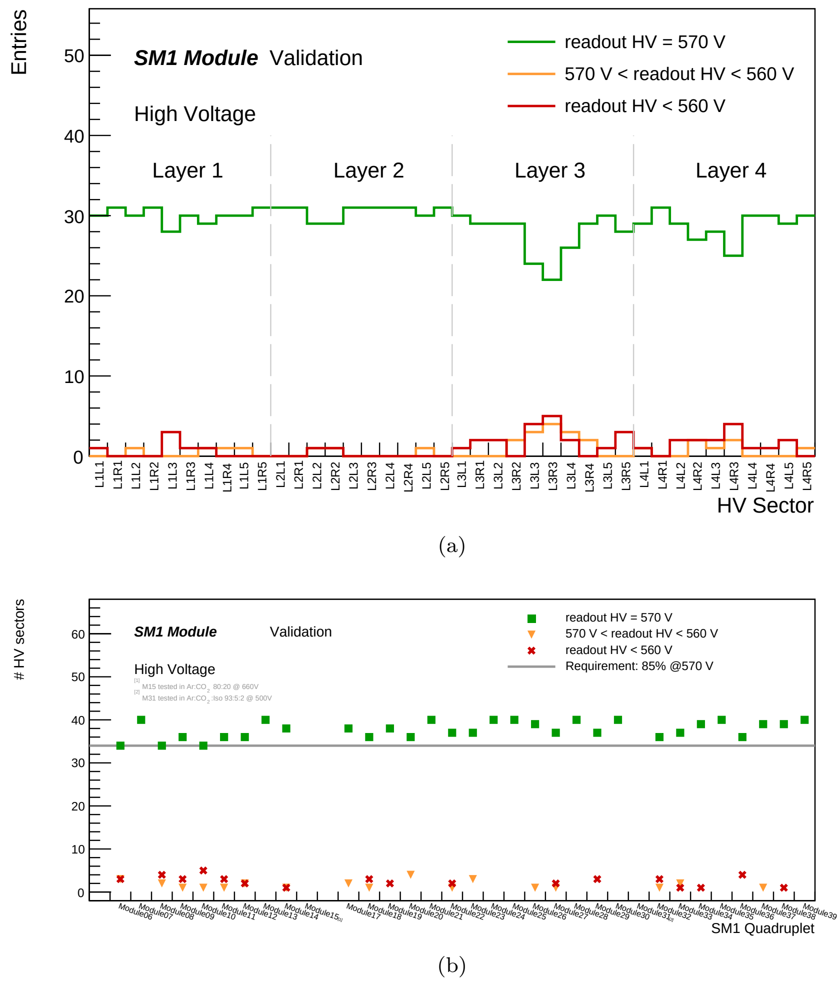

Figure 4.30: Summary HV results.

SM1 Module	Area at 570 V	Mean Efficiency	Validation at LNF	Where it is
M01	-	-	-	used for mechanical integration test on the Wheel → Disassembled
M02	-	-	-	used for electronics integration test on the Wheel → Disassembled
M03	-	-	Yes	Disassembled
M04	-	-	Yes	Disassembled
M05	-	-	No	Disassembled
M06	88.5 %	89.3 %	Yes	CERN on A14 (IP)
M07	100 %	95.1 %	Yes	CERN on C12 (HO)
M08	80.0 %	88.6 %	Yes	CERN on C12 (IP)
M09	87.8 %	89.9 %	Yes	CERN on A14 (HO)
M10	76.3 %	90.4 %	Yes	CERN on A04 (HO)
M11	87.3 %	91.5 %	Yes	CERN on C04 (HO)
M12	92.2 %	87.4 %	Yes	CERN on A16 (IP)
M13	100 %	96.3 %	Yes	CERN on A16 (HO)
M14	94.9 %	96.7 %	Yes	CERN on A08 (IP)
M15	100% in Ar:CO_2 80:20	98.0 %	Yes	CERN on A08 (HO)
M16	-	-	No	Disassembled
M17	100 %	96.2 %	Yes	CERN on A12 (HO)
M18	88.5 %	94.1 %	Yes	CERN on A12 (IP)
M19	89.8 %	91.8 %	Yes	CERN on A06 (IP)
M20	100 %	95.2 %	Yes	CERN on A06 (HO)
M21	100 %	92.2 %	Yes	CERN on A10 (HO)
M22	94.9 %	93.1 %	Yes	CERN on A02 (HO)
M23	100 %	94.8 %	Yes	CERN on A02 (IP)
M24	100 %	95.4 %	Yes	CERN on A10 (IP)
M25	100 %	94.4 %	Yes	CERN on C14 (IP)
M26	100 %	96.1 %	Yes	CERN on C10 (IP)
M27	91.1 %	91.5 %	Yes	CERN on C14 (HO)
M28	100%	96 %	Yes	CERN on C02 (HO)
M29	96.1 %	96.3 %	Yes	CERN on C10 (HO)
M30	100 %	96.1 %	Yes	CERN on A04 (IP)
M31	100% in Ar:CO_2:Iso 93:5:2	90.8 %	Yes	CERN will be on C04 (IP)
M32	94.9 %	92.8 %	Yes	CERN on C16 (HO)
M33	94.9 %	96.2 %	Yes	CERN on C16 (IP)
M34	93.6 %	95.7 %	Yes	CERN will be on C08 (HO)
M35	93.6 %	94.4 %	Yes	CERN (spare)
M36	80.7 %	80.8 %	Yes	CERN on C06 (HO)
M37	100 %	94.1 %	Yes	CERN on C06 (IP)
M38	94.9 %	95.1 %	Yes	CERN on C08 (IP)
M39	100 %	93.8 %	Yes	CERN on C02 (IP)

Table 4.2: Summary validation table of all the SM1 modules assembled and tested at LNF.

4.2 High Voltage stability studies on SM1 modules

The HV stability has been a critical part of the Micromegas commissioning. For this purpose, a limited R&D program restarted addressing the main issues:

- Correlation of the currents with the humidity
- Mesh mechanical imperfections
- Residual ionic contamination on PCBs and panels
- Non – uniform resistivity on the anode PCBs

Several studies have been performed to overcome these issues and solutions have been implemented in the module assembly workflow.

In the following sections some of these studies are described in details.

4.2.1 Relative humidity and gas flux

From the very first tests on the Micromegas modules, the impact of the relative humidity inside the chamber on the HV behaviour has been observed to be not negligible. A relative humidity higher than 15% leads to a contamination of the gas mixture, compromising the performance of the chamber. To reduce this, a solution is to increase the gas flux up to 20 L/h. At LNF usually several chambers are tested in parallel. To maximise the benefit of the high gas flux, two SM1 modules are connected in series as in Figure 4.31. The relative humidity is monitored with the RH sensor Vaisala connected at the output of each chamber. In Figure 4.32, the variation of the RH in time of two chambers connected in series is shown. It is clear the reduction of the RH from the increasing of the gas flow. The modulation of the curves are due to the day-night cycle.

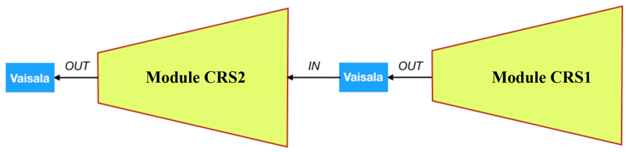

Figure 4.31: SM1 modules gas line connected in series. The output gas is monitored with RH sensor Vaisala.

4.2.2 Mesh Polishing

The imperfections, as small defects, on the meshes can sensitively change the electric field in the amplification gap. Figure 4.33b shows the modification of the electric field due to a single point defect of 2µm size, which can be 100 times larger than the nominal value. As consequence, it has an impact on the High Voltage behaviour of the Micromegas, leading to a sparky regime of the chamber.

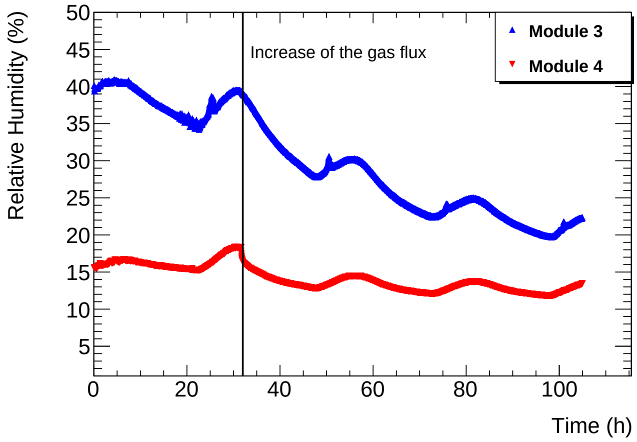

Figure 4.32: Relative humidity in time of the SM1 modules M3 and M4 connected in series (M3→M4). It shows the decrease of the RH with the increase of the gas flux.

The effects of these imperfections can be mitigated and solved by *polishing* the mesh. The polishing is performed on the finalised drift panels in two steps, with two different grades of sand papers. The first step is done with grade 2500 sand paper to polish few microns of wire and remove the wider imperfections. In the second step, a 10000 grade sand paper is used to perform the precision polishing to uniform the mesh surface.

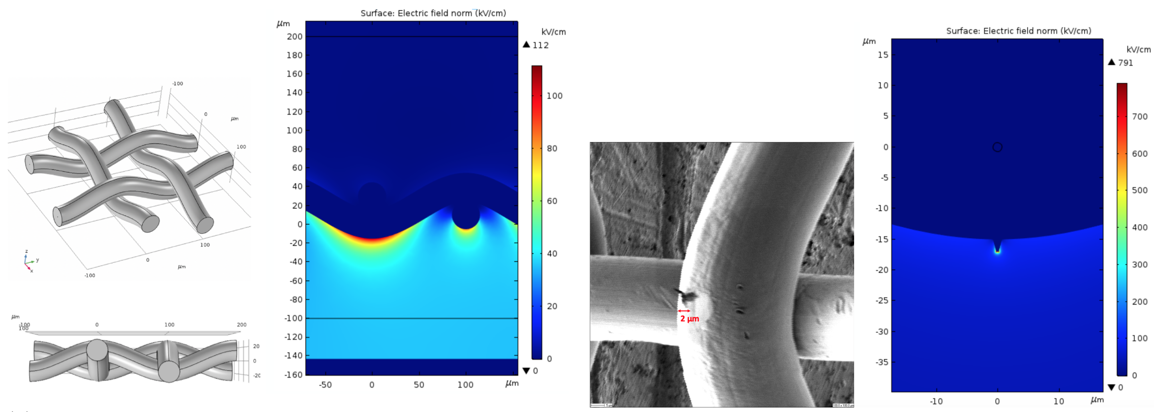

(a) Standard mesh pattern: wire diameter of 30 μm and a pitch of 100 μm (then a edge-to-edge distance of 70 μm) on the left. Simulation of the electric field of this pattern.

(b) SEM image of a defect of 2µm size on the micromesh on the left and simulation of the electric field due to this single point defect on the right.

Figure 4.33: Comparison of mesh electric field simulation in presence of mesh imperfections with nominal.

4.2.3 Cleaning

During the PCB and panels production, organic residuals can deposit on the surfaces, leading to instability problem in the High Voltage of the chambers. For this reason, a cleaning procedure has been developed to guarantee the removal of the most of the organic residuals (Figure 4.34).

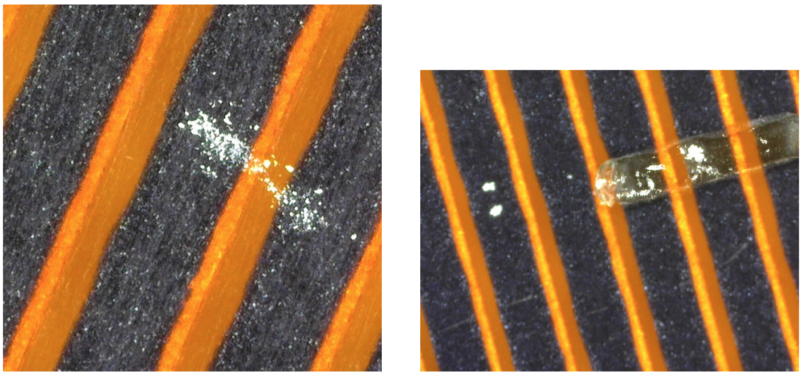

Figure 4.34: Residuals of the previous NGL treatment on the PCB.

The cleaning occurs with the panels placed in vertical position in a custom made *washing machine*. Detergents are distributed on the whole panel surfaces with the use of soft brushes, to properly remove the residuals that can be trapped on the pillar edges, and with warm tap water (T$\sim$ 40°). Different detergents are used according to the panel: the Readout panel is cleaned with micro crystal multipurpose cleaner Cif® cream detergent, the Drift panels with NGL Cleaning Technology® 17.40 cleaner. Alternative cleaning procedure for the Readout panels have been tested using caustic soda and pumice powder.

Measurements of the ionic contamination have been performed by ELTOS on the PCBs with the Resistivity of Solvent Extract (ROSE) test, to test the presence and measure the average concentration of soluble ionic contaminants, using different detergents. The test results is reported in Table 4.3 in terms of total equivalent NaCl [mg/sq inch] for a non-washed PCB, for a PCB immersed in a tank with caustic soda for 30 minutes and for one hour, and finally a PCB cleaned only with Cif®. They show that the cleaning with Cif® gives the best performance in terms of reduction of ionic contamination.

Test on PCB	**NaCl equivalent**
Non-washed	209.6
Caustic Soda 30 min	165.0
Caustic Soda 1 hour	27.7
Only Cif ®	7.6

Table 4.3: PCB ionic contamination results from ROSE test.

The pumice powder is used to smooth the Readout panels edges before the passivation (described in Section 4.2.4.3). It results in a deeper cleaning of the area, to avoid any possible impurity to be trapped below the passivation, leading to bad HV behaviour.

The detergent is removed by rinsing the panels with warm tap water (T$\sim$ 40°) using garden shower and a soft paint brush. Further rinsing is performed with 25-40 L/surface of deionised water using a high pressure ($\sim$ 60-70 bar) Kärcher®, kept at a safe distance of 30-40 cm from the surface. This is to eliminate all remnants of the tap water and for the final mechanical action to remove sticky dirt, especially around pillars. Deionised water is also sprayed inside the inlet/outlet of the gas distribution tubes, mounted on the Drift panels, to check that sprays come out from the little holes along the tubes. After the rinsing step, clean room tissues and nitrogen flux are used to remove water drops from assembly holes, rims and gas tubes. The panels are then transported and mounted directly in the drying station.

The drying station is a custom made structure able to host 5 panels in vertical position (as much as needed for a MM module), located close to the clean room, where the module will be assembled. It is equipped with a ventilation system to filter the air and the drying temperature is around 40°.

In Figure 4.35, the different steps of the cleaning procedure and the final stock of the panels in the oven are shown.

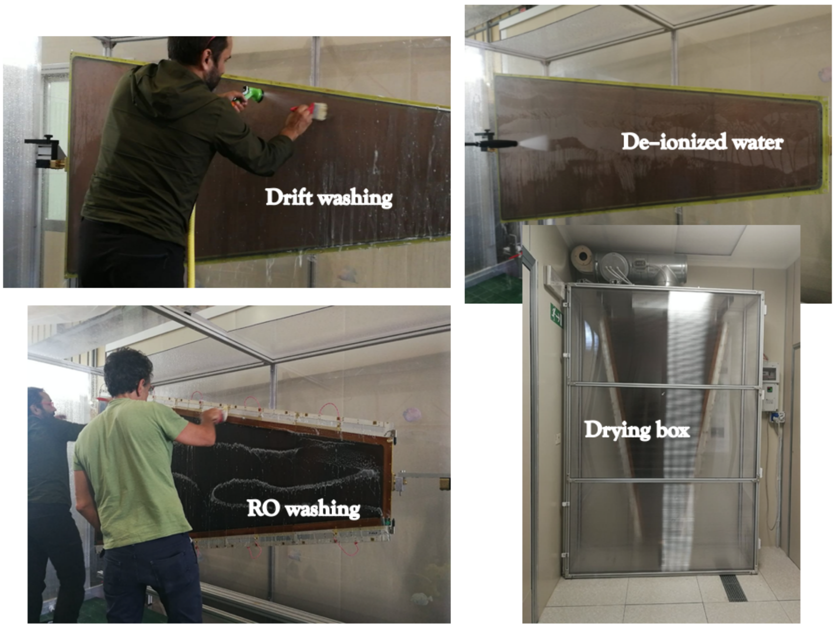

Figure 4.35: Different steps of the cleaning procedure. Drift panels are washed with NGL and Readout panel with CIF. Both are rinsed before with hot tap water and then with de-ionised water. Finally the washed panels are put in the drying box at 40°.

4.2.4 Resistivity of the Readout board

The resistive strips on the PCB are ink-printed on Kapton® support. Their layout presents interconnections with a defined pattern, as shown in Figure 4.36. The resistive pattern consists of strips congruent to the readout layer, but with an array of bridges connecting each strip alternating with its top or bottom neighbour every 10 mm. This yields a more homogeneous surface resistivity which is less effected by damages than single lines. Finally the strips are interrupted in their centre to divide the surface into two High Voltage sectors, interconnecting all resistive lines.

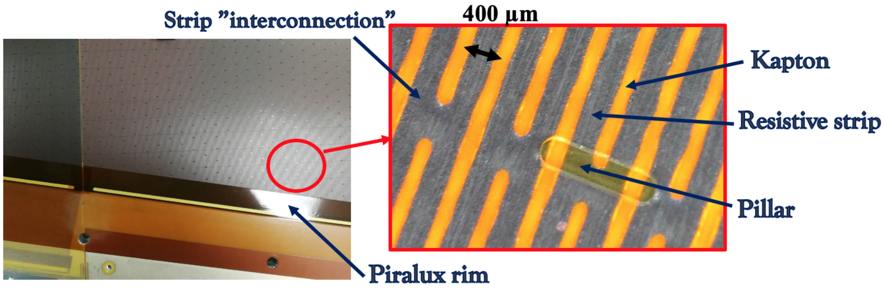

Figure 4.36: The resistive strips on PCBs shows a defined pattern with an array of interconnection between one strip and the next one at regular distance of 10 mm.

During the Micromegas chamber production, it has been observed that the layout of the PCB has an impact on the HV behaviour of the section. This is due to the fact that this layout leads to a non-uniformity of the resistivity on the board anyway.

In particular, the resistance values measured near the piralux rim, along the PCB edges, are very low, below the acceptance threshold of 0.28 MΩ/sq. This fact itself does not represent a problem, but in presence of a defect on the readout panel, or on the mesh, a low resistivity area on the board becomes a weak point for the stability in HV, where sparks occurs.

4.2.4.1 SM1 PCB Layout

For the SM1 modules there are 2 type of PCB: Eta and Stereo, of 5 different size. Looking at the Gerber files of the two type of PCB (Figure 4.37), it can be seen that the pattern of the interconnection bridges is different between Eta and Stereo. In particular for the Stereo, the first line of interconnections near to the PCB edge ends below the piralux rim, which is 1 cm wide. This means that the shortest strip (above the piralux line) on that PCB is 1 cm long, leading to a lower value of resistance in that area.

4.2.4.2 Resistivity measurements

The resistivity measurements performed at CERN on the PCBs show that the minimum value of the resistance measured in some cases goes below the acceptable threshold of 0.28 MΩ/sq. A set of the measurements on PCB foils performed at CERN is showed in Figure 4.38. It shows both the minimum values and the average values of the resistance.

Further measurements are performed in Pavia, when the PCB are glued to the final Readout panel. They measure the resistance both on the right and left side of the PCB, given that they correspond to two different HV sections. Those measurements have been correlated with the HV measurements performed at LNF for each section.

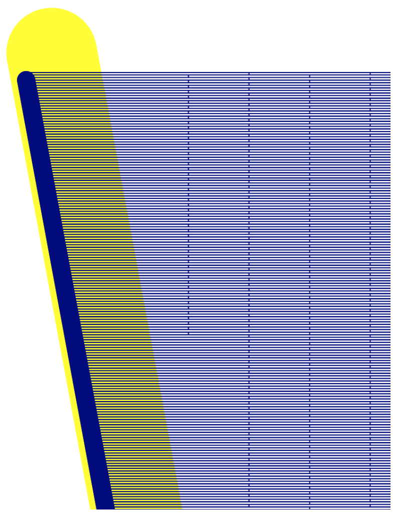

(a) Layout of Eta PCB

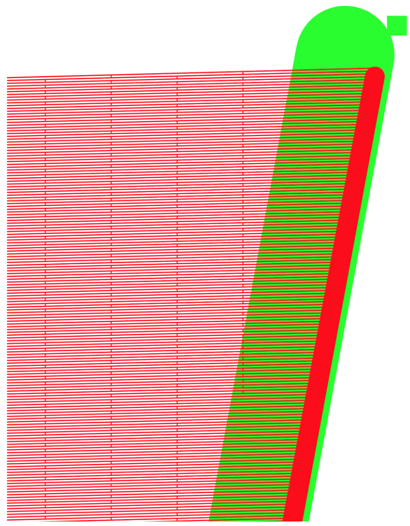

(b) Layout of Stereo PCB

Figure 4.37

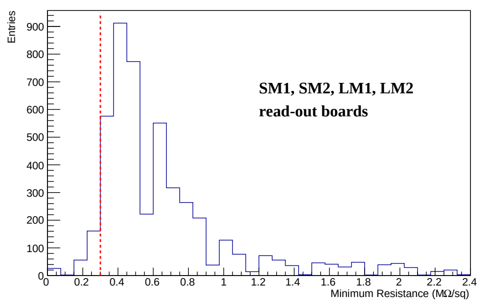

(a) Minimum value of the resistance per PCB foil.

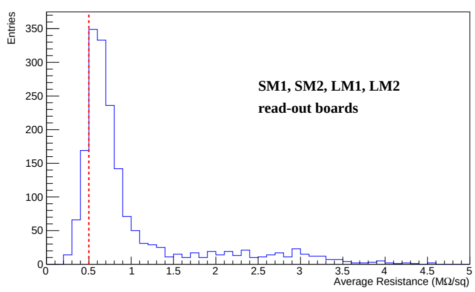

(b) Average value of the resistance per PCB foil.

Figure 4.38

From this study, a clear correlation can be seen between the minimum value of the resistance on the PCB and the maximum HV value reached by that sector, as reported in Figure 4.39. It shows that PCB with lower value of R_{min} cannot reach the working point at 570 V. In particular, looking at separate measurements of the Eta and Stereo PCBs, it is evident that the worse HV sections are more frequently on the Stereo PCBs, sign of a correlation of this behaviour with the PCB layout.

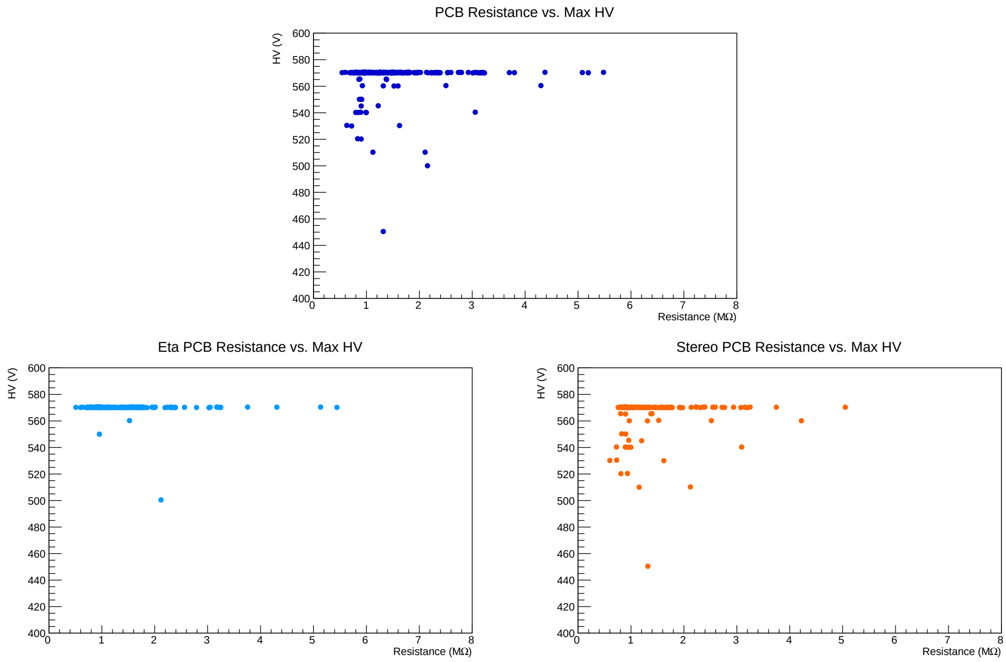

Figure 4.39: Correlation between the resistance measurement performed at Pavia on the PCBs and the HV value of the corresponding HV section measured at LNF. The plots on the bottom show the same statistics, but splitted for Eta PCBs and Stereo PCBs.

The effect of the HV tests on the problematic PCBs has been investigated with several visual inspections of the readout panels, when a problematic SM1 module has to be disassembled. These inspections have shown that in many cases the damages due to the sparks are localised on the resistive strips junctions crossing the piralux rim, where the resistance is usually lower (Figure 4.40).

4.2.4.3 PCB Edge Passivation

To mitigate the problem of the low resistance along the PCB sides, the *edge passivation* procedure has been developed for the SM1 modules and transferred to the other construction sites. This procedure consists in the passivation of the region along the sides of the active area through a deposit of a thin layer of araldite or polyurethane. The thickness of the area which must be passivated varies from 0 to 3 cm, according to the distance from the PCB edge in which the resistance value has a value above the threshold. Figure 4.41 shows the steps of the passivation procedure.

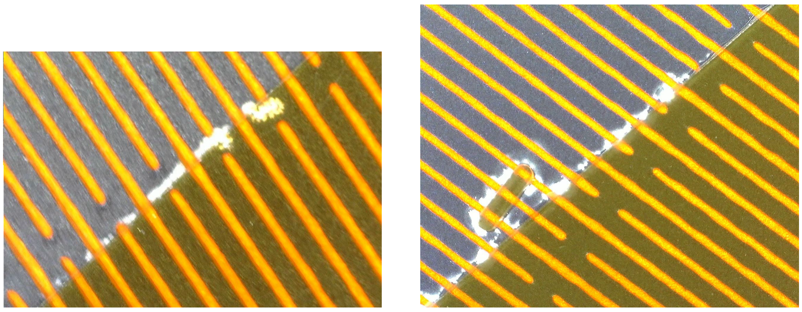

Figure 4.40: Damages due to the discharges along the piralux rim.

The Readout panels have to be cleaned both before and after the passivation step. In particular, the pumice powder is used to clean the Readout panels edges before the passivation, to avoid that impurities can be trapped below the passivation.

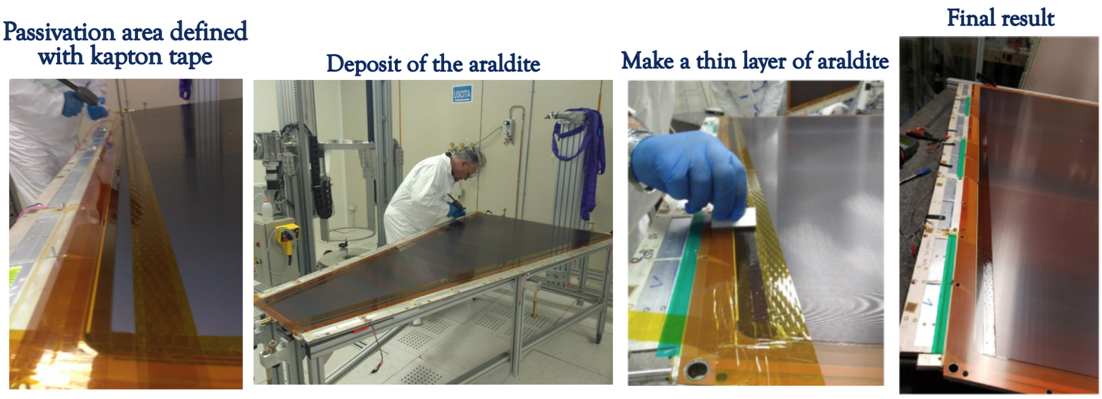

Figure 4.41: Different steps of the passivation procedure.

4.2.4.4 PCB circuit model

In this section, a study on the PCB layout and its relation with the resistance is presented. The idea is to build a model of the resistive PCB circuit to see the behaviour of the resistance as function of the PCB layout.

The circuit of the PCB can be modelled from the pattern of the interconnection bridges (this pattern is also called *ladder*): each interconnection represents a node of the circuit, and each portion of strip, from one interconnection and the next one, represents a resistance. An example of a real Eta PCB ladders layout is shown in Figure 4.42. The parameters of the PCB are then:

- First interconnection distance d: it varies for each PCB and each strips, following a given pattern related also to the angle of the PCB.
- Ladder step L: it is the distance between one interconnection on a strip and the next interconnection presents on the neighbour strip. Its values is fixed to be 10 mm.

- Resistivity ρ: it is the linear resistivity of the strip. It should be of the order of $\sim$10 MΩ/cm.

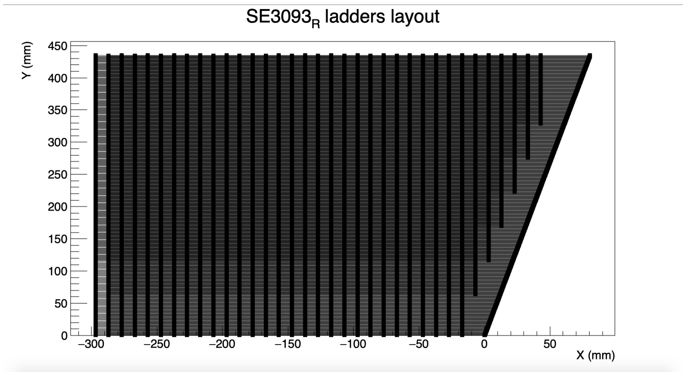

Figure 4.42: Eta PCB *ladder* layout.

Simulation

A first step is to build a simulation of the PCB circuit. As such some simplifications are needed. A first simplification can be done by assuming that the distance of the first interconnection is equal to the ladder steps: d=L=10 mm. We can neglect the angle of the PCB and then assume that all the strips have the same length, and also d is always long 10 mm.

The simulation of the PCB circuit is shown in Figure 4.43. All the resistances in the circuit are 1 MΩ. We are interested in modelling the resistance along the strip, which is computed by powering the circuit with 1 kV. For this reason, looking at the central circuit branch in the picture, at each step there are two resistance defined such as their sum is equal to 1 MΩ. Varying the values of these two resistances and measuring the resistance at their ends, it is possible to evaluate the effective resistance along the branch of the circuit based on the position in which the measurement is performed. Focusing on the first four ladders, the resistance as function of the distance from the coverlay in the simulation is shown in Figure 4.44. It can be seen that at each step the resistance decreases when it comes close to the next interconnection. The overall behaviour shows an enhancement of the resistance with the coverlay distance.

Recursive Model

The next step is to develop a model to reproduce the simulated data. We can start from a simple configuration, in which we want to measure the resistance value at some distance from the coverlay, between the second and the third interconnection. A sketch of the circuit is shown in Figure 4.45a. In this configuration, we are neglecting the contributions from neighbour strips between the second and the third interconnection, taking into account only the resistance at lower steps, given that we expect that their contribution is dominant.

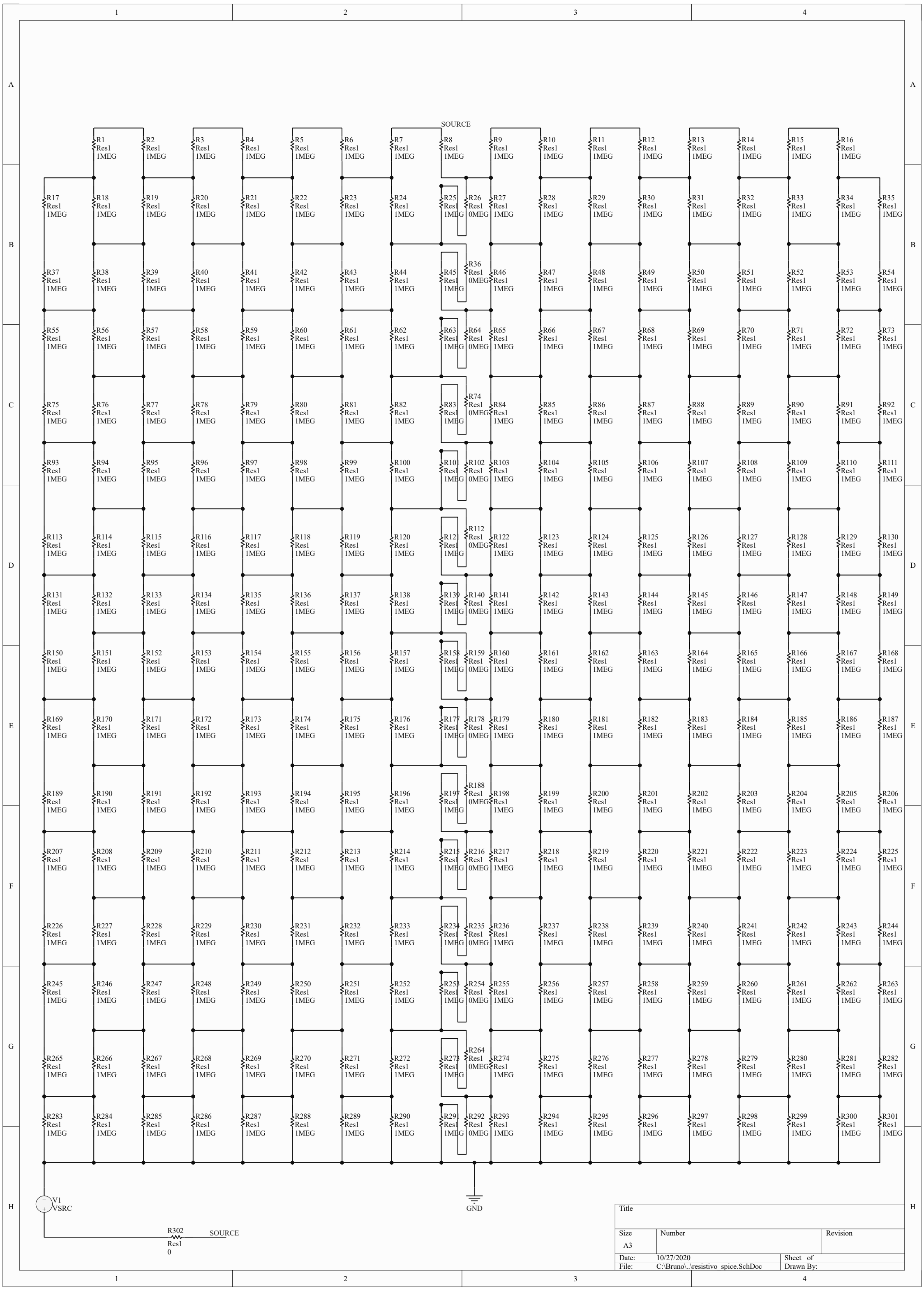

Figure 4.43: Simulation of the PCB circuit.

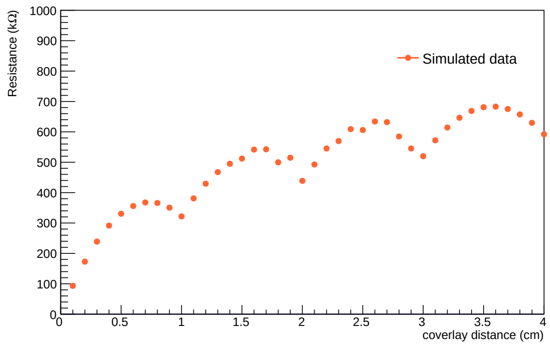

Figure 4.44: Strip resistance as function of the distance from the coverlay in the simulated data.

Then in this scheme different resistance have been defined as follow:

$$R_d = \rho \cdot d \ ; \ R_{L1} = R_{L2} = \rho \cdot L \ ; \ R_x = \rho \cdot (x - d - L) \ ; \ R_{Lx} = \rho \cdot (2L + d - x) \qquad (4.2.1)$$

where x is the distance from the coverlay in which we are measuring the resistance. In Figure 4.45b and 4.45c, there are further simplification steps of the circuit, to obtain the final equivalent circuit using the following resistance definitions:

$$R_{dp} = R_d \ || \ R_d \ ; \ R_{Lp1} = (R_{L1} + Rdp) \ || \ (R_{L1} + Rdp) \qquad (4.2.2)$$

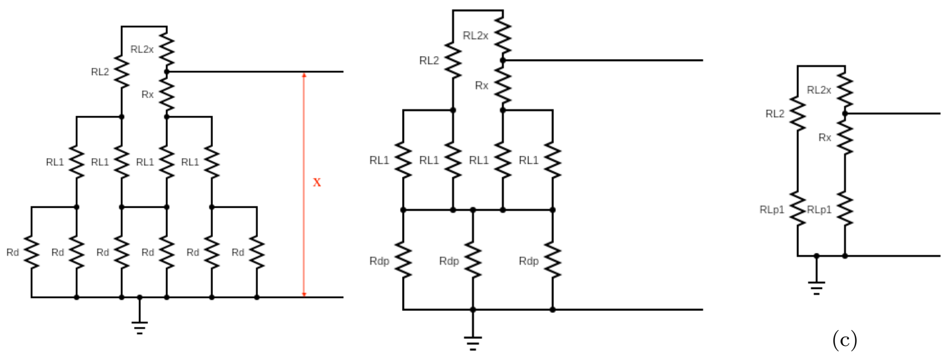

(a) (b) (c)

Figure 4.45: Sketch of the PCB circuit with approximation used to built the recursive model. The three figure show the equivalent circuits of the first one (a) after the resistance re-definitions.

Since the very first tests, it was clear that this model is affected by many approximations, as we are neglecting a huge part of the circuit. A way to compensate these approximations is to add some *scale factors* (*SF*) to the resistances that do not belong to the strip in which we are performing the measurement (R_x and R_{Lx}).

In this way, it is possible to extend this model also at further steps, above the third interconnection, defining an recursive model represented by the circuit in Figure 4.46, in which the resistance along the strip is:

$$R_{strip,i} = (R_{xi} + R_{Lpi} \cdot SF1_i) \mid\mid (R_{Lxi} + R_{Lpi} \cdot SF2_i) \tag{4.2.3}$$

Two scale factors are required at each step i, defining two effective resistances.

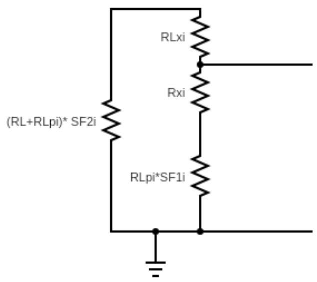

Figure 4.46: Sketch of the PCB circuit used to built the recursive model.

Figure 4.47 shows the simulated data fitted with the recursive model defined in Equation 4.2.3. In this fit, the first interconnection distance d was fixed at 10 mm, and the scale factors and the resistivity were free. The resistivity value obtained from the fit is 1.083 MΩ/cm, which shows the fit is able to recover the input value used in the simulation.

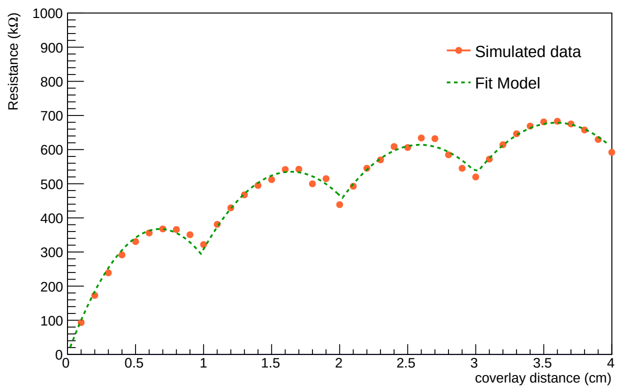

Figure 4.47: Strip resistance as function of the distance from the coverlay in the simulated data fitted with the recursive model.

Fit on experimental data

The final step of this study is to use this model to fit real resistance measurements performed on a real PCB. The goal is to extract the distance of the first interconnection d from the fit and see if the fit is able to recover the pattern periodicity of the strips in the PCB layout (Figure 4.42).

The resistance of the strips along lines parallel to the coverlay at steps of 1 cm has been measured isolating the neighbour strips. The measurements has been performed on

45 strips, one every 10 mm. Figure 4.48 shows the resistance map of the PCB used for this test.

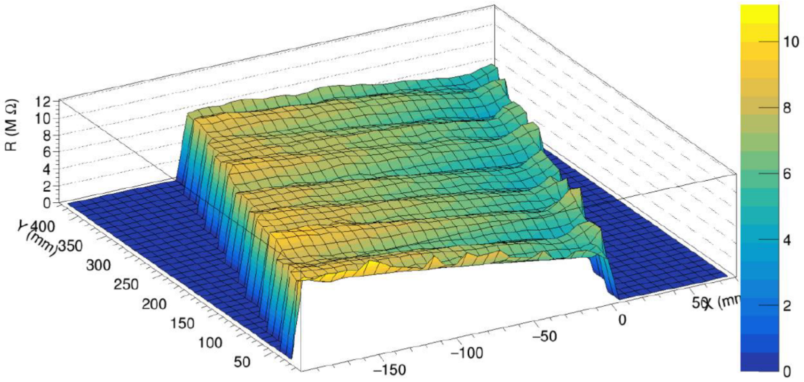

Figure 4.48: 2D resistance map of an SM1 Eta PCB.

The measured data has been then fitted with the model described previously. In this case, the scale factors has been fixed using the values obtained from the fit on the simulation. This has been done assuming that these scale factors do not depend from the resistivity ρ neither on the distance of the first interconnection d, which are the free parameters in the data fit. The parameters fit results on the n-th strip are used as input to initialise the parameters for the fit on the $(n+1)$-th strip.

Figure 4.49 shows the distance from the first interconnection extracted from the fit on each measured strip. It is possible to see that the fit is able to recover the periodicity of the ladder layout, even if the angle of the PCB has not been used in the model. Figure 4.50 shows the fit on the data for four example strips. Finally, Figure 4.51 shows the distribution of the resistivity values obtained from the fit. The values are in a range of 7-10 MΩ/cm with a mean value around 8.5 MΩ/cm.

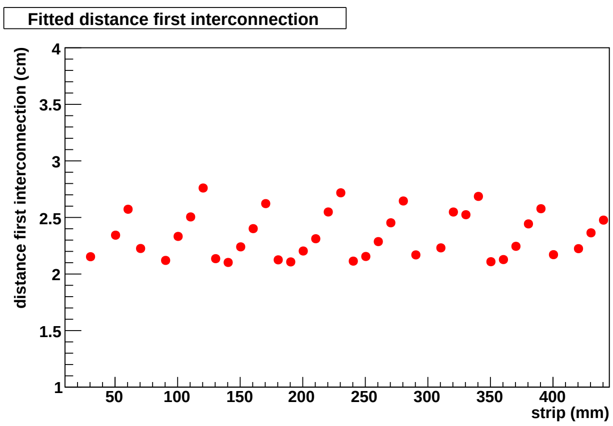

Figure 4.49: First interconnection distance d obtained from the fit on the measured resistance along the strips.

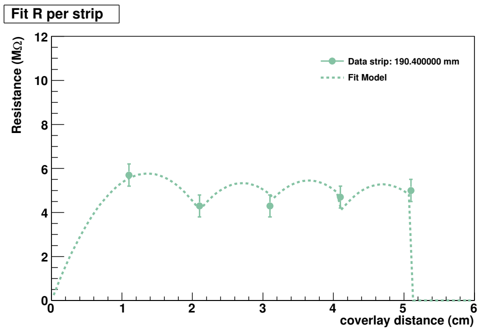

(a)

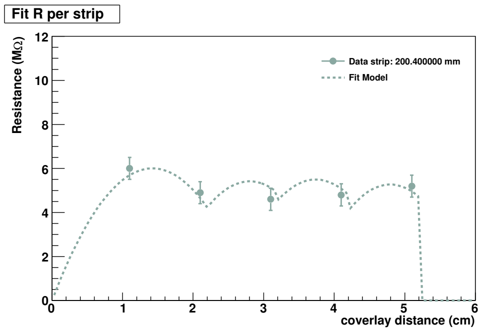

(b)

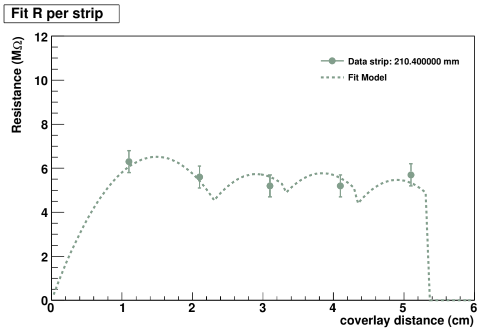

(c)

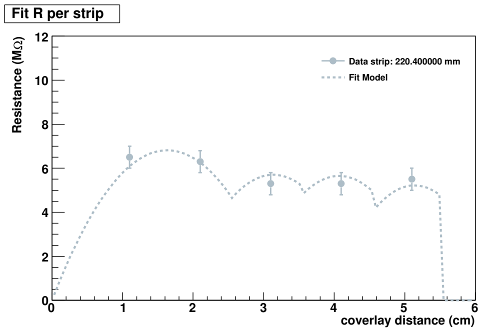

(d)

Figure 4.50: Fit on the measured data for four example strips.

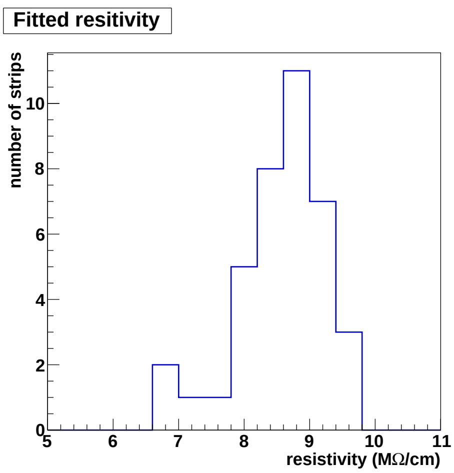

Figure 4.51: Distribution of the linear resistivity ρ obtained from the fit.

Conclusions

The goal of the study presented in this section was to find a model able to describe the resistance along the strips of the readout PCB used for the Micromegas detector.

The PCBs are characterised by a specific layout in which the resistive strips are connected at regular steps. This layout should uniform the resistance along the PCB and the pattern of these interconnections has a crucial role at this end. Figure 4.52 shows the resistance as function of the coverlay distance with and without the interconnections ("no ladder") in the PCB layout. The interconnection case is represented with the model described previously and different cases are reported, with different value of the first interconnection distance d: 1 cm, 2 cm and 3 cm, to show how the resistance changes with the tuning of the layout parameters. It can be seen that the ladder layout leads to a uniformity of the resistance along the strips with respect to the case with no ladder, but also that the distance of the first interconnection plays an important role to have a resistance value high enough in the area close to HV line, which has been demonstrated to be a weak point, in which sparks can occur more frequently.

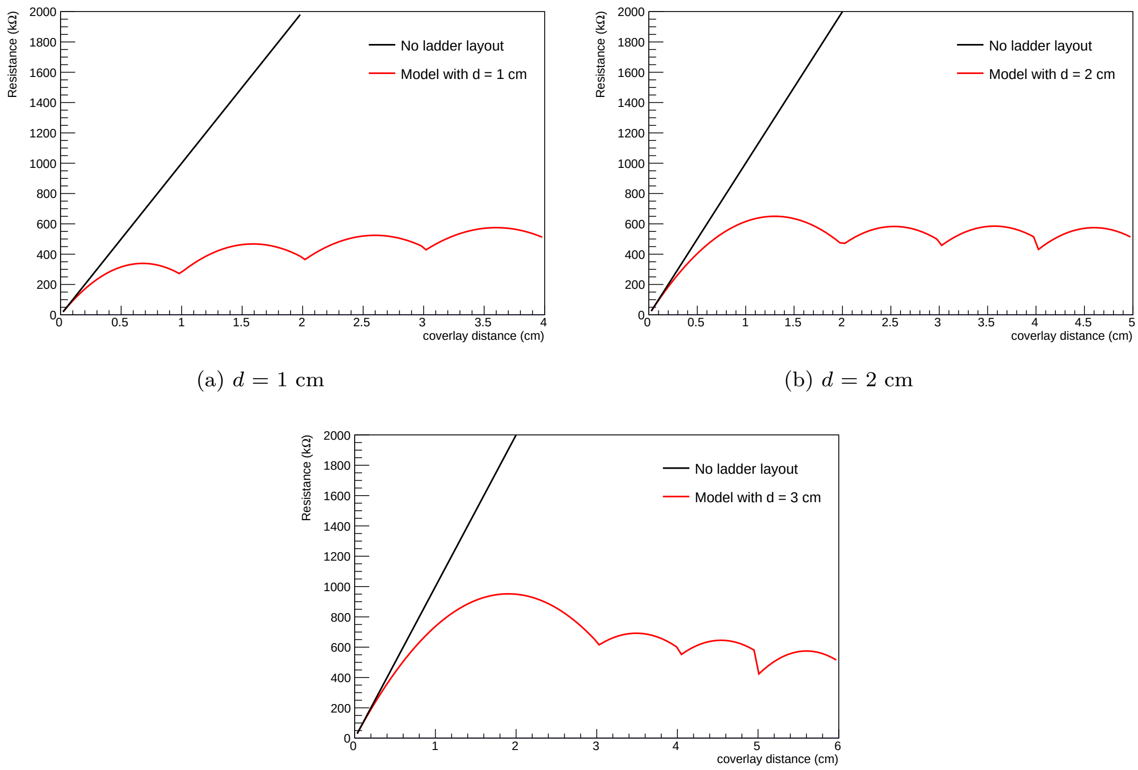

(a) $d = 1$ cm

(b) $d = 2$ cm

(c) $d = 3$ cm

Figure 4.52: Comparison between the resistance as function of the coverlay distance with (red line) and without (black line) the interconnection pattern in the PCB layout. The three plots show different first interconnection distance values: (a) 1 cm, (b) 2 cm and (c) 3 cm.

4.3 Integration of SM1 module at CERN

Once the SM1 modules are validated at LNF, they are sent to CERN for the final integration on the New Small Wheel. The integration workflow is show in Figure 4.53.

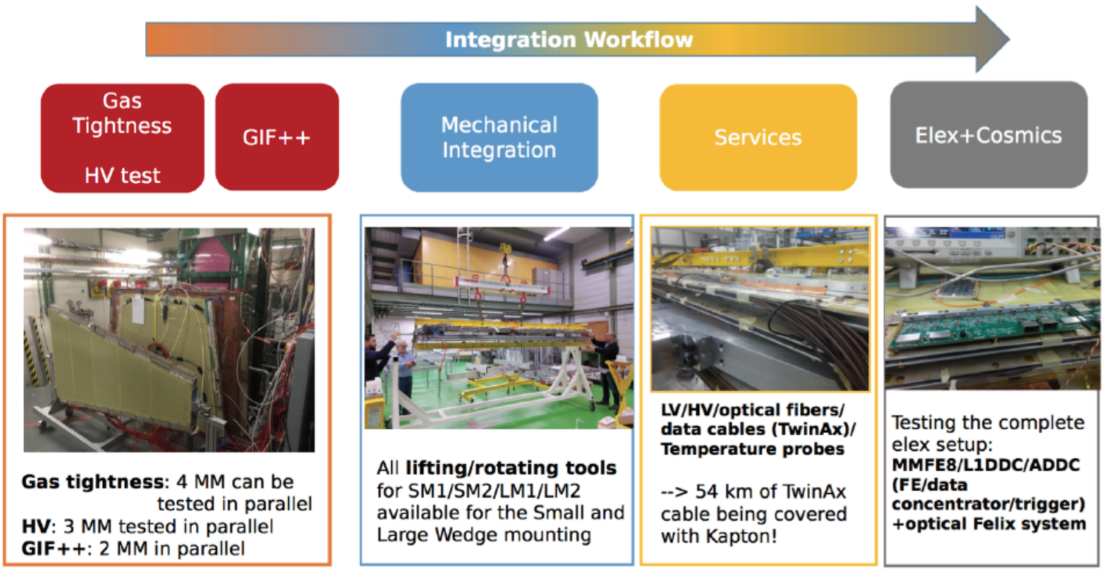

Figure 4.53: Micromegas modules integration workflow at CERN Building BB5.

The modules arrive at CERN Building BB5 where further gas tightness and High Voltage tests are performed on the chambers to ensure that they have not been damaged or compromised during the transportation.

4.3.1 Irradiation Test at GIF++

On some of the modules, an irradiation test is performed at the Gamma Ray Irradiation Facility (GIF++) [89]. This facility uses a ^{137}Cs source of $\sim$ 14 TBq which provides a spectrum of 662 keV photons. The chamber is then exposed to the photon flux and the intensity depends on the distance of the chamber from the source. The intensity can be further tuned using a set of filters, to guarantee a uniform irradiation per plane making the facility especially suitable for large areas detectors, as the ATLAS Micromegas modules.

By applying a photon flux of 6.4×10^7 photons/cm^{2}s^{-1}, it is possible to induce a current at the avalanche stage compatible to the one foreseen at the High-Luminosity LHC operation, with an expected particle rate at the NSW surface of 15 kHz/cm^2. Figure 4.54 shows the expected beam background rates from different sources at a luminosity of 3×10^{34}cm^{-2}s^{-1} as function of the distance from the interaction point: cavern background (both correlated and uncorrelated [2]) and the pile-up events [7].

[2] Background hits in the muon spectrometer arise from low energy photons and neutrons. They are generated by synchronous proton collisions with the bunch crossing that triggers the ATLAS data-taking mechanism (correlated), or by collisions that happen one to several bunch crossing earlier (uncorrelated).

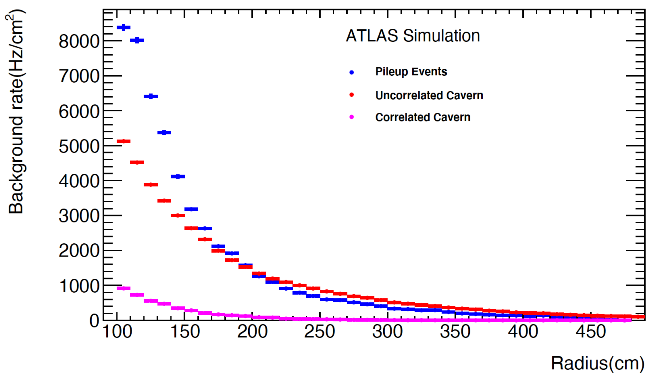

Figure 4.54: Beam background rates from different sources at a luminosity of $3 \times 10^{34}\mathrm{cm}^{-2}\mathrm{s}^{-1}$. The red, blue and pink points are rates from pile-up events, uncorrelated cavern, background and correlated cavern background, respectively [7].

In this way, it is possible to compute approximately the expected background rate for each PCB, based on their distance from the interaction point, and the corresponding current drawn from them, based on their area:

$$I_{\mathrm{pcb}} = \mathrm{Rate} \times (e \cdot 100 \cdot 10^4) \times \mathrm{A}_{\mathrm{pcb}} \tag{4.3.1}$$

where Rate($\mathrm{Hz/cm^2}$) is the background rate, $\mathrm{A}_{\mathrm{pcb}}$ in the PCB area, e the electron charge, 100 is the expected number of primary electrons in 5 mm with Ar:CO_2 93:7 gas mixture and 10^4 is the amplification factor. In Table 4.4, the expected background rate at the distance corresponding to the centre of the PCB and the current drawn by it for both Small and Large modules are reported.

PCB	Rate ($\mathrm{Hz/cm^2}$)	Small Module I(μA)	Large Module I(μA)
1	13450	2.8	3.9
2	5800	1.5	2.2
3	2750	0.9	1.3
4	1700	0.6	1.0
5	1000	0.4	0.7
6	650	0.3	0.5
7	350	0.2	0.3
8	275	0.2	0.2

Table 4.4: Current drawn by each PCB of both Small and Large modules based on the expected background rate in ATLAS at luminosity of $3 \times 10^{34}\mathrm{cm}^{-2}\mathrm{s}^{-1}$.

For this reason, an attenuation scan is made on the module by changing the photon flux, and recording the current induced. In this way, the HV stability can be studied to see the chamber behaviour in high background environment. In Figure 4.55, an example of the attenuation scan of an SM1 HV section is reported. Up to now, no degradation effects have been observed on the tested modules due to the irradiation.

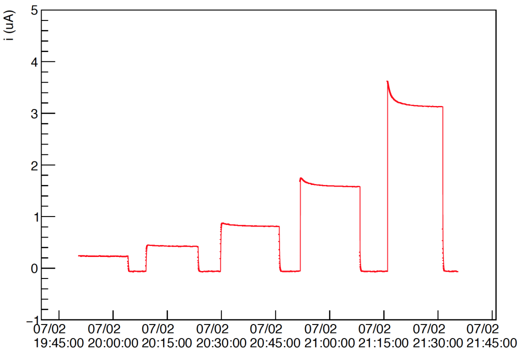

Figure 4.55: Attenuation scan performed at GIF++ of Micromegas modules. In Figure 4.55 the monitored current in time during the data taking is reported. The different steps show the increase of the mean current drawn by the HV section using different filters: 22, 10, 6.9, 4.6 and 1. This numbers represents the attenuation factor with respect to the photon flux emitted by the source at the peak of 662 keV.

4.3.2 Double-Wedge validation at BB5

The modules which pass the acceptance criteria at the reception step in BB5 and at GIF++, are then integrated in a Micromegas *Double Wedge* (DW). In particular, the SM1 modules are part of the *Small Double Wedges*, which consist of two wedges, each one with an SM1 module and a SM2 module positioned as in Figure 4.56a. In the same way, a *Large Double Wedge* can be defined, which consists of two LM1 and two LM2 modules (Figure 4.56b).

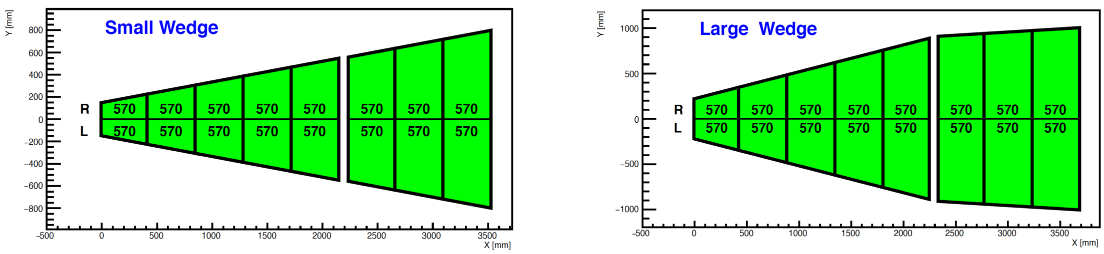

(a) Small Wedge

(b) Large Wedge

Figure 4.56: Example of (a) a Small and (b) a Large Wedge. A Double Wedge consists of 2 wedges back-to-back to the other.

Once the Double Wedge is mechanically assembled, all the services are then installed and the DW is equipped with the full read-out electronics, ready to be tested at the Cosmic Ray Stand. The Double Wedge is positioned as in Figure 4.57.

Figure 4.57: Cosmic Ray Stand setup at CERN. A Small Double Wedge is in place ready to take data.

4.3.2.1 High Voltage test

In a single Wedge there are 64 HV sections (40 HV section for the type 1 modules and 24 HV section for the type 2 modules). Thereby, in a Double Wedge, there are 128 HV sections. These 128 HV sections are not powered separately, as in the usual configuration used for the tests at the Construction Sites and the reception in BB5 or GIF++.

The final HV scheme distribution for the Micromegas modules in the NSW requires that the HV sections of each layer are connected all together at the same HV channel in the power supply. This configuration is achieved using a *splitter box*. One splitter box is used to power one Wedge and it consists of 10 HV lines to power the readout and 2 HV lines to power the drift. Then per module, there are 4 HV lines to power each layer, which are called **Main lines**, and 1 HV line called **Hospital line** used to put the HV sections that cannot reach the nominal HV value of 570 V.

Once a DW arrives at the Cosmic Ray Stand, it is connected to the gas line and it is flushed at 50 L/h each wedge and splitted on the four layers. The gas flow goes from the large basis of the type 2 chamber to the small basis of the type 1 chamber. The HV cables are then plugged to the splitter box. When the relative humidity reaches a value below 13%, the HV test starts.

The test procedure is similar to the one implemented at LNF. The DW is slowly ramped up until it reaches the nominal voltage of 570 V. Given that in the splitter box configuration all the HV section of one layer are connected together to just one power supply channel, it is important as first step to perform what is called *section scan*. This is performed by powering each HV section separately to check its working HV value with respect to the value obtained in the previous HV tests.

Once the HV map of the DW is obtained, it can be connected with the final HV scheme to the splitter box. The sections that can reach the working point 570 V are connected in the main line, and the ones that cannot, are connected to the hospital line. It is powered with an HV chosen as the one of the worst behaving section, with a minimum acceptable value of 500 V. If an HV section has a value below 500 V, it is not connected at all. Figure 4.58 show an example of the HV map of the Double Wedge A14.

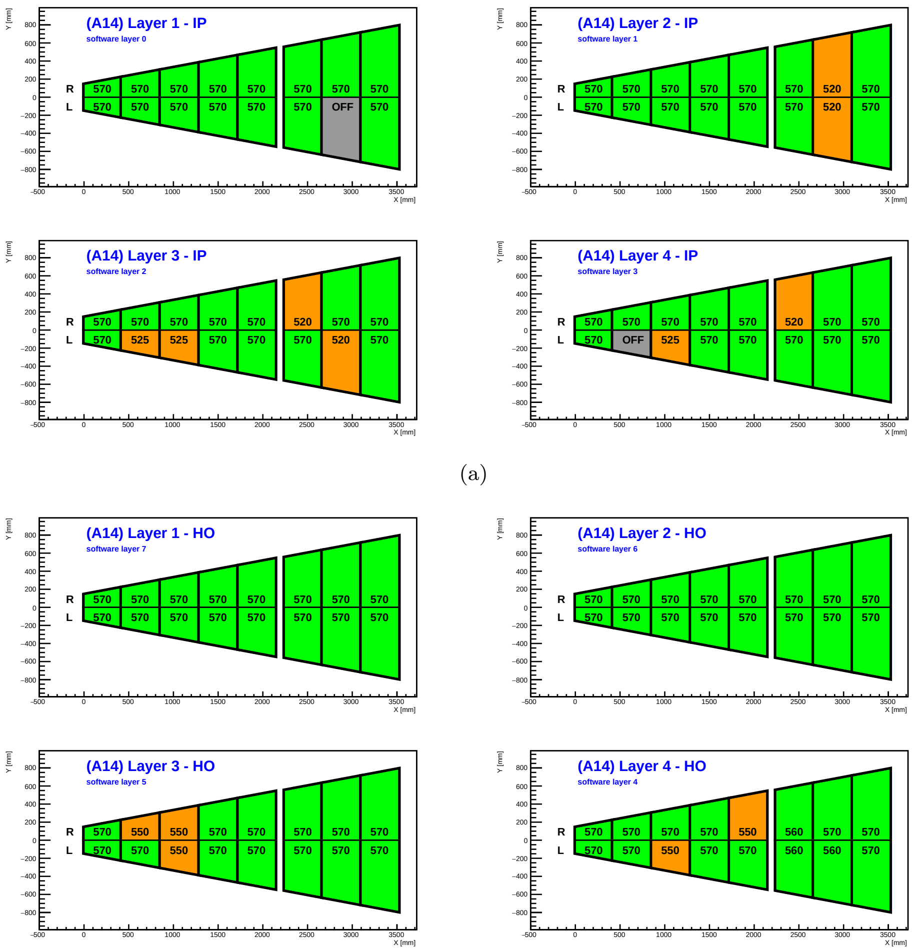

(a)

(b)

Figure 4.58: Final HV map of the Double Wedge A14: (a) IP and (b) HO side.

The HV test is then performed, validating the HV stability in time for the DW. The HV and the currents are monitored using a DCS system developed at CERN. The data are recorded and then analysed to evaluated the spark rate, as done at LNF. A DW is considered validated when the 80% of the sections are connected to the main line and show a stable behaviour.

Figure 4.59 shows the percentage of the section connected at different HV values or disconnected. The A04 DW had several problematic sections, for this reason the problematic chamber on this DW have been substituted.

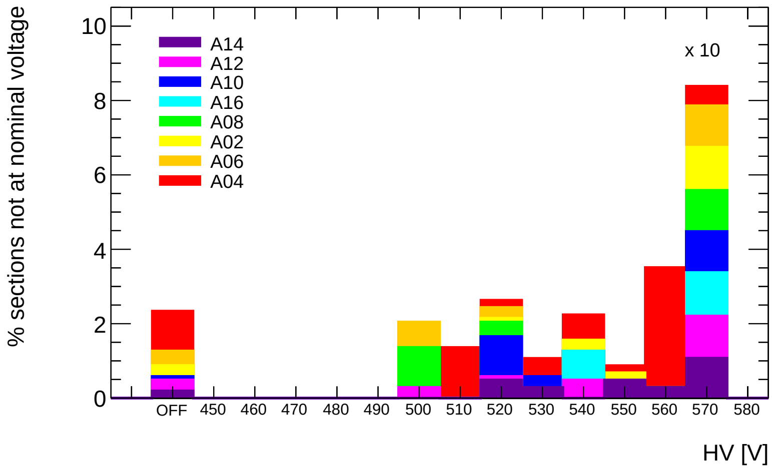

Figure 4.59: Summary of the HV values applied at each section of the Small Double Wedges following the splitter box scheme. The plot shows the percentage of the sections connected at a given HV value. The data at 570 V have to be scales ×10.

New HV scheme: half-granularity

The HV scheme described using the *splitter box* with a MAIN line and an HOSPITAL line, showed several limitations. If in the same chamber two HV sections have a maximum HV reachable value 560 V and 500 V, both of them have to be set at the lower value (500 V), leading to a loss in terms of chamber performance. This effect is more significant in DWs with several HV sections that cannot reach the nominal value of 570 V. The other limitation is the handling of the HV once the NSW will be in ATLAS: if a HV section will go in short or its HV value need to be lowered, it means that all the other HV sections connected to the same HV channel will be lowered or even switched off.

For this reason, a new HV scheme has been proposed and will be implemented on ATLAS as final configuration. In this configuration, called *half-granularity*, the HV sections are grouped together per PCB instead of per Layer, and there is no more Hospital line. Then for each DW, 68 HV channels are needed to power the amplification gap: 20 HV sections for type 1 modules (5 PCBs × 4 layers) and 12 HV sections for type 2 modules (3 PCBs × 4 layers). In this way, if a HV section will go in short or need to be lowered, only the corresponding PCB will be lowered or switched off.

In terms of chambers performance, this solution can lead to a lowering in the efficiency, given that both HV section of a PCB need to be powered at same HV value. If before the two sections of a PCB were powered at 500 V on one side and 570 V on the other side, now they have to be powered both at 500 V. But the improvement that we obtain to manage the HV of each PCB is significant once the chambers will be in the experiment. In any case, DWs with several HV sections which cannot stay at nominal value, will gain also in terms of performance.

As A04 DW showed some HV problems, its SM1-IP module has been substituted and this DW has been the first one tested with the new HV scheme. Figure 4.60 shows the HV map of the HO side of the Double Wedge A04, in which the SM1 and SM2 modules are the same before and after the replacement, tested both with old splitter box HV scheme and with the new half-granularity configuration. Even if a couple of sections need to be lowered, the overall HV picture is improved with respect to the old HV scheme. It will be possible to further improve the picture once the DW is installed on the experiment.

Figure 4.61 shows the percentage of the section connected at different HV values or disconnected with the new A04 DW tested with the new HV configuration.

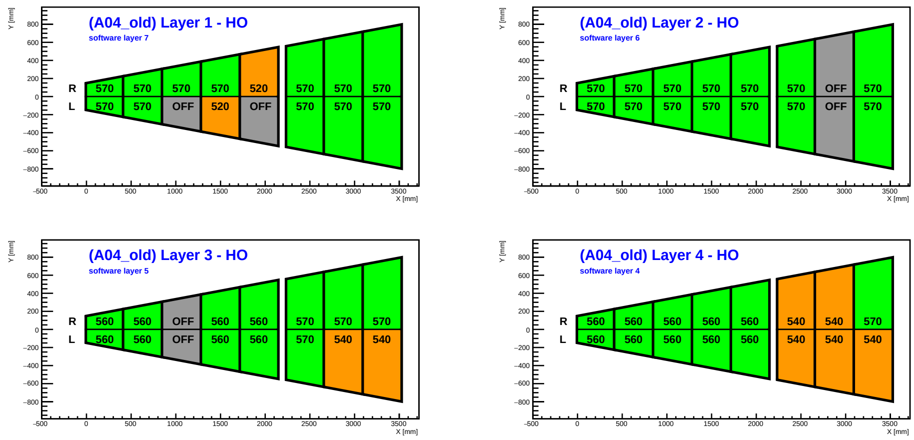

(a)

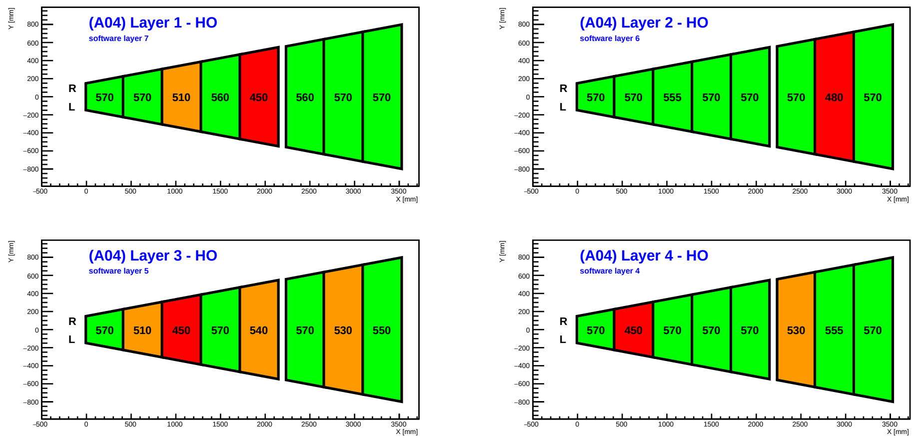

(b)

Figure 4.60: Comparison of the HV maps of the Double Wedge A04 HO side with the two different HV scheme: (a) old *splitter box* and (b) new *half-granularity* configuration

4.3.2.2 Cosmics results

Finally the cosmic test is performed on the DW to validate its performance and estimate its efficiency. The Cosmic Ray Stand in BB5 is shown in Figure 4.57 and it is composed of two layers of scintillators for the trigger, achieving a rate of ~ 105 Hz. The module is

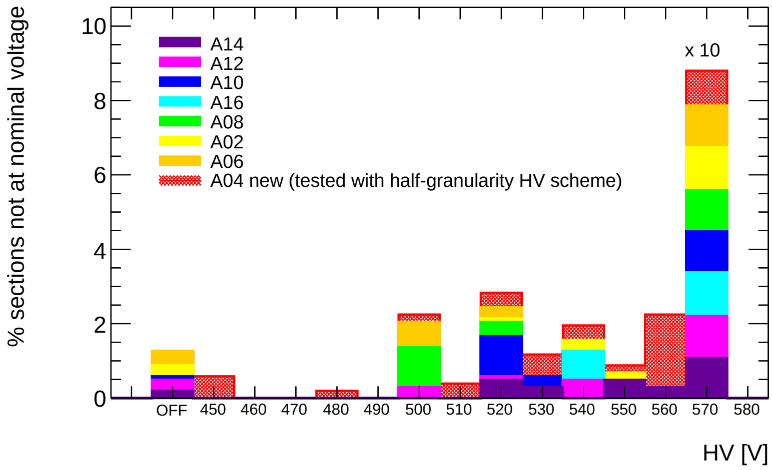

Figure 4.61: Summary of the HV values applied at each section of all the Small Double Wedges including the new A04 tested with the half-granularity HV scheme. The plot shows the percentage of the sections connected at a given HV value. The data at 570 V have to be scales ×10.

equipped with the final front-end electronics. For the ATLAS NSW, a custom Application Specific Integrated Circuit (ASIC) called *VMM* has been developed. Each PCB of a MM chamber is connected to two read-out boards, called MMFE8 which carries eight front-end chips VMM of 64 channels each one.

A 3D self-tracking algorithm is used to reconstruct the track, requiring at least 5 layers (of which at least two Eta and two Stereo) and excluding the layer under study. In Figure 4.62a, the hit map of the reconstructed track on a layer of a DW is shown.

Then the efficiency of each layer of the DW can be estimate, as shown in Figure 4.62b. Figure 4.63 shows the measured layer efficiency as a function of the HV in the amplification region for the layers of each DW.

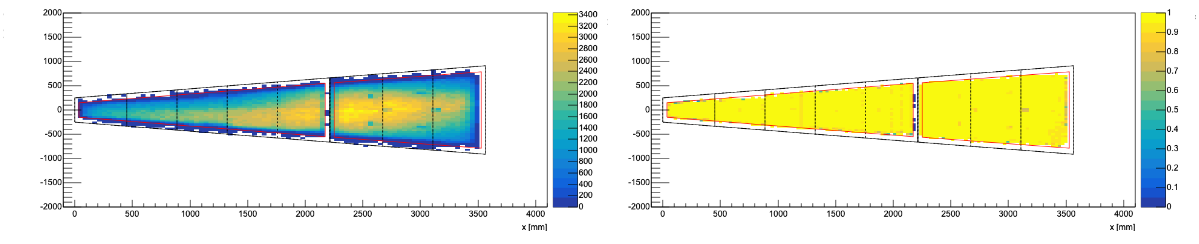

(a) (b)

Figure 4.62: (a) Reconstructed track map and (b) efficiency map of software layer 0 (which corresponds to Layer 1 of the IP-side modules) from the cosmic results on A02.

4.3.2.3 Summary

In Table 4.5, the status of the small Double Wedges of the NSW-A tested is summarised. It reports the percentage of the HV sections at nominal voltage of 570 V and with values

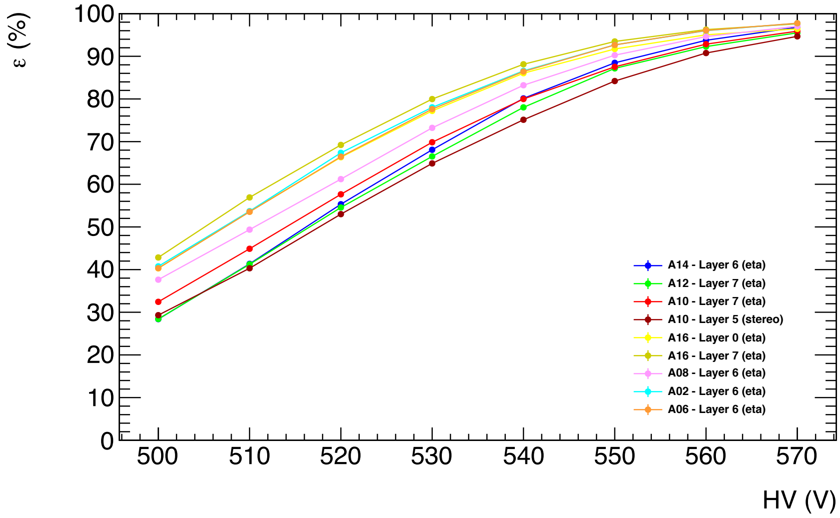

Figure 4.63: Measured layer efficiency as a function of the HV on the Small Double Wedges.

≥ 550 V and the corresponding mean efficiency of the full DW measured with cosmic data.

Small Double Wedges	HV sections at 570 V	HV sections >550 V	Mean Efficiency with cosmics
A14	85.9 %	88.2 %	88.1%
A12	90.6 %	90.6 %	90.8%
A10	93.8 %	93.8 %	94.5 %
A16	88.3 %	88.3 %	90.9%
A08	88.3 %	88.3 %	92.0 %
A02	93.0 %	93.0 %	94.5 %
A06	89.1 %	89.1 %	90.0 %
A04	59.3 %	76.6 %	85.0 %

Table 4.5: Summary validation table of the small Double Wedges for the NSW-A.

Expected segment reconstruction efficiency

From the efficiency scan performed as function of the HV for the Small Double Wedges with cosmics for one DW layer, it is possible to build an average efficiency curve as function of the HV and fit it with a *logistic function* or *sigmoid* to extract a theoretical expected efficiency, $\varepsilon_{\text{theo}}$:

$$\varepsilon_{\text{theo}}(\text{HV}) = \frac{\varepsilon_{\text{theo}}^{\text{max}}}{1 + e^{-k(\text{HV}-\text{HV}_0)}} \tag{4.3.2}$$

where the free parameters in the fit are: the curve's maximum $\varepsilon_{\text{th.exp}}^{\text{max}}$, the HV value of the sigmoid's midpoint HV_0 and the logistic growth rate k. Figure 4.64 shows the theoretical efficiency curve for a layer of a small DW obtained from the average of the curves showed in Figure 4.63, fitted with the sigmoid function.

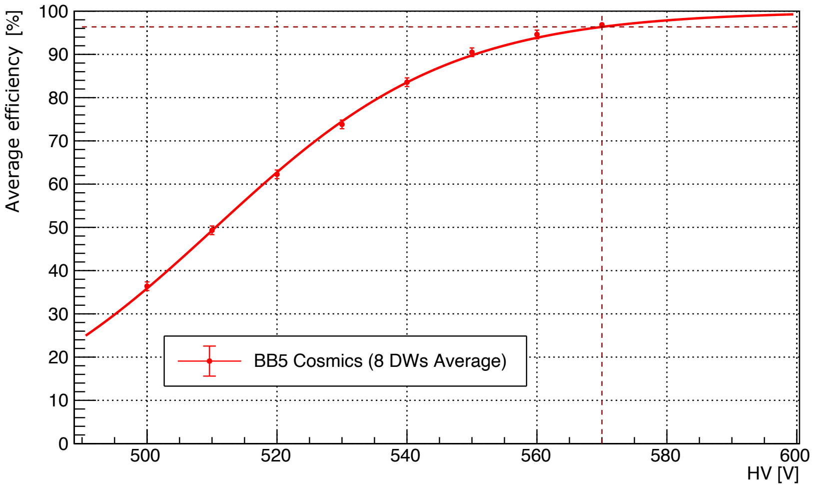

Figure 4.64: Average efficiency as a function of the HV of the Small Double Wedges.

From this theoretical efficiency, it is possible to build the expected efficiency maps for all the layers of a DW knowing the HV applied at each HV section. Requiring specific combination of the layers, it is possible to estimate the *segment reconstruction efficiency* in the NSW using only the Micromegas chambers. Then three different working points are defined:

- *Loose*: a segment is reconstructed if at least 4 layers over the total 8 layers are efficient. A further selection is applied requiring that of the 4 layers, two must be Eta and the other two must be Stereo, to be able to reconstruct also the second coordinate. The 2D map of the segment reconstruction efficiency (computed from the HV map) of the NSW-A made by the only small sectors is shown in Figure 4.65a.
- *Medium*: a segment is reconstructed if at least 5 layers (over 8) are efficient. Also in this case at least two Eta and two Stereo layers are required, but a further requirement is made on the Stereo layers. One of the Stereo layers must have the strips tilted by $+1.5°$ and the other tilted by $-1.5°$. The 2D segment reconstruction efficiency map of the NSW-A is shown in Figure 4.65b.
- *Tight*: a segment is reconstructed if at least 6 layers (over 8) are efficient. In this case at least three Eta and three Stereo are required to be efficient. The 2D segment reconstruction efficiency map of the NSW-A for this working point is shown in Figure 4.65c

In the New Small Wheel pictures shown for the three working point, the green regions are the ones with a segment reconstruction efficiency of at least 95 %. This picture has been done considering only the Micromegas detectors. Then the inclusion of sTGC in the combination of the efficient layers will improve the segment reconstruction efficiency in the experiment.

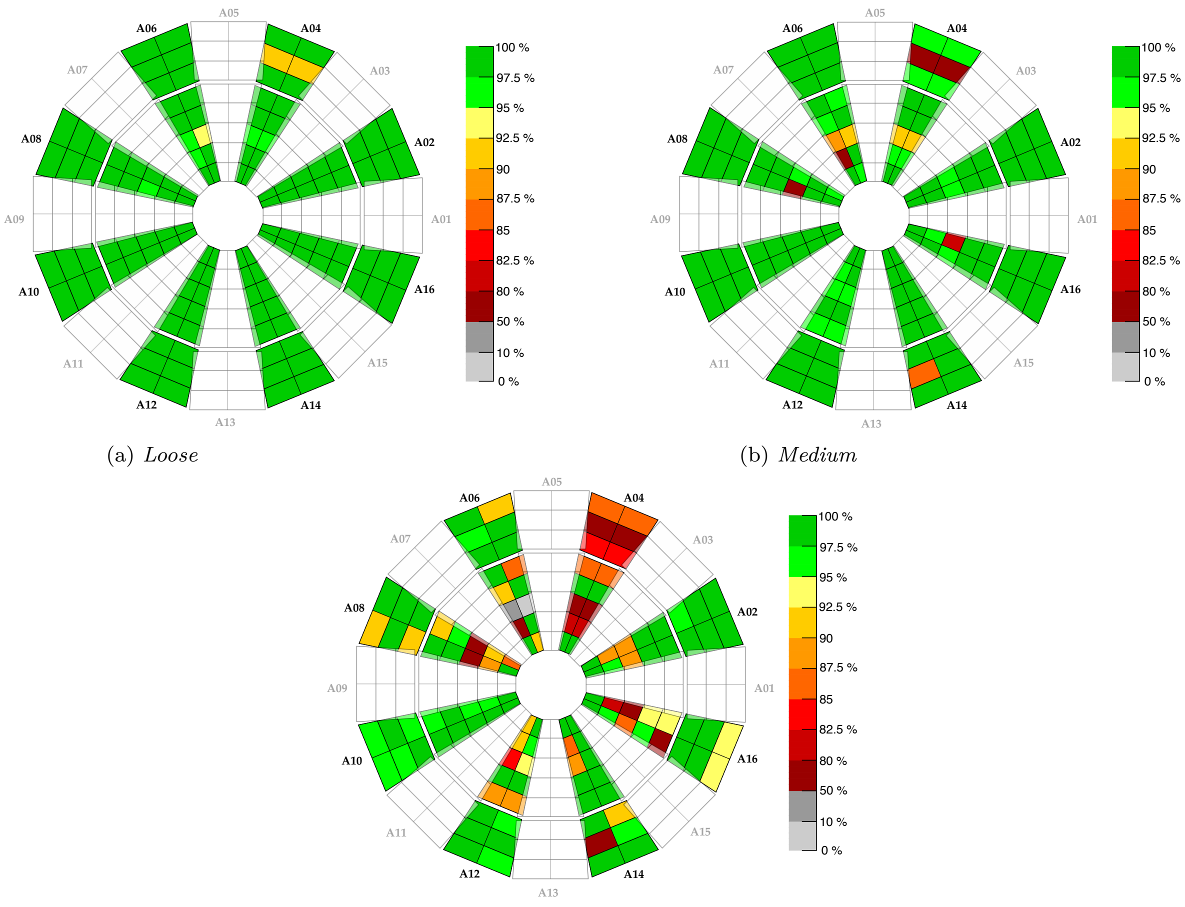

(a) *Loose* (b) *Medium*

(c) *Tight*

Figure 4.65: 2D map of the segment reconstruction efficiency using the small Micromegas DWs of the NSW-A for three different working points: (a) *Loose*, (b) *Medium* and (c) *Tight*. This efficiency has been computed using the theoretical curve extrapolated from the average efficiency curve of the Small Double Wedges, based on the HV maps of each DW.

The same computation can be performed also using the actual data measured at the Cosmic Ray Stand in BB5. From the average efficiency measured of each layer, the same combinations described above can be realised and the results are shown in Figure 4.66. In this case, we do not have the segmentation in HV sections, but it is an average on the whole DW area and this numbers come directly from cosmic data. The three different graphs represent the three different working points, and each point is the segment reconstruction efficiency of a single DW. It is possible to see that all the DW, averaging on their whole area, have efficiencies higher than 97% for the *Medium* working point.

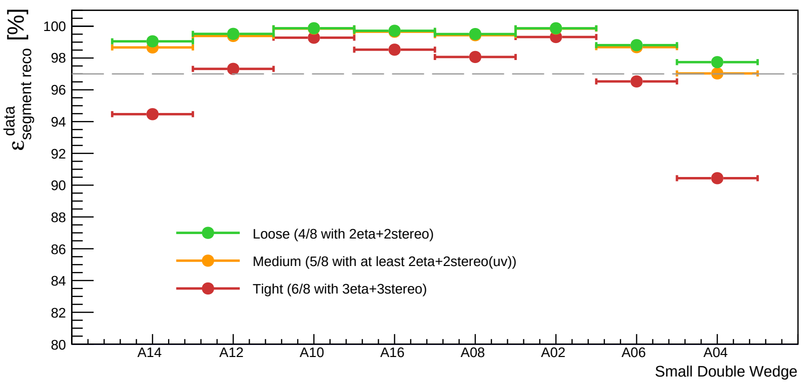

Figure 4.66: Segment reconstruction efficiency of the Small Double Wedges computed from the experimental efficiency measured from the cosmic data. The green, orange and red points represent the three working points *Loose*, *Medium* and *Tight* respectively. The grey line represent the 97% efficiency level.

Chapter 5

The $H \to ZZ^* \to 4l$ decay channel

Contents

The $H \to ZZ^* \to 4l$ decay channel is referred to as the *Golden Channel* due to the high signal-background ratio ($\sim$ 2) and due to a clean signature for the triggering on the high-p_T leptons that comes from the Z bosons decays. The limit of this decay channel is the low Branching Ratio ($\sim$3%), which lowers the available statistics. However the increase of the integrated luminosity to 139 fb^{-1}, leads to a lowering of the statistic error on the measurements, as it is the main contribution to the errors in this channel.

Four different final states can be distinguished in the 4ℓ decay channel: $\mu^+\mu^-\mu^+\mu^-$ (4μ), $e^+\mu^-e^+\mu^-$ ($2e2\mu$), $\mu^+\mu^-e^+e^-$ ($2\mu 2e$), $e^+e^-e^+e^-$ ($4e$), where the first lepton pair is defined to be the one with the di-lepton invariant mass closest to the Z boson mass ($\sim$ 91.2 GeV [90]). Leptons are reconstructed with high efficiency, high momentum and energy resolution, which leads to an high invariant mass resolution for all four final states. As the mass of the Higgs boson is less than twice the Z boson mass, only one intermediate Z boson can be on-shell, while the other one has to be off-shell (Z^*).

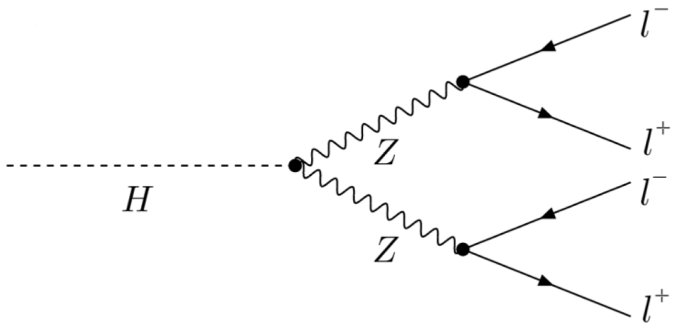

Figure 5.1: Feynman diagram of $H \to ZZ^* \to 4l$ decay channel.

There are three main SM background processes for this channel. The dominant contribution is from the continuum $(Z^{(*)}/\gamma^*)$ $(Z^{(*)}/\gamma^*)$ production, with $Z^{(*)}$ or γ^* decaying to lepton pairs. This production constitutes the irreducible background as it has the same signature and similar event topology of the signal.

A much smaller contribution to total background is expected from the so-called *reducible background*, which is from $Z+$jets and $t\bar{t}$ production with two prompt leptons, where the additional charged lepton candidates arise from decays of hadrons with $b-$ or $c-$quark content or misidentified jets as leptons; and WZ production. Finally minor backgrounds are present with four or more correctly identified isolated leptons such as tribosons (VVV) and all-leptonic $t\bar{t}$+V.

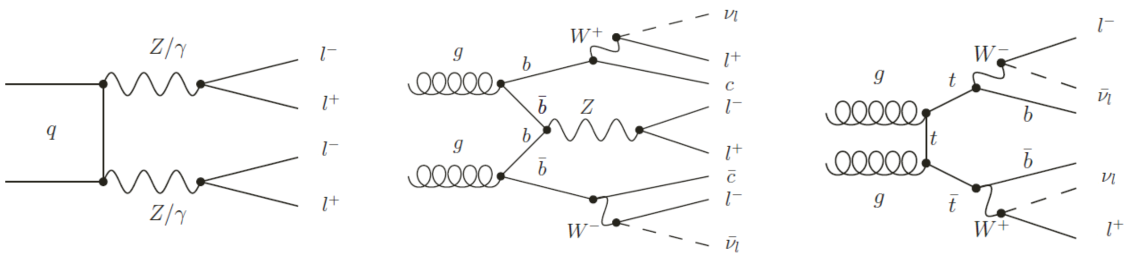

(a) (b) (c)

Figure 5.2: Feynman diagrams for the dominant background processes in the $H \to ZZ^* \to 4l$ decay channel: (a) $(Z^{(*)}/\gamma^*)$ $(Z^{(*)}/\gamma^*)$ continuum production, (b) $Z + jets$ production and (c) $t\bar{t}$ production.

5.1 Event samples

5.1.1 Data samples

For the analysis presented in this thesis, the Full Run 2 dataset, consisting of all proton-proton collision data collected from 2015-2018 at $\sqrt{s} = 13$ TeV with a 25 ns bunch spacing configuration, has been used. The data are subjected to quality requirements and events recorded during periods when the relevant detector components were not operating normally are rejected. The events which pass the requirements build the dataset called "Good for physics", which are the one used in the analyses. In Table 5.1 the integrated luminosity of the proton-proton collision delivered in each year of the Run 2 data taking is shown, together with the data recorded by the ATLAS detector and the one used in the analysis.

Data taking period	Integrated Luminosity [fb^{-1}] Delivered	Recorded	Good for physics	Average pile-up $< \mu >$
2015	3.88	3.63	3.22	13.4
2016	38.0	35.5	33.0	25.1
2017	49.0	46.4	44.39	37.8
2018	62.1	60.0	58.5	36.1
Full Run 2	156	147	139	33.7

Table 5.1: The integrated luminosity for each year of the Run 2 data taking, as delivered by the LHC, recorded by the ATLAS detector and analysed in this thesis. The corresponding average amount of pile-up interactions is also shown.

5.1.2 Monte Carlo samples

The simulation of a particle scattering event in a Monte Carlo event generator is factorised into several event phases. The hard process can be calculated in fixed order perturbation theory in the coupling constants based on matrix element that can be provided by *Matrix Element generators* (ME). The QCD evolution is described by *Parton Showers* (PS), which connects the hard scale of coloured parton creation with the hadronisation scale where the transition to the colourless hadrons occurs, and it also simulates the initial and final state radiation. The generated events are then fully simulated using the ATLAS detector simulation [91] within the GEANT4 framework [92]. The simulation of the additional pp interactions (pile-up) is done in a separate step in the simulation chain where the minimum bias events are superimposed on the simulated signal events.

For simulating both the 2015 and 2016 data-taking conditions, only one MC set has been used (called *mc16a* campaign). Separate MC campaigns are used to simulate the 2017 (*mc16d*) and 2018 (*mc16e*) data-taking conditions.

5.1.2.1 Higgs signal samples

The production of the SM Higgs boson via gluon–gluon fusion (ggF), via vector-boson fusion (VBF), with an associated vector boson (VH, where V is a W or Z boson), and with a top quark pair ($t\bar{t}H$) is modelled with the POWHEG-BOX v2 Monte Carlo (MC) event generator [93–99]. Table 5.2 summarises the predicted SM production cross sections and branching ratios for the $H \to ZZ^{(*)} \to 4\ell$ decay for $m_H = 125$ GeV together with their theoretical accuracy.

Production process		Accuracy	σ [pb]
ggF	$(gg \to H)$	N^{3}LO in QCD, NLO in EW	48.6 ± 2.4
VBF	$(qq' \to Hqq')$	(approximate) NNLO in QCD, NLO in EW	3.78 ± 0.08
WH	$\left(q\bar{q}' \to WH\right)$	NNLO in QCD, NLO in EW	1.373 ± 0.028
ZH	$(q\bar{q}/gg \to ZH)$	NNLO in QCD, NLO in EW	0.88 ± 0.04
$t\bar{t}H$	$(q\bar{q}/gg \to t\bar{t}H)$	NLO in QCD, NLO in EW	0.51 ± 0.05
$b\bar{b}H$	$\left(q\bar{q}/gg \to b\bar{b}H\right)$	NNLO (NLO) in QCD for 5FS (4FS)	0.49 ± 0.12
tH	$(q\bar{q}/gg \to tH)$	NLO in QCD	0.09 ± 0.01
Decay process		NLO in QCD, NLO in EW	$\mathcal{B}$ $[\cdot\, 10^{-4}]$
$H \to ZZ^*$			262 ± 6
$H \to ZZ^{(*)} \to 4\ell$			1.240 ± 0.027

Table 5.2: Predicted SM Higgs boson production cross sections (σ) for ggF, VBF and five associated production modes in pp collisions for $m_H = 125$ GeV at $\sqrt{s} = 13$ TeV [13, 26, 100–105, 107–129]. For bbH the accuracy of calculations in the 4- and 5-flavour schemes (FS) is reported. The quoted uncertainties correspond to the total theoretical systematic uncertainties calculated by adding in quadrature the uncertainties due to missing higher-order corrections and PDF+α_s. The decay branching ratios ($\mathcal{B}$) with the associated uncertainty for $H \to ZZ^*$ and $H \to ZZ^{(*)} \to 4\ell$, with $\ell = e, \mu$, are also given.

For ggF, the PDF4LHC next-to-next-to-leading-order (NNLO) set of parton distribution functions (PDF) is used, while for all other production modes, the PDF4LHC next-to-leading-order (NLO) set is used [126].

The simulation of ggF Higgs boson production uses the POWHEG method for merging the NLO Higgs + jet cross section with the parton shower and the MINLO method [130] to simultaneously achieve NLO accuracy for the inclusive Higgs boson production. In a second step, a reweighting procedure (NNLOPS) [131], exploiting the Higgs boson rapidity distribution, is applied using the HNNLO program [132, 133] to achieve NNLO accuracy in the strong coupling constant α_s.

The matrix elements of the VBF, $q\bar{q} \to VH$ and $t\bar{t}H$ production mechanisms are calculated to NLO accuracy in QCD. For VH production, the MINLO method is used to merge 0- and 1-jet events [99, 130]. The $gg \to ZH$ contribution is modelled at leading order (LO) in QCD.

The production of a Higgs boson in association with a bottom quark pair ($b\bar{b}H$) is simulated at NLO with MADGRAPH5_AMC@NLO v2.3.3 [134], using the CT10 NLO PDF [135]. The production in association with a single top quark (tH+X where X is either jb or W, defined in the following as tH) is simulated at NLO with MADGRAPH5_AMC@NLO v2.6.0 using the NNPDF30 PDF set [129].

For all production mechanisms the PYTHIA 8 [136] generator is used for the $H \to ZZ^{(*)} \to 4\ell$ decay as well as for the parton shower modelling. The AZNLO set of tuned parameters [137] is used, except for $t\bar{t}H$, where, like for the $t\bar{t}$ samples, the A14 tune [138] is employed. The event generator is interfaced to EVTGEN v1.2.0 [139] for simulation of the bottom and charm hadron decays. All signal samples are simulated for a Higgs boson mass

$m_H = 125$ GeV.

The ggF sample is also generated with MadGraph5_aMC@NLO for additional checks. This simulation has NLO QCD accuracy for zero, one and two additional partons merged with the FxFx merging scheme [140, 141], and top and bottom quark mass effects are taken into account [142–144]. Higgs boson are decayed using Madspin [145, 146].

The differential cross sections results reported in this thesis, for variables defined for the events with at least one jets, are also compared with ggF predictions calculated with RadISH, which provides resummation at N^3LL+NNLO accuracy [147–151] and uses MATRIX for the fixed-order calculation [152, 153], as well with ggF predictions obtained from NNLOJET [154–156]. Instead the results for several of the variables that probe the kinematics of the Higgs boson decay products include comparisons with Hto4l and Prophecy4f. These two programs include the full NLO electroweak corrections to the Higgs boson decay into four charged leptons [123–125, 157–162].

The samples are normalised to cross sections obtained from the best available predictions as provided in Refs. [13, 25, 26, 100, 121, 122, 127–129]. The SM branching ratio prediction, taken from Prophecy4f [123, 158], includes the full NLO EW corrections, and interference effects which result in a branching ratio that is 10% higher for same-flavour final states (4μ and $4e$) than for different-flavour states ($2e2\mu$ and $2\mu2e$).

Beyond Standard Model samples For the BSM interpretation in the Pseudo-Observable framework, described in Section 7.1.1, deviations from the SM are studied using a ggF sample generated with MadGraph5_aMC@NLO using the HPOprodMFV UFO model [30] with FeynRules [163] at LO and the NNPDF23 PDF set. The sample is interfaced to Pythia 8 using the A14 parameter set [138]. For studies of the Yukawa couplings described in Section 7.1.2, the gluon-initiated component of the prediction is calculated using RadISH, while MadGraph5_aMC@NLO is used for the quark-initiated component with FxFx merging for 0- and 1-jet final states. For the interpretation within Effective Field Theory framework, described in Section 7.2, VBF+VH hadronic samples are generated at LO QCD with MadGraph5_aMC@NLO. SMEFT model is implemented with SMEFTsim package [27].

5.1.2.2 Background samples

The ZZ^* continuum background from quark–antiquark annihilation is modelled using Sherpa 2.2.2 [164–166], which provides a matrix element calculation accurate to NLO in α_s for 0- and 1-jet final states, and LO accuracy for 2- and 3-jet final states. The merging with the Sherpa parton shower [167] is performed using the ME+PS@NLO prescription [176]. The NLO EW corrections are applied as a function of the invariant mass of the ZZ^* system m_{ZZ^*} [168, 169].

The gluon-induced ZZ^* production is modelled by Sherpa 2.2.2 at LO in QCD for 0- and 1-jet final states. The higher-order QCD effects for the $gg \to ZZ^*$ continuum production are calculated for massless quark loops [170–172] in the heavy top-quark approximation [173], including the $gg \to H^* \to ZZ$ processes [174, 175]. The $gg \to ZZ^*$ simulation cross section is scaled by a K-factor of 1.7±1.0, defined as the ratio of the higher-order to leading-order cross section predictions. Production of ZZ^* via vector-boson scattering is simulated at LO in QCD with the Sherpa 2.2.2 generator.

The WZ background is modelled using Powheg-Box v2 interfaced to Pythia 8 and EvtGen v1.2.0 for the simulation of bottom and charm hadron decays. The triboson backgrounds ZZZ, WZZ, and WWZ with four or more prompt leptons (denoted by VVV hereafter) were modelled using Sherpa 2.2.2. The simulation of $t\bar{t}+Z$ events with both top quarks decaying semileptonically and the Z boson decaying leptonically is performed with MadGraph5_aMC@NLO interfaced to Pythia 8. The total cross section is normalised to the prediction of Ref. [117]. The smaller tWZ, $t\bar{t}W^+W^-$, $t\bar{t}t$, $t\bar{t}t\bar{t}$ and tZ background processes are simulated with MadGraph5_aMC@NLO interfaced to Pythia 8.

The modelling of events containing Z bosons with associated jets ($Z+$jets) is performed using the Sherpa 2.2.1 generator. Matrix elements are calculated for up to two partons at NLO and four partons at LO using Comix [165] and OpenLoops [166], and merged with the Sherpa parton shower [167] using the ME+PS@NLO prescription [176]. The NNPDF3.0 NNLO PDF set is used in conjunction with a dedicated set of tuned parton shower parameters.

The $t\bar{t}$ background is modelled using Powheg-Box v2 interfaced to Pythia 8 for parton showering, hadronisation, and the underlying event, and to EvtGen v1.2.0 for heavy-flavour hadron decays. For this sample, the A14 tune is used [177]. Simulated $Z+$jets and $t\bar{t}$ background samples are normalised to the data-driven estimates described in Section 5.3.2.

5.2 Event Selection

5.2.1 Object Definitions

Electrons. They are reconstructed using the supercluster algorithm which is able to recover the low energy radiated photons, as described in Section 2.3.2. It takes the information from the Inner Detector (ID) and the Electromagnetic Calorimeter (ECal): topological clusters from deposits in the EM calorimeter are matched to a well constructed ID track. A *Loose* likelihood (LH) selection is applied, which maintains an high efficiency of about 95%. The electrons are required to have $E_T > 7$ GeV and $|\eta| < 2.47$.

Muons. They are reconstructed as tracks in the ID and the muon spectrometer (MS), and their identification is primarily based on the presence of a matching track or tag in the MS. In this analysis the *Loose* working point for muons is used, as described in Section 2.3.3. In this way the muons are required to have $p_T > 5$ GeV and the Segment-tagged (ST) muons are limited to the centre of the barrel region $|\eta| < 0.1$, instead for combined (CB) muons the coverage is extended up to $2.5 < |\eta| < 2.7$ (MS), for stand-alone (SA) muons the coverage is only within $2.5 < |\eta| < 2.7$. The calorimeter-tagged (CT) muons must to pass the *Loose* selection and have $p_T > 15$ GeV. At most one calorimeter-tagged or stand-alone or silicon-associated forward muon is allowed per event.

Jets. They are reconstructed from the output of the particle-flow algorithm using the anti-k_T algorithm with a radius parameter $R = 0.4$, as described in Section 2.3.4. They are required to have $p_T > 30$ GeV and $|\eta| < 4.5$, The contribution from pile-up jets is reduced by applying a cut on the Jet-Vertex Tagger (JVT) discriminant. This is a multivariate combination of the fraction of the total momentum of tracks in the jet associated with the primary vertex and a track-based variable related to the scalar sum p_T of the tracks associated with the jet. For a discriminant value JVT< 0.59, the selection efficiency is about 92% for hard scatter jets. Finally, the MV2c10 b-tagging algorithm is used to assign a b-tagging weight to jets with $|\eta| < 2.5$, with a pseudo-continuous calibration applied.

Overlap Removal. It is necessary to require an overlap ambiguity removal to resolve different objects that could be reconstructed from the same detector information. For an electron and a muon which share the same ID track, if the muon is obtained from a calorimeter-tagged reconstruction, it is rejected and the electrons is selected, otherwise the electron is rejected. Additionally, the reconstructed jets which overlap with electrons or muons in a cone of radius $R = 0.2$ are removed.

5.2.2 Event Selection

Events are required to have at least one vertex with two associated tracks with $p_T > 500$ MeV. The primary vertex is chosen to be the reconstructed vertex with the largest $\sum p_T$. A selection on the impact parameter of each lepton along the beam axis (z_0) is applied, such that the four leptons should come from the primary vertex. The lepton tracks must have $|z_0 \cdot \sin\theta| < 0.5$ mm from the primary vertex. Further selection is applied on the transverse impact parameter d_0 to reject cosmic rays and to select leptons from non primary vertex: $d_0 < 1$ mm. Figure 5.3 shows a description of both impact parameter: longitudinal z_0 and transverse d_0.

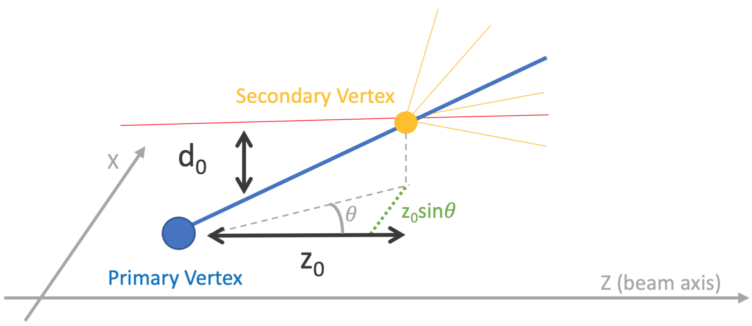

Figure 5.3: Sketch of the impact parameters definition.

Four-lepton events are selected and classified according to their final state: 4μ, $2e2\mu$, $2\mu2e$, $4e$. Higgs boson candidates are formed by selecting two same-flavour, opposite-sign lepton pairs (a lepton quadruplet) in an event.

Quadruplet Selection. Multiple quadruplets within a single event are possible: for four muons or four electrons there are two ways to pair the masses, and for five or more leptons there are multiple ways to choose the leptons to form a quadruplets. The same-flavour opposite-charge lepton pair with the mass closest to the Z boson mass is referred to as the leading di-lepton pair (Z_1). Its invariant mass is referred to as m_{12} and is required to be in the range 50 GeV$< m_{12} <$ 106 GeV. The second subleading (Z_2), pair is chosen from the remaining leptons as the pair closest in mass to the Z boson. The invariant mass (m_{34}) requirement is $m_{\text{threshold}} < m_{34} < 115\,\text{GeV}$, where $m_{\text{threshold}}$ is 12 GeV for the four-lepton invariant mass $m_{4\ell}$ below 140 GeV, rising linearly to 50 GeV at $m_{4\ell} = 190\,\text{GeV}$ and then remaining at 50 GeV for all higher $m_{4\ell}$ values. In a proton-proton collision, the characteristic of the hard scattering process between partons is the production of particles with high p_T. In this case, the four leptons produced are ordered in p_T: the highest p_T lepton in the quadruplet must satisfy $p_T >$ 20 GeV, and the second and third leptons in p_T order must satisfy $p_T >$ 15 GeV and $p_T >$ 10 GeV respectively. All possible same-flavour opposite-charge di-lepton combinations in the quadruplet must satisfy $m_{4l} >$ 5 GeV to remove events containing $J/\psi \to ll$ ($m_{J/\psi}$ = 3.097 GeV [90]). Finally all lepton pairs within the quadruplet must have an angular separation of $\Delta R = \sqrt{(\Delta y)^2 + (\Delta\phi)^2} > 0.1$.

Impact parameter and Vertex Selection. The requirements on the impact parameter are applied to suppress the background from heavy-flavour hadrons. The impact parameter significance $|d_0|/\sigma_{d_0}$, is required to be lower than 3 for muons and 5 for electrons. In order to further reduce the reducible background, the four leptons are required to be within the same vertex, then a χ^2 selection is applied: $\chi^2/ndof < 6$ for 4μ and $\chi^2/ndof < 9$ for the other final states. These cuts maintain a signal efficiency of 99.5% rejecting 20-30% of the $Z+$jets and $t\bar{t}$ events.

Isolation requirement. These requirements are used in order to select signal events and reject backgrounds. Usually they are track-based or calorimeter-based isolation criteria on each leptons.

For the track-based isolation a new variable has been defined in Run 2. The p_T of tracks in a cone of radius ΔR around the lepton, which additionally satisfy a $p_{T,\text{threshold}}$ cut and a primary vertex requirement or have $|z_0 \cdot \sin\theta| <$ 3 mm, are summed to create this new isolation variable. This variable is called *pt(var)cone[cone]_TightTTVA_pt[$p_T$cut]*, where "cone" is the cone size and "p_T cut" is the cutoff for including tracks in the calculation ($p_{T,\text{threshold}}$). In this analysis the values chosen are: p_T>500 MeV and for leptons with p_T>33 GeV, the cone size decreases linearly with p_T from ΔR=0.3 to a minimum cone size of ΔR=0.2 at 50 GeV. For the calorimeter-based isolation, a new variable also has been defined and the major improvement is its pile-up robustness, which comes from the use of the particle-flow method to calculate the calorimeter isolation. The new variable is called *newflowisol[cone]* with "cone" as the cone size in which the usual $\sum E_T$ is computed. In this analysis, the cone size for the calorimeter-based isolation is fixed at ΔR=0.20.

To determine the best isolation working point (WP), several combinations of the previous variables have been studied, looking for the right balance between signal efficiency, background rejection and pile-up robustness. The one chosen in this round of the analysis is the *FixedCutPFlowLoose*, which is a particular triangular cut to combine the new "ptvarcone" and the particle flow calorimeter isolation (*newpflowisol*) variables into a single selection. The combination of the track isolation variable and the 40% of the calorimeter isolation explained before is required to be less than 16% of the lepton p_T.

Best Quadruplet. Multiple quadruplets may pass these selections, but only one per event is selected as the candidate. Several criteria must be passed by the event to be chosen as the best quadruplet, if more than one events satisfy the previous selection criteria:

- leading pair closest to the Z boson mass
- subleading lepton pair closest to the Z boson mass
- the quadruplet from the channel with highest efficiency. The signal selection efficiencies are 31%, 21%, 17% and 16%, in the 4μ, $2e2\mu$, $2\mu2e$ and $4e$ channels, respectively.
- if more than one quadruplet has been selected (passed all the previous criteria), a matrix element for the Higgs boson decay is computed and the quadruplet with largest value selected as the final Higgs boson candidate.

Final State Radiation (FSR) Correction. The shape of the di-lepton invariant mass spectrum in the $Z \to l^+l^-$ decays are affected by the final state radiation (FSR). This radiation reduces the lepton energy leading to radiative tails in the four-lepton invariant mass spectrum towards lower values. Collinear FSR photons and electrons candidates are added to muons to the leading lepton pair ($66 < m_{12} < 89$ GeV). The non-collinear (far) FSR candidates include only photon candidates, but they are added to both electrons and muons from both leading and subleading lepton pair.

The FRS candidates are selected based on several criteria: the fraction f_1 of energy deposited in the front sampling of the calorimeter over the total energy to reduce background from muon ionisation, the angular distance $\Delta R_{\text{cluster},\mu}$ between the candidate calorimeter cluster and the muon, and the candidate E_T which must be at least 1 GeV. The selection criteria for FRS candidates are:

- Collinear FSR candidate with $E_T < 3.5$ GeV: f_1>0.2 and $\Delta R_{\text{cluster},\mu}< 0.08$
- Collinear FSR candidate with $E_T > 3.5$ GeV: f_1>0.1 and $\Delta R_{\text{cluster},\mu}< 0.15$

- Non-collinear FSR candidate: $E_T > 10$ GeV, $\Delta R_{\text{cluster},\mu}$>0.15 and pass the *Tight* identification selection and the *FixedCutLoose* isolation selection.

Only one FSR candidate is included in the quadruplet with preference given to collinear FSR and to the candidate with highest E_T. The candidate is rejected if the mass of the lepton pair and the FSR particle is above 100 GeV. Approximately 3% of reconstructed Higgs boson candidates have an FSR candidate and its impact on the expected invariant mass distribution is shown in Figure 5.4.

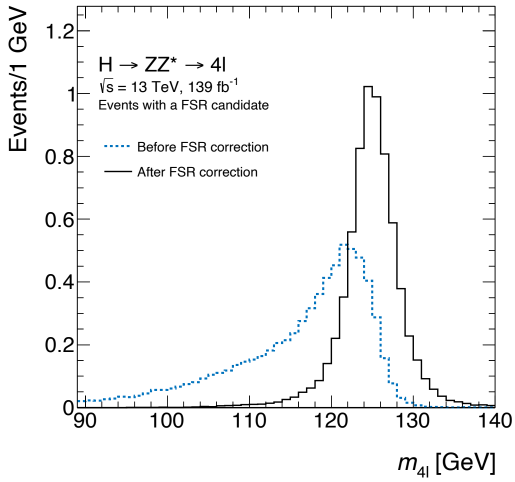

Figure 5.4: Feynman diagrams for final state radiation in leptonic Z boson decays.

Finally, Higgs boson candidates in the $m_{4\ell}$ range [115, 130] GeV are used for the analyses. A comprehensive summary of all the cuts and requirements used in the event selection is given in Table 5.3.

5.3 Background Estimation

The main backgrounds in the $H \to ZZ^* \to 4\ell$ analysis have been mentioned before. They can be classified as the so-called *irreducible background* in which there are four prompt and isolated leptons as the ZZ^*, $t\bar{t}$+V and VVV; and as the so-called *reducible background* processes as $Z+$jets and $t\bar{t}$ and WZ production, with non-prompt or misidentified leptons.

5.3.1 Irreducible Backgrounds

The main contribution comes from the ZZ^* production via $q\bar{q}$ annihilation, and then from gluon fusion. In the previous analyses in this decay channel, this contribution was estimated from Monte Carlo simulation. However, with the increasing Run 2 data statistics, the normalisation for these processes can be obtained using a data-driven approach. The details will be discussed in section 6.4.3.1.

Lepton and Jets selection	
ELECTRON Loose likelihood quality electrons with hit in innermost layer with E_T>7 GeV and $\|\eta\|< 2.47$ Interaction point constraint: $\|z_0 \cdot \sin\theta\| < 0.5$ mm (if ID track is available)	
MUON Loose identification with p_T>5 GeV and $\|\eta\|< 2.7$ Calo-tagged with p_T>15 GeV and $\|\eta\|< 0.1$, segment-tagged with $\|\eta\|< 0.1$ Stand-alone and silicon-associated forward restricted to $2.5\|\eta\|< 2.7$ Combined, stand-alone (with ID hits if available) and segment tagged muons with p_T>5 GeV Interaction point constraint: $\|z_0 \cdot \sin\theta\| < 0.5$ mm (if ID track is available)	
JETS anti-k_t jets with *bad-loose* identification, p_T>30 GeV and $\|\eta\|< 4.5$ Jets with $p_T< 60$ GeV and $\|\eta\|< 2.4$ and passing pile-up jet rejection requirements at the 92% working point (JVT score >0.59)	
Event Selection	
QUADRUPLET SELECTION	- Require at least one quadruplet of leptons consisting of two pairs of same flavour opposite-charge leptons fulfilling the following requirements: - p_T threshold for three leading leptons: 20, 15 and 10 GeV - At most one calo-tagged, stand-alone or silicon-associated muon per quadruplet - Leading di-lepton mass requirement: 50 GeV $<m_{12}<$ 106 GeV - Subleading di-lepton mass requirement: $m_{\text{threshold}} <m_{34}<$ 115 GeV - Remove quadruplet if alternative same-flavour opposite-charge di-lepton gives $m_{ll}<$ 5 GeV - $\Delta R(l,l')$>0.10 for all lepton pairs in the quadruplet - Keep all the quadruplets passing the above selection
ISOLATION	- Contribution from the other leptons of the quadruplet is subtracted max(ptcone20_TightTTVA_pt500, ptvarcone30_TightTTVA_pt500)+ $+0.4 \cdot$ neflowisol20/p_T < 0.16 (FixedCutPflowLoose)
IMPACT PARAMETER SIGNIFICANCE	- Apply impact parameter significance cut to all leptons of the quadruplet - For electrons: $\|d_0/\sigma_{d_0}\|< 5$ - For muons: $\|d_0/\sigma_{d_0}\|< 3$
VERTEX SELECTION	- Require a common vertex for the leptons - $\chi^2/ndof < 6$ for 4μ and $\chi^2/ndof < 9$ for others.
BEST QUADRUPLET	- If more than one quadruplet has been selected, choose the quadruplet with highest Higgs decay ME according to channel: 4μ, $2e2\mu$, $2\mu2e$, $4e$

Table 5.3: Schematic summary of the selection criteria in order to select the four lepton candidates on the $H \to ZZ^* \to 4l$ decay channel.

The other relevant background are triboson processes (ZZZ, WZZ, and WWZ) and they are taken directly from Monte Carlo simulation.

5.3.2 Reducible Backgrounds

The contribution of the reducible background is estimated using data-driven methods by defining control regions (CRs) of data with enhanced background and suppressed signal contributions. These CRs are built by relaxing or inverting selections and/or lepton identification requirements and the background composition in each of them can be studied through different shape models. The expected yields of different backgrounds components can be obtained performing a simultaneous fit in all the CRs. The estimation of these background in the Signal Region (SR) can be extrapolated from the CRs using *Transfer Factors* (TF). These factors are determined from the ratio of the signal lepton efficiency to pass the nominal selection and the efficiency to pass the relaxed or inverted selection requirement in the given CR.

The dominant background components vary according to the flavour of the leptons of the subleading lepton pair. As such the background analysis is performed separately for the $\ell\ell + \mu\mu$ and $\ell\ell + ee$ final states, where the $\ell\ell$ comes from a on-shell Z boson. The muon background comes mostly from heavy-flavour jets (HF) produced in association with a Z boson or in $t\bar{t}$ decays. The electron background also has a large contribution from light-flavour jets (LF) produced in association with a Z boson that are misidentified as electrons.

5.3.3 $\ell\ell + \mu\mu$ background

The dominant contribution to the $\ell\ell + \mu\mu$ background is from Z production accompanied by leptons from semi-leptonic decays of heavy flavour hadrons. There is a smaller contribution from Z production accompanied by leptons from in-flight decays of π/K from light-flavour jets. The sum of these two components is denoted as Z+jets. Another contribution is from top quark pair production $t\bar{t}$ and diboson production WZ.

The estimation of these backgrounds is performed with a simultaneous fit in multiple control regions. Each CR is enhanced with different sources of background and different fitting model is used to estimated the contribution of each background component.

The control regions are orthogonal to the signal region and they are defined as below:

- *Inverted d_0 CR (enhanced in heavy-flavour jets)*: the subleading dilepton pair has the d_0 significance selection inverted for at least one lepton. This control region is enhanced in Z+HF and $t\bar{t}$ since leptons from heavy-flavour hadrons are characterised by a large d_0 significance.

- *$e\mu$+$\mu\mu$ CR (enhanced in $t\bar{t}$)*: an opposite-charge different-flavour leading dilepton is required. In this way the leading lepton pair cannot originate from a Z boson decay, guaranteeing a pure $t\bar{t}$ CR.

- *Inverted isolation CR (enhanced in light-flavour jets)*: the subleading dilepton pair is required to pass the d_0 significance selection but have at least one lepton failing the standard isolation selection. This control region aims to enhance the Z+LF over the Z+HF.

- *Same-sign (SS) CR*: the subleading dilepton are required to have same charge. This same-sign control region is not dominated by a specific background.

Additionally, a further validation region called *Relaxed CR*, is used in the measurement, though not in the fits. This is a higher-statistics region obtained by applying the standard four-lepton analysis selection to the quadruplet, except that d_0 and isolation selections are not applied to the subleading lepton pair, as well as the vertexing cut is also not applied. It includes also the SR, but is used to validate the normalisation of the background components after the fit.

In table 5.4 the selection criteria in each CR are summarised.

Control Region	Vertex Selection	m_{12}	$\mu\mu$ requirements m_{34}	d_0 significance	Isolation
Inverted d_0	✘	-	-	inverted	✘
$e\mu + \mu\mu$	✘	OF OS	SF (OS + SS)	✘	✘
Inverted isolation	✔	-	-	✔	inverted
Same-Sign	✘	-	SF SS	✘	✘
Relaxed Region	✘	-	-	✘	✘

Table 5.4: Selection criteria of $\ell\ell+\mu\mu$ Control Regions and Relaxed Region. The check mark (✔) and crosses (✘) indicate whether a requirement is applied or not. The flavour and sign of the dilepton pairs are defined as SF = same-flavour, OF = opposite-flavour, SS = same-sign and OS=opposite-sign.

The data is then fitted to the shapes obtained from Monte Carlo in the different control regions to get the normalisation of each background component in the data. The simultaneous fit is performed on the distribution of the leading dilepton mass m_{12}, which allows a good separation of the Z+jets and $t\bar{t}$ components as the m_{12} distribution of the first forms a Z peak while the latter is non-resonant. The $t\bar{t}$ background shape is modelled by a 2^{nd} order Chebyshev polynomial in all CRs. The Z+HF and Z+LF jets resonant shape is described by a Breit-Wigner (BW) function convolved with a Crystal Ball (CB) function in all the CRs except the $e\mu$+$\mu\mu$ one, in which the leading dilepton cannot originate from a Z decay, so the non-resonant m_{12} is modelled with a first order polynomial.

The normalisation obtained from the fit is tested with data in the relaxed region and then extrapolated to the signal region by the application of transfer factors to take into account selection efficiencies and other selection effects. Figures 5.5a-5.5b show the distributions of m_{12} for the contributing background components, compared to the data in two of the CRs, after the fit has been performed (top panels) along with the fit pulls (bottom panels).

Figure 5.5c shows the comparison between the data and the background estimation of the fitting procedure expressed in the relaxed region.

Fit results together with the transfer factors and final SR estimates are shown in Table 5.5.

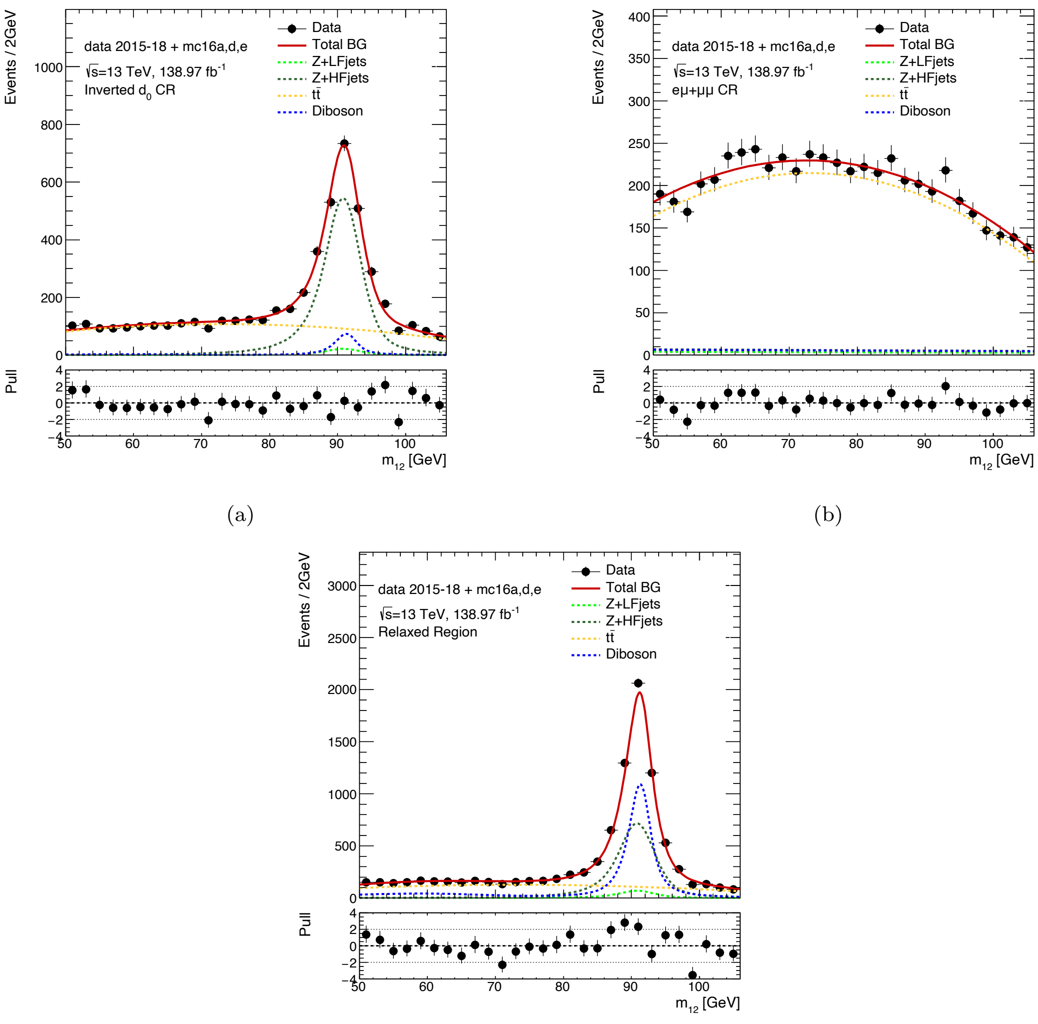

Figure 5.5: Distributions of m_{12} for the full Run2 data compared to the modelled background components in the (a) inverted-d0 and (b) $e\mu$+$\mu\mu$ CRs and in the (c) Relaxed region. The lower panels show the fit pulls.

In this table, the fit results in the relaxed region are shown with their statistical uncertainty from the data. The transfer factors are shown with their statistical uncertainty, due to the limited size of simulated samples, and their systematic uncertainty. This systematics come from the differences between data and simulation. To evaluate this uncertainty a further control region has been defined, $Z+\mu$, in which the isolation and d_0 significance efficiencies in data are studied to correct the Monte Carlo. In order to improve the Z+LF

Background type	Yields in *Relaxed region*	Transfer Factor	Yields in *Signal region*
$t\bar{t}$	3074 ± 45	0.0024 ± 0.0002	$7.38 \pm 0.11 \pm 0.71$
Z+jets (HF)	2862 ± 110	0.0043 ± 0.0004	$12.39 \pm 0.48 \pm 1.11$
Z+jets (LF)	277 ± 63	0.0108 ± 0.0011	$2.98 \pm 0.68 \pm 0.30$
WZ	MC-based estimation		4.53 ± 0.52

Table 5.5: Final $\ell\ell + \mu\mu$ background estimates in the relaxed region for each of the contributing background components, corresponding to the full m_{4l} range. The second column shows the transfer factors to the SR along with the corresponding statistical uncertainties. The last column shows the estimates for the SR yields with both statistical and systematic uncertainties.

estimation, the relative contribution of the Z+LF with respect to the dominant Z+HF jets background component is further enhanced in this control region. The Z+LF contribution originates from Z boson production accompanied by muons from in-flight decays. These are detected only in the muon spectrometer, while the π and K, from which the muons should come, are detected in the inner detector. Then defining the muon momentum balance $(p_{\mathrm{T}}^{\mathrm{ID}} - p_{\mathrm{T}}^{\mathrm{MS}})/p_{\mathrm{T}}^{\mathrm{ID}}$, the Z+LF background can be enhanced requiring at least one muon with a value greater than 0.2. In the Z+LF jets samples a significant data-MC differences have been observed in the Z+μ control sample, then transfer factor for Z+LF is taken from data.

Finally the WZ contribution is taken from MC in the SR.

5.3.4 $\ell\ell + ee$ background

The main background in the $\ell\ell + ee$ process arises from the misidentification of light-flavour jets as electrons, photon conversions and the semi-leptonic decays of heavy-flavour hadrons. The estimation of the electron background is extracted from a control region, denoted as $3\ell + X$ CR, where the first three leptons pass the full analysis selection, but the identification criteria for the lower p_T electron in the subleading pair are relaxed. In fact, the X electron is only required to have a minimum number of hits in the ID and the same charge as the other subleading electron, to ensure the orthogonality to the signal region, and the d_0 significance and vertex cut are applied.

The main contributions to $\ell\ell + ee$ background come from light jets with deposits in the calorimeter. They are referred as fake electrons (f). The other contributions are electrons coming from photon conversions or FSR (γ) and the ones which come from semileptonic decays of heavy quarks (q).

The background estimation is targeted to discriminate the different components using the n_{InnerPix} observable, which counts the number of IBL hits. This variable have a good discriminating power between electron backgrounds from γ and $f + q$, given that the first are expected to populate $n_{\mathrm{InnerPix}} = 0$ in the distribution, instead the other sources are expected to leave at least one hit in the IBL. Given that the f and q are not really discriminated by this observable, the small q contributions is estimated from simulation, as well the small

ZZ^* contributions which populates this control region.

The estimation of each background component is obtained performing a template fit based on the distribution of n_{InnerPix} for events falling in this control region. The templates are obtained from Monte Carlo simulation in a further complementary control region denoted as $Z+X$ CR, which has much more statistics with respect to the $3\ell+X$ CR. In this CR only one electron is required in addition to the leading lepton pair which has to satisfy the same criteria as $3\ell+X$ CR except the vertex cut, which is not applied (given that we are requiring less than four leptons).

In Table 5.6 the selection criteria in the two CR used in the $\ell\ell+ee$ background estimation are summarised.

Control Region	Vertex Selection	m_{34}	X requirements		
			ID	d_0 significance	Isolation
$3\ell+X$	✔	SF SS	relaxed	✔	✘
$Z+X$	✘	-	relaxed	✔	✘

Table 5.6: Selection criteria of $\ell\ell+ee$ in $3\ell+X$ and $Z+X$ control regions. The check mark (✔) and crosses (✘) indicate whether a requirement is applied or not. The flavour and sign of the dilepton pairs are defined as SF = same-flavour, OF = opposite-flavour, SS = same-sign and OS=opposite-sign. The ID column represents the identification requirements.

The resulting shapes in $Z+X$ CR for the observables used in the fit are shown in Figure 5.6a. The plot also includes the template for electrons from heavy-flavour decays that contribute in the $3\ell+X$ CR for comparison, even though this component is derived directly from MC-simulated $3\ell+X$ events. The fit on the n_{InnerPix} distribution described above is performed on data combining the $2\mu 2e$ and $4e$ channels. The distributions of the data and the fit result in the $3\ell+X$ CR are shown in Figure 5.6b: the lower panel shows the fit pulls.

Finally the efficiency of a background object to pass the nominal electron selections is used to extrapolate the fitted background yields in the 3ℓ+X CR to the signal region. These efficiencies are estimated as a function of the X p_{T} and the number of jets in the event, which are calculated separately from MC simulation in the Z+X CR and then corrected to better reproduce the efficiencies measured in data. The final estimation for f and γ background in the SR is obtained separately for the two components with the simple function:

$$N_{\mathrm{SR}} = \sum_i s_i \sum_j \varepsilon_{ij} \cdot w^{ij},$$

where the index i runs over the p_{T} intervals and j over the n_{jet} intervals. ε is the efficiency for the given background component, s is the corresponding p_{T} efficiency scale factor and w is the probability being f or γ background obtained from the fit. The fit results together with the transfer factors and final SR estimates are shown in Table 5.7.

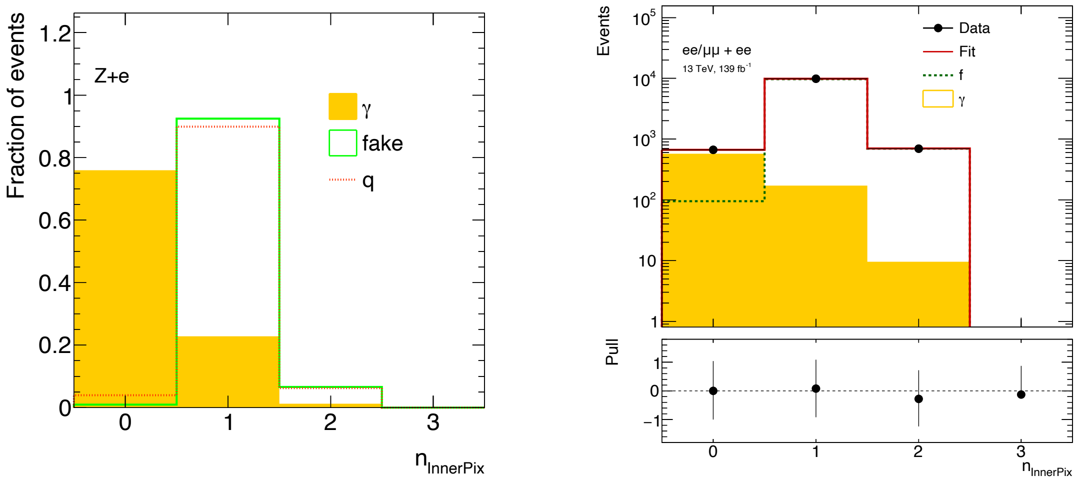

(a) (b)

Figure 5.6: In (a) templates used in the $3\ell + X$ fit to n_{InnerPix} for the different sources of background (γ, f), extracted from MC simulation in the $Z + X$ control sample. The q component (real electrons from heavy-flavour decays) is extracted from $3\ell + X$ events in simulation. All distributions are normalised to unit area. In (b) data 3ℓ+X events and result of the fit to n_{InnerPix}, combining $2\mu 2e$ and $4e$ channels for the full Run-2 dataset: the lower panel shows the fit pulls. The fit components modeling f and γ contributions are also shown.

Background type	Yields in $3\ell + X$ *CR*	Transfer Factor	Yields in *Signal region*
f	10451 ± 104	0.0016 ± 0.0003	$14.79 \pm 0.55 \pm 2.33$
γ	754 ± 34	0.0066 ± 0.0013	$4.18 \pm 0.73 \pm 0.84$
q	(MC-based estimation)		12.10 ± 3.63

Table 5.7: Fit result for yields in the $3\ell + X$ CR with statistical errors, shown together with the transfer factor used to extrapolate the yields to the SR. The SR yields for the f and γ components are quoted with statistical uncertainty as returned from the data fit and systematic uncertainty of the efficiency and the fit. For the q component that is not fitted in the data, the SR yield is taken directly from MC simulation and is quoted with its total uncertainty.

5.4 Results

The observed number of events in each of the four decay final states, and the expected signal and background yields are presented in Table 5.8. These events have passed the event selection and fall in the signal region 115< $m_{4\ell}$ <130 GeV. The mass spectrum for the FSR-corrected $m_{4\ell}$ is shown in Figure 5.7 for the signal region 115 − 130 GeV and the larger 80 − 170 GeV region compared to the signal and background expectations. The corresponding plots for the individual channels in the full mass range are given in Figure 5.8.

Final state	Signal	ZZ^* Background	Other Background	Total expected	S/B	Observed
4μ	78 ± 5	38.0 ± 2.1	2.79 ± 0.18	119 ± 5	1.9	115
$2e2\mu$	53.0 ± 3.1	26.1 ± 1.4	2.94 ± 0.19	82.0 ± 3.4	1.8	96
$2\mu 2e$	40.1 ± 2.9	17.3 ± 1.3	3.5 ± 0.5	60.9 ± 3.2	1.9	57
$4e$	35.3 ± 2.6	15.0 ± 1.5	2.73 ± 0.33	53.0 ± 3.1	2.0	42
Total	206 ± 13	96 ± 6	11.9 ± 0.9	315 ± 14	1.9	310

Table 5.8: The number of events expected and observed for a $m_H = 125\,\text{GeV}$ hypothesis for the four-lepton final states in a window of $115 < m_{4\ell} < 130\,\text{GeV}$, using the FSR-corrected $m_{4\ell}$. The columns show the number of expected signal events, the number of expected irreducible and reducible background events, the expected S/B ratio for each final state, and the number of observed events, for 139 fb^{-1} at $\sqrt{s} = 13\,\text{TeV}$.

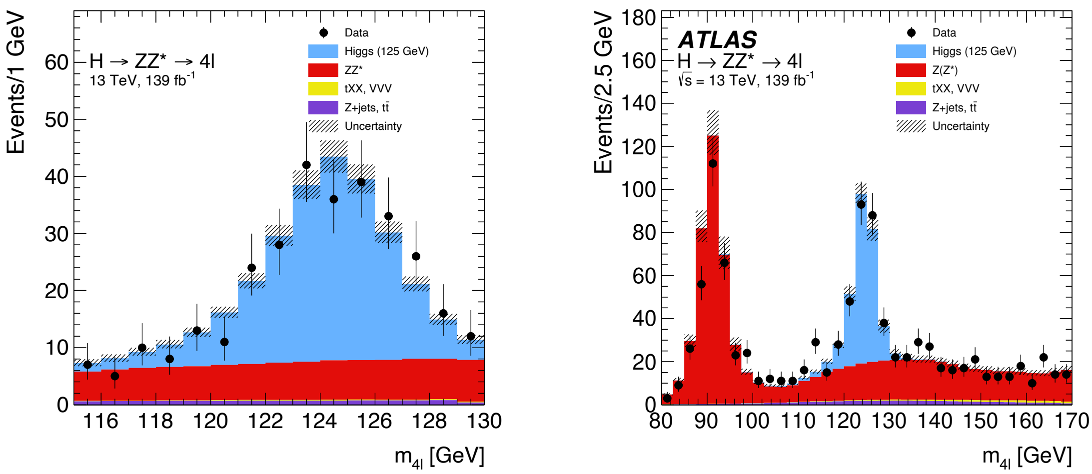

(a) (b)

Figure 5.7: FSR-corrected $m_{4\ell}$ distribution of the selected candidates, compared to the background expectation (a) in the low mass region and (b) in the whole mass spectrum of the analysis.

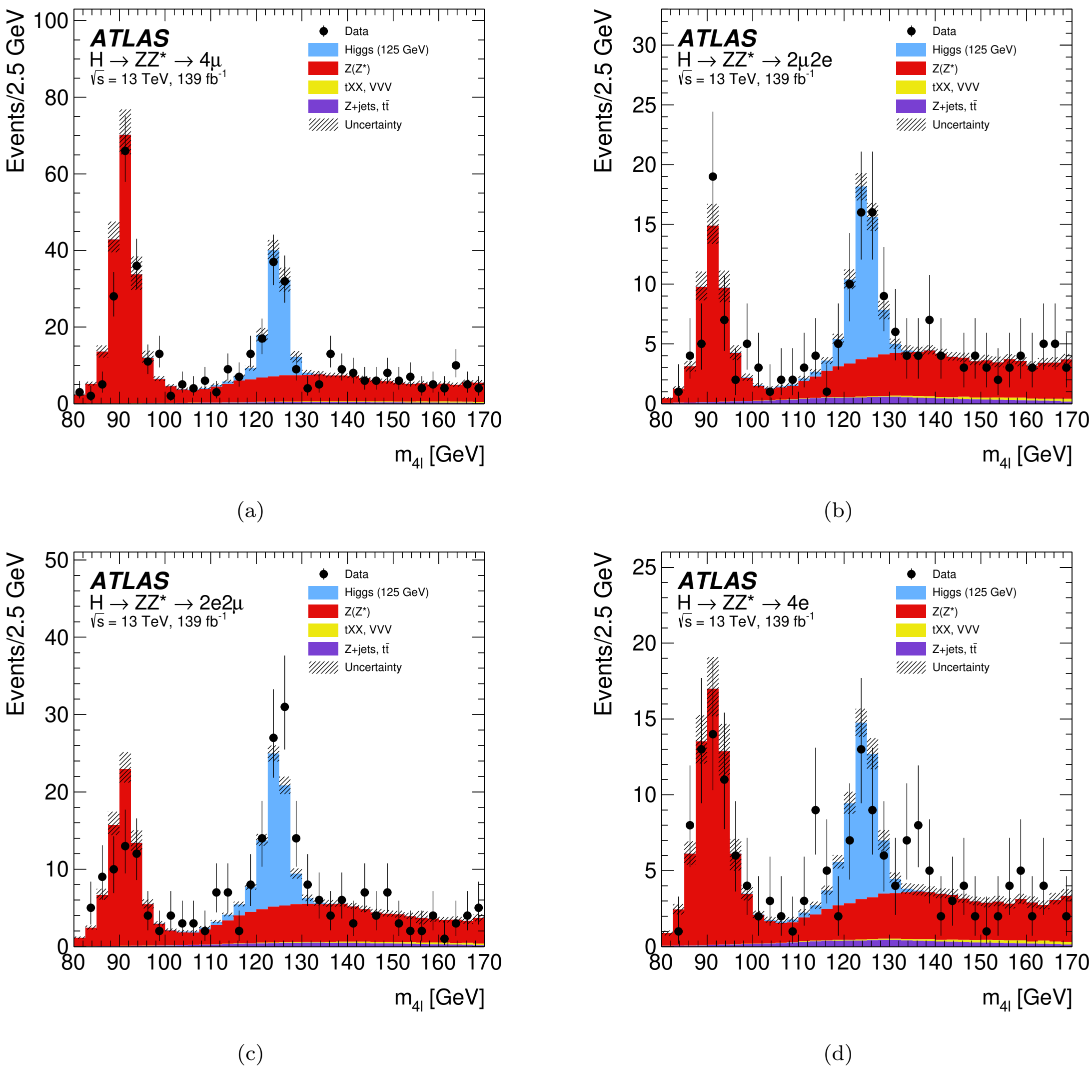

Figure 5.8: FSR-corrected $m_{4\ell}$ distribution of the selected candidates for the different channels of the analysis, compared to the signal and background expectations in the region $80 - 170\,\text{GeV}$: (a) 4μ, (b) $2\mu 2e$, (c) $2e2\mu$, (d) $4e$. The contribution of the reducible background is also shown separately.

Chapter 6

Fiducial inclusive and differential cross section measurements in $H \to ZZ^* \to 4l$ decay channel

Contents

The measurements of the differential cross section of the Higgs boson in the $H \to ZZ^{(*)} \to 4\ell$ decay channel plays a crucial role in studying possible deviations from the SM. This is due to the fact that the differential cross section can be expressed in terms of variables sensitive to possible Beyond Standard Model effects. In this analysis the Full Run 2 dataset of 139 fb^{-1}has been used.

The main goal of this analysis is to have a model-independent result to be more sensitive to possible deviations from the SM. The cross section measurement is then performed within a fiducial phase-space defined to mimic the selection described in Section 5.2 for the reconstruction of Higgs boson decays in the four lepton final state. The signal is extracted from a fit to the invariant mass distribution of the four lepton system.

The inclusive fiducial cross section measurement has been performed in different four lepton finale states: 4μ, $4e$, $2e2\mu$ and $2\mu 2e$. The combination in all final states and the total cross section have been also measured. The differential fiducial cross section measurements are performed on several variables of interest, which either describe the Higgs kinematics or are sensitive to the details of the Higgs boson production and double-differential cross section measurements are also presented. The variables used in the differential measurement are described in Section 6.3 and they are sensitive to different Higgs boson properties and to possible BSM effects in its couplings with the other SM particles. For example the decay angles of the four leptons and the angle in the transverse plane of the two leading jet are sensitive to the spin-CP properties of the Higgs boson. The transverse momentum spectrum is very important to test the theoretical cross section predictions and it is sensitive to the charm and bottom Yukawa couplings, and it is described in detail in Chapter 7. The jet-related variables are sensitive to different production mechanisms and then to their theoretical model. The fiducial inclusive and differential cross section results are presented in Section 6.6. Further variables built to be sensitive to CP-odd effects have been studied in this thesis and the preliminary expected results are reported in Section 6.7.

6.1 Analysis Strategy

The total cross section is defined as:

$$\sigma^{\text{tot}} = \frac{N_s}{\varepsilon_{\text{tot}} \cdot BR \cdot \mathcal{L}_{\text{int}}} \,, \tag{6.1.1}$$

where BR$= 1.25 \pm 0.03 \times 10^{-4}$ [13] is the branching ratio of the $H \to ZZ^* \to 4\ell$ final state, N_s is the number of observed signal events, $\mathcal{L}_{\text{int}}$ is the integrated luminosity, ε_{tot} is the efficiency for detecting signal, taking into account for trigger, reconstruction and identification efficiencies. This parameter is very model-dependent quantity since it takes into account events which are outside the detector acceptance. Then the total cross section is a measurement extrapolated to regions of phase space in which the detector has no sensitivity.

This model dependency can be removed factorising out the acceptance from the definition of the detector efficiency:

$$\varepsilon_{\text{tot}} = \mathcal{A} \cdot \varepsilon_{\text{fid}}, \tag{6.1.2}$$

where $\mathcal{A}$ is the fiducial acceptance and ε_{fid} the fiducial efficiency. In this way the fiducial cross section can be defined as:

$$\sigma^{\text{fid}} = \sigma^{\text{tot}} \cdot \mathcal{A} \cdot BR = \frac{N_s}{\varepsilon_{\text{fid}} \cdot \mathcal{L}_{\text{int}}} \; . \tag{6.1.3}$$

The fiducial phase space is defined closely to the selection cuts used in reconstruction of the Higgs boson decays to four lepton. The signal is unfolded at particle-level using the matrix inversion method. This method allows to correct for detector efficiency and resolution taking into account of migration effects between the bins of the distributions.

The cross sections in each bin of the differential distribution or in each final states for the inclusive analysis, are measured performing a binned fit to the $m_{4\ell}$ distribution to extract the number of signal events. The contribution of the non-resonant ZZ^* background is estimated by introducing a floating ZZ^* normalisation, which is fitted simultaneously with the signal in an extended mass window of $105 < m_{4\ell} < 160$ GeV.

Finally the possibility to perform a VBF fiducial cross section measurements has been also studied. The key point of the measurement is to discriminate the VBF-like events from the ggF-like ones during the fit to extract the cross sections. The ggF production represents a background source in this case and its contribution can be constrained from the data as it has been done for the ZZ^* background by adding a floating ggF normalisation. The fit is then performed on a variable build to distinguish all the three contributions: VBF, ggF and ZZ^*. Tests on two different template variables have been performed and their results are presented in Section 6.8.

6.2 Fiducial Selection

The fiducial selection is defined to mirror the reconstruction event selection described in Section 5.2 in order to minimise the extrapolation outside of the detector acceptance.

Particles selection

Each event at truth-level simulation has a collection of finale states which are initially classified using the Particle Data Group Identification (PDGID) [178] numbering schemes stored in the High Energy Monte Carlo (HepMC) record [179], which traces the particle evolution throughout the simulation.

Truth lepton definitions can be divided into three categories based on how QED radiation effects are handled:

- *Bare* leptons are the stable leptons after QED Final State Radiation (FSR).

- *Born* leptons are leptons before QED FSR.
- *Dressed* leptons are bare leptons in which the QED FSR recovery is mimicked, collecting all stable photons inside a cone or jet algorithm around the charged lepton.

The photons for clustering are required to be stable, not come from hadron and have to be within a ΔR of 0.1 from bare lepton.

In this analysis, dressed lepton have been used to describe the truth lepton kinematics. This represents a difference with respect to the reconstructed event selection in which the FSR correction is performed and it leads to a small non-overlap between the dressing and FSR correction, but only 0.8% of events have an FSR with $\Delta R > 0.1$ and only 0.003% of events migrate in or out of our signal mass window due to FSR correction in the non-overlapping region.

- **Electrons.** Electrons (e) are required to have $p_{\mathrm{T}}^{e} > 5$ GeV, $|\eta^{e}| < 2.7$ and to originate from Z and W decays (not from hadron decays).
- **Muons.** The construction of muons (μ) is similar to electrons with the exception of the kinematic and geometric cuts: $p_{\mathrm{T}}^{\mu} > 5$ GeV, $|\eta^{\mu}| < 2.7$.
- **Jets.** Particle-level jets (j) are reconstructed from final states neutral and charged particles excluding those originating from the Higgs and leptonic vector boson decays. Stable particles are clustered using the anti-k_{t} algorithm [79] with radius parameter $R = 0.4$. Each jet is required to have $p_{\mathrm{T}}(\mathrm{j}) > 30$ GeV and $|y(j)| < 4.4$ and they are removed if they are within a cone of size $\Delta R < 0.1$ of any truth electron or muon. A fiducial jet is labelled as a b-jet if there is a b-hadron within a cone around the jet axis of radius $\Delta R = 0.3$ with a transverse momentum greater than 5 GeV.

Higgs candidate

Once the particles are defined, the final quadruplet have to be defined. Only stable particles are considered in the formation of the fiducial volume and some fiducial selection requirements are in common with the reconstructed event selection:

- two pairs of same flavour opposite sign (SFOS) truth lepton;
- the leading pair as the SFOS lepton pair with invariant mass closest to the PDG Z mass (m_Z) and the subleading pair as the second SFOS lepton pair with invariant mass closest to the m_Z;
- the three leading leptons are required to have p_{T}^{ℓ} >20, 15, 10 GeV respectively;
- the leading pair invariant mass must be $50 < m_{12} < 106$ GeV;
- the subleading pair invariant mass must be $12 < m_{34} < 106$ GeV (different from reconstructed event selection in with the lower threshold is $m_{4\ell}$-dependent);

- the event is removed if $m_{\ell_i,\ell_j} \leq 5$ GeV (J/ψ veto);
- the quadruplet is required to have $105 < m_{4\ell} < 160$ GeV.

The mass window cut has been defined to optimise the ZZ^* background estimation. In cases where multiple Higgs candidates can be formed, the best candidate is selected using a matrix element based method, as is done in the event selection described in Section 5.2. This method reduce the possibility of a "lepton mispairing" due to additional lepton in the final states which characterise the VH or $t\bar{t}H$ production signatures. The fiducial region selection is summarised in Tab. 6.1.

Table 6.1: List of event selection requirements which define the fiducial phase space for the cross-section measurement. SFOC lepton pairs are same-flavour opposite-charge lepton pairs.

Leptons and jets	
Leptons	$p_{\mathrm{T}} > 5$ GeV, $\lvert\eta\rvert < 2.7$
Jets	$p_{\mathrm{T}} > 30$ GeV, $\lvert y\rvert <$ 4.4
Lepton selection and pairing	
Lepton kinematics	$p_{\mathrm{T}} > 20, 15, 10$ GeV
Leading pair (m_{12})	SFOC lepton pair with smallest $\lvert m_Z - m_{\ell\ell}\rvert$
Subleading pair (m_{34})	remaining SFOC lepton pair with smallest $\lvert m_Z - m_{\ell\ell}\rvert$
Event selection (at most one quadruplet per event)	
Mass requirements	50 GeV$< m_{12} <$ 106 GeV and 12 GeV$< m_{34} <$ 115 GeV
Lepton separation	$\Delta R(\ell_i, \ell_j) > 0.1$
Lepton/Jet separation	$\Delta R(\ell_i, \mathrm{jet}) > 0.1$
J/ψ veto	$m(\ell_i, \ell_j) > 5$ GeV for all SFOC lepton pairs
Mass window	105 GeV$< m_{4\ell} <$ 160 GeV
If extra lepton with $p_{\mathrm{T}} > 12$ GeV	Quadruplet with largest matrix element value

6.3 Variable Definitions

The $H \to ZZ^{(*)} \to 4\ell$ decay channel is a very interesting channel to perform study of the Higgs couplings due to the fact that the reconstructed events contain the full kinematic information of the Higgs since all four leptons can be measured. The Higgs four-vectors can be used to calculate the differential cross section of the Higgs as a function of any variable of interest. The Higgs production properties can also be investigated with differential cross section measurement in the variables related to jets present in the final states.

6.3.1 Higgs boson kinematic variables

The kinematics of the Higgs particle in a pp collision can be described by the transverse momentum p_T, azimuthal direction Φ_H, and rapidity y. The decay to four leptons is described by the invariant mass of the leading lepton pair m_{12}, the invariant mass of the subleading lepton pair m_{34}, and five decay angles (Φ_H, Φ_1, θ^*, θ_1, θ_2) between the leptons as shown in Figure 6.1. The angular variable definitions can be found in [182].

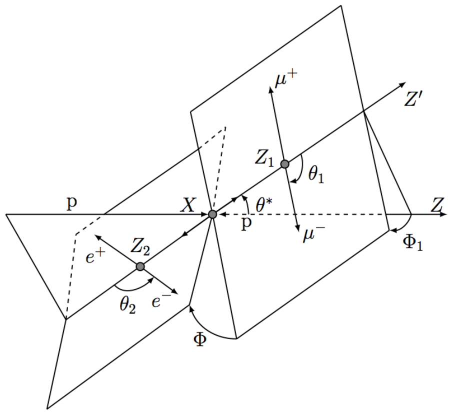

Figure 6.1: Diagram of decay angles for the $H \to 4\ell$ decay.

This analysis measures the differential cross sections of:

- $p_T^{4\ell}$, $|y_{4\ell}|$: transverse momentum and rapidity of the four-lepton system;
- m_{12}, m_{34}: invariant mass of the leading and subleading lepton pair;
- $|\cos(\theta^*)|$: magnitude of the cosine of the decay angle of the leading lepton pair in the four-lepton rest frame relative to the beam axis;
- $\cos(\theta_1)$, $\cos(\theta_2)$: production angles of the anti-leptons from the two Z bosons, where the angle is relative to the Z vector;
- ϕ, ϕ_1: two azimuthal angles between the three planes constructed from the Z boson and leptons in the Higgs rest frame.

The Higgs boson differential transverse momentum cross section is of particular interest as the theoretical cross section predictions have been studied extensively (see e.g. [105,106,180,181]). In particular, the treatment of the top and bottom quark masses in the calculation of the ggF production mode cross section can lead to order 10% differences in the differential transverse momentum cross section [105,106]. The rapidity of the Higgs is a measure of the relativistic angle between the $x-y$ plane in the ATLAS coordinate and the direction of the emitted Higgs and it can be used as constraint of the gluon Parton Distribution Function in the ggF production at high parton momentum fraction. The invariant mass of the leading and subleading lepton pair are sensitive to higher order electroweak (EW) corrections to the Higgs boson decay, and to BSM contributions. These two variable and the angular variables $\cos(\theta_1)$, $\cos(\theta_2)$, ϕ, and ϕ_1 are investigated due to their sensitivity to the spin and parity of the Higgs, as well as to the same-flavour pair final state interference and EW corrections.

In addition to the single observables listed, the observable m_{12} vs. m_{34} is built to perform a double differential cross section measurement. This 2D variable captures the correlations between the leading and subleading lepton pair invariant mass. In a BSM Effective Field Theory framework, such as the Pseudo-Observable one described in Section 1.1.2.3, with extra contact couplings between the Higgs and the final lepton pairs that modifies the HZZ vertex, m_{12} vs. m_{34} would be more sensitive than m_{12} or m_{34} on their own since their contact term affects both distributions.

6.3.2 Jet-related variables

The measurement of the jet related variables probes both QCD radiation effects and contributions from the various production modes of the Higgs boson.

In this analysis differential cross sections have been measured in:

- N_{jets}, $N_{\text{b-jets}}$: jet and b-jet multiplicity;
- $p_T^{\text{lead. jet}}$, $p_T^{\text{sublead. jet}}$: transverse momentum of the leading and subleading jet, for events with at least one and two jets respectively. The leading jet refers to the jet with the highest p_{T} in the event, while the subleading refers to the jet with the second-highest p_{T};
- m_{jj}, $|\Delta\eta_{jj}|$ and $\Delta\phi_{jj}$: invariant mass, difference in pseudorapidity and signed difference in ϕ of the leading and subleading jets for events with at least two jets, defined as:

$$\Delta\phi_{jj} = \begin{cases} \phi_{j1} - \phi_{j2}, & \text{if } \eta_{j1} > \eta_{j2} \\ \phi_{j2} - \phi_{j1}, & \text{if } \eta_{j2} > \eta_{j1} \\ \Delta\phi_{jj} + 2\pi, & \text{if } \Delta\phi_{jj} < 0 \end{cases} \tag{6.3.1}$$

The jet multiplicity is sensitive to different production mechanisms given that the fraction of events coming from non-ggF production modes increases with jet multiplicity due to the presence of hadronic decays of the particles produced in association with the Higgs boson. It also provides sensitivity to the theoretical modelling of high-p_T quark and gluon emission. The transverse momentum of the jets directly probes the quark and gluon radiation. The invariant mass of the two leading jets is also sensitive to the production mechanisms of the Higgs boson. The $\Delta\phi_{jj}$ variable is sensitive to spin-CP effects in the HZZ production vertex in case of VBF or VH production mode.

Additional variables which combine the properties related to the kinematics of the Higgs boson and the jets have been considered for the differential measurements:

- $m_{4\ell j}$, $p_{T4\ell j}$: transverse momentum and invariant mass of the four-lepton system and leading jet, for events with at least one jet;
- $m_{4\ell jj}$, $p_{T4\ell jj}$: transverse momentum and invariant mass of the four-lepton system and leading and subleading jets, for events with at least two jets.

The $4\ell+1j$ observables are sensitive to resummation effects: $p_{T4\ell j}$ is a "1/2-jet resolution variable" that probes the second emission in Higgs+1 jet events. The $4\ell + 2j$ observables are instead sensitive to additional jet activity in the events: $p_{T4\ell jj}$ is a proxy for events with $\geq$ 3 jets, in particular of the third jet p_T, instead $m_{4\ell jj}$ provides the energy scale of the Higgs+2 jet process.

In addition to the single observables listed, the following double differential observables are built using variables defined below: $p_{\mathrm{T}}^{4\ell}$ vs. N_{jets}, $p_{\mathrm{T}}^{4\ell}$ vs. $p_{\mathrm{T}}^{\text{lead. jet}}$, $p_{\mathrm{T}}^{4\ell}$ vs. $p_{\mathrm{T}}^{4\ell\mathrm{j}}$, $p_{\mathrm{T}}^{4\ell}$ vs. $|y_{4\ell}|$, $p_{\mathrm{T}}^{4\ell\mathrm{j}}$ vs. $m_{4\ell j}$, $p_{\mathrm{T}}^{\text{lead. jet}}$ vs. $p_{\mathrm{T}}^{\text{sublead. jet}}$, and $p_{\mathrm{T}}^{\text{lead. jet}}$ vs. $|y^{\text{lead. jet}}|$ (where $|y^{\text{lead. jet}}|$ | is the rapidity of the leading jet). These variables probes the effects of QCD resummation.

6.3.3 CP-odd sensitive variables

Several theories Beyond Standard Model require an extended Higgs sector featuring several neutral Higgs boson of both even and odd CP-parity. The search of CP-violation in the $H \to ZZ^{(*)} \to 4\ell$ decay channel can be performed, by looking for an anomalous CP-odd coupling in the HZZ decay vertex as well as in the VBF and VH production vertex (Figure 6.2). For this reason, observables sensitive to this effects have been defined.

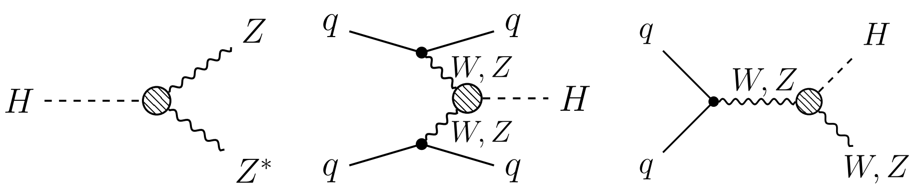

Figure 6.2: Feynman Diagram of the HZZ Higgs decay and VBF and VH Higgs production with effective HVV vertex.

Asymmetric CP angular observables [183]. One possibility to study CP violation is through angular-function asymmetries arising in case of CP violation effect. Six observable angular-functions can be defined:

$$O_1 = \frac{(\vec{p}_{2Z} - \vec{p}_{1Z}) \cdot (\vec{p}_{3H} + \vec{p}_{4H})}{|\vec{p}_{2Z} - \vec{p}_{1Z}||\vec{p}_{3H} + \vec{p}_{4H}|} \equiv \cos\theta_1 \tag{6.3.2}$$

$$O_2 = \frac{(\vec{p}_{2Z} - \vec{p}_{1Z}) \cdot (\vec{p}_{3H} \times \vec{p}_{4H})}{|\vec{p}_{2Z} - \vec{p}_{1Z}||\vec{p}_{3H} \times \vec{p}_{4H}|} \equiv -\sin\phi\cos\theta_1 \tag{6.3.3}$$

$$O_3 = O_1 O_{3a} O_{3b} \equiv \cos\theta_1 \sin\theta_2 \cos\theta_2 \sin\phi \tag{6.3.4}$$

$$\text{where:} \quad O_{3a} = \frac{(\vec{p}_{4Z} - \vec{p}_{3Z}) \cdot (\vec{p}_{1H} \times \vec{p}_{2H})}{|\vec{p}_{4Z} - \vec{p}_{3Z}||\vec{p}_{1H} \times \vec{p}_{2H}|} \quad \text{and} \quad O_{3b} = \frac{(\vec{p}_{3Z} - \vec{p}_{4Z}) \cdot (\vec{p}_{1H} + \vec{p}_{2H})}{|\vec{p}_{3Z} - \vec{p}_{4Z}||\vec{p}_{1H} + \vec{p}_{2H}|} \tag{6.3.5}$$

$$O_4 = \frac{[(\vec{p}_{3H} \times \vec{p}_{4H}) \cdot \vec{p}_{1H}][(\vec{p}_{3H} \times \vec{p}_{4H}) \cdot (\vec{p}_{1H} \times \vec{p}_{2H})}{|\vec{p}_{3H} + \vec{p}_{4H}|^2|\vec{p}_{1H} + \vec{p}_{2H}||\vec{p}_{3Z} - \vec{p}_{4Z}|^2|\vec{p}_{1Z} - \vec{p}_{2Z}|/16} \equiv \sin^2\theta_1 \sin^2\theta_2 \sin\phi\cos\phi \tag{6.3.6}$$

$$O_5 = \frac{[(\vec{p}_{4H} \times \vec{p}_{3H}) \cdot \vec{p}_{1H}][(\vec{p}_{1Z} - \vec{p}_{2Z}) \cdot \vec{p}_{3Z}]}{|\vec{p}_{3H} + \vec{p}_{4H}||\vec{p}_{3Z} - \vec{p}_{4Z}|^2|\vec{p}_{1Z} - \vec{p}_{2Z}|^2/8} \equiv \sin\theta_1 \sin\theta_2 \sin\phi[\sin\theta_1 \sin\theta_2 \cos\phi - \cos\theta_1 \cos\theta_2] \tag{6.3.7}$$

$$O_6 = \frac{[(\vec{p}_{1Z} - \vec{p}_{2Z}) \cdot (\vec{p}_{3H} + \vec{p}_{4H})][(\vec{p}_{3H} \times \vec{p}_{4H}) \cdot \vec{p}_{1H}}{|\vec{p}_{1Z} - \vec{p}_{2Z}|^2 |\vec{p}_{3H} + \vec{p}_{4H}|^2 |\vec{p}_{3Z} - \vec{p}_{4Z}|/4} \equiv \sin\theta_1 \cos\theta_1 \sin\theta_2 \sin\phi \qquad (6.3.8)$$

Here $\vec{p}_i$, i=1,2,3,4 are the 3-moments of the final state leptons in the order $\ell_1\bar{\ell}_1\ell_2\bar{\ell}_2$. The subscripts Z and H denote that the corresponding 3-vector is taken in the Z or in the Higgs boson rest frames. Figure 6.3 shows the shape modification in presence of CP-odd coupling at the VBF vertex for the O_2 and O_5.

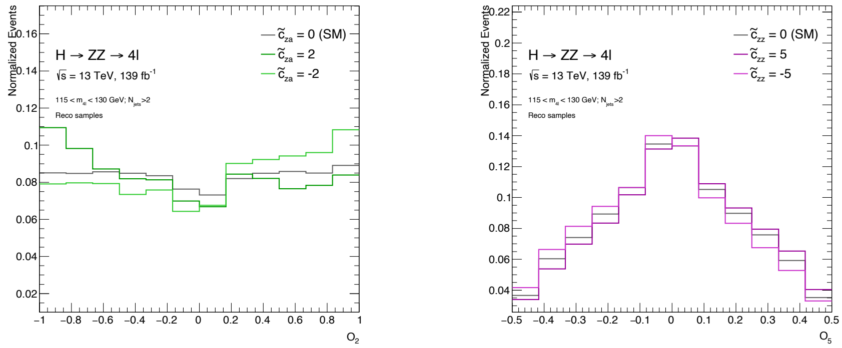

(a) O_2 with CP-odd $\widetilde{c}_{za}$ = ± 2

(b) O_5 with CP-odd $\widetilde{c}_{zz}$ = ± 5

Figure 6.3: Shape modification in presence of CP-odd coupling at the VBF vertex for the O_2 (a) and O_5 (b).

Optimal Observables ($\mathcal{OO}$) [184]. The lepton and jets variables alone could be not sensitive at very low values of BSM couplings. Instead the matrix element of a physics process contains all the kinematic information of an event. For this reason, a Matrix Element (ME) based observable should provide maximal information for a process, combining all low-level quantities (lepton and jets kinematics) into a higher-level observable.

Starting from the matrix element of the Higgs boson interaction as sum of CP-even contribution from SM and a BSM CP-odd contribution, the squared amplitude can be computed (which is the only physical observable quantity):

$$\mathcal{M}_{\text{Mix}}(\boldsymbol{c}) = \mathcal{M}_{\text{SM}} + \mathcal{M}_{\text{BSM}}(\boldsymbol{c}) \implies |\mathcal{M}_{\text{Mix}}(\boldsymbol{c})|^2 = |\mathcal{M}_{\text{SM}}|^2 + 2\Re(\mathcal{M}_{\text{SM}}\mathcal{M}^*_{\text{BSM}}(\boldsymbol{c})) + |\mathcal{M}_{\text{BSM}}(\boldsymbol{c})|^2 \qquad (6.3.9)$$

where $\boldsymbol{c}$ is the CP-odd couplings which parametrises a BSM hypothesis under which the matrix elements are computed. It is possible to define several observables built on the ratios of the matrix element. The Optimal Observable of first order in the BSM amplitude is defined as the ratio of the interference term $2\Re(\mathcal{M}_{\text{SM}}\mathcal{M}^*_{\text{BSM}}(\boldsymbol{c}))$ and the squared amplitude of the SM process:

$$\mathcal{OO}_1(\boldsymbol{c}) = \frac{|\mathcal{M}_{\text{Mix}}(\boldsymbol{c})|^2 - |\mathcal{M}_{\text{SM}}|^2 - |\mathcal{M}_{\text{BSM}}(\boldsymbol{c})|^2}{|\mathcal{M}_{\text{SM}}|^2} \qquad (6.3.10)$$

The distribution of this observable has the interesting property of being symmetric for a

Standard Model - like events and asymmetric if a CP-odd contribution is present. A second observable can be defined as the second order in BSM amplitude Optimal Observable. It is defined as the ratio of the pure BSM contribution matrix element and the SM one:

$$\mathcal{OO}_2(\boldsymbol{c}) = \frac{|\mathcal{M}_{\mathrm{BSM}}(\boldsymbol{c})|^2}{|\mathcal{M}_{\mathrm{SM}}|^2} \tag{6.3.11}$$

This observable does not have an asymmetry in case of CP-odd contributions. Its results are less sensitive given that it is not able to distinguish between CP-even and CP-odd contributions. However, it brings additional information regarding the magnitude of the coupling.

Furthermore, two different Optimal Observable of the first and second order can be defined, based on which process we are computing the BSM matrix element, namely which is the HVV vertex under investigation. If the BSM coupling is probed in the VBF vertex we are defining the *production only* ME and then a production only $\mathcal{OO}$, denoted as $\mathcal{OO}_{1,jj}$ for the first order. If the BSM coupling is probed in the $H \to 4\ell$ decay vertex we are defining the *decay only* ME and then a decay only $\mathcal{OO}$, denoted as $\mathcal{OO}_{1,4\ell}$ for the first order. Figure 6.4 shows an example of the distribution of the first order production only Optimal Observable $\mathcal{OO}_{1,jj}(\widetilde{c}_{zz} = 1)$, where $\widetilde{c}_{zz}$ represents one of the CP-odd coupling constant in the *Higgs basis*, described in Section 1.1.2.2, which is zero in the SM. It can be seen that for different CP-odd coupling values the $\mathcal{OO}_{1,jj}$ shape becomes asymmetric.

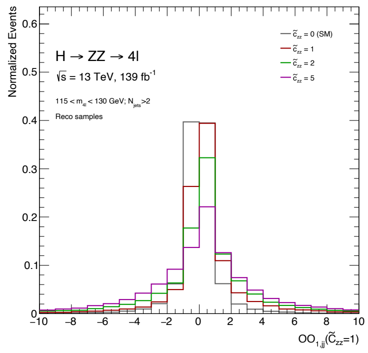

(a) $\mathcal{OO}_{1,jj}(\widetilde{c}_{zz} = 1)$ with CP-odd $\widetilde{c}_{zz}$ = +1,+2,+5

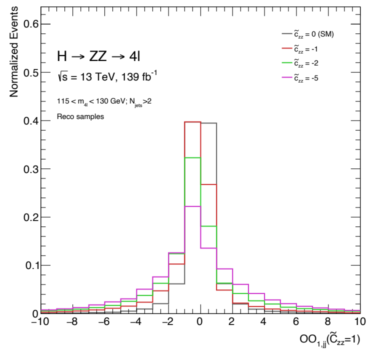

(b) $\mathcal{OO}_{1,jj}(\widetilde{c}_{zz} = 1)$ with CP-odd $\widetilde{c}_{zz}$ = -1,-2,-5

Figure 6.4: Shape modification in presence of CP-odd coupling at the VBF vertex for the $\mathcal{OO}_{1,jj}(\widetilde{c}_{zz} = 1)$.

6.4 Signal Extraction and Unfolding

The number of signal events is extracted performing a fit on the $m_{4\ell}$ distribution in a mass window $105 < m_{4\ell} < 160$ GeV, constraining the ZZ^* background normalisation from data. The unfolding procedure is described in this section together with the definitions of the main factors needed to unfold the observable distributions as the acceptance, detector response matrix and the fiducial leakage. Finally, the profile likelihood method used to extract the cross sections from the observed events is described.

6.4.1 Fiducial definitions and Unfolding

6.4.1.1 Fiducial factors

In the previous section, the fiducial selection has been described. Then several quantities in the fiducial phase space have to be defined to perform the fiducial cross section measurement, such as the acceptance, the efficiency and the fiducial leakage. These factors are defined in the following section and their behaviour for different production mode and their combination has been investigated in all the four final states and in the inclusive one.

Fiducial acceptance

The fiducial acceptance is defined as the ratio between the events which pass the fiducial selection N_{Fid} and the total number of generated events, N_{Tot}:

$$\mathcal{A} = \frac{N_{\mathrm{Fid}}}{N_{\mathrm{Tot}}} \,. \tag{6.4.1}$$

The fiducial selection of the phase space is performed to minimise the extrapolation outside of the detector acceptance. It selects the objects and the events based on the quantities measurable experimentally and on the reconstruction level selection explained in Section 5.2. The acceptance must be estimated from simulation given that is not possible to measure it from data, introducing a model dependence in the cross section measurement. Figure 6.5 shows the acceptance for different production modes in the four final states. The acceptance values between the different final states are very close and they are within 10% for all the Higgs production modes. In particular, for the $t\bar{t}H$ $+tH$ production the fiducial acceptance is higher than the other production modes due to the fact that this mechanism has a larger lepton multiplicity . This results in a combinatorially increasing number of possible pairings, leading to an higher efficiency for the m_{12} and m_{34} requirements and then to a larger fiducial acceptance.

Fiducial efficiency: correction factor

The detector fiducial efficiency is defined as the number of reconstructed events divided by the number of fiducial events:

$$\varepsilon_{\mathrm{fid}} = \frac{N_{\mathrm{Reco}}}{N_{\mathrm{Fid}}} \,. \tag{6.4.2}$$

and it is also called *correction factor*. It can be seen from Figure 6.6 that the detector efficiency is significantly higher in the 4μ channel due to the higher reconstruction efficiency for muons. The reduced detector correction factor in $t\bar{t}H$ $+tH$ is the result of a decreased reconstruction efficiency due to the lepton isolation requirements. The reconstructed leptons are less isolated because of the presence of the additional jets (from top decays) within the event and no isolation requirements are imposed at particle-level.

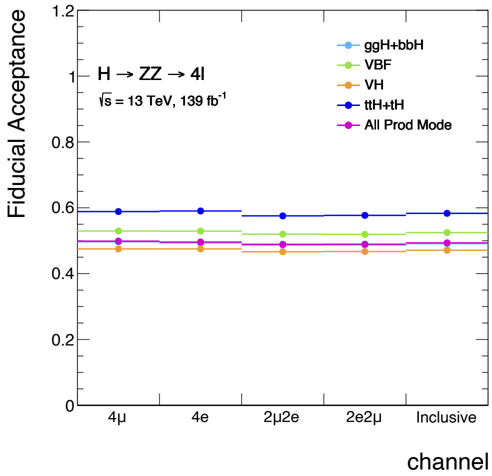

Figure 6.5: Comparison of the acceptance at $m_H = 125$ GeV using the dressed truth lepton definition in the mass range $105 < m_{4\ell} < 160$ GeV for different production mode in the four final states.

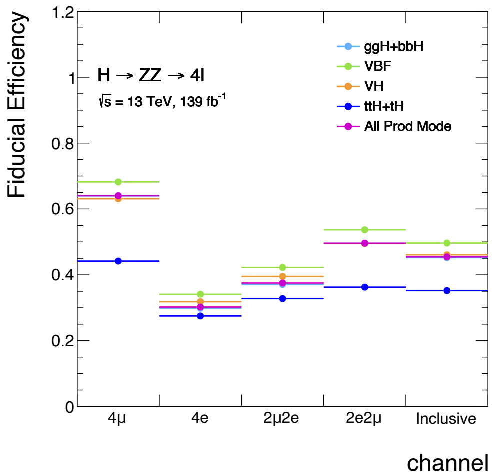

Figure 6.6: Comparing the fiducial efficiency at $m_H = 125$ GeV using the dressed truth lepton definition in the mass range $105 < m_{4\ell} < 160$ GeV for different production mode in the four final states.

Fiducial leakage: non-fiducial factor

Ideally the reconstructed events should be a subset of the fiducial events, but it is not true due to the fact that there are some events which are not in the fiducial region at particle level, but they are reconstructed inside anyway. This will cause a migration effects at the edge of the fiducial region.

It is important to take into account of the fraction of the events which are outside the fiducial region but they are reconstructed within the signal region. They represents events produced by signal process, but they should be considered as background given that they are outside the fiducial region. This quantity is called *non-fiducial factor* f_{nonfid}, defined as follows:

$$f_{\text{nonfid}} = \frac{N_{\text{reco}} - N_{\text{reco\&fid}}}{N_{\text{reco}}} \ . \qquad (6.4.3)$$

This contribution is expected to be of the order of 1-2% for all the production mode, as show in Figure 6.7. The VH and $t\bar{t}H$ production have a larger leakage due to the increased lepton multiplicity in their final states when the leptonic decay of the vector boson associated or of W boson from top quark decay are considered.

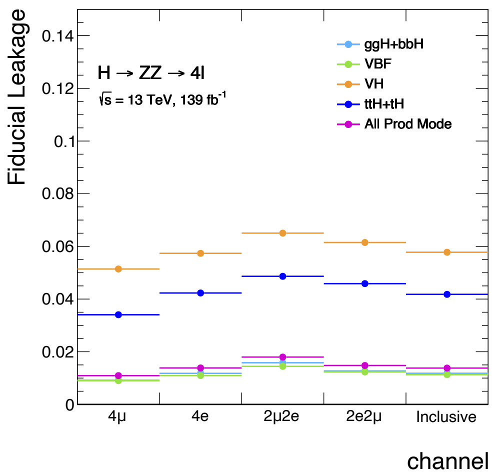

Figure 6.7: Comparing the fiducial leakage at $m_H = 125$ GeV using the dressed truth lepton definition in the mass range $105 < m_{4\ell} < 160$ GeV for different production mode in the four final states.

6.4.1.2 Unfolding

When we need to measure a quantity x , we actually measure a related quantity y. For example, we are able to measure the transverse momentum of the 4-lepton system $p_{\mathrm{T}}^{4\ell}$, which is related to the Higgs boson momentum p_T^H, that we are not able to measure directly. Then an unfolding method is needed to extract the information at particle level (also referred as *truth* level) from a distribution at reconstruction level, which corrects for detector effects and for the transformation from a quantity y to a quantity x.

For this analysis, the *detector response matrix* has been used as unfolding method, based on a binning scheme. The detector response matrix $\epsilon_{i,j}$ is defined as the number of reconstructed events in a bin i that can be matched to a truth event in bin j, normalised to the number of truth events in bin j. It represents the probability for an event with a given true value of some observable, categorised in a given truth bin, to be reconstructed with a different value, which is categorised in a different reconstructed event bin. The matrix is represented as follow:

- Y-axis = x_{truth} and X-axis = x_{reco};

- for each truth bin, the percentage of the reconstructed events in the corresponding reconstructed event bin is reported;

The response matrix encodes the information about the correlation in the migration between bins and also the reconstruction efficiency. This reconstruction efficiency has a different definition with respect to the fiducial efficiency explained in the previous section. This is due to the fact that in this case we are considering *only* the reconstructed events which match with a truth event passing the fiducial selection. Then this efficiency is not taking into account the fiducial leakage, which must be estimated separately.

The migration between different bins can be investigated defining the *migration matrix*, in which the elements are not normalised to the total number of truth events, but just to the number of truth events that match with reconstructed events.

The matrix unfolding method take into account of the detector effects only, but as it is estimated from simulation, then it assumes a model of the signal composition for each production mode. The kinematics of various production modes, as the two forward jets well separated in rapidity characteristic of the VBF production, can cause events to fall in and out of the fiducial volume. This has an impact of the response matrix and then it can introduce a bias when the matrix is used to unfold the data.

Another limitation of this approach happens if the matrix is ill-conditioned. It means that is characterised by a large condition number, which is defined as the ratio between the maximum and the minimum singular values of the matrix. If the condition number is close to 1, the matrix is considered well-conditioned. The ill-conditioning of the matrix can lead to possible amplification of small fluctuations in the data. For this reason the condition numbers of the matrices for all the variables has been computed and they resulting numbers are all below 2.5, then the matrices are considered well-conditioned and will not be largely affected by small fluctuations.

Alternative unfolding method: bin-by-bin correction factor

In the previous round of the fiducial cross section analysis in the $H \to ZZ^* \to 4\ell$ decay channel with lower statistics (20.3 fb^{-1}during Run 1 and 36.1 fb^{-1}during early Run 2) another unfolding method has been used: *bin-by-bin correction factor* $\mathcal{C}_i$.

In this approach the reconstructed events are unfolded using the correction factor, which has been defined previously as the fiducial efficiency, computed in each bin i of the distribution, defined as:

$$\mathcal{C}_i = \frac{N^i_{\text{Reco}}}{N^i_{\text{Fid}}} \,. \tag{6.4.4}$$

This unfolding method does not take into account of the migrations between the bins of the distribution due to detector effects. This effect can be neglected in a regime in which the statistical uncertainty is much higher than the systematics. Indeed this method is known to introduce a systematic bias into the measurement because the correction factors are derived from the signal simulation, which may or may not reproduce the true underlying distributions. This bias can be quantified as [185]:

$$< \delta\mu_i >= s_i \times \left(\left(\frac{\mu_i}{s_i} \right)_{\text{Model}} - \left(\frac{\mu_i}{s_i} \right)_{\text{Truth}} \right), \tag{6.4.5}$$

where μ_i is the number of true events, s_i is the number of reconstructed signal events, and $< \delta\mu_i >$ is the average bias in the i-th bin. This bias can be difficult to estimate as it depends on the difference between the truth and the model, which is not known *a priori.* However, it can also be shown that the bias is proportional to the off-diagonal terms of the response matrix, ϵ_{ij}:

$$< \delta\mu_i >= s_i \times \sum_{i \neq j} \epsilon_{ij}^{-1} \left(\left(\frac{s_j}{s_i} \right)_{\text{Model}} - \left(\frac{s_j}{s_i} \right)_{\text{Truth}} \right). \tag{6.4.6}$$

given that $\mu_i = \sum_j \epsilon_{ij}^{-1} s_j$ and when $j = i$ the parenthesis in Equation 6.4.6 becomes zero. Therefore, the size of this bias goes to zero as the response matrix becomes diagonal that correspond to a small bin-to-bin migrations.

6.4.1.3 Unfolding Bias Studies

Bias test with Pseudo-data

The unfolding bias on the differential measurement can be estimated performing a test with toys for each bin of the variable distribution. Each pseudo experiment is generated with true cross section value varied in a range corresponding to the expected uncertainty of the unfolded measurement of the tested bin. Then the reco-level pseudo dataset is obtained by folding the truth-level distribution of the generated dataset, taking into account of the detector effects using the migration matrix. The fit on the pseudo dataset in the given bin is performed using the matrix unfolding method to estimate the corresponding cross section.

In this way, for each toy a relative bias can be defined as the difference between the estimated cross section from the fit and the true cross section value. Generating 10000 toys for each bin, the result is a mean relative bias, which can be reported as function of the true cross section. Figures 6.8 show the biases computed for $p_{\mathrm{T}}^{4\ell}$, N_{jets}, O_1 and $\mathcal{OO}_{1,jj}(\tilde{c}_{zz} = 1)$ distributions with two unfolding methods: matrix inversion and bin-by-bin correction factor. The biases result very small for the matrix unfolding method. In case of a jet variable, as the number of jets or the Optimal Observable, the bin-by-bin unfolding method show larger biases overall, due to the large migrations between the bins. In all the cases, the biases are comparable with the statistical uncertainties.

Unfolding BSM MC data

Another bias test which can be performed is to evaluate the limit of unfolding procedure validity in case of data with BSM behaviour. The idea is to generate simulated BSM data distribution and unfold them with the nominal SM response matrix, and compare this results with the expected BSM cross sections.

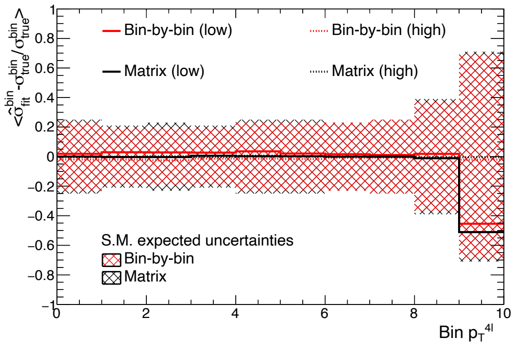

(a) Bias with toys $p_{\mathrm{T}}^{4\ell}$

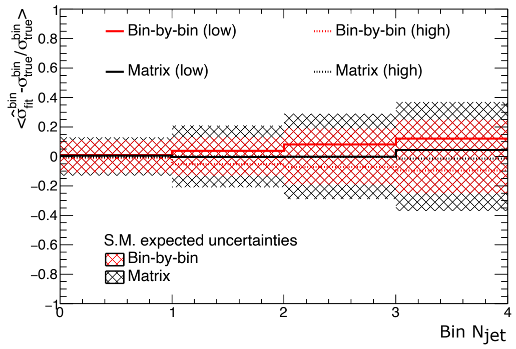

(b) Bias with toys N_{jets}

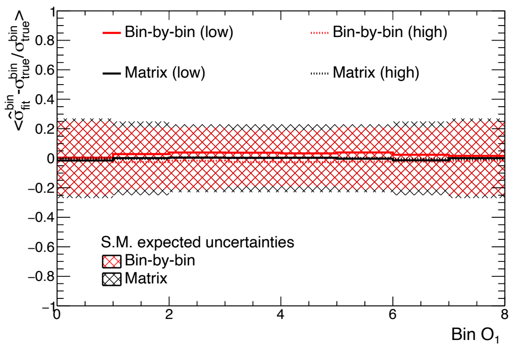

(c) Bias with toys O_1

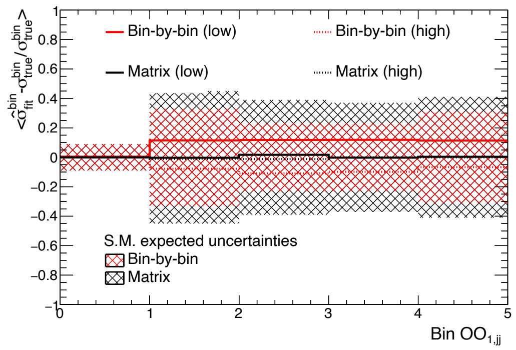

(d) Bias with toys $\mathcal{OO}_{1,jj}(\tilde{c}_{zz} = 1)$

Figure 6.8: Mean cross section bias, as obtained from pseudo experiments tests on samples with different true cross section, as a function of the true cross section for each bin of the variable (a) $p_{\mathrm{T}}^{4\ell}$, (b) N_{jets},(c) O_1 and (d) $\mathcal{OO}_{1,jj}(\tilde{c}_{zz} = 1)$. The black and red continuous (dotted) lines show cross section bias for the matrix and bin-by-bin unfolding methods when the truth cross-section is varied within the +1 (-1) sigma expected statistical uncertainty, respectively. The shaded areas show the median statistical uncertainty as obtained from ensemble tests with the true cross section (SM) equal to that used to derive the correction factors and matrices.

The BSM contribution is given by the introduction of a CP-odd anomalous coupling in the VBF vertex production. The simulated data are generated with LHCXSWG production mode cross section predictions for the ggF, VH, $t\bar{t}H$ and $b\bar{b}H$ production and with BSM VBF cross section predictions from Madgraph5_aMC@NLO SMEFT samples for different BSM coupling values.

This test has been performed on the Optimal Observable $\mathcal{OO}_{1,jj}(\tilde{c}_{zz} = 1)$, which is sensitive to CP-odd effects in the VBF vertex. The simulated data have been generated for different coupling values $\tilde{c}_{zz}$: $\pm1, \pm2, \pm5$. Figure 6.9 shows the pre-fit distribution of the BSM simulated data for two different coupling values $\tilde{c}_{zz}$ =+1 and $\tilde{c}_{zz}$ =+5, compared with the SM expectation. In this test, just the $qqZZ^*$ background has been considered as background process.

The unfolded results are shown in Figure 6.10, in which the *Fit* points represent the BSM simulated data unfolded using SM input response matrices, and the *Expected* are the expected fiducial BSM cross sections values. On the bottom panel, the ratio between the fit and the expected cross sections is reported. The behaviour is symmetric for the positive and negative value of the coupling, as expected due to the features of the $\mathcal{OO}_{1,jj}$ variable. The results show that the discrepancy between the expected and fit cross sections is within the relative uncertainty on the measurements. The extreme case of $\widetilde{c}_{zz} = \pm 5$ there is a discrepancy between the cross sections of the order of 20-22% despite a relative uncertainty of 15-19 % on the measurement.

Looking to the expected limits on the values of $\widetilde{c}_{zz}$ from the analyses described in the next chapter in Section 7.2, at the 95% CL, they are close to $\pm$ 2, then the unfolding procedure is reliable inside the expected limits of an anomalous CP-odd coupling.

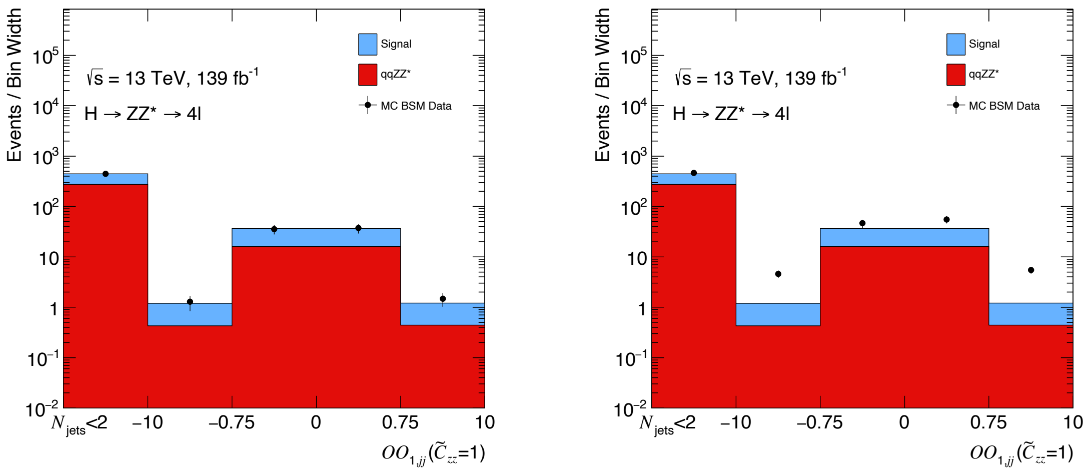

(a) MC data $\widetilde{c}_{zz}$ =+1

(b) MC data $\widetilde{c}_{zz}$ =+5

Figure 6.9: The SM expected distributions of the $\mathcal{OO}_{1,jj}(\widetilde{c}_{zz} = 1)$ in the range $105 < m_{4\ell} < 160$ GeV compared with the BSM simulated data (black dots) for coupling value of (a) $\widetilde{c}_{zz} = +1$ and (b) $\widetilde{c}_{zz} = +5$.

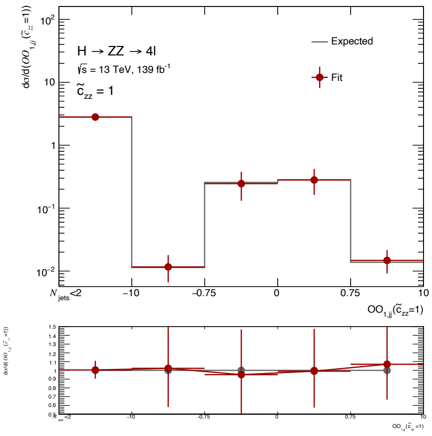

(a) XS fit MC data $\widetilde{c}_{zz}$ =+1

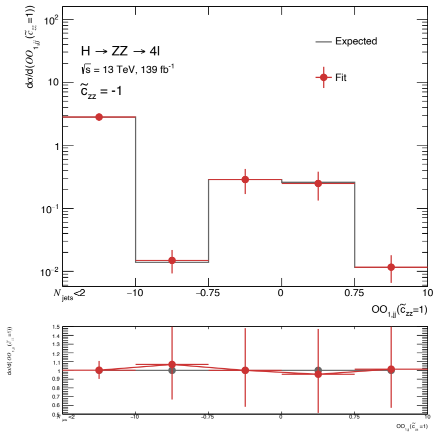

(b) XS fit MC data $\widetilde{c}_{zz}$ =-1

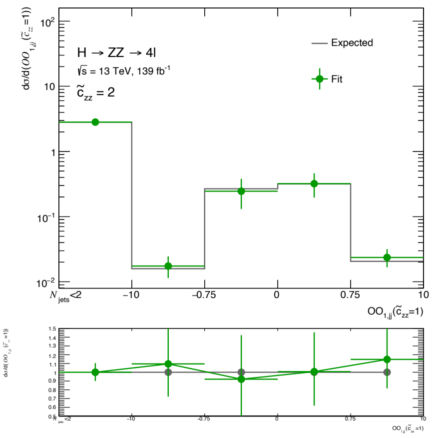

(c) XS fit MC data $\widetilde{c}_{zz}$ =+2

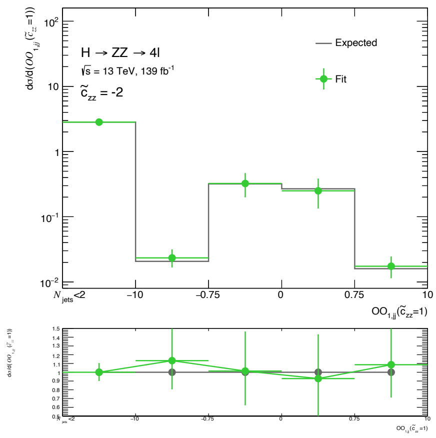

(d) XS fit MC data $\widetilde{c}_{zz}$ =-2

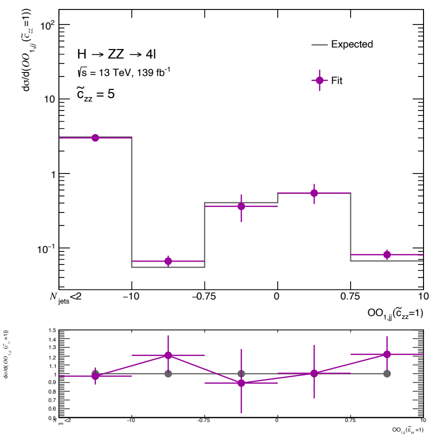

(e) XS fit MC data $\widetilde{c}_{zz}$ =+5

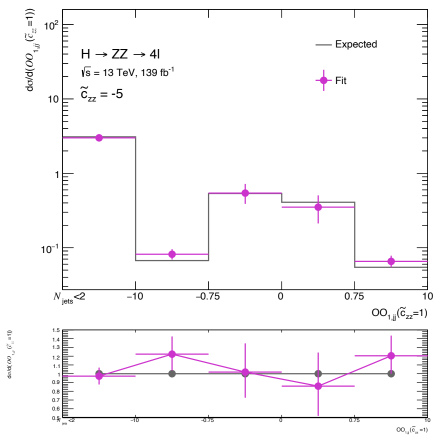

(f) XS fit MC data $\widetilde{c}_{zz}$ =-5

Figure 6.10: Differential cross section results of $\mathcal{OO}_{1,jj}(\widetilde{c}_{zz} = 1)$ obtained using unfolding BSM simulated data with SM response matrix compared with the BSM expected cross section in each bin for different coupling values: (a) $\widetilde{c}_{zz}$ = +1, (b) $\widetilde{c}_{zz}$ = -1, (c) $\widetilde{c}_{zz}$ = +2, (d) $\widetilde{c}_{zz}$ = -2, (e) $\widetilde{c}_{zz}$ = +5, (f) $\widetilde{c}_{zz}$ = -5. In the bottom panel the ratio between the fit and the expected cross sections is reported.

6.4.2 Binning and Migration studies

The binning of the observables is defined using simulation. The basic criteria to choose the number of bins and their width are to achieve an expected significance of at least 2 sigma and to keep the event bin migration as low as possible. The expected significance is defined as:

$$\text{significance} = S/\sqrt{S+B}, \tag{6.4.7}$$

where S and B are the inclusive signal and background yields. Together with the previous definition of the significance, also the significance versus the null hypothesis applicable in a low stats regime Z_0 can be computed, and it is defined as:

$$Z_0 = \sqrt{2((S+B)\cdot ln(1+S/B)-S)}\,. \tag{6.4.8}$$

In this section the binning choice and the migration studies of some selected observables considered for the differential cross section measurements are reported. One of the selected variables is the transverse momentum of the Higgs boson $p_{\mathrm{T}}^{4\ell}$ from the Higgs kinematic variables, given that there are several theoretical interest behind. In particular, the region at low-p_{T} is sensitive to charm and bottom Yukawa couplings. Constraint on these couplings has been set in this thesis work and they are described in Section 7.1.2.

For the jet related variables the N_{jets} and m_{jj} are presented, given that they are very sensitive to the Higgs production mechanisms, playing an important role in the VBF selection used in this thesis for the CP-violation searches described in Section 7.2.

For the double-differential distribution, the selected variable is the invariant mass of the leading di-lepton pair versus the invariant mass of the subleading di-lepton pair (m_{12} versus m_{34}). The differential measurement in this variable correspond to the amplitude decay of the Higgs boson in the two Z boson system. This quantity is sensitive to possible BSM effects which can be study with anomalous couplings defined in the Pseudo-Observable framework. Constraints on these anomalous couplings have been set and they are described in Section 7.1.1.

Higgs kinematic: $p_{\mathrm{T}}^{4\ell}$

Table 6.2 shows the binning choice performed for all the Higgs kinematic variables.

Looking a bit more in detail on the $p_{\mathrm{T}}^{4\ell}$ variable, the binning choice for this has been performed both to follow the previous criteria, but also to try to maximise the sensitivity to possible BSM effects. Figure 6.11 shows the distributions of this variable together with the binning choice and the expected yields for signal and backgrounds, estimated in the mass range $115 < m_{4\ell} < 130$ GeV. Figure 6.12 shows the migration matrix and the response matrix for this variable. For the kinematic variables in general the migration matrix is nearly diagonal because the detector resolution is much smaller than the bin width. Bin-to-bin migrations are of order of 20% or less for these variables. In this case, also the unfolding technique based on bin-by-bin correction factor is well-defined and the expected bias on the measurement is small, as showed in the previous section.

Variable	Bin Edges	N_{bins}
p_T	0, 10, 20, 30, 45, 60, 80, 120, 200, 350, 1000 GeV	10
m_{12}	50, 73, 64, 85, 106 GeV	4
m_{34}	12, 20, 24, 28, 32, 40, 55, 65 GeV	7
$\|y\|$	0.0, 0.15, 0.3, 0.45, 0.6, 0.75, 0.9, 1.2, 1.6, 2.0, 2.5	10
$\|cos(\theta^*)\|$	0, 0.125, 0.25, 0.375, 0.5, 0.625, 0.75, 0.875, 1.0	8
$cos(\theta_1)$	-1.0, -0.75, -0.50, -0.25, 0.0, 0.25, 0.50, 0.75, 1.0	8
$cos(\theta_2)$	-1.0, -0.75, -0.50, -0.25, 0.0, 0.25, 0.50, 0.75, 1.0	8
ϕ	$-\pi$, $-\frac{3\pi}{4}$, $-\frac{2\pi}{4}$, $-\frac{\pi}{4}$, 0, $\frac{\pi}{4}$, $\frac{2\pi}{4}$, $\frac{3\pi}{4}$, π	8
ϕ_1	$-\pi$, $-\frac{3\pi}{4}$, $-\frac{2\pi}{4}$, $-\frac{\pi}{4}$, 0, $\frac{\pi}{4}$, $\frac{2\pi}{4}$, $\frac{3\pi}{4}$, π	8

Table 6.2: Binning chosen for Higgs kinematic variables of interest.

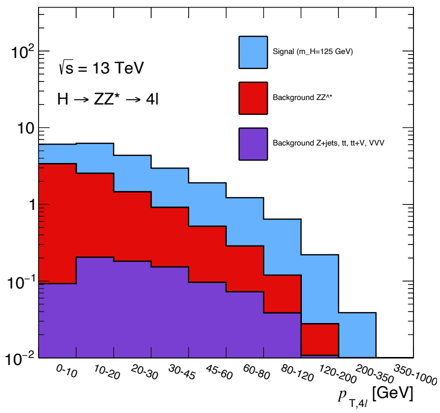

Bin	Signal	ZZ	Z+jets/$t\bar{t}$	$t\bar{t}V + VVV$	S/B	significance	Z_0
0	27.02	32.95	0.91	0.01	0.8	3.5	4.2
1	37.15	23.36	1.87	0.17	1.5	4.7	6.2
2	29.03	12.78	1.68	0.13	2.0	4.4	6.1
3	30.82	11.40	2.01	0.29	2.3	4.6	6.6
4	20.91	6.33	1.16	0.28	2.7	3.9	5.7
5	18.75	4.28	1.10	0.36	3.3	3.8	5.8
6	20.92	3.25	0.93	0.60	4.4	4.1	6.7
7	15.44	1.36	0.48	0.37	7.0	3.7	6.5
8	5.43	0.26	0.03	0.10	14.1	2.3	4.6
9	0.77	0.03	0.01	0.01	17.2	0.9	1.8

Figure 6.11: Distribution and binning choice for p_T: for each bin, signal and background yields are reported for $115 < m_{4\ell} < 130$ GeV together with S/B and expected significance values. A SM Higgs with $m_H = 125$ GeV has been assumed.

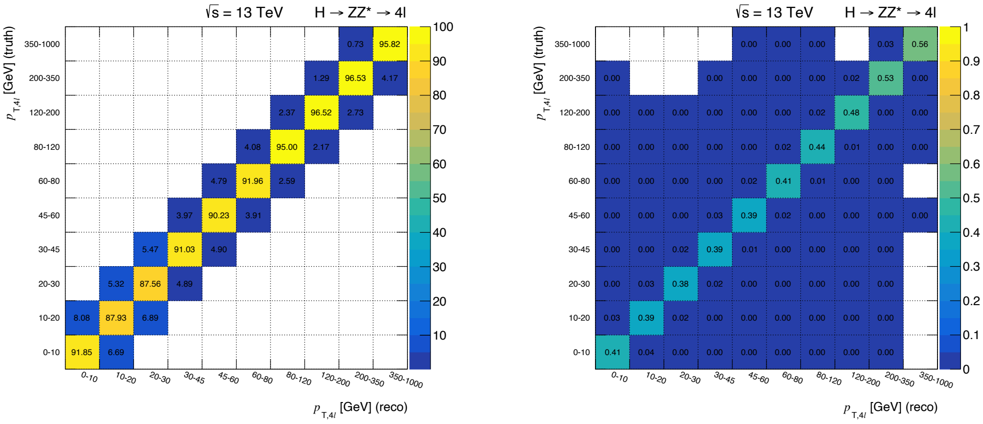

(a) $p_{\mathrm{T}}^{4\ell}$ Migration Matrix

(b) $p_{\mathrm{T}}^{4\ell}$ Response Matrix

Figure 6.12: (a) Migration and (b) response matrix for $p_{\mathrm{T}}^{4\ell}$, evaluated using signal MC (mc16a+mc16d+mc16e) at $m_H = 125$ GeV for mass window of $105 < m_{4\ell} < 160$ GeV (summing over all production modes). Only reconstructed events that have been matched to truth events are included.

Jet variables: N_{jets} and m_{jj}

Table 6.3 shows the binning choice performed for all the jet variables.

Variable	Bin Edges	N_{bins}
N_{jets}	$=0$, $=1$, $=2$, ≥ 3	4
$N_{b-\mathrm{jets}}$	0 jets, 0 b-jets, ≥ 1 b-jets	3
$p_T^{\mathrm{lead.\ jet}}$	N_{jets}=0, 30, 60, 120, 350 GeV	4
$p_T^{\mathrm{sublead.\ jet}}$	N_{jets}=0, 30, 60, 120, 350 GeV	4
m_{jj}	$N_{\mathrm{jets}} < 2$, 0, 120, 450, 3000 GeV	4
$\Delta\eta_{jj}$	$N_{\mathrm{jets}} < 2$, 0, 1, 2.5, 9	4
$\Delta\phi_{jj}$	$N_{\mathrm{jets}} < 2$, 0, $\frac{1}{2}\pi$, π, $\frac{3}{2}\pi$, 2π	5

Table 6.3: Binning chosen for jet variables of interest.

The measurement of the jet multiplicity and other jet properties allow to probe several feature of the Higgs production modes, as for example the VBF production which is characterised by the presence of two forward jets at high p_{T}. For this reason the di-jet variables are very interesting given that they can be used to discriminate a process which come from ggF, VBF production or *VH* production. For example applying a cut on m_{jj} at 120 GeV, we can distinguish events which come from the hadron decay of the vector boson produced in association with the Higgs in the *VH* production (m_{jj} <120 GeV), or events which most probably come from a VBF production (m_{jj} >120 GeV).

Figures 6.13 and 6.14 show the distributions of N_{jets} and m_{jj} variables together with the binning choice and the expected yields for signal and backgrounds, estimated in the mass range $115 < m_{4\ell} < 130$ GeV. For the p_{T} of the jets and di-jet variables, the underflow bin has been considered, in order to consider migrations with $N_{\mathrm{jet}} = 0$ or $N_{\mathrm{jet}} < 2$ cases, given that those variables are defined for events with one, two *or more* jets. Figures 6.15 - 6.16 show the migration matrices and the response matrices for these variables. The variables related

3633 to the jets have off diagonal terms of the migration matrix often $> 30\%$. For this reason
3634 to response matrix unfolding is more suitable choice given that it takes these off-diagonal
3635 elements into account.

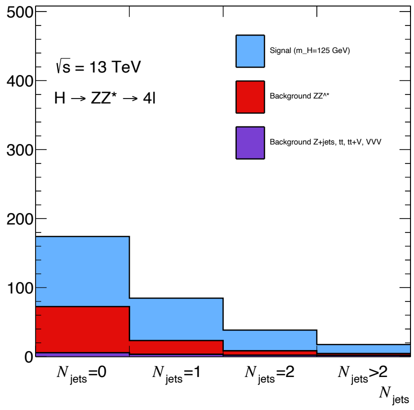

Bin	Signal	ZZ	Z+jets/$t\bar{t}$	$t\bar{t}V + VVV$	S/B	significance	Z_0
0	101.62	66.91	5.46	0.13	1.4	7.7	10.1
1	61.45	20.02	2.78	0.45	2.6	6.7	9.8
2	30.07	6.34	1.21	0.81	3.6	4.8	7.6
3	13.09	2.74	0.74	0.93	3.0	3.1	4.7

Figure 6.13: Distribution and binning choice for N_{jets}: for each bin, signal and background yields are reported for $115 < m_{4\ell} < 130$ GeV together with S/B and expected significance values. A SM Higgs with $m_H = 125$ GeV has been assumed.

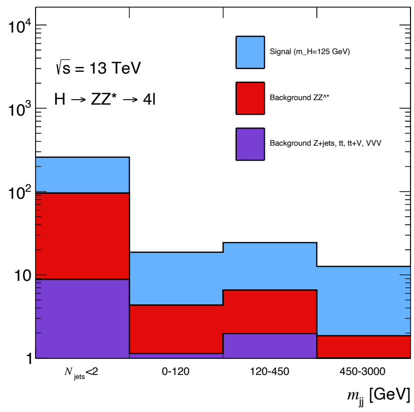

Bin	Signal	ZZ	Z+jets/$t\bar{t}$	$t\bar{t}V + VVV$	S/B	significance	Z_0
0	163.27	86.93	8.24	0.58	1.7	10.1	13.7
1	14.37	3.20	0.70	0.43	3.3	3.3	5.1
2	17.82	4.59	0.96	1.02	2.7	3.6	5.3
3	10.78	1.28	0.28	0.29	5.8	3.0	5.2

Figure 6.14: Distribution and binning choice for m_{jj}: for each bin, signal and background yields are reported for $115 < m_{4\ell} < 130$ GeV together with S/B and expected significance values. A SM Higgs with $m_H = 125$ GeV has been assumed.

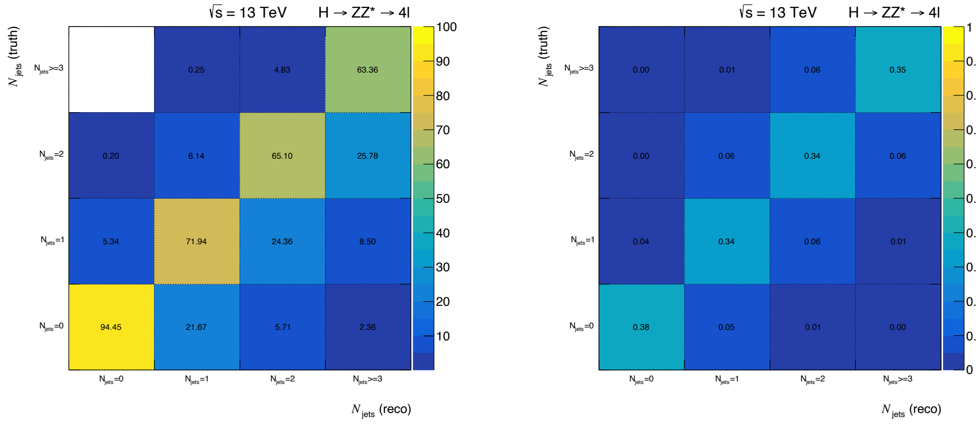

(a) N_{jets} Migration Matrix (b) N_{jets} Response Matrix

Figure 6.15: (a) Migration and (b) response matrix for N_{jets}, evaluated using signal MC (mc16a+mc16d+mc16e) at $m_H = 125$ GeV for mass window of $105 < m_{4\ell} < 160$ GeV (summing over all production modes). Only reconstructed events that have been matched to truth events are included.

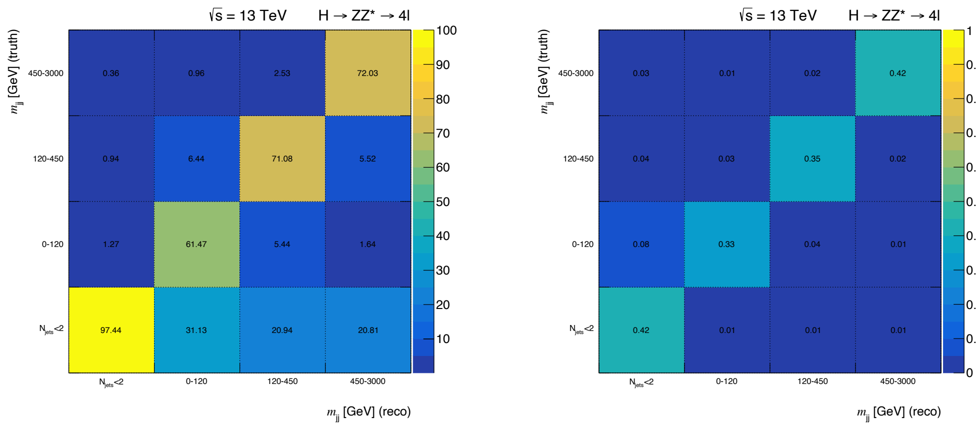

(a) m_{jj} Migration Matrix (b) m_{jj} Response Matrix

Figure 6.16: (a) Migration and (b) response matrix for m_{jj}, evaluated using signal MC (mc16a+mc16d+mc16e) at $m_H = 125$ GeV for mass window of $105 < m_{4\ell} < 160$ GeV (summing over all production modes). Only reconstructed events that have been matched to truth events are included.

Double-differential: m_{12} vs. m_{34}

In this analysis six pairs of variables have been considered for the double-differential cross section measurements. The binning choices for these variables are summarised in Table 6.4

Variable	Bin Edges		N_{bins}
$p_{T,4\ell}$ vs. N_{jets}	$N_{\text{jets}} = 0$	$p_{T,4\ell}$ {0, 15, 30, 120, 350}	
	$N_{\text{jets}} = 1$	$p_{T,4\ell}$ {0, 60, 80, 120, 350}	12
	$N_{\text{jets}} = 2$	$p_{T,4\ell}$ {0, 120, 350}	
	$N_{\text{jets}} \geq 3$	$p_{T,4\ell}$ {0, 120, 350}	
m_{12} vs. m_{34}	$m_{12} < 82$	$m_{34} < 32$	
	$m_{12} < 74$	$m_{34} > 32$	
	$m_{12} > 74$	$m_{34} > 32$	5
	$m_{12} > 82$	$24 < m_{34} < 32$	
	$m_{12} > 82$	$m_{34} < 24$	
$p_{T,4\ell}$ vs. $\|y\|$	$0.0 < \|y\| < 0.5$	$p_{T,4\ell}$ {0, 45, 120, 350}	
	$0.5 < \|y\| < 1.0$	$p_{T,4\ell}$ {0, 45, 120, 350}	12
	$1.0 < \|y\| < 1.5$	$p_{T,4\ell}$ {0, 45, 120, 350}	
	$1.5 < \|y\| < 2.5$	$p_{T,4\ell}$ {0, 45, 120, 350}	
$p_{T,4\ell}$ vs. $p_{T,\text{lead.jet}}$	$N_{\text{jets}} = 0$		
	$30 < p_{T,\text{lead.jet}} < 60$	$p_{T,4\ell}$ {0, 80, 350}	7
	$60 < p_{T,\text{lead.jet}} < 120$	$p_{T,4\ell}$ {0, 120, 350}	
	$120 < p_{T,\text{lead.jet}} < 350$	$p_{T,4\ell}$ {0, 120, 350}	
$p_{T,4\ell}$ vs. $p_{T,4\ell,j}$	$N_{\text{jets}} = 0$		
	$0 < p_{T,4\ell,j} < 60$	$p_{T,4\ell}$ {0, 120, 350}	5
	$60 < p_{T,4\ell,j} < 350$	$p_{T,4\ell}$ {0, 120, 350}	
$p_{T,4\ell,j}$ vs. $m_{4\ell,j}$		$N_{\text{jets}} = 0$	
	$120 < m_{4\ell,j} < 220$	$0 < p_{T,4\ell,j} < 350$	
	$220 < m_{4\ell,j} < 350$	$p_{T,4\ell,j}$ {0, 60, 350}	5
	$350 < m_{4\ell,j} < 2000$	$0 < p_{T,4\ell,j} < 350$	
$p_T^{\text{lead. jet}}$ vs. $p_T^{\text{sublead. jet}}$	$N_{\text{jets}} = 0$		
	$p_T^{\text{lead. jet}}$ {30, 60, 350}	$N_{\text{jets}} = 1$	
	$30 < p_T^{\text{lead. jet}} < 60$	$30 < p_T^{\text{sublead. jet}} < 60$	6
	$60 < p_T^{\text{lead. jet}} < 350$	$30 < p_T^{\text{sublead. jet}} < 60$	
	$60 < p_T^{\text{lead. jet}} < 350$	$60 < p_T^{\text{sublead. jet}} < 350$	
$p_T^{\text{lead. jet}}$ vs. $\|y^{\text{lead. jet}}\|$	$N_{\text{jets}} = 0$		
	$30 < p_T^{\text{lead. jet}} < 120$	$0.0 < \|y^{\text{lead. jet}}\| < 0.8$	
	$30 < p_T^{\text{lead. jet}} < 120$	$0.8 < \|y^{\text{lead. jet}}\| < 1.7$	
	$30 < p_T^{\text{lead. jet}} < 120$	$\|y^{\text{lead. jet}}\| > 1.7$	6
	$120 < p_T^{\text{lead. jet}} < 350$	$0 < \|y^{\text{lead. jet}}\| > 1.7$	
	$120 < p_T^{\text{lead. jet}} < 350$	$\|y^{\text{lead. jet}}\| > 1.7$	

Table 6.4: Binning choices for the double differential variables.

For the m_{12} vs. m_{34} variable, total of five bins are defined. Table 6.5 shows the binning chosen as well as expected signal and background yields and significance per bin. Figure 6.17a shows the expected signal and backgrounds distribution for each bin of m_{12} vs. m_{34}. Figure 6.18 shows the migration matrix and the response matrix for this variable.

Bin	m_{12} and m_{34} values [GeV]	Signal	ZZ	Z+jets/$t\bar{t}$	$t\bar{t}V + VVV$	S/B	significance	Z_0
0	$m_{12} < 82$ and $m_{34} < 32$	18.22	11.37	1.54	0.48	1.4	3.2	4.2
1	$m_{12} < 74$ and $m_{34} > 32$	26.61	5.94	1.96	0.41	3.2	4.5	6.9
2	$m_{12} > 74$ and $m_{34} > 32$	29.71	5.92	0.79	0.21	4.3	4.9	7.9
3	$m_{12} > 82$ and $24 < m_{34} < 32$	69.68	18.32	1.72	0.42	3.4	7.3	11.3
4	$m_{12} > 82$ and $m_{34} < 24$	62.03	54.45	4.17	0.81	1.0	5.6	7.0

Table 6.5: Binning and expected signal and background yields for m_{12} vs. m_{34}.

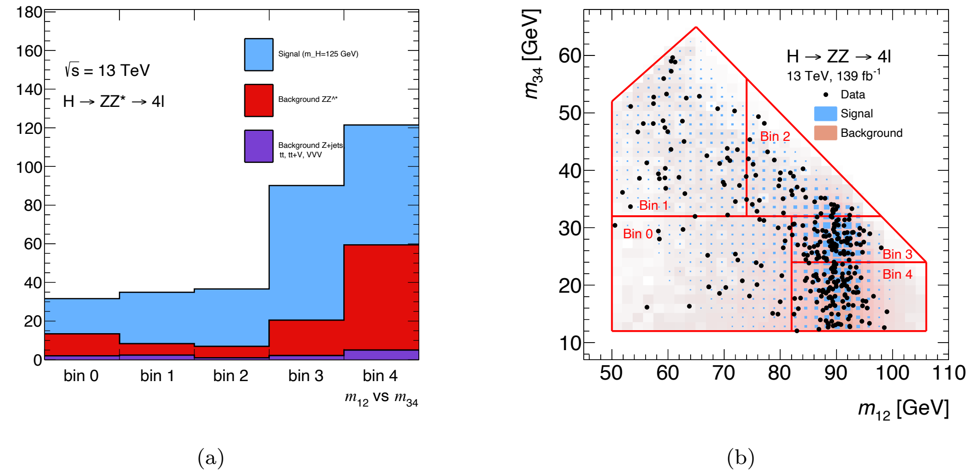

Figure 6.17: Expected m_{12} vs. m_{34} distribution of signal and ZZ^* background for $115 < m_{4\ell} < 130$ GeV (a) and the corresponding bin boundaries (b). A SM Higgs with $m_H = 125$ GeV has been assumed, with a luminosity of 138.9 fb^{-1}.

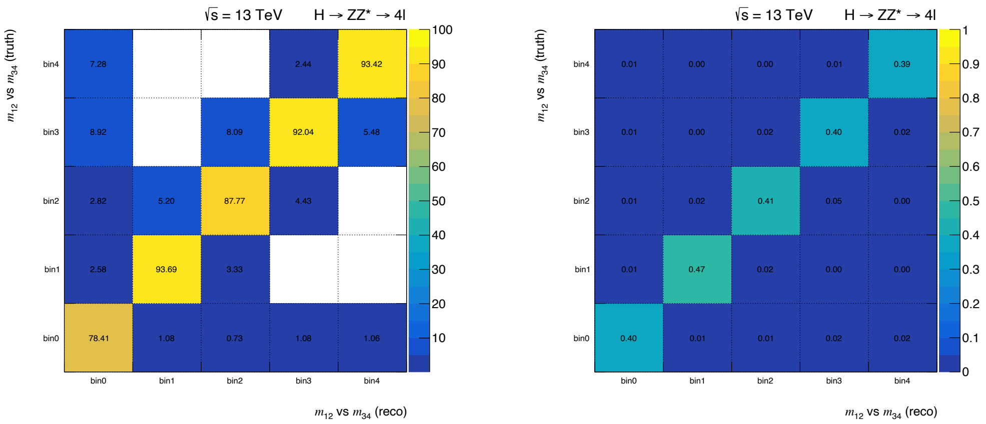

(a) m_{12} vs. m_{34} Migration Matrix

(b) m_{12} vs. m_{34} Response Matrix

Figure 6.18: (a) Migration and (b) response matrix for for m_{12} vs. m_{34}, evaluated using signal MC (mc16a+mc16d+mc16e) at $m_H = 125$ GeV for mass window of $105 < m_{4\ell} < 160$ GeV (summing over all production modes). Only reconstructed events that have been matched to truth events are included.

Preliminary studies on CP-sensitive variables

The CP-odd angular observables are variables related to the kinematics of the Higgs boson decay into four leptons. In particular they are a combination of the leptons and Z decay angles. The migration matrices for these variables looks nearly diagonal. Except for the O_1, the other variables show a matrix with far-off diagonal elements. This effect can be explained by a mis-pairing of the leptons in the final states 4μ and $4e$. As these variables are defined as function of $\sin\phi$ as described in Section 6.3.3, a mis-pairing of the leptons between the leading and the subleading lepton pair can lead to a mis-reconstruction of the ϕ angle, and subsequently of $\sin\phi$. In Figure 6.19 the migration matrices and the response matrices for O_2 and O_5 variables are shown, both computed in the expanded mass range $105 < m_{4\ell} < 160$ GeV, given that it is the one used in the unfolding.

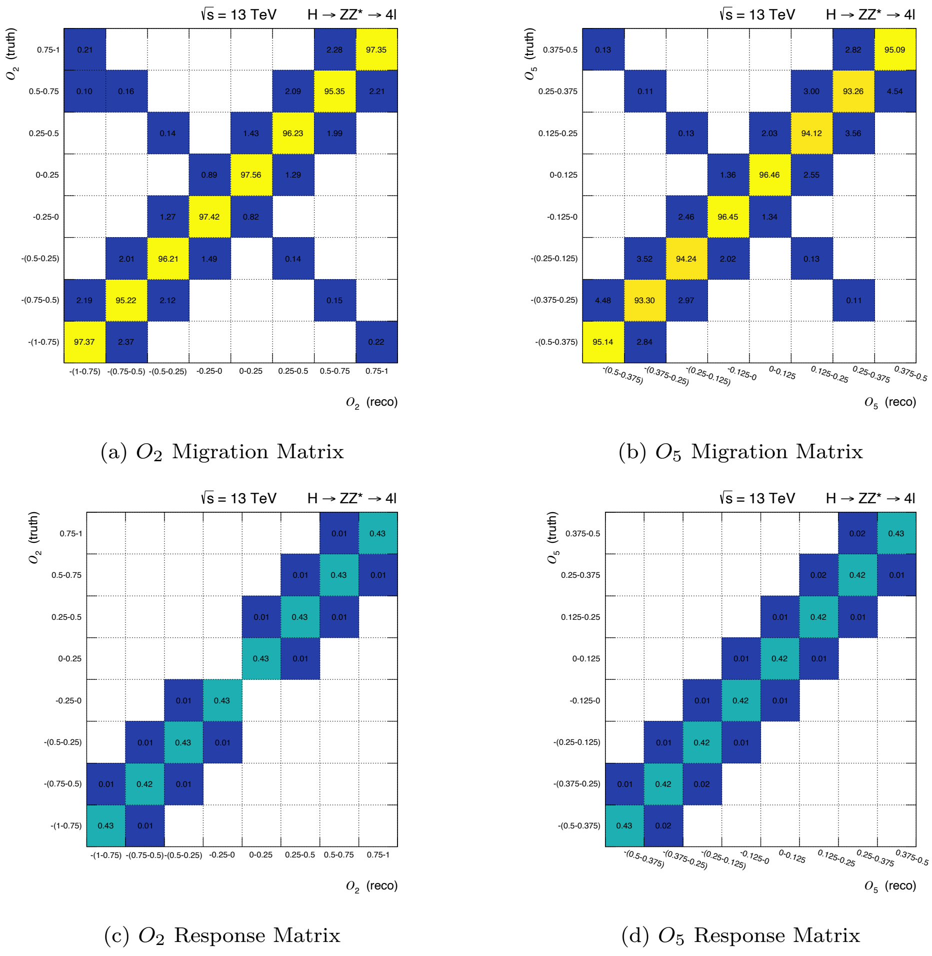

(a) O_2 Migration Matrix (b) O_5 Migration Matrix

(c) O_2 Response Matrix (d) O_5 Response Matrix

Figure 6.19: Migration and response matrices for or the CP-odd angular observable O_2 (a and c) and O_5 (b and d), evaluated using signal MC (mc16a+mc16d+mc16e) at $m_H = 125$ GeV for mass window of $105 < m_{4\ell} < 160$ GeV (summing over all production modes). Only reconstructed events that have been matched to truth events are included.

The Optimal Observables studied are the jet related $\mathcal{OO}_{1,jj}$. They are defined for events with at least two jets. The underflow bin with $N_{jets} < 2$ has been considered in the distribution to take into account the migrations with $N_{jets} < 2$ cases. For the $\mathcal{OO}_{1,jj}$ variables, the migrations are much larger than the CP angular observables, where the off-diagonal terms can be >30%. These values are reached when events at truth-level with <2 jets are reconstructed as events with at least 2 jets. In case of ggF events, almost all of these mis-reconstructed events are from pileup jets. Instead in case of VBF events, about 80% of them are from pileup jets, the other 20% comes from smearing effects on jet-p_T and different jet-η cut in fiducial and reconstructed event selection (the fiducial cut is $|\eta| < 4.4$ instead the cut at reconstruction level is $|\eta| < 4.5$).

For the $\mathcal{OO}_{1,jj}(\tilde{c}_{zz} = 1)$ variable, different binning choices has been studied to find the best compromise between the bins migration and the statistical uncertainties in the cross section measurements. Three different configurations for the binning choice have been tested:

A) $[N_{jets} < 2, -10.0, -0.50, 0.0, 0.50., 10]$

B) $[N_{jets} < 2, -10.0, -0.75, 0.0, 0.75., 10]$

C) $[N_{jets} < 2, -10.0, -1.0, 0.0, 1.0., 10]$

Looking to the shape of the $\mathcal{OO}_{1,jj}$ variable (as in Figure 6.4a and 6.4b), the outer bins have lower statistics, hence larger outer bins can lead to lower errors. The yields for the three different cases are shown in Table 6.6. At the same time, Figure 6.20 shows that larger outer bins lead to larger migrations. As consequence, the best compromise for the binning choice for $\mathcal{OO}_{1,jj}$ variable is $[N_{jets} < 2, -10.0, -0.75, 0.0, 0.75., 10]$. In Figure 6.21, the migration matrix are reported together with the response matrix computed in the expanded mass range $105 < m_{4\ell} < 160$ GeV.

Bin	(S+B) case A	(S+B) case B	(S+B) case C
1	10.84	7.77	5.90
2	15.08	18.0	20.02
3	15.16	18.0	20.09
4	10.86	7.81	5.93

Table 6.6: Total Signal+Background (S+B) yields in each $\mathcal{OO}_{1,jj}(\tilde{c}_{zz} = 1)$ bin are reported for the three different binning choices (the underflow bin is not shown) in the mass range $105 < m_{4\ell} < 160$ GeV.

The final bin choice for the CP-sensitive variable distributions studied are summarised in Table 6.7.

In this preliminary study, for the CP-odd angular observables only the $qqZZ^*$, $Z+$jets and $t\bar{t}$ have been considered in the background ($ggZZ^*$,VVV and $t\bar{t}V$ are not included). For the Optimal Observable only the $qqZZ^*$ has been considered.

Figures 6.22 and 6.23 show the distributions of O_2 and O_5 variables respectively and Figure 6.24 shows the distributions of the Optimal Observables $\mathcal{OO}_{1,jj}(\tilde{c}_{zz} = 1)$, together

3685 with the binning choice and the expected yields for signal and backgrounds, estimated in
3686 the mass range $115 < m_{4\ell} < 130$ GeV.

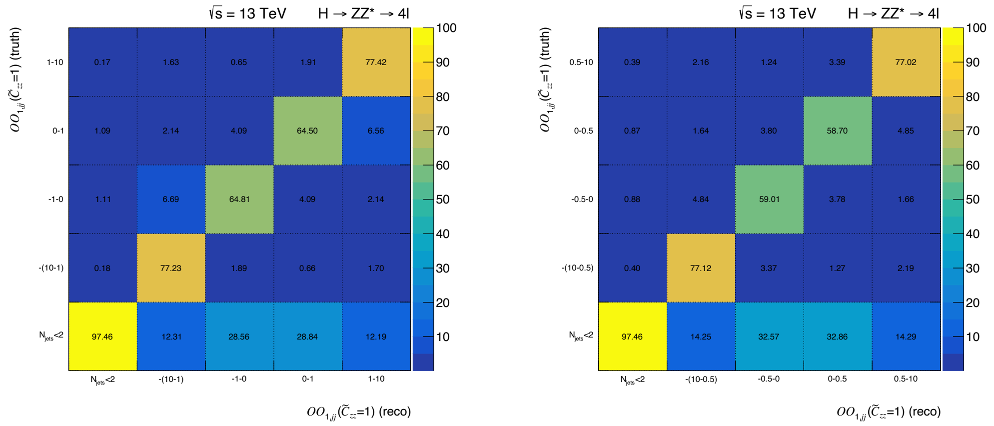

(a) (b)

Figure 6.20: Migration matrices for the Optimal Observable $\mathcal{OO}_{1,jj}(\tilde{c}_{zz} = 1)$ using two different binning choices: (a) $[N_{jets} < 2, -10.0, -1.0, 0.0, 1.0., 10]$ and (b) $[N_{jets} < 2, -10.0, -0.50, 0.0, 0.50., 10]$. In the second case in which the external bin width is 9.5, the migration is larger with respect to first case with a bin width of 9; and the central bins show diagonal elements <60%. Figure 6.21a shows the middle case with binning choice $[N_{jets} < 2, -10.0, -0.75, 0.0, 0.75., 10]$, with an acceptable level of migration of the central bins.

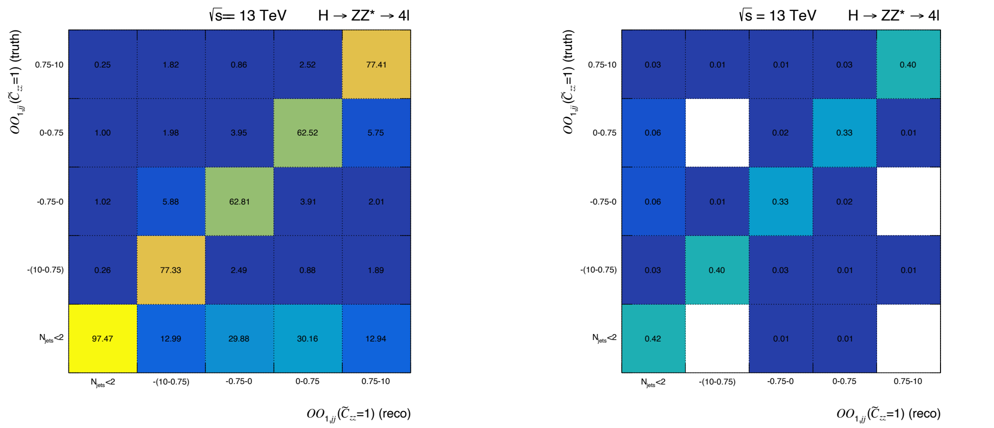

(a) (b)

Figure 6.21: Migration matrix (a) and response matrix (b) evaluated using signal MC (mc16a+mc16d+mc16e) at $m_H = 125$ GeV for mass window of $105 < m_{4\ell} < 160$ GeV (summing over all production modes) for the Optimal Observable $\mathcal{OO}_{1,jj}(\tilde{c}_{zz} = 1)$. Only reconstructed events that have been matched to truth events are included.

Variable	Bin Edges	N_{bins}
O_1	-1.0, -0.75, -0.50, -0.25, 0.0, 0.25, 0.50, 0.75, 1.0	8
O_2	-1.0, -0.75, -0.50, -0.25, 0.0, 0.25, 0.50, 0.75, 1.0	8
O_3	-0.50, -0.225, -0.125, -0.05, 0.0, 0.05, 0.125, 0.225, 0.50	8
O_4	-0.50, -0.35, -0.225, -0.10, 0.0, 0.10, 0.225, 0.35, 0.50	8
O_5	-0.50, -0.375, -0.25, -0.125, 0.0, 0.125, 0.25, 0.375, 0.50	8
O_6	-0.50, -0.35, -0.225, -0.10, 0.0, 0.10, 0.225, 0.35, 0.50	8
$\mathcal{OO}_{1,jj}(\widetilde{c}_{zz}=1)$	$N_{jets} < 2$, -10.0, -0.75, 0.0, 0.75, 10.0	5

Table 6.7: Binning chosen for CP-odd angular observables and Optimal Observables $\mathcal{OO}_{1,jj}$.

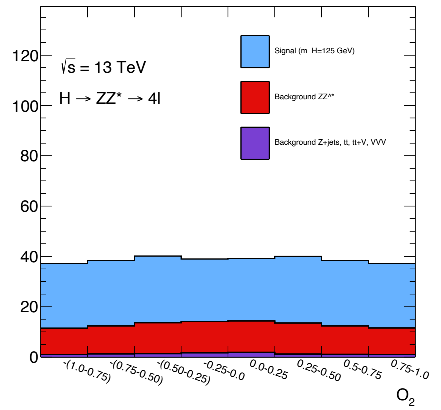

Bin	Signal	ZZ	Z+jets/$t\bar{t}$	$t\bar{t}V + VVV$	S/B	significance	Z_0
0	25.69	10.45	0.96	-	2.2	4.2	6.0
1	26.07	11.13	1.19	-	2.1	4.2	5.9
2	26.53	12.29	1.30	-	2.0	4.2	5.8
3	24.82	12.51	1.63	-	1.8	4.0	5.4
4	24.89	12.44	1.86	-	1.7	4.0	5.4
5	26.53	12.34	1.15	-	2.0	4.2	5.8
6	26.00	11.25	1.07	-	2.1	4.2	5.9
7	25.71	10.48	1.03	-	2.2	4.2	6.0

Figure 6.22: Distribution and binning choice for O_2: for each bin, signal and background yields ($ggZZ^*$, $ttV + VVV$ not included) are reported for $115 < m_{4\ell} < 130$ GeV together with S/B and expected significance values.

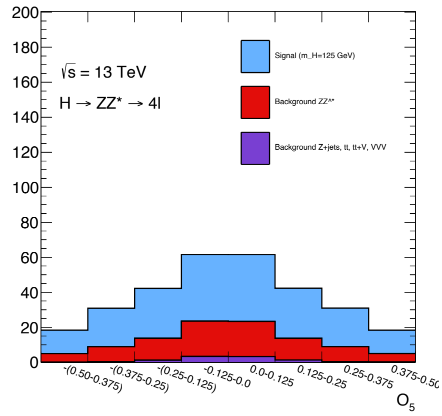

Bin	Signal	ZZ	Z+jets/$t\bar{t}$	$t\bar{t}V + VVV$	S/B	significance	Z_0
0	13.36	4.85	0.15	-	2.7	3.1	4.6
1	22.02	8.57	0.32	-	2.5	4.0	5.7
2	28.56	12.51	1.21	-	2.1	4.4	6.2
3	38.08	20.16	3.35	-	1.6	4.9	6.5
4	38.18	20.06	3.30	-	1.6	4.9	6.5
5	28.64	12.39	1.31	-	2.1	4.4	6.2
6	22.02	8.60	0.33	-	2.5	4.0	5.7
7	13.33	4.80	0.22	-	2.7	3.1	4.6

Figure 6.23: Distribution and binning choice for O_5: for each bin, signal and background yields ($ggZZ^*$, $ttV + VVV$ not included) are reported for $115 < m_{4\ell} < 130$ GeV together with S/B and expected significance values.

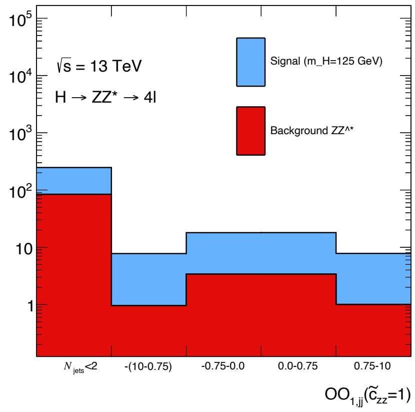

Bin	Signal	ZZ	Z+jets/$t\bar{t}$	$t\bar{t}V+VVV$	S/B	significance	Z_0
0	163.07	84.14	-	-	1.9	10.4	14.4
1	6.81	0.96	-	-	7.1	2.4	4.3
2	14.60	3.39	-	-	4.3	3.4	5.6
3	14.65	3.39	-	-	4.3	3.4	5.6
4	6.81	1.00	-	-	6.8	2.4	4.3

Figure 6.24: Distribution and binning choice for $\mathcal{OO}_{1,jj}(\widetilde{c}_{zz}=1)$: for each bin, signal and background yields (only $qqZZ^*$) are reported for $115 < m_{4\ell} < 130$ GeV together with S/B and expected significance values.

6.4.3 Cross section extraction

The cross section measurement is performed with a fit on the $m_{4\ell}$ distribution to extract the number of signal events in each bin of the differential distribution of the observable under test or in each decay final state for the inclusive fiducial cross section measurement. The number of the expected events N_i in each observable reconstruction bin i (final state for the inclusive measurement), expressed as a function of $m_{4\ell}$ is given by:

$$N_i(m_{4\ell}) = \sum_j r_{ij} \cdot (1 + f_i^{\rm nonfid}) \cdot \sigma_j^{\rm fid} \cdot \mathcal{P}_i(m_{4\ell}) \cdot \mathcal{L}_{\rm int} + N_i^{\rm bkg}(m_{4\ell}) \ , \tag{6.4.9}$$

where $\sigma_j^{\rm fid}$ is the fiducial cross section in bin j, defined as in Equation 6.1.3, and represents the *Parameter of Interest* (POI) that can be extracted from the likelihood fit using this signal parametrisation.

The first part of the Equation 6.4.9 represents the number of signal events in bin i. The term $\mathcal{P}_i(m_{4\ell})$ is the $m_{4\ell}$ signal shape, given by the fraction of the signal expected events in the bin i as function of the $m_{4\ell}$. The normalisation factors are the integrated luminosity $\mathcal{L}_{\rm int}$, the detectors response matrix r_{ij} and the non-fiducial factor $f_i^{\rm nonfid}$ defined as in Equation 6.4.3. Both the response matrix and the non-fiducial factor are determined from simulation, sum over all production modes. $N_i^{\rm bkg}(m_{4\ell})$ represents instead the background contribution.

Given this signal parametrisation, the inclusive and differential cross section measurement for each category can be extracted defining different POI.

For the inclusive fiducial cross section measurement, four categories, corresponding to the four final states (4μ, $4e$, $2e2\mu$, $2\mu2e$) are defined, then in this case the $\sigma_j^{\rm fid}$ correspond to the cross section in each final state j. The fiducial cross sections in the four final states can be summed to obtain and inclusive fiducial cross section, or can be combined assuming the SM $ZZ^* \to 4\ell$ relative branching ratios. The latter combination is more model dependent, but benefits from a smaller statistical uncertainty. Finally, also the total cross section can be measured extrapolating the combined inclusive cross section to the full phase space. Then the following POIs are defined:

- fiducial cross section per final state (category i):

$$\mathrm{POI}_{\mathrm{fs},i} = [\sigma_{tot} \times \mathrm{BR}(H \to 4\ell)_i] \times A_i \ = \sigma^{\mathrm{fid}}_{\mathrm{fs},i}; \tag{6.4.10}$$

  where $\mathrm{BR}(H \to 4\ell)_i$ and A_i correspond to the branching ratio and the acceptance in each final state and the fit is performed on the corresponding $m_{4\ell}$ distribution.

- fiducial cross section for 4ℓ ($4\mu + 4e$) and $2\ell 2\ell$ ($2e2\mu + 2\mu 2e$):

$$\mathrm{POI}_{4\ell} = \sigma_{tot} \times [\mathrm{BR}(H \to 4\ell)_{4e} \times A_{4e} + \mathrm{BR}(H \to 4\ell)_{4\mu} \times A_{4\mu}] = \sigma^{\mathrm{fid}}_{4\ell}; \tag{6.4.11}$$

$$\mathrm{POI}_{2\ell 2\ell} = \sigma_{tot} \times [\mathrm{BR}(H \to 4\ell)_{2e2\mu} \times A_{2e2\mu} + \mathrm{BR}(H \to 4\ell)_{2\mu 2e} \times A_{2\mu 2e}] = \sigma^{\mathrm{fid}}_{2\ell 2\ell}; \tag{6.4.12}$$

- inclusive fiducial cross section as sum of all final states (i):

$$\mathrm{POI}_{\mathrm{sum}} = \sum_i \sigma_{tot} \times \mathrm{BR}(H \to 4\ell)_i \times A_i = \sigma^{\mathrm{fid}}_{\mathrm{sum}}; \tag{6.4.13}$$

- inclusive fiducial cross section as combination of all final states (i):

$$\mathrm{POI}_{\mathrm{comb}} = [\sigma_{tot} \times \mathrm{BR}(H \to 4\ell)_i] \times \bar{A} = \sigma^{\mathrm{fid}}_{\mathrm{comb}}; \tag{6.4.14}$$

  where $\bar{A}$ is the acceptance averaged on the four final states;

- total cross section:

$$\mathrm{POI}_{\mathrm{tot}} = \sigma_{tot}. \tag{6.4.15}$$

The differential cross section measurement for each bin i can be measured defining the following POI:

$$\mathrm{POI}_i = [\sigma_{tot} \times \mathrm{BR}(H \to 4\ell)] \times A_i \ = \sigma^{\mathrm{fid}}_i. \tag{6.4.16}$$

In this case the event selected are not categorised in final states, so the inclusive $m_{4\ell}$ distribution is used in the fit.

6.4.3.1 Background estimation

Fitting ZZ^* normalisation with data

The ZZ^* normalisation is extracted from data, unlike the previous analysis [186] in which this contribution was estimated from MC. The introduction of a floating normalisation with respect to a fixed one increases the statistical error in the nominal mass region between 115-130 GeV. A widening of the $m_{4\ell}$ window to $105 < m_{4\ell} < 160$ GeV showed an improvement of the relative errors. As such normalisation factors for ZZ^* contribution are introduced and they are profiled during the fit on the $m_{4\ell}$ to extract the ZZ^* normalisation from the sidebands.

The $m_{4\ell}$ distribution has 33 bins: thirty bins of 0.5 GeV size in the range 115-130 GeV, and further three sideband bins 105-115 GeV, 130-135 GeV and 135-160 GeV to fit simultaneously the ZZ^* normalisation.

For the total and fiducial cross sections in different final states, the same normalisation factor is used for the ZZ^* contribution. In the differential cross sections, the number of ZZ^* normalisation factors are different for each variable. In principle they should be as much as the number of bins of the observable distribution, but they also introduce a degradation of the errors. For the ZZ^* estimations the bins are merged together until the degradation of the relative uncertainty on the expected cross section is under 5% of the uncertainty considering just one ZZ^* normalisation factor. The same normalisation factor is applied in each bin of the observable distribution that has been merged.

Reducible background

The $Z+$ jets and $t\bar{t}$ are estimated using data-driven methodology already described in Section 5.3.2. Several control regions are defined with enhanced background components. In this way the expected yields of different backgrounds components can be estimated in thos regions and their contribution in the signal region extrapolated with Transfer Factors.

For the $\ell\ell\mu\mu$ background, the shapes of the observables used in the differential cross-section analysis are obtained by performing the fits separately in each bin of the distribution. In some bins, the fit fails due to low statistics, in which case the model shape parameters are fixed to those from the inclusive fit. In the case of bins in the tails of distributions where no transfer factor can be obtained, the TF from the last bin where it is possible to calculate one is used. For the $\ell\ell ee$ background, the shapes are obtained following the method used in the inclusive estimation.

6.4.3.2 Statistical Method

In this section, the statistical method used to extract the best estimation of the cross section σ_{fid} from the total number of events, as well as the 68% confidence level (which corresponds to $\pm 1\sigma$ uncertainty on the measurement) is described. The method is based on maximum likelihood estimator, which is calculated by maximising the likelihood function $\mathcal{L}$.

The number of observed events produced for a given luminosity, defined as n^{obs}, can be described as a random variable which follows a Poisson distribution:

$$\text{Poisson}(n^{\text{obs}}|n^{\text{exp}} = n_s + n_b) = \frac{(n_s + n_b)^{n^{\text{obs}}}}{n^{\text{obs}}!} e^{n_s + n_b}; \tag{6.4.17}$$

where $n^{\text{exp}} = n_s + n_b$ are the expected number of events, sum of the signal and background events.

The number of the background events is sum of each background component $n_b = \sum_i^{bkg} n_b^i$.

Given that the $m_{4\ell}$ distribution for signal and background events have different shapes, the two contributions can be extracted by the maximum likelihood method with a binned template fit on $m_{4\ell}$. Then the likelihood function can be defined as follow:

$$\mathcal{L}(n^{\text{obs}}, m_{4\ell}|n_s, n_b) = \text{Poisson}(n^{\text{obs}}|n_s + n_b) \times P(m_{4\ell}|n_s, n_b) \tag{6.4.18}$$

where $P(m_{4\ell}|n_s, n_b)$ is the modelling of the signal and different backgrounds:

$$P(m_{4\ell}|n_s, n_b) = \frac{n_s}{n_s + n_b} F_s(m_{4\ell}|n_s) + \frac{n_b}{n_s + n_b} \sum_i^{\text{bkg}} F_b^i(m_{4\ell}|n_b^i) \tag{6.4.19}$$

where F_s and F_b^i are respectively the probability distribution function for the $m_{4\ell}$ shape of signal and $i - th$ background.

Including systematic uncertainties in the fit, they are considered as *nuisance parameters*, which are parameters we are not interested to extract but which add additional degrees of freedom to the analysis. Then gaussian constraints on the systematic uncertainties is added to the likelihood. The gaussian constraint is defined as $\text{Gaus}(\Theta_k|\theta_k, \alpha_k)$, where Θ_k is the random variable (which can be the systematic variation for a measured quantity) with mean θ_k and standard deviation α_k.

Then the final likelihood function is:

$$\mathcal{L}(n^{\text{obs}}, m_{4\ell}|n_s, n_b) = \text{Poisson}(n^{\text{obs}}|n_s + n_b) \times P(m_{4\ell}|n_s, n_b) \times \prod_i^{\text{syst}} \text{Gaus}(\Theta_k|\theta_k, \alpha_k) \tag{6.4.20}$$

in which the $n_s + n_b$ term corresponds to the number of events described by the Equation 6.4.9.

To deal with the nuisance parameters when extracting the best fit value of the fiducial cross section σ^{fid}, the profile likelihood ratio fit is used. It is defined:

$$\lambda(m_{4\ell}|\sigma^{\text{fid}}) = \frac{\mathcal{L}(m_{4\ell}|\sigma^{\text{fid}}, \hat{\hat{\theta}})}{\mathcal{L}(m_{4\ell}|\hat{\sigma}^{\text{fid}}, \hat{\theta})} \tag{6.4.21}$$

where, for a given parameter x (which is θ in this case), the numerator denotes the conditional likelihood estimator of x, (*i.e.*, $\hat{\hat{x}}$ is the value of x that maximises the likelihood function for a given σ^{fid}), and the denominator denotes the maximised (unconditional) likelihood estimator. The effect of the nuisance parameters is to broaden the profile likelihood ratio, which is a function of σ^{fid}, reflecting the loss of information originated from the inclusion of systematic uncertainties.

The profile likelihood ratio is evaluated within the RooFit/RooStats framework [187, 188], and it is also used to determine the upper and lower limit on the cross section within a 68% confidence level interval. This result relies on the assumption that the negative logarithm of the profile likelihood multiplied by a factor 2, $-2\ln\lambda$, behaves as a χ^2 distribution with one degree of freedom (*asymptotic approximation*). Then for each parameter of interest, a scan of the $-2 \ln \lambda$ is performed while profiling all other parameters (they are fitted to the values that minimise the negative log likelihood for each value of the POI).

6.5 Systematic Uncertainties

The systematic uncertainties include experimental uncertainties, such as those in object reconstruction, identification, isolation, resolution, and trigger efficiencies, as well as theoretical uncertainties related to the modelling of the signal and background processes. The impacts of the experimental and theoretical uncertainties on the measurements are summarised in Table 6.8.

6.5.1 Experimental uncertainties

The experimental uncertainties can be categorised into *normalisation* and *shape* systematic uncertainties. The *normalisation* systematic uncertainties impact only the expected yields and they originate from uncertainties on the reconstruction of lepton and jets, identification, isolation and trigger efficiencies. The *shape* systematic uncertainties impact on the variable shape given that they are related to the energy scale and resolution measurement of lepton and jets.

Two of the experimental uncertainties that affect the predicted yields are the ones related to the integrated luminosity and pile-up modelling. The uncertainty in the integrated luminosity is 1.7% and affects the signal yields and simulated background estimates when not constrained by the sidebands. The uncertainty due to pile-up modelling ranges between 1% and 2%.

Lepton uncertainties.

The electron and muon reconstruction and identification efficiency uncertainties are approximately 1.0–2.0% and $< 1.0\%$ respectively. The uncertainty in the expected yields due to the muon and electron isolation efficiencies is also considered, and is approximately 1%. Lepton energy momentum scale and resolution uncertainties have impacts smaller than 1% and then have not been considered on the presented results.

Jets uncertainties.

The impact of uncertainties in the jet energy scale and resolution (of between 1% and 3%) is only relevant for the jet-related differential cross-section measurements, where their impact is typically between 3% and 5%, and is negligible in the other measurements. The uncertainty on the efficiency of the b-tagging algorithm is at the level of a few percent over most of the jet p_{T} range [189].

Reducible background uncertainties.

The uncertainties affecting the data-driven measurement of the reducible background can be classified into three sources: statistical uncertainty of the fit in the CR, overall systematic uncertainty for each of $\ell\ell\mu\mu$ and $\ell\ell ee$ originates from the difference between data and simulation, and a shape systematic uncertainty which varies with the differential variable. Impacts from these sources of uncertainty range from less than 1% to a maximum of around 3%. The inclusive reducible background estimate has a relatively small (3%) statistical uncertainty, which has minimal impact on the cross section.

6.5.2 Theory Uncertainties

Theory uncertainties account for the uncertainty on theoretical modelling of signal and background processes, such as the choice of the renormalisation and factorisation scales (QCD scale), missing higher-order corrections, parton shower, PDF+α_{s} uncertainties. For the cross sections extrapolated to the full phase space, an additional uncertainty (2.2%) related to the $H \to ZZ^*$ branching ratio [123, 124] is included in the measurement.

Signal theory uncertainties.

For measurements of the cross section, the impact of these theory systematic uncertainties on the signal comes from their effects on the response matrix.

QCD renormalisation and factorisation scales. The effect of the renormalisation (μ_R) and factorisation (μ_F) scales choices are obtained by varying μ_R and μ_F simultaneously between 0.5 and 2 times their nominal value (8 total variations). This is done for VH and $t\bar{t}H$ process.

For the ggF production mode, QCD scale uncertainty from the factorisation and renormalisation scales, resummation scales, and migrations between N-jet phase-space bins are considered [107, 190–193]. The impact of QCD scale variations on the Higgs boson p_{T} distribution as well as the uncertainty of the p_{T} distribution in the 0-jet bins are also taken into account. Higher-order impacts on the p_{T} distribution predictions due to treating the top quark mass as infinite in the heavy-quark loop are accounted for by comparing these predictions with finite-mass calculations.

For the VBF production mode, the uncertainty due to missing higher orders in QCD are considered, including migration effects in number of jets, transverse momentum of the Higgs boson, transverse momentum of the Higgs boson and leading dijet system, and the invariant mass of the two leading jets as outlined in the scheme presented in Ref. [194].

Alternative parton distribution functions. Uncertainties related to the choice of PDF set are evaluated by taking the Hessian error of the PDF4LHC variations [126], which is a combination of the eigenvector variations of the baseline (NNPDF3.0) and the central values of alternative (MMHT2014 and CT14) PDF sets. The Hessian error is given by

$$\Delta X = \sqrt{\sum_i (X_{i+} - X_{i-})^2} \tag{6.5.1}$$

where X_{i+} and X_{i-} are the *up* and *down* PDF variation in the set.

Parton shower simulation uncertainties. The effects of parton shower and multiple-parton interaction modelling uncertainties on the acceptance are estimated using tune eigenvector variations within the nominal parton shower generator tune, as well as using an alternative parton shower generator. The uncertainties from the parton shower tune in the nominal generator are estimated using the automated shower variations in PYTHIA 8 of the renormalisation scales μ_R^{FSR} and μ_R^{ISR} for QCD emissions in final and initial state state radiations, respectively. The parton shower uncertainties have also been evaluated comparing between acceptances calculated with PYTHIA 8 and HERWIG 7 parton showering algorithms.

ZZ^* background uncertainties.

Since the ZZ^* process normalisation is constrained by performing a simultaneous fit of sideband regions enriched in this contribution together with the signal region, most of the theoretical uncertainty in the normalisation for this background vanishes. This is not more valid in cases where the cross-section bins are merged into a single ZZ^* bin, where the relative normalisation uncertainties are included.

As for the signal theory uncertainties, also the ZZ^* background is affected by the uncertainties related to the theory predictions. The uncertainties on missing information from higher-order terms in QCD are estimated by varying the factorisation and renormalisation QCD scales by a factor of two. The impact on the PDF uncertainty is estimated using the alternative PDF of the NNPDF3.0 PDF set. Uncertainties due to the parton shower modelling for the ZZ^* process are considered as well. The impact of these uncertainties is below 2% for all the fiducial differential cross sections.

In addition, the $m_{4\ell}$ shape obtained from SHERPA is compared with that obtained from POWHEG and MADGRAPH5_AMC@NLO and the difference is taken as an additional source of systematic uncertainty. In each $m_{4\ell}$ bin, the largest difference between SHERPA and POWHEG or MADGRAPH5_AMC@NLO is used, and the systematic uncertainty is determined by interpolating between these shapes. Typically, SHERPA and POWHEG have the largest difference in the predicted $m_{4\ell}$ shape, with the impact linearly varying from approximately $\pm 10\%$ at low $m_{4\ell}$ to $\mp 2\%$ at high $m_{4\ell}$.

The uncertainty in the gluon-induced ZZ^* process is taken into account as well by changing the relative composition between the quark-initiated and gluon-initiated ZZ^* components according to the theoretical uncertainty in the predicted cross sections.

Unfolding systematics

Unfolding-related uncertainties arise from uncertainties in the production mode composition that affect the response matrices, as well as from uncertainties in the bias introduced by the unfolding method.

Higgs mass. The effect of the uncertainty of the Higgs mass on the acceptance and response matrix is evaluated by shifting the nominal values m_H to the $\pm 1\sigma$ experimental uncertainty on m_H (± 240 MeV) and re-evaluating these factors.

Signal composition. This uncertainty is related to the relative fraction of each production mode of the Higgs. It is assessed by varying the production cross sections within their measured uncertainties taken from the measured ratios and correlations between the ggF and the VBF, WH, ZH, $t\bar{t}H$ production modes (Ref. [195]). The impact is less than 1%.

Bias. This uncertainty is estimated from the bias test described in 6.4.1.3. The impact of this uncertainty is typically negligible in distributions such as $p_{\mathrm{T}}^{4\ell}$, where the response matrix is largely diagonal, but can be of the order of 10% in distributions with larger bin migrations, such as N_{jets}.

6.5.3 Ranking plot

In order to understand the impact of each individual source of systematic uncertainty, a so-called *ranking* of nuisance parameters (NPs) is performed.

Firstly, the unconditional fit of the statistical model on the data is performed to extract the best fit value of the POI (the cross sections) and also the variations of each nuisance parameters corresponding to one standard deviation ($\pm 1\sigma$) are determined. Then the value of a given parameter is fixed to $\pm 1\sigma$ away from the nominal (it is referred as the *pulling* of the NP) and the fit is performed again with this fixed value, extracting a new fit result for the POI. This procedure is performed for each systematic uncertainty. Then the impact of a given systematic corresponds to the difference between the value of the fitted cross section from the unconditional fit and from the fit with the NP pulled to $\pm 1\sigma$.

The rank of the impacts of each systematic uncertainty is called *ranking plot*. The ranking plots for the cross section measured in the $p_{\mathrm{T}}^{4\ell}$ bin 1 and N_{jets} bin 3 are reported as an example in Figure 6.25. Regarding the experimental systematics, for the Higgs kinematic variables the systematics with larger impact is the uncertainty on the integrated luminosity; for the jet-related variables instead the jet energy scale uncertainties have a relevant impact.

Observable	Stat. unc. [%]	Syst. unc. [%]	Dominant systematic components [%]						
			Lumi.	e/μ	Jets	Other Bkg.	ZZ^* Th.	Sig. Th.	Comp.
σ_{comb}	9	3	1.7	2	< 0.5	< 0.5	1	1.5	< 0.5
$\sigma_{4\mu}$	15	4	1.7	3	< 0.5	< 0.5	1.5	1	< 0.5
$\sigma_{4\mathrm{e}}$	26	8	1.7	7	< 0.5	< 0.5	1.5	1.5	< 0.5
$\sigma_{2\mu 2\mathrm{e}}$	20	7	1.7	5	< 0.5	< 0.5	2	1.5	< 0.5
$\sigma_{2\mathrm{e}2\mu}$	15	3	1.7	2	< 0.5	< 0.5	1	1.5	< 0.5
$\mathrm{d}\sigma\ /\ \mathrm{d}p_{\mathrm{T}}^{4\ell}$	20–46	2–8	1.7	1–3	1–2	< 0.5	1–6	1–2	< 1
$\mathrm{d}\sigma\ /\ \mathrm{d}m_{12}$	12–42	3–6	1.7	2–3	< 1	< 0.5	1–2	1–2	< 1
$\mathrm{d}\sigma\ /\ \mathrm{d}m_{34}$	20–82	3–12	1.7	2–3	< 1	1–2	1–8	1–3	< 1
$\mathrm{d}\sigma\ /\ \mathrm{d}\lvert y_{4\ell}\rvert$	22–81	3–6	1.7	2–3	< 1	< 0.5	1–5	1–3	< 1
$\mathrm{d}\sigma\ /\ \mathrm{d}\lvert\cos\theta^*\rvert$	23–113	3–6	1.7	2–3	< 1	1–2	1–7	1–3	< 0.5
$\mathrm{d}\sigma\ /\ \mathrm{d}\cos\theta_1$	23–44	3–6	1.7	2–3	< 1	< 0.5	1–3	1–2	< 1
$\mathrm{d}\sigma\ /\ \mathrm{d}\cos\theta_2$	22–39	3–6	1.7	2–3	< 1	< 0.5	1–3	1–3	< 1
$\mathrm{d}\sigma\ /\ \mathrm{d}\phi$	20–29	2–5	1.7	2–3	< 1	< 0.5	1–3	1–2	< 0.5
$\mathrm{d}\sigma\ /\ \mathrm{d}\phi_1$	22–33	3–6	1.7	2–3	< 1	< 0.5	1–2	1–3	< 0.5
$\mathrm{d}\sigma\ /\ \mathrm{d}N_{\mathrm{jets}}$	15–37	6–14	1.7	1–3	4–10	< 0.5	1–4	3–7	1–4
$\mathrm{d}\sigma\ /\ \mathrm{d}N_{b-\mathrm{jets}}$	15–67	6–15	1.7	1–3	4–5	1–3	1–2	3–9	1–4
$\mathrm{d}\sigma\ /\ \mathrm{d}p_{\mathrm{T}}^{\mathrm{lead.\ jet}}$	15–34	3–13	1.7	1–3	4–10	< 0.5	1–2	1–5	< 0.5
$\mathrm{d}\sigma\ /\ \mathrm{d}p_{\mathrm{T}}^{\mathrm{sublead.\ jet}}$	11–67	5–22	1.7	1–3	2–12	< 1	1–3	2–15	1–5
$\mathrm{d}\sigma\ /\ \mathrm{d}m_{\mathrm{jj}}$	11–50	5–18	1.7	1–3	1–11	< 0.5	1–3	2–15	1–2
$\mathrm{d}\sigma\ /\ \mathrm{d}\eta_{jj}$	11–57	5–17	1.7	1–3	2–10	< 0.5	1–2	2–14	1–4
$\mathrm{d}\sigma\ /\ \mathrm{d}\phi_{jj}$	11–50	4–18	1.7	1–3	2–9	< 0.5	1–3	2–14	1–6
$\mathrm{d}\sigma\ /\ \mathrm{d}m_{4\ell\mathrm{j}}$	15–66	4–19	1.7	1–3	3–9	< 0.5	1–6	3–14	1–8
$\mathrm{d}\sigma\ /\ \mathrm{d}m_{4\ell\mathrm{jj}}$	11–182	5–67	1.7	1–3	4–24	< 0.5	1–5	2–35	1–9
$\mathrm{d}\sigma\ /\ \mathrm{d}p_{\mathrm{T}}^{4\ell\mathrm{j}}$	15–76	6–13	1.7	1–3	2–8	< 1	1–5	3–9	1–3
$\mathrm{d}\sigma\ /\ \mathrm{d}p_{\mathrm{T}}^{4\ell\mathrm{jj}}$	11–76	5–27	1.7	2–3	2–9	1–2	1–4	3–17	1–12
$\mathrm{d}^2\sigma\ /\ \mathrm{d}m_{12}\ \mathrm{d}m_{34}$	16–65	3–11	1.7	2–3	< 1	1–2	1–9	1–3	1–2
$\mathrm{d}^2\sigma\ /\ \mathrm{d}p_{\mathrm{T}}^{4\ell}\ \mathrm{d}\lvert y_{4\ell}\rvert$	23–63	2–13	1.7	1–3	1–2	< 1	1–6	1–5	1–2
$\mathrm{d}^2\sigma\ /\ \mathrm{d}p_{\mathrm{T}}^{4\ell}\ \mathrm{d}N_{\mathrm{jets}}$	23–93	4–193	1.7	2–14	2–25	1–3	1–7	1–12	1–92
$\mathrm{d}^2\sigma\ /\ \mathrm{d}p_{\mathrm{T}}^{4\ell\mathrm{j}}\ \mathrm{d}m_{4\ell\mathrm{j}}$	15–41	4–12	1.7	1–3	2–8	< 0.5	1–5	2–9	< 1
$\mathrm{d}^2\sigma\ /\ \mathrm{d}p_{\mathrm{T}}^{4\ell}\ \mathrm{d}p_{\mathrm{T}}^{4\ell\mathrm{j}}$	15–53	3–10	1.7	1–3	2–8	< 1	1–2	2–6	1–2
$\mathrm{d}^2\sigma\ /\ \mathrm{d}p_{\mathrm{T}}^{4\ell}\ \mathrm{d}p_{\mathrm{T}}^{\mathrm{lead.\ jet}}$	15–84	3–21	1.7	1–3	2–18	1–10	1–3	2–9	1–3
$\mathrm{d}^2\sigma\ /\ \mathrm{d}p_{\mathrm{T}}^{\mathrm{lead.\ jet}}\ \mathrm{d}\lvert y^{\mathrm{lead.\ jet}}\rvert$	15–38	3–11	1.7	1–3	2–9	< 0.5	1–2	1–4	1–2
$\mathrm{d}^2\sigma\ /\ \mathrm{d}p_{\mathrm{T}}^{\mathrm{lead.\ jet}}\ \mathrm{d}p_{\mathrm{T}}^{\mathrm{sublead.\ jet}}$	15–63	5–22	1.7	1–3	4–15	< 0.5	1–4	3–11	1–7

Table 6.8: Fractional uncertainties for the inclusive fiducial and total cross sections, and ranges of systematic uncertainties for the differential measurements. The columns 'e/μ' and 'Jets' represent the experimental uncertainties in lepton and jet reconstruction and identification, respectively. The $Z+$jets, $t\bar{t}$, tXX (Other Bkg.) column includes uncertainties related to the estimation of these background sources. The ZZ^* theory (ZZ^* th.) uncertainties include the PDF and scale variations. Signal theory (Sig th.) uncertainties include PDF choice, QCD scale, and shower modelling of the signal. Finally, the column labelled 'Comp.' contains uncertainties related to production mode composition and unfolding bias which affect the response matrices. The uncertainties have been rounded to the nearest 0.5%, except for the luminosity uncertainty, which has been measured to be 1.7%.

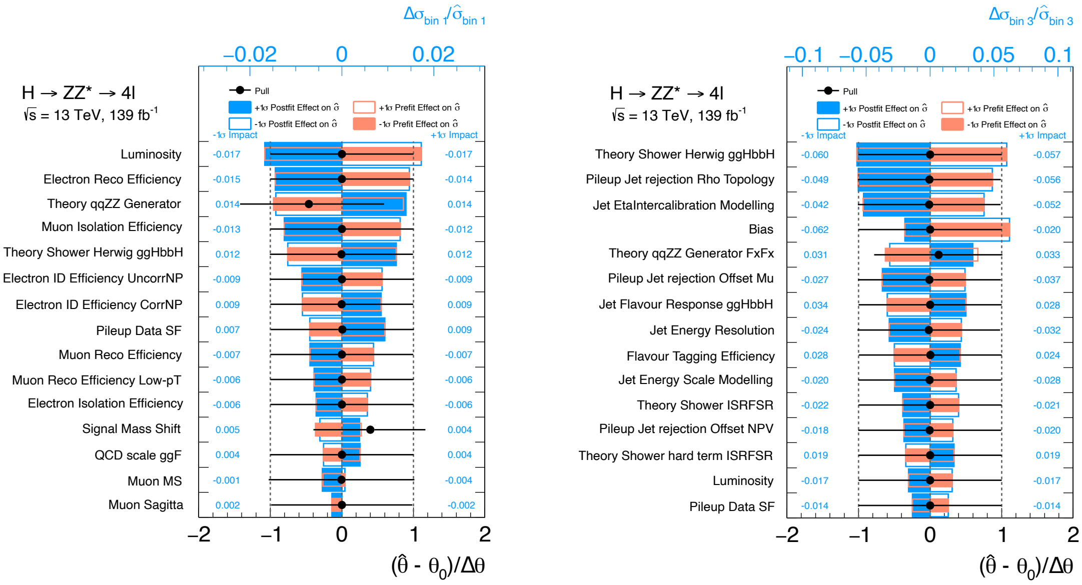

(a) $p_{\mathrm{T}}^{4\ell}$ ranking plot in Bin 1

(b) N_{jets} ranking plot in Bin 3

Figure 6.25: Ranking plots for (a) $p_{\mathrm{T}}^{4\ell}$ and (b) N_{jets} distribution for response matrix unfolding. Only the first 15 most highly ranked parameters are shown. The pink rectangles correspond to the pre-fit impact on the cross section $\hat{\sigma}$ instead the blue rectangles to the post-fit impact, in case that the NP is fixed to $+1\sigma$ (empty rectangles) or -1σ (filled rectangles) away from the nominal values θ_0. The impact of each nuisance parameter $\Delta\sigma$ on the cross section is computed by comparing the nominal best-fit value σ with the result of the fit when fixing the considered nuisance parameter to its best fit value $\hat{\theta}$, shifted by its pre-fit (post-fit) uncertainties $\pm\Delta\theta(\pm\Delta\hat{\theta})$. The impact on the cross section with fixed NP to $\pm1\sigma$, $\Delta\sigma/\hat{\sigma}$ refers to the scale on the top axis, and the $\pm1\sigma$ impact of each NP is written on the side of rectangles. The black points show the pulls of the nuisance parameters relative to their nominal values, θ_0. These pulls and their relative post-fit errors $(\hat{\theta} - \theta_0)/\Delta\theta$, refer to the scale on the bottom axis.

6.6 Results

In this section the fiducial inclusive and the differential cross section measurements of the variables described previously in this chapter ($p_{\mathrm{T}}^{4\ell}$, N_{jets}, m_{jj} and m_{12} vs. m_{34}) are presented. The results of all the other variables are reported in Appendix A.

Measured data yields

The observed number of events in each of the four decay final states, and the expected signal and background yields before fitting the data (pre-fit) in the mass range $115 < m_{4\ell} < 130$ GeV, are presented in Tables 6.9. Figure 6.27 shows the expected and observed four-lepton invariant mass distributions in the inclusive final state 4ℓ in the signal mass window $105 < m_{4\ell} < 160$ GeV. Figure 6.28 shows the expected and observed four-lepton invariant mass distributions in each final state.

Final state	Signal	ZZ^* background	Other backgrounds	Total expected	Observed
4μ	78 ± 5	38.0 ± 2.1	2.85 ± 0.18	119 ± 5	115
$2e2\mu$	53.0 ± 3.1	26.1 ± 1.4	2.98 ± 0.19	82.0 ± 3.4	96
$2\mu 2e$	40.1 ± 2.9	17.3 ± 1.3	3.6 ± 0.5	61.0 ± 3.2	57
$4e$	35.3 ± 2.6	15.0 ± 1.5	2.91 ± 0.33	53.2 ± 3.1	42
Total	206 ± 13	96 ± 6	12.2 ± 1.0	315 ± 14	310

Table 6.9: Expected (pre-fit) and observed numbers of events in the four decay final states after the event selection, in the mass range 115< $m_{4\ell}$ <130 GeV. The sum of the expected number of SM Higgs boson events and the estimated background yields is compared with the data.

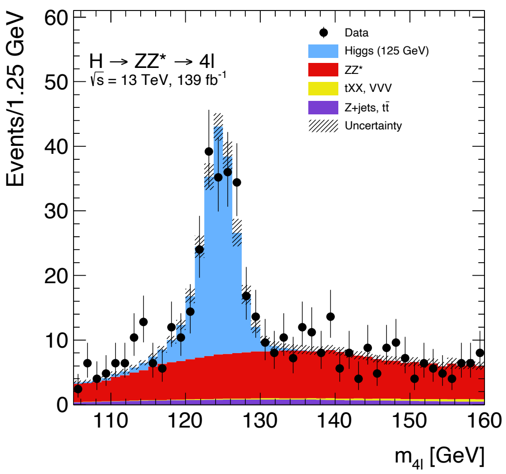

Figure 6.26: $105 < m_{4\ell} < 160$ GeV

Figure 6.27: The observed and expected (pre-fit) distributions four lepton invariant mass distribution for the selected Higgs boson candidates in the inclusive final state in the mass range $105 < m_{4\ell} < 160$ GeV. The uncertainty in the prediction is shown by the hatched band, which include the theoretical uncertainties of the SM cross section for the signal and ZZ^* background.

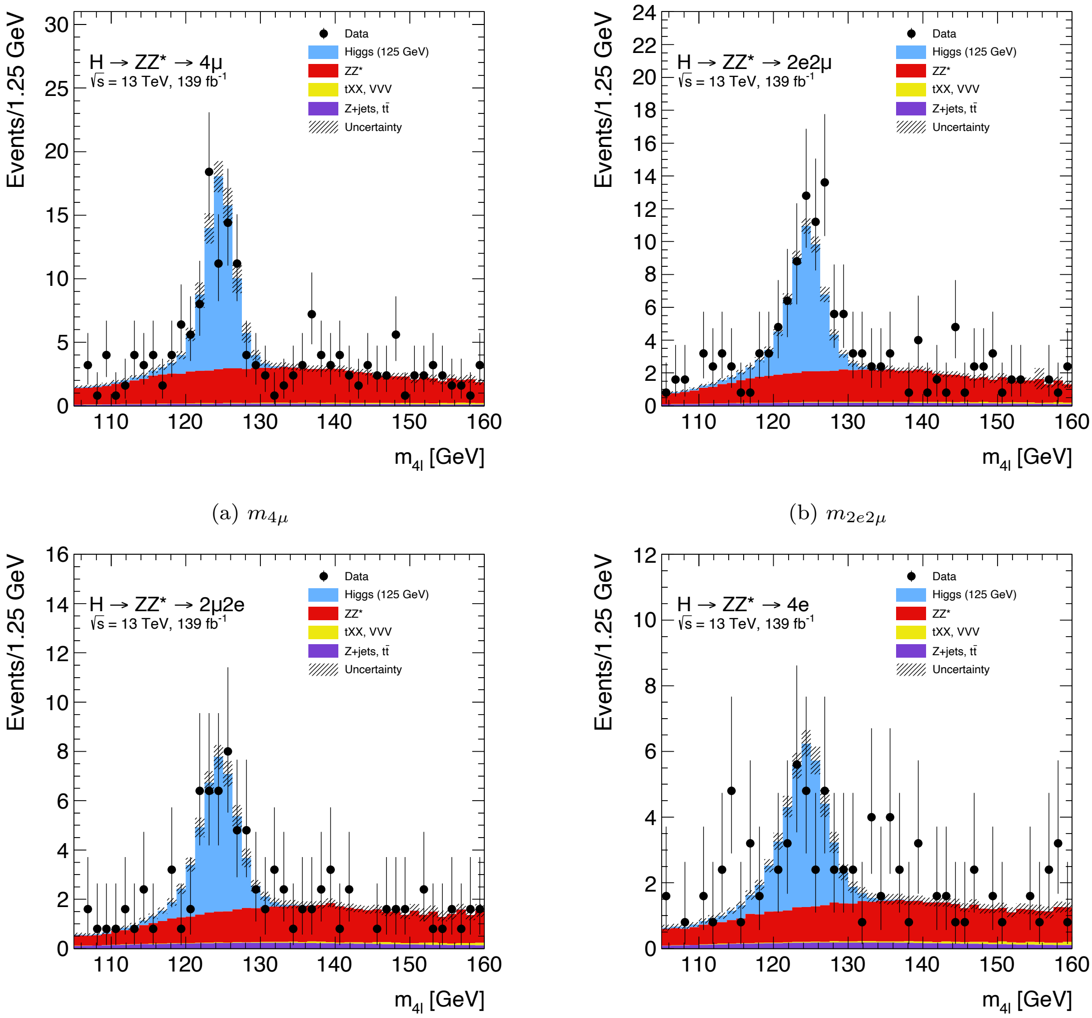

(a) $m_{4\mu}$ (b) $m_{2e2\mu}$

(c) $m_{2\mu 2e}$ (d) m_{4e}

Figure 6.28: The observed and expected (pre-fit) distributions four lepton invariant mass distribution for the selected Higgs boson candidates in the range of $115 < m_{4\ell} < 130$ GeV for the different decay final states (a) 4μ, (b) $2e2\mu$, (c) $2\mu 2e$ and (d) $4e$. The uncertainty in the prediction is shown by the hatched band, which include the theoretical uncertainties of the SM cross section for the signal and ZZ^* background.

The expected and the observed distribution of the variable previously described in this section, are shown in Figures 6.29-6.32. In each figure are shown the distribution of the events selected both in the enlarged mass window $105 < m_{4\ell} < 160$ GeV and in the signal mass window $115 < m_{4\ell} < 130$ GeV

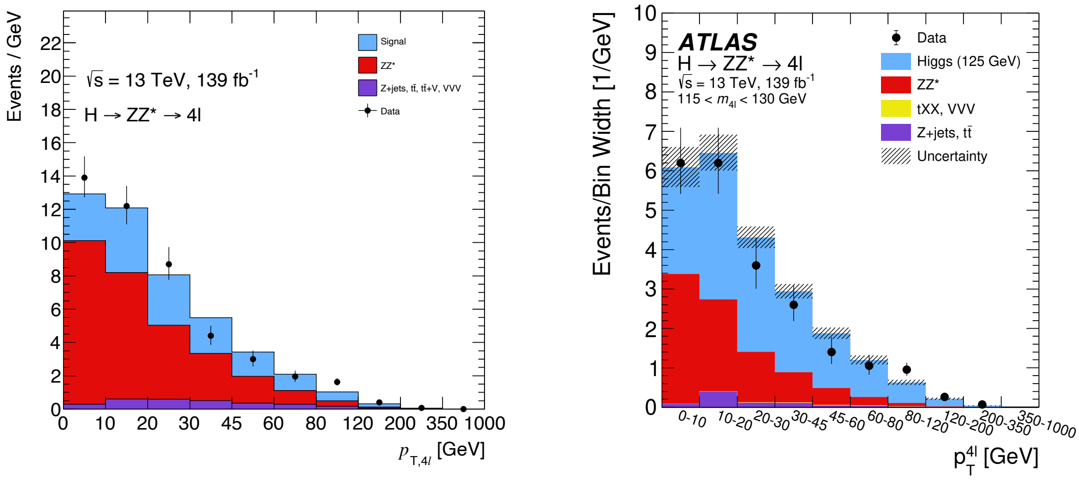

(a) $p_T^{4\ell}$ pre-fit distribution
$105 < m_{4\ell} < 160$ GeV

(b) $p_T^{4\ell}$ pre-fit distribution
$115 < m_{4\ell} < 130$ GeV

Figure 6.29: The observed and expected (pre-fit) distributions of $p_T^{4\ell}$ in the range of (a)$105 < m_{4\ell} < 160$ GeV and (b) $115 < m_{4\ell} < 130$ GeV. The black dots depict pre-fit data while the blue, red and violet (and yellow) areas represent the signal, the ZZ^* background and the reducible background, respectively. In (b) the uncertainty in the prediction is shown by the hatched band, which include the theoretical uncertainties of the SM cross section for the signal and ZZ^* background.

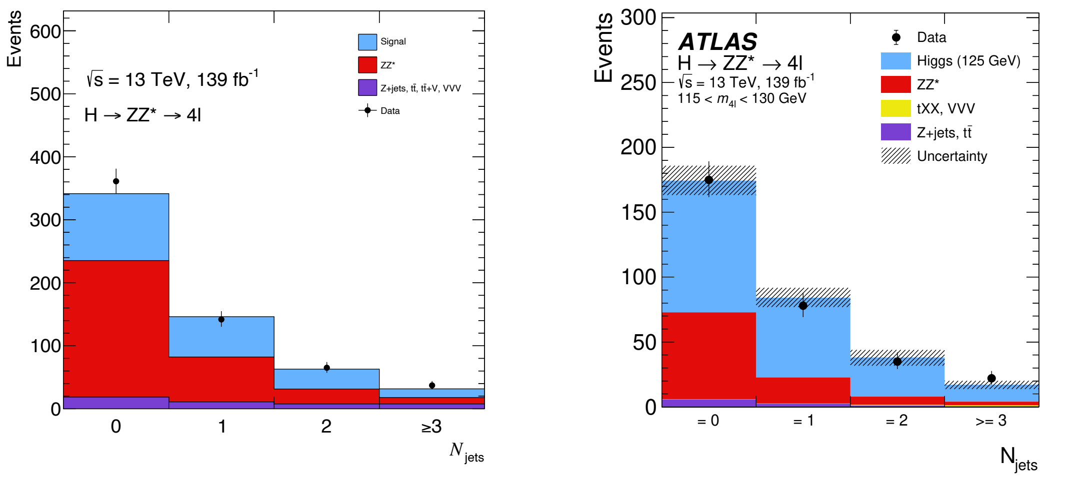

(a) N_{jets} pre-fit distribution
$105 < m_{4\ell} < 160$ GeV

(b) N_{jets} pre-fit distribution
$115 < m_{4\ell} < 130$ GeV

Figure 6.30: The observed and expected (pre-fit) distributions of N_{jets} in the range of (a)$105 < m_{4\ell} < 160$ GeV and (b) $115 < m_{4\ell} < 130$ GeV. The black dots depict pre-fit data while the blue, red and violet (and yellow) areas represent the signal, the ZZ^* background and the reducible background, respectively. In (b) the uncertainty in the prediction is shown by the hatched band, which include the theoretical uncertainties of the SM cross section for the signal and ZZ^* background.

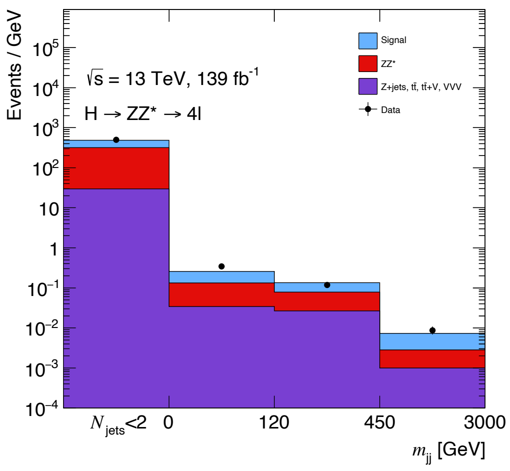

(a) $m_{\rm jj}$ pre-fit distribution
$105 < m_{4\ell} < 160$ GeV

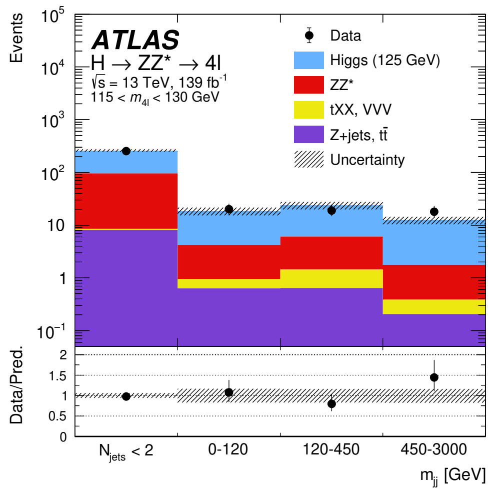

(b) $m_{\rm jj}$ pre-fit distribution
$115 < m_{4\ell} < 130$ GeV

Figure 6.31: The observed and expected (pre-fit) distributions of $m_{\rm jj}$ in the range of (a)$105 < m_{4\ell} < 160$ GeV and (b) $115 < m_{4\ell} < 130$ GeV. The black dots depict pre-fit data while the blue, red and violet (and yellow) areas represent the signal, the ZZ^* background and the reducible background, respectively. In (b) the uncertainty in the prediction is shown by the hatched band, which include the theoretical uncertainties of the SM cross section for the signal and ZZ^* background.

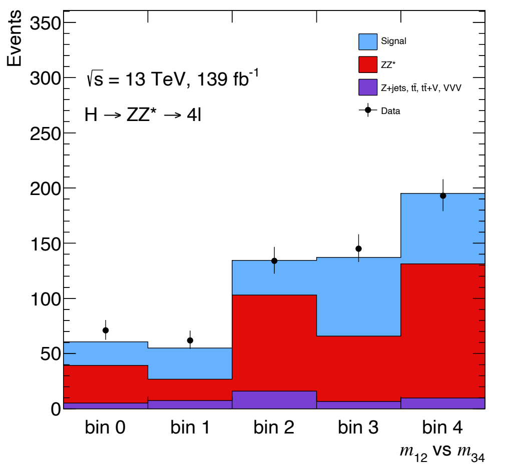

(a) m_{12} vs. m_{34} pre-fit distribution
$105 < m_{4\ell} < 160$ GeV

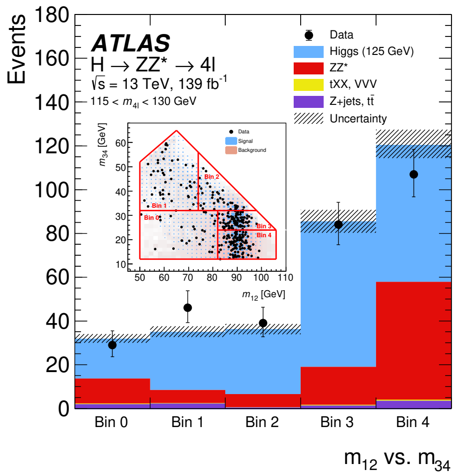

(b) m_{12} vs. m_{34} pre-fit distribution
$115 < m_{4\ell} < 130$ GeV

Figure 6.32: The observed and expected (pre-fit) distributions of m_{12} vs. m_{34} in the range of (a)$105 < m_{4\ell} <$ 160 GeV and (b) $115 < m_{4\ell} < 130$ GeV. The black dots depict pre-fit data while the blue, red and violet (and yellow) areas represent the signal, the ZZ^* background and the reducible background, respectively. In (b) the uncertainty in the prediction is shown by the hatched band, which include the theoretical uncertainties of the SM cross section for the signal and ZZ^* background.

6.6.1 Inclusive cross section results

The fiducial inclusive cross sections of the $H \to ZZ^{(*)} \to 4\ell$ process are presented in Figure 6.33 and Table 6.10. The left panel in Figure 6.33a shows the fiducial cross sections for the four individual decay final states: 4μ, $4e$ decays (hereafter referred to as same flavour), and $2\mu 2e$, $2e2\mu$ decays (hereafter referred to as different flavour). The middle panel shows the cross sections for same- and different-flavour decays, which can provide a probe of same-flavour interference effects, as well as the inclusive fiducial cross sections obtained by either summing all 4ℓ decay final states or combining them assuming relative SM branching ratios.

The data are compared with the SM prediction after accounting for the fiducial acceptance as determined from the SM Higgs boson simulated samples (see Section 5.1.2).

The combined inclusive fiducial cross section is extrapolated to the full phase space, as shown in the right panel of Figure 6.33a, using the fiducial acceptance as well as the branching ratios, with the uncertainties described in Section 6.5. The total cross section is also compared with the cross sections predicted by NNLOPS, MadGraph5_aMC@NLO-FxFx (MG5-FxFx) and Hres 2.3 [105, 106] for ggF, while for all other production modes the predictions described in Section 5.1.2 are used. For ggF, all generators predict cross sections that are lower than the N^{3}LO calculation.

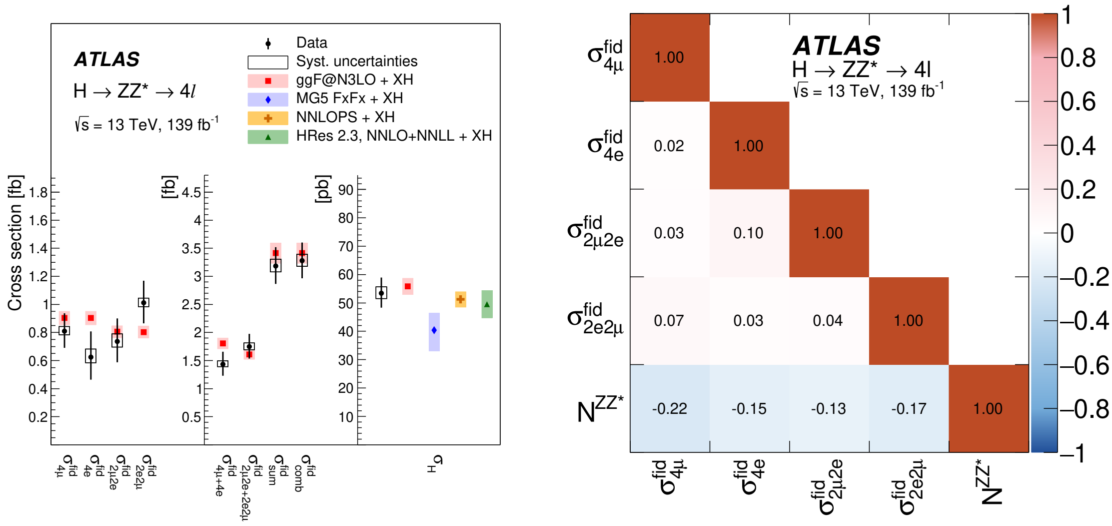

(a)

(b)

Figure 6.33: (a) The fiducial cross sections (left two panels) and total cross section (right panel) of Higgs boson production measured in the 4ℓ final state. The fiducial cross sections are shown separately for each decay final state, and for same- and different-flavour decays. The inclusive fiducial cross section is measured as the sum of all final states, as well as by combining the per-final-state measurements assuming SM $ZZ^* \to 4\ell$ relative branching ratios. The error bars on the data points show the total uncertainties, while the systematic uncertainties are indicated by the boxes. The shaded bands around the theoretical predictions indicate the PDF and scale uncertainties. (b) The correlation between the fiducial cross sections for the four individual decay final states and the ZZ^* normalisation factor.

Table 6.10 shows also the p-values, quantifying the probability of compatibility of the measurements and the SM predictions. Given that the statistical analysis assume the asymptotic approximation in which the NLL behaves as a χ^2 distribution with one degree of freedom, the p-value is defined as the probability that a χ^2 distribution is greater than the results of the χ^2 test performed on the data. In this case it can be defined as:

$$p\text{-value} = \int_{\text{NLL}(\hat{\sigma^{\text{obs}}})}^{\infty} \chi^2(\text{NLL})\,\mathrm{d}\text{NLL} \quad \text{where} \quad \text{NLL} = -2\ln\frac{L(m_{4\ell}|\sigma^{\text{fid,pred}},\hat{\hat{\theta}})}{L(m_{4\ell}|\hat{\sigma^{\text{fid}}},\hat{\theta})} \tag{6.6.1}$$

The probability of compatibility of the measured fiducial cross section (σ_{comb}) and the Standard Model expectation is at the level of 67%.

Cross section [fb]	Data	± (stat.)	± (syst.)	Standard Model prediction	p-value [%]
$\sigma_{4\mu}$	0.81	±0.12	±0.03	0.90 ± 0.05	46
σ_{4e}	0.62	±0.17	±0.05	0.90 ± 0.05	14
$\sigma_{2\mu 2e}$	0.74	±0.15	±0.05	0.80 ± 0.04	67
$\sigma_{2e2\mu}$	1.01	±0.15	±0.03	0.80 ± 0.04	15
$\sigma_{4\mu+4e}$	1.43	±0.21	±0.05	1.81 ± 0.10	10
$\sigma_{2\mu 2e+2e2\mu}$	1.75	±0.21	±0.06	1.61 ± 0.09	51
σ_{sum}	3.18	±0.31	±0.11	3.41 ± 0.18	49
σ_{comb}	3.28	±0.30	±0.11	3.41 ± 0.18	67
σ_{tot} [pb]	53.5	±4.9	±2.1	55.7 ± 2.8	66

Table 6.10: The fiducial and total cross sections of Higgs boson production measured in the 4ℓ final state. The fiducial cross sections are given separately for each decay final state, and for same- and different-flavour decays. The inclusive fiducial cross section is measured as the sum of all final states (σ_{sum}), as well as by combining the per-final-state measurements assuming SM $ZZ^* \to 4\ell$ relative branching ratios (σ_{comb}). For the total cross section (σ_{tot}), the Higgs boson branching ratio at $m_H = 125$ GeV is assumed. The p-values indicating the probability of compatibility of the measurement and the SM prediction are shown as well.

6.6.2 Differential cross section measurement

Cross section results with data and Asimov comparison

Here the cross section results in each variable bin are presented. This results are obtained using data from Run 2 and from the Asimov dataset [196].

The Asimov dataset is used to understand the performance in terms of statistical error on the fiducial measurement for each parameter of interest. The Asimov dataset is generated assuming SM expectation for signal ($m_H = 125$ GeV) and ZZ^* background and reducible background, implicitly assuming that the nuisance parameters are set to their nominal values (then the systematics are set to be zero). Minimising the Negative Log Likelihood from generated Asimov data the expected cross section $\hat{\sigma^{\text{fid}}}$ and its uncertainty can be estimated. This procedure relies on the assumption that the asymptotic approximation for which $-2\ln\lambda$ behaves as a χ^2 is true. Then the PDF of $\hat{\sigma}^{\text{fid}}$ from which the Asimov data are generated is set to behave as a χ^2 distribution with one degree of freedom. In this way the minimum of $-2\ln\lambda(\hat{\sigma}^{\text{fid}})$ is the "truth" σ^{fid}.

Figure 6.34 shows the scans of the Negative Log Likelihood in the first three bin of the Higgs p_{T} as example. The cross section results as well as their relative errors (including systematics) in each bin of the variables, described in Section 6.4.2, are shown in Tables 6.11-6.14.

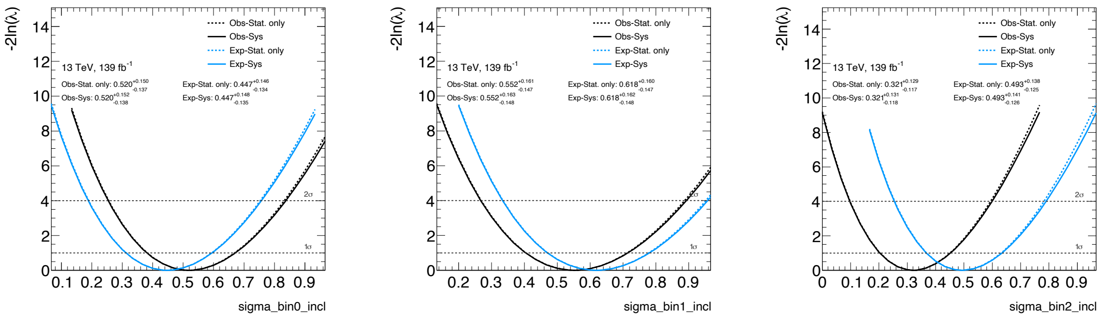

(a) p_T bin 0 NLL scan (b) p_T bin 1 NLL scan (c) p_T bin 2 NLL scan

Figure 6.34: Negative log likelihood scans of the cross sections in the first three bin of the $p_{\text{T}}^{4\ell}$ distribution for response matrix unfolding using data (in black) and the Asimov dataset (in blue) with luminosity 139 fb^{-1} for $105 < m_{4\ell} < 160$ GeV has been considered. Expected and observed cross sections are reported. Systematic uncertainties are included.

POI	XS $_{\text{inj}}$ [fb]	XS $^{\text{asimov}}_{\text{fit}}$ [fb]	Rel. Error [%]	XS $^{\text{data}}_{\text{fit}}$ [fb]	Rel. Error [%]
σ_{bin0}	0.45	$0.45 \pm 0.14 \pm 0.02$	$\pm 31.1 \pm 4.4$	$0.52 \pm 0.14 \pm 0.02$	$\pm 26.9 \pm 2.8$
σ_{bin1}	0.62	$0.62 \pm 0.15 \pm 0.02$	$\pm 24.1 \pm 3.2$	$0.55 \pm 0.15 \pm 0.02$	$\pm 27.2 \pm 3.6$
σ_{bin2}	0.49	$0.49 \pm 0.13^{+0.03}_{-0.02}$	$\pm 26.5^{+6.1}_{-4.1}$	$0.32 \pm 0.12^{+0.02}_{-0.01}$	$\pm 37.5^{+6.2}_{-3.1}$
σ_{bin3}	0.53	$0.53 \pm 0.13 \pm 0.02$	$\pm 24.5 \pm 3.8$	$0.47 \pm 0.12^{+0.02}_{-0.01}$	$\pm 25.5^{+4.3}_{-2.1}$
σ_{bin4}	0.36	$0.36 \pm 0.10^{+0.02}_{-0.01}$	$\pm 27.8^{+5.6}_{-2.8}$	$0.222 \pm 0.085^{+0.011}_{-0.006}$	$\pm 38.3^{+5.0}_{-2.7}$
σ_{bin5}	0.32	$0.32 \pm 0.09 \pm 0.01$	$\pm 28.1 \pm 3.1$	$0.17 \pm 0.08 \pm 0.01$	$\pm 45.9^{+8.1}_{-6.4}$
σ_{bin6}	0.34	$0.34 \pm 0.09 \pm 0.01$	$\pm 26.5 \pm 2.9$	$0.55 \pm 0.11^{+0.02}_{-0.01}$	$\pm 20.0^{+3.6}_{-1.8}$
σ_{bin7}	0.230	$0.230 \pm 0.065^{+0.009}_{-0.006}$	$\pm 28.2^{+3.9}_{-2.6}$	$0.287 \pm 0.072^{+0.011}_{-0.007}$	$\pm 25.0^{+3.8}_{-2.4}$
σ_{bin8}	0.073	$0.073\ ^{+0.038}_{-0.029}{}^{+0.004}_{-0.002}$	${}^{+52.0}_{-39.7}{}^{+5.4}_{-2.7}$	$0.125\ ^{+0.047}_{-0.037}{}^{+0.006}_{-0.003}$	${}^{+37.6}_{-29.6}{}^{+4.8}_{-2.4}$

Table 6.11: Expected and observed cross sections in each category of $p_{\text{T}}^{4\ell}$ using the Asimov dataset and data, assuming an integrated luminosity of 139 fb^{-1} for $105 < m_{4\ell} < 160$ GeV, with full statistical plus systematic uncertainties.

POI	XS $_{\text{inj}}$ [fb]	XS $^{\text{asimov}}_{\text{fit}}$ [fb]	Rel. Error [%]	XS $^{\text{data}}_{\text{fit}}$ [fb]	Rel. Error [%]
σ_{bin0}	1.85	1.85 $\pm 0.26 \pm 0.12$	$\pm 14.0 \pm 6.5$	1.75 $\pm 0.26 \pm 0.12$	$\pm 14.9 \pm 6.8$
σ_{bin1}	0.95	0.95 $\pm 0.22 \pm 0.06$	$\pm 23.1 \pm 6.3$	0.83 $\pm 0.21 \pm 0.06$	$\pm 25.3 \pm 7.2$
σ_{bin2}	0.43	0.43 $\pm 0.15 \pm 0.04$	$\pm 34.9 \pm 9.3$	0.40 $\pm 0.15 \pm 0.04$	$\pm 37.5 \pm 10.0$
σ_{bin3}	0.18	0.18 $\pm 0.09 \pm 0.04$	$\pm 50.0 \pm 22.2$	0.29 $\pm 0.10 \pm 0.04$	$\pm 34.5 \pm 13.8$

Table 6.12: Expected and observed cross sections in each category of N_{jets} using the Asimov dataset and data, assuming an integrated luminosity of 139 fb^{-1} for 105 < $m_{4\ell}$ < 160 GeV, with full statistical plus systematic uncertainties.

POI	XS $_{\text{inj}}[fb]$	XS $^{\text{asimov}}_{\text{fit}}$ [fb]	Rel. Error [%]	XS $^{\text{data}}_{\text{fit}}$ [fb]	Rel. Error [%]
σ_{bin0}	2.81	2.81 $\pm 0.29 \pm 0.13$	$\pm 10.3 \pm 4.6$	2.57 $\pm 0.29 \pm 0.12$	$\pm 11.3 \pm 4.7$
σ_{bin1}	0.20	0.20 $\pm 0.10 \pm 0.04$	$\pm 50.0 \pm 20.0$	0.21 $\pm 0.11 \pm 0.04$	$\pm 52.4 \pm 19.0$
σ_{bin2}	0.27	0.27 $\pm 0.11 \pm 0.04$	$\pm 40.7 \pm 14.8$	0.21 $\pm 0.10 \pm 0.04$	$\pm 47.6 \pm 19.0$
σ_{bin3}	0.14	0.14 $\pm 0.06 \pm 0.02$	$\pm 42.8 \pm 14.3$	0.25 $\pm 0.08 \pm 0.02$	$\pm 32.0 \pm 8.0$

Table 6.13: Expected and observed cross sections in each category of m_{jj} using the Asimov dataset and data, assuming an integrated luminosity of 139 fb^{-1} for 105 < $m_{4\ell}$ < 160 GeV, with full statistical plus systematic uncertainties.

POI	XS $_{\text{inj}}$ [fb]	XS $^{\text{asimov}}_{\text{fit}}$ [fb]	Rel. Error [%]	XS $^{\text{data}}_{\text{fit}}$ [fb]	Rel. Error [%]
σ_{bin0}	0.30	0.30 $\pm 0.12 \pm 0.02$	$\pm 40.0 \pm 6.7$	0.18 $\pm 0.12 \pm 0.02$	$\pm 66.7 \pm 11.1$
σ_{bin1}	0.40	0.40 $\pm 0.09 \pm 0.02$	$\pm 22.5 \pm 5.0$	0.50 $\pm 0.11 \pm 0.03$	$\pm 22.0 \pm 6.0$
σ_{bin2}	0.47	0.47 $\pm 0.11^{+0.03}_{-0.02}$	$\pm 23.4^{+6.4}_{-4.3}$	0.49 $\pm 0.11^{+0.03}_{-0.02}$	$\pm 22.4^{+6.1}_{-4.1}$
σ_{bin3}	1.17	1.17 $\pm 0.18^{+0.05}_{-0.03}$	$\pm 15.4^{+4.3}_{-2.6}$	1.14 $\pm 0.18^{+0.04}_{-0.03}$	$\pm 15.8^{+3.5}_{-2.6}$
σ_{bin4}	1.07	1.07 $\pm 0.21^{+0.05}_{-0.03}$	$\pm 19.6^{+4.7}_{-2.8}$	0.83 $\pm 0.20^{+0.04}_{-0.03}$	$\pm 24.1^{+4.8}_{-3.6}$

Table 6.14: Expected and observed cross sections in each category of m_{12} vs. m_{34} using the Asimov dataset and data, assuming an integrated luminosity of 139 fb^{-1} for 105 < $m_{4\ell}$ < 160 GeV, with full statistical plus systematic uncertainties.

Differential cross section results

The measured differential production cross sections for the transverse momentum $p_{\text{T}}^{4\ell}$ of the Higgs boson, the number of jets N_{jets}, the invariant mass of the di-jet system m_{jj} and the double-differential distribution m_{12} vs. m_{34} are shown in Figures 6.35-6.38. For the double-differential distribution m_{12} vs. m_{34} also the differential cross section distributions in the two different $\ell\ell\mu\mu$ and $\ell\ell ee$ final states are reported. These results have been used to put constraints on effective BSM Higgs couplings in one of the Pseudo-Observable scenarios investigated in Section 7.1.1. The correlation matrices between the measured cross sections and the ZZ^{*} background normalisation factors are shown in all figures along with the cross-section measurements.

The data are compared with SM expectations constructed from the ggF predictions provided by NNLOPS and MadGraph5_aMC@NLO-FxFx. Certain distributions related to the production of the Higgs boson also include a comparison with the predictions from NNLOJET and RadISH and some of the measurements related to the Higgs boson decay are compared also with predictions from Hto4l and Prophecy4f. The ggF predictions from MadGraph5_aMC@NLO-FxFx and NNLOPS are normalised to the N^{3}LO prediction while the normalisations for NNLOJET and RadISH are to their respective predicted cross sections. All the other Higgs boson production modes (labelled as XH) are normalised to the most accurate SM predictions. The error bars on the data points show the total uncertainties, while the systematic uncertainties are indicated by the boxes. The shaded bands on the expected cross sections indicate the PDF and scale uncertainties. This includes the uncertainties related to the XH production modes. The central panel of the figures shows the ratio of different predictions to the data, and the grey area represents the total uncertainty of the measurement. Finally the bottom panel shows the ratios of the fitted values of the ZZ^* normalisation factors to the predictions from MC simulation discussed in Section 5.1.2. As indicated by the horizontal error bars, the ZZ^* normalisation is estimated in each of the first three $p_{\mathrm{T}}^{4\ell}$ bins separately, while the next two bins share a common estimation factor, as do the last five bins. For the N_{jets} and m_{jj} the last two bins share a common normalisation factor, as the first two bins of m_{12} vs. m_{34}. The figures include the p-values quantifying the probability of compatibility of the measurements and the SM predictions.

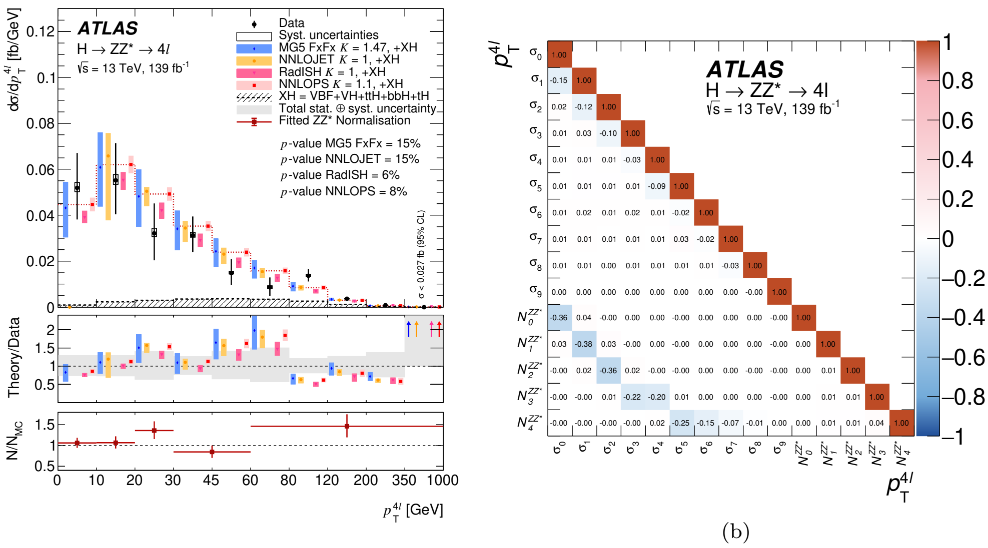

(a) (b)

Figure 6.35: (a) Differential fiducial cross section for the transverse momentum $p_{\mathrm{T}}^{4\ell}$ of the Higgs boson, along with (b) the corresponding correlation matrix between the measured cross sections and the ZZ^* background normalisation factors.

The p-value for the differential cross section measurement is computed from the Equation

6.6.1, considering the full likelihood as the product of the likelihood of each bin, and the $\sigma^{\text{fid,pred}}$ in each bin is fixed to the cross sections predicted by theory. Under the asymptotic assumption $\textsc{nll}(\sigma^{\text{fid,pred}})$ behaves as a χ^2 with the number of degrees of freedom equal to the number of bins.

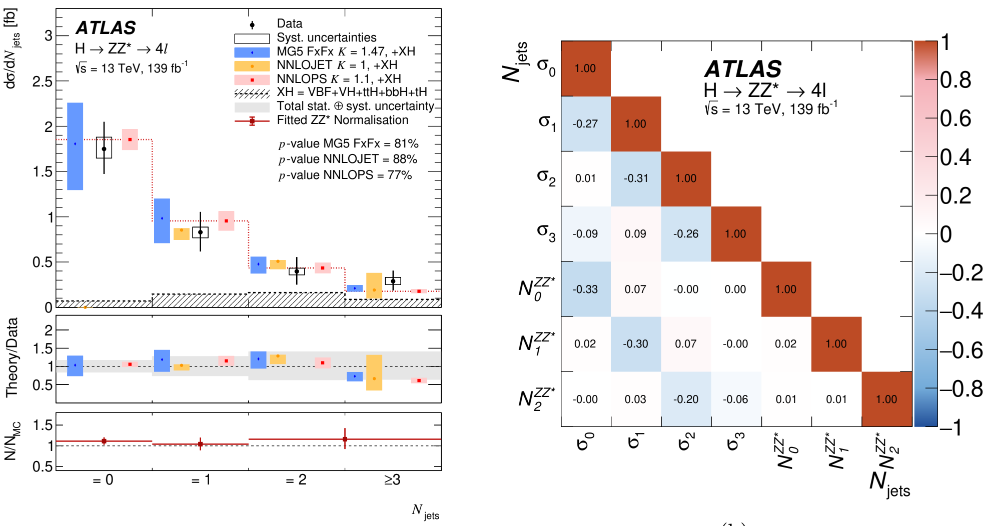

(a)

(b)

Figure 6.36: (a) Differential fiducial cross section for the number of jets N_{jets}, along with (b) the corresponding correlation matrix between the measured cross sections and the ZZ^* background normalisation factors.

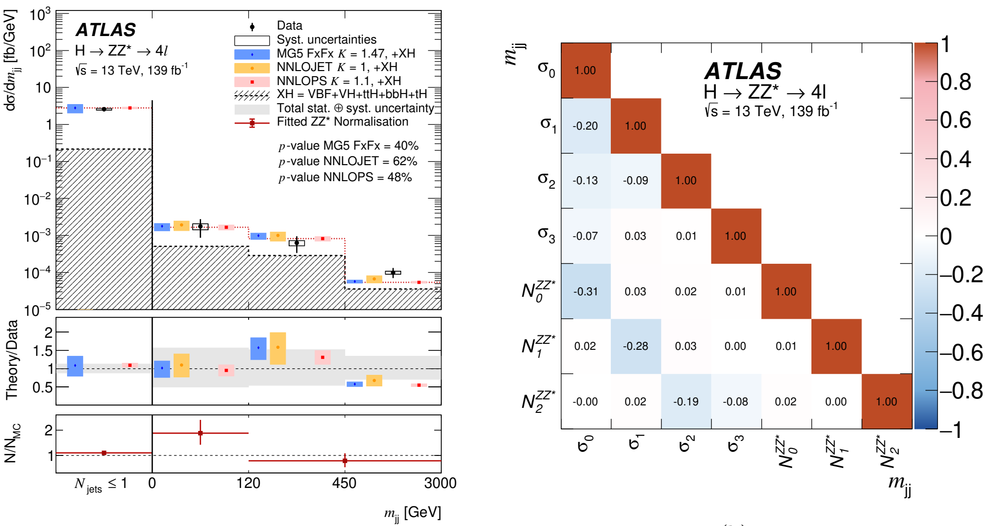

(a)

(b)

Figure 6.37: (a) Differential fiducial cross section for the di-jet invariant mass m_{jj}, along with (b) the corresponding correlation matrix between the measured cross sections and the ZZ^* background normalisation factors.

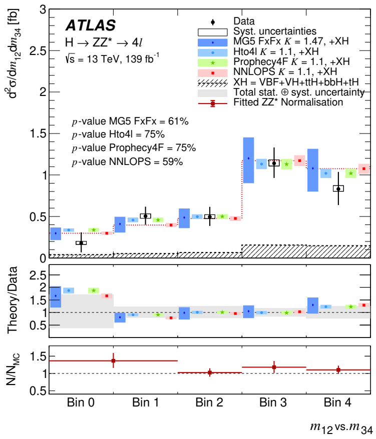

(a)

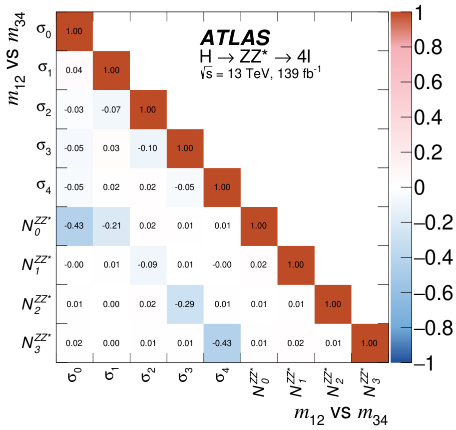

(b)

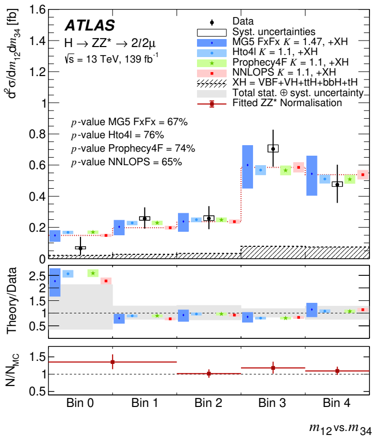

(c)

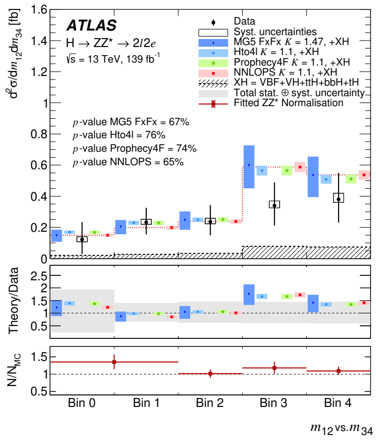

(d)

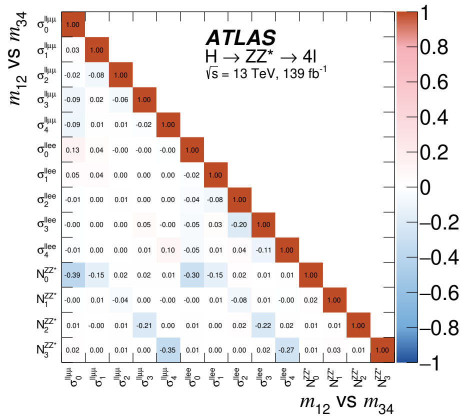

(e)

Figure 6.38: (a) Differential fiducial cross section for the leading vs. subleading Z boson mass m_{12} vs. m_{34}, in (a) inclusive final state and split in (c) $\ell\ell\mu\mu$ and (d) $\ell\ell ee$ final states, along with the corresponding correlation matrix between the measured cross sections and the ZZ^* background normalisation factors ((b) inclusive and (e) splitted final states).

6.7 Preliminary expected results on CP sensitive variables

In this section, the preliminary expected results for the CP-odd angular variables O_2 and O_5 and the Optimal Observables $\mathcal{OO}_{1,jj}(\tilde{c}_{zz} = 1)$ are presented. The expected results of the other CP-odd variable as shown in Appendix B. The expected distributions of these variables in the mass window $105 < m_{4\ell} < 160$ GeV are shown in Figure 6.39. The black dots correspond to the Asimov dataset. The expected cross section value in each bin and the corresponding uncertainty (including systematics) from the Asimov data fit are shown in Tables 6.15 - 6.17. Finally the expected differential cross section for those variables are shown in Figures 6.40 - 6.42. They show the Asimov data results compared with SM prediction from the ggF production provided by NNLOPS. The correlation matrices between the expected cross sections and the ZZ^* background normalisation factors are also reported in all the figures along with the cross section measurements.

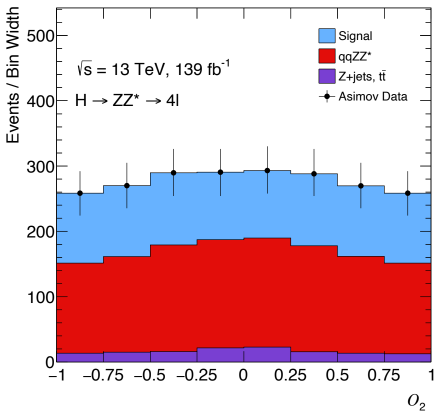

(a) O_2 pre-fit distribution

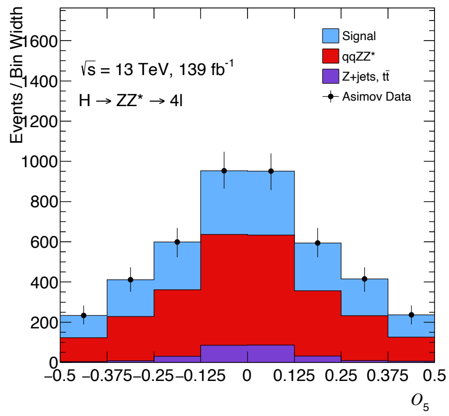

(b) O_5 pre-fit distribution

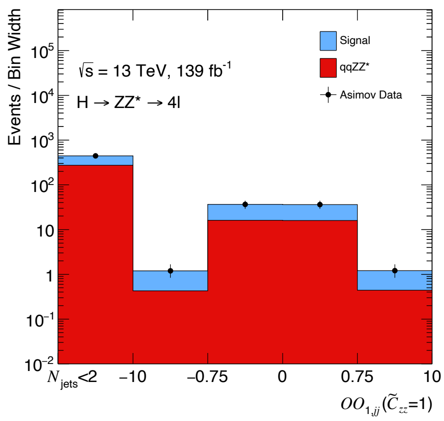

(c) $\mathcal{OO}_{1,jj}(\tilde{c}_{zz} = 1)$ pre-fit distribution

Figure 6.39: The expected (pre-fit) distributions of (a) O_2, (b) O_5 and (c) $\mathcal{OO}_{1,jj}(\tilde{c}_{zz} = 1)$, in the range of $105 < m_{4\ell} < 160$ GeV. The black dots depict pre-fit asimov data while the blue, red and violet areas represent the signal, the ZZ^* background and the reducible background, respectively.

POI	XS $_{\text{inj}}$ [fb]	$\text{XS}^{\text{asimov}}_{\text{fit}}$ [fb]	Rel. Error [%]
σ_{bin0}	0.43	$0.43 \pm 0.10\ ^{+0.02}_{-0.01}$	$\pm 23.2\ ^{+4.6}_{-2.3}$
σ_{bin1}	0.43	$0.43 \pm 0.11\ ^{+0.02}_{-0.01}$	$\pm 25.6\ ^{+4.6}_{-2.3}$
σ_{bin2}	0.43	$0.43 \pm 0.11\ ^{+0.02}_{-0.01}$	$\pm 25.6\ ^{+4.6}_{-2.3}$
σ_{bin3}	0.41	$0.41 \pm 0.10\ ^{+0.02}_{-0.01}$	$\pm 24.4\ ^{+4.9}_{-2.4}$
σ_{bin4}	0.41	$0.41 \pm 0.10\ ^{+0.02}_{-0.01}$	$\pm 24.4\ ^{+4.9}_{-2.4}$
σ_{bin5}	0.43	$0.43 \pm 0.11\ ^{+0.02}_{-0.01}$	$\pm 25.6\ ^{+4.6}_{-2.3}$
σ_{bin6}	0.43	$0.43 \pm 0.11\ ^{+0.02}_{-0.01}$	$\pm 25.6\ ^{+4.6}_{-2.3}$
σ_{bin7}	0.43	$0.43 \pm 0.10\ ^{+0.02}_{-0.01}$	$\pm 23.2\ ^{+4.6}_{-2.3}$

Table 6.15: Expected cross sections in each category of O_2 using the Asimov dataset, assuming an integrated luminosity of $139\,\text{fb}^{-1}$ for $105 < m_{4\ell} < 160$ GeV, with full statistical plus systematic uncertainties.

POI	XS $_{\text{inj}}$ [fb]	$\text{XS}^{\text{asimov}}_{\text{fit}}$ [fb]	Rel. Error [%]
σ_{bin0}	0.216	$0.216^{+0.078}_{-0.066}\ ^{+0.009}_{-0.005}$	$^{+36.1}_{-30.8}\ ^{+4.0}_{-2.1}$
σ_{bin1}	0.359	$0.359 \pm 0.098\ ^{+0.014}_{-0.008}$	$\pm 27.3\ ^{+3.9}_{-2.4}$
σ_{bin2}	0.47	$0.47 \pm 0.11\ ^{+0.02}_{-0.01}$	$\pm 23.4\ ^{+4.0}_{-2.7}$
σ_{bin3}	0.64	$0.64 \pm 0.13\ \pm 0.02$	$\pm 20.3\ ^{+3.7}_{-2.6}$
σ_{bin4}	0.64	$0.64 \pm 0.13\ \pm 0.02$	$\pm 20.3\ ^{+3.7}_{-2.6}$
σ_{bin5}	0.47	$0.47 \pm 0.11\ ^{+0.02}_{-0.01}$	$\pm 23.4\ ^{+4.0}_{-2.7}$
σ_{bin6}	0.359	$0.359 \pm 0.098\ ^{+0.014}_{-0.008}$	$\pm 23.7\ ^{+3.9}_{-2.4}$
σ_{bin7}	0.214	$0.214^{+0.077}_{-0.066}\ ^{+0.008}_{-0.004}$	$^{+36.1}_{-30.8}\ ^{+3.8}_{-2.1}$

Table 6.16: Expected cross sections in each category of O_5 using the Asimov dataset, assuming an integrated luminosity of $139\,\text{fb}^{-1}$ for $105 < m_{4\ell} < 160$ GeV, with full statistical plus systematic uncertainties.

POI	XS $_{\text{inj}}$ [fb]	$\text{XS}^{\text{asimov}}_{\text{fit}}$ [fb]	Rel. Error [%]
σ_{bin0}	2.82	$2.82 \pm 0.29\ \pm 0.11$	$\pm 10.4\ ^{+4.3}_{-3.6}$
σ_{bin1}	0.094	$0.094^{+0.056}_{-0.044}\ ^{+0.007}_{-0.005}$	$^{+59.5}_{-46.9}\ ^{+7.1}_{-5.8}$
σ_{bin2}	0.20	$0.20 \pm 0.10\ \pm 0.03$	$\pm 50.0\ \pm 15.0$
σ_{bin3}	0.20	$0.20 \pm 0.10\ \pm 0.03$	$\pm 50.0\ \pm 15.0$
σ_{bin4}	0.095	$0.095^{+0.056}_{-0.044}\ ^{+0.007}_{-0.006}$	$^{+59.6}_{-47.0}\ ^{+7.4}_{-6.1}$

Table 6.17: Expected cross sections in each category of $\mathcal{OO}_{1,jj}(\widetilde{c}_{zz} = 1)$ using the Asimov dataset, assuming an integrated luminosity of $139\,\text{fb}^{-1}$ for $105 < m_{4\ell} < 160$ GeV, with full statistical plus systematic uncertainties.

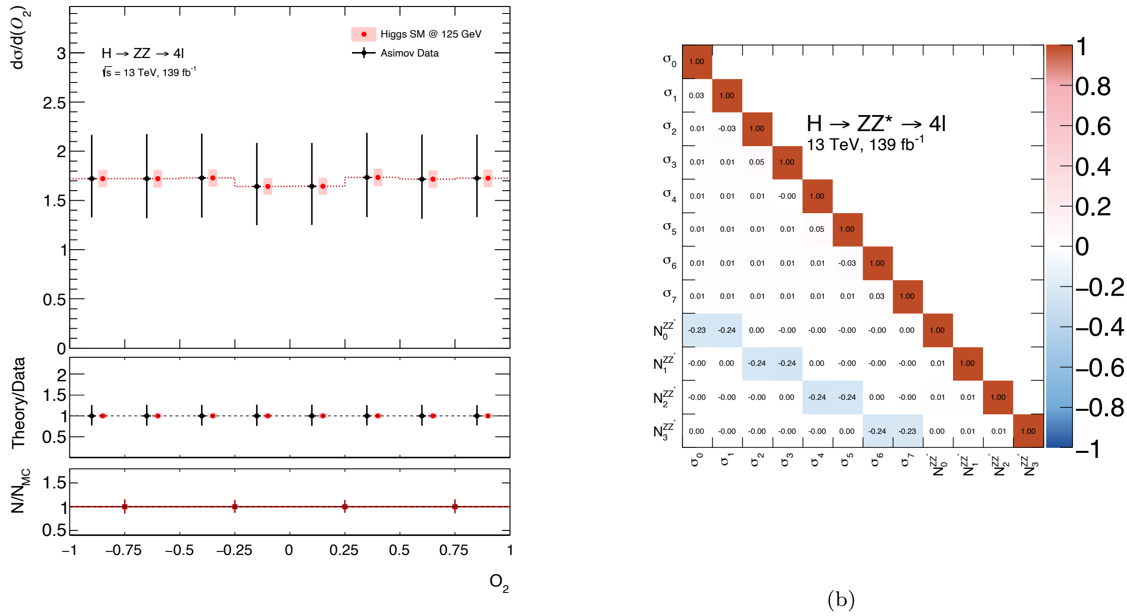

(a) (b)

Figure 6.40: (a) Expected results for differential fiducial cross section for O_2 observable, along with (b) the corresponding correlation matrix between the measured cross sections and the ZZ^* background normalisation factors.

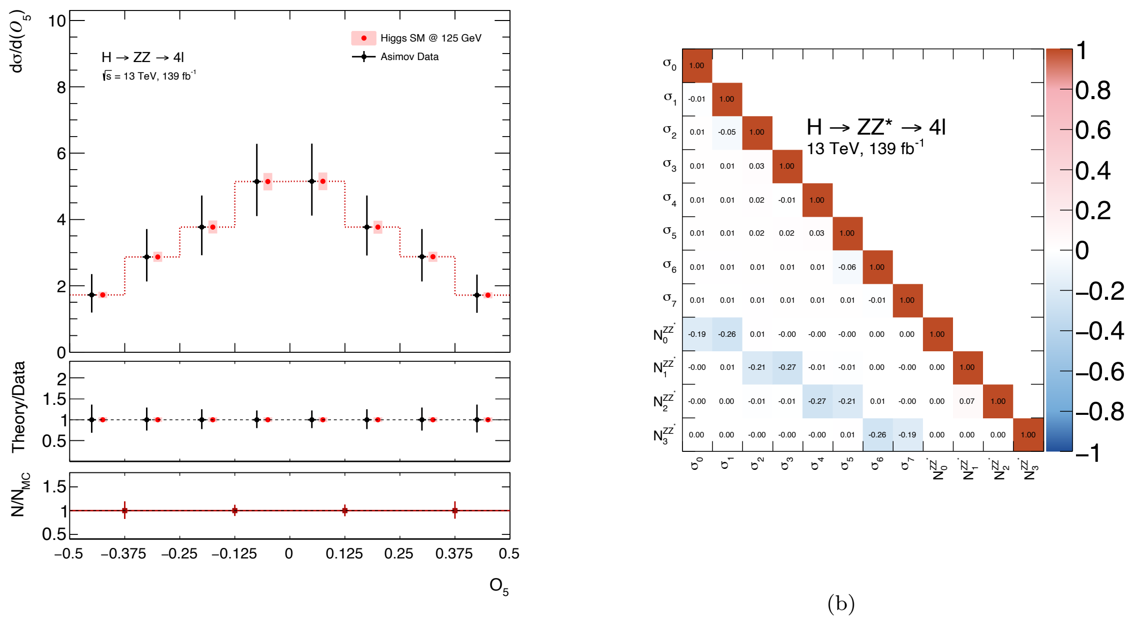

(a) (b)

Figure 6.41: (a) Expected results for differential fiducial cross section for O_5 observable, along with (b) the corresponding correlation matrix between the measured cross sections and the ZZ^* background normalisation factors.

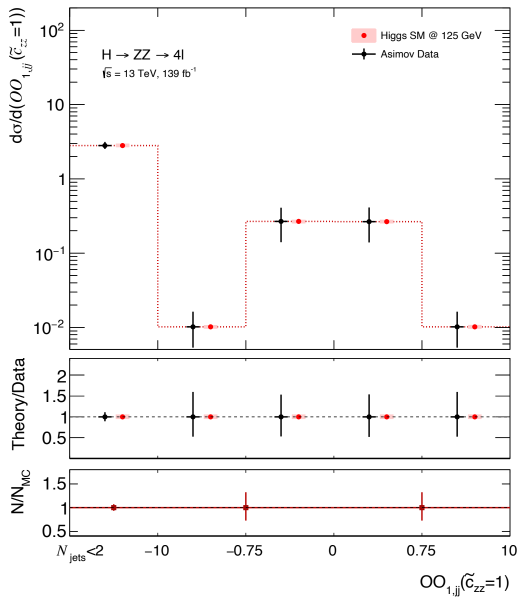

(a)

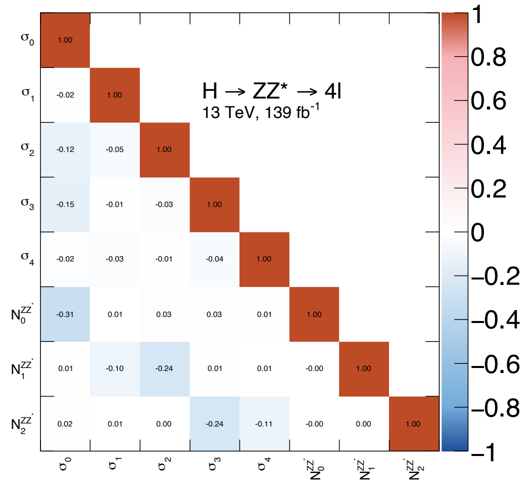

(b)

Figure 6.42: (a) Expected results for differential fiducial cross section for $\mathcal{OO}_{1,jj}(\tilde{c}_{zz} = 1)$ optimal observable, along with (b) the corresponding correlation matrix between the measured cross sections and the ZZ^* background normalisation factors.

6.8 Prospects: VBF Fiducial cross section measurement

A feasibility study has been performed to have a VBF fiducial cross section measurement. The idea is to select the VBF-like signal without applying any further cut on the event selection, but building a PDF able to discriminate the dominant ggF production from the VBF one and also to estimate the ggF contribution itself, as the fit of $m_{4\ell}$ has been used to extract the ZZ^* background in the measurement described in the previous section.

Given that the expected VBF events with the Full Run 2 dataset in the mass window $105 < m_{4\ell} < 160$ GeV are 17.0 ± 0.8 [197], we do not have enough statistics to perform a fiducial differential measurement in this production mode. Anyway, the prospect of this measurement at higher luminosity (300 fb^{-1}with Run 3 and 3000 fb^{-1}with HL-LHC) has been also investigated with the $\mathcal{OO}_{1,jj}(\tilde{c}_{zz} = 1)$ observable in two differential bins.

This study has been performed mainly to evaluate the sensitivity to this kind of measurement, only the ggF and VBF production has been considered as signal (VH, $t\bar{t}H$ and $b\bar{b}H$ are not included) and with only $qqZZ^*$ background process as background ($ggZZ^*$, $Z+$jets, $t\bar{t}$, VVV and $t\bar{t}V$ are not included). Also the systematic uncertainty have not been considered in this test, but their impact is expected to be negligible with respect to the statistical uncertainty due to the low statistics regime.

6.8.1 Signal Extraction

This test has been performed using the $\mathcal{OO}_{1,jj}(\tilde{c}_{zz} = 1)$ observable, defining two bins: $N_{jets} < 2$ and $N_{jets} \geq 2$. This is not a real differential distribution in $\mathcal{OO}_{1,jj}(\tilde{c}_{zz} = 1)$, but it is an inclusive measurement in the phase space in which the variable is defined, namely for events with at least 2 jets.

Two different variables to build the PDF for the fit have been tested: m_{jj} vs. $\Delta\eta_{jj}$ and the Neural Network used as discriminant observable in the 2-jet category for the STXS analysis [197]: NN^{2j}_{VBF}. The m_{jj} vs. $\Delta\eta_{jj}$ template distribution has been built applying cuts on m_{jj} and $\Delta\eta_{jj}$ to maximise the VBF contribution in the bins, in a mass window $115 < m_{4\ell} < 130$ GeV. Figure 6.43 shows the 2D distribution of the ggF signal and VBF signal respectively.

The choice to build a PDF from the m_{jj} vs. $\Delta\eta_{jj}$ is based on the idea to have a PDF related to simple kinematic variables, reducing possible theoretical uncertainties on the estimation and minimising the model dependency. On the other hand, the use of the Neural Network improves the discrimination of the VBF signal from the ggF one, at the cost of a more model dependent measurement.

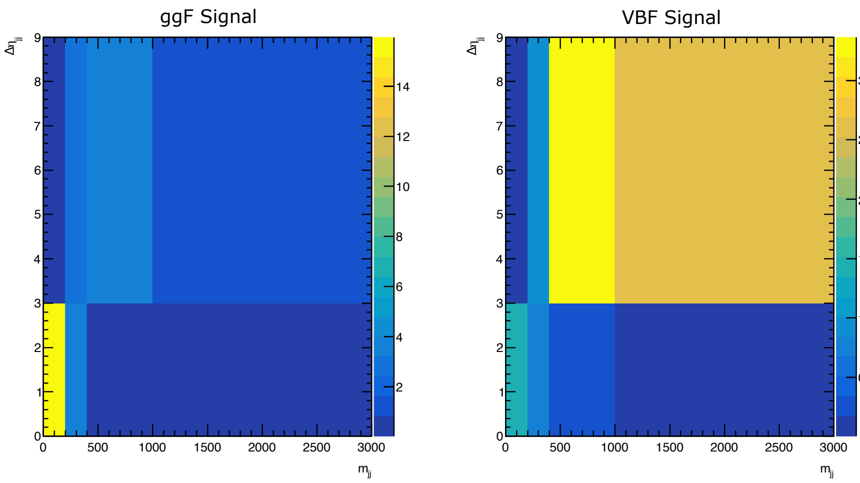

Figure 6.43: 2D events distribution for the ggF signal (*on the left*) and VBF signal (*on the right*) in m_{jj} vs. $\Delta\eta_{jj}$, in a mass region $115 < m_{4\ell} < 130$ GeV.

The number of the expected events $N_{\geq 2\text{ jets}}$ in the bin $N_{jets} \geq 2$, expressed as a function of m_{jj} vs. $\Delta\eta_{jj}$, but is the same function for NN^{2j}_{VBF}, is given by a formula inspired to the one used for the all production mode measurement:

$$N_{i=\geq 2\text{ jets}}(m_{jj}\Delta\eta_{jj}) = \sum_j r_{ij} \cdot (1 + f_i^{\text{nonfid}}) \cdot \sigma_j^{\text{VBF-fid}} \cdot \mathcal{P}_i(m_{jj}\Delta\eta_{jj}) \cdot \mathcal{L} + \tag{6.8.1}$$

$$+ N_i^{\text{ggF-bkg}}(m_{jj}\Delta\eta_{jj}) + N_i^{\text{ZZ-bkg}}(m_{jj}\Delta\eta_{jj}) \tag{6.8.2}$$

where the bin $i = N_{jets} \geq 2$ and j runs over the two bins $N_{jets} < 2$ and $N_{jets} \geq 2$.

The VBF fiducial cross section to extract from the fit is $\sigma_j^{\mathrm{VBF-fid}}$. In this case the signal events are the VBF events. The ggF production represents a background source and its contribution is treated similarly as the ZZ^* background: $N_i^{\mathrm{ggF-bkg}}(m_{jj}\Delta\eta_{jj})$ and $N_i^{\mathrm{ZZ-bkg}}(m_{jj}\Delta\eta_{jj})$. The term $\mathcal{P}_i(m_{jj}\Delta\eta_{jj})$ is the m_{jj} vs. $\Delta\eta_{jj}$ shape used in the fit to extract the VBF cross section and simultaneously estimate the background normalisation.

The number of the expected events $N_{<2\ \mathrm{jets}}$ in the bin $N_{jets} < 2$ is computed using the Equation 6.4.9, performing the fit on $m_{4\ell}$ as in this region VBF events are not expected and there are not enough jets to build an alternative template distribution for the fit.

The measurement is performed with a simultaneous fit on both $N_{jets} < 2$ and $N_{jets} \geq 2$ bins, even if just in the $N_{jets} \geq 2$ bin the VBF fiducial cross section measurement can be really measured.

6.8.2 Floating background normalisations

The ZZ^* background normalisation is estimated from the data (in this case just preliminary results are shown, then the estimation is performed on the Asimov data), as done with the all production mode measurement. An additional bin to the template distribution is added, containing all the events in the sidebands $105 < m_{4\ell} < 115$ GeV and $130 < m_{4\ell} < 160$ GeV to perform this measurement, given that these sidebands are ZZ^* enriched.

The ggF signal instead gives its main contribution in the signal region $115 < m_{4\ell} < 130$ GeV. Its normalisation can also be constrained from data, introducing floating normalisation factors to the ggF contribution in the fit. This method leads to an enhancement of the statistical error, for this reason also the estimation with fixed ggF normalisation factor are reported.

The m_{jj} vs. $\Delta\eta_{jj}$ and NN_{VBF}^{2j} distributions in the bin $N_{jets} \geq 2$ are shown in Figure 6.44. The last bin of the template represents the *sideband-bin* and all the contributions from ggF, VBF and ZZ^* processes are reported together with the full signal distribution. It can be seen that the Neural Network has a better discriminating power with respect to the m_{jj} vs. $\Delta\eta_{jj}$ distribution.

6.8.3 Expected Results

Table 6.18 shows the expected results of the VBF fiducial cross section measurement in the bin $N_{jets} \geq 2$, performing the fit both on m_{jj} vs. $\Delta\eta_{jj}$ and NN_{VBF}^{2j} and both with floating and fixed ggF normalisation factor. The results show that the sensitivity for this measurement is very low. The best sensitivity reached is about 70% and it is obtained performing the fit on the NN_{VBF}^{2j} and extracting the ggF contribution from MC (fixed normalisation factor).

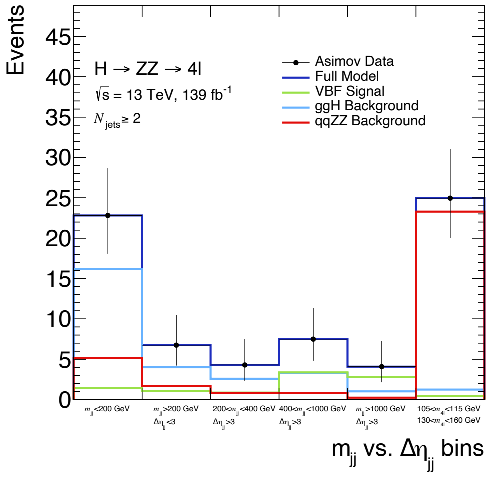

(a) m_{jj} vs. $\Delta\eta_{jj}$ shape

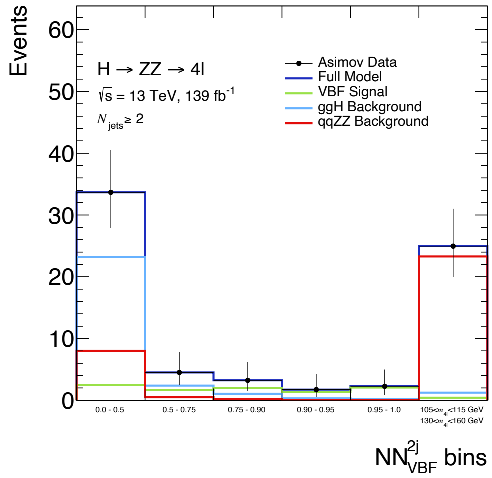

(b) NN^{2j}_{VBF} shape

Figure 6.44: Shape for the bin $N_{jets} \geq 2$ of the a m_{jj} vs. $\Delta\eta_{jj}$ and b NN^{2j}_{VBF} template distributions in the range $115 < m_{4\ell} < 130$ GeV. The last bin of the template represents the *sideband-bin* with all the events in $105 < m_{4\ell} < 115$ GeV and $130 < m_{4\ell} < 160$ GeV.

POI	$\mathrm{XS}^{\mathrm{asimov}}_{\mathrm{fit}}$ [fb]	Relative Error ggF factor float [%]		Relative Error ggF factor fixed [%]	
		Fit on m_{jj} vs. $\Delta\phi_{jj}$	Fit on NN^{2j}_{VBF}	Fit on m_{jj} vs. $\Delta\phi_{jj}$	Fit on NN^{2j}_{VBF}
$\sigma^{\mathrm{VBF}}_{\geq 2\ \mathrm{jets}}$	0.131	$+84.0$ -115	$+77.8$ -114	$+79.4$ -73.3	$+73.3$ -67.2

Table 6.18: Expected results for the Fiducial VBF cross section measurement in the bin $N_{jets} \geq 2$ for different tested configurations.

Prospects on differential cross section measurement

The possibility to perform a differential measurement with higher statistics has been investigated. The study has been performed always on the $\mathcal{OO}_{1,jj}(\tilde{c}_{zz} = 1)$ observable defining two differential bins, besides the underflow bin:

$$[N_{jets} < 2, -10.0, 0.0, 10.0] \tag{6.8.3}$$

Following the same strategy to extract the signal and to estimate the ggF and ZZ^* background, the expected results with enhanced statistics have been estimated, scaling the luminosity up to 300 fb^{-1}and 3000 fb^{-1}. Figure 6.45 shows the profile likelihood fit with the corresponding cross section measurement in the two differential $\mathcal{OO}_{1,jj}(\tilde{c}_{zz} = 1)$ bins at 139 fb^{-1}, 300 fb^{-1}and 3000 fb^{-1}, both fitting m_{jj} vs. $\Delta\eta_{jj}$ and NN^{2j}_{VBF}. The ggF background normalisation is constrained from data by adding one floating normalisation parameter. As for the inclusive study, systematic uncertainties are not considered, even if their impact at higher luminosity could have a larger impact with respect to the Run 2.

As expected, the sensitivity at 139 fb^{-1}is too low to perform this measurement. At Run 3, with 300 fb^{-1}, an improvement of the sensitivity is expected, with a reduction on the

4116 statistical uncertainty of about 30%, then with a sensitivity of 80% of the measurement in
4117 each bin. At 3000 fb^{-1}, the statistical uncertainty in each bin is expected to be reduced of
4118 a further 70%, reaching a sensitivity of 30% at 1σ.

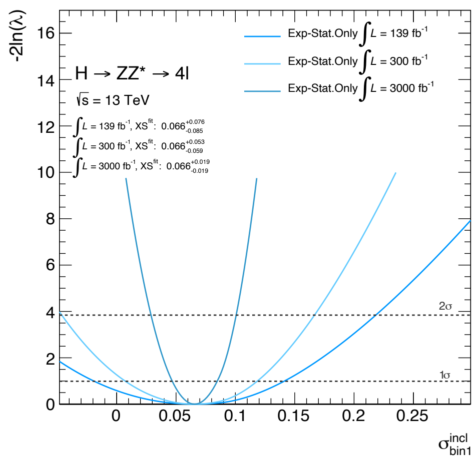

(a) m_{jj} vs. $\Delta\eta_{jj}$ XS fit in Bin 1

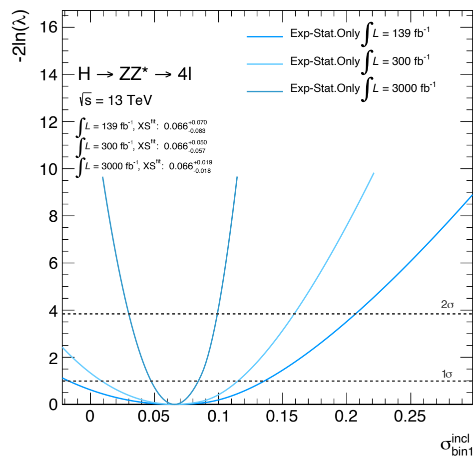

(b) NN_{VBF}^{2j} XS fit in Bin 1

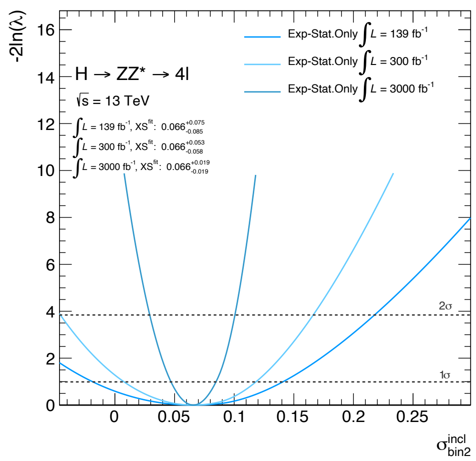

(c) m_{jj} vs. $\Delta\eta_{jj}$ XS fit in Bin 2

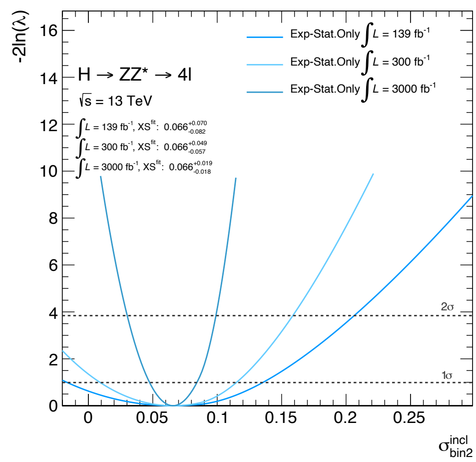

(d) NN_{VBF}^{2j} XS fit in Bin 2

Figure 6.45: Expected results for the fiducial differential VBF cross section measurement in $\mathcal{OO}_{1,jj}(\widetilde{c}_{zz} = 1)$ bins at 139 fb^{-1}, 300 fb^{-1}and 3000 fb^{-1}and for different template fit variable: m_{jj} vs. $\Delta\eta_{jj}$ (a and c) and NN_{VBF}^{2j} (b and d). Only statistical uncertainties have been considered.

Chapter 7

Limits on Beyond Standard Model Physics from $H \to ZZ^* \to 4l$ decay channel

Contents

7.1 Interpretation of the differential cross section measurements

In this section, the interpretation of the results shown in the previous Chapter 6 are presented. The results have been used to constrain possible Beyond Standard Model contact interaction of the Higgs or Z boson with leptons, or non-Standard Model values of the b- and $c-$ quark Yukawa couplings.

7.1.1 Pseudo-Observables

Limits are set on modified Higgs boson interactions within the framework of Pseudo-Observables [15]. In this analysis, the couplings related to the both flavour universal and flavour violating contact-interaction of the Higgs decay are considered as outlined in [30]. The considered scenarios are:

1. **Linear EFT-inspired:** (κ_{ZZ} vs. $\epsilon_{Z\ell(\mathrm{R})}$), where $\epsilon_{Z\ell(\mathrm{L})} = 0.48\ \epsilon_{Z\ell(\mathrm{R})}$ [29], $\epsilon_{Ze(\mathrm{R,L})} = \epsilon_{Z\mu(\mathrm{R,L})}$ and other $\epsilon \to 0$.

2. **Flavor universal contact terms:** ($\epsilon_{Z(\mathrm{R})}$ vs. $\epsilon_{Z(\mathrm{L})}$): where $\epsilon_{Ze(\mathrm{L})} = \epsilon_{Z\mu(\mathrm{L})}$, $\epsilon_{Ze(\mathrm{R})} = \epsilon_{Z\mu(\mathrm{R})}$, $\kappa_{ZZ} = 1$ and other $\epsilon \to 0$.

3. **Flavor non-universal vector contact terms:** ($\epsilon_{Ze(\mathrm{R})}$ vs. $\epsilon_{Z\mu(\mathrm{R})}$), where $\epsilon_{Ze(\mathrm{L})} = \epsilon_{Ze(\mathrm{R})}$, $\epsilon_{Z\mu(\mathrm{L})} = \epsilon_{Z\mu(\mathrm{R})}$, $\kappa_{ZZ} = 1$ and other $\epsilon \to 0$.

4. **Flavor non-universal axial contact terms:** ($\epsilon_{Ze(\mathrm{R})}$ vs. $\epsilon_{Z\mu(\mathrm{R})}$), where $\epsilon_{Z\ell(\mathrm{L})} =$ -$\epsilon_{Z\ell(\mathrm{R})}$, $\kappa_{ZZ} = 1$ and other $\epsilon \to 0$.

Figure 7.1 shows the Feynman diagrams of the process involved in these scenarios, based on the equations derived in Section 1.1.2.3. The contact terms have the same Lorentz structure as the SM term, therefore, the angular distributions are not modified and the contact terms only affect the di-lepton invariant mass spectra. Other Pseudo-Observables affecting the angular distributions, such as $\epsilon^{(CP)}_{ZZ}$, $\epsilon^{(CP)}_{Z\gamma}$ and $\epsilon^{(CP)}_{\gamma\gamma}$, are not considered in this analysis. Assuming the SM values for all but the tested parameters, limits are set on the contact-interaction coupling strength.

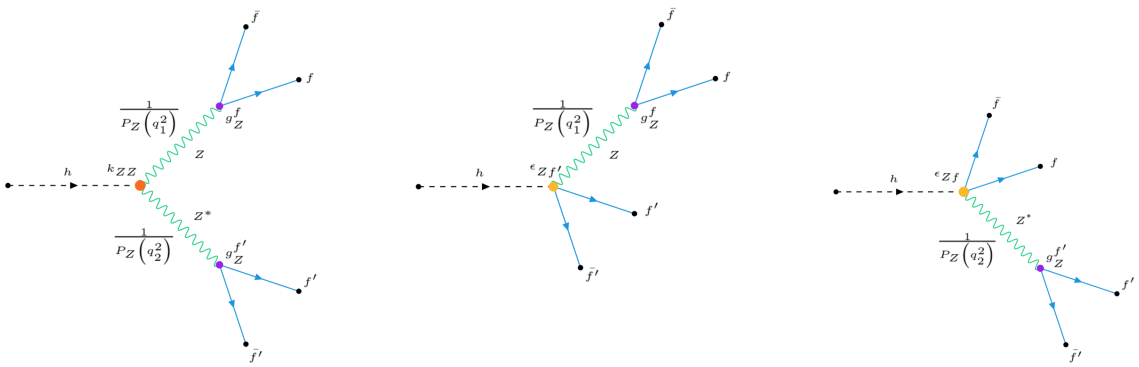

Figure 7.1: Feynman diagrams Pseudo-Observables.

The unfolded observable that is sensitive to modifications and able to probe this contact terms is m_{12} vs. m_{34}.

Figures 7.2-7.3 show some examples of how the m_{12} and m_{34} shape changes for different coupling values. It can be observed that κ_{ZZ} has no impact on the shape modification, given that it only affect the overall normalisation of all $h \to 4\ell$ decays and consequently can only be probed through its effects on the total rates. The contact terms operators, which couple the Higgs to the intermediate boson and two leptons, impact of the shape of the dilepton masses. These could arise via a heavy Z' that is integrated out, or via other mechanisms that might not even involve two intermediate bosons.

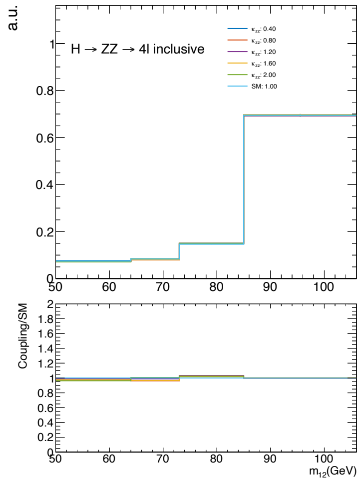

(a) m_{12} in κ_{ZZ}

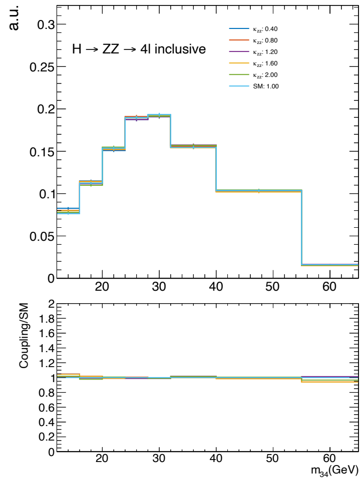

(b) m_{34} in κ_{ZZ}

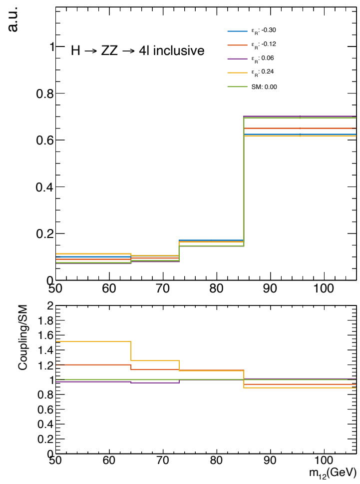

(c) m_{12} in $\epsilon_{Z\ell(\mathrm{R})}$

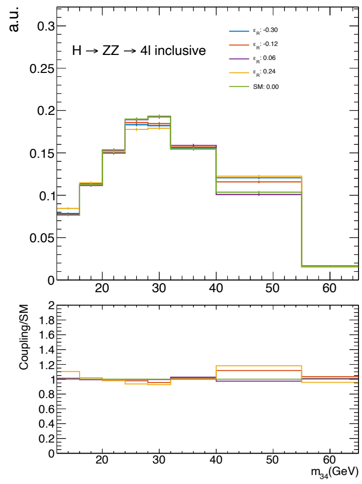

(d) m_{34} in $\epsilon_{Z\ell(\mathrm{R})}$

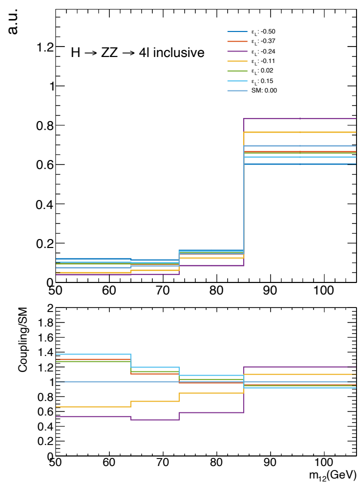

(e) m_{12} in $\epsilon_{Z\ell(\mathrm{R})}$

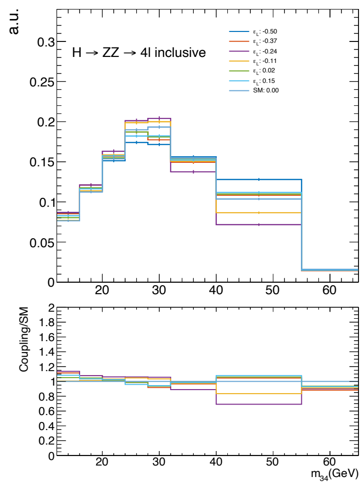

(f) m_{34} in $\epsilon_{Z\ell(\mathrm{R})}$

Figure 7.2: Modification of the m_{12} and m_{34} spectra in $2e2\mu$ final state for different value of κ_{ZZ}, $\epsilon_{Z\ell(\mathrm{R})}$ and $\epsilon_{Z\ell(\mathrm{L})}$ coupling values in inclusive four lepton final state.

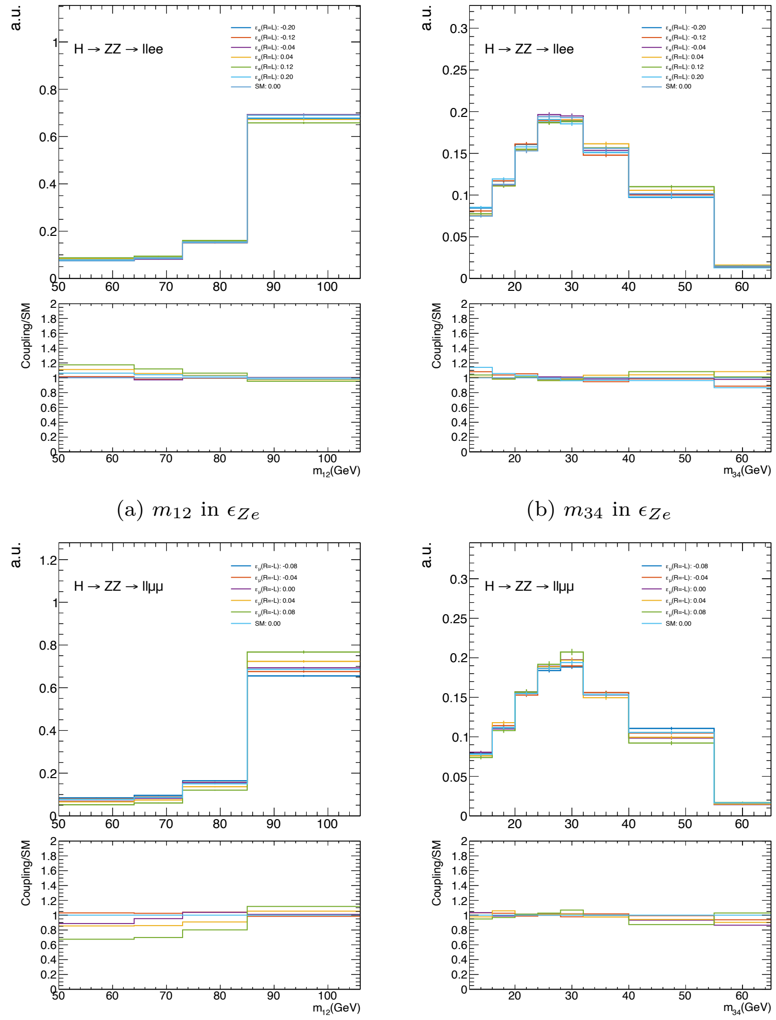

(a) m_{12} in ϵ_{Ze} (b) m_{34} in ϵ_{Ze}

(c) m_{12} in $\epsilon_{Z\mu}$ (d) m_{34} in $\epsilon_{Z\mu}$

Figure 7.3: Modification of the m_{12} and m_{34} spectra for non-universal flavour couplings ϵ_{Ze} (with $\epsilon_{Z\ell(\mathrm{L})}$ = $\epsilon_{Z\ell(\mathrm{R})}$) in $\ell\ell ee$ final state and $\epsilon_{Z\mu}$ (with $\epsilon_{Z\ell(\mathrm{L})}$ = -$\epsilon_{Z\ell(\mathrm{R})}$) in $\ell\ell\mu\mu$ final state.

7.1.1.1 Signal parametrisation and validation

In Section 1.1.2.3 the decay amplitude of an on-shell Higgs boson in four lepton final states has been expressed as function of the POs. If we consider a decay channel $h \to 2e2\mu$, the double differential decay distribution in q_1 (m_{12}) and q_2 (m_{34}) leads to a quadratic polynomial function in k= (k_{ZZ}, ϵ_{ZeL}, $\epsilon_{Z\mu L}$, ϵ_{ZeR}, $\epsilon_{Z\mu R}$), therefore the decay amplitude can be written as a function of the POs as follows:

$$\frac{d^2\Gamma_{h\to 2e2\mu}}{dm_{12}dm_{34}} = \sum_{j\geq i} A_{ij}k_ik_j \tag{7.1.1}$$

The total cross section in each bin of the m_{12} vs. m_{34} distribution can then be parametrised as a quadratic function of the POs. However, the acceptance depending on the coupling value can change this form. The acceptance variation as function of the coupling with respect to the SM expectation has been studied in each bin and it is shown in Figure 7.4. It changes less than 5% across the coupling values. This small variations can be taken into account by directly parametrising the fiducial cross section with a quadratic function.

The fiducial cross section in each bin has been calculated by simulating a grid of coupling values for a given parameter. These values are then fitted with a 2D quadratic function. For the Linear EFT-inspired and universal contact terms scenario, the fit has been performed in the inclusive final state. For the two non-universal lepton flavour scenarios the fit has been done in $\ell\ell ee$ and $\ell\ell\mu\mu$ final states separately.

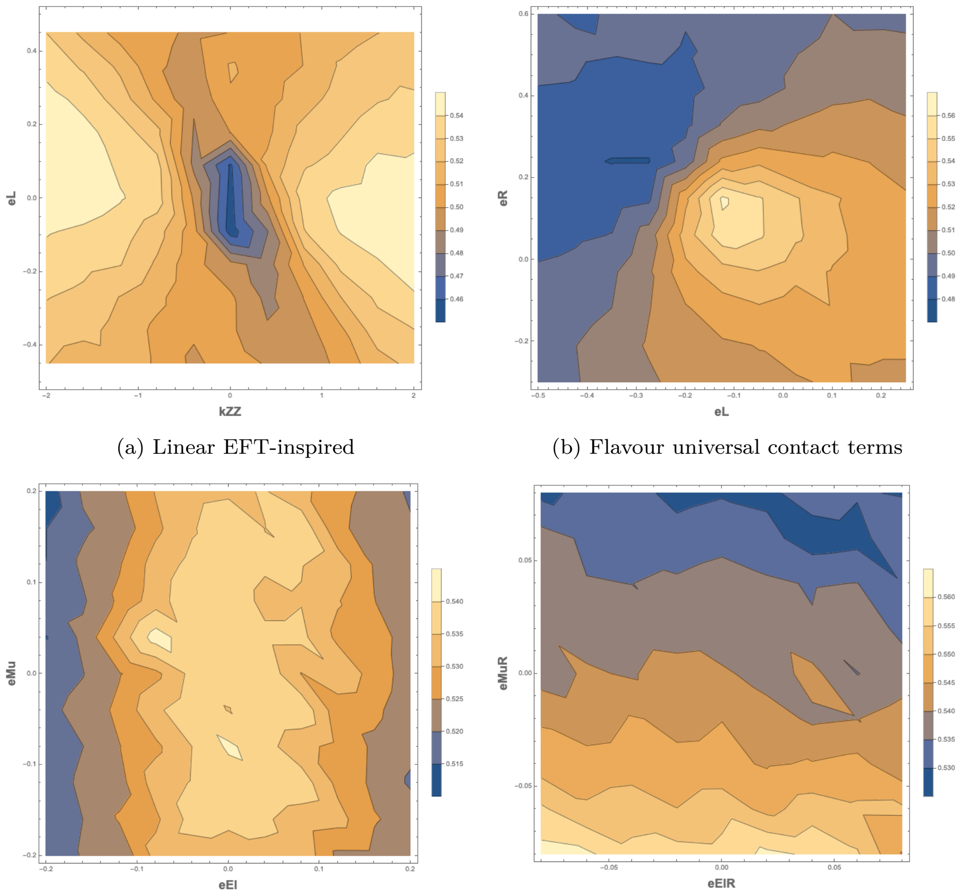

(a) Linear EFT-inspired

(b) Flavour universal contact terms

(c) Flavour non-universal vector contact terms

(d) Flavour non-universal axial contact terms

Figure 7.4: Acceptance variation in the inclusive fiducial phase space as a function of the POs for linear-EFT inspired and flavour universal contact terms scenarios in inclusive final state and flavour non-universal with vector and axial contact terms scenarios in the $\ell\ell ee$ and $\ell\ell\mu\mu$ final states.

Figure 7.5 shows the ratio between the predicted cross section at a given coupling value over the predicted Standard Model cross section as function of one coupling, while scanning the other. Figure 7.6 shows the 2D fit of the cross section with the parabolic function. The equations themselves can be found in Appendix C.1.

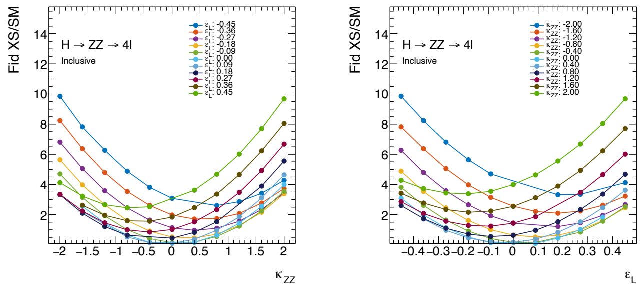

(a) Linear EFT-inspired

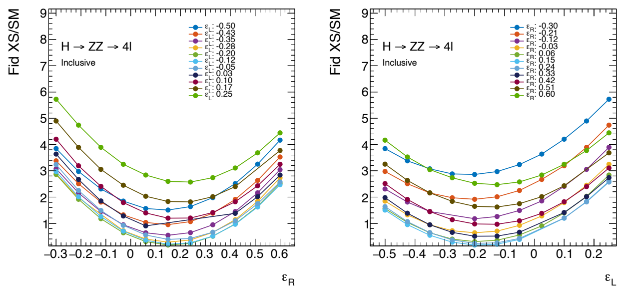

(b) Flavour universal contact terms

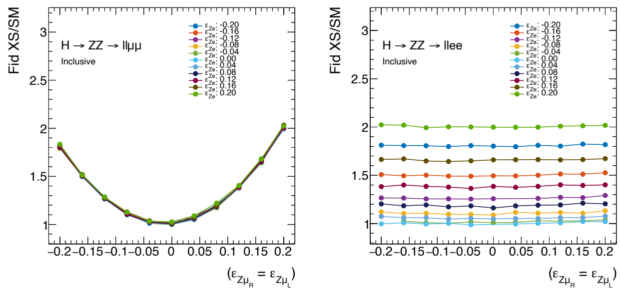

(c) Flavour non-universal vector contact terms

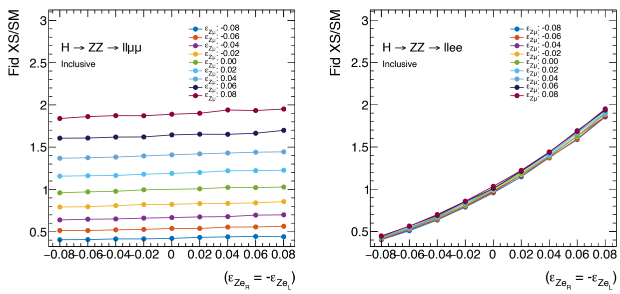

(d) Flavour non-universal axial contact terms

Figure 7.5: Modification of the predicted XS in the inclusive fiducial phase space as a function of the POs for linear-EFT inspired and flavour universal contact terms scenarios in inclusive final state and flavour non-universal with vector and axial contact terms scenarios in the $\ell\ell ee$ and $\ell\ell\mu\mu$ final states.

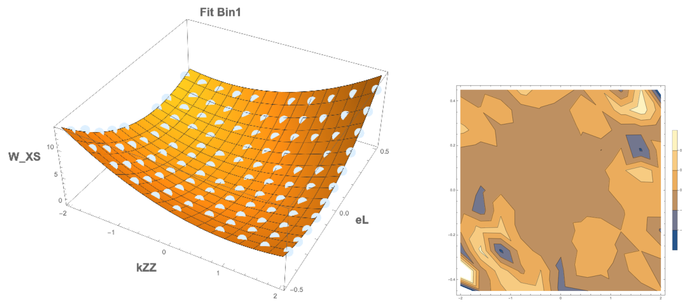

(a) Linear EFT-inspired

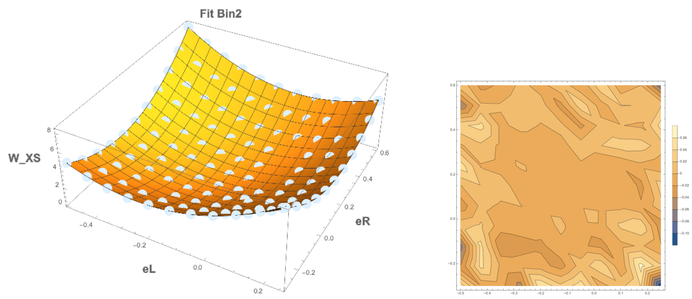

(b) Flavour universal contact terms

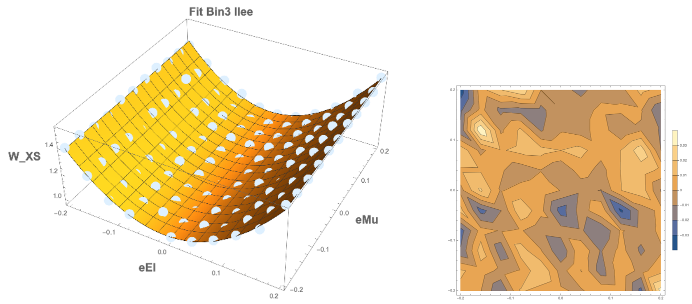

(c) Flavour non-universal vector contact terms

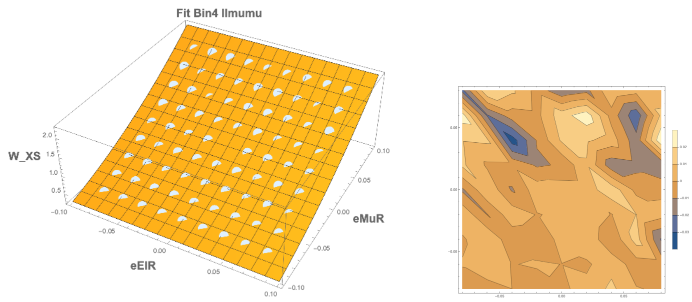

(d) Flavour non-universal axial contact terms

Figure 7.6: Modification of the predicted XS in 2D coupling space in differential bins on m_{12} vs m_{34} as a function of the POs in linear-EFT inspired and flavour universal contact terms scenarios in inclusive final state and flavour non-universal with vector and axial contact terms scenarios in the $\ell\ell ee$ and $\ell\ell\mu\mu$ final states. White dots are the Montecarlo points, while the orange surface is the fitted 2D quadratic function. The fit residuals are shown on the right plots.

In the lepton flavour violation scenarios the different coupling values only impact the cross section in the final states in which the sub-leading lepton pair has the same flavour as the anomalous contact coupling. Different $\epsilon_{Z\mu}$ change the cross sections in the $\ell\ell\mu\mu$ decay channel, but ϵ_{Ze} has no impact on this final state.

To extract the expected exclusion limits on the couplings in each scenario, the parametrisation of the cross sections are incorporated into the likelihood. The detail of the statistical analysis are described in the Section 7.1.1.2.

To check the validity of the parameterisation, additional points are generated around the expected 68% and 95% limits. For these, the expected exclusion is calculated using the parametrised function ($\mathrm{NLL}(\mathrm{xs}_{\mathrm{param}})$) and the unfolded results for each simulated point ($\mathrm{NLL}(\mathrm{xs}_{\mathrm{MC}})$). For all interpretations the difference between the two methods has been evaluated:

$$\Delta\mathrm{NLL} = \frac{\mathrm{NLL}(\mathrm{xs}_{\mathrm{param}}) - \mathrm{NLL}(\mathrm{xs}_{\mathrm{MC}})}{\mathrm{NLL}(\mathrm{xs}_{\mathrm{param}})} \tag{7.1.2}$$

and it results $< 5\%$, as shown in Figure 7.7. Figure 7.8 shows the simulated points around the expected 68% and 95% limits for the Linear-EFT inspired and flavour universal contact scenarios.

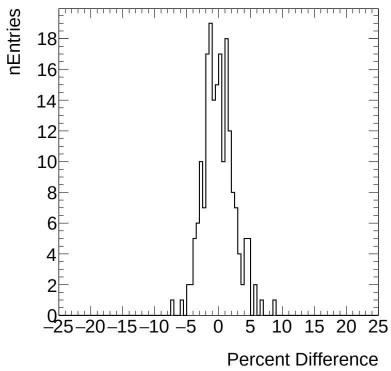

Linear EFT-inspired

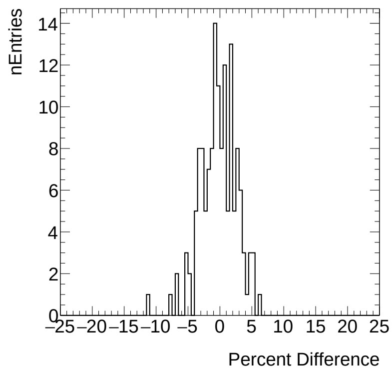

Flavour universal contact terms

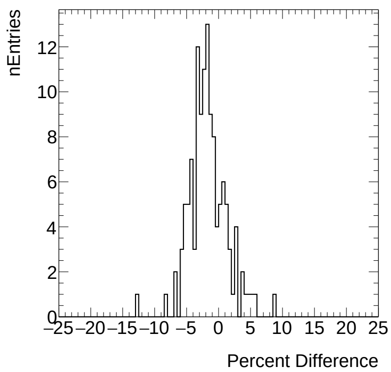

Flavour non-universal vector contact terms

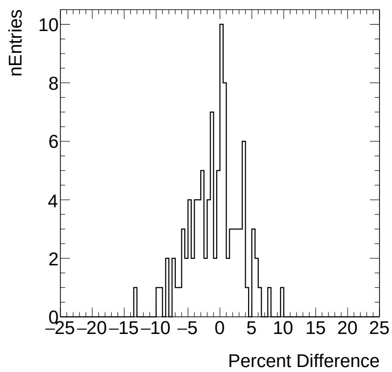

Flavour non-universal axial contact terms

Figure 7.7: Percent difference between the two exclusion methods for all the interpretation scenarios.

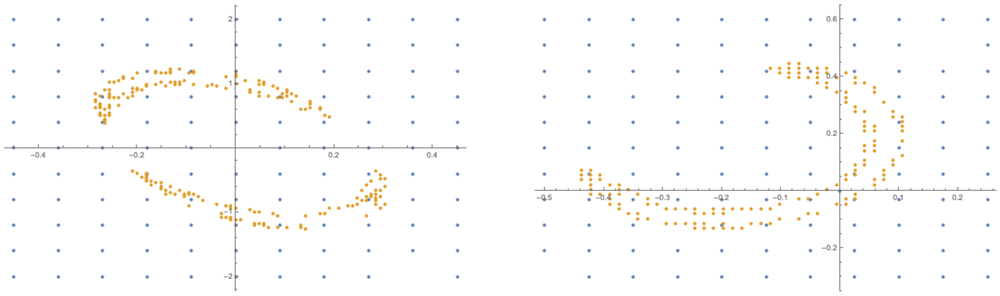

Figure 7.8: Generated point around the expected 68% and 95% limits for the Linear-EFT inspired and flavour universal contact term scenarios.

7.1.1.2 Statistical Analysis and Coverage Studies

The cross section parametrisation is implemented in the likelihood function in Equation 6.4.20 through the cross sections σ_j^{fid} in Equation 6.4.9. The new Parameters of Interest (POI) are the Pseudo-Observables (which will be referred to simply as general κ in this section for simplicity).

The profile likelihood ratio is used as statistical test, which is always computed with respect to a given hypothesis (corresponding to the denominator in the Equation 6.4.21). The profile likelihood ratio is computed with respect to the best fit value from the parametrised model with κ the couplings $\sigma(\hat{\kappa})$:

$$-2\ln\lambda = -2\ln\frac{\mathcal{L}(\sigma(\kappa),\hat{\hat{\theta}}(\kappa))}{\mathcal{L}(\sigma(\hat{\kappa}),\hat{\theta})} \;. \tag{7.1.3}$$

The double-differential cross section measurements in m_{12} vs m_{34} are performed in five m_{12} vs m_{34} bins, which are then mapped to an exclusion plane in 2 coupling dimensions (2 POI) to determine the 68% and 95% confidence level interval in the two couplings under investigation in a given scenario.

The profile likelihood ratio method relies on the assumption that the quantity $-2\ln\lambda$ behaves as a χ^2 distribution, and the number of degrees of freedom (DOF) is given by the number of POI that we are fitting. In this case, it should behave as a χ^2 distribution with two degrees of freedom.

To validate this assumption, $\sim$10000 toy datasets have been generated at the Standard Model point ($\kappa = 1$ and ϵ=0) and then fitted to extract the corresponding coupling values and check the coverage. Figure 7.9 show the results of the coverage test. The 2D plots show the distribution of the toy results distributed in the 2D coupling phase space together with the expected confidence level at 68% and 95%. The distribution of the $-2\ln\lambda$ is also reported with a χ^2 fit function to check the number of degrees of freedom.

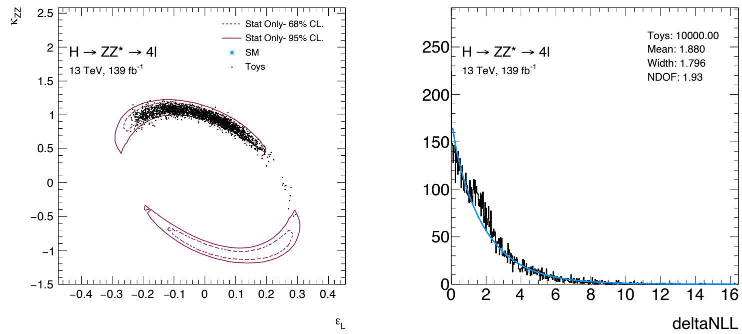

(a) Linear EFT-inspired

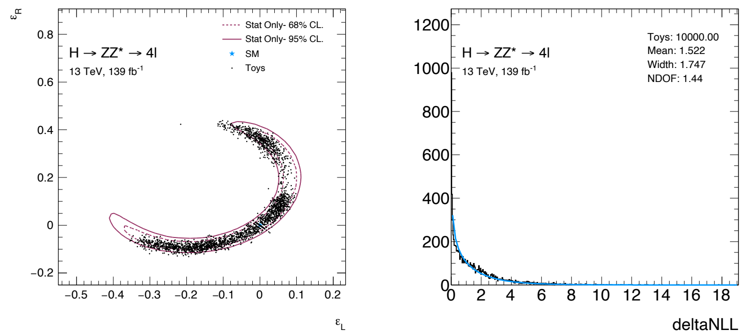

(b) Flavour universal contact terms

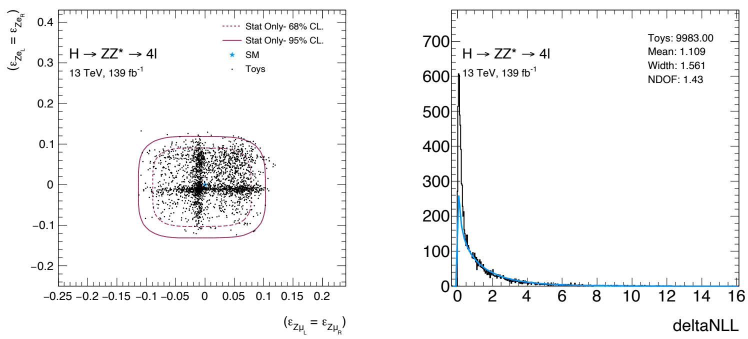

(c) Flavour non-universal vector contact terms

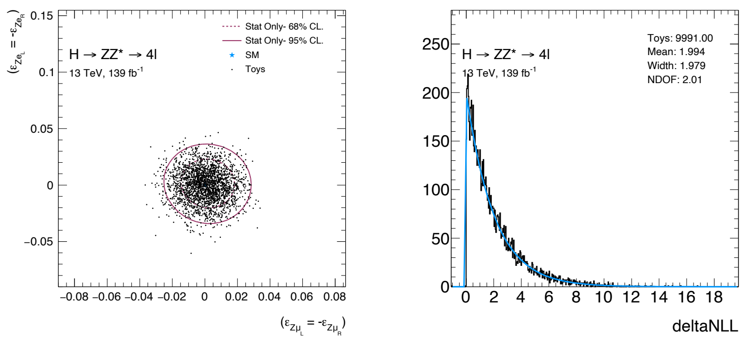

(d) Flavour non-universal axial contact terms

Figure 7.9: The right plots show the 2D distribution of the toys generated at SM point together with the expected confidence level at 68% and 95%. The left plots show the distribution of the $-2\ln\lambda$ with a χ^2 fit function to check the number of degrees of freedom.

It can be seen that for some scenarios the fitted number of degrees of freedom is far from the expected value of 2, and the distribution of the fitted coupling points in the 2D phase space is not uniform as expected. These effects are related to the model used for the cross section parametrisation. For example in the flavour non-universal vector contact term scenario, the cross section model in Figure 7.5c shows a minimum when the Beyond Standard Model cross section is equal to the Standard Model one. This means that all the downward fluctuations of the data cannot be absorbed by the parametrisation, and all the toys with cross section values below the SM expectation, provide coupling values close to the minimum of the model. All the points in Figure 7.9c accumulate around $\epsilon_{Ze} = 0$ and $\epsilon_{Z\mu} = 0$.

An alternative statistical approach has been used to provide the limits on the POs which is able to deal with the downward fluctuation of the data and respect the coverage and the asymptotic approximation.

The profile likelihood ratio is computed with respect to the best fit value from the cross section measurements in m_{12} vs m_{34} bins $\hat{\sigma}$:

$$-2\ln\lambda = -2\ln\frac{\mathcal{L}(\sigma(\kappa),\hat{\hat{\theta}}(\kappa))}{\mathcal{L}(\hat{\sigma},\hat{\theta})}\ . \tag{7.1.4}$$

The conditional fit (numerator) is the same as the previous approach. But the unconditional fit (denominator) is now computed to extract the cross sections from m_{12} vs m_{34} distribution and not more the couplings κ. In this case, the POIs are the 5 cross sections in m_{12} vs m_{34} bins for the lepton flavour universal scenarios, and 10 POIs for the lepton flavour non-universal scenarios given that the measured is performed in the two final states $\ell\ell\mu\mu$ and $\ell\ell ee$. In this case, the profile likelihood ratio should behaves as a χ^2 distribution with 5 or 10 degrees of freedom.

Also in this case, ~10000 toy datasets have been generated at the Standard Model point ($\sigma_i = \sigma_i^{\mathrm{exp}}$) and then fitted to extract the corresponding cross section values and check the coverage.

Figure 7.10 show the distribution of the $-2\ln\lambda$ fitted with a χ^2 function to check the number of degrees of freedom. It can be seen that the number of degrees of freedom is close to the expected values. The number of DOF obtained from these fits in all the scenarios have been used to calibrate the limits in the exclusion plots. The number of degrees of freedom obtained with the two approaches are summarised in Table 7.1.

After adjusting the number of DOF, a further check of coverage has been done, given that in this case the toys generated in the cross section phase space cannot be mapped to the coupling phase space. To check the coverage in the coupling space, toy datasets have been generated at each couple of coupling value $(PO1, PO2)$. A negative log-likelihood distribution has been built for each toy dataset and an exclusion area at the point $(PO1, PO2)$ has been computed from the integral of the NLL distribution with values greater than the NLL obtained from the usual conditional fit $-2\ln\mathcal{L}(\sigma(\kappa),\hat{\hat{\theta}}(\kappa))$.

Figure 7.11 show an example of this check performed on the Linear-EFT inspired sce-

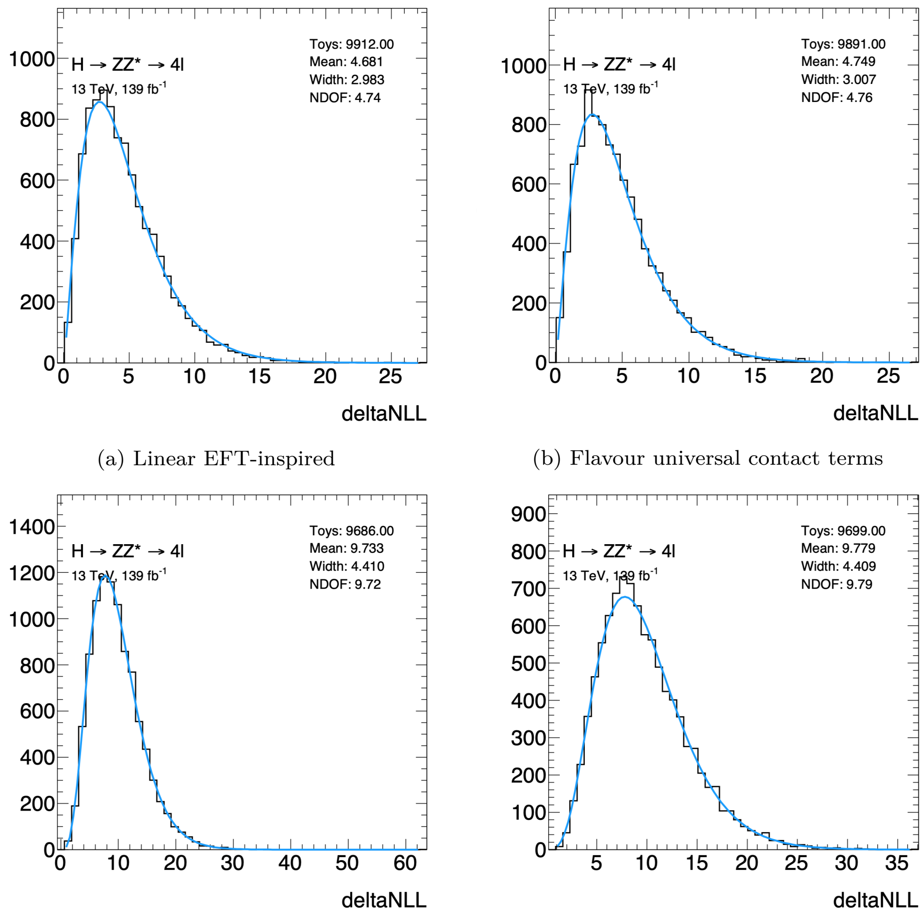

(a) Linear EFT-inspired

(b) Flavour universal contact terms

(c) Flavour non-universal vector contact terms

(d) Flavour non-universal axial contact terms

Figure 7.10: Distribution of the $-2\ln\lambda$ of the toys generated at SM point with a χ^2 fit function to check the number of degrees of freedom.

Scenario	#DOF PO model	#DOF XS measurements
Linear - EFT inspired	1.93	4.74
LFU contact term	1.44	4.76
LFV vector contact term	1.43	9.72
LFV axial contact term	2.01	9.79

Table 7.1: Number of DOF obtained from toys with the two statistical approaches for the Pseudo-Observable scenarios.

nario. The blue line correspond to the 68% and 95% CL obtained from the profile likelihood fit and the orange are the CL obtained from the percentage of toys excluded (32% and 5% respectively), and they match. Examples of the NLL distribution at given points ($PO1, PO2$) with the NLL value from the conditional fit (red line) are also reported. This further test

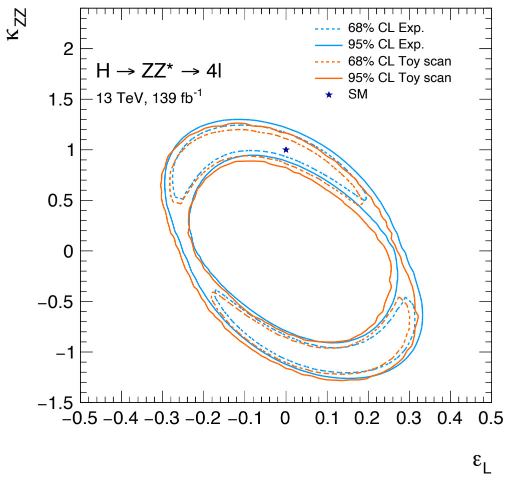

(a) Linear EFT-inspired toy scan

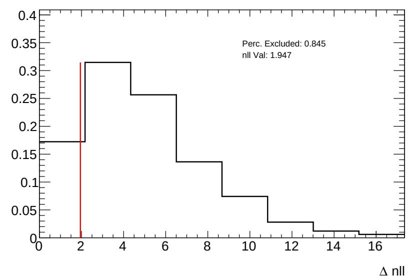

(b) NLL toy in $\kappa_{ZZ} = 1.02, \epsilon_L = -0.1$

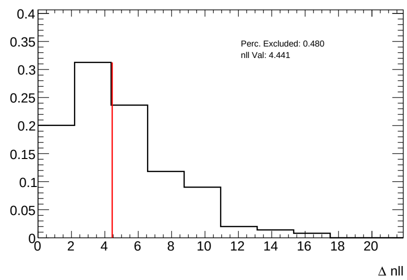

(c) NLL toy in $\kappa_{ZZ} = 0.9, \epsilon_L = 0$

Figure 7.11: a 2D toy scan performed generating toys in a grid of 50x50 points (κ_{ZZ}, ϵ_L). The blue line correspond to the 68% and 95% CL obtained from the profile likelihood fit and the orange are the CL obtained from the percentage of toys excluded (32% and 5% respectively). NLL distribution in b ($\kappa_{ZZ} = 1.02, \epsilon_L = -0.1$) and c ($\kappa_{ZZ} = 0.9, \epsilon_L = 0$) with the NLL value from the conditional fit (red line)

validate the respect of the asymptotic approximation of the second approach.

7.1.1.3 Systematics

The impact of the systematics was investigated by varying the renormalization and factorization scale in Madgraph. These variation are approximately the same across all coupling values across all bins sensitive to modification. Examples of the systematics for different scenarios are shown in Figure 7.12.

These systematics modify the production modes, therefore, we can apply this as a flat systematic for each bin of m_{12} versus m_{34}. However, as the MC is at NLO accuracy, the derived scale variation are significantly large. Instead, we choose to apply the Higgs systematics recommended by the LHCXSWG as the theoretical uncertainty as they are calculated at a higher order and have an approximately 5% impact across the mass spectrum.

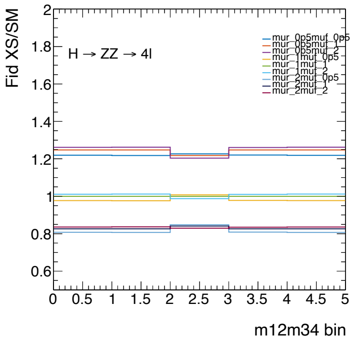

Linear EFT-inspired

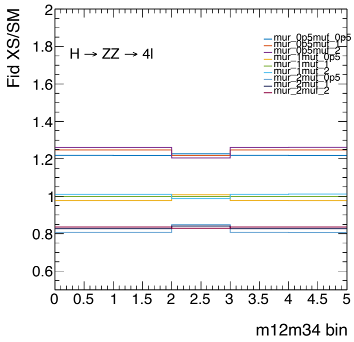

Flavour universal contact terms

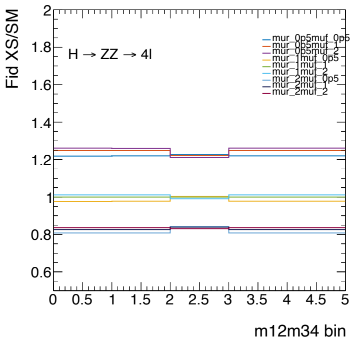

Flavour non-universal vector contact terms

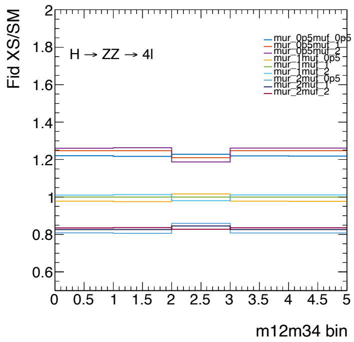

Flavour non-universal axial contact terms

Figure 7.12: Systematic variations for all the interpretation scenarios.

7.1.1.4 Results

In this section, the expected and observed results are reported with both statistical approaches described in the previous section. They are shown in Figure 7.13 and in all the plots the p-value is reported. It represents the probability of compatibility between the data and the m_{12} vs m_{34} prediction corresponding to the best-fit values of POs, in each scenario. It is computed from the unconditional fits performed with the two approaches: the "PO model" approach provides the best-fit values of POs instead the "XS measurement" approach provides the best-fit of the cross sections, then:

$$p\text{-value} = \int_{\textsc{nll}(\hat{\sigma^{\text{obs}}})}^{\infty} \chi^2(\textsc{nll})\, \mathrm{d}\textsc{nll} \quad \text{where} \quad \textsc{nll} = -2\ln\frac{\mathcal{L}(\sigma(\hat{\kappa}),\hat{\theta})}{\mathcal{L}(\hat{\sigma},\hat{\theta})} \tag{7.1.5}$$

In this way, the exclusion limits of the "XS measurement" approach ($\textsc{nll}_\sigma$) and the exclusion limits of the "PO model" ($\textsc{nll}_\kappa$) can be related given that the two negative log-likelihood are related:

$$\mathrm{CL}(\textsc{nll}_\sigma) = p\text{-value} \times \mathrm{CL}(\textsc{nll}_\kappa) \;\Rightarrow\; \frac{\mathcal{L}(\sigma(\kappa),\hat{\hat{\theta}}(\kappa))}{\mathcal{L}(\hat{\sigma},\hat{\theta})} = \frac{\mathcal{L}(\sigma(\hat{\kappa}),\hat{\theta})}{\mathcal{L}(\hat{\sigma},\hat{\theta})} \times \frac{\mathcal{L}(\sigma(\kappa),\hat{\hat{\theta}}(\kappa))}{\mathcal{L}(\sigma(\hat{\kappa}),\hat{\theta})} \tag{7.1.6}$$

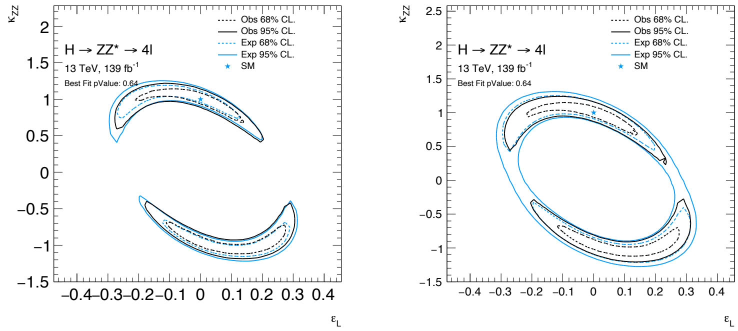

(a) Linear EFT-inspired

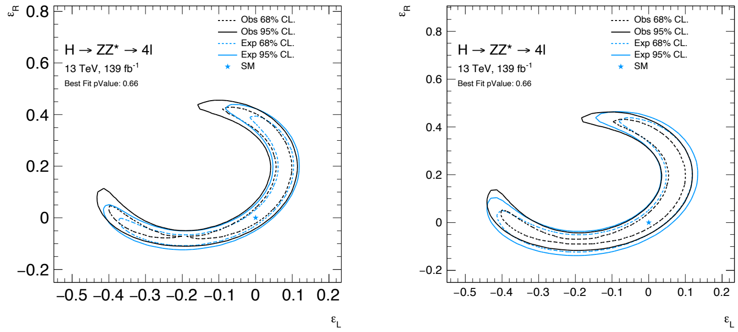

(b) Flavour universal contact terms

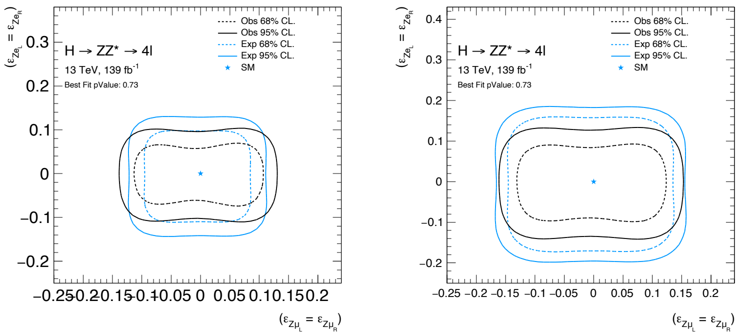

(c) Flavour non-universal vector contact terms

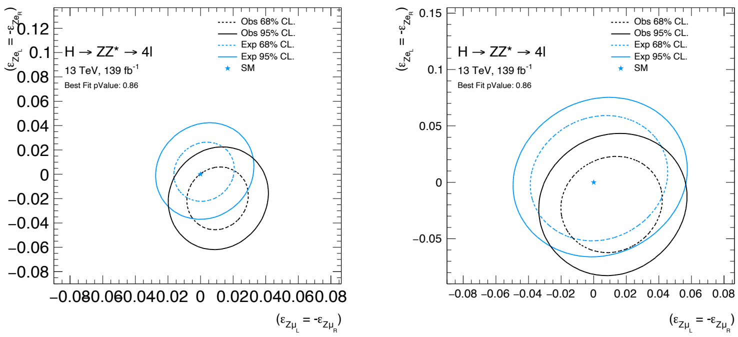

(d) Flavour non-universal axial contact terms

Figure 7.13: Observed (black line) and expected (blue line) exclusion plots for the four scenarios with the two statistical approaches: "PO model" on the right and "XS measurement" on the left. The dashed line represents the 68% CL and the continuous line the 95% CL.

The final results have been provided in the "PO model" approach, given that it provides limits to the best fit of the POs, which is a BSM measurement of the couplings, together with the p-value with respect to the data. Figure 7.14 shows the observed results. The corresponding 95% confidence intervals for each of the parameters are listed in Table 7.2.

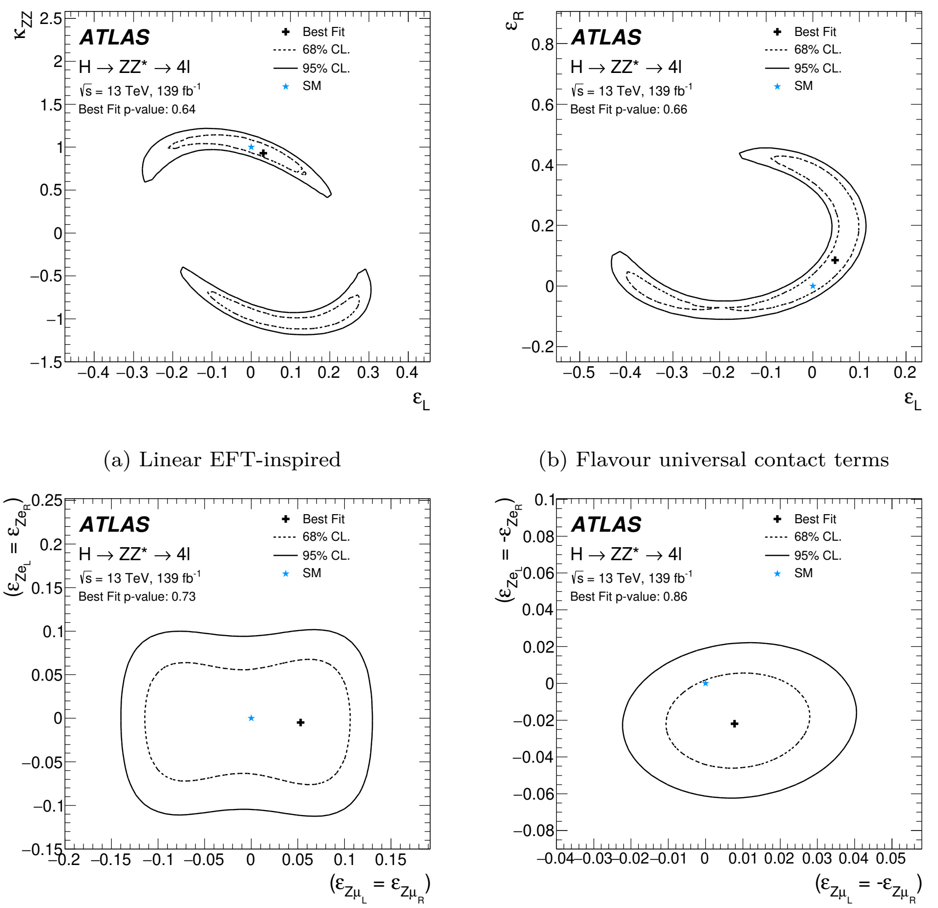

(a) Linear EFT-inspired

(b) Flavour universal contact terms

(c) Flavour non-universal vector contact terms

(d) Flavour non-universal axial contact terms

Figure 7.14: Observed exclusion plots for the four scenarios. The dashed line represents the 68% CL and the continuous line the 95% CL.

Further checks: profiled Asimov test

The observed exclusion limits in Section 7.1.1, based on the profile likelihood ratio test, shows different shapes with respect to the expected limits. For example, in the universal contact terms scenario, the 68% CL shows a discontinuity for coupling value (ϵ_L, ϵ_R) around (-0.20,-0.05). To verify that this effect is due to the statistical fluctuations, Asimov datasets have been generated with the observed cross sections and several checks have been done on the bins with the most significant fluctuations. We expect that the effect of these fluctuations is linked to the quadratic model used to parametrise the cross section as function of the

Interpretation	Parameter best-fit value	95% confidence interval
EFT-inspired	$\epsilon_L = 0.03$	$[-0.25, 0.17]$
	$\kappa_{ZZ} = 0.93$	$[0.51, 1.16]$
Flavour non-universal vector	$\epsilon_{Ze} =$ -0.005	$[-0.097, 0.082]$
	$\epsilon_{Z\mu} = 0.054$	$[-0.131, 0.114]$
Flavour non-universal axial-vector	$\epsilon_{Ze} =$ -0.022	$[-0.056, 0.012]$
	$\epsilon_{Z\mu} = 0.008$	$[-0.016, 0.033]$

Table 7.2: Confidence intervals for the scenarios considered in the Pseudo-Observables framework. Based on the observed 2D exclusion contours, 1D exclusion intervals are provided for the EFT-inspired, flavour non-universal vector, and flavour non-universal axial-vector scenarios. The observed limits are calculated while profiling the other parameters of interest. For the EFT-inspired interpretation, the limits are derived assuming $\kappa_{ZZ} \geq 0$. This constraint has no impact on the limit as the analysis is not sensitive to the sign of this parameter.

coupling values, making them more or less probable, depending on the observed cross section values.

Looking at the cross section results in the universal contact term scenario in Table 7.3, the observed cross section in bin 1 has been chosen for this test given that it is 29% higher than the expected. Three different asimov datasets have been generated, changing the value of this injected cross section from the expected cross section value to the 29% higher. The injected cross section values chosen are then 1, 1.2, 1.29 times the expected value. The results are shown in Figure 7.15. The fluctuations of the cross section measurements in this bin result in the break of 68% CL for the coupling values $(\epsilon_L, \epsilon_R) \sim (-0.20., -0.05)$ for which the model shows a minimum (Figure 7.17 - on the left). Similar effect can be seen in the Linear-EFT scenario (Figure 7.16), in which we have miss the 68% CL around the couplings values corresponding to a minimum of the model (Figure 7.17 - on the right).

This test has been done also in the non-universal scenarios. Looking at the cross sections in Table 7.4, the one in bin 3 has been used for the test, because it is 42% lower in the $\ell\ell ee$ final state than the expected. As for the flavour universal contact term scenario, three asimov datasets have been generated, injecting a cross section in bin 3 equal to 1, 0.8, 0.58 times the expected value and the results are shown in Figure 7.18 and Figure 7.19. In this case the fluctuations of the cross sections result in a shift of the exclusion limits in the axial scenario, and in a change of the ϵ_{Ze} limit in the vector case, due to the asymmeric shape of the model in the first case (Figure 7.20 - on the top) and to the parabolic behaviour around the SM value in the second case (Figure 7.20 - on the bottom). In these scenarios, the check has been done also changing the bin 3 cross section in $\ell\ell\mu\mu$ final state, that is 19% higher than the expected, and the exclusion limits change in the opposite way with respect to the previous case.

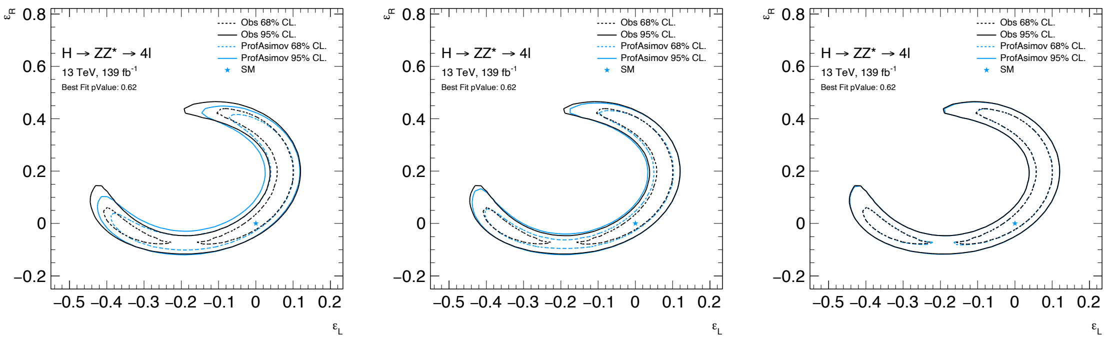

Figure 7.15: Observed exclusion limits (*black lines*) compared with ones obtained from the asimov dataset (*blue lines*) generated with $\sigma_{bin1_{incl}}$ equal to 1 (*on the left*), 1.2 (*in the center*), 1.29 (*on the right*) times the expected value, and the others XS equal to the SM value, in the universal contact terms scenario.

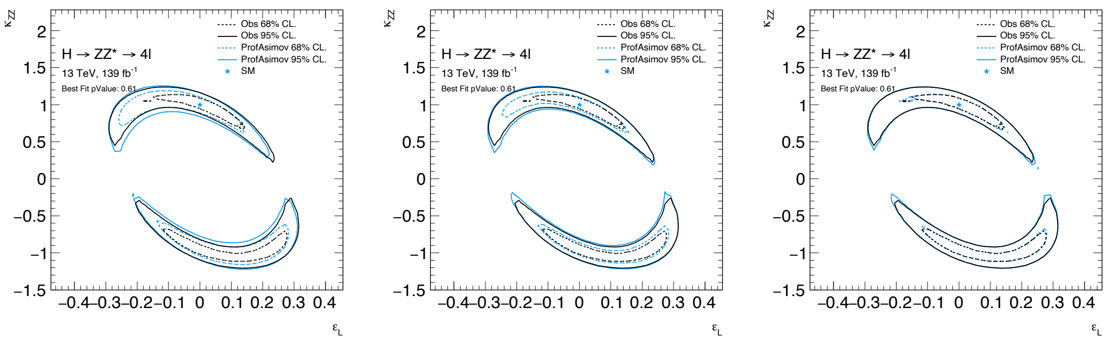

Figure 7.16: Observed exclusion limits (*black lines*) compared with ones obtained from the asimov dataset (*blue lines*) generated with $\sigma_{bin1_{incl}}$ equal to 1 (*on the left*), 1.2 (*in the center*), 1.29 (*on the right*) times the expected value, and the others XS equal to the SM value, in the Linear-EFT scenario.

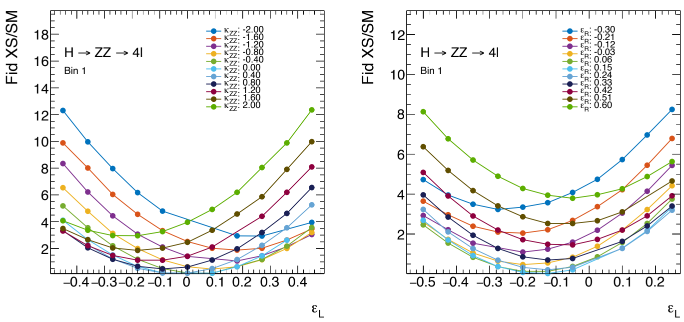

Figure 7.17: Modification of the predicted cross section in bin1 of m_{12} vs. m_{34} distribution as function of the ϵ_L for Linear-EFT (*on the left*) and universal contact terms (*on the right*) scenarios.

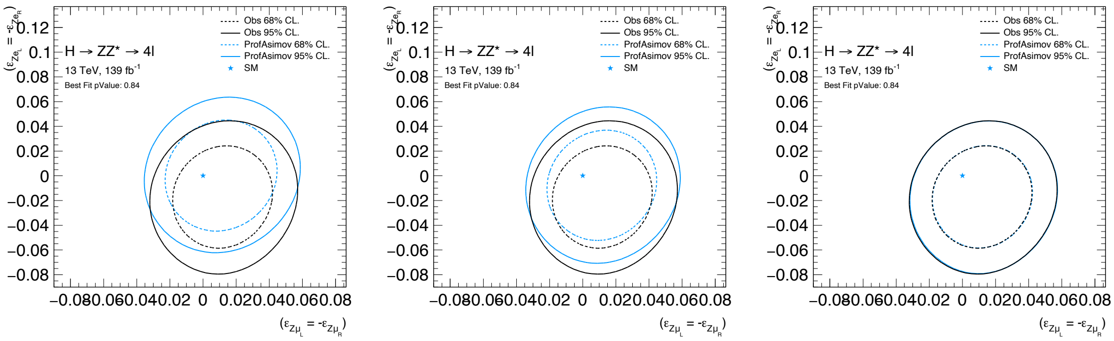

Figure 7.18: Observed exclusion limits (*black lines*) compared with ones obtained from the asimov dataset (*blue lines*) generated with $\sigma_{bin3_{\ell\ell ee}}$ equal to 1 (*on the left*), 0.8 (*in the center*), 0.58 (*on the right*) times the expected value, and the others XS equal to the SM value, in the non-universal axial contact terms scenario.

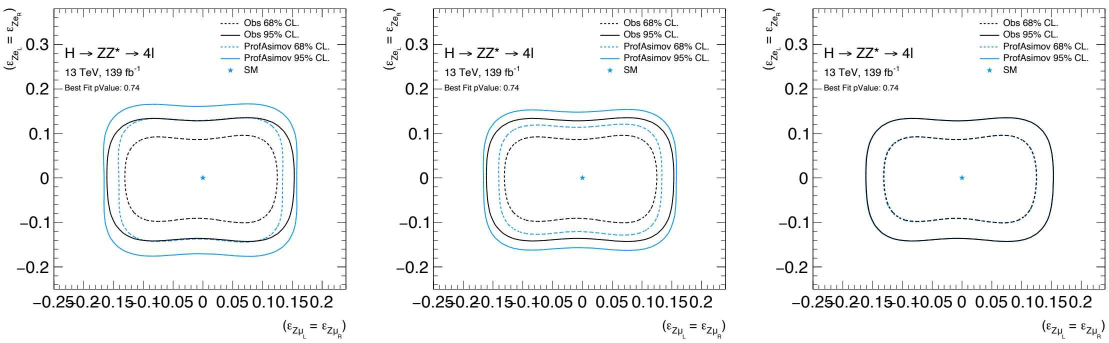

Figure 7.19: Observed exclusion limits (*black lines*) compared with ones obtained from the asimov dataset (*blue lines*) generated with $\sigma_{bin3_{\ell\ell ee}}$ equal to 1 (*on the left*), 0.8 (*in the center*), 0.58 (*on the right*) times the expected value, and the others XS equal to the SM value, in the non-universal vector contact terms scenario.

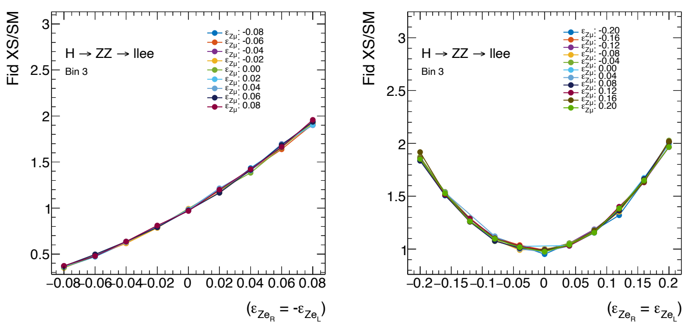

Figure 7.20: Modification of the predicted cross section in bin1 of m_{12} vs. m_{34} distribution as function of the ϵ_{Ze} in $\ell\ell ee$ final states for the non-universal axial (*on the left*) and vector (*on the right*) contact terms scenarios.

POI	XS $_{\text{Exp}}$ [fb]	XS $_{\text{Obs}}$ [fb]	Rel. Error	$\frac{\text{XS}_{\text{Obs}}}{\text{XS}_{\text{Exp}}}$
$\sigma_{bin0_{incl}}$	$0.30^{+0.13}_{-0.12}$	$0.19^{+0.13}_{-0.11}$	$^{+68.6\%}_{-59.0\%}$	0.63
$\sigma_{bin1_{incl}}$	$0.40^{+0.10}_{-0.09}$	$0.51^{+0.12}_{-0.10}$	$^{+22.9\%}_{-20.3\%}$	1.29
$\sigma_{bin2_{incl}}$	$0.47^{+0.13}_{-0.110}$	$0.49^{+0.13}_{-0.11}$	$^{+25.5\%}_{-22.2\%}$	1.04
$\sigma_{bin3_{incl}}$	$1.17^{+0.20}_{-0.184}$	$1.14^{+0.20}_{-0.18}$	$^{+17.7\%}_{-16.1\%}$	0.97
$\sigma_{bin4_{incl}}$	$1.07^{+0.23}_{-0.211}$	$0.83^{+0.21}_{-0.19}$	$^{+25.5\%}_{-22.8\%}$	0.78

Table 7.3: Expected and observed cross sections in each category of m_{12} vs. m_{34} distribution in the inclusive final state, using data corresponding to an integrated luminosity of 139 fb^{-1}. The columns correspond to the parameter of interest, the expected and the observed cross section with errors, the corresponding relative errors listed in percentage and the ratio between the observed and expected cross sections.

POI	XS $_{\text{Exp}}$ [fb]	XS $_{\text{Obs}}$ [fb]	Rel. Error	$\frac{\text{XS}_{\text{Obs}}}{\text{XS}_{\text{Exp}}}$
$\sigma_{bin0_{\ell\ell\mu\mu}}$	$0.15^{+0.08}_{-0.07}$	$0.07^{+0.07}_{-0.05}$	$^{+100\%}_{-65.7\%}$	0.47
$\sigma_{bin1_{\ell\ell\mu\mu}}$	$0.20^{+0.07}_{-0.06}$	$0.26^{+0.07}_{-0.06}$	$^{+29.0\%}_{-24.7\%}$	1.31
$\sigma_{bin2_{\ell\ell\mu\mu}}$	$0.24^{+0.08}_{-0.07}$	$0.26^{+0.08}_{-0.07}$	$^{+30.7\%}_{-26.4\%}$	1.10
$\sigma_{bin3_{\ell\ell\mu\mu}}$	$0.59^{+0.12}_{-0.11}$	$0.70^{+0.13}_{-0.12}$	$^{+18.6\%}_{-16.9\%}$	1.19
$\sigma_{bin4_{\ell\ell\mu\mu}}$	$0.54^{+0.13}_{-0.12}$	$0.48^{+0.13}_{-0.12}$	$^{+27.5\%}_{-25.0\%}$	0.89
$\sigma_{bin0_{\ell\ell ee}}$	$0.15^{+0.11}_{-0.09}$	$0.12^{+0.11}_{-0.09}$	$^{+92.7\%}_{-74.8\%}$	0.83
$\sigma_{bin1_{\ell\ell ee}}$	$0.20^{+0.08}_{-0.07}$	$0.24^{+0.09}_{-0.08}$	$^{+38.5\%}_{-31.2\%}$	1.23
$\sigma_{bin2_{\ell\ell ee}}$	$0.24^{+0.11}_{-0.09}$	$0.23^{+0.11}_{-0.09}$	$^{+46.4\%}_{-37.8\%}$	0.99
$\sigma_{bin3_{\ell\ell ee}}$	$0.58^{+0.18}_{-0.16}$	$0.34^{+0.15}_{-0.13}$	$^{+44.2\%}_{-38.1\%}$	0.58
$\sigma_{bin4_{\ell\ell ee}}$	$0.54^{+0.19}_{-0.17}$	$0.38^{+0.17}_{-0.15}$	$^{+44.9\%}_{-38.7\%}$	0.72

Table 7.4: Expected and observed cross sections in each category of m_{12} vs. m_{34} distribution in the $\ell\ell ee$ and $\ell\ell\mu\mu$ final states, using data corresponding to an integrated luminosity of 139 fb^{-1}. The columns correspond to the parameter of interest, the expected and the observed cross section with errors, the corresponding relative errors listed in percentage and the ratio between the observed and expected cross sections.

7.1.2 κ-framework: constraint on Yukawa couplings

The coupling of the Higgs boson to the top and bottom quark have been previosuly measured. Measuring the coupling of the Higgs boson to lighter quarks, such as the charm quark, has been much more difficult due to small branching fractions in channels ($h \to J/\psi\gamma \to \mu^+\mu^-$) or large QCD backgrounds ($VH(\to c\bar{c})$). However, it was recently proposed that the coupling can be constrained with current LHC data by analysing modifications to the p_{T}^{H} shape [16]. In particular the effects of BSM contributions to the coupling modifiers for the Higgs boson to charm quark ,κ_c, and for the Higgs boson to bottom quarks, κ_b, have been investigated in this interpretation.

For this interpretation, three scenarios have been considered, based on which quantities can be modified by the presence of the anomalous couplings, with an increasing level of model dependency:

1. The cross section is fixed to the SM but the p_{T}^{H} shape can be modified
2. The cross section and p_{T}^{H} shape can be modified
3. The cross section and p_{T}^{H} shape and branching ratio can be modified

In these interpretations κ_b is simultaneous fit alongside κ_c. This is so that any large deviations for lighter generation quark with charge = -1/3 can be seen from κ_b.

The coupling between the Higgs boson and the charm quark can be investigated in different signatures of gluon and quark initiated processes, as shown in Figure 7.21. In this analysis, the gluon predictions have been provided by the authors of the paper [16] using RaDISH and the quark initiated have been generated using Madgraph using the 5FS and LHAPDF.

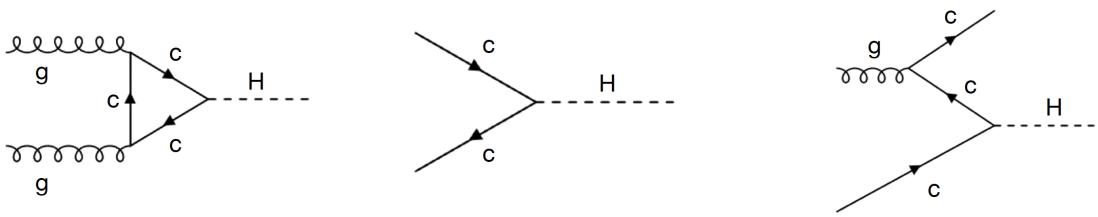

Figure 7.21: Feynman diagrams showing coupling between the Higgs boson and charm quark.

Figure 7.22 show how the p_{T}^{H} shape changes for different κ_c values for both gluon and quark initiated processes.

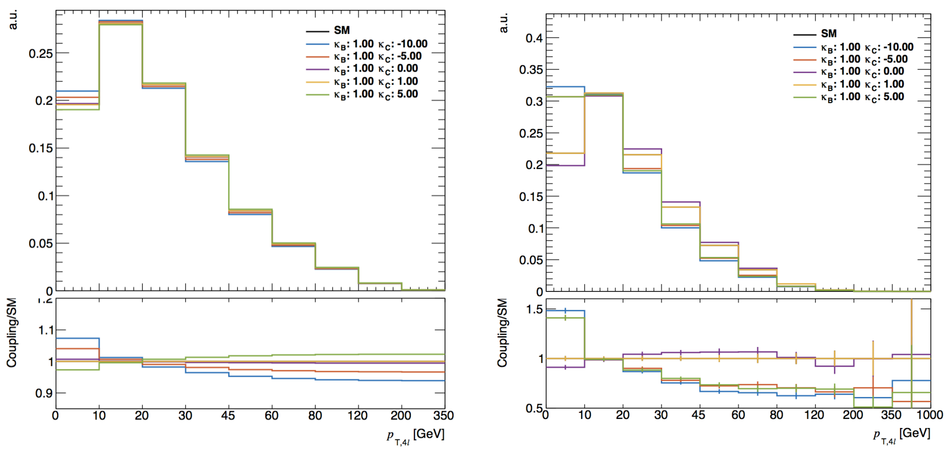

(a) Gluon initiated process

(b) Quark initiated process

Figure 7.22: Modification to the p_{T}^{H} shape from gluon- (left) and quark- (right) initiated processed.

7.1.2.1 Signal parametrisation

This interpretation follows the same strategy used for the Pseudo-Observables interpretation, with some differences in the three scenarios:

- **Modification to only on $p_T^{4\ell}$ shape.** The total cross section is assumed to be the one fitted from data. The cross sections in each p_T^H bin have been parametrised as a function of κ_b and κ_c values, adding a normalisation factor μ common to all the parametrised cross sections:

$$\frac{XS_{\mathrm{bin}}^{\mathrm{BSM}}}{XS_{\mathrm{bin}}^{\mathrm{SM}}} = \mu \sum_{i \geq j} c_{i,j}^{\mathrm{bin}} \kappa_i \kappa_j \tag{7.1.7}$$

  where $c_{i,j}^{\mathrm{bin}}$ are the coefficient of the quadratic function used in the parametrisation for each p_T^H bin.

- **Modifications to $p_T^{4\ell}$ differential cross section.** Same approach has been used for the Pseudo-Observable, the cross section has parametrised as a function of κ_b and κ_c values in each bin of p_T^H:

$$\frac{XS_{\mathrm{bin}}^{\mathrm{BSM}}}{XS_{\mathrm{bin}}^{\mathrm{SM}}} = \sum_{i \geq j} c_{i,j}^{\mathrm{bin}} \kappa_i \kappa_j \tag{7.1.8}$$

- **Modifications to $p_T^{4\ell}$ differential cross section and to BR.** The cross section has been parametrised as before, and also the Branching Ratio $H \to ZZ^*$ has been parametrised as function of κ_b and κ_c as follow:

$$\frac{\mathcal{BR}_{\mathrm{ZZ}}^{\mathrm{BSM}}}{\mathcal{BR}_{\mathrm{ZZ}}^{\mathrm{SM}}} = \frac{\Gamma_{\mathrm{tot}}}{\kappa_b^2 \cdot \Gamma_{b\bar{b}} + \kappa_c^2 \cdot \Gamma_{c\bar{c}} + f(\kappa_b, \kappa_c) \cdot \Gamma_{gg} + \Gamma_{\mathrm{rest}}} \tag{7.1.9}$$

  where $f(\kappa_b, \kappa_c)$ is assumed to follow the same dependance as the cross section for the $H \to gg$ decay and $\Gamma_{\mathrm{rest}} = \Gamma_{\tau\tau} + \Gamma_{\gamma\gamma} + \Gamma_{Z\gamma} + \Gamma_{ZZ} + \Gamma_{WW}$.

Figure 7.23 shows the modification of the cross section as function of the coupling with 2D parabolic fit for the first two scenarios; *Shape only* and *Cross section only* in a couple of $p_T^{4\ell}$ example bin.

The modification of the acceptances for the quark initiated samples are also reported in Figure 7.24. For the gluon initiated processes the acceptance has been taken from NNLOPS. Similar to the Pseudo-Observable approach, as the parametrisation is performed on the fiducial cross section measurement, the acceptance modifications are factorised.

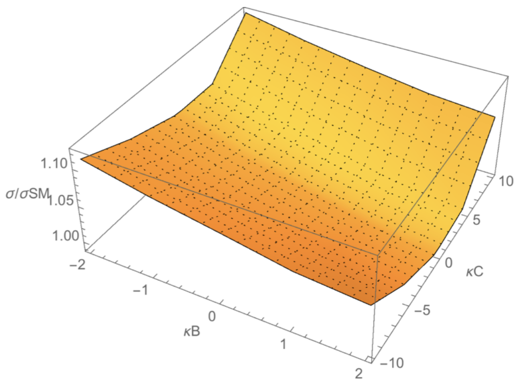

(a) Shape Only

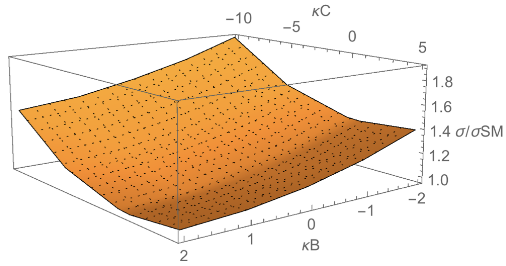

(b) XS Only

Figure 7.23: Modification of the predicted XS in different bins of p_{T}^{H} as a function of κ_b and κ_c.

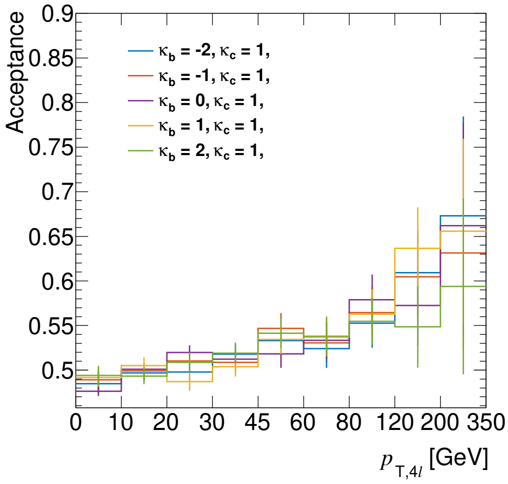

(a)

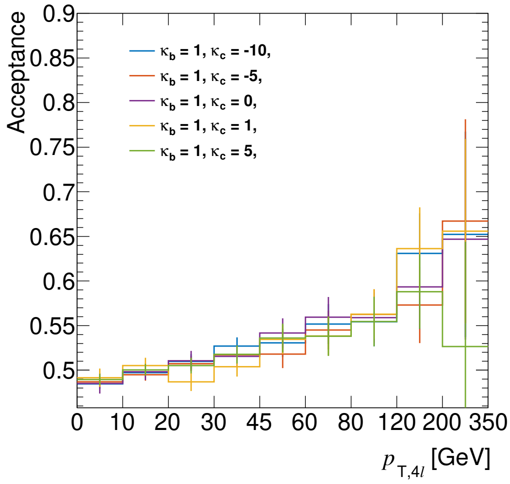

(b)

Figure 7.24: Modification of the acceptance in p_{T}^{H} bin for different (a) κ_b (with $\kappa_c = 1$) and (b) κ_c (with $\kappa_b = 1$) values.

7.1.2.2 Statistical Analysis and Coverage Studies

In this interpretation, the same statistical analysis of the Pseudo-Observable described in Section 7.1.1.2 has been used. Also in this case both the statistical approaches have been tested:

- **"Yukawa model".** The profile likelihood ratio $-2\ln\lambda$ is computed with respect to the best fit value from the parametrised model with the κ couplings $\sigma(\hat{\kappa})$. The asymptotic approximation lies on the assumption that $-2\ln\lambda$ behaves as a χ^2 distribution with two DOF (POI: κ_b, κ_c).
- **"XS measurement".** The profile likelihood ratio $-2\ln\lambda$ is computed with respect to the best fit value from the cross section measurements in $p_{\mathrm{T}}^{4\ell}$ bins $\hat{\sigma}$. The asymptotic approximation lies on the assumption that $-2\ln\lambda$ behaves as a χ^2 distribution with ten DOF (POI: σ in each $p_{\mathrm{T}}^{4\ell}$ bin).

For this interpretation, the model presents the same coverage issue shown for the Pseudo-Observable. The BSM model presents a minimum when the BSM cross section is equal to the SM and the downward fluctuations cannot be absorbed. It can be seen by generating $\sim$ 10000 toys at SM point for each scenario. Figure 7.25 show the 2D distribution of the toy results distributed in the coupling phase space together with the expected confidence level at 68% and 95%. The distribution of the $-2\ln\lambda$ is also reported with a χ^2 fit function to check the number of degrees of freedom.

Also in this case, the alternative "XS measurement" approach has been investigated and the coverage checked always generating $\sim$ 10000 toys at SM point for each scenario. Figure 7.26 show the distribution of the $-2\ln\lambda$ fitted with a χ^2 function to check the number of degrees of freedom. It can be seen that the number of degrees of freedom is close to the expected value of 10. The number of DOF obtained from these fits in all the scenarios have been used to calibrate the limits in the exclusion plots. The number of degrees of freedom obtained with the two approaches are summarised in Table 7.5.

Scenario	#DOF Yukawa model	#DOF XS measurements
Shape Only	2.15	9.48
XS Only	0.78	9.57
XS and BR	1.30	9.53

Table 7.5: Number of DOF obtained from toys with the two statistical approaches for the Yukawa couplings interpretation.

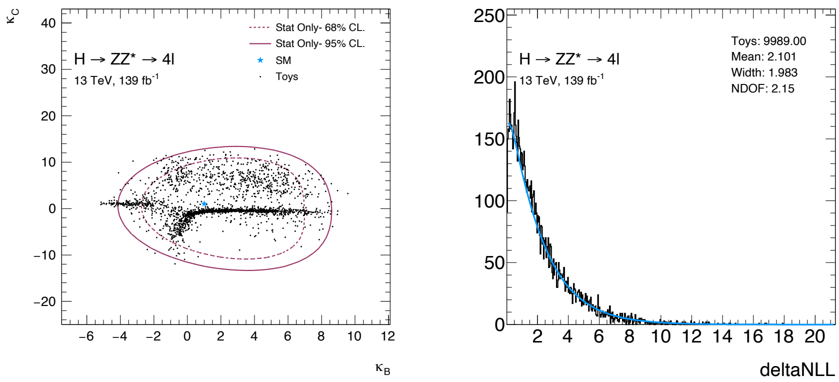

(a) Shape Only

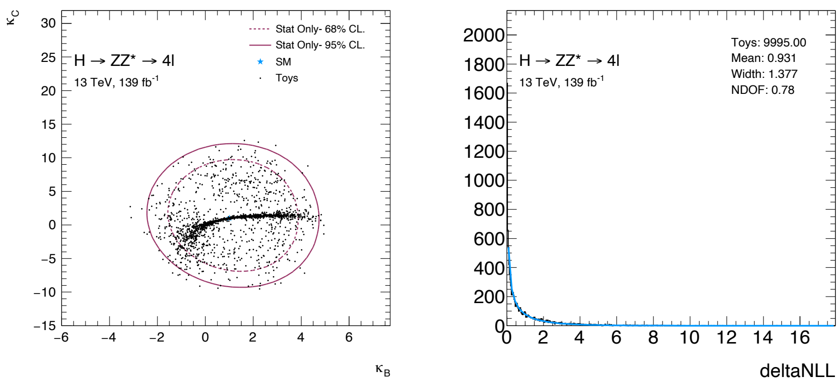

(b) XS Only

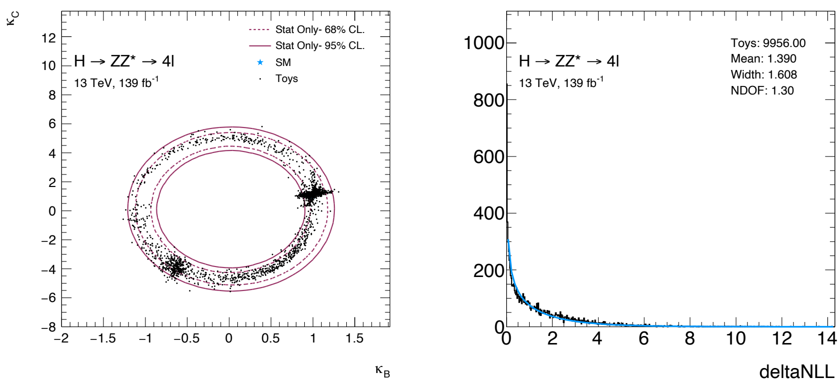

(c) XS and BR

Figure 7.25: The right plots show the 2D distribution of the toys generated at SM point together with the expected confidence level at 68% and 95%. The left plots show the distribution of the $-2\ln\lambda$ with a χ^2 fit function to check the number of degrees of freedom.

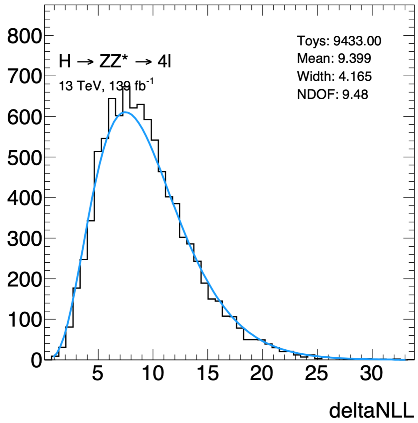

(a) Shape Only

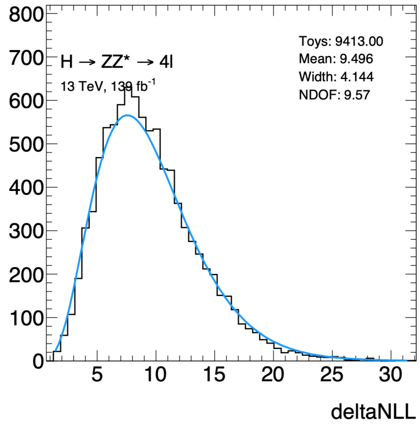

(b) XS Only

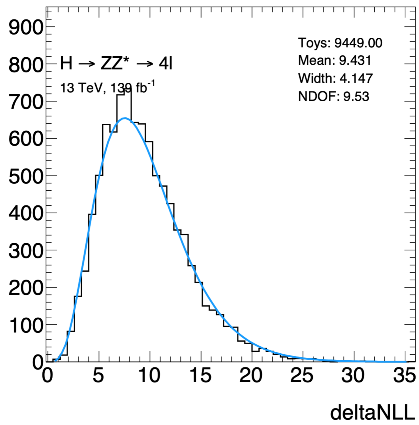

(c) XS and BR

Figure 7.26: Distribution of the $-2\ln\lambda$ of the toys generated at SM point with a χ^2 fit function to check the number of degrees of freedom.

7.1.2.3 Systematics

Theory systematics are considered separately for gluon and quark initiated processes. For gluon initiated processes, variations in the renormalisation, factorisation and matching scale are considered. The largest up and down variation across all κ_b and κ_c values is taken and applied as a flat systematic for each p_{T}^{H} bin. For quark initiated processes the normalisation and factorisation scale are varied in an 8-point variation. Again, the largest variation across all κ_b and κ_c is applied as a flat systematic in each p_{T}^{H} bin. The variations for the SM point are shown in Figure 7.27 for the gluon initiated process on the left and the quark initiated process on the right. Note that the last bin is not considered when choosing the largest variation. Approximately, a 20% impact is observed in the expected limits.

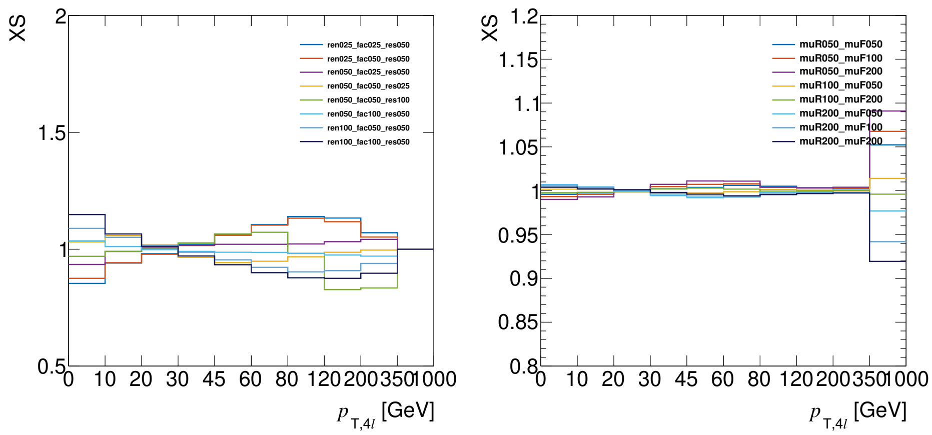

Figure 7.27: Scale variations for the gluon (left) and quark (right) initiated processes for the SM point

7.1.2.4 Results

In this section the expected and observed results are reported with both statistical approaches described in the previous section. They are shown in Figure 7.28 and in all the plots the p-value is reported. It represents the probability of compatibility between the data and the $p_{\mathrm{T}}^{4\ell}$ prediction corresponding to the best-fit values of κ_b, κ_c in each scenario.

Comparison between statistical approaches

In this interpretation, the coverage problem leads to a quite different results in terms of exclusion limits. Indeed in all the scenarios the p-value is about 10%. It can be seen that in the "XS measurement" approach, the 68% CL is not shown, given that the compatibility between the data and the model used for the parametrisation is 10%. Instead in the "Yukawa model" approach, the limit is showed.

It is possible to verify the relation between the two approaches, given by Equation 7.1.6. Given that the model is compatible with the data at 10%, to have an exclusion limits of 5% in the "XS measurement" approach (NLL_σ), an exclusion limit at 50% have to be set in the "Yukawa model" approach (NLL_κ). The comparison between the two limits is shown in Figure 7.29 for the Shape Only and XS Only scenarios and they match. This means that to provide the results using the theoretical model approach in the statistical analysis, it is necessary provide also the p-value as complementary information.

The final results have been provided in the "Yukawa model" approach, as has been done for the Pseudo-Observables. Figure 7.30 shows the observed results. The NLL scans along the κ_c coupling with free κ_b coupling in the fit for the three scenarios are shown in Figure 7.31. In Figure 7.32, the $p_{\mathrm{T}}^{4\ell}$ differential cross section measurement is reported together with prediction at 95% CL from the Shape Only scenario overlaid (with SM κ_b=1).

The 95% confidence intervals for the first and second scenarios are also listed in Table 7.6. These are comparable to results from direct searches in $VH, H \to c\bar{c}$ [198,199]. Constraining κ_b to the results from Ref. [200] leads to a less than 5% improvement in the observed limits

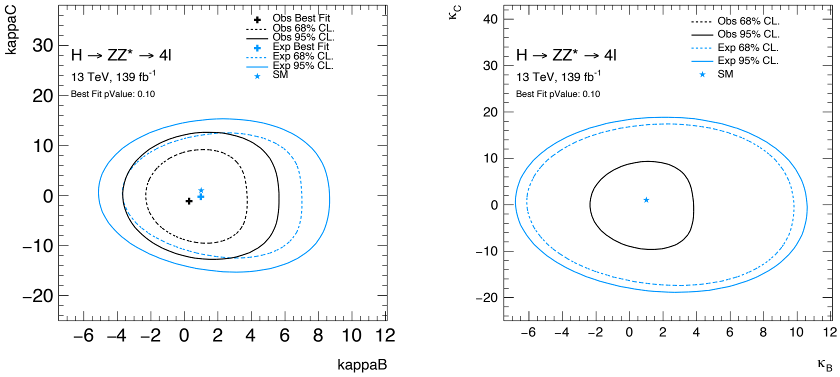

(a) Shape Only

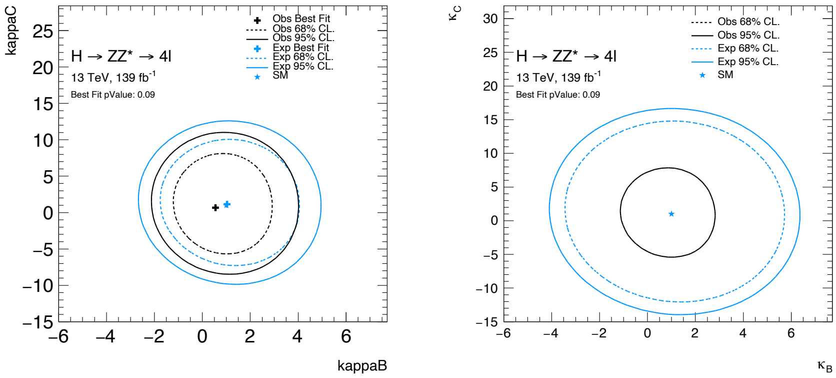

(b) XS Only

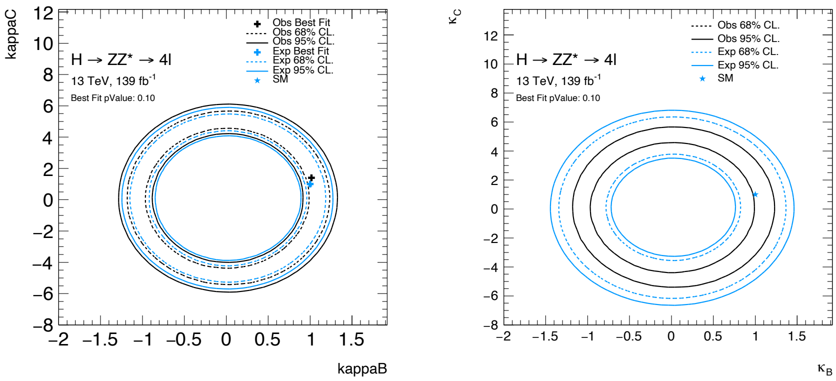

(c) XS and BR

Figure 7.28: Observed (black line) and expected (blue line) exclusion plots for the three scenarios with the two statistical approaches: "Yukawa model" on the right and "XS measurement" on the left. The dashed line represents the 68% CL and the continuous line the 95% CL.

4438 for κ_c for the scenarios considered.

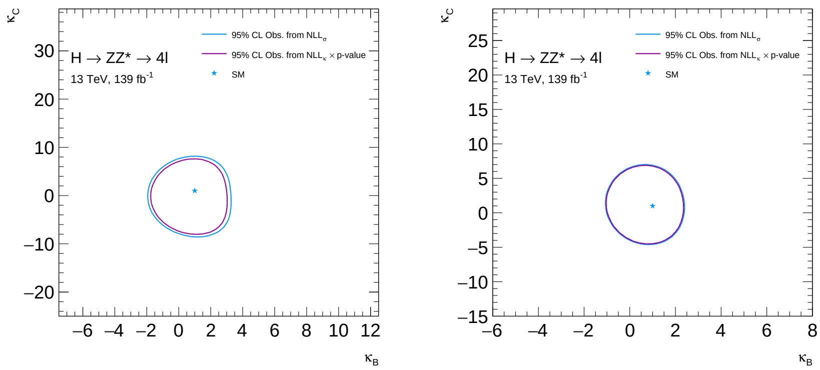

(a) Shape Only (b) XS Only

Figure 7.29: Comparison between the two 95% CL obtained with the "XS measurement" approach and with the "Yukawa model" taking into account the compatibility with the data using the p-value for the Shape Only and XS Only scenarios .

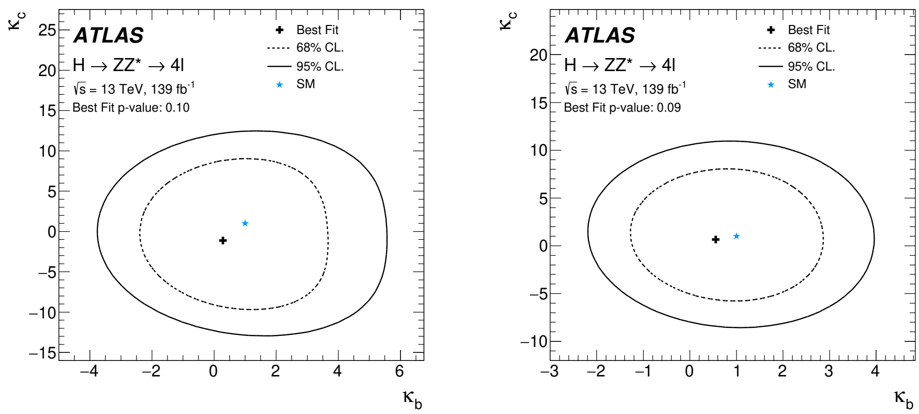

(a) Shape Only (b) XS Only

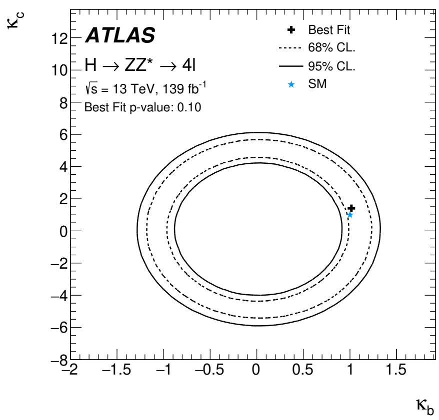

(c) XS and BR

Figure 7.30: Observed exclusion plots for the four scenarios. The dashed line represents the 68% CL and the continuous line the 95% CL.

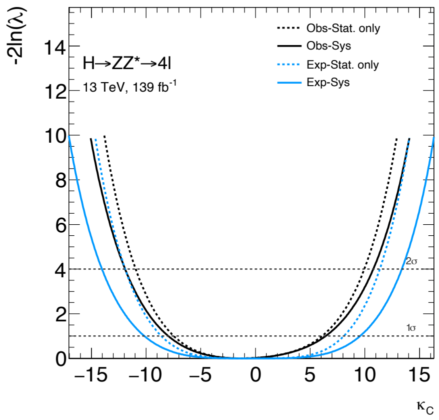

(a) Shape Only

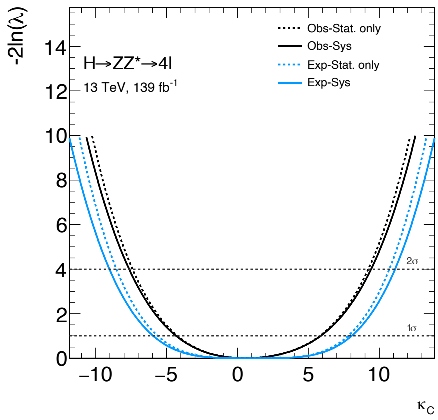

(b) XS Only

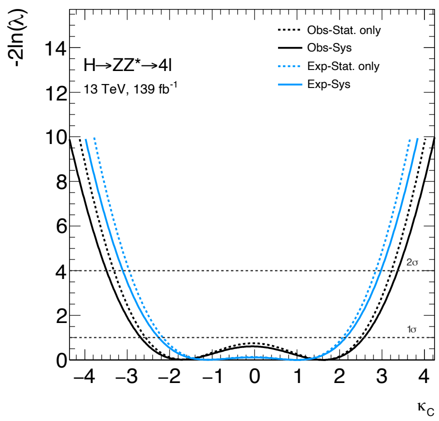

(c) XS and BR

Figure 7.31: Expected and observed NLL scan for the Yukawa coupling κ_C.

Interpretation	Parameter best-fit value	95% confidence interval
Modifications to only $p_T^{4\ell}$ shape	$\kappa_c = -1.1$	$[-11.7,\ 10.5]$
	$\kappa_b = 0.28$	$[-3.21,\ 4.50]$
Modifications to $p_T^{4\ell}$ predictions	$\kappa_c = 0.66$	$[-7.46,\ 9.27]$
	$\kappa_b = 0.55$	$[-1.82,\ 3.34]$

Table 7.6: Confidence intervals for the Yukawa couplings. Based on the observed 2D exclusion contours, 1D exclusion intervals are only provided for interpretations where modification to the $p_T^{4\ell}$ shape and predictions are considered. The observed limits are calculated while profiling the other parameter of interest.

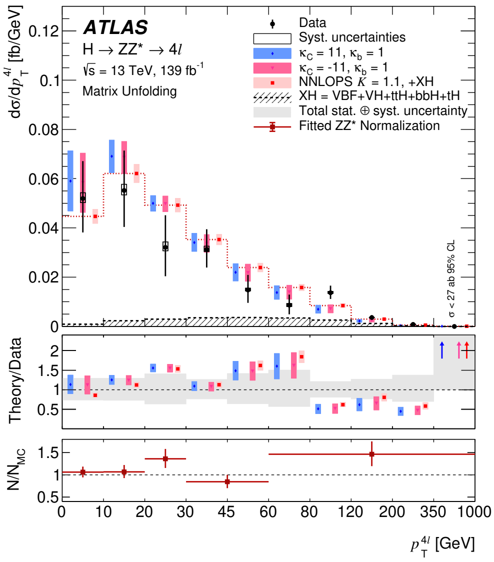

Figure 7.32: $p_{T,4\ell}$ differential cross section measurement compared with predictions at 95% confidence level for κ_C for the Shape Only scenario.

7.2 CP-violation in Effective Field Theory using Optimal Observables

In this section some preliminary expected results for the CP violation search in the $H \to ZZ^{(*)} \to 4\ell$ decay channel are presented.

The limits on possible BSM CP-odd couplings to the HVV vertex can be set with two approaches. One way is the interpretation of the differential cross section measurement of a variable sensitive to CP-odd effects, as the Optimal Observable. Then following exactly the same analysis strategy used for the previous interpretations, a constraint on CP-odd couplings can be set. An alternative approach is with a *shape-based* analysis. This approach factorise out any possible BSM contribution in the rate, focusing just on the impact on the shape of the variable. Also in this case, the Optimal Observable are the most sensitive to probe this effect.

For these preliminary studies, the BSM contribution has been probed only in the VBF vertex, and only VBF BSM samples have been used. All the other signals are SM, but for the shape-based analysis only the ggF and VH have been taken into account ($t\bar{t}H$ and $b\bar{b}H$ has not been included). For the background, only the ZZ^* process has been considered.

7.2.1 Expected Limits from differential cross section measurement

Possible CP-odd Higgs boson couplings can be studied in the Effective Field Theory framework, described in Section 1.1.2.2. These couplings can be defined in different basis, it depends if we are dealing with the field eigenstates (*Warsaw basis*) or with mass eigenstate

(*Higgs basis*). This study focuses on constraining the $\widetilde{c}_{zz}$ coupling in the Higgs basis. The presence of an anomalous $\widetilde{c}_{zz}$ couplings in the VBF vertex can be probed using the differential cross section distribution of the Optimal Observable $\mathcal{OO}_{1,jj}(\widetilde{c}_{zz}=1)$. The anomalous CP-odd coupling impacts the cross section measurement in each bin of the $\mathcal{OO}_{1,jj}(\widetilde{c}_{zz}=1)$ as can be seen in Figure 7.33. The acceptance variations due to anomalous $\widetilde{c}_{zz}$ couplings are shown in Figure 7.34.

As for the previous interpretations, also in this case the cross sections have a parabolic behaviour as function of the BSM couplings, and the cross section in each bin can be parametrised with a quadratic function of $\widetilde{c}_{zz}$. The cross section in the underflow bin $N_{jets} < 2$ has not been parametrised given that the anomalous coupling $\widetilde{c}_{zz}$ is present only in VBF events, which require at least 2 jets.

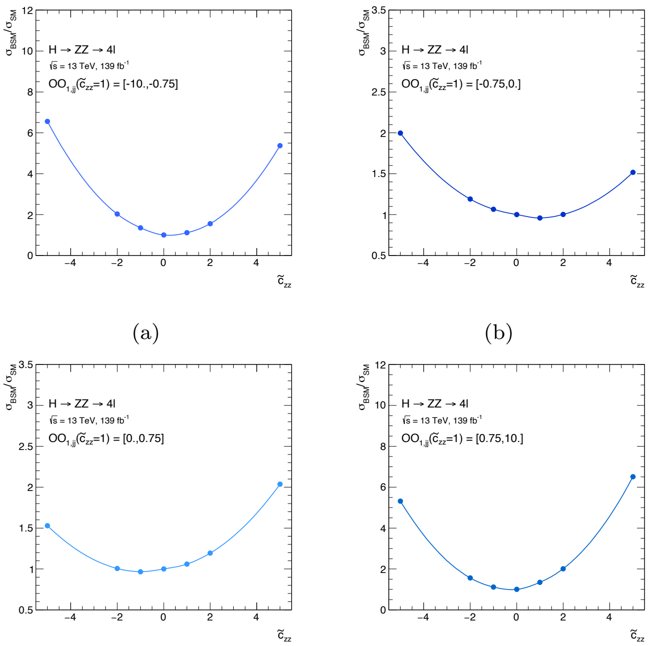

(a) (b)

(c) (d)

Figure 7.33: Modification of the predicted XS in different $\mathcal{OO}_{1,jj}(\widetilde{c}_{zz}=1)$ bins as a function of $\widetilde{c}_{zz}$.

In this analysis, only one coupling is probed, while all the other couplings in the Effective Lagrangian ($\widetilde{c}_{za}$ and $\widetilde{c}_{aa}$ for the Higgs basis) are set to the SM value, then to be zero. The cross section parametrisation is then implemented in the likelihood function in Equation 6.4.20 through the cross sections σ_j^{fid} in Equation 6.4.9. The statistical analysis to determine the exclusion limits on $\widetilde{c}_{zz}$ (which is the new POI) is based on a profile likelihood fit computed with respect to the best fit value from the parametrised model:

$$-2\ln\lambda = -2\ln\frac{\mathcal{L}(\sigma(\widetilde{C}_{zz}),\hat{\hat{\theta}}(\widetilde{C}_{zz}))}{\mathcal{L}(\hat{\sigma}(\widetilde{C}_{zz}),\hat{\theta})} \tag{7.2.1}$$

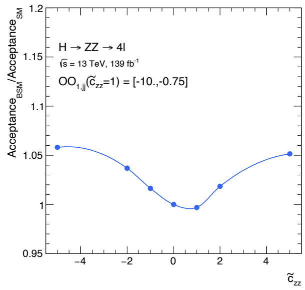

(a)

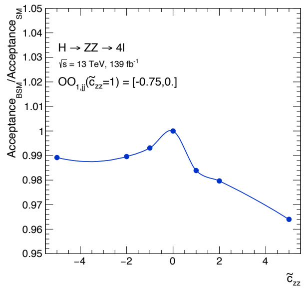

(b)

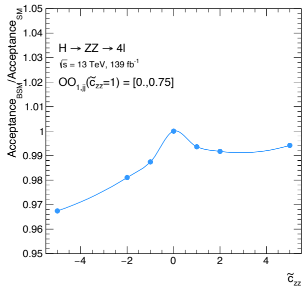

(c)

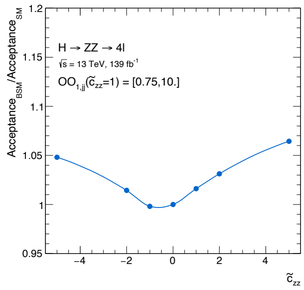

(d)

Figure 7.34: Modification of the acceptance in different $\mathcal{OO}_{1,jj}(\widetilde{c}_{zz} = 1)$ bins as a function of $\widetilde{c}_{zz}$.

Figure 7.35 show the expected limits on $\widetilde{c}_{zz}$ using the $\mathcal{OO}_{1,jj}(\widetilde{c}_{zz} = 1)$ differential cross section measurement:

$$\widetilde{c}_{zz} = -0.004 \quad 68\% \text{ CL} : [-1.31, 1.33] \quad 95\% \text{ CL} : [-1.97, 1.99] \tag{7.2.2}$$

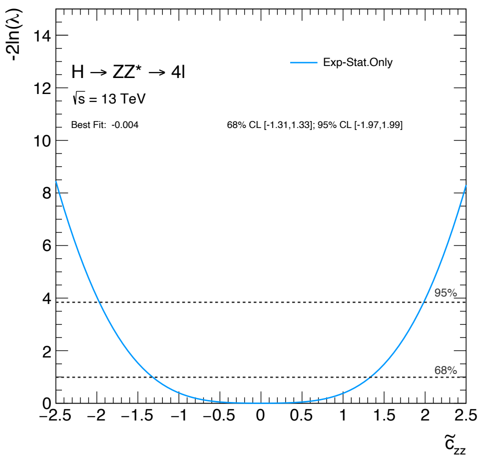

Figure 7.35: Expected NLL scan and expected exclusion limits for $\widetilde{c}_{zz}$. The dashed horizontal lines represent the 68% CL and the 95% CL.

7.2.2 Expected Limits from Shape-based analysis in VBF production

To constraint possible CP-odd Higgs boson couplings an alternative approach rate-independent can be used, relying only on the shapes of the distributions of the kinematic variables. In general this approach is less sensitive to BSM couplings with respect to the rate approach, but the observables can be chosen in a way in which they are sensitive only to CP-odd effects, providing a direct probe of CP-violation in the Higgs sector.

In this section, a sensitivity study for a shape-based analysis to test CP violation at the HVV vertex in the VBF Higgs boson production is presented, to constraint of EFT Wilson coefficients targeting CP-odd Higgs boson coupling with vector bosons.

7.2.2.1 Analysis Strategy

In the shape-based measurement, the shapes of the kinematic variables distributions are used to discriminate between SM and BSM coupling contributions, normalising the distributions to the expected yields or to the data by adding a normalisation parameter μ independent from the BSM coupling.

The most sensitive observables to CP-odd effects are the ones already described in Section 6.3.3. In particular, the production Optimal Observables are matrix element based observable which combine all the the jets and the Higgs boson kinematics information, providing higher sensitivity compared to the other jets or leptons variables. The first order Optimal Observable $\mathcal{OO}_{1,jj}$ is more sensitive to CP-odd effects given that it becomes asymmetric in presence of CP-odd contribution. This observable has been used in this analysis.

The BMS signal is modelled with simulated VBF $+VH$-Had samples (LO in QCD) to take into account of interference Feynman diagrams between the two productions, and including the ggF production with its SM contribution. The signal event yields for VBF $+VH$-Had are scaled to the ones given by the nominal samples VBF and VH, which includes higher order effects.

The constraints on possible CP-odd coupling are obtained by performing a binned likelihood fit of the expected distributions of the Optimal Observables to the data. The likelihood function is constructed from the Poisson distributions of the observable given an expected signal $n_s(\kappa_{\text{BSM}})$, which depends from the couplings, and an expected background n_b:

$$\mathcal{L}(n^{\text{obs}}, \mathcal{OO}|\kappa_{\text{BSM}}) = \text{Poisson}(n^{\text{obs}}|\mu \cdot n_s(\kappa_{\text{BSM}}) + n_b) \times P(\mathcal{OO}|\mu \cdot n_s(\kappa_{\text{BSM}}), n_b) \quad (7.2.3)$$

where $P(\mathcal{OO}|\mu \cdot n_s(\kappa_{\text{BSM}}), n_b)$ is the model of the signal and backgrounds, and μ is the normalisation factor which is a free parameter independent from the BSM coupling, so that the analysis only exploits the shape of the distribution of the Optimal Observable.

The exclusion limits on the CP-odd couplings are obtained with the profile likelihood ratio statistical test, scanning the negative-log likelihood to extract the 68% and 95% CL:

$$-2\ln\lambda = -2\ln\frac{\mathcal{L}(\mathcal{OO}|\kappa_{\text{BSM}})}{\mathcal{L}(\mathcal{OO}|\hat{\kappa}_{\text{BSM}})} \quad (7.2.4)$$

Signal modelling: Morphing

To constraint the BSM couplings using the shape-information, the distribution of the Optimal Observables needs to be modelled, starting from several input shapes of the $\mathcal{OO}$ at different coupling values. The signal model is based on the so-called *morphing method.* This technique allows for a signal prediction in an arbitrary point of the multi-dimensional BSM parameter space by means of interpolation between the cross section predictions at discrete points of this space. It provides a continuous multi-dimensional model starting from few simulated point in the BSM phase space. In this analysis, only one EFT coupling is probed each time. The morphing technique holds under the assumption that the physical quantity T (e.g. cross sections or differential distributions) which needs to be morphed, is proportional to the matrix element of the underlying process:

$$T(\boldsymbol{g}) \propto |\mathcal{M}(\boldsymbol{g})|^2 \quad \text{with} \quad \mathcal{M}(\boldsymbol{g}) = \sum_i g_i \mathcal{M}_i \tag{7.2.5}$$

where $\boldsymbol{g}$ is a set of couplings $g_i, \cdots, g_i, \cdots$ corresponding to a set of matrix elements $\mathcal{M}_i$. Then, the squared matrix element is a polynomial in the couplings.

The other key point of the morphing is that the so-called *target* distribution of the quantity T, $T_{\text{target}}(\boldsymbol{g})$, can be written as a linear combination of some input distributions of T, $T_{\text{input},j}$, coming from simulation:

$$T_{\text{target}}(\boldsymbol{g}) \sum_j w_j(\boldsymbol{g}) T_{\text{input},j} \quad \text{with} \quad w_j(\boldsymbol{g}) = \sum_i c_{i,j} \cdot g_{i,j} \tag{7.2.6}$$

where $w_j(\boldsymbol{g})$ are the weights which are related to the couplings g_i through polynomial coefficients. In this analysis, there is a single BSM coupling parameter which appears in the morphing g_{BSM} ($\tilde{c}_{zz}$, $\tilde{c}_{za}$, etc.), and the SM coupling, g_{SM}, then $\boldsymbol{g} = g_{\text{SM}}, g_{\text{BSM}}$. The couplings in the VBF production mode in the $H \to ZZ^{(*)} \to 4\ell$ decay channel appears twice: in the production vertex and in the decay one. The squared matrix element for the VBF $H \to 4\ell$ process is:

$$|\mathcal{M}(g_{\text{SM}}, g_{\text{BSM}})|^2 = |\mathcal{M}^{\text{prod}}(g_{\text{SM}}, g_{\text{BSM}})|^2 \cdot |\mathcal{M}^{\text{dec}}(g_{\text{SM}}, g_{\text{BSM}})|^2 \tag{7.2.7}$$

becoming a fourth order polynomial with respect to the g_i, with five independent terms. To produce the $T_{\text{target}}(g_{\text{SM}}, g_{\text{BSM}})$, five *base samples* $T_{\text{input},j}(g_{\text{SM},j}, g_{\text{BSM},j})$ for $j \in [1, 5]$ are needed.

The resulting linear system of equations is called morphing matrix and the c_i coefficients in the weight $w_j(\boldsymbol{g})$ definition can be computed by inverting the morphing matrix.

The base samples choice is an important point of the morphing method, given that from this controls the extrapolation power of the morphing itself. The wider the basis choice is, the higher the prediction power of the morphing, but it can become less reliable in the interpolation part. Given that the goal of the analysis is to perform a sensitivity measurement, the best choice for the morphing base is to choose points close to the expected limits at 68% and 95% CL, to minimise poor extrapolation effects for the larger limits at 95% and have the better estimation of the ones at 68%.

Very preliminary studies for the CP-odd measurement in the VBF production using Optimal Observables, showed a good sensitivity in $\tilde{c}_{zz}$ and $\tilde{c}_{za}$ couplings in the Higgs basis, and in $c_{H\widetilde{W}}$ in the Warsaw basis. In Table 7.7, the bases chosen for this analysis are reported.

Coupling	Basis
$\tilde{c}_{zz}$	$0, \pm 1, \pm 2$
$\tilde{c}_{za}$	$0, \pm 2, \pm 5$
$c_{H\widetilde{W}}$	$0, \pm 2, \pm 4$

Table 7.7: Morphing bases choice for the CP-odd measurement in VBF production in the most sensitive couplings.

Optimisation of the measurement

In the CP-odd analysis, the Higgs boson candidates are selected in 4ℓ mass window $115 < m_{4\ell} < 130$ GeV, as done also for the differential cross section analysis. The VBF Higgs boson production mode is targeted by selecting Higgs boson candidates which fall into the VBF-enriched category by requiring at least two jets in the final state with an invariant mass of the two leading jets larger than 120 GeV.

The major background contribution in the VBF-enriched category comes from the ggF production mode and from the ZZ^* background, besides the minor signal production ttH and bbH and reducible background. The presence of background decrease the sensitivity of the measurements. It is important to improve the discrimination between the VBF $+VH$ signal and the background processes. This can be achieved with multivariate discriminants using Neural Networks. Based on machine learning technique, these discriminants have been used in the most recent Higgs boson production cross-section measurements analysis in the $H \to ZZ^{(*)} \to 4\ell$ decay channel at 139 fb^{-1}performed in the STXS framework [197]. In this CP-odd analysis the Neural Network NN^{2j}_{VBF} has been used. This NN has been trained in the STXS 2-jet category, which requires at least two jets and $m_{\mathrm{jj}} < 120$ GeV or $p_{\mathrm{T}}^{4\ell} < 200$ GeV, to discriminate the VBF signal from the ggF and ZZ^* background process.

The events can be categorised in different NN bins. Choosing the same NN binning used in [197], the percentage of the expected yields in each category are summarised in Figure 7.36. The binned likelihood fit can be performed simultaneously in all the categories (NN bins) to extract the VBF signal.

In the VBF production the expected yields is very low (~ 17 events). As such, the binning of the Optimal Observable distribution used to perform the fit have to be optimised to maximise the sensitivity with enough statistics in each bin. The best choice is to define equally populated bins of the Optimal Observable (including all the signals and background events). In Figure 7.37, it can be seen that the equally populated binning choice is much more sensitive to BSM effects in the VBF $+VH$ production.

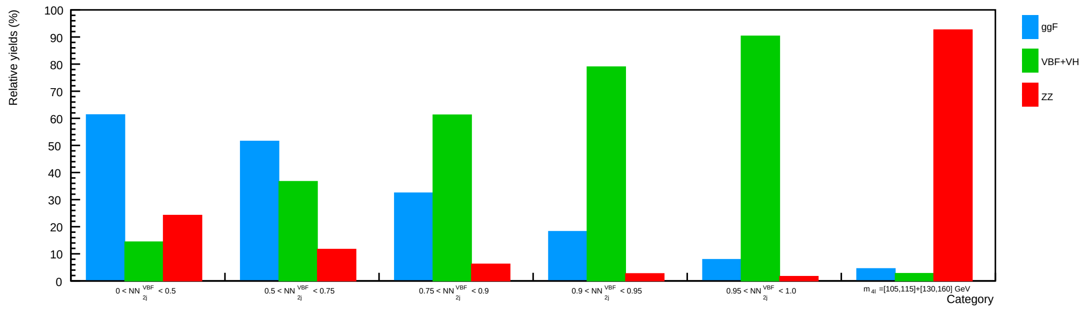

Figure 7.36: Expected percentage contribution of each process ggF, VBF $+VH$ and ZZ^{*} in each NN bin in the $m_{4\ell}$ Signal Region and in the $m_{4\ell}$ Control Region.

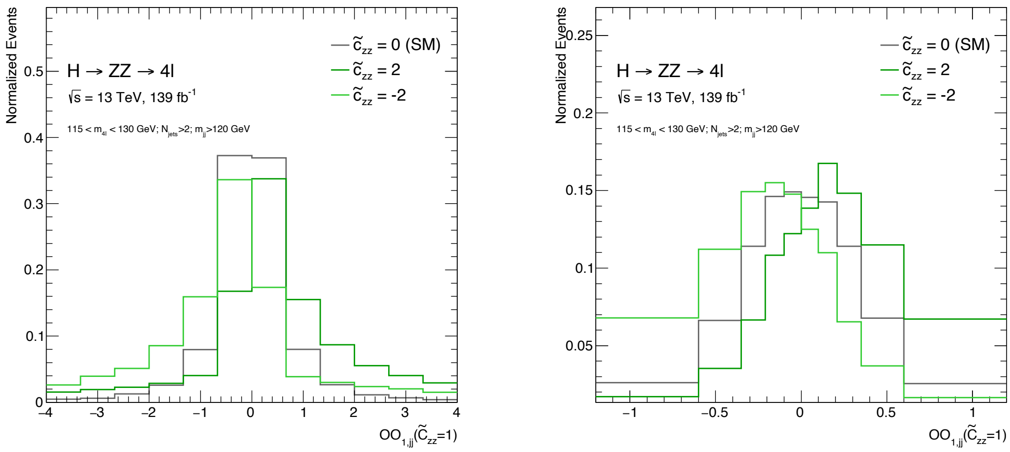

(a) Equally sized bins

(b) Equally populated bins

Figure 7.37: Optimal Observable $\mathcal{OO}_{1,jj}(\tilde{c}_{zz} = 1)$ distribution for VBF $+VH$ SM sample with different CP-odd coupling value $\tilde{c}_{zz} = \pm\, 2$ with equally sized populated bins (a) and with equally populated bins (a).

Figure 7.38 show the comparison of different negative log-likelihood scans performed using $\mathcal{OO}_{1,jj}(\tilde{c}_{zz} = 1)$ observable on $\tilde{c}_{zz}$ couplings as example, with different configurations: only VBF-enriched categorisation, adding the Neural Network categories and using $\mathcal{OO}_{1,jj}(\tilde{c}_{zz} = 1)$ distribution with 12 equally sized bins in the range $[-4, 4]$ or 12 equally populated bins in the range $[-10, 10]$. It can be seen that the introduction of the Neural Network gives the largest improvement in the sensitivity, of about 40% on the exclusion limits. The equally populated bins provide a further improvement of about 10%.

Finally, as done also in the differential cross section measurement analysis, the main backgrounds can be constrained from the data. In this case, the ggF process is a background source, and adding a floating normalisation factor μ_{ggF} in the PDF, its contribution can be constrained from the fit. The ZZ^{*} background does not have a such large contribution in the Signal Region $115 < m_{4\ell} < 130$ GeV to be constrained.

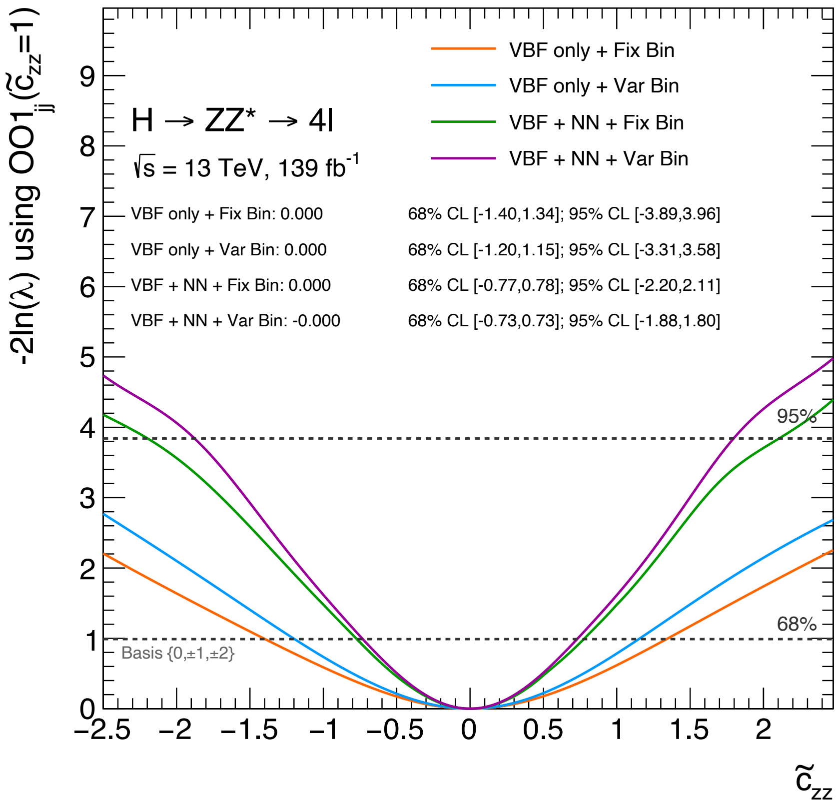

Figure 7.38: NLL comparison with different configurations: only VBF-enriched category using $\mathcal{OO}_{1,jj}(\tilde{c}_{zz} = 1)$ distribution with 12 equally sized bins (orange line), only VBF-enriched category using $\mathcal{OO}_{1,jj}(\tilde{c}_{zz} = 1)$ distribution with 12 equally populated bins (blue line) and adding NN categories (green and purple lines respectively)

Then a Control Region is defined from the $m_{4\ell}$ sidebands $105 < m_{4\ell} < 115$ GeV and $130 < m_{4\ell} < 160$ GeV, and it is added to the fit categories together with another floating normalisation factor μ_{ZZ}, which is constrained from the fit.

Figure 7.39a show the impact on the limits of the floating normalisation factors in the fit as well as the presence of the Control Region. It can be seen that the impact is negligible on the expected limits. In particular in Figures 7.39b and 7.39c, the fitted μ_{ggF} and μ_{ZZ} extracted in the negative log-likelihood scan are reported. It can be seen that the presence of the Control Region constraints the μ_{ZZ} factor.

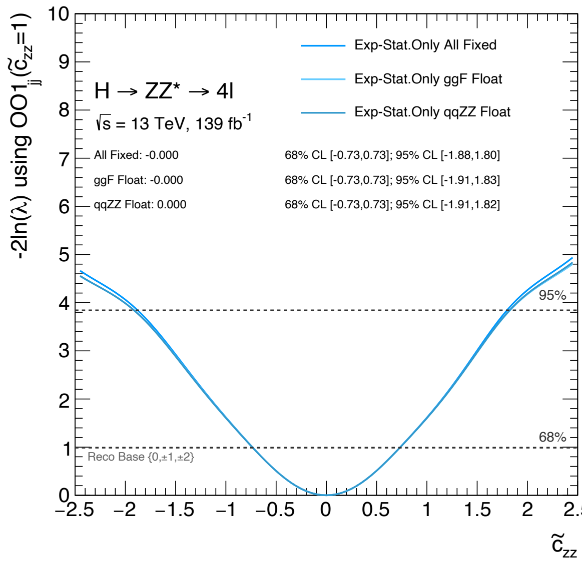

(a) NLL scan

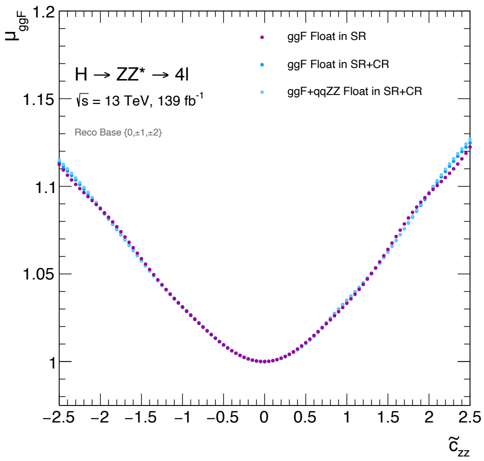

(b) μ_{ggF} scan results

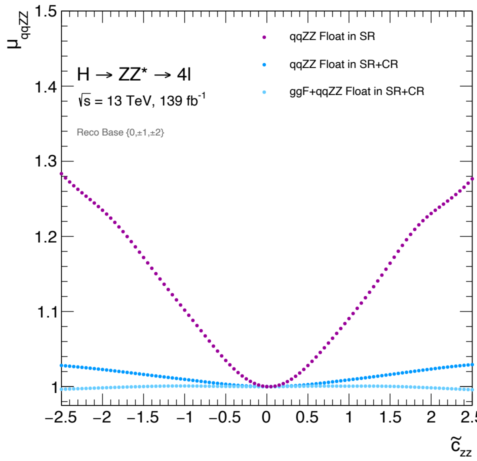

(c) μ_{ZZ} scan results

Figure 7.39: a NLL scan including the floating normalisation factors to constraint background contribution ggF b and ZZ^* c

7.2.2.2 Expected sensitivity

The expected sensitivity results in the most sensitive couplings $\tilde{c}_{zz}$, $\tilde{c}_{za}$ and $c_{H\widetilde{W}}$ using $\mathcal{OO}_{1,jj}(\tilde{c}_{zz} = 1)$, $\mathcal{OO}_{1,jj}(\tilde{c}_{za} = 1)$ and $\mathcal{OO}_{1,jj}(c_{H\widetilde{W}} = 1)$ Optimal Observable distributions, are showed in Figure 7.40. In Table 7.8, the best limits of each coupling at 68% and 95% CLs are reported.

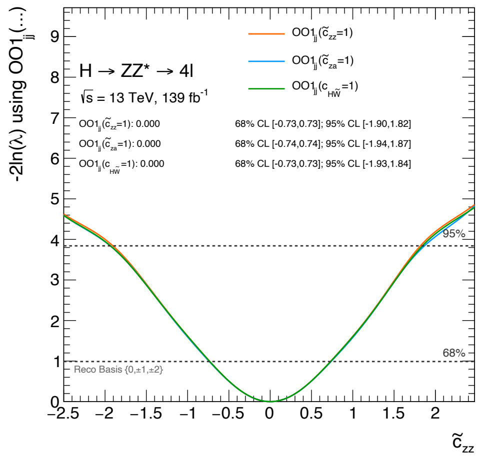

(a) NLL scan on $\widetilde{c}_{zz}$

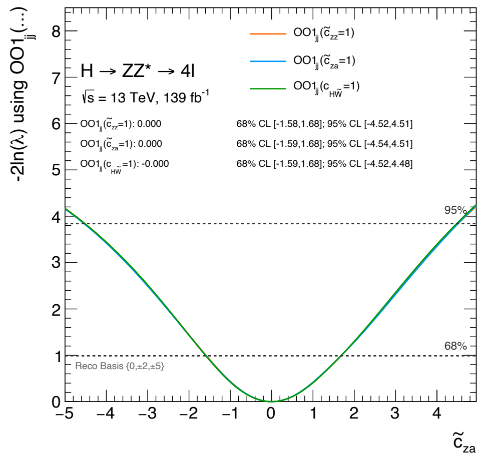

(b) NLL scan on $\widetilde{c}_{za}$

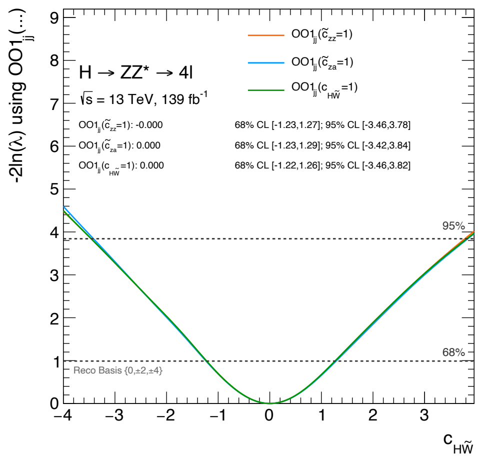

(c) NLL scan on $c_{H\widetilde{W}}$

Figure 7.40: NLL scan along $\widetilde{c}_{zz}$ (a), $\widetilde{c}_{za}$ (b) and $c_{H\widetilde{W}}$ (c) fittin Optimal Observables $\mathcal{OO}_{1,jj}(\widetilde{c}_{zz} = 1)$, $\mathcal{OO}_{1,jj}(\widetilde{c}_{za} = 1)$ and $\mathcal{OO}_{1,jj}(c_{H\widetilde{W}} = 1)$.

Coupling	68% CL	95% CL
$\widetilde{c}_{zz}$	$[-0.73, 0.73]$	$[-1.90, 1.82]$
$\widetilde{c}_{za}$	$[-1.59, 1/68]$	$[-4.54, 4.51]$
$c_{H\widetilde{W}}$	$[-1.22, 1.26]$	$[-3.46, 3.82]$

Table 7.8: Expected exclusion limits at 68% and 95% CL for CP-odd couplings $\widetilde{c}_{zz}$, $\widetilde{c}_{za}$ and $c_{H\widetilde{W}}$ from shape-based measurement

Conclusions

In the first part of this thesis work, the challenge for the ATLAS detectors upgrade has been presented. The New Small Wheel Upgrade of the muon spectrometer has entered the mass production phase for what concern the Micromegas quadruplet, with the goal to build all the detectors in time for their installation of the two NSW (NSW-A and NSW-C) during the LS2.

At the Frascati National Laboratories has been developed an assembly and validation procedure of the SM1 chambers. Several validation tests is performed on SM1 modules: planarity, readout strips alignment, gas tightness and high voltage stability test. Finally a test with cosmic rays is done to test the performance of the chambers.

The high voltage stability has been presented as a critical point of the MM production, and several sources of this problem have been identified and solved. The residual ionic contamination has been reduced with a cleaning procedure, the mesh imperfections with a polishing of the mesh itself, the gas humidity has been solved by increasing the gas flux and the non-uniformity of the readout board resistivity passivating the edge of the board. An extensive study on the resistance of the PCB board related to the layout of the resistive strips has been performed. This work will lead to future improvements on the design of the PCB boards to minimise low resistivity regions and then potential weak points for the high voltage.

To date 33 SM1 modules have been produced, 32 to be installed on both NSW and one spare, and they are all at CERN. The first 16 modules has been already installed on the Double-Wedges corresponding to the 8 sectors of the NSW-A. Once the modules arrive at CERN, further HV tests are performed together with irradiation tests at Gamma Ray Irradiation (GIF++) facility. They are then integrated in the Double-Wedges. The final HV test with a different HV scheme (done using a *splitter box*) is performed together with the final electronics test at Cosmic Ray Stand to validate the DW performance.

In the second part inclusive fiducial and differential cross section measurements of the Higgs boson in the $H \to ZZ^* \to 4l$ decay channel has been presented. They are based on 139 fb^{-1} of $\sqrt{s} = 13$ TeV proton–proton collisions recorded by the ATLAS detector at the LHC in 2015-2018.

The inclusive fiducial cross section is measured to be:

$$\sigma^{\text{fid}} = 3.38 \pm 0.30(\text{stat.}) \pm 0.11(\text{syst.})\ \text{fb},$$

in agreement with the Standard Model prediction $\sigma_{SM}^{fid} = 3.41 \pm 0.18$ fb. Differential cross sections defined in a fiducial region are measured of several observables sensitive to Higgs boson properties and to possible BSM effects. Also in this case a good agreement is found between the data and the predictions of the Standard Model. Respect with the old analysis, several changes as been made as the lepton isolation criteria in the event selection and a matrix unfolding method has been used instead the bin-by-bin correction factor method.

Observed results of differential cross section measurements for some variables have been presented in detail in this thesis, those function of the transverse momentum $p_T^4 l$, of the number of jets N_{jets}, of the invariant mass of the di-jet system m_{jj}, and of the double-differential m_{12} vs. m_{34}. Furthermore, also some preliminary expected results of unfolded CP-odd sensitive observables distribution has been presented, in particular of O_2, O_5 and the Optimal Observable $\mathcal{OO}_{1,jj}(\tilde{c}_{zz} = 1)$.

The prospect to perform a fiducial VBF measurement in the $H \to ZZ^* \to 4l$ decay channel has been investigated. With the current available statistics, the expected sensitivity is very low (70% of statistical uncertainty), with an expected VBF fiducial cross section of:

$$\sigma_{\text{VBF}}^{\text{fid}} = 0.131^{+0.096}_{-0.088}(\text{stat.})\ \text{fb}.$$

The expected results with enhanced statistics at 300 fb^{-1}and 3000 fb^{-1}have been investigated, looking at the possibility to have a differential VBF cross section measurement in $\mathcal{OO}_{1,jj}(\tilde{c}_{zz} = 1)$. An improvement of the sensitivity is expected up to 30% at 3000 fb^{-1}.

The differential cross section measurements have been interpreted in different theoretical framework to put constraint on anomalous Higgs boson couplings. The double-differential cross section has been interpreted in the Pseudo-Observables framework, in which the lepton flavour non-universal scenarios have been investigated for the first time and also a parametrisation of the cross section $h \to 4l$ has been used to extrapolated the exclusion plots. Several coverage test with toys has been performed to validate the statistical analysis. New and more stringent constraints on contact terms interactions in the $h \to 4l$ amplitudes has been introduced, in particular for the flavour non-universal scenarios with helicity structure of the couplings fixed to be vector ($\varepsilon_R = \varepsilon_L$) or axial ($\varepsilon_R = -\varepsilon_L$), the observed limits at 95% CL are:

$$\text{Vector: } \varepsilon_{Ze} \in [-0.097, 0.082]\ @\ 95\%\ CL\ ; \varepsilon_{Z\mu} \in [-0.131, 0.114]\ @\ 95\%\ CL,$$
$$\text{Axial: } \varepsilon_{Ze} \in [-0.056, 0.012]\ @\ 95\%\ CL\ ; \varepsilon_{Z\mu} \in [-0.016, 0.033]\ @\ 95\%\ CL.$$

The Higgs boson transverse momentum spectrum has been used to constrain the Yukawa couplings with $b-$ and $c-$ quark, using different approaches with different level of model-dependency. In the most model-independent approach which look at only the modification of the p_T^{4l} shape, the observed limits at 95% CL of κ_c are:

$$\kappa_c \in [-11.7, 10.5] \text{ @ } 95\% \; CL.$$

Finally also preliminary sensitivity studies has been performed for CP-violation search in the $H \to ZZ^* \to 4l$ decay channel, both as an interpretation of the differential cross section measurements of the $\mathcal{OO}_{1,jj}(\widetilde{c}_{zz} = 1)$, and with a shape-based analysis looking at BSM effects only on the shape of the Optimal Observable. The expected limits at 95% CL obtained with the two approaches on the $\widetilde{c}_{zz}$ coupling are:

$$\widetilde{c}_{zz} \in [-1.97, 1.99] \text{ @ } 95\% \; CL,$$

$$\widetilde{c}_{zz} \in [-1.90, 1.82] \text{ @ } 95\% \; CL.$$

Appendices

Appendix A

Fiducial differential cross section results

A.1 Measured Data Yields

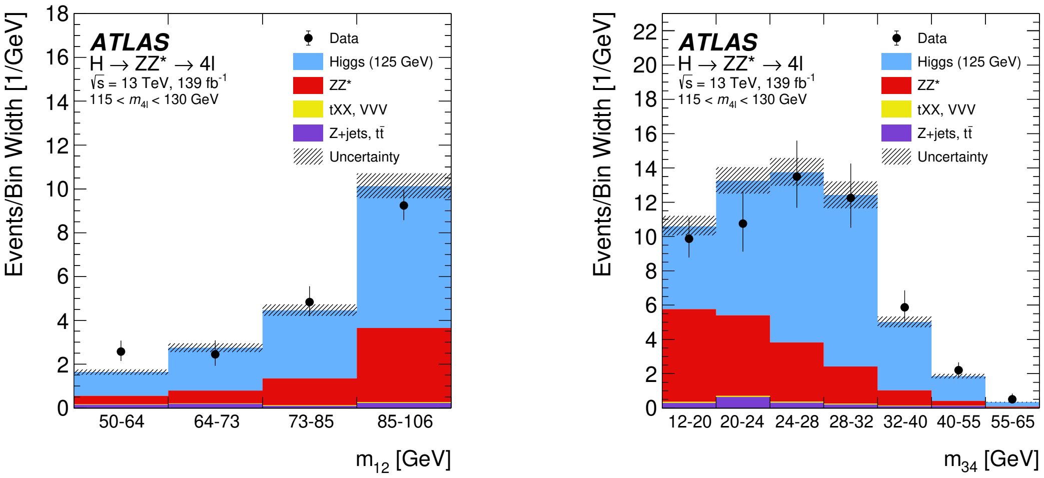

(a) (b)

Figure A.1: The observed and expected (pre-fit) distributions of a m_{12}, and b m_{34} in the mass region $115 < m_{4\ell} < 130$ GeV, for an integrated luminosity of 139 fb^{-1} collected at $\sqrt{s} = 13$ TeV. A SM Higgs boson signal with a mass $m_H = 125$ GeV is assumed. The uncertainty in the prediction is shown by the hatched band, which includes the theoretical uncertainties of the SM cross section for the signal and the ZZ^* background.

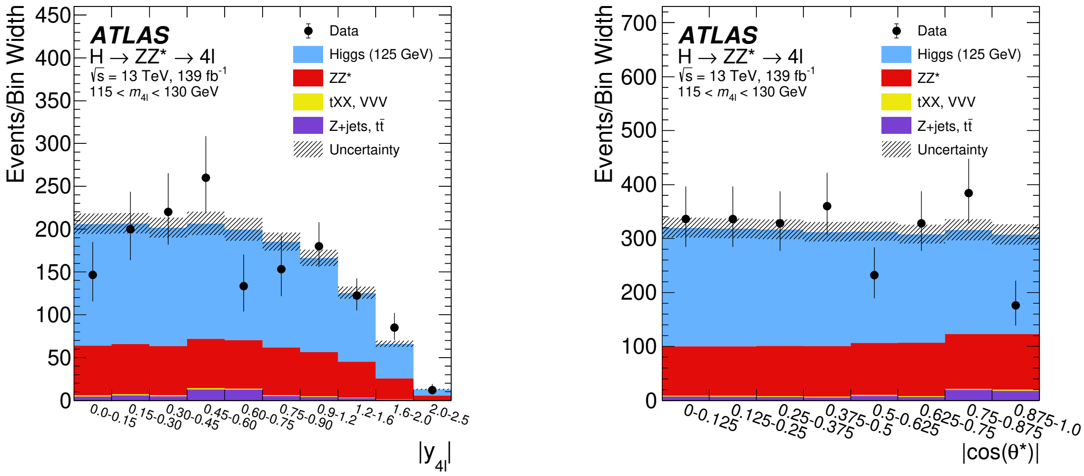

(a) (b)

Figure A.2: The observed and expected (pre-fit) distributions of a $|y_{4\ell}|$ and b $|\cos\theta^*|$ in the mass region $115 < m_{4\ell} < 130$ GeV, for an integrated luminosity of 139 fb^{-1} collected at $\sqrt{s} = 13$ TeV. A SM Higgs boson signal with a mass $m_H = 125$ GeV is assumed. The uncertainty in the prediction is shown by the hatched band, which includes the theoretical uncertainties of the SM cross section for the signal and the ZZ^* background.

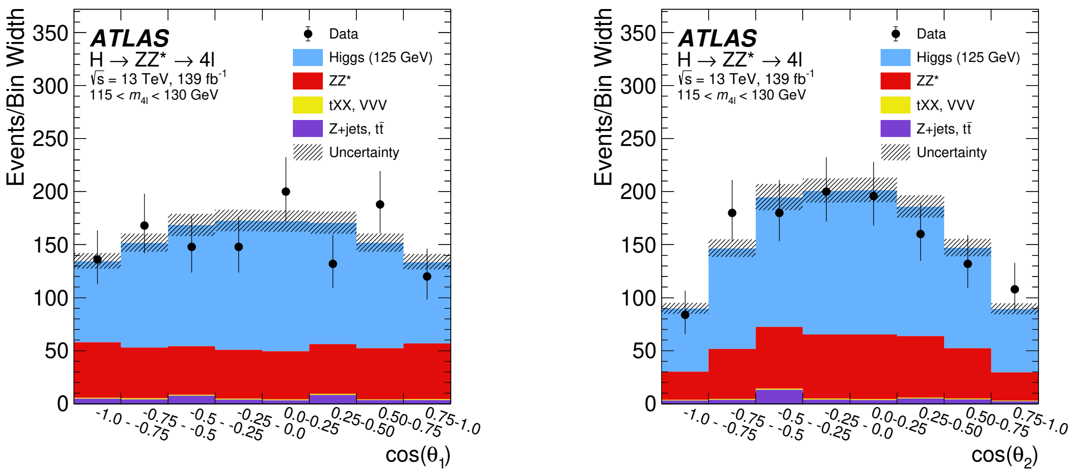

(a) (b)

Figure A.3: The observed and expected (pre-fit) distributions of a $\cos\theta_1$ and b $\cos\theta_2$ in the mass region $115 < m_{4\ell} < 130$ GeV, for an integrated luminosity of 139 fb^{-1} collected at $\sqrt{s} = 13$ TeV. A SM Higgs boson signal with a mass $m_H = 125$ GeV is assumed. The uncertainty in the prediction is shown by the hatched band, which includes the theoretical uncertainties of the SM cross section for the signal and the ZZ^* background.

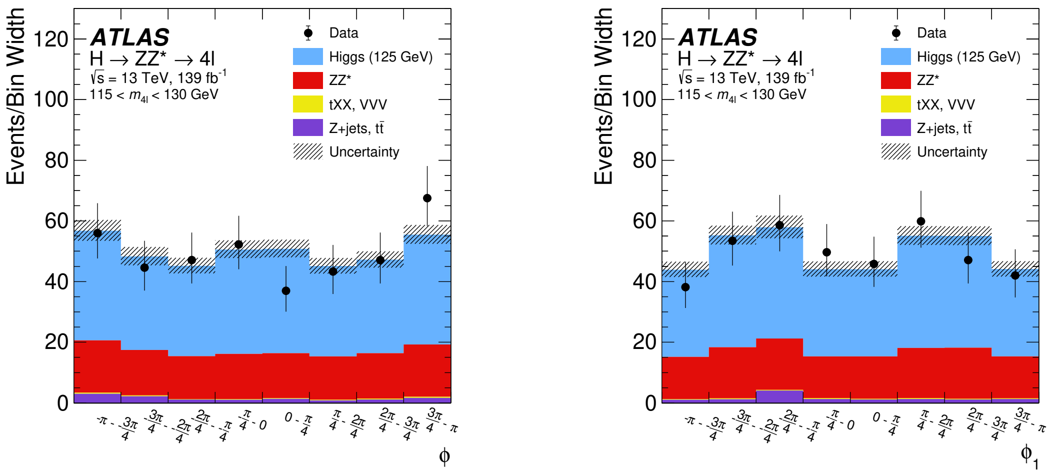

(a) (b)

Figure A.4: The observed and expected (pre-fit) distributions of a ϕ, and b ϕ_1 in the mass region $115 < m_{4\ell} < 130$ GeV, for an integrated luminosity of 139 fb^{-1} collected at $\sqrt{s} = 13$ TeV. A SM Higgs boson signal with a mass $m_H = 125$ GeV is assumed. The uncertainty in the prediction is shown by the hatched band, which includes the theoretical uncertainties of the SM cross section for the signal and the ZZ^* background.

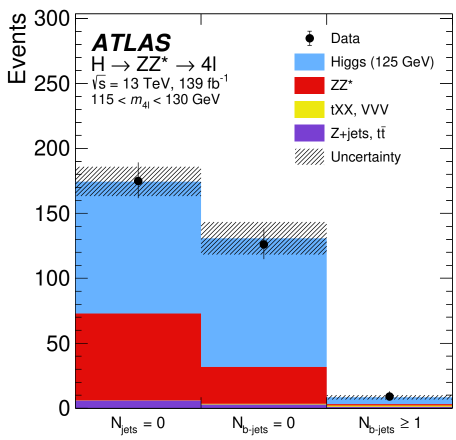

Figure A.5: The observed and expected (pre-fit) distributions of $N_{b-\mathrm{jets}}$ in the mass region $115 < m_{4\ell} < 130$ GeV, for an integrated luminosity of 139 fb^{-1} collected at $\sqrt{s} = 13$ TeV. A SM Higgs boson signal with a mass $m_H = 125$ GeV is assumed. The uncertainty in the prediction is shown by the hatched band, which includes the theoretical uncertainties of the SM cross section for the signal and the ZZ^* background.

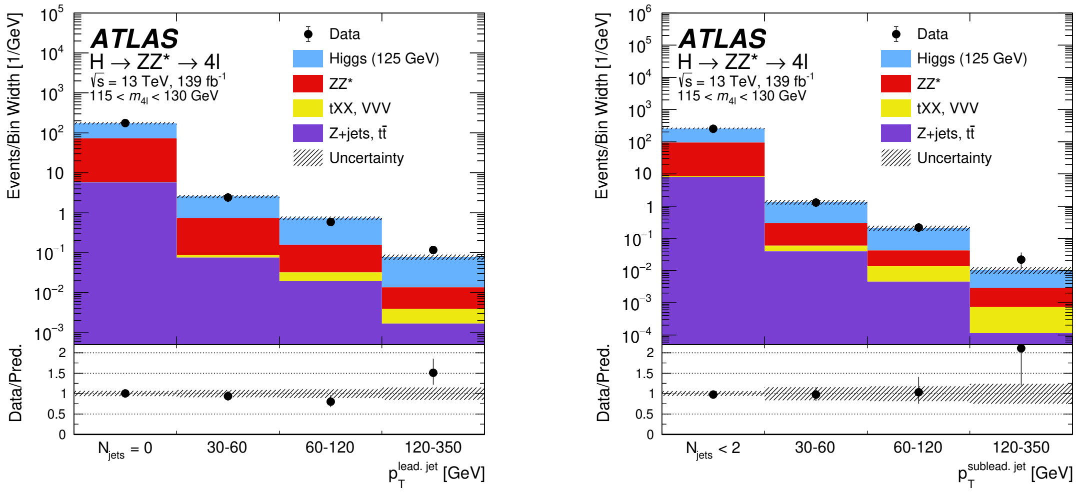

(a) (b)

Figure A.6: The observed and expected (pre-fit) distributions of a $p_{\mathrm{T}}^{\text{lead. jet}}$, and b $p_{\mathrm{T}}^{\text{sublead. jet}}$ in the mass region $115 < m_{4\ell} < 130$ GeV, for an integrated luminosity of 139 fb^{-1} collected at $\sqrt{s} = 13$ TeV. A SM Higgs boson signal with a mass $m_H = 125$ GeV is assumed. The uncertainty in the prediction is shown by the hatched band, which includes the theoretical uncertainties of the SM cross section for the signal and the ZZ^* background.

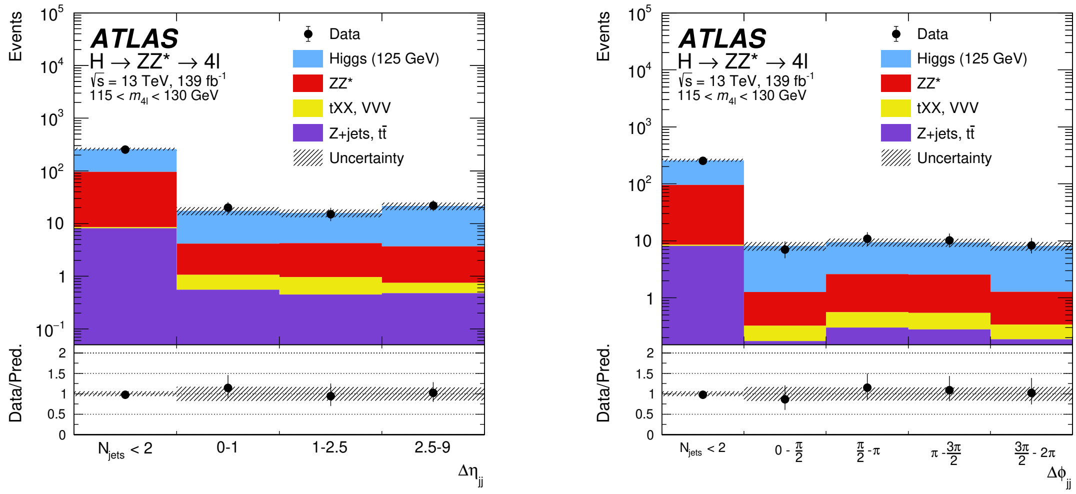

(a) (b)

Figure A.7: The observed and expected (pre-fit) distributions of a $\Delta\eta_{\mathrm{jj}}$, and b $\Delta\phi_{\mathrm{jj}}$ in the mass region $115 < m_{4\ell} < 130$ GeV, for an integrated luminosity of 139 fb^{-1} collected at $\sqrt{s} = 13$ TeV. A SM Higgs boson signal with a mass $m_H = 125$ GeV is assumed. The uncertainty in the prediction is shown by the hatched band, which includes the theoretical uncertainties of the SM cross section for the signal and the ZZ^* background.

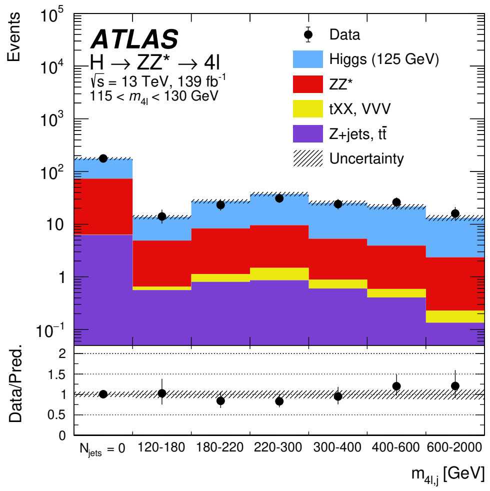

(a)

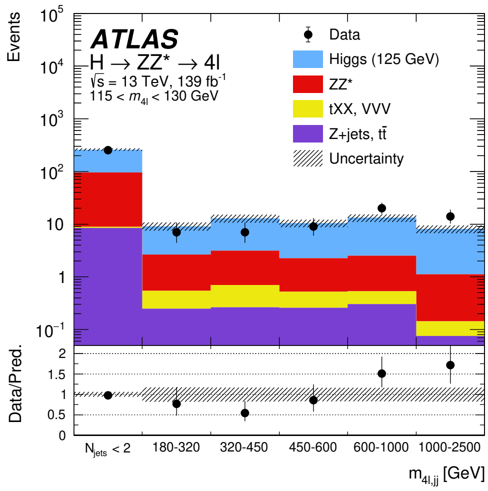

(b)

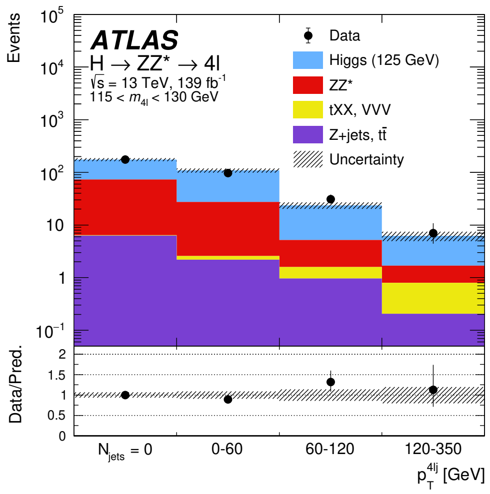

(c)

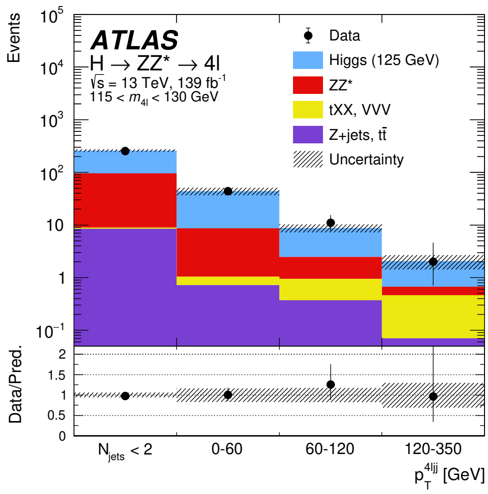

(d)

Figure A.8: The observed and expected (pre-fit) distributions of a $m_{4\ell\mathrm{j}}$, b $m_{4\ell\mathrm{jj}}$, c $p_{\mathrm{T}}^{4\ell\mathrm{j}}$, and d $p_{\mathrm{T}}^{4\ell\mathrm{jj}}$ in the mass region $115 < m_{4\ell} < 130$ GeV, for an integrated luminosity of 139 fb^{-1} collected at $\sqrt{s} = 13$ TeV. A SM Higgs boson signal with a mass $m_H = 125$ GeV is assumed. The uncertainty in the prediction is shown by the hatched band, which includes the theoretical uncertainties of the SM cross section for the signal and the ZZ^* background.

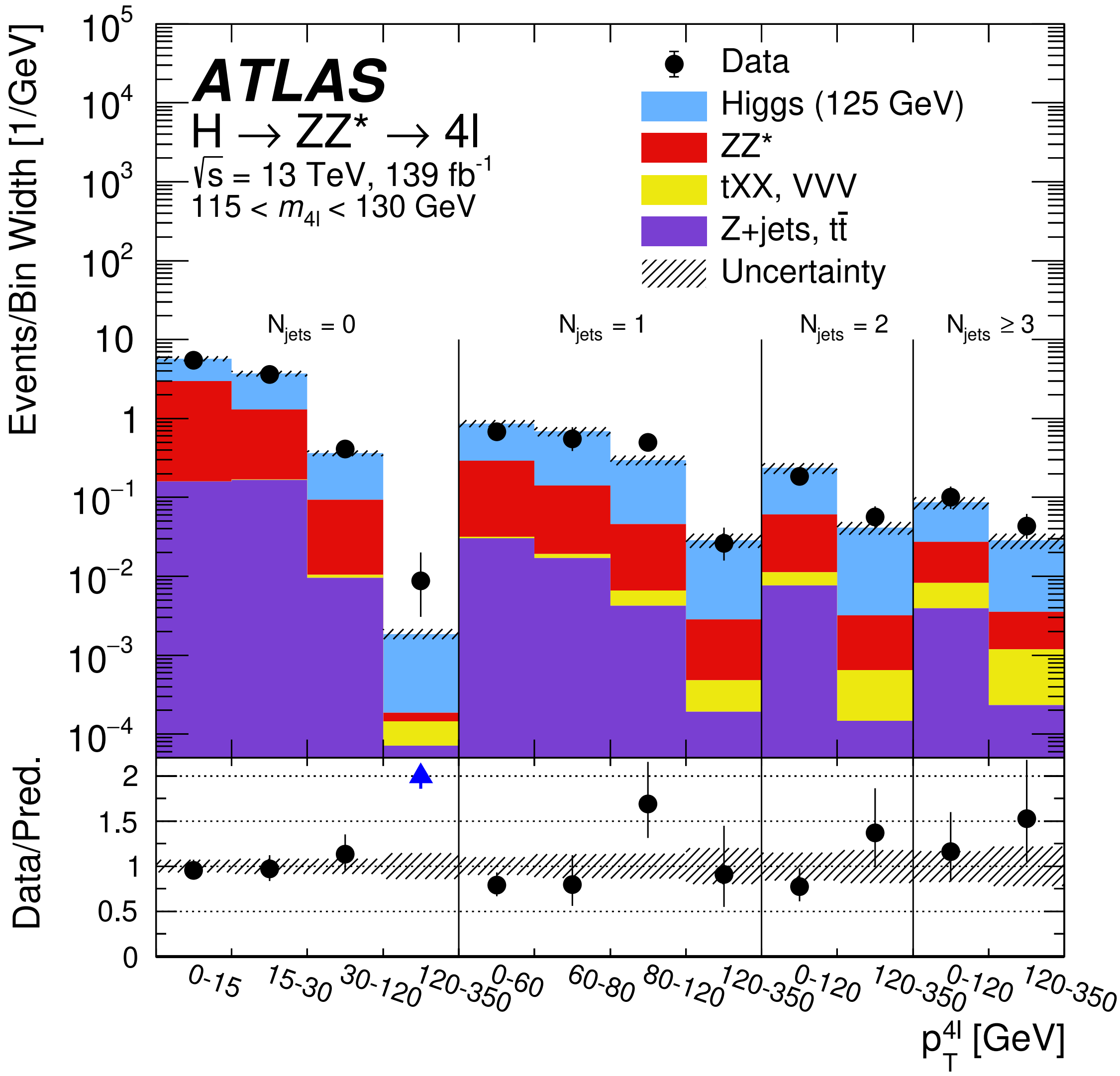

Figure A.9: The observed and expected (pre-fit) distributions of $p_{\mathrm{T}}^{4\ell}$ in N_{jets} bins in the mass region $115 < m_{4\ell} < 130$ GeV, for an integrated luminosity of 139 fb^{-1} collected at $\sqrt{s} = 13$ TeV. A SM Higgs boson signal with a mass $m_H = 125$ GeV is assumed. The uncertainty in the prediction is shown by the hatched band, which includes the theoretical uncertainties of the SM cross section for the signal and the ZZ^* background.

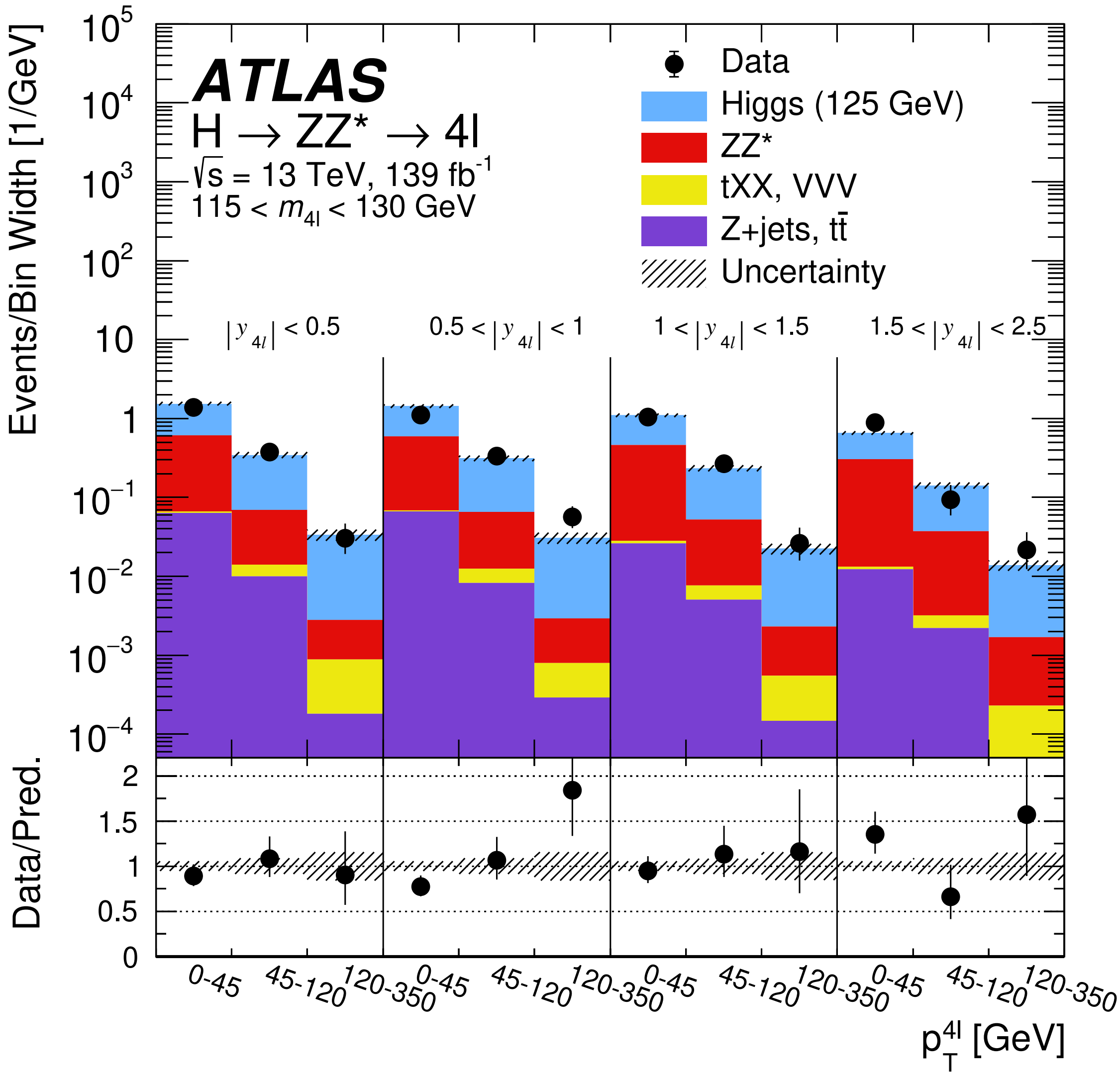

Figure A.10: The observed and expected (pre-fit) distributions of $p_{\mathrm{T}}^{4\ell}$ in $|y_{4\ell}|$ bins in the mass region $115 < m_{4\ell} < 130$ GeV, for an integrated luminosity of 139 fb^{-1} collected at $\sqrt{s} = 13$ TeV. A SM Higgs boson signal with a mass $m_H = 125$ GeV is assumed. The uncertainty in the prediction is shown by the hatched band, which includes the theoretical uncertainties of the SM cross section for the signal and the ZZ^* background.

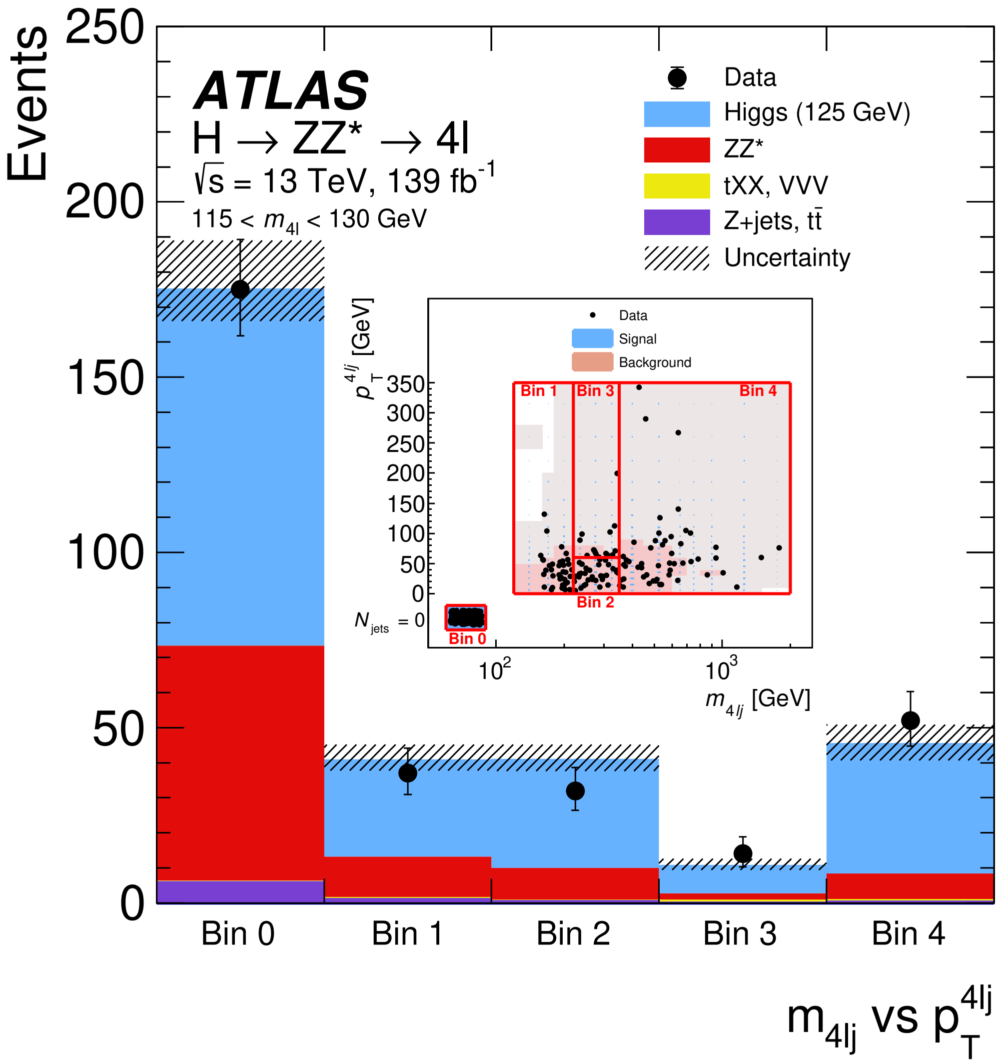

Figure A.11: The observed and expected (pre-fit) distribution in bins of the transverse momentum of the four-lepton plus leading-jet system vs. the invariant mass of the four-lepton plus leading-jet system, $p_{\mathrm{T}}^{4\ell\mathrm{j}}$ vs. $m_{4\ell\mathrm{j}}$. The same distribution in the 2D plane is provided in the inset plot, where the black dots depict data and the blue and pink shaded areas represent simulated signal and background, respectively. The red lines depict the bin boundaries. These distributions correspond to the mass region $115 < m_{4\ell} < 130$ GeV, for an integrated luminosity of 139 fb^{-1} collected at $\sqrt{s} = 13$ TeV. A SM Higgs boson signal with a mass $m_H = 125$ GeV is assumed. The uncertainty in the prediction is shown by the hatched band, which includes the theoretical uncertainties of the SM cross section for the signal and the ZZ^* background.

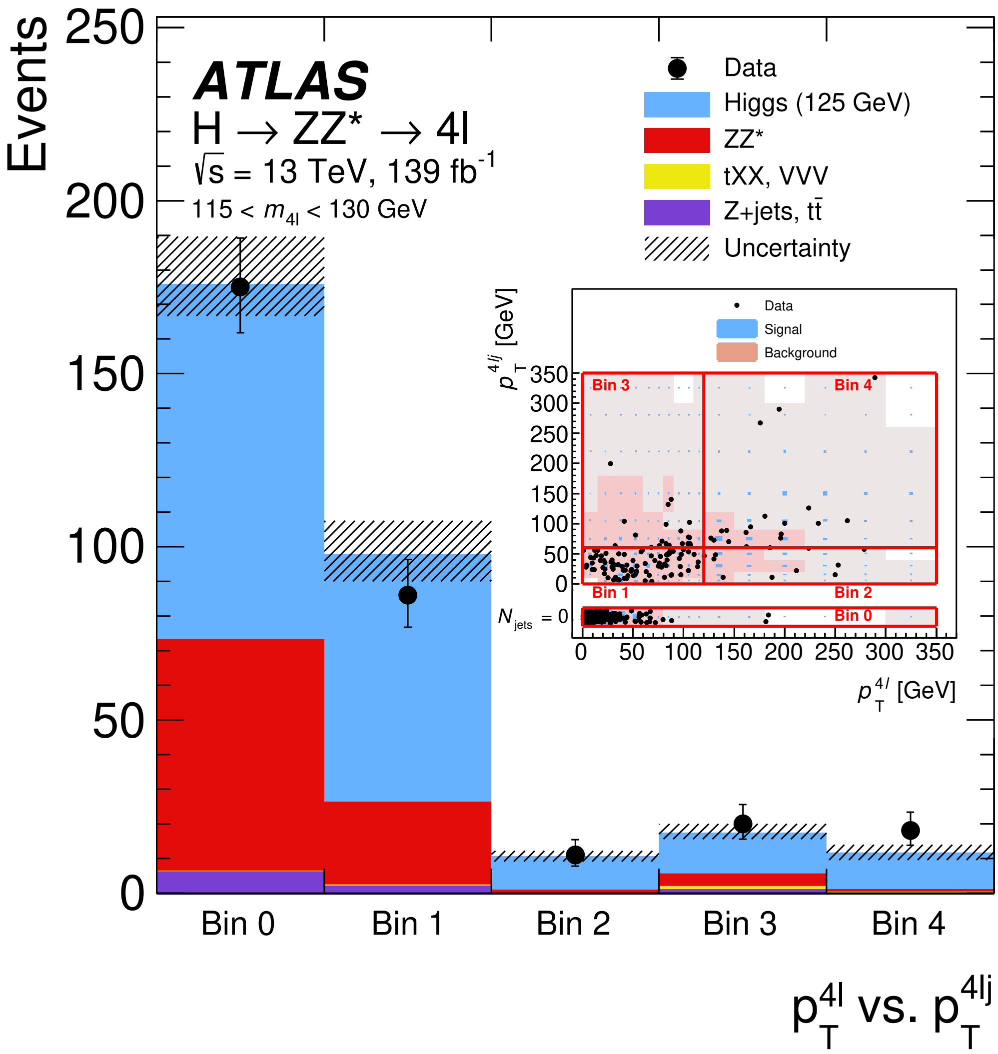

Figure A.12: The observed and expected (pre-fit) distribution in bins of the transverse momentum of the four-lepton system vs. the transverse momentum of the four-lepton plus leading-jet system, $p_{\mathrm{T}}^{4\ell}$ vs. $p_{\mathrm{T}}^{4\ell j}$. The same distribution in the 2D plane is provided in the inset plot, where the black dots depict data and the blue and pink shaded areas represent simulated signal and background, respectively. The red lines depict the bin boundaries. These distributions correspond to the mass region $115 < m_{4\ell} < 130$ GeV, for an integrated luminosity of 139 fb^{-1} collected at $\sqrt{s} = 13$ TeV. A SM Higgs boson signal with a mass $m_H = 125$ GeV is assumed. The uncertainty in the prediction is shown by the hatched band, which includes the theoretical uncertainties of the SM cross section for the signal and the ZZ^* background.

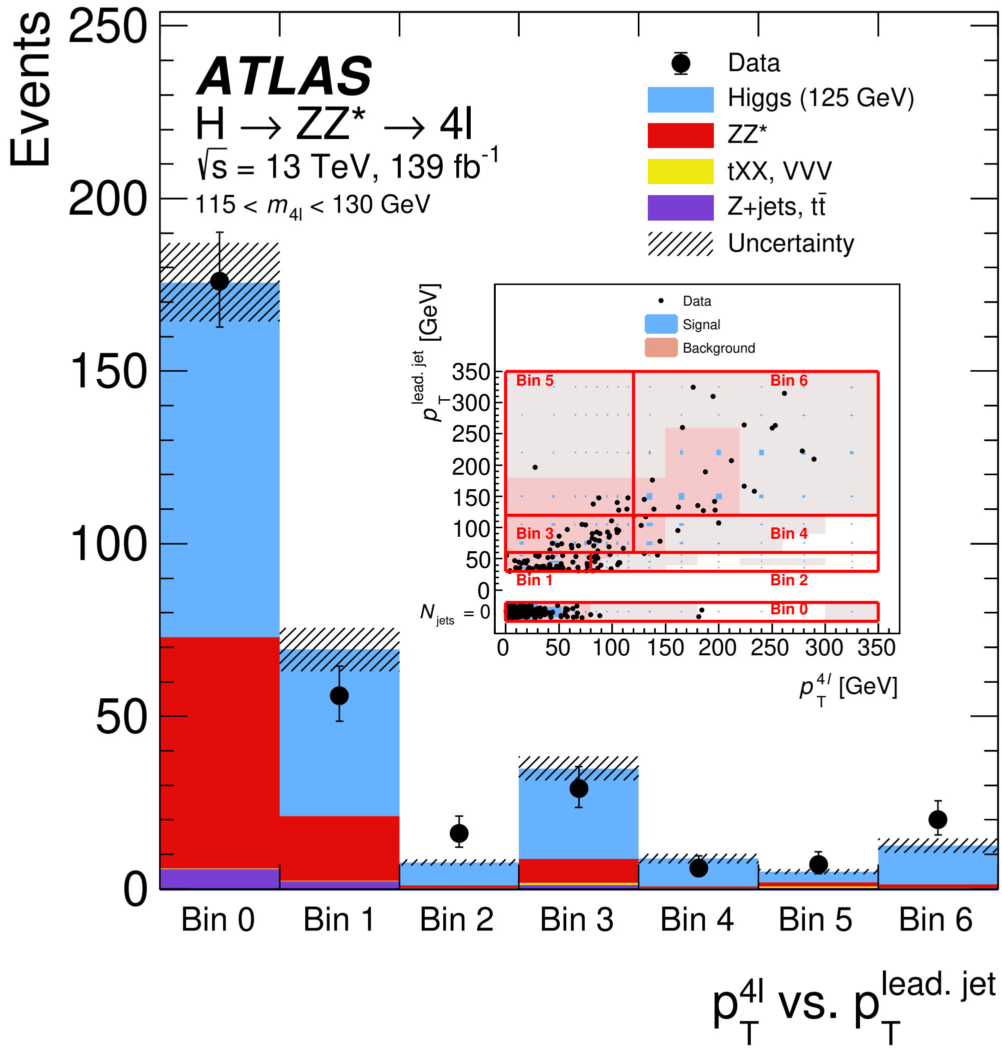

Figure A.13: The observed and expected (pre-fit) distribution in bins of the transverse momentum of the four-lepton system vs. the transverse momentum of the leading jet, $p_{\mathrm{T}}^{4\ell}$ vs. $p_{\mathrm{T}}^{\mathrm{lead.\ jet}}$. The same distribution in the 2D plane is provided in the inset plot, where the black dots depict data and the blue and pink shaded areas represent simulated signal and background, respectively. The red lines depict the bin boundaries. These distributions correspond to the mass region $115 < m_{4\ell} < 130$ GeV, for an integrated luminosity of 139 fb^{-1} collected at $\sqrt{s} = 13$ TeV. A SM Higgs boson signal with a mass $m_H = 125$ GeV is assumed. The uncertainty in the prediction is shown by the hatched band, which includes the theoretical uncertainties of the SM cross section for the signal and the ZZ^* background.

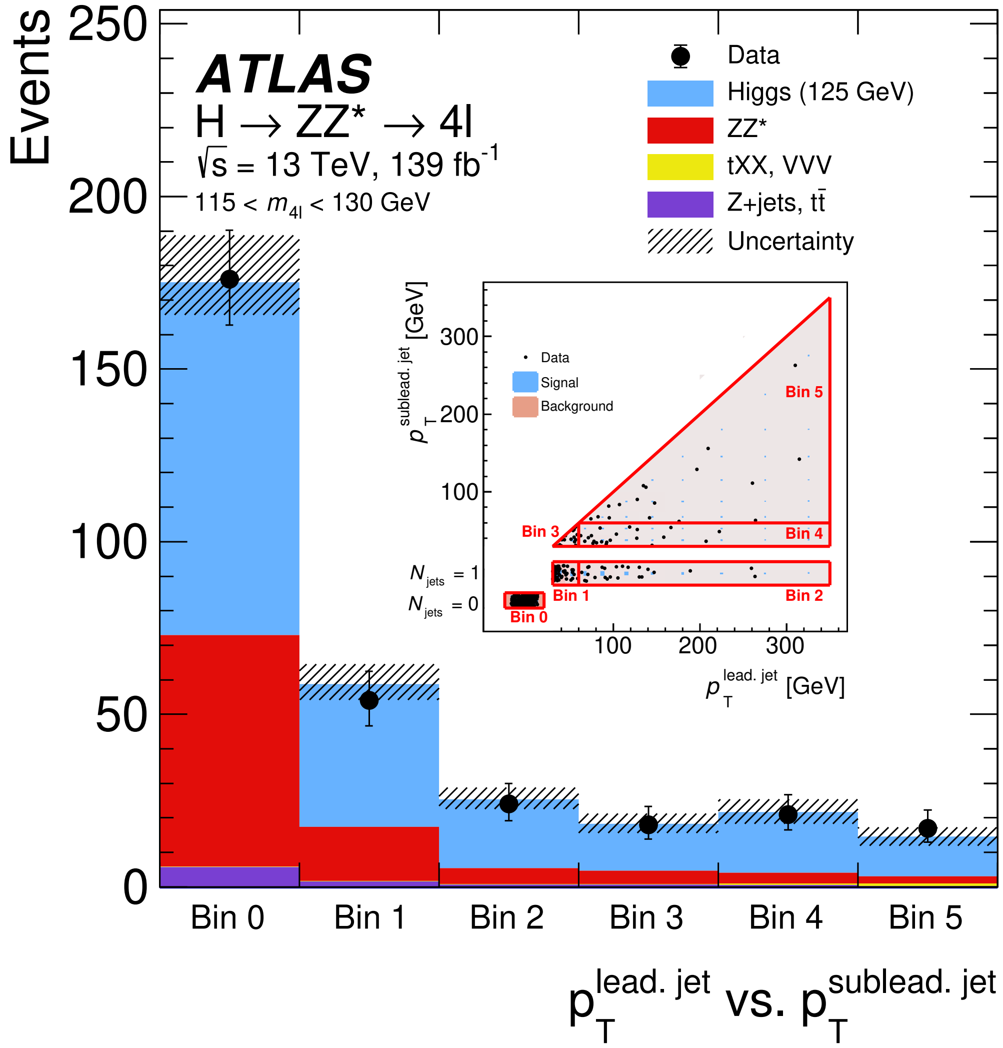

Figure A.14: The observed and expected (pre-fit) distribution in bins of the transverse momentum of the leading vs. subleading jet, $p_{\mathrm{T}}^{\text{lead. jet}}$ vs. $p_{\mathrm{T}}^{\text{sublead. jet}}$. The same distribution in the 2D plane is provided in the inset plot, where the black dots depict data and the blue and pink shaded areas represent simulated signal and background, respectively. The red lines depict the bin boundaries. These distributions correspond to the mass region $115 < m_{4\ell} < 130$ GeV, for an integrated luminosity of 139 fb^{-1} collected at $\sqrt{s} = 13$ TeV. A SM Higgs boson signal with a mass $m_H = 125$ GeV is assumed. The uncertainty in the prediction is shown by the hatched band, which includes the theoretical uncertainties of the SM cross section for the signal and the ZZ^* background.

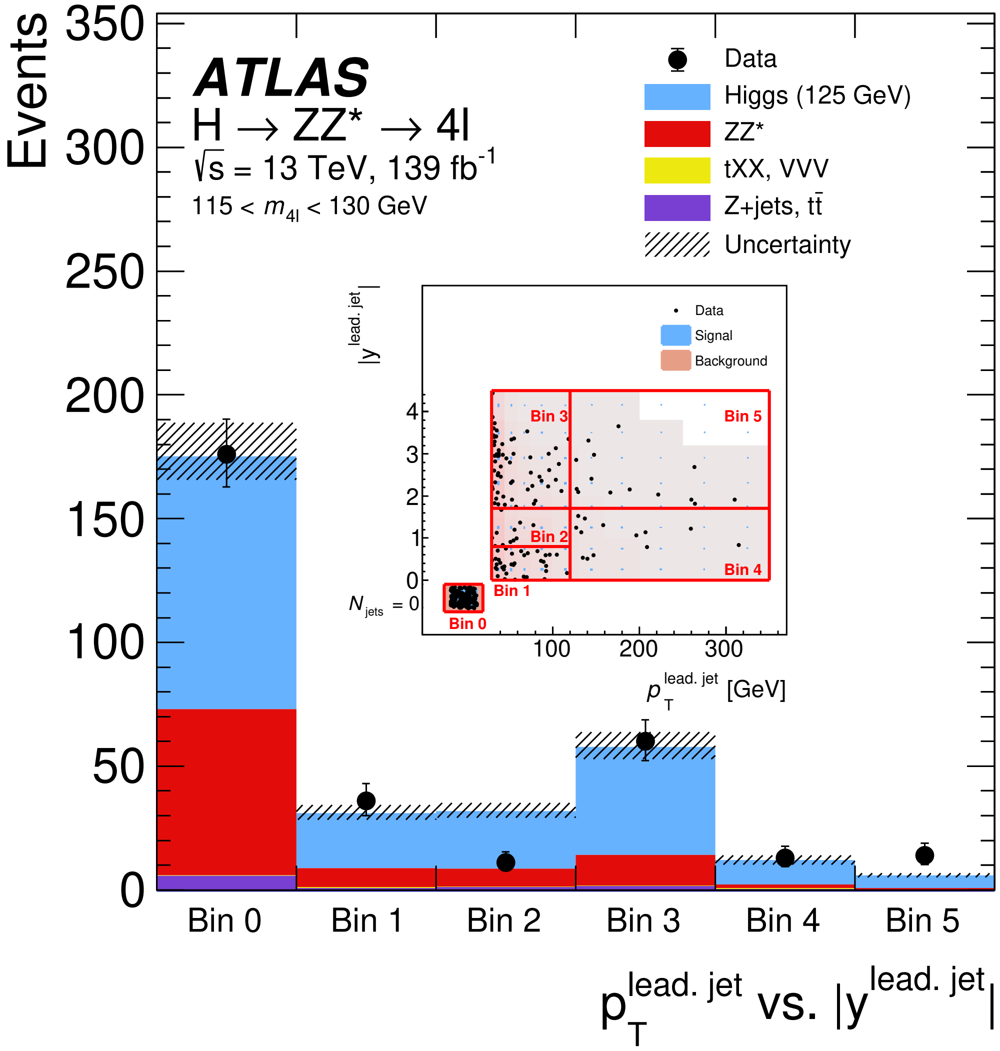

Figure A.15: The observed and expected (pre-fit) distribution in bins of the transverse momentum vs. the rapidity of the leading jet, $p_{\mathrm{T}}^{\text{lead. jet}}$ vs. $|y^{\text{lead. jet}}|$. The same distribution in the 2D plane is provided in the inset plot, where the black dots depict data and the blue and pink shaded areas represent simulated signal and background, respectively. The red lines depict the bin boundaries. These distributions correspond to the mass region $115 < m_{4\ell} < 130$ GeV, for an integrated luminosity of 139 fb^{-1} collected at $\sqrt{s} = 13$ TeV. A SM Higgs boson signal with a mass $m_H = 125$ GeV is assumed. The uncertainty in the prediction is shown by the hatched band, which includes the theoretical uncertainties of the SM cross section for the signal and the ZZ^* background.

A.2 Summary Plot

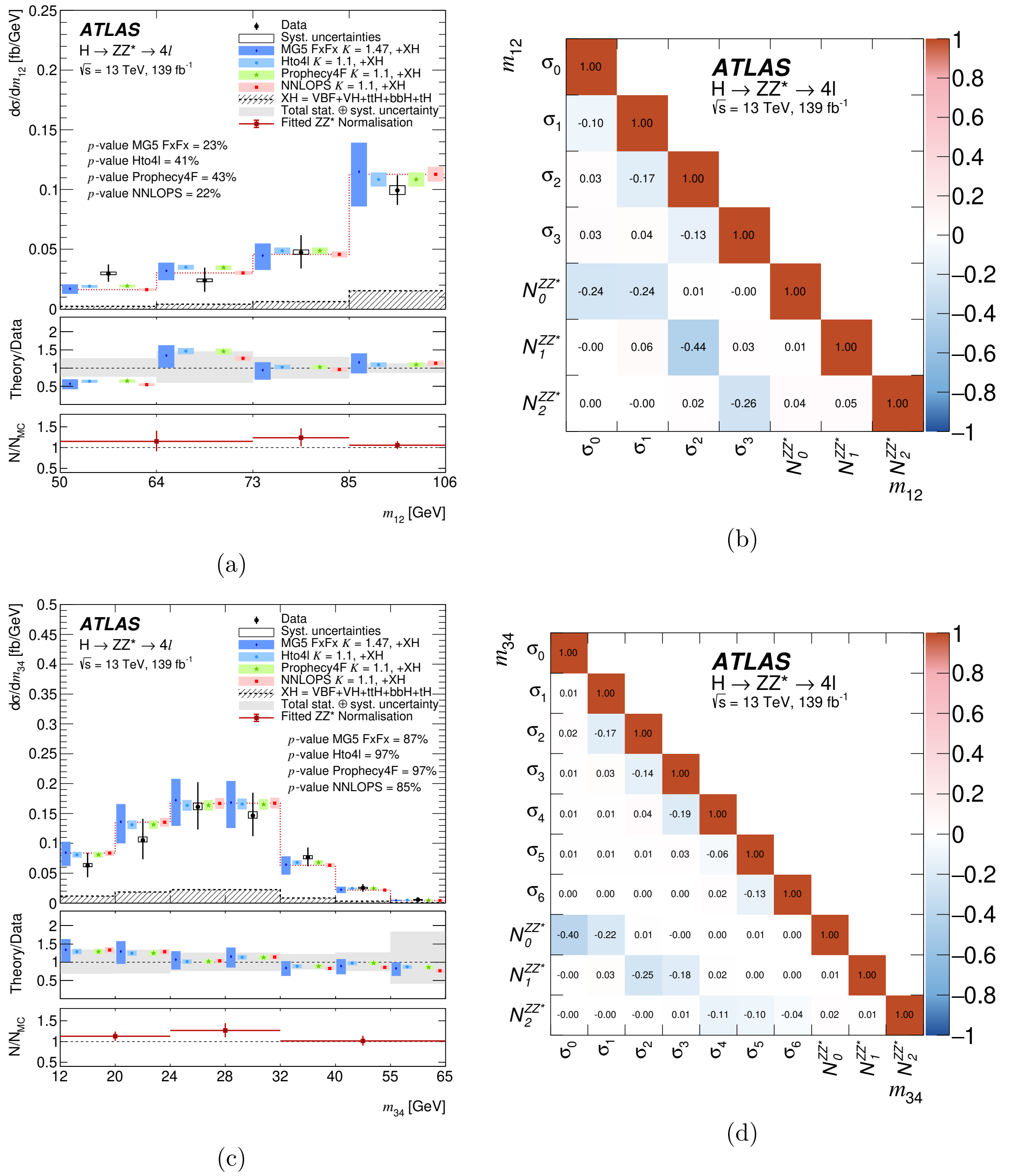

Figure A.16: Differential fiducial cross sections for a the invariant mass m_{12} of the leading Z boson and c the invariant mass m_{34} of the subleading Z boson, along with the corresponding correlation matrices between the measured cross sections and the ZZ^* background normalisation factors (b and d).

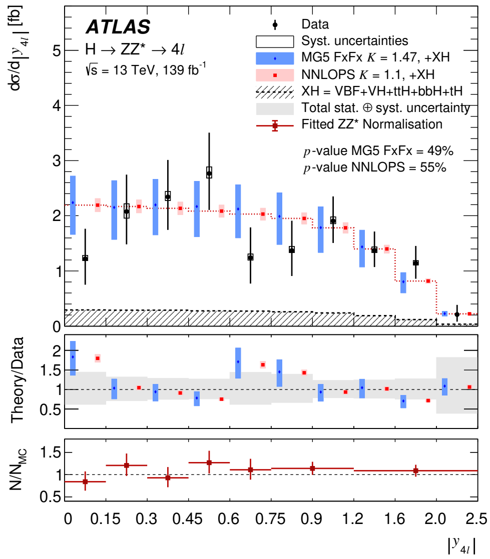

(a)

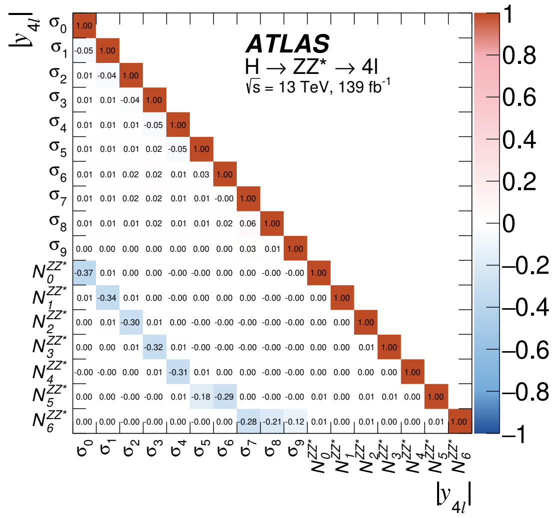

(b)

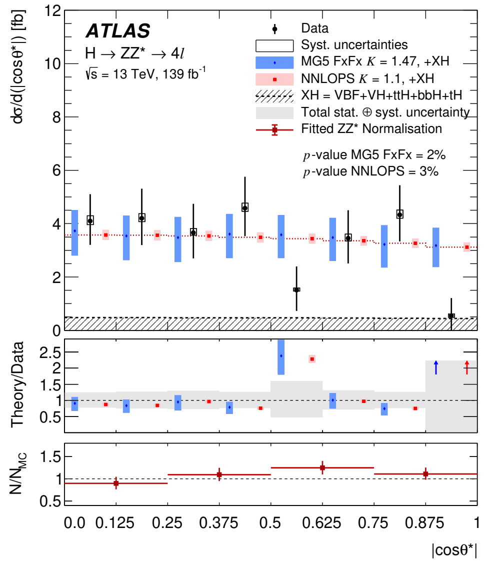

(c)

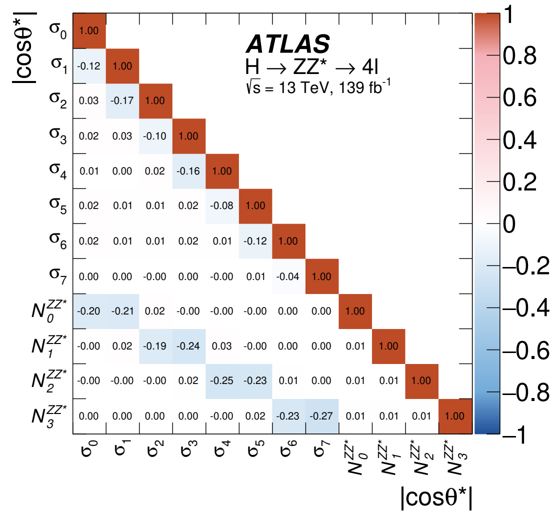

(d)

Figure A.17: Differential fiducial cross sections for a the rapidity, $|y_{4\ell}|$, of the Higgs boson and c the production angle, $|\cos\theta^*|$, of the leading Z boson. The corresponding correlation matrices between the measured cross sections and the ZZ^* background normalisation factors are also shown (b and d).

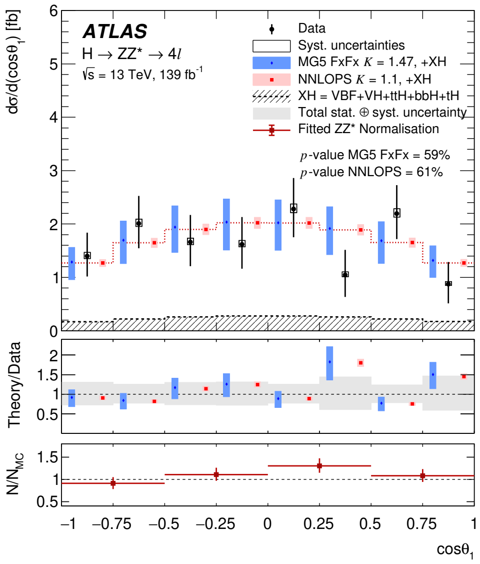

(a)

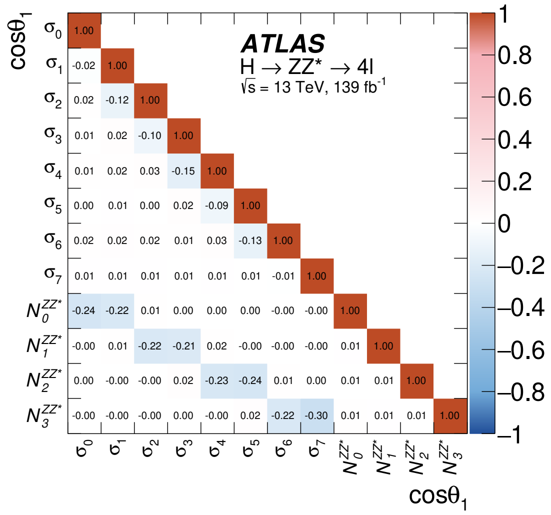

(b)

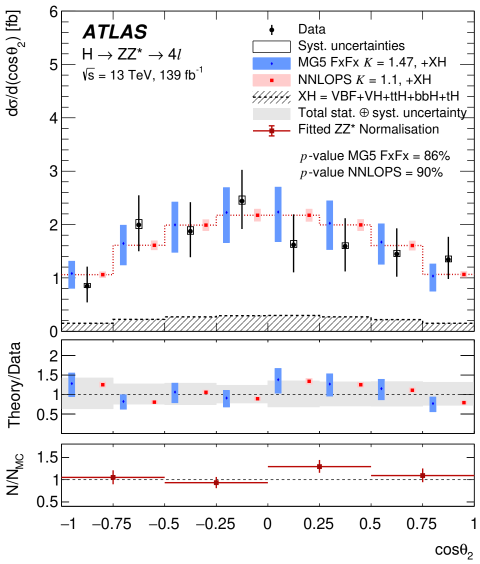

(c)

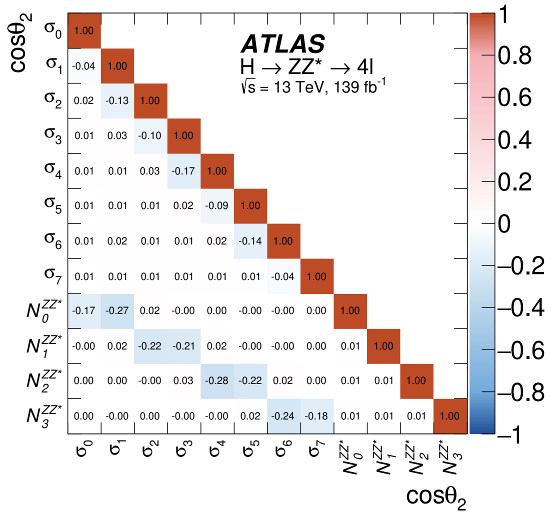

(d)

Figure A.18: Differential fiducial cross sections for a production angle, $\cos\theta_1$, of the anti-lepton from the leading Z boson and c the production angle, $\cos\theta_2$, of the anti-lepton from the subleading Z boson. The corresponding correlation matrices between the measured cross sections and the ZZ^* background normalisation factors are also shown (b and d).

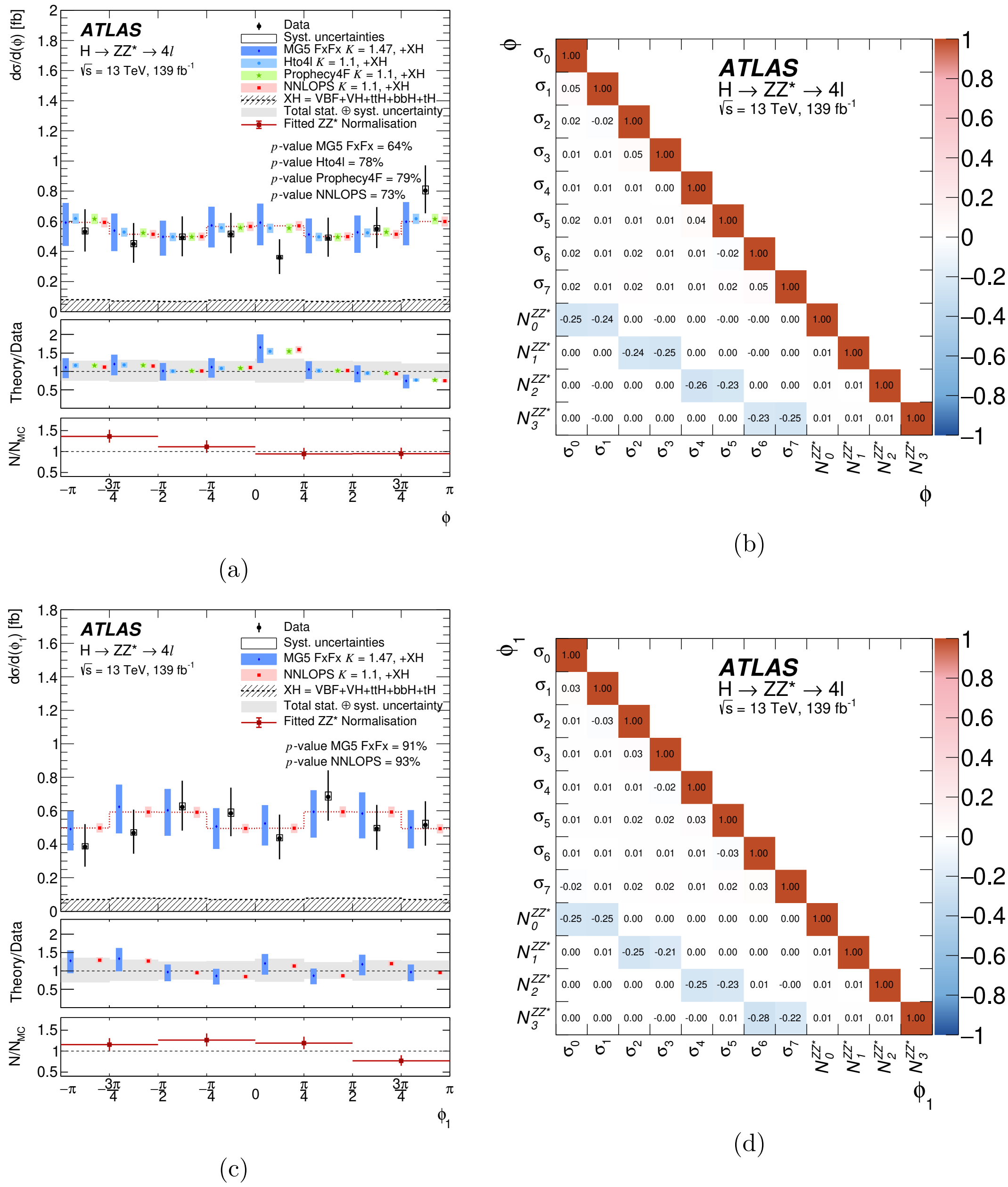

Figure A.19: Differential fiducial cross sections for a the azimuthal angle, ϕ, between the decay planes of the two reconstructed Z bosons and c the azimuthal angle, ϕ_1, between the decay plane of the leading Z boson and the plane formed by its four-momentum and the z-axis. The corresponding correlation matrices between the measured cross sections and the ZZ^* background normalisation factors are also shown (b and d).

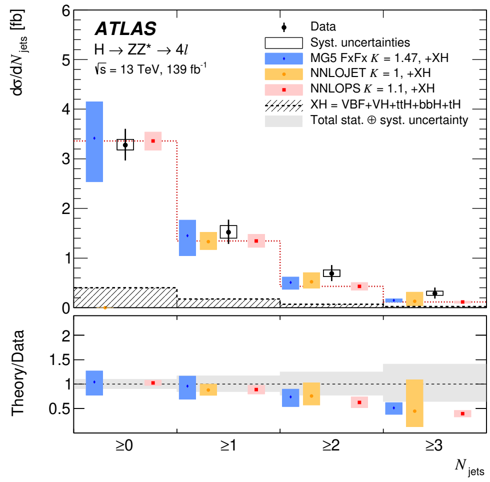

Figure A.20: Differential fiducial cross sections for the inclusive jet multiplicity. In this N_{jets} distribution all bins are inclusive, with the first bin including all events, the second including all events with at least one jet, and so on.

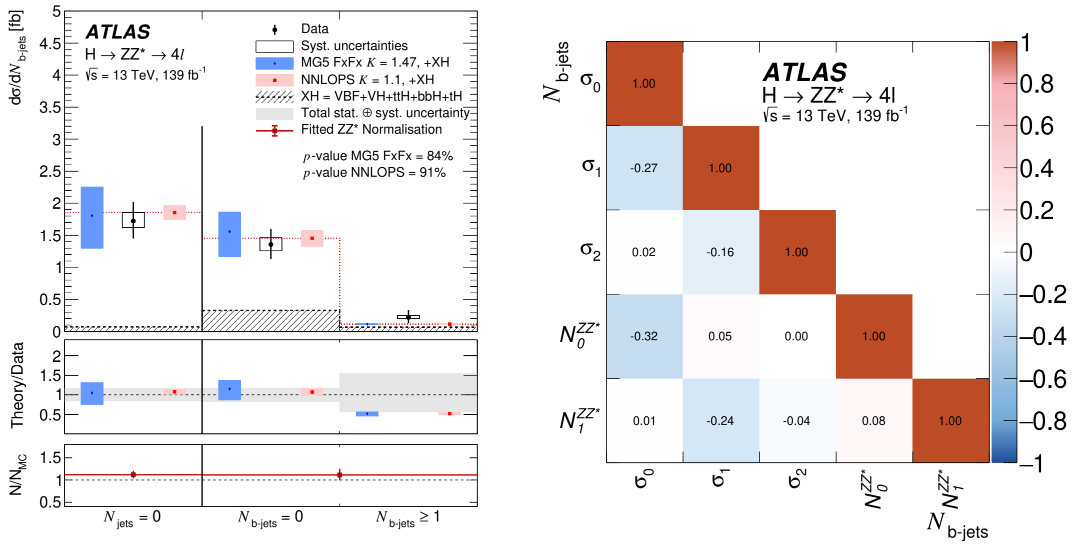

(a)

(b)

Figure A.21: a Differential fiducial cross section as function of the b-jet multiplicity, $N_{b-\text{jets}}$. Three bins are considered. The first bin is filled with events which do not have any jets, the second is filled with events with at least one jet but no b-tagged jets, while the third includes all events with at least one b-tagged jet. The corresponding correlation matrices between the measured cross sections and the ZZ^* background normalisation factors are also shown in b).

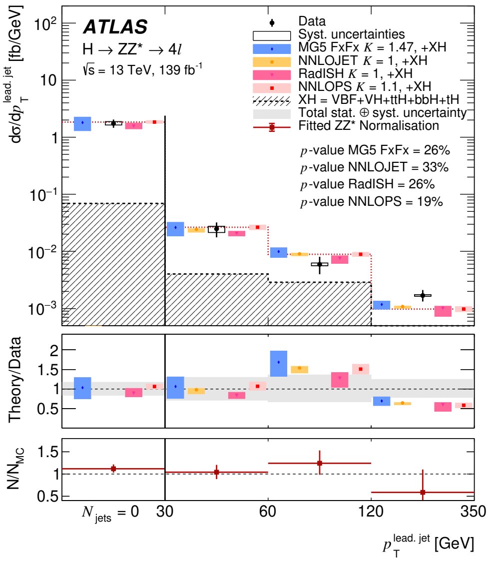

(a)

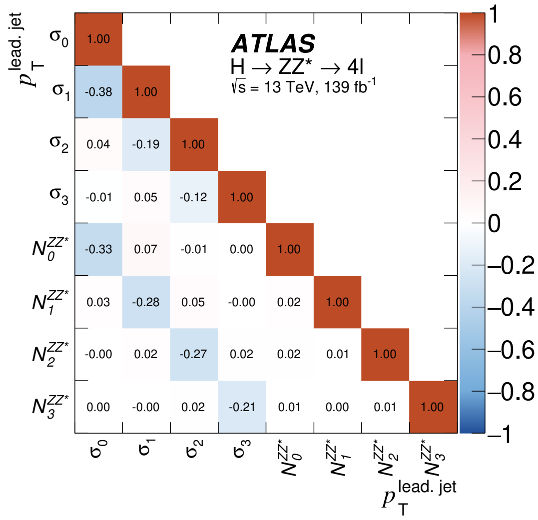

(b)

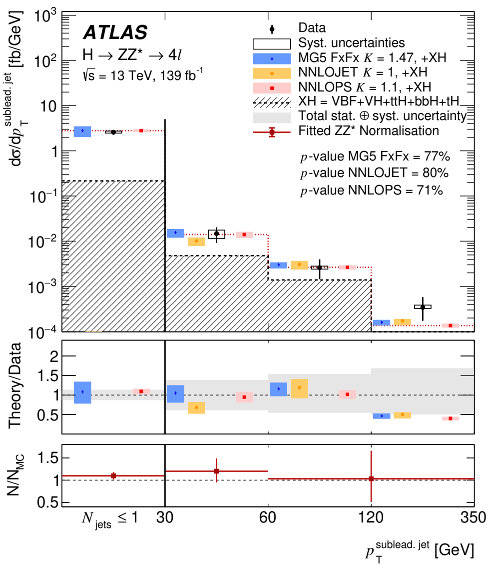

(c)

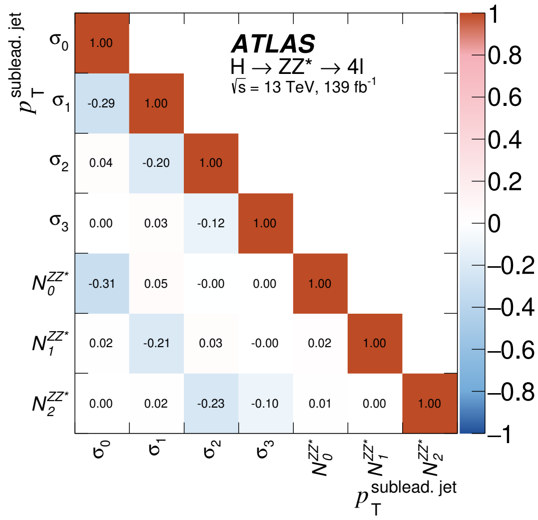

(d)

Figure A.22: Differential fiducial cross sections for a the transverse momentum of the leading jet, $p_{\mathrm{T}}^{\mathrm{lead.\ jet}}$, in events with at least one jet, and c the transverse momentum of the subleading jet, $p_{\mathrm{T}}^{\mathrm{sublead.\ jet}}$, in events with at least two jets. Leading and subleading jets refer to the jets with the highest and second-highest transverse momenta. The first bin contains events which do not pass the jet requirements. The corresponding correlation matrices between the measured cross sections and the ZZ^* background normalisation factors are also shown (b and d).

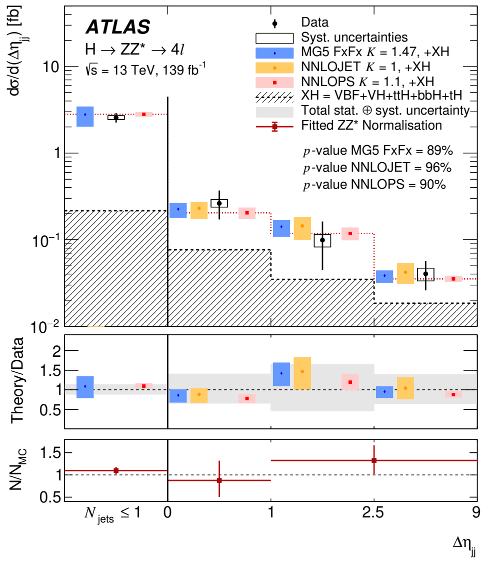

(a)

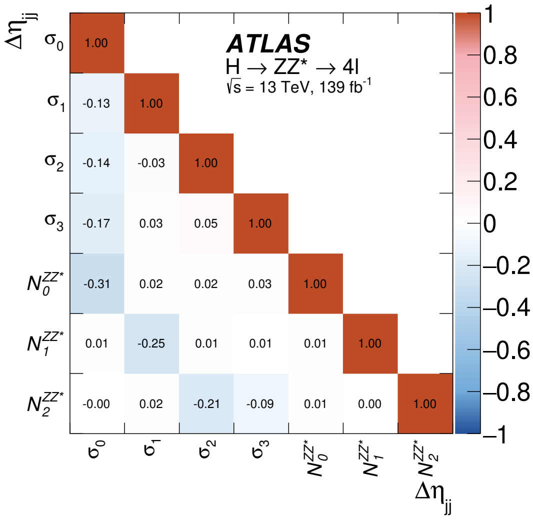

(b)

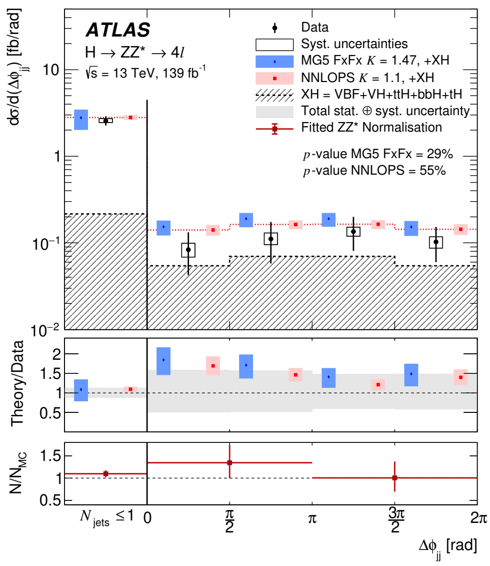

(c)

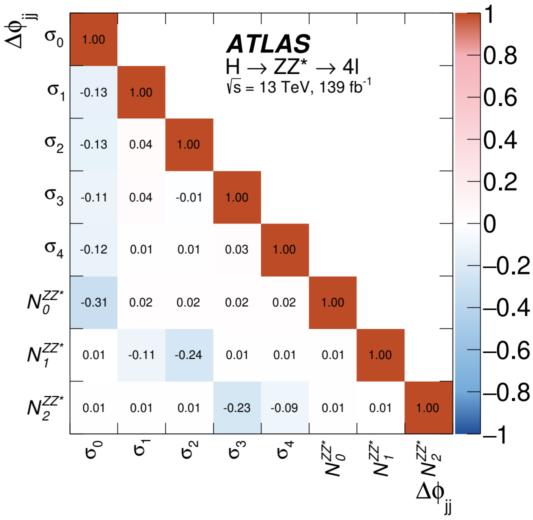

(d)

Figure A.23: Differential fiducial cross sections for a the distance between these two jets in pseudorapidity, $\Delta\eta_{\mathrm{jj}}$, and c the distance between the two jets in ϕ, $\Delta\phi_{\mathrm{jj}}$. The first bin contains events with fewer than two jets that pass the jet selection requirements. Finally, the corresponding correlation matrices between the measured cross sections and the ZZ^* background normalisation factors are provided (b and d).

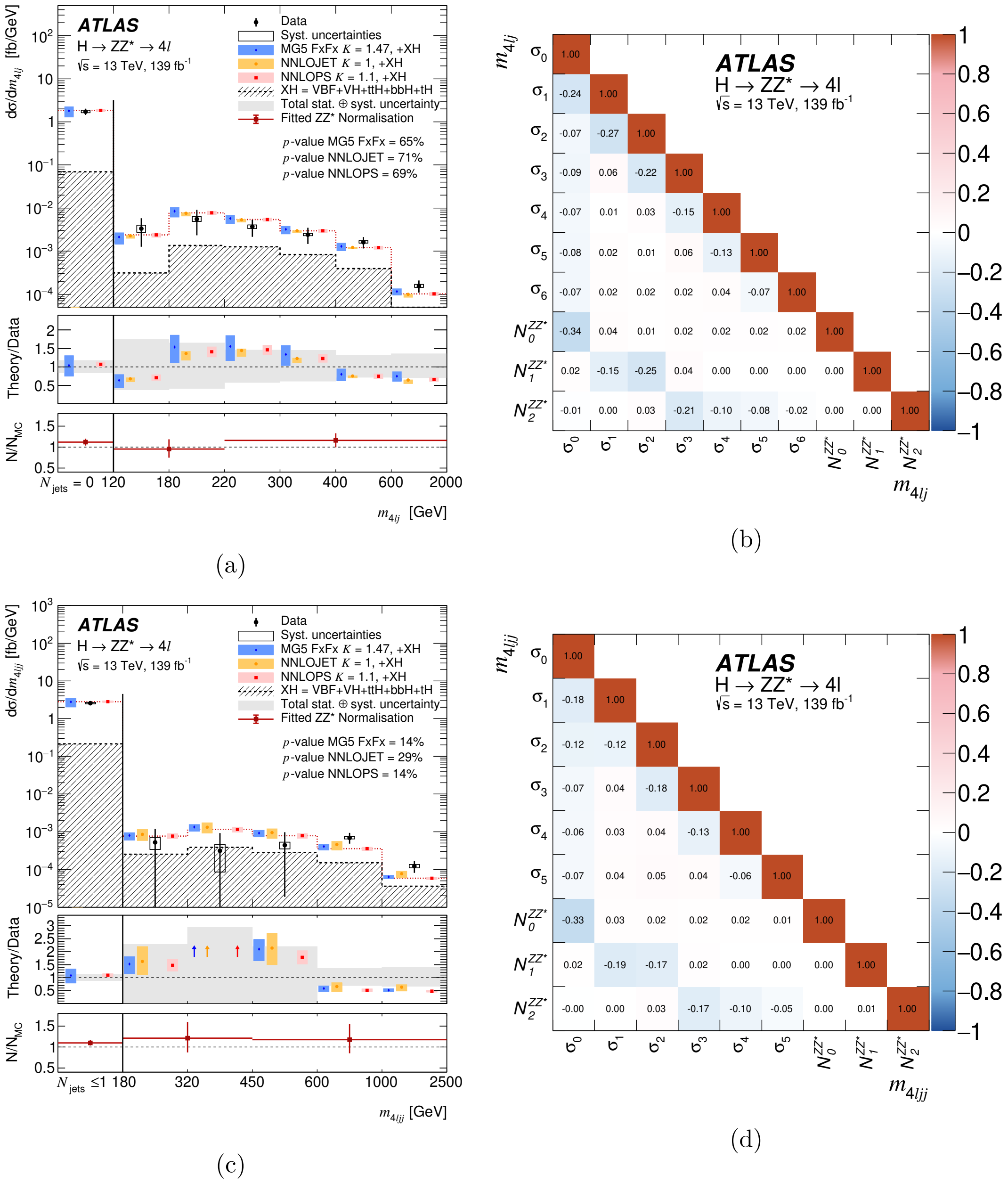

Figure A.24: Differential fiducial cross sections for a the invariant mass of the four-lepton plus jet system, in events with at least one jet, and c the invariant mass of the four-lepton plus dijet system, in events with at least two jets. The corresponding correlation matrices between the measured cross sections and the ZZ^* background normalisation factors are also shown (b and d).

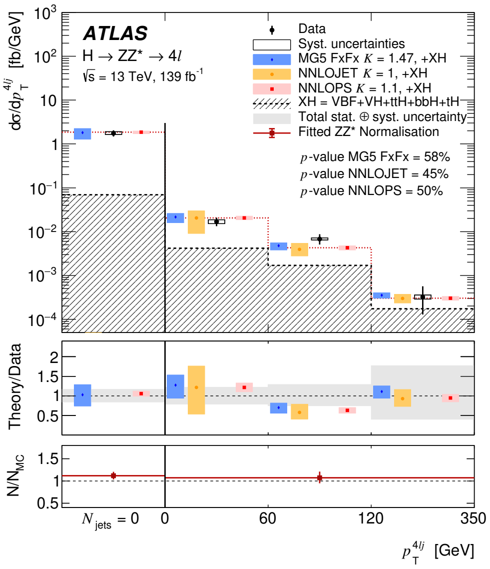

(a)

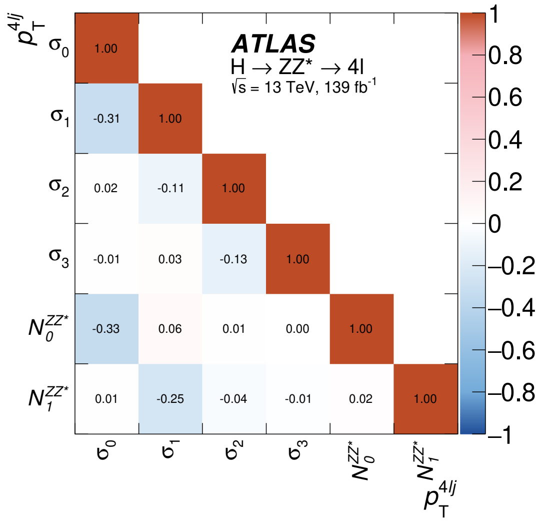

(b)

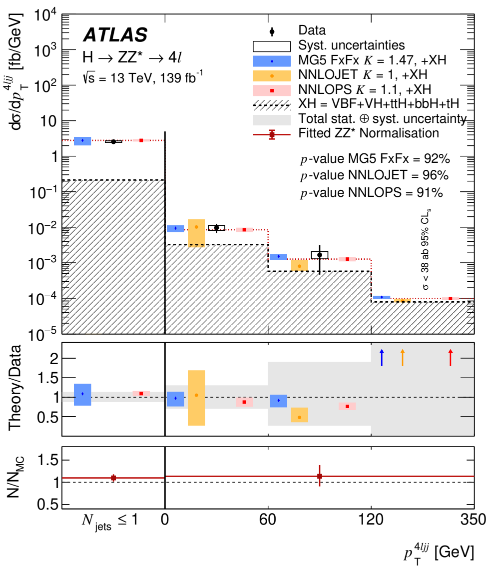

(c)

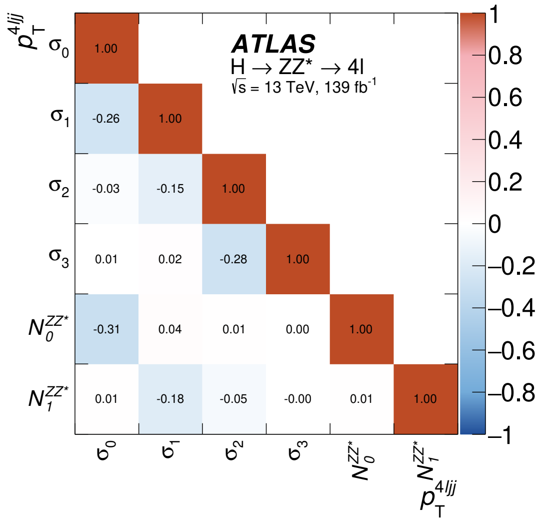

(d)

Figure A.25: Differential fiducial cross sections for a the transverse momentum of the four-lepton plus jet system, in events with at least one jet, and c the transverse momentum of the four-lepton plus dijet system, in events with at least two jets. The corresponding correlation matrices between the measured cross sections and the ZZ^* background normalisation factors are also shown (b and d).

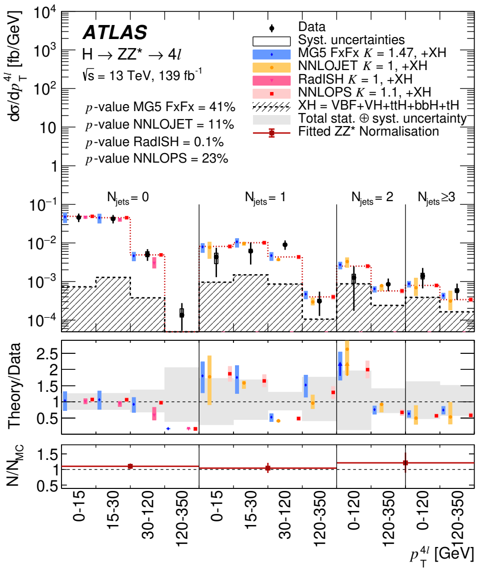

(a)

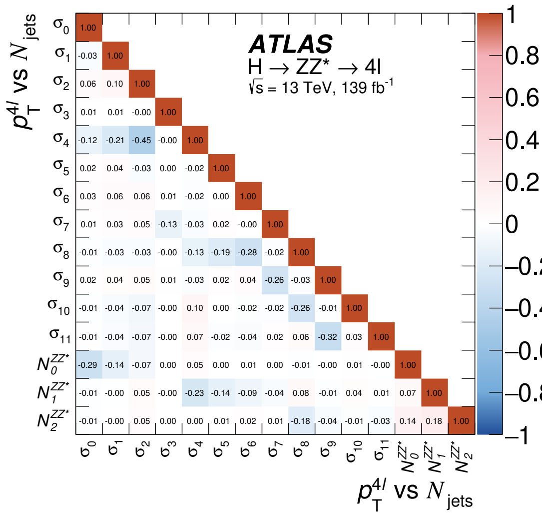

(b)

Figure A.26: a Double differential fiducial cross sections of the $p_{\mathrm{T}}^{4\ell}$ distribution in N_{jets} bins. The corresponding correlation matrix between the measured cross sections and the ZZ^* background normalisation factors is shown in b. The p-values shown are calculated for all bins across both $p_{\mathrm{T}}^{4\ell}$ and N_{jets} simultaneously.

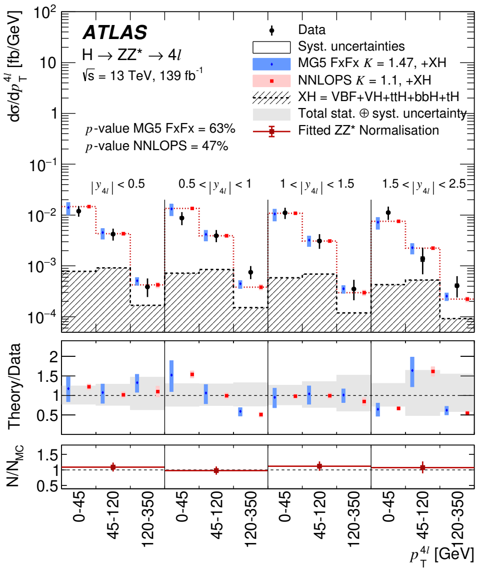

(a)

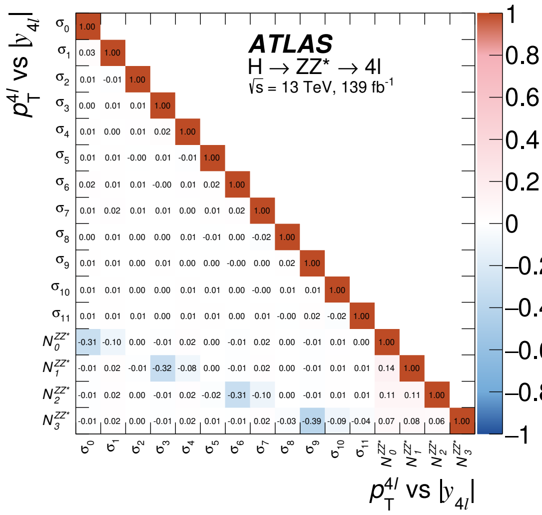

(b)

Figure A.27: a Double differential fiducial cross sections of the $p_{\mathrm{T}}^{4\ell}$ distribution in $|y_{4\ell}|$ bins. The corresponding correlation matrix between the measured cross sections and the ZZ^* background normalisation factors is shown in b. The p-values shown are calculated for all bins across both $p_{\mathrm{T}}^{4\ell}$ and $|y_{4\ell}|$ simultaneously.

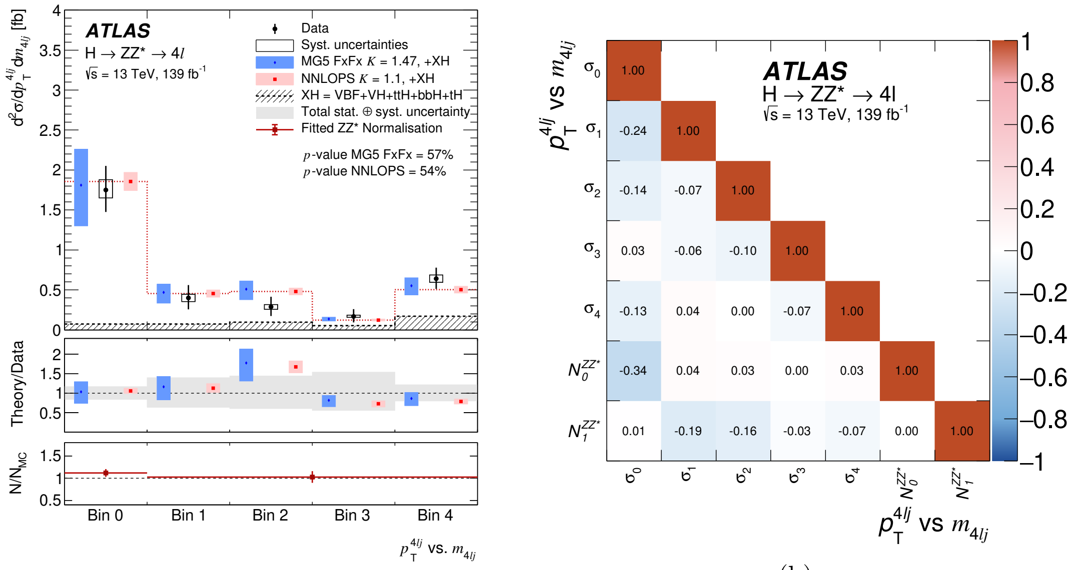

(a) (b)

Figure A.28: a Double differential fiducial cross section for the transverse momentum of the four-lepton plus jet system vs. the invariant mass of the four-lepton plus jet system, $p_{\mathrm{T}}^{4\ell\mathrm{j}}$ vs. $m_{4\ell\mathrm{j}}$ and b the corresponding correlation matrix between the measured cross sections and the ZZ^* background normalisation factors. The bin boundaries are defined in Figure A.11.

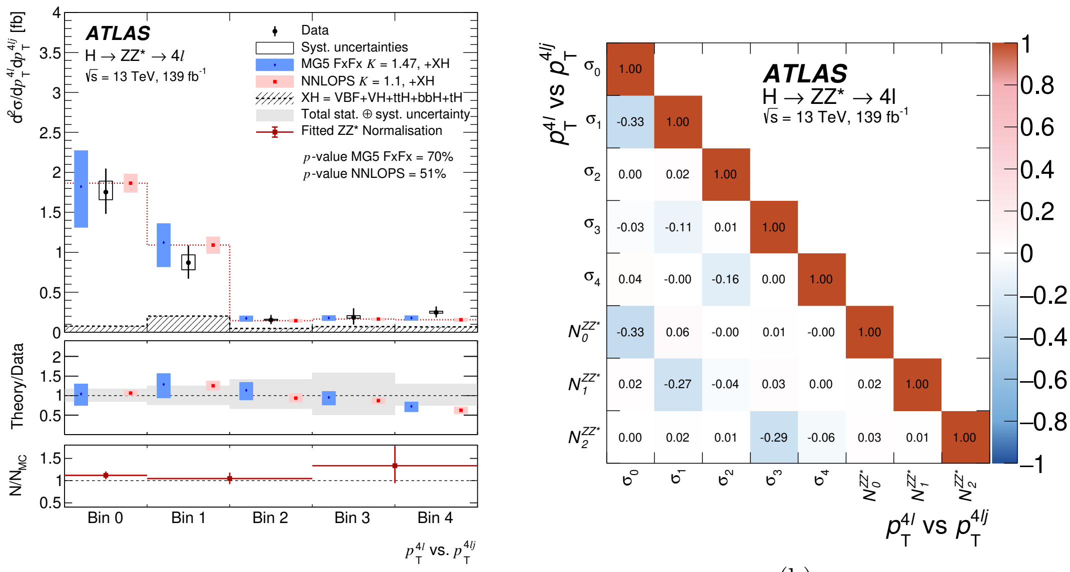

(a) (b)

Figure A.29: a Differential fiducial cross section for the transverse momentum of the four-lepton system vs. the transverse momentum of the four-lepton plus jet system, $p_{\mathrm{T}}^{4\ell}$ vs. $p_{\mathrm{T}}^{4\ell\mathrm{j}}$ and b the corresponding correlation matrix between the measured cross sections and the ZZ^* background normalisation factors. The bin boundaries are defined in Figure A.12.

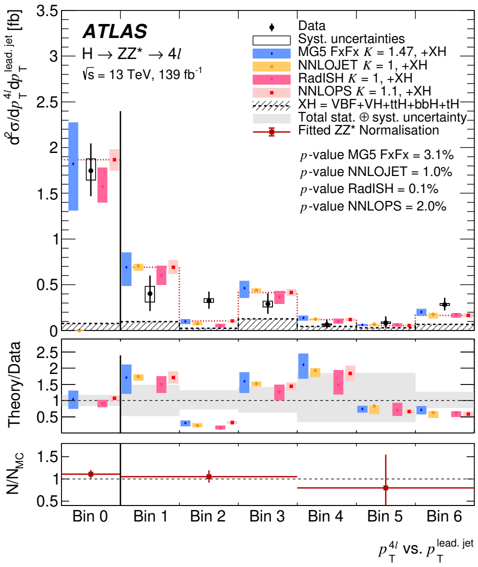

(a)

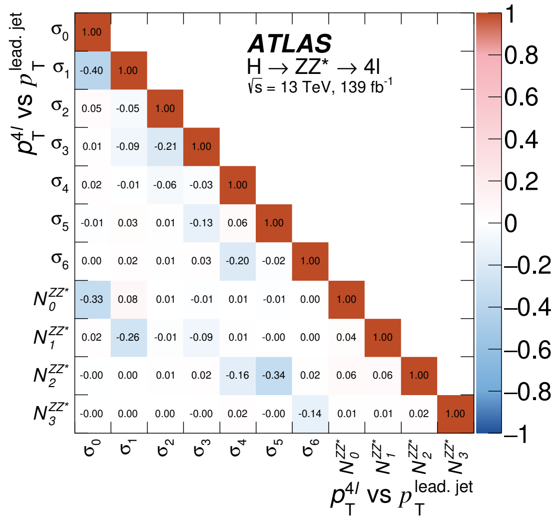

(b)

Figure A.30: a Double differential fiducial cross section for the transverse momentum of the four-lepton system vs. the transverse momentum of the leading jet, $p_{\mathrm{T}}^{4\ell}$ vs. $p_{\mathrm{T}}^{\mathrm{lead.\ jet}}$, and b the corresponding correlation matrix between the measured cross sections and the ZZ^* background normalisation factors. The bin boundaries are defined in Figure A.13.

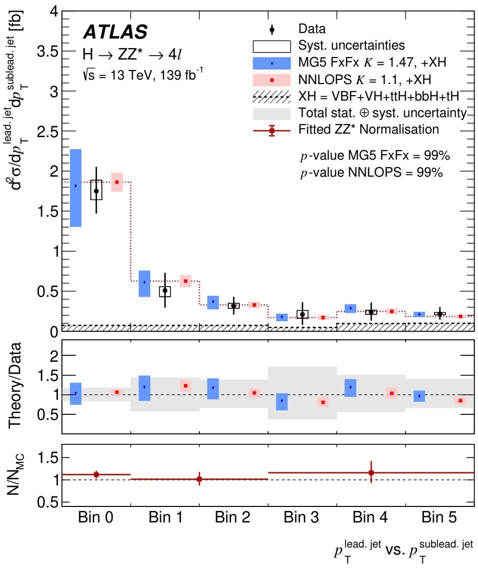

(a)

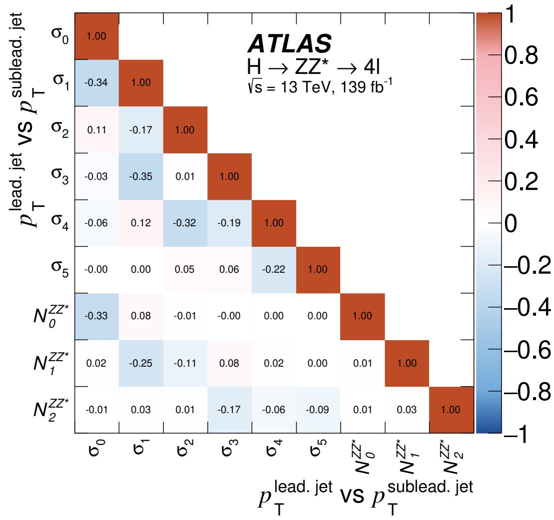

(b)

Figure A.31: a Double differential fiducial cross section for the transverse momentum of leading vs. subleading jet, $p_{\mathrm{T}}^{\mathrm{lead.\ jet}}$ vs. $p_{\mathrm{T}}^{\mathrm{sublead.\ jet}}$, and b the corresponding correlation matrix between the measured cross sections and the ZZ^* background normalisation factor. The bin boundaries are defined in Figure A.14.

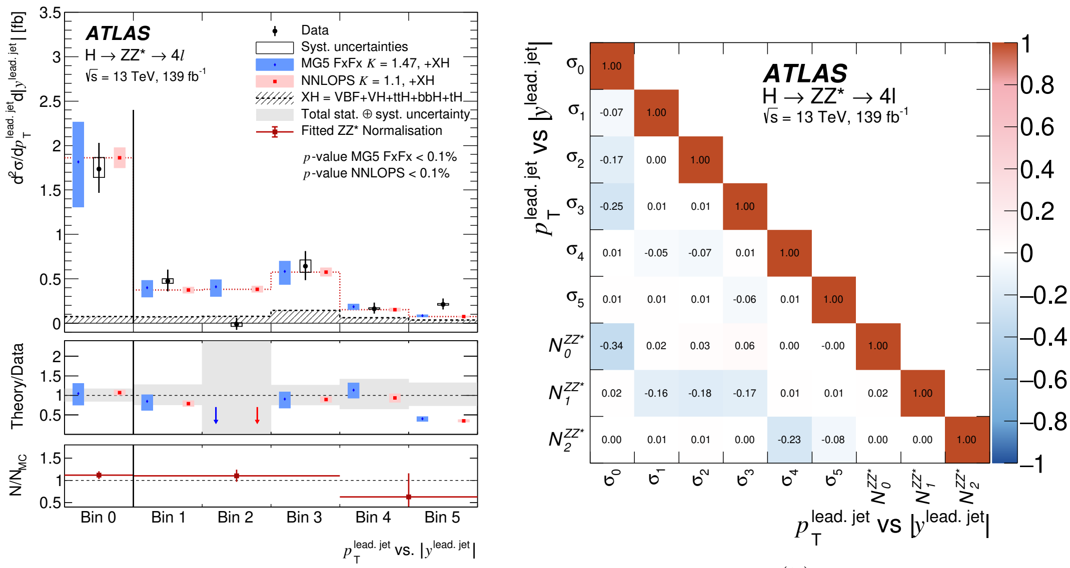

(a)

(b)

Figure A.32: a Double differential fiducial cross section for the transverse momentum of the leading jet vs. the rapidity of the leading jet, $p_{\mathrm{T}}^{\text{lead. jet}}$ vs. $|y^{\text{lead. jet}}|$, and b the corresponding correlation matrix between the measured cross sections and the ZZ^* background normalisation factors. The bin boundaries are defined in Figure A.15.

Appendix B

Preliminary expected unfolded results on CP-odd observables

B.1 Expected Yields

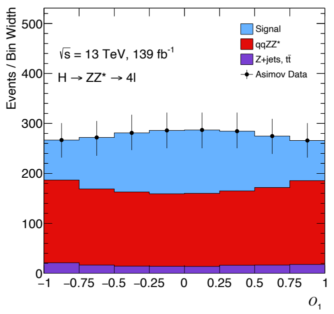

(a) O_1 pre-fit distribution

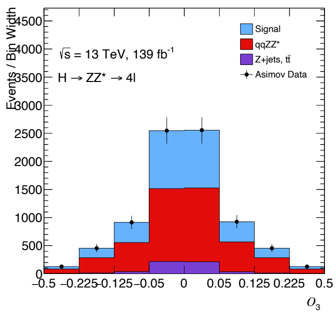

(b) O_3 pre-fit distribution

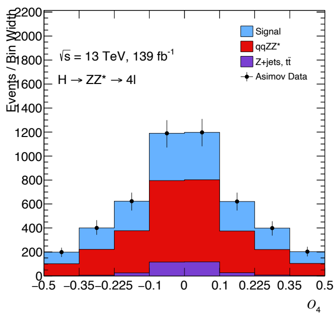

(c) O_4 pre-fit distribution

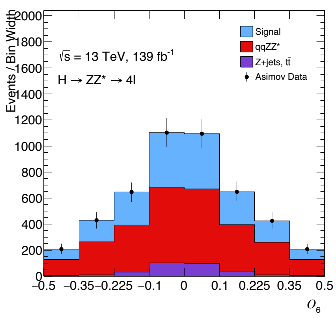

(d) O_6 pre-fit distribution

Figure B.1: The expected (pre-fit) distributions of (a) O_1, (b) O_3, (c) O_4 and (d) O_6 in the range of $105 < m_{4\ell} < 160$ GeV. The black dots depict pre-fit asimov data while the blue, red and violet areas represent the signal, the ZZ^* background and the reducible background, respectively.

B.2 Expected Summary Plot

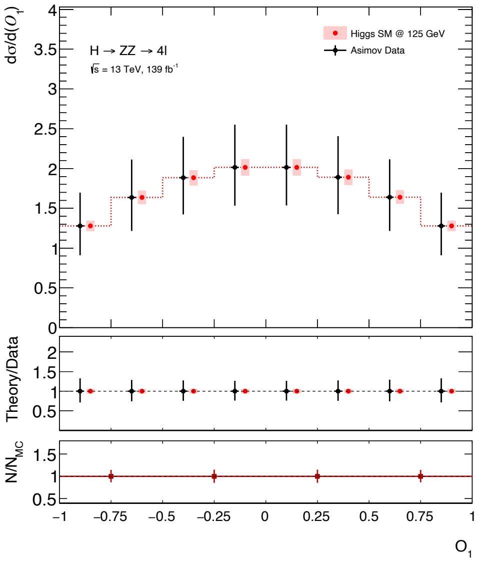

(a)

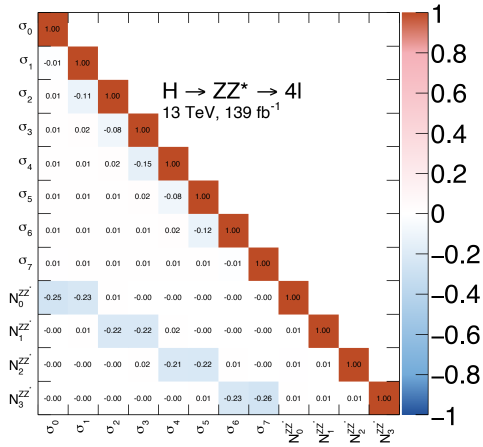

(b)

Figure B.2: a Expected results for differential fiducial cross section for O_1 observable, along with b the corresponding correlation matrix between the measured cross sections and the ZZ^* background normalisation factors.

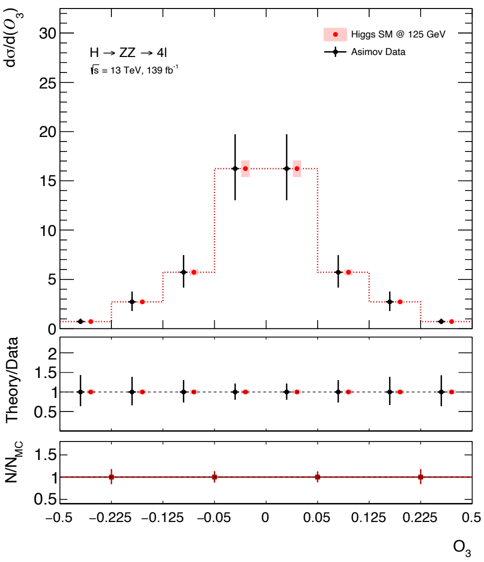

(a)

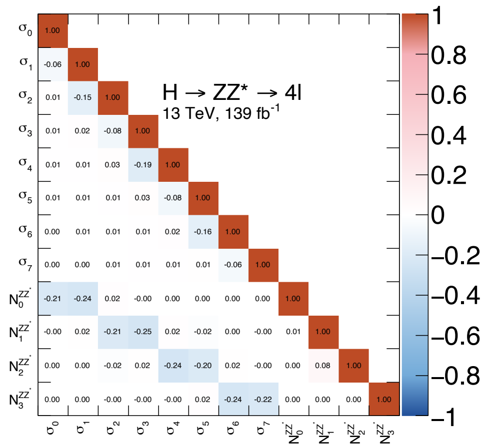

(b)

Figure B.3: a Expected results for differential fiducial cross section for O_3 observable, along with b the corresponding correlation matrix between the measured cross sections and the ZZ^* background normalisation factors.

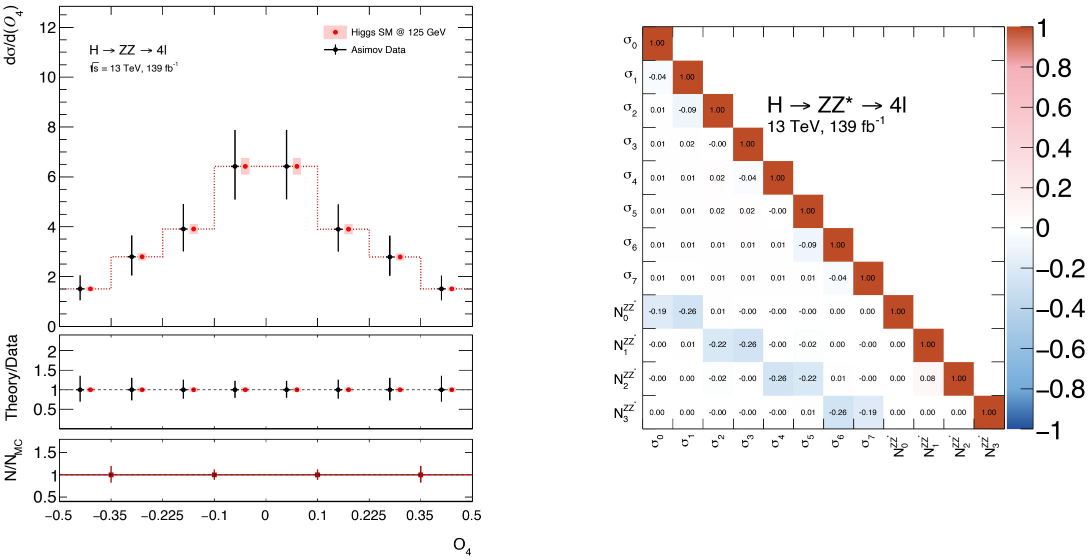

(a) (b)

Figure B.4: a Expected results for differential fiducial cross section for O_4 observable, along with b the corresponding correlation matrix between the measured cross sections and the ZZ^* background normalisation factors.

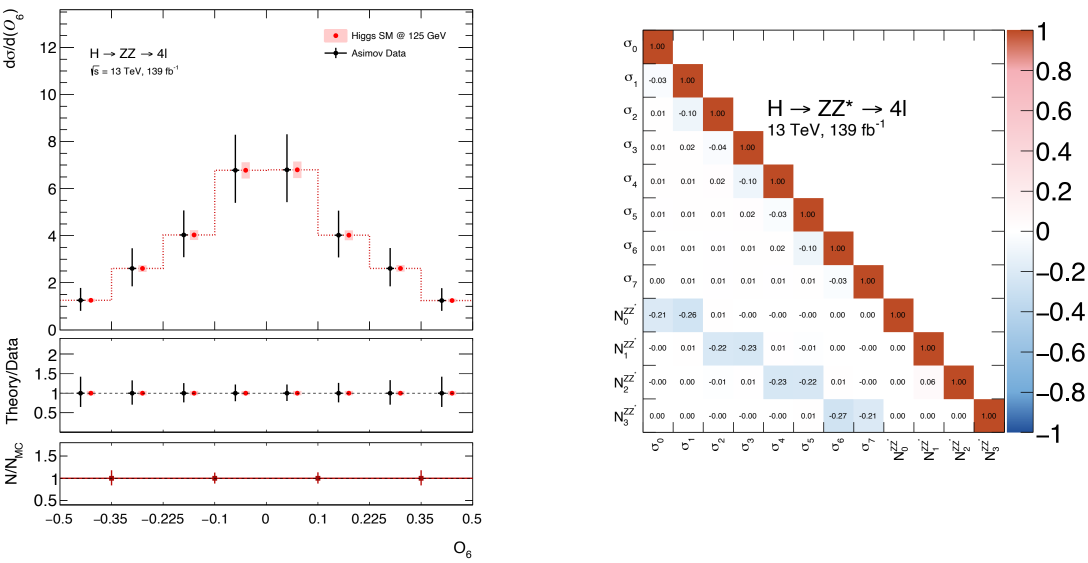

(a) (b)

Figure B.5: a Expected results for differential fiducial cross section for O_6 observable, along with b the corresponding correlation matrix between the measured cross sections and the ZZ^* background normalisation factors.

Appendix C

Interpretations

C.1 Parametrisation Equations

The cross section for a range of coupling values is fit with a 2D quadratic function in each observable bin. The equations themselves for POs and light Yukawa are given below.

C.1.1 Pseudo-observables

Flavour Universal EFT-Inspired

$$\sigma_{\mathrm{inc}}(k_{ZZ}, \varepsilon_L) = 0.00419268 - 0.0033989k_{ZZ} + 0.996947k_{ZZ}^2 - 0.205695\varepsilon_L + 3.10671k_{ZZ}\varepsilon_L + 14.8321\varepsilon_L^2$$

$$\sigma_{\mathrm{bin1}}(k_{ZZ}, \varepsilon_L) = (0.0118545 + 0.00473493k_{ZZ} + 0.976461k_{ZZ}^2 - 0.169253\varepsilon_L + 4.39928k_{ZZ}\varepsilon_L + 21.5267\varepsilon_L^2) * 0.298125$$

$$\sigma_{\mathrm{bin2}}(k_{ZZ}, \varepsilon_L) = (0.00291446 + 0.00634187k_{ZZ} + 0.978697k_{ZZ}^2 - 0.0569087\varepsilon_L + 4.59441k_{ZZ}\varepsilon_L + 20.9932\varepsilon_L^2) * 0.3968493$$

$$\sigma_{\mathrm{bin3}}(k_{ZZ}, \varepsilon_L) = (0.00166876 - 0.00151507k_{ZZ} + 0.99964k_{ZZ}^2 - 0.0679888\varepsilon_L + 1.69709k_{ZZ}\varepsilon_L + 7.55031\varepsilon_L^2) * 0.4749392$$

$$\sigma_{\mathrm{bin4}}(k_{ZZ}, \varepsilon_L) = (0.0055631 - 0.00810194k_{ZZ} + 0.997235k_{ZZ}^2 - 0.259348\varepsilon_L + 3.14499k_{ZZ}\varepsilon_L + 14.859\varepsilon_L^2) * 1.167774$$

$$\sigma_{\mathrm{bin5}}(k_{ZZ}, \varepsilon_L) = (0.00289313 - 0.00747054k_{ZZ} + 1.00792k_{ZZ}^2 - 0.362549\varepsilon_L + 3.28721k_{ZZ}\varepsilon_L + 16.645\varepsilon_L^2) * 1.073738$$

Flavour Universal Contact Terms

$$\sigma_{\text{inc}}(\varepsilon_L,\varepsilon_R) = 0.998222 + 5.08817\varepsilon_L + 13.0995\varepsilon_L^2 - 4.56355\varepsilon_R - 2.38422\varepsilon_L\varepsilon_R + 12.4207\varepsilon_R^2$$

$$\sigma_{\text{bin1}}(\varepsilon_L,\varepsilon_R) = (0.979371 + 7.08214\varepsilon_L + 20.5079\varepsilon_L^2 - 6.02912\varepsilon_R - 6.4808\varepsilon_L\varepsilon_R + 18.1969\varepsilon_R^2) * 0.298125$$

$$\sigma_{\text{bin2}}(\varepsilon_L,\varepsilon_R) = (0.987121 + 7.49835\varepsilon_L + 21.169\varepsilon_L^2 - 6.18274\varepsilon_R - 9.01672\varepsilon_L\varepsilon_R + 18.3019\varepsilon_R^2) * 0.3968493$$

$$\sigma_{\text{bin3}}(\varepsilon_L,\varepsilon_R) = (1.00112 + 2.80277\varepsilon_L + 6.829\varepsilon_L^2 - 2.4738\varepsilon_R - 1.8205\varepsilon_L\varepsilon_R + 6.46017\varepsilon_R^2) * 0.4749392$$

$$\sigma_{\text{bin4}}(\varepsilon_L,\varepsilon_R) = (0.998971 + 5.18013\varepsilon_L + 12.335\varepsilon_L^2 - 4.77457\varepsilon_R - 0.588961\varepsilon_L\varepsilon_R + 12.2517\varepsilon_R^2) * 1.167774$$

$$\sigma_{\text{bin5}}(\varepsilon_L,\varepsilon_R) = (1.00459 + 5.3831\varepsilon_L + 13.6594\varepsilon_L^2 - 5.089\varepsilon_R - 0.383903\varepsilon_L\varepsilon_R + 13.6127\varepsilon_R^2) * 1.073738$$

Flavour Violation Vector Terms

$$\sigma_{\text{bin1},ll\mu}(\varepsilon_\mu,\varepsilon_e) = 0.149488*(0.965949+0.0837411\varepsilon_e+1.63634\varepsilon_e^2+0.960177\varepsilon_\mu+0.0667985\varepsilon_e\varepsilon_\mu+30.1589\varepsilon_\mu^2)$$

$$\sigma_{\text{bin1},lle}(\varepsilon_\mu,\varepsilon_e) = 0.148512 * (0.997272 + 1.00082\varepsilon_e + 31.229\varepsilon_e^2 + 0.0702626\varepsilon_\mu + 0.0154327\varepsilon_e\varepsilon_\mu + 1.38876\varepsilon_\mu^2)$$

$$\sigma_{\text{bin2},ll\mu}(\varepsilon_\mu,\varepsilon_e) = 0.198426*(0.980452+0.161354\varepsilon_e+3.06736\varepsilon_e^2+1.12356\varepsilon_\mu+0.471118\varepsilon_e\varepsilon_\mu+26.9644\varepsilon_\mu^2)$$

$$\sigma_{\text{bin2},lle}(\varepsilon_\mu,\varepsilon_e) = 0.198448 * (0.994118 + 1.17375\varepsilon_e + 27.6509\varepsilon_e^2 + 0.172134\varepsilon_\mu - 0.384523\varepsilon_e\varepsilon_\mu + 2.90482\varepsilon_\mu^2)$$

$$\sigma_{\text{bin3},ll\mu}(\varepsilon_\mu,\varepsilon_e)0.237858*(1.00841+0.0211637\varepsilon_e-0.0958445\varepsilon_e^2+0.319301\varepsilon_\mu-0.0116292\varepsilon_e\varepsilon_\mu+11.4768\varepsilon_\mu^2)$$

$$\sigma_{\text{bin3},lle}(\varepsilon_\mu,\varepsilon_e) = 0.237134*(0.992386+0.301243\varepsilon_e+11.4301\varepsilon_e^2+0.0218458\varepsilon_\mu-0.0711554\varepsilon_e\varepsilon_\mu+0.154839\varepsilon_\mu^2)$$

$$\sigma_{\text{bin4},ll\mu}(\varepsilon_\mu,\varepsilon_e) = 0.584551 * (1.00439 - 0.0102651\varepsilon_e + 0.257413\varepsilon_e^2 + 0.383446\varepsilon_\mu 0.127734\varepsilon_e\varepsilon_\mu + 24.113\varepsilon_\mu^2)$$

$$\sigma_{\text{bin4},lle}(\varepsilon_\mu,\varepsilon_e) = 0.583308*(0.984277+0.382427\varepsilon_e+23.581\varepsilon_e^2+0.00125059\varepsilon_\mu-0.0218768\varepsilon_e\varepsilon_\mu+0.00140188\varepsilon_\mu^2)$$

$$\sigma_{\text{bin5},ll\mu}(\varepsilon_\mu,\varepsilon_e) = 0.538241*(1.00139-0.0039792\varepsilon_e-0.116811\varepsilon_e^2+0.291238\varepsilon_\mu-0.0496207\varepsilon_e\varepsilon_\mu+26.7701\varepsilon_\mu^2)$$

$$\sigma_{\text{bin5},lle}(\varepsilon_\mu,\varepsilon_e) = 0.535183*(1.00664+0.330428\varepsilon_e+27.0753\varepsilon_e^2-0.0106102\varepsilon_\mu+0.00186087\varepsilon_e\varepsilon_\mu+0.0886525\varepsilon_\mu^2)$$

Flavour Violation Axial Terms

$$\sigma_{\text{bin1},ll\mu}(\varepsilon_\mu,\varepsilon_e) = 0.149488*(0.971877+1.28135\varepsilon_e+0.579641\varepsilon_e^2+11.6692\varepsilon_\mu+6.96666\varepsilon_e\varepsilon_\mu+35.0948\varepsilon_\mu^2)$$

$$\sigma_{\text{bin1},lle}(\varepsilon_\mu,\varepsilon_e) = 0.148512*(0.995975+12.0443\varepsilon_e+38.3885 varepsilon_e^2+1.36448\varepsilon_\mu+7.25375\varepsilon_e\varepsilon_\mu+0.640143\varepsilon_\mu^2)$$

$$\sigma_{\text{bin2},ll\mu}(\varepsilon_\mu,\varepsilon_e) = 0.198426*(0.974009+2.18613\varepsilon_e+4.06525\varepsilon_e^2+11.541\varepsilon_\mu+9.04715\varepsilon_e\varepsilon_\mu+38.2336\varepsilon_\mu^2)$$

$$\sigma_{\text{bin2},lle}(\varepsilon_\mu,\varepsilon_e) = 0.198448*(0.983832+11.7236\varepsilon_e+39.3417\varepsilon_e^2+2.16866\varepsilon_\mu+9.28273\varepsilon_e\varepsilon_\mu+4.08212\varepsilon_\mu^2)$$

$$\sigma_{\text{bin3},ll\mu}(\varepsilon_\mu,\varepsilon_e) = 0.237858*(0.999248+0.213919\varepsilon_e-0.0579672\varepsilon_e^2+5.04664\varepsilon_\mu+0.782157\varepsilon_e\varepsilon_\mu+14.3319\varepsilon_\mu^2)$$

$$\sigma_{\text{bin3},lle}(\varepsilon_\mu,\varepsilon_e) = 0.237134*(0.996155+5.02171\varepsilon_e+25.6665\varepsilon_e^2+0.0694762\varepsilon_\mu+0.0938681\varepsilon_e\varepsilon_\mu+0.61464\varepsilon_\mu^2)$$

$$\sigma_{\text{bin4},ll\mu}(\varepsilon_\mu,\varepsilon_e) = 0.584551*(1.00694+0.0444484\varepsilon_e-0.116497\varepsilon_e^2+9.99591\varepsilon_\mu+0.0131965\varepsilon_e\varepsilon_\mu+25.311\varepsilon_\mu^2)$$

$$\sigma_{\text{bin4},lle}(\varepsilon_\mu,\varepsilon_e) = 0.583308*(0.979121+9.82652\varepsilon_e+25.0379\varepsilon_e^2-0.0696026\varepsilon_\mu-0.772898\varepsilon_e\varepsilon_\mu-0.318693\varepsilon_\mu^2)$$

$$\sigma_{\text{bin5},ll\mu}(\varepsilon_\mu,\varepsilon_e) = 0.538241*(1.0031+0.0109809\varepsilon_e-0.917898\varepsilon_e^2+10.3854\varepsilon_\mu+1.08422\varepsilon_e\varepsilon_\mu+26.7298\varepsilon_\mu^2)$$

$$\sigma_{\text{bin5},lle}(\varepsilon_\mu,\varepsilon_e) = 0.535183*(1.00986+10.4788\varepsilon_e+27.7145\varepsilon_e^2-0.00924963\varepsilon_\mu+0.298521\varepsilon_e\varepsilon_\mu-0.648294\varepsilon_\mu^2)$$

C.1.2 Light Yukawa

Light Yukawa XS and Shape Terms

$$\sigma_{\text{bin0}}(\kappa_b,\kappa_c) = 0.447918*(1.086-0.0995398\kappa_b+0.0211969\kappa_b^2-0.0127267\kappa_c+0.00112476\kappa_b\kappa_c+0.00394341\kappa_c^2)$$

$$\sigma_{\text{bin1}}(\kappa_b,\kappa_c) = 0.620297*(1.04051-0.0572372\kappa_b+0.020424\kappa_b^2-0.00671966\kappa_c+0.0004592191\kappa_b\kappa_c+0.00255965\kappa_c^2)$$

$$\sigma_{\text{bin2}}(\kappa_b,\kappa_c) = 0.49342*(1.01621-0.0331328\kappa_b+0.0185667\kappa_b^2-0.00386386\kappa_c+0.000273466\kappa_b\kappa_c+0.00194292\kappa_c^2)$$

$$\sigma_{\text{bin3}}(\kappa_b,\kappa_c) = 0.528859*(1.00094-0.0176483\kappa_b+0.0168945\kappa_b^2-0.00198147\kappa_c+0.000199086\kappa_b\kappa_c+0.00159783\kappa_c^2)$$

$$\sigma_{\text{bin4}}(\kappa_b,\kappa_c) = 0.357714*(0.991561-0.00696091\kappa_b+0.0149863\kappa_b^2-0.00105533\kappa_c+0.000224571\kappa_b\kappa_c+0.00124394\kappa_c^2)$$

$$\sigma_{\text{bin5}}(\kappa_b,\kappa_c) = 0.313951*(0.987178-0.000231589\kappa_b+0.0122641\kappa_b^2-0.000289526\kappa_c+0.0000873691\kappa_b\kappa_c+0.000991461\kappa_c^2)$$

$$\sigma_{\text{bin6}}(\kappa_b,\kappa_c) = 0.337929*(0.985648+0.00448924\kappa_b+0.00886693\kappa_b^2+0.000303749\kappa_c+1.96141*10^-6\kappa_b\kappa_c+0.000690375\kappa_c^2)$$

$$\sigma_{\text{bin7}}(\kappa_b,\kappa_c) = 0.229145*(0.987913+0.00660564\kappa_b+0.0046578\kappa_b^2+0.000410833\kappa_c-7.62124*10^-6\kappa_b\kappa_c+0.000420321\kappa_c^2)$$

$$\sigma_{\text{bin8}}(\kappa_b,\kappa_c) = 0.0724372*(0.989735+0.00620547\kappa_b+0.00342841\kappa_b^2+0.000304243\kappa_c-7.38116*10^-6\kappa_b\kappa_c+0.00033449\kappa_c^2)$$

$\sigma_{\text{bin9}}(\kappa_b, \kappa_c) = 0.00974789 * (0.989735 + 0.00620547\kappa_b + 0.00342841\kappa_b^2 + 0.000304243\kappa_c - 7.38116 * 10^-6\kappa_b\kappa_c + 0.00033449\kappa_c^2)$

Light Yukawa XS, Shape and BR Terms

For this intepretation the parametrization is the same as above but multipled with the branching ratio of Higgs decays where a $\kappa_{b/c}^2$ dependancy enters for relevant decays. For $H \to gg$ we assume the same depedance as for the cross section.

Light Yukawa Shape Only Terms

$\sigma_{\text{bin0}}(\kappa_b, \kappa_c) = 0.447918*\mu*(1.04665-0.0512018\kappa_b+0.00162496\kappa_b^2+0.0000338729\kappa_c+0.00053128\kappa_b\kappa_c+ 0.00235781\kappa_c^2)$

$\sigma_{\text{bin1}}(\kappa_b, \kappa_c) = 0.620297*\mu*(1.01387-0.0173241\kappa_b+0.00252584\kappa_b^2+0.000204705\kappa_c+0.0000310473\kappa_b\kappa_c+ 0.000688825\kappa_c^2)$

$\sigma_{\text{bin2}}(\kappa_b, \kappa_c) = 0.49342*\mu*(0.996298+0.00218594\kappa_b+0.00158421\kappa_b^2+0.0000895628*@1-0.0000675553\kappa_b\kappa_c- 0.0000901347\kappa_c^2)$

$\sigma_{\text{bin3}}(\kappa_b, \kappa_c) = 0.528859*\mu*(0.984389+0.0149804\kappa_b+0.000779814\kappa_b^2+0.00039613\kappa_c-0.0000412635\kappa_b\kappa_c- 0.000504231\kappa_c^2)$

$\sigma_{\text{bin4}}(\kappa_b, \kappa_c) = 0.357714*\mu*(0.978097+0.0231324\kappa_b-0.000517927\kappa_b^2+0.000332973*@1-0.000157022\kappa_b\kappa_c- 0.000887341\kappa_c^2)$

$\sigma_{\text{bin5}}(\kappa_b, \kappa_c) = 0.313951*\mu*(0.97634+0.0282538\kappa_b-0.00279408\kappa_b^2-0.000281031\kappa_c-0.000278456\kappa_b\kappa_c- 0.00124009\kappa_c^2)$

$\sigma_{\text{bin6}}(\kappa_b, \kappa_c) = 0.337929*\mu*(0.975551+0.032276\kappa_b-0.00541302\kappa_b^2-0.000645668\kappa_c-0.000193265\kappa_b\kappa_c- 0.00157458\kappa_c^2)$

$\sigma_{\text{bin7}}(\kappa_b, \kappa_c) = 0.229145*\mu*(0.979509+0.0332076\kappa_b-0.00887264\kappa_b^2-0.00158589\kappa_c-0.000331683\kappa_b\kappa_c- 0.00192662\kappa_c^2)$

$\sigma_{\text{bin8}}(\kappa_b, \kappa_c) = 0.0724372*\mu*(0.980562+0.0331471\kappa_b-0.00983821\kappa_b^2-0.00165352\kappa_c-0.00023104\kappa_b\kappa_c- 0.00198635\kappa_c^2)$

$\sigma_{\text{bin9}}(\kappa_b, \kappa_c) = 0.00974789*\mu*(0.980562+0.0331471\kappa_b-0.00983821\kappa_b^2-0.00165352\kappa_c-0.00023104\kappa_b\kappa_c- 0.00198635\kappa_c^2)$

Bibliography

[1] ATLAS Collaboration, "Observation of a new particle in the search for the Standard Model Higgs boson with the ATLAS detector at the LHC," Phys. Lett. B **716** (2012), 1-29 [arXiv:1207.7214 [hep-ex]]. pages 1, 14, 15

[2] CMS Collaboration, "Observation of a New Boson at a Mass of 125 GeV with the CMS Experiment at the LHC," Phys. Lett. B **716** (2012), 30-61 [arXiv:1207.7235 [hep-ex]]. pages 1, 14, 15

[3] ATLAS Collaboration, "The ATLAS Experiment at the CERN Large Hadron Collider," JINST **3** (2008), S08003 pages 1, 38, 40, 41, 44, 46, 48

[4] CMS Collaboration, "The CMS Experiment at the CERN LHC," JINST **3** (2008), S08004 pages 1, 38

[5] ATLAS Collaboration, *Letter of Intent for the Phase-I Upgrade of the ATLAS Experiment*. Technical Report CERN-LHCC-2011-012. LHCC-I-020, CERN, Geneva, Nov 2011. pages 1, 52

[6] ATLAS Collaboration, *Letter of Intent for the Phase-II Upgrade of the ATLAS Experiment*. Technical Report CERN-LHCC-2012-022. LHCC-I-023, CERN, Geneva, Dec 2012. pages 1, 52

[7] T. Kawamoto *et al.*, "New Small Wheel Technical Design Report", CERN-LHCC-2013-006, ATLAS-TDR-020. pages 1, 52, 62, 64, 65, 70, 71, 120, 121

[8] Y. Giomataris, P. Rebourgeard, J. P. Robert and G. Charpak, "*MICROMEGAS: A High granularity position sensitive gaseous detector for high particle flux environments*", Nucl. Instrum. Meth. A **376** (1996) 29. pages 1

[9] M. Iodice [ATLAS Muon Collaboration], "Micromegas detectors for the Muon Spectrometer upgrade of the ATLAS experiment", JINST **10** (2015) no.02, C02026. pages 1, 71

[10] S. Majewski, G. Charpak, A. Breskin and G. Mikenberg, “A Thin Multiwire Chamber Operating In The High Multiplication Mode", Nucl. Instrum. Meth. **217** (1983) 265. pages 1

[11] J.Wotschack, “The development of large-area Micromegas detectors for the ATLAS upgrade", Mod. Phys. Lett. A **28** (2013), 1340020 pages 1, 72, 73

[12] T. Alexopoulos, M. Alviggi, M. Antonelli, F. Anulli, C. Arcangeletti, P. Bagnaia, A. Baroncelli, M. Beretta, C. Bini and J. Bortfeldt, *et al.* “Construction techniques and performances of a full-size prototype Micromegas chamber for the ATLAS muon spectrometer upgrade,” Nucl. Instrum. Meth. A **955** (2020), 162086 [arXiv:1808.09752 [physics.ins-det]]. pages 1

[13] S. Dittmaier *et al.* [LHC Higgs Cross Section Working Group], “Handbook of LHC Higgs Cross Sections: 1. Inclusive Observables,” [arXiv:1101.0593 [hep-ph]]. pages 2, 135, 136, 152

[14] ATLAS Collaboration, “Measurements of the Higgs boson inclusive and differential fiducial cross sections in the 4ℓ decay channel at $\sqrt{s}$ = 13 TeV,” Eur. Phys. J. C **80** (2020) no.10, 942 [arXiv:2004.03969 [hep-ex]]. pages 2, 3, 33, 34

[15] M. Gonzalez-Alonso, A. Greljo, G. Isidori and D. Marzocca, “Pseudo-observables in Higgs decays,” Eur. Phys. J. C **75** (2015), 128 [arXiv:1412.6038 [hep-ph]]. pages 2, 16, 19, 209

[16] F. Bishara, U. Haisch, P. F. Monni and E. Re, "*Constraining Light-Quark Yukawa Couplings from Higgs Distributions*", Phys. Rev. Lett. **118** (2017) no.12, 121801 [arXiv:1606.09253 [hep-ph]]. pages 2, 228, 229

[17] I. Brivio and M. Trott, "*The Standard Model as an Effective Field Theory*", Phys. Rept. **793** (2019) 1 [arXiv:1706.08945 [hep-ph]]. pages 3, 16, 17

[18] S. L. Glashow, “Partial Symmetries of Weak Interactions,” Nucl. Phys. **22** (1961), 579-588 pages 6

[19] S. Weinberg, “A Model of Leptons,” Phys. Rev. Lett. **19** (1967), 1264-1266 pages 6

[20] A. Salam, “Weak and Electromagnetic Interactions,” Conf. Proc. C **680519** (1968), 367-377 pages 6

[21] F. Englert and R. Brout, “Broken Symmetry and the Mass of Gauge Vector Mesons,” Phys. Rev. Lett. **13** (1964), 321-323 pages 10

[22] P. W. Higgs, “Broken Symmetries and the Masses of Gauge Bosons,” Phys. Rev. Lett. **13** (1964), 508-509 pages 10

[23] G. Aad *et al.* [ATLAS and CMS], "Combined Measurement of the Higgs Boson Mass in pp Collisions at $\sqrt{s} = 7$ and 8 TeV with the ATLAS and CMS Experiments," Phys. Rev. Lett. **114** (2015), 191803 [arXiv:1503.07589 [hep-ex]]. pages 14

[24] ATLAS and CMS Collaboration, "Measurements of the Higgs boson production and decay rates and constraints on its couplings from a combined ATLAS and CMS analysis of the LHC pp collision data at $\sqrt{s} = 7$ and 8 TeV," JHEP **08** (2016), 045 [arXiv:1606.02266 [hep-ex]]. pages

[25] D. de Florian *et al.* [LHC Higgs Cross Section Working Group], "Handbook of LHC Higgs Cross Sections: 4. Deciphering the Nature of the Higgs Sector," [arXiv:1610.07922 [hep-ph]]. pages 16, 22, 23, 136

[26] S. Heinemeyer *et al.* [LHC Higgs Cross Section Working Group], "Handbook of LHC Higgs Cross Sections: 3. Higgs Properties," [arXiv:1307.1347 [hep-ph]]. pages 16, 24, 135, 136

[27] I. Brivio, Y. Jiang and M. Trott, "The SMEFTsim package, theory and tools," JHEP **12** (2017), 070 [arXiv:1709.06492 [hep-ph]]. pages 19, 136

[28] A. Falkowski, B. Fuks, K. Mawatari, K. Mimasu, F. Riva and V. Sanz, Eur. Phys. J. C **75** (2015) no.12, 583 [arXiv:1508.05895 [hep-ph]]. pages 19

[29] M. Gonzalez-Alonso, A. Greljo, G. Isidori and D. Marzocca, "Electroweak bounds on Higgs pseudo-observables and $h \to 4\ell$ decays," Eur. Phys. J. C **75** (2015), 341 [arXiv:1504.04018 [hep-ph]]. pages 210

[30] J. S. Gainer, M. González-Alonso, A. Greljo, S. Isaković, G. Isidori, A. Korytov, J. Lykken, D. Marzocca, K. T. Matchev and P. Milenović, *et al.* "Adding pseudo-observables to the four-lepton experimentalist's toolbox," JHEP **10** (2018), 073 [arXiv:1808.00965 [hep-ph]]. pages 136, 209

[31] ATLAS Collaboration, "Cross-section measurements of the Higgs boson decaying into a pair of τ-leptons in proton-proton collisions at $\sqrt{s} = 13$ TeV with the ATLAS detector," Phys. Rev. D **99** (2019), 072001 [arXiv:1811.08856 [hep-ex]]. pages 24, 25

[32] CMS Collaboration, "Observation of the Higgs boson decay to a pair of τ leptons with the CMS detector," Phys. Lett. B **779** (2018), 283-316 [arXiv:1708.00373 [hep-ex]]. pages 24, 25

[33] ATLAS Collaboration, "Observation of Higgs boson production in association with a top quark pair at the LHC with the ATLAS detector," Phys. Lett. B **784** (2018), 173-191 [arXiv:1806.00425 [hep-ex]]. pages 25, 26

[34] CMS Collaboration, "Observation of $\mathrm{t\bar{t}H}$ production," Phys. Rev. Lett. **120** (2018) no.23, 231801 [arXiv:1804.02610 [hep-ex]]. pages 25, 26

[35] ATLAS Collaboration, "Observation of $H \to b\bar{b}$ decays and VH production with the ATLAS detector," Phys. Lett. B **786** (2018), 59-86 [arXiv:1808.08238 [hep-ex]]. pages 26, 27

[36] CMS Collaboration, "Observation of Higgs boson decay to bottom quarks," Phys. Rev. Lett. **121** (2018) no.12, 121801 [arXiv:1808.08242 [hep-ex]]. pages 26, 27

[37] ATLAS Collaboration, "A search for the dimuon decay of the Standard Model Higgs boson with the ATLAS detector," *Preprint* [arXiv:2007.07830 [hep-ex]]. pages 27, 28

[38] CMS Collaboration, "Measurement of Higgs boson decay to a pair of muons in proton-proton collisions at $\sqrt{s} = 13\,\text{TeV}$," CMS-PAS-HIG-19-006. https://cds.cern.ch/record/2725423/ pages 28

[39] ATLAS Collaboration, "Measurement of the Higgs boson mass in the $H \to ZZ^* \to 4\ell$ and $H \to \gamma\gamma$ channels with $\sqrt{s} = 13$ TeV pp collisions using the ATLAS detector," Phys. Lett. B **784** (2018), 345-366 (*Preprint* [arXiv:1806.00242 [hep-ex]]). pages 29

[40] ATLAS Collaboration, "Measurement of the Higgs boson mass in the $H \to ZZ^* \to 4\ell$ decay channel with $\sqrt{s} = 13$ TeV pp collisions using the ATLAS detector at the LHC," ATLAS-CONF-2020-005. http://cdsweb.cern.ch/record/2714883/ pages 29

[41] CMS Collaboration, "A measurement of the Higgs boson mass in the diphoton decay channel," Phys. Lett. B **805** (2020), 135425 [arXiv:2002.06398 [hep-ex]]. pages 29

[42] ATLAS Collaboration, "Study of the spin and parity of the Higgs boson in diboson decays with the ATLAS detector," Eur. Phys. J. C **75** (2015) no.10, 476 [erratum: Eur. Phys. J. C **76** (2016) no.3, 152] [arXiv:1506.05669 [hep-ex]]. pages 29, 30, 31

[43] CMS Collaboration, "Constraints on the spin-parity and anomalous HVV couplings of the Higgs boson in proton collisions at 7 and 8 TeV," Phys. Rev. D **92** (2015) no.1, 012004 [arXiv:1411.3441 [hep-ex]]. pages 30, 31

[44] ATLAS Collaboration, "CP Properties of Higgs Boson Interactions with Top Quarks in the $t\bar{t}H$ and tH Processes Using $H \to \gamma\gamma$ with the ATLAS Detector," Phys. Rev. Lett. **125** (2020) no.6, 061802 (*Preprint* [arXiv:2004.04545 [hep-ex]]). pages 31

[45] CMS Collaboration, "Measurements of $\mathrm{t\bar{t}}H$ Production and the CP Structure of the Yukawa Interaction between the Higgs Boson and Top Quark in the Diphoton Decay Channel," Phys. Rev. Lett. **125** (2020) no.6, 061801 [arXiv:2003.10866 [hep-ex]]. pages 31

[46] ATLAS Collaboration, "Test of CP invariance in vector-boson fusion production of the Higgs boson in the $H \to \tau\tau$ channel in proton−proton collisions at $\sqrt{s} = 13$ TeV with the ATLAS detector," Phys. Lett. B **805** (2020), 135426 (*Preprint* [arXiv:2002.05315 [hep-ex]]). pages 32

[47] CMS Collaboration, "Analysis of the CP structure of the Yukawa coupling between the Higgs boson and τ leptons in proton-proton collisions at $\sqrt{s} = 13$ TeV," CMS-PAS-HIG-20-006. https://cds.cern.ch/record/2725571 pages 32

[48] ATLAS Collaboration, "Constraints on off-shell Higgs boson production and the Higgs boson total width in $ZZ \to 4\ell$ and $ZZ \to 2\ell 2\nu$ final states with the ATLAS detector," Phys. Lett. B **786** (2018), 223-244 (*Preprint* [arXiv:1808.01191 [hep-ex]]). pages

[49] CMS Collaboration, "Measurements of the Higgs boson width and anomalous HVV couplings from on-shell and off-shell production in the four-lepton final state," Phys. Rev. D **99** (2019) no.11, 112003 [arXiv:1901.00174 [hep-ex]]. pages

[50] ATLAS Collaboration, "Measurements and interpretations of Higgs-boson fiducial cross sections in the diphoton decay channel using 139 fb^{-1} of pp collision data at $\sqrt{s} = 13$ TeV with the ATLAS detector," ATLAS-CONF-2019-029. https://cds.cern.ch/record/2682800 pages 33

[51] ATLAS Collaboration, "Combined measurement of the total and differential cross sections in the $H \to \gamma\gamma$ and the $H \to ZZ^* \to 4\ell$ decay channels at $\sqrt{s}$ =13 TeV with the ATLAS detector," ATLAS-CONF-2019-032. https://cds.cern.ch/record/2682844 pages 33, 35

[52] CMS Collaboration, "Measurement and interpretation of differential cross sections for Higgs boson production at $\sqrt{s} = 13$ TeV," Phys. Lett. B **792** (2019), 369-396 [arXiv:1812.06504 [hep-ex]]. pages 33, 35

[53] CMS Collaboration, "Measurement and interpretation of differential cross sections for Higgs boson production at $\sqrt{s} = 13$ TeV," Phys. Lett. B **792** (2019), 369-396 [arXiv:1812.06504 [hep-ex]]. pages 33, 35

[54] CMS Collaboration, "Measurements of properties of the Higgs boson in the four-lepton final state in proton-proton collisions at $\sqrt{s} = 13$ TeV," CMS-PAS-HIG-19-001. pages 33, 34

[55] N. Berger, *et al.* "Simplified Template Cross Sections - Stage 1.1," *Preprint* [arXiv:1906.02754 [hep-ph]]. pages 34

[56] ATLAS Collaboration, "A combination of measurements of Higgs boson production and decay using up to 139 fb^{-1} of proton–proton collision data at $\sqrt{s} = 13$ TeV collected with the ATLAS experiment," ATLAS-CONF-2020-027. https://cds.cern.ch/record/2725733 pages 35, 36

[57] CMS Collaboration, "Combined Higgs boson production and decay measurements with up to 137 fb-1 of proton-proton collision data at sqrts = 13 TeV," CMS-PAS-HIG-19-005. https://cds.cern.ch/record/2706103 pages 36

[58] L. Evans and P. Bryant, “LHC Machine,” JINST **3** (2008), S08001 pages 37

[59] O. S. Bruning, P. Collier, P. Lebrun, S. Myers, R. Ostojic, J. Poole and P. Proudlock, “LHC Design Report Vol.1: The LHC Main Ring,” pages 37

[60] K. Aamodt *et al.* [ALICE], “The ALICE experiment at the CERN LHC,” JINST **3** (2008), S08002 pages 38

[61] A. A. Alves, Jr. *et al.* [LHCb], “The LHCb Detector at the LHC,” JINST **3** (2008), S08005 pages 38

[62] ATLAS Collaboration, “Luminosity Public Results", url: https://twiki.cern.ch/twiki/bin/view/AtlasPublic/LuminosityPublicResultsRun2 pages 39

[63] ATLAS Collaboration, “The Superconducting magnet system for the ATLAS detector at CERN,” CERN-OPEN-2001-064. pages 42

[64] ATLAS Collaboration, “ATLAS inner detector: Technical design report. Vol. 1,” CERN-LHCC-97-16. pages 43

[65] ATLAS Collaboration, “ATLAS inner detector: Technical design report. Vol. 2,” CERN-LHCC-97-17. pages 43

[66] ATLAS Collaboration, “ATLAS Insertable B-Layer Technical Design Report,” CERN-LHCC-2010-013. pages 43

[67] ATLAS Collaboration, “ATLAS calorimeter performance Technical Design Report,” CERN-LHCC-96-40. pages 45

[68] ATLAS Collaboration, “ATLAS muon spectrometer: Technical design report,” CERN-LHCC-97-22. pages 48

[69] ATLAS Collaboration, “ATLAS first level trigger: Technical design report,” CERN-LHCC-98-14. pages 50

[70] ATLAS Collaboration, “ATLAS high-level trigger, data acquisition and controls: Technical design report,” CERN-LHCC-2003-022. pages 50

[71] L. Rossi and O. Brüning, “Introduction to the HL-LHC Project,” Adv. Ser. Direct. High Energy Phys. **24** (2015), 1-17 pages 52

[72] ATLAS Collaboration, “Technical Design Report for the ATLAS Inner Tracker Strip Detector,” CERN-LHCC-2017-005. CERN, Geneva, 2017 pages 52

[73] ATLAS Collaboration, “Performance of the ATLAS Track Reconstruction Algorithms in Dense Environments in LHC Run 2,” Eur. Phys. J. C **77** (2017) no.10, 673 [arXiv:1704.07983 [hep-ex]]. pages 53

[74] ATLAS Collaboration, "Reconstruction of primary vertices at the ATLAS experiment in Run 1 proton–proton collisions at the LHC," Eur. Phys. J. C **77** (2017) no.5, 332 [arXiv:1611.10235 [physics.ins-det]]. pages 53

[75] ATLAS Collaboration, "Electron and photon performance measurements with the ATLAS detector using the 2015–2017 LHC proton-proton collision data," JINST **14** (2019) no.12, P12006 [arXiv:1908.00005 [hep-ex]]. pages 54, 56

[76] ATLAS Collaboration, "Topological cell clustering in the ATLAS calorimeters and its performance in LHC Run 1," Eur. Phys. J. C **77** (2017), 490 [arXiv:1603.02934 [hep-ex]]. pages 54

[77] ATLAS Collaboration, "Muon reconstruction and identification efficiency in ATLAS using the full Run 2 pp collision data set at $\sqrt{s} = 13$ TeV," [arXiv:2012.00578 [hep-ex]]. pages 57, 59

[78] ATLAS Collaboration, "Jet reconstruction and performance using particle flow with the ATLAS Detector," Eur. Phys. J. C **77** (2017) no.7, 466 [arXiv:1703.10485 [hep-ex]]. pages 60

[79] M. Cacciari, G. P. Salam and G. Soyez, "The anti-k_t jet clustering algorithm," JHEP **04** (2008), 063 [arXiv:0802.1189 [hep-ph]]. pages 60, 154

[80] ATLAS Collaboration, "ATLAS b-jet identification performance and efficiency measurement with $t\bar{t}$ events in pp collisions at $\sqrt{s} = 13$ TeV," Eur. Phys. J. C **79** (2019) no.11, 970 [arXiv:1907.05120 [hep-ex]]. pages 61

[81] A. Abusleme, C. Bélanger-Champagne, A. Bellerive, Y. Benhammou, J. Botte, H. Cohen, M. Davies, Y. Du, L. Gauthier, T. Koffas, S. Kuleshov, B. Lefebvre, C. Li, N. Lupu, G. Mikenberg, D. Mori, J. P. Ochoa-Ricoux, E. Perez Codina, S. Rettie, A. Robichaud-Véronneau, R. Rojas, M. Shoa, V. Smakhtin, B. Stelzer, O. Stelzer-Chilton, A. Toro, H. Torres, P. Ulloa, B. Vachon, G. Vasquez, A. Vdovin, S. Viel, P. Walker, S. Weber and C. Zhu, "Performance of a Full-Size Small-Strip Thin Gap Chamber Prototype for the ATLAS New Small Wheel Muon Upgrade", Nucl. Instrum. Meth. A **817** (2016), 85-92 [arXiv:1509.06329 [physics.ins-det]]. pages 70, 71

[82] The Roma1 MM group, "The vacuum bag technique for the MicroMega panel construction", ATL-COM-MUON-2014-024

[83] P. Iengo *et al.*, "Construction of a large-size four plane micromegas detector", PoS TIPP **2014**, 058 (2014). pages 78

[84] M. Beker *et al.*, "The Rasnik 3-point optical alignment system", JINST **14**, no. 08, P08010 (2019). pages 79

[85] Raether, H, "Electron avalanches and breakdown in gases", Butterworths, London (1964) pages 80, 90

[86] I. Giomataris, R. De Oliveira, S. Andriamonje, S. Aune, G. Charpak, P. Colas, A. Giganon, P. Rebourgeard and P. Salin, "Micromegas in a bulk", Nucl. Instrum. Meth. A **560** (2006), 405-408 [arXiv:physics/0501003 [physics]]. pages 72

[87] J. H. Burge, P. Su, C. Zhao, and T. Zobrist, “Use of a commercial laser tracker for optical alignment", Optical System Alignment and Tolerancing **vol. 6676** (2007), p. 66760E. pages 73

[88] Kevan Hashemi, “Rasnik Analysis. Brandeis University", (2007-2016). url: `http://www.bndhep.net/Devices/RASNIK/Analysis.html` pages 86

[89] D. Pfeiffer, G. Gorine, H. Reithler, B. Biskup, A. Day, A. Fabich, J. Germa, R. Guida, M. Jaekel and F. Ravotti, “The radiation field in the Gamma Irradiation Facility GIF++ at CERN,” Nucl. Instrum. Meth. A **866** (2017), 91-103 [arXiv:1611.00299 [physics.ins-det]]. pages 90

pages 120

[90] C. Patrignani et al., *Particle Data Group*, Chin. Phys. C, 40, 100001 (2016) pages 132, 139

[91] ATLAS Collaboration, “The ATLAS Simulation Infrastructure,” Eur. Phys. J. C **70** (2010), 823-874 [arXiv:1005.4568 [physics.ins-det]]. pages 134

[92] S. Agostinelli *et al.* [GEANT4], “GEANT4–a simulation toolkit,” Nucl. Instrum. Meth. A **506** (2003), 250-303 pages 134

[93] S. Alioli, P. Nason, C. Oleari and E. Re, “A general framework for implementing NLO calculations in shower Monte Carlo programs: the POWHEG BOX,” JHEP **06** (2010), 043 [arXiv:1002.2581 [hep-ph]]. pages 134

[94] S. Frixione, P. Nason and C. Oleari, “Matching NLO QCD computations with Parton Shower simulations: the POWHEG method,” JHEP **11** (2007), 070 [arXiv:0709.2092 [hep-ph]]. pages 134

[95] P. Nason, “A New method for combining NLO QCD with shower Monte Carlo algorithms,” JHEP **11** (2004), 040 [arXiv:hep-ph/0409146 [hep-ph]]. pages 134

[96] E. Bagnaschi, G. Degrassi, P. Slavich and A. Vicini, “Higgs production via gluon fusion in the POWHEG approach in the SM and in the MSSM,” JHEP **02** (2012), 088 [arXiv:1111.2854 [hep-ph]]. pages 134

[97] U. Aglietti, R. Bonciani, G. Degrassi and A. Vicini, “Two loop light fermion contribution to Higgs production and decays,” Phys. Lett. B **595** (2004), 432-441 [arXiv:hep-ph/0404071 [hep-ph]]. pages 134

[98] K. Hamilton, P. Nason and G. Zanderighi, “Finite quark-mass effects in the NNLOPS POWHEG+MiNLO Higgs generator,” JHEP **05** (2015), 140 [arXiv:1501.04637 [hep-ph]]. pages 134

[99] G. Luisoni, P. Nason, C. Oleari and F. Tramontano, “$HW^{\pm}$/HZ + 0 and 1 jet at NLO with the POWHEG BOX interfaced to GoSam and their merging within MiNLO,” JHEP **10** (2013), 083 [arXiv:1306.2542 [hep-ph]]. pages 134, 135

[100] S. Dittmaier, C. Mariotti, G. Passarino, R. Tanaka, S. Alekhin, J. Alwall, E. A. Bagnaschi, A. Banfi, J. Blumlein and S. Bolognesi, *et al.* “Handbook of LHC Higgs Cross Sections: 2. Differential Distributions,” [arXiv:1201.3084 [hep-ph]]. pages 135, 136

[101] C. Anastasiou, C. Duhr, F. Dulat, F. Herzog and B. Mistlberger, “Higgs Boson Gluon-Fusion Production in QCD at Three Loops,” Phys. Rev. Lett. **114** (2015), 212001 [arXiv:1503.06056 [hep-ph]]. pages 135

[102] C. Anastasiou, C. Duhr, F. Dulat, E. Furlan, T. Gehrmann, F. Herzog, A. Lazopoulos and B. Mistlberger, “High precision determination of the gluon fusion Higgs boson cross-section at the LHC,” JHEP **05** (2016), 058 [arXiv:1602.00695 [hep-ph]]. pages 135

[103] S. Actis, G. Passarino, C. Sturm and S. Uccirati, “NLO Electroweak Corrections to Higgs Boson Production at Hadron Colliders,” Phys. Lett. B **670** (2008), 12-17 0809.1301[arXiv:0809.1301 [hep-ph]]. pages 135

[104] C. Anastasiou, R. Boughezal and F. Petriello, “Mixed QCD-electroweak corrections to Higgs boson production in gluon fusion,” JHEP **04** (2009), 003 [arXiv:0811.3458 [hep-ph]]. pages 135

[105] M. Grazzini and H. Sargsyan, “Heavy-quark mass effects in Higgs boson production at the LHC,” JHEP **09** (2013), 129 [arXiv:1306.4581 [hep-ph]]. pages 135, 156, 194

[106] D. de Florian, G. Ferrera, M. Grazzini and D. Tommasini, “Higgs boson production at the LHC: transverse momentum resummation effects in the H->2gamma, H->WW->lnu lnu and H->ZZ->4l decay modes,” JHEP **06** (2012), 132 [arXiv:1203.6321 [hep-ph]]. pages 156, 194

[107] I. W. Stewart and F. J. Tackmann, “Theory Uncertainties for Higgs and Other Searches Using Jet Bins,” Phys. Rev. D **85** (2012), 034011 [arXiv:1107.2117 [hep-ph]]. pages 135, 185

[108] M. Ciccolini, A. Denner and S. Dittmaier, “Strong and electroweak corrections to the production of Higgs + 2jets via weak interactions at the LHC,” Phys. Rev. Lett. **99** (2007), 161803 [arXiv:0707.0381 [hep-ph]]. pages 135

[109] M. Ciccolini, A. Denner and S. Dittmaier, “Electroweak and QCD corrections to Higgs production via vector-boson fusion at the LHC,” Phys. Rev. D **77** (2008), 013002 [arXiv:0710.4749 [hep-ph]]. pages 135

[110] P. Bolzoni, F. Maltoni, S. O. Moch and M. Zaro, “Higgs production via vector-boson fusion at NNLO in QCD,” Phys. Rev. Lett. **105** (2010), 011801 [arXiv:1003.4451 [hep-ph]]. pages 135

[111] O. Brein, A. Djouadi and R. Harlander, “NNLO QCD corrections to the Higgs-strahlung processes at hadron colliders,” Phys. Lett. B **579** (2004), 149-156 [arXiv:hep-ph/0307206 [hep-ph]]. pages 135

[112] A. Denner, S. Dittmaier, S. Kallweit and A. Muck, “Electroweak corrections to Higgs-strahlung off W/Z bosons at the Tevatron and the LHC with HAWK,” JHEP **03** (2012), 075 [arXiv:1112.5142 [hep-ph]]. pages 135

[113] L. Altenkamp, S. Dittmaier, R. V. Harlander, H. Rzehak and T. J. E. Zirke, “Gluon-induced Higgs-strahlung at next-to-leading order QCD,” JHEP **02** (2013), 078 [arXiv:1211.5015 [hep-ph]]. pages 135

[114] W. Beenakker, S. Dittmaier, M. Kramer, B. Plumper, M. Spira and P. M. Zerwas, “NLO QCD corrections to t anti-t H production in hadron collisions,” Nucl. Phys. B **653** (2003), 151-203 [arXiv:hep-ph/0211352 [hep-ph]]. pages 135

[115] S. Dawson, C. Jackson, L. H. Orr, L. Reina and D. Wackeroth, “Associated Higgs production with top quarks at the large hadron collider: NLO QCD corrections,” Phys. Rev. D **68** (2003), 034022 [arXiv:hep-ph/0305087 [hep-ph]]. pages 135

[116] Y. Zhang, W. G. Ma, R. Y. Zhang, C. Chen and L. Guo, “QCD NLO and EW NLO corrections to $t\bar{t}H$ production with top quark decays at hadron collider,” Phys. Lett. B **738** (2014), 1-5 [arXiv:1407.1110 [hep-ph]]. pages 135

[117] S. Frixione, V. Hirschi, D. Pagani, H. S. Shao and M. Zaro, “Electroweak and QCD corrections to top-pair hadroproduction in association with heavy bosons,” JHEP **06** (2015), 184 [arXiv:1504.03446 [hep-ph]]. pages 135, 137

[118] S. Dawson, C. B. Jackson, L. Reina and D. Wackeroth, “Exclusive Higgs boson production with bottom quarks at hadron colliders,” Phys. Rev. D **69** (2004), 074027 [arXiv:hep-ph/0311067 [hep-ph]]. pages 135

[119] S. Dittmaier, M. Krämer and M. Spira, “Higgs radiation off bottom quarks at the Tevatron and the CERN LHC,” Phys. Rev. D **70** (2004), 074010 [arXiv:hep-ph/0309204 [hep-ph]]. pages 135

[120] R. V. Harlander and W. B. Kilgore, “Higgs boson production in bottom quark fusion at next-to-next-to leading order,” Phys. Rev. D **68** (2003), 013001 [arXiv:hep-ph/0304035 [hep-ph]]. pages 135

[121] A. Djouadi, J. Kalinowski and M. Spira, “HDECAY: A Program for Higgs boson decays in the standard model and its supersymmetric extension,” Comput. Phys. Commun. **108** (1998), 56-74 [arXiv:hep-ph/9704448 [hep-ph]]. pages 135, 136

[122] A. Djouadi, M. M. Muhlleitner and M. Spira, "Decays of supersymmetric particles: The Program SUSY-HIT (SUspect-SdecaY-Hdecay-InTerface)," Acta Phys. Polon. B **38** (2007), 635-644 [arXiv:hep-ph/0609292 [hep-ph]]. pages 135, 136

[123] A. Bredenstein, A. Denner, S. Dittmaier and M. M. Weber, "Precise predictions for the Higgs-boson decay H —> WW/ZZ —> 4 leptons," Phys. Rev. D **74** (2006), 013004 [arXiv:hep-ph/0604011 [hep-ph]]. pages 135, 136, 185

[124] A. Bredenstein, A. Denner, S. Dittmaier and M. M. Weber, "Radiative corrections to the semileptonic and hadronic Higgs-boson decays H —> W W / Z Z —> 4 fermions," JHEP **02** (2007), 080 [arXiv:hep-ph/0611234 [hep-ph]]. pages 135, 136, 185

[125] S. Boselli, C. M. Carloni Calame, G. Montagna, O. Nicrosini and F. Piccinini, "Higgs boson decay into four leptons at NLOPS electroweak accuracy," JHEP **06** (2015), 023 [arXiv:1503.07394 [hep-ph]]. pages 135, 136

[126] J. Butterworth, S. Carrazza, A. Cooper-Sarkar, A. De Roeck, J. Feltesse, S. Forte, J. Gao, S. Glazov, J. Huston and Z. Kassabov, *et al.* "PDF4LHC recommendations for LHC Run II," J. Phys. G **43** (2016), 023001 [arXiv:1510.03865 [hep-ph]]. pages 135, 185

[127] S. Dulat, T. J. Hou, J. Gao, M. Guzzi, J. Huston, P. Nadolsky, J. Pumplin, C. Schmidt, D. Stump and C. P. Yuan, "New parton distribution functions from a global analysis of quantum chromodynamics," Phys. Rev. D **93** (2016) no.3, 033006 [arXiv:1506.07443 [hep-ph]]. pages 135, 136

[128] L. A. Harland-Lang, A. D. Martin, P. Motylinski and R. S. Thorne, "Parton distributions in the LHC era: MMHT 2014 PDFs," Eur. Phys. J. C **75** (2015) no.5, 204 [arXiv:1412.3989 [hep-ph]]. pages 135, 136

[129] R. D. Ball *et al.* [NNPDF], "Parton distributions for the LHC Run II," JHEP **04** (2015), 040 [arXiv:1410.8849 [hep-ph]]. pages 135, 136

[130] K. Hamilton, P. Nason, C. Oleari and G. Zanderighi, "Merging H/W/Z + 0 and 1 jet at NLO with no merging scale: a path to parton shower + NNLO matching," JHEP **05** (2013), 082 [arXiv:1212.4504 [hep-ph]]. pages 135

[131] K. Hamilton, P. Nason, E. Re and G. Zanderighi, "NNLOPS simulation of Higgs boson production," JHEP **10** (2013), 222 [arXiv:1309.0017 [hep-ph]]. pages 135

[132] S. Catani and M. Grazzini, "An NNLO subtraction formalism in hadron collisions and its application to Higgs boson production at the LHC," Phys. Rev. Lett. **98** (2007), 222002 [arXiv:hep-ph/0703012 [hep-ph]]. pages 135

[133] M. Grazzini, "NNLO predictions for the Higgs boson signal in the H —> WW —> lnu lnu and H —> ZZ —> 4l decay channels," JHEP **02** (2008), 043 [arXiv:0801.3232 [hep-ph]]. pages 135

[134] M. Wiesemann, R. Frederix, S. Frixione, V. Hirschi, F. Maltoni and P. Torrielli, "Higgs production in association with bottom quarks," JHEP **02** (2015), 132 [arXiv:1409.5301 [hep-ph]]. pages 135

[135] H. L. Lai, M. Guzzi, J. Huston, Z. Li, P. M. Nadolsky, J. Pumplin and C. P. Yuan, "New parton distributions for collider physics," Phys. Rev. D **82** (2010), 074024 [arXiv:1007.2241 [hep-ph]]. pages 135

[136] T. Sjostrand, S. Mrenna and P. Z. Skands, "A Brief Introduction to PYTHIA 8.1," Comput. Phys. Commun. **178** (2008), 852-867 [arXiv:0710.3820 [hep-ph]]. pages 135

[137] ATLAS Collaboration, "Measurement of the Z/γ^* boson transverse momentum distribution in pp collisions at $\sqrt{s} = 7$ TeV with the ATLAS detector," JHEP **09** (2014), 145 [arXiv:1406.3660 [hep-ex]]. pages 135

[138] ATLAS Collaboration, "ATLAS Pythia 8 tunes to 7 TeV data," ATL-PHYS-PUB-2014-021, CERN (2014). pages 135, 136

[139] D. J. Lange, "The EvtGen particle decay simulation package," Nucl. Instrum. Meth. A **462** (2001), 152-155 pages 135

[140] J. Alwall, R. Frederix, S. Frixione, V. Hirschi, F. Maltoni, O. Mattelaer, H. S. Shao, T. Stelzer, P. Torrielli and M. Zaro, "The automated computation of tree-level and next-to-leading order differential cross sections, and their matching to parton shower simulations," JHEP **07** (2014), 079 [arXiv:1405.0301 [hep-ph]]. pages 136

[141] R. Frederix and S. Frixione, "Merging meets matching in MC@NLO," JHEP **12** (2012), 061 [arXiv:1209.6215 [hep-ph]]. pages 136

[142] R. Frederix, S. Frixione, E. Vryonidou and M. Wiesemann, "Heavy-quark mass effects in Higgs plus jets production," JHEP **08** (2016), 006 [arXiv:1604.03017 [hep-ph]]. pages 136

[143] H. Mantler and M. Wiesemann, "Hadronic Higgs production through NLO + PS in the SM, the 2HDM and the MSSM," Eur. Phys. J. C **75** (2015) no.6, 257 [arXiv:1504.06625 [hep-ph]]. pages 136

[144] H. Mantler and M. Wiesemann, "Top- and bottom-mass effects in hadronic Higgs production at small transverse momenta through LO+NLL," Eur. Phys. J. C **73** (2013) no.6, 2467 [arXiv:1210.8263 [hep-ph]]. pages 136

[145] S. Frixione, E. Laenen, P. Motylinski and B. R. Webber, "Angular correlations of lepton pairs from vector boson and top quark decays in Monte Carlo simulations," JHEP **04** (2007), 081 [arXiv:hep-ph/0702198 [hep-ph]]. pages 136

[146] P. Artoisenet, R. Frederix, O. Mattelaer and R. Rietkerk, "Automatic spin-entangled decays of heavy resonances in Monte Carlo simulations," JHEP **03** (2013), 015 [arXiv:1212.3460 [hep-ph]]. pages 136

[147] A. Banfi, P. F. Monni, G. P. Salam and G. Zanderighi, "Higgs and Z-boson production with a jet veto," Phys. Rev. Lett. **109** (2012), 202001 [arXiv:1206.4998 [hep-ph]]. pages 136

[148] A. Banfi, F. Caola, F. A. Dreyer, P. F. Monni, G. P. Salam, G. Zanderighi and F. Dulat, "Jet-vetoed Higgs cross section in gluon fusion at N^3LO+NNLL with small-R resummation," JHEP **04** (2016), 049 [arXiv:1511.02886 [hep-ph]]. pages 136

[149] P. F. Monni, E. Re and P. Torrielli, "Higgs Transverse-Momentum Resummation in Direct Space," Phys. Rev. Lett. **116** (2016) no.24, 242001 1604.02191[arXiv:1604.02191 [hep-ph]]. pages 136

[150] W. Bizon, P. F. Monni, E. Re, L. Rottoli and P. Torrielli, "Momentum-space resummation for transverse observables and the Higgs $p_\perp$ at N^3LL+NNLO," JHEP **02** (2018), 108 [arXiv:1705.09127 [hep-ph]]. pages 136

[151] P. F. Monni, L. Rottoli and P. Torrielli, "Higgs transverse momentum with a jet veto: a double-differential resummation," Phys. Rev. Lett. **124** (2020) no.25, 252001 [arXiv:1909.04704 [hep-ph]]. pages 136

[152] M. Grazzini, S. Kallweit and M. Wiesemann, "Fully differential NNLO computations with MATRIX," Eur. Phys. J. C **78** (2018) no.7, 537 [arXiv:1711.06631 [hep-ph]]. pages 136

[153] M. Grazzini, S. Kallweit, D. Rathlev and M. Wiesemann, "Transverse-momentum resummation for vector-boson pair production at NNLL+NNLO," JHEP **08** (2015), 154 [arXiv:1507.02565 [hep-ph]]. pages 136

[154] X. Chen, T. Gehrmann, E. W. N. Glover and M. Jaquier, "Precise QCD predictions for the production of Higgs + jet final states," Phys. Lett. B **740** (2015), 147-150 [arXiv:1408.5325 [hep-ph]]. pages 136

[155] X. Chen, J. Cruz-Martinez, T. Gehrmann, E. W. N. Glover and M. Jaquier, "NNLO QCD corrections to Higgs boson production at large transverse momentum," JHEP **10** (2016), 066 [arXiv:1607.08817 [hep-ph]]. pages 136

[156] X. Chen, T. Gehrmann, E. W. N. Glover and A. Huss, "Fiducial cross sections for the four-lepton decay mode in Higgs-plus-jet production up to NNLO QCD," JHEP **07** (2019), 052 [arXiv:1905.13738 [hep-ph]]. pages 136

[157] S. Boselli, C. M. Carloni Calame, G. Montagna, O. Nicrosini, F. Piccinini and A. Shivaji, "Higgs decay into four charged leptons in the presence of dimension-six operators," JHEP **01** (2018), 096 [arXiv:1703.06667 [hep-ph]]. pages 136

[158] A. Bredenstein, A. Denner, S. Dittmaier and M. M. Weber, “Precision calculations for the Higgs decays H —> ZZ/WW —> 4 leptons,” Nucl. Phys. B Proc. Suppl. **160** (2006), 131-135 [arXiv:hep-ph/0607060 [hep-ph]]. pages 136

[159] L. Altenkamp, S. Dittmaier and H. Rzehak, “Renormalization schemes for the Two-Higgs-Doublet Model and applications to h → WW/ZZ → 4 fermions,” JHEP **09** (2017), 134 [arXiv:1704.02645 [hep-ph]]. pages 136

[160] L. Altenkamp, S. Dittmaier and H. Rzehak, “Precision calculations for $h \to WW/ZZ \to 4$ fermions in the Two-Higgs-Doublet Model with Prophecy4f,” JHEP **03** (2018), 110 [arXiv:1710.07598 [hep-ph]]. pages 136

[161] L. Altenkamp, M. Boggia and S. Dittmaier, “Precision calculations for $h \to WW/ZZ \to 4$ fermions in a Singlet Extension of the Standard Model with Prophecy4f,” JHEP **04** (2018), 062 [arXiv:1801.07291 [hep-ph]]. pages 136

[162] A. Denner, S. Dittmaier and J. N. Lang, “Renormalization of mixing angles,” JHEP **11** (2018), 104 [arXiv:1808.03466 [hep-ph]]. pages 136

[163] A. Alloul, N. D. Christensen, C. Degrande, C. Duhr and B. Fuks, “FeynRules 2.0 - A complete toolbox for tree-level phenomenology,” Comput. Phys. Commun. **185** (2014), 2250-2300 [arXiv:1310.1921 [hep-ph]]. pages 136

[164] T. Gleisberg, S. Hoeche, F. Krauss, M. Schonherr, S. Schumann, F. Siegert and J. Winter, “Event generation with SHERPA 1.1,” JHEP **02** (2009), 007 [arXiv:0811.4622 [hep-ph]]. pages 136

[165] T. Gleisberg and S. Hoeche, “Comix, a new matrix element generator,” JHEP **12** (2008), 039 [arXiv:0808.3674 [hep-ph]]. pages 136, 137

[166] F. Cascioli, P. Maierhofer and S. Pozzorini, “Scattering Amplitudes with Open Loops,” Phys. Rev. Lett. **108** (2012), 111601 [arXiv:1111.5206 [hep-ph]]. pages 136, 137

[167] S. Schumann and F. Krauss, “A Parton shower algorithm based on Catani-Seymour dipole factorisation,” JHEP **03** (2008), 038 [arXiv:0709.1027 [hep-ph]]. pages 136, 137

[168] B. Biedermann, A. Denner, S. Dittmaier, L. Hofer and B. Jäger, “Electroweak corrections to $pp \to \mu^+\mu^-e^+e^- + X$ at the LHC: a Higgs background study,” Phys. Rev. Lett. **116** (2016) no.16, 161803 [arXiv:1601.07787 [hep-ph]]. pages 136

[169] B. Biedermann, A. Denner, S. Dittmaier, L. Hofer and B. Jager, “Next-to-leading-order electroweak corrections to the production of four charged leptons at the LHC,” JHEP **01** (2017), 033 [arXiv:1611.05338 [hep-ph]]. pages 136

[170] F. Caola, K. Melnikov, R. Röntsch and L. Tancredi, “QCD corrections to ZZ production in gluon fusion at the LHC,” Phys. Rev. D **92** (2015) no.9, 094028 [arXiv:1509.06734 [hep-ph]]. pages 136

[171] F. Caola, K. Melnikov, R. Röntsch and L. Tancredi, “QCD corrections to W^+W^- production through gluon fusion,” Phys. Lett. B **754** (2016), 275-280 [arXiv:1511.08617 [hep-ph]]. pages 136

[172] J. M. Campbell, R. K. Ellis, M. Czakon and S. Kirchner, “Two loop correction to interference in $gg \to ZZ$,” JHEP **08** (2016), 011 [arXiv:1605.01380 [hep-ph]]. pages 136

[173] K. Melnikov and M. Dowling, “Production of two Z-bosons in gluon fusion in the heavy top quark approximation,” Phys. Lett. B **744** (2015), 43-47 [arXiv:1503.01274 [hep-ph]]. pages 136

[174] M. Bonvini, F. Caola, S. Forte, K. Melnikov and G. Ridolfi, “Signal-background interference effects for ggßHßW^+W^- beyond leading order,” Phys. Rev. D **88** (2013) no.3, 034032 [arXiv:1304.3053 [hep-ph]]. pages 137

[175] C. S. Li, H. T. Li, D. Y. Shao and J. Wang, “Soft gluon resummation in the signal-background interference process of gg(→ h*)→ ZZ,” JHEP **08** (2015), 065 [arXiv:1504.02388 [hep-ph]]. pages 137

[176] S. Hoeche, F. Krauss, M. Schonherr and F. Siegert, “QCD matrix elements + parton showers: The NLO case,” JHEP **04** (2013), 027 [arXiv:1207.5030 [hep-ph]]. pages 136, 137

[177] ATLAS Collaboration, “Studies on top-quark Monte Carlo modelling for Top2016,” ATL-PHYS-PUB-2016-020, CERN (2016) pages 137

[178] K. A. Olive *et al.* [Particle Data Group], “Review of Particle Physics,” Chin. Phys. C **38** (2014), 090001 pages 153

[179] M. Dobbs and J. B. Hansen, “The HepMC C++ Monte Carlo event record for High Energy Physics,” Comput. Phys. Commun. **134** (2001), 41-46 pages 153

[180] G. Bozzi, S. Catani, D. de Florian and M. Grazzini, “Transverse-momentum resummation and the spectrum of the Higgs boson at the LHC,” Nucl. Phys. B **737** (2006), 73-120 [arXiv:hep-ph/0508068 [hep-ph]]. pages 156

[181] D. de Florian, G. Ferrera, M. Grazzini and D. Tommasini, “Transverse-momentum resummation: Higgs boson production at the Tevatron and the LHC,” JHEP **11** (2011), 064 [arXiv:1109.2109 [hep-ph]]. pages 156

[182] S. Bolognesi, Y. Gao, A. V. Gritsan, K. Melnikov, M. Schulze, N. V. Tran and A. Whitbeck, “On the spin and parity of a single-produced resonance at the LHC,” Phys. Rev. D **86** (2012), 095031 [arXiv:1208.4018 [hep-ph]]. pages 156

[183] N. Belyaev, R. Konoplich, L. E. Pedersen and K. Prokofiev, “Angular asymmetries as a probe for anomalous contributions to HZZ vertex at the LHC,” Phys. Rev. D **91** (2015) no.11, 115014 [arXiv:1502.03045 [hep-ph]]. pages 158

[184] ATLAS Collaboration, "Test of CP Invariance in vector-boson fusion production of the Higgs boson using the Optimal Observable method in the ditau decay channel with the ATLAS detector," Eur. Phys. J. C **76** (2016) no.12, 658 [arXiv:1602.04516 [hep-ex]]. pages 159

[185] G. Cowan, "A survey of unfolding methods for particle physics," Conf. Proc. C **0203181** (2002), 248-257 pages 165

[186] ATLAS Collaboration, "Measurement of inclusive and differential cross sections in the $H \to ZZ^* \to 4\ell$ decay channel in pp collisions at $\sqrt{s} = 13$ TeV with the ATLAS detector," JHEP **10** (2017), 132 [arXiv:1708.02810 [hep-ex]]. pages 181

[187] W. Verkerke and D. P. Kirkby, "The RooFit toolkit for data modeling," eConf **C0303241** (2003), MOLT007 [arXiv:physics/0306116 [physics]]. pages 183

[188] L. Moneta, K. Belasco, K. S. Cranmer, S. Kreiss, A. Lazzaro, D. Piparo, G. Schott, W. Verkerke and M. Wolf, "The RooStats Project," PoS **ACAT2010** (2010), 057 [arXiv:1009.1003 [physics.data-an]]. pages 183

[189] ATLAS Collaboration, "Measurements of b-jet tagging efficiency with the ATLAS detector using $t\bar{t}$ events at $\sqrt{s} = 13$ TeV," JHEP **08** (2018), 089 [arXiv:1805.01845 [hep-ex]]. pages 184

[190] I. W. Stewart, F. J. Tackmann, J. R. Walsh and S. Zuberi, "Jet p_T resummation in Higgs production at $NNLL' + NNLO$," Phys. Rev. D **89** (2014) no.5, 054001 [arXiv:1307.1808 [hep-ph]]. pages 185

[191] X. Liu and F. Petriello, "Reducing theoretical uncertainties for exclusive Higgs-boson plus one-jet production at the LHC," Phys. Rev. D **87** (2013) no.9, 094027 [arXiv:1303.4405 [hep-ph]]. pages 185

[192] R. Boughezal, X. Liu, F. Petriello, F. J. Tackmann and J. R. Walsh, "Combining Resummed Higgs Predictions Across Jet Bins," Phys. Rev. D **89** (2014) no.7, 074044 [arXiv:1312.4535 [hep-ph]]. pages 185

[193] S. Gangal and F. J. Tackmann, "Next-to-leading-order uncertainties in Higgs+2 jets from gluon fusion," Phys. Rev. D **87** (2013) no.9, 093008 [arXiv:1302.5437 [hep-ph]]. pages 185

[194] J. R. Andersen, J. Bellm, J. Bendavid, N. Berger, D. Bhatia, B. Biedermann, S. Bräuer, D. Britzger, A. G. Buckley and R. Camacho, *et al.* "Les Houches 2017: Physics at TeV Colliders Standard Model Working Group Report," [arXiv:1803.07977 [hep-ph]]. pages 185

[195] ATLAS Collaboration, "Measurement of the Higgs boson coupling properties in the $H \to ZZ^* \to 4\ell$ decay channel at $\sqrt{s} = 13$ TeV with the ATLAS detector," JHEP **03** (2018), 095 [arXiv:1712.02304 [hep-ex]]. pages 187

[196] G. Cowan, K. Cranmer, E. Gross and O. Vitells, "Asymptotic formulae for likelihood-based tests of new physics," Eur. Phys. J. C **71** (2011), 1554 [erratum: Eur. Phys. J. C **73** (2013), 2501] [arXiv:1007.1727 [physics.data-an]]. pages 195

[197] ATLAS Collaboration, "Higgs boson production cross-section measurements and their EFT interpretation in the 4ℓ decay channel at $\sqrt{s}$ =13 TeV with the ATLAS detector," Eur. Phys. J. C **80** (2020) no.10, 957 [arXiv:2004.03447 [hep-ex]]. pages 204, 205, 244

[198] CMS Collaboration, "A search for the standard model Higgs boson decaying to charm quarks," JHEP **03** (2020), 131 [arXiv:1912.01662 [hep-ex]]. pages 235

[199] ATLAS Collaboration, "Search for the Decay of the Higgs Boson to Charm Quarks with the ATLAS Experiment," Phys. Rev. Lett. **120** (2018) no.21, 211802 [arXiv:1802.04329 [hep-ex]]. pages 235

[200] ATLAS Collaboration, "Combined measurements of Higgs boson production and decay using up to 80 fb^{-1} of proton-proton collision data at $\sqrt{s}$ = 13 TeV collected with the ATLAS experiment," Phys. Rev. D **101** (2020) no.1, 012002 [arXiv:1909.02845 [hep-ex]]. pages 235

[201] G. Mancini, *Study of the Higgs boson properties in $H \to ZZ^* \to 4l$ decay channel with the ATLAS detector at LHC using data recorded at $\sqrt{s}$ = 13 TeV*, PhD Thesis pages